

THE BEHAVIOUR OF PIPE BENDS UNDER INTERNAL PRESSURE AND IN-PLANE
BENDING LOADING

by

Diana Abdulhameed

A thesis submitted in partial fulfillment of the requirements for the degree of

Doctor of Philosophy

in

Structural Engineering

Department of Civil and Environmental Engineering
University of Alberta

© Diana Abdulhameed, 2018

ABSTRACT

The behaviour of pipe bends differ according to the type of applied load whether it is internal pressure, pure bending or a combined load of pressure and bending. Pipe bends under internal pressure tend to straighten-out and the stress levels and deformations are higher than predicted using simple beam theory. Due to the special geometry characteristic of a pipe bend, outward forces are generated that tend to open the bend generating additional hoop and longitudinal stresses. This phenomenon is known as the “Bourdon effect”. This phenomenon was ignored in past studies and no thorough investigation was found to understand the bend’s behaviour under internal pressure. The behaviour of pipe bends under in-plane bending differs based on the direction of bending moment. The initially circular cross-section deforms into an oval shape when subjected to opening in-plane bending and the bend gains more stiffness. On the other hand, a closing in-plane bending moment deforms the cross-section into a flattened shape where the pipe bend gains flexibility by loading. Therefore, the behaviour of the pipe bend and its flexibility is highly affected by the direction of bending moment applied. Moreover, the combined loading of internal pressure and in-plane bending results in a behaviour that is much complicated than to be solved using theoretical approaches. The bending moment tends to deform the initially circular cross-section of the bend into an oval or flattened shape for opening and closing bending moments, respectively. However, the internal pressure tends to resist the cross-sectional deformation resulted from the bending moment and tends to straighten out the pipe bend due to the generated outward forces. These two behaviours are nonlinear where the stresses cannot be added based on superposition. Past studies proposed a “Pressure reduction factor” that accounts for the reduced stress generated due to adding internal pressure to a closing in-plane bending moment. This factor is used by the current codes without modification for the case of in-plane opening bending or out-

of-plane bending moments. Moreover, these factors ignored the effect of the pipe bend angle on the generated stresses which is found to be highly significant.

In this thesis, an extensive numerical investigation is conducted on pipe bends under internal pressure. The results show that Bourdon effect increases the stresses on pipe bends by up to 48% when compared to the stresses on a straight pipe. Based on this study, a new “Pressure factor” is proposed to account for the increase in stresses due to the “Bourdon effect”. Moreover, a mathematical model is derived to evaluate the Bourdon outward forces that are beneficial in designing any lateral supports at bend locations. The stress intensification factors presented in current design codes are reassessed for the in-plane bending moment using large deformation finite element analysis. The study is extended to assess the pressure reduction factor presented in the ASME B31.1 code that accounts for the internal pressure effect on in-plane bending moments. Comparing the results presented in this thesis with the CSA-Z662 and ASME B31.1 codes confirms that the ASME piping code underestimates the stresses on pipe bends under internal pressure and bending moment. However, for pure bending, the codes are conservative in some cases and un-conservative in other cases depending on the bending moment direction, the pipe bend geometry and size. New stress intensification factors and pressure correction factors are proposed in this thesis that accounts for the effect of the bending moment direction and the pipe bend angle on the stresses. These proposed factors are beneficial for the piping industry since it considers more parameters and it covers a wider range of pipe sizes and geometry.

Preface

The thesis is an original work by Diana Abdulhameed. No part of this thesis has been previously published. Due Acknowledgement must always be made of the use any material contained in, or derived from, this thesis.

Acknowledgments

“Happiness does not come from doing easy work but from the afterglow of satisfaction that comes after the achievement of a difficult task that demanded our best” Theodore Isaac.

After four years of hard work, today is the day. Writing this note of thanks is the finishing touch of my dissertation. It has been a period of intense learning for me, not only in the scientific area, but also on a personal level. Writing this dissertation has had a big impact on me. I would like to reflect on the people who have supported and helped me throughout this period.

First of all, I would like to express my sincere gratitude to my supervisor, Dr. Samer Adeeb, for his continuous support of my Ph.D study and research, for his patience, motivation, enthusiasm, encouragement, and immense knowledge. I would like further to express my sincere appreciation to the rest of my thesis committee: Professor Roger Chang, Dr. Mustafa Gul, Dr. Carlos Cruz and Dr. Magdy Mohareb for their encouragement, insightful comments and recommendations. My sincere thanks also goes to Mr. Michael Martens for offering me an internship opportunity in his group and gaining valuable software skills from his team.

To my life-coaches, my dear parents: because I owe it all to you, saying Thank you is not enough. My parents raised me to believe that I could achieve anything I set my mind to. My Father and Mother, have been there for me through the hard times, and are an endless source of great joy and love. Their continuous support and encouragement helped me achieve my goals especially during hardships. I would also like to thank my siblings, Dina, Mohammad and Ahmad for their wise counsel and sympathetic ear. You are always there for me in the good and hard times. I always feel that with your presence I can achieve anything in life. I'm blessed for having you with me. To my soul mate, my dearest companion and my best friend, Hayssam, Thank you. I love you for everything, for being so understanding and for putting up with me through the toughest moments of my life. I thank God for enlightening my life with your presence. Sweet heart I love you!

Finally, there are my friends. We were not only able to support each other by deliberating over our problems and findings, but also happily talking about things other than just our papers.

Thank you everyone!

TABLE OF CONTENTS

CHAPTER 1: INTRODUCTION AND LITERATURE REVIEW

1.1.	INTRODUCTION	1
1.2.	LITERATURE REVIEW	3
1.2.1.	PIPE BENDS UNDER INTERNAL PRESSURE LOADING	3
1.2.2.	PIPE BENDS UNDER PRESSURE AND BENDING MOMENT LOADS	6
1.2.2.1.	<i>Minimum Potential Energy Approach</i>	7
1.2.2.2.	<i>Mechanics-of-Materials Approach</i>	11
1.2.2.3.	<i>Thin-Shell Theory Approach</i>	11
1.2.2.4.	<i>Experimental Work</i>	12
1.2.2.5.	<i>Numerical Analysis Approach</i>	13
1.3.	PROBLEM STATEMENT	15
1.4.	AIM OF THE THESIS	17

CHAPTER 2: THE BOURDON EFFECT AND BEHAVIOUR OF PRESSURIZED PIPE BENDS

2.1.	INTRODUCTION	19
2.2.	METHODOLOGY	20
2.2.1.	DEVELOPING A MATHEMATICAL MODEL FOR THE BOURDON EFFECT FORCES	21
2.2.2.	EVALUATING THE BOURDON EFFECT USING SHELL ELEMENT MODELS	23
2.2.2.1.	<i>Current design Methodology by CSA-Z662</i>	24
2.2.2.2.	<i>Modelling pipe bends using SHELL elements in ABAQUS</i>	25
2.2.2.3.	<i>Developing a pressure factor K_p</i>	28
2.2.3.	PROPOSE A MODELLING APPROACH	29
2.2.3.1.	<i>Different elements used in modelling</i>	29
2.2.3.1.1.	<i>Beam element (PIPE31)</i>	29
2.2.3.1.2.	<i>Elbow element (ELBOW31)</i>	29
2.2.3.2.	<i>Finite element modelling</i>	30
2.2.3.3.	<i>Check validity of the proposed modelling approach for back-to-back pipe bends</i>	31
2.2.4.	COMPARISON BETWEEN FEA RESULTS AND PAST STUDIES	32
2.3.	RESULTS	33
2.3.1.	VALIDATING THE PROPOSED MATHEMATICAL MODEL FOR THE BOURDON EFFECT FORCES	33
2.3.2.	EVALUATING THE BOURDON EFFECT USING SHELL ELEMENT MODELS	34
2.3.2.1.	<i>Current Methodology by CSA-Z662</i>	34
2.3.2.2.	<i>Proposed pressure factor (K_p)</i>	38
2.3.3.	PROPOSED MODELLING APPROACH:	43
2.3.3.1.	<i>Check validity of the proposed modelling approach for back-to-back pipe bends</i>	47
2.3.4.	COMPARISON BETWEEN FEA RESULTS AND PAST STUDIES	50
2.4.	SIGNIFICANCE OF THE PRESSURE FACTOR (K_p)	53

2.4.1.	PREDICTING PRELIMINARY PIPE BEND WALL THICKNESS:.....	53
2.4.2.	DESIGN OF PIPE BENDS:	54
2.4.3.	MODELLING OF PIPE BENDS IN ABAQUS:	54
2.5.	DISCUSSION	55
2.6.	CONCLUSION.....	58

CHAPTER 3: PIPE BENDS SUBJECTED TO IN-PLANE OPENING AND CLOSING BENDING MOMENTS

3.1.	INTRODUCTION.....	60
3.2.	METHODOLOGY	62
3.2.1.	FINITE ELEMENT MODELLING AND ANALYSIS	62
3.3.	RESULTS.....	67
3.3.1.	VERIFICATION OF THE FINITE ELEMENT MODEL.....	67
3.3.2.	SHAPE OF OVALIZATION	68
3.3.3.	LINEARITY OF THE RESPONSE AND EFFECT OF THE BENDING MOMENT DIRECTION	72
3.3.4.	EFFECT OF BENDING MOMENT DIRECTION.....	76
3.3.4.1.	<i>Pipe bends with large bend angles (40 to 140 degrees):</i>	76
3.3.4.2.	<i>Pipe bends with small bend angles (10 and 20 degrees):</i>	81
3.3.4.3.	<i>Stress distribution on the mid-layer of pipe bends</i>	88
3.3.5.	COMPARISON BETWEEN THE FEA AND THE CSA-Z662 STRESSES.....	91
3.3.5.1.	<i>Stresses at mid-layer of the pipe wall thickness</i>	92
3.3.5.2.	<i>Stresses at the inner and outer layer of the pipe wall thickness</i>	95
3.4.	DISCUSSION AND CONCLUSION	98

CHAPTER 4: DEVELOPED STRESS INTENSIFICATION FACTORS

4.1.	INTRODUCTION & BACKGROUND.....	106
4.2.	METHODOLOGY	107
4.2.1.	SENSITIVITY ANALYSIS AND MODEL FORMULATION	107
4.2.2.	REGRESSION ANALYSIS.....	111
4.3.	THE DEVELOPED STRESS INTENSIFICATION FACTORS.....	113
4.3.1.	OPENING BENDING MOMENT:.....	113
4.3.2.	CLOSING BENDING MOMENT:	116

CHAPTER 5: THE INTERACTION BETWEEN INTERNAL PRESSURE AND BENDING MOMENT FOR PIPE BENDS

5.1.	INTRODUCTION	119
5.2.	METHODOLOGY	121
5.2.1.	FINITE ELEMENT MODELLING AND ANALYSIS	121
5.2.2.	LOADING AND BOUNDARY CONDITIONS	122
5.2.3.	PREDICTED STRESSES ACCORDING TO THE CURRENT DESIGN CODES	124
5.3.	RESULTS	126
5.3.1.	PIPE BENDS UNDER INTERNAL PRESSURE LOADING	126
5.3.2.	BENDING MOMENT LOADING	133
5.3.2.1.	<i>Linearity of the response</i>	133
5.3.2.2.	<i>Effect of bending moment direction</i>	136
5.3.2.3.	<i>Comparison between the FEA and the CSA-Z662 Code results</i>	143
5.3.2.4.	<i>Effect of changing the End Boundary Conditions on the Bend Behaviour</i>	145
5.3.3.	INTERNAL PRESSURE AND BENDING MOMENT LOADING	151
5.3.3.1.	<i>Linearity of the response and the effect of bending moment direction</i>	151
5.3.3.2.	<i>Effect of Bend Angle (α) on the stress distribution</i>	155
5.3.3.3.	<i>Comparison between the FEA with CSA-Z662 and ASME B31.1</i>	157
5.4.	DISCUSSION	159

CHAPTER 6: DEVELOPED STRESS INTENSIFICATION FACTORS FOR BENDS UNDER INTERNAL PRESSURE AND BENDING MOMENT

6.1.	INTRODUCTION & BACKGROUND	172
6.2.	METHODOLOGY	173
6.2.1.	EVALUATING THE DATA POINTS REQUIRED FOR THE REGRESSION ANALYSIS	173
6.2.1.1.	<i>In-plane bending moment (Stress Intensification Factor)</i>	173
6.2.1.2.	<i>Internal pressure and in-plane bending moment (Pressure Effect Factor)</i>	173
6.2.2.	SENSITIVITY ANALYSIS AND MODEL FORMULATION	174
6.2.2.1.	<i>In-plane bending moment</i>	174
6.2.2.2.	<i>Internal pressure and In-plane bending moment</i>	176
6.3.	EQUATIONS DEVELOPMENT:	179
6.3.1.	THE DEVELOPED STRESS INTENSIFICATION FACTOR	180
6.3.2.	THE DEVELOPED PRESSURE REDUCTION FACTOR (X_{PROPOSED})	185
6.4.	INFLUENCE OF THE END EFFECTS	187

CHAPTER 7: CONCLUSIONS AND RECOMMENDATIONS

7.1.	CONCLUSIONS	189
7.2.	RECOMMENDATIONS AND FUTURE WORK	192

<u>APPENDIX (A): PIPE BENDS UNDER IN-PLANE BENDING MOMENT</u>	196
--	-----

<u>APPENDIX (B): DEVELOPED STRESS INTENSIFICATION FACTORS</u>	223
--	-----

<u>APPENDIX (C): DEVELOPED STRESS INTENSIFICATION FACTORS FOR BENDS UNDER INTERNAL PRESSURE AND BENDING MOMENT</u>	241
---	-----

LIST OF FIGURES

FIGURE 2. 1. THE INFINITESIMAL AREA ON PIPE ELBOW SURFACE. -----	20
FIGURE 2. 2 BOUNDARY CONDITIONS AND LOADING FOR A STAND-ALONE PIPE ELBOW. -----	22
FIGURE 2. 3. BOUNDARY CONDITIONS AND GEOMETRY OF THE PIPE MODEL. -----	25
FIGURE 2. 4. STRESS AND DISPLACEMENT EVALUATED AT SECTION (A-A) & (B-B). -----	25
FIGURE 2. 5. GEOMETRY AND BOUNDARY CONDITIONS FOR PIPE MODELS USING BEAM ELEMENT. -----	29
FIGURE 2. 6. GEOMETRY AND BOUNDARY CONDITION FOR A BACK TO BACK S-SHAPE PIPELINE SYSTEM USING SHELL ELEMENTS (S4R). ---	30
FIGURE 2. 7. GEOMETRY AND BOUNDARY CONDITION FOR A BACK TO BACK S-SHAPE PIPELINE SYSTEM USING PIPE ELEMENTS (PIPE31). 30	
FIGURE 2. 8. TRESCA STRESS RESULT FROM THE SHELL MODEL VS CSA-Z662 FOR SHORT RADIUS BENDS SUBJECTED TO INTERNAL PRESSURE CAUSING 80% SMYS HOOP STRESS.-----	34
FIGURE 2. 9. TRESCA STRESS RESULT FROM THE SHELL MODEL VS CSA-Z662 FOR LONG RADIUS BENDS SUBJECTED TO INTERNAL PRESSURE CAUSING 80% SMYS HOOP STRESS. -----	34
FIGURE 2. 10. TRESCA STRESS RESULT FROM THE SHELL MODEL VS CSA-Z662 FOR SHORT RADIUS BENDS SUBJECTED TO INTERNAL PRESSURE CAUSING 30% SMYS HOOP STRESS.-----	35
FIGURE 2. 11. TRESCA STRESS RESULT FROM THE SHELL MODEL VS CSA-Z662 FOR LONG RADIUS BENDS SUBJECTED TO INTERNAL PRESSURE CAUSING 30% SMYS HOOP STRESS.-----	35
FIGURE 2. 12. TRESCA STRESS RESULT VS THE BEND ANGLE FOR DIFFERENT PIPE BEND SIZE SUBJECTED TO INTERNAL PRESSURE CAUSING 80% SMYS HOOP STRESS.-----	36
FIGURE 2. 13. FEA RESULTANT DISPLACEMENT VS THE BEND ANGLE FOR DIFFERENT PIPE BEND SIZE SUBJECTED TO INTERNAL PRESSURE CAUSING 80% SMYS HOOP STRESS. -----	36
FIGURE 2. 14. EFFECT OF RADIUS RATIO (R/R) ON THE TRESCA STRESSES FOR DIFFERENT PIPE BEND SIZE SUBJECTED TO INTERNAL PRESSURE CAUSING 80% SMYS HOOP STRESS. -----	37
FIGURE 2. 15. EFFECT OF BEND SLENDERNESS RATIO (D/T) ON TRESCA STRESSES FOR DIFFERENT PIPE BEND SIZE SUBJECTED TO INTERNAL PRESSURE CAUSING 80% SMYS HOOP STRESS.-----	37
FIGURE 2. 16. TRESCA STRESS RESULTS FROM THE SHELL ELEMENT MODEL VS THE CSA RESULTS AND THE FACTORED CSA RESULTS FOR PIPES SUBJECTED TO INTERNAL PRESSURE CAUSING 80% SMYS.-----	39
FIGURE 2. 17. TRESCA STRESS RESULTS FROM THE SHELL ELEMENT MODEL VS THE CSA RESULTS AND THE FACTORED CSA RESULTS FOR PIPES SUBJECTED TO INTERNAL PRESSURE CAUSING 30% SMYS.-----	39
FIGURE 2. 18 THE DISTRIBUTION OF TRESCA STRESSES ALONG HALF THE PIPE CROSS-SECTION AT THE MID-SECTION OF PIPE BEND FOR SHELL ELEMENT MODEL. -----	42
FIGURE 2. 19. THE DISTRIBUTION OF HOOP STRESS ALONG THE PIPE CROSS-SECTION AT MID-SECTION OF PIPE BEND FOR PIPE AND ELBOW ELEMENT MODEL. -----	43
FIGURE 2. 20. TRESCA STRESS RESULTS FROM PIPE MODEL USING SHELL, PIPE AND ELBOW ELEMENT. -----	43
FIGURE 2. 21. THE DISTRIBUTION OF TRESCA STRESS ALONG THE PIPE CROSS-SECTION AT MID-SECTION OF PIPE BEND FOR SHELL ELEMENT AND ELBOW ELEMENT MODEL.-----	44
FIGURE 2. 22. TRESCA STRESS RESULTS FROM THE PROPOSED APPROACH OF MODELLING PIPE BENDS USING THE MODIFIED INTERNAL PRESSURE LOAD FOR PIPE AND ELBOW ELEMENTS.-----	45
FIGURE 2. 23. BACK TO BACK 90 DEGREE ELBOW MODEL. -----	46
FIGURE 2. 24. TRESCA STRESS EVALUATED FROM PAST STUDIES COMPARED WITH THE FEA RESULTS AND THE CSA RESULTS.-----	50
FIGURE 2. 25. LATERAL SUPPORTS USED AT PIPE BENDS. -----	53
FIGURE 3. 1. PIPE BEND CONFIGURATION WITH ATTACHED STRAIGHT PIPES.-----	61
FIGURE 3. 2. PIPE MESHING-----	62
FIGURE 3. 3.MODEL BOUNDARY CONDITIONS.-----	62
FIGURE 3. 4.APPLIED LOADING AND PIPE GEOMETRY-----	63
FIGURE 3. 5. APPLIED END ROTATION VS VON MISES STRESS FOR NPS 12 PIPE BEND WITH SHORT BEND RADIUS (R = 1D)-----	64
FIGURE 3. 6. THE VERTICAL DISPLACEMENT FROM THE FEA VERSUS THE TEST RESULTS FOR BEND 1.-----	66
FIGURE 3. 7. THE VERTICAL DISPLACEMENT FROM THE FEA VERSUS THE TEST RESULTS FOR BEND 3.-----	66
FIGURE 3. 8. OVALIZATION EQUATION DIMENSIONS-----	67
FIGURE 3. 9. THE CROSS-SECTIONAL DEFORMATION OF HALF A PIPE BEND SUBJECTED TO OPENING OR CLOSING ROTATIONS. -----	67
FIGURE 3. 10. OVALIZATION RATIO VS BEND ANGLE FOR PIPE BENDS WITH SHORT BEND RADIUS (R=1D).-----	69
FIGURE 3. 11. OVALIZATION RATIO VS D/T RATIO FOR PIPE BENDS WITH SHORT BEND RADIUS (R=1D).-----	69
FIGURE 3. 12. OVALIZATION RATIO VS D/T RATIO FOR PIPE BENDS WITH LONG BEND RADIUS (R=5D).-----	70
FIGURE 3. 13. END ROTATION VS REACTION MOMENT FOR 12" PIPE WITH 1D BEND RADIUS. -----	71

FIGURE 3. 14. END ROTATION VS REACTION MOMENT FOR 42" PIPE WITH 1D BEND RADIUS.	71
FIGURE 3. 15. END ROTATION VS REACTION MOMENT FOR 12" PIPE WITH 5D BEND RADIUS.	72
FIGURE 3. 16. END ROTATION VS REACTION MOMENT FOR 42" PIPE WITH 5D BEND RADIUS.	72
FIGURE 3. 17. VON MISES STRESS VS REACTION MOMENT FOR 12" PIPE WITH 1D BEND RADIUS.	73
FIGURE 3. 18. VON MISES STRESS VS REACTION MOMENT FOR 42" PIPE WITH 1D BEND RADIUS.	73
FIGURE 3. 19. REACTION BENDING MOMENT VS BEND ANGLE FOR PIPE BENDS WITH SHORT BEND RADIUS (R=1D).	74
FIGURE 3. 20. TYPICAL VON MISES STRESS DISTRIBUTION FOR A 40-DEGREE PIPE BEND WITH SHORT BEND RADIUS (R = 1D) SUBJECTED TO AN OPENING BENDING MOMENT.	76
FIGURE 3. 21. VON MISES STRESS DISTRIBUTION ALONG THE CRITICAL SECTION OF A PIPE BEND WITH BEND ANGLE 90O AND SHORT BEND RADIUS (R = 1D) SUBJECTED TO AN OPEN BENDING MOMENT-----	76
FIGURE 3. 22. VON MISES STRESS DISTRIBUTION ALONG THE CRITICAL SECTION OF A PIPE BEND WITH BEND ANGLE 90O AND SHORT BEND RADIUS (R = 1D) SUBJECTED TO A CLOSING BENDING MOMENT-----	77
FIGURE 3. 23. HOOP STRESS DISTRIBUTION ALONG THE CRITICAL SECTION OF A PIPE BEND WITH BEND ANGLE 90O AND SHORT BEND RADIUS (R = 1D) SUBJECTED TO OPENING BENDING MOMENT.	77
FIGURE 3. 24. HOOP STRESS DISTRIBUTION ALONG THE CRITICAL SECTION OF A PIPE BEND WITH BEND ANGLE 90O AND SHORT BEND RADIUS (R = 1D) SUBJECTED TO CLOSING BENDING MOMENT.	78
FIGURE 3. 25. LONGITUDINAL STRESS DISTRIBUTION ALONG THE CRITICAL SECTION OF A PIPE BEND WITH BEND ANGLE 90O AND SHORT BEND RADIUS (R = 1D) SUBJECTED TO OPENING BENDING MOMENT.	79
FIGURE 3. 26. LONGITUDINAL STRESS DISTRIBUTION ALONG THE CRITICAL SECTION OF A PIPE BEND WITH BEND ANGLE 90O AND SHORT BEND RADIUS (R = 1D) SUBJECTED TO CLOSING BENDING MOMENT.	79
FIGURE 3. 27. VON MISES STRESS DISTRIBUTION FOR 10-DEGREE PIPE BENDS WITH 12" OUTER DIAMETER AND SHORT BEND RADIUS (R = 1D) SUBJECTED TO OPENING BENDING MOMENT.	81
FIGURE 3. 28. VON MISES STRESS DISTRIBUTION ALONG THE CRITICAL SECTION OF AN NPS 12 PIPE BEND WITH BEND ANGLE 10O AND SHORT BEND RADIUS (R = 1D) -----	81
FIGURE 3. 29. VON MISES STRESS DISTRIBUTION ALONG THE CRITICAL SECTION OF AN NPS 12 PIPE BEND WITH BEND ANGLE 10O AND LONG BEND RADIUS (R = 5D) -----	82
FIGURE 3. 30. VON MISES STRESS DISTRIBUTION ALONG THE CRITICAL SECTION OF A NPS 36 PIPE BEND WITH BEND ANGLE 20O AND SHORT BEND RADIUS (R = 1D) -----	82
FIGURE 3. 31. HOOP STRESS DISTRIBUTION ALONG THE CRITICAL SECTION OF A PIPE BEND WITH BEND ANGLE 10O AND SHORT BEND RADIUS (R = 1D)-----	84
FIGURE 3. 32. LONGITUDINAL STRESS DISTRIBUTION ALONG THE CRITICAL SECTION OF A PIPE BEND WITH BEND ANGLE 10O AND SHORT BEND RADIUS (R = 1D) -----	84
FIGURE 3. 33. HOOP STRESS DISTRIBUTION ALONG THE CRITICAL SECTION OF A PIPE BEND WITH BEND ANGLE 10O AND LONG BEND RADIUS (R = 5D)-----	84
FIGURE 3. 34. LONGITUDINAL STRESS DISTRIBUTION ALONG THE CRITICAL SECTION OF A PIPE BEND WITH BEND ANGLE 10O AND LONG BEND RADIUS (R = 5D)-----	85
FIGURE 3. 35. HOOP STRESS DISTRIBUTION ALONG THE CRITICAL SECTION OF AN NPS 36 PIPE BEND WITH BEND ANGLE 20O AND SHORT BEND RADIUS (R = 1D) -----	85
FIGURE 3. 36. LONGITUDINAL STRESS DISTRIBUTION ALONG THE CRITICAL SECTION OF AN NPS 36 PIPE BEND WITH BEND ANGLE 20O AND SHORT BEND RADIUS (R = 1D) -----	86
FIGURE 3. 37. VON MISES STRESS DISTRIBUTION AT MID-LAYER OF PIPE WALL AT AN APPLIED END ROTATION 0.1 RADIAN FOR DIFFERENT D/T RATIOS FOR PIPE BENDS WITH BEND ANGLE 10 AND 140 DEGREES HAVING SHORT BEND RADIUS (R = 1D).-----	87
FIGURE 3. 38. VON MISES STRESS DISTRIBUTION AT MID-LAYER OF PIPE WALL AT AN APPLIED END ROTATION 0.1 RADIAN FOR DIFFERENT D/T RATIOS FOR PIPE BENDS WITH BEND ANGLE 10 AND 140 DEGREES HAVING LONG BEND RADIUS (R = 5D).-----	87
FIGURE 3. 39. THE MAXIMUM VON MISES STRESS VS THE BEND RADIUS FOR PIPE SIZE NPS 12 WITH DIFFERENT BEND ANGLES.	88
FIGURE 3. 40. THE MAXIMUM VON MISES STRESS VS THE BEND RADIUS FOR PIPE SIZE NPS 42 WITH DIFFERENT BEND ANGLES.	88
FIGURE 3. 41. VON MISES STRESS DISTRIBUTION AT MID-LAYER OF PIPE WALL AT AN APPLIED END ROTATION 0.1 RADIAN FOR DIFFERENT D/T RATIOS FOR PIPE BENDS WITH SHORT BEND RADIUS (R = 1D) AND VARYING BEND ANGLES.	88
FIGURE 3. 42. VON MISES STRESS DISTRIBUTION AT MID-LAYER OF PIPE WALL AT AN APPLIED END ROTATION 0.1 RADIAN FOR DIFFERENT D/T RATIOS FOR PIPE BENDS WITH SHORT BEND RADIUS (R = 1D) AND VARYING BEND ANGLES.	89
FIGURE 3. 43. VON MISES STRESS DISTRIBUTION AT MID-LAYER OF PIPE WALL AT AN APPLIED END ROTATION 0.1 RADIAN FOR DIFFERENT D/T RATIOS FOR PIPE BENDS WITH LONG BEND RADIUS (R = 5D) AND VARYING BEND ANGLES.	89
FIGURE 3. 44. STRESS DISTRIBUTION AT APPLIED END ROTATION 0.1 RADIAN FOR SHORT RADIUS PIPE BENDS WITH BEND ANGLE 10 DEGREES.	91
FIGURE 3. 45. STRESS DISTRIBUTION AT APPLIED END ROTATION 0.1 RADIAN FOR SHORT RADIUS PIPE BENDS WITH BEND ANGLE 20 DEGREES.	91

FIGURE 3. 46. STRESS DISTRIBUTION AT APPLIED END ROTATION 0.1 RADIAN FOR SHORT RADIUS PIPE BENDS WITH BEND ANGLE 90 DEGREES. -----	92
FIGURE 3. 47. STRESS DISTRIBUTION AT APPLIED END ROTATION 0.1 RADIAN FOR SHORT RADIUS PIPE BENDS WITH BEND ANGLE 140 DEGREES. -----	92
FIGURE 3. 48. STRESS DISTRIBUTION AT APPLIED END ROTATION 0.1 RADIAN FOR LONG RADIUS PIPE BENDS WITH BEND ANGLE 10 DEGREES. -----	92
FIGURE 3. 49. STRESS DISTRIBUTION AT APPLIED END ROTATION 0.1 RADIAN FOR LONG RADIUS PIPE BENDS WITH BEND ANGLE 20 DEGREES. -----	92
FIGURE 3. 50. STRESS DISTRIBUTION AT APPLIED END ROTATION 0.1 RADIAN FOR LONG RADIUS PIPE BENDS WITH BEND ANGLE 90 DEGREES. -----	93
FIGURE 3. 51. STRESS DISTRIBUTION AT APPLIED END ROTATION 0.1 RADIAN FOR LONG RADIUS PIPE BENDS WITH BEND ANGLE 140 DEGREES. -----	93
FIGURE 3. 52. INNER LAYER STRESS DISTRIBUTION AT APPLIED END ROTATION 0.1 RADIAN FOR SHORT RADIUS PIPE BENDS WITH BEND ANGLE 10 DEGREES. -----	94
FIGURE 3. 53. INNER LAYER STRESS DISTRIBUTION AT APPLIED END ROTATION 0.1 RADIAN FOR SHORT RADIUS PIPE BENDS WITH BEND ANGLE 140 DEGREES. -----	94
FIGURE 3. 54. INNER LAYER STRESS DISTRIBUTION AT APPLIED END ROTATION 0.1 RADIAN FOR LONG RADIUS PIPE BENDS WITH BEND ANGLE 10 DEGREES. -----	95
FIGURE 3. 55. INNER LAYER STRESS DISTRIBUTION AT APPLIED END ROTATION 0.1 RADIAN FOR SHORT RADIUS PIPE BENDS WITH BEND ANGLE 90 DEGREES. -----	95
FIGURE 3. 56. OUTER LAYER STRESS DISTRIBUTION AT APPLIED END ROTATION 0.1 RADIAN FOR SHORT RADIUS PIPE BENDS WITH BEND ANGLE 10 DEGREES. -----	96
FIGURE 3. 57. OUTER LAYER STRESS DISTRIBUTION AT APPLIED END ROTATION 0.1 RADIAN FOR SHORT RADIUS PIPE BENDS WITH BEND ANGLE 90 DEGREES. -----	96
FIGURE 3. 57. OUTER LAYER STRESS DISTRIBUTION AT APPLIED END ROTATION 0.1 RADIAN FOR LONG RADIUS PIPE BENDS WITH BEND ANGLE 10 DEGREES. -----	96
FIGURE 3. 58. OUTER LAYER STRESS DISTRIBUTION AT APPLIED END ROTATION 0.1 RADIAN FOR LONG RADIUS PIPE BENDS WITH BEND ANGLE 140 DEGREES. -----	96
FIGURE 3. 60. THE SHAPE OF DEFORMATION OF A PIPE BEND SUBJECTED TO IN-PLANE OPENING OR CLOSING BENDING MOMENT. -----	97
FIGURE 3. 61. THE RATIO OF THE MAJOR AND MINOR AXIS OF THE OVAL SHAPE CROSS-SECTION VERSUS THE D/T RATIO FOR DIFFERENT BEND ANGLES. -----	99
FIGURE 3. 62. BENDING STRESSES RESULTED FROM THE CROSS-SECTIONAL DEFORMATIONS OF THE PIPE BEND SUBJECTED TO OPENING AND CLOSING BENDING MOMENT. -----	101
FIGURE 4. 1. STRESS INTENSIFICATION FACTORS FOR SHORT RADIUS PIPE BENDS WITH VARIOUS BEND ANGLES. -----	107
FIGURE 4. 2. STRESS INTENSIFICATION FACTORS FOR LONG RADIUS PIPE BENDS WITH VARIOUS BEND ANGLES. -----	107
FIGURE 4. 3. STRESS INTENSIFICATION FACTORS PIPE BENDS SUBJECTED TO OPENING BENDING MOMENT. -----	108
FIGURE 4. 4. STRESS INTENSIFICATION FACTORS PIPE BENDS SUBJECTED TO CLOSING BENDING MOMENT. -----	108
FIGURE 4. 5. DEVIATION OF THE SIF DEVELOPED FORMULA FROM THE FEA RESULTS FOR THE MID-LAYER OF THE WALL THICKNESS ----	112
FIGURE 4. 6. DEVIATION OF THE SIF DEVELOPED FORMULA FROM THE FEA RESULTS FOR THE INNER LAYER OF THE WALL THICKNESS ---	112
FIGURE 4. 7. DEVIATION OF THE SIF DEVELOPED FORMULA FROM THE FEA RESULTS FOR THE OUTER LAYER OF THE WALL THICKNESS ---	113
FIGURE 4. 8. THE MID-LAYER FEA SIF (DOTTED) COMPARED TO THE PROPOSED SIF FORMULA (BLUE LINE) FOR NPS12 BENDS WITH SHORT BEND RADIUS (R=1D) -----	113
FIGURE 4. 9. THE FEA SIF (DOTTED) COMPARED TO THE PROPOSED SIF FORMULA (BLUE LINE) FOR BENDS WITH BEND ANGLE = 140o	113
FIGURE 4. 10. THE FEA SIF (DOTTED) COMPARED TO THE PROPOSED SIF FORMULA (BLUE LINE) FOR BENDS WITH BEND ANGLE = 10o	113
FIGURE 4. 11. DEVIATION OF THE SIF DEVELOPED FORMULA FROM THE FEA RESULTS FOR THE MID-LAYER OF THE WALL THICKNESS ---	115
FIGURE 4. 12. DEVIATION OF THE SIF DEVELOPED FORMULA FROM THE FEA RESULTS FOR THE INNER LAYER OF THE WALL THICKNESS--	115
FIGURE 4. 13. DEVIATION OF THE SIF DEVELOPED FORMULA FROM THE FEA RESULTS FOR THE OUTER LAYER OF THE WALL THICKNESS -	116
FIGURE 4. 14. THE FEA SIF (DOTTED) COMPARED TO THE PROPOSED SIF FORMULA (BLUE LINE) FOR BENDS WITH BEND ANGLE = 10o	116
FIGURE 4. 15. THE FEA SIF (DOTTED) COMPARED TO THE PROPOSED SIF FORMULA (BLUE LINE) FOR BENDS WITH BEND ANGLE = 140o -----	116
FIGURE 5. 1. PIPE BEND CONFIGURATION WITH ATTACHED STRAIGHT PIPES. -----	119
FIGURE 5. 2. PIPE MESHING -----	120
FIGURE 5. 3. MODEL BOUNDARY CONDITIONS. -----	121
FIGURE 5. 4. VON MISES STRESS AT MID-LAYER FOR PIPE BENDS WITH SHORT BEND RADIUS (R = 1D) -----	125
FIGURE 5. 5. VON MISES STRESS AT MID-LAYER FOR PIPE BENDS WITH LONG BEND RADIUS (R = 3D) -----	125
FIGURE 5. 6. VON MISES STRESS AT MID-LAYER FOR PIPE BENDS WITH LONG BEND RADIUS (R = 5D) -----	125

FIGURE 5. 7. VON MISES STRESS AT INNER LAYER FOR PIPE BENDS WITH SHORT BEND RADIUS ($R = 1D$)	125
FIGURE 5. 8. VON MISES STRESS AT INNER LAYER FOR PIPE BENDS WITH LONG BEND RADIUS ($R = 3D$)	126
FIGURE 5. 9. VON MISES STRESS AT INNER LAYER FOR PIPE BENDS WITH LONG BEND RADIUS ($R = 5D$)	126
FIGURE 5. 10. VON MISES STRESS AT OUTER LAYER FOR PIPE BENDS WITH SHORT BEND RADIUS ($R = 1D$)	126
FIGURE 5. 11. VON MISES STRESS AT OUTER LAYER FOR PIPE BENDS WITH LONG BEND RADIUS ($R = 3D$)	126
FIGURE 5. 12. VON MISES STRESS AT OUTER LAYER FOR PIPE BENDS WITH LONG BEND RADIUS ($R = 5D$)	127
FIGURE 5. 13. VON MISES STRESS DISTRIBUTION ALONG THE CIRCUMFERENCE OF THE CRITICAL SECTION OF A 12" PIPE BEND WITH SHORT BEND RADIUS AND BEND ANGLE 40 DEGREES.	128
FIGURE 5. 14. VON MISES STRESS DISTRIBUTION ALONG THE CIRCUMFERENCE OF THE CRITICAL SECTION OF A 42" PIPE BEND WITH SHORT BEND RADIUS AND BEND ANGLE 40 DEGREES.	128
FIGURE 5. 15. COMPARISON BETWEEN THE MID-LAYER HOOP STRESSES OF THE 12" AND 42" PIPE SIZE.	128
FIGURE 5. 16. COMPARISON BETWEEN INNER AND OUTER LAYER HOOP STRESSES OF THE 12" AND 42" PIPE SIZE.	128
FIGURE 5. 17. COMPARISON BETWEEN THE MID-LAYER LONGITUDINAL STRESSES OF THE 12" AND 42" PIPE SIZE.	129
FIGURE 5. 18. COMPARISON BETWEEN THE MID-LAYER LONGITUDINAL STRESSES OF THE 12" AND 42" PIPE SIZE.	129
FIGURE 5. 19. BOURDON FORCES AND END REACTION MOMENTS ON PIPE BENDS.	130
FIGURE 5. 20. END ROTATION VS REACTION MOMENT FOR 12" PIPE WITH 1D BEND RADIUS.	132
FIGURE 5. 21. END ROTATION VS REACTION MOMENT FOR 12" PIPE WITH 5D BEND RADIUS.	132
FIGURE 5. 22. END ROTATION VS REACTION MOMENT FOR 42" PIPE WITH 1D BEND RADIUS.	133
FIGURE 5. 23. END ROTATION VS REACTION MOMENT FOR 42" PIPE WITH 5D BEND RADIUS.	133
FIGURE 5. 24. MID-LAYER VON MISES STRESS VS REACTION MOMENT FOR 12" PIPE WITH 1D BEND RADIUS.	133
FIGURE 5. 25. MID-LAYER VON MISES STRESS VS REACTION MOMENT FOR 12" PIPE WITH 5D BEND RADIUS.	133
FIGURE 5. 26. MID-LAYER VON MISES STRESS VS REACTION MOMENT FOR 42" PIPE WITH 1D BEND RADIUS.	133
FIGURE 5. 27. MID-LAYER VON MISES STRESS VS REACTION MOMENT FOR 42" PIPE WITH 5D BEND RADIUS.	133
FIGURE 5. 28. TYPICAL VON MISES STRESS DISTRIBUTION FOR PIPE BENDS WITH BEND ANGLES RANGING FROM 40 TO 140 DEGREES AND BEND RADIUS FROM 1D TO 5D.	134
FIGURE 5. 29. VON MISES STRESS DISTRIBUTION ALONG THE CRITICAL SECTION OF A PIPE BEND WITH BEND ANGLE 90° AND BEND RADIUS ($R = 3D$) SUBJECTED TO AN OPENING BENDING MOMENT.	136
FIGURE 5. 30. VON MISES STRESS DISTRIBUTION ALONG THE CRITICAL SECTION OF A PIPE BEND WITH BEND ANGLE 90° AND BEND RADIUS ($R = 3D$) SUBJECTED TO AN CLOSING BENDING MOMENT.	136
FIGURE 5. 31. THE CROSS-SECTIONAL OVALIZATION AT THE MID-LENGTH OF THE PIPE BEND SUBJECTED TO AN OPENING BENDING MOMENT.	137
FIGURE 5. 32. THE CROSS-SECTIONAL FLATTENING DEFORMATION AT THE MID-LENGTH OF THE PIPE BEND SUBJECTED TO AN CLOSING BENDING MOMENT.	137
FIGURE 5. 33. VON MISES STRESS DISTRIBUTION ALONG THE CRITICAL SECTION OF A PIPE BEND WITH BEND ANGLE 90° AND BEND RADIUS ($R = 3D$) SUBJECTED TO AN OPENING BENDING MOMENT.	137
FIGURE 5. 34. VON MISES STRESS DISTRIBUTION ALONG THE CRITICAL SECTION OF A PIPE BEND WITH BEND ANGLE 90° AND BEND RADIUS ($R = 3D$) SUBJECTED TO AN CLOSING BENDING MOMENT.	137
FIGURE 5. 35. VON MISES STRESS DISTRIBUTION ALONG THE CRITICAL SECTION OF A PIPE BEND WITH BEND ANGLE 90° AND BEND RADIUS ($R = 3D$) SUBJECTED TO AN OPENING BENDING MOMENT.	138
FIGURE 5. 36. VON MISES STRESS DISTRIBUTION ALONG THE CRITICAL SECTION OF A PIPE BEND WITH BEND ANGLE 90° AND BEND RADIUS ($R = 3D$) SUBJECTED TO AN CLOSING BENDING MOMENT.	138
FIGURE 5. 37. MID-LAYER VON MISES STRESS VS THE D/T RATIO FOR PIPE BENDS WITH SHORT BEND RADIUS ($R=1D$).	138
FIGURE 5. 38. INNER-LAYER VON MISES STRESS VS THE D/T RATIO FOR PIPE BENDS WITH LONG BEND RADIUS ($R=3D$).	138
FIGURE 5. 39. OUTER-LAYER VON MISES STRESS VS THE D/T RATIO FOR PIPE BENDS WITH LONG BEND RADIUS ($R=5D$).	139
FIGURE 5. 40. VON MISES STRESS DISTRIBUTION FOR 20-DEGREE PIPE BENDS WITH 12" OUTER DIAMETER AND SHORT BEND RADIUS ($R = 1D$) SUBJECTED TO OPENING BENDING MOMENT.	140
FIGURE 5. 41. VON MISES STRESS DISTRIBUTION ALONG THE CRITICAL SECTION OF A NPS 42 PIPE BEND WITH BEND ANGLE 20° AND SHORT BEND RADIUS ($R = 1D$) SUBJECTED TO OPENING BENDING.	140
FIGURE 5. 42. MID-LAYER VON MISES STRESS VS D/T RATIO FOR SHORT RADIUS PIPE BENDS ($R = 1D$) WITH BEND ANGLES 20 & 40 DEGREES.	142
FIGURE 5. 43. MID-LAYER VON MISES STRESS VS D/T RATIO FOR SHORT RADIUS PIPE BENDS ($R = 1D$) WITH BEND ANGLES 90 & 140 DEGREES.	142
FIGURE 5. 44. INNER LAYER VON MISES STRESS VS D/T RATIO FOR SHORT RADIUS PIPE BENDS ($R= 1D$) WITH BEND ANGLE 20 & 40 DEGREES.	142
FIGURE 5. 45. INNER LAYER VON MISES STRESS VS D/T RATIO FOR LONG RADIUS PIPE BENDS ($R= 3D$) WITH BEND ANGLE 90 & 140 DEGREES.	142

FIGURE 5. 46. INNER LAYER VON MISES STRESS VS D/T RATIO FOR SHORT RADIUS PIPE BENDS ($R= 1D$) WITH BEND ANGLE 20 & 40 DEGREES. -----	143
FIGURE 5. 47. INNER LAYER VON MISES STRESS VS D/T RATIO FOR LONG RADIUS PIPE BENDS ($R= 3D$) WITH BEND ANGLE 90 & 140 DEGREES. -----	143
FIGURE 5. 48. INNER AND OUTER LAYER VON MISES STRESS VS D/T RATIO FOR SHORT RADIUS PIPE BENDS ($R= 1D$) WITH BEND ANGLE 140 DEGREES. -----	143
FIGURE 5. 49. MID-LAYER VON MISES STRESS VS D/T RATIO FOR PIPES WITH 1D BEND RADIUS AND 40 DEGREES BEND ANGLE. -----	145
FIGURE 5. 50. INNER LAYER VON MISES STRESS VS D/T RATIO FOR PIPES WITH 1D BEND RADIUS AND 140 DEGREES BEND ANGLE. -----	145
FIGURE 5. 51. OUTER LAYER VON MISES STRESS VS D/T RATIO FOR PIPES WITH 3D BEND RADIUS AND 90 DEGREES BEND ANGLE. -----	145
FIGURE 5. 52. MID-LAYER VON MISES STRESS VS D/T RATIO FOR PIPES WITH 1D BEND RADIUS SUBJECTED TO AN OPENING BENDING MOMENT.-----	146
FIGURE 5. 53. MID-LAYER VON MISES STRESS VS D/T RATIO FOR PIPES WITH 1D BEND RADIUS SUBJECTED TO CLOSING BENDING MOMENT. -----	146
FIGURE 5. 54. MID-LAYER VON MISES STRESS VS D/T RATIO FOR PIPES WITH 5D BEND RADIUS SUBJECTED TO AN OPENING BENDING MOMENT.-----	147
FIGURE 5. 55. MID-LAYER VON MISES STRESS VS D/T RATIO FOR PIPES WITH 5D BEND RADIUS SUBJECTED TO A CLOSING BENDING MOMENT.-----	147
FIGURE 5. 56. INNER LAYER VON MISES STRESS VS D/T RATIO FOR PIPES WITH 1D BEND RADIUS SUBJECTED TO AN OPENING BENDING MOMENT.-----	147
FIGURE 5. 57. INNER LAYER VON MISES STRESS VS D/T RATIO FOR PIPES WITH 1D BEND RADIUS SUBJECTED TO CLOSING BENDING MOMENT.-----	147
FIGURE 5. 58. OUTER LAYER VON MISES STRESS VS D/T RATIO FOR PIPES WITH 3D BEND RADIUS SUBJECTED TO AN OPENING BENDING MOMENT.-----	148
FIGURE 5. 59. OUTER LAYER VON MISES STRESS VS D/T RATIO FOR PIPES WITH 3D BEND RADIUS SUBJECTED TO CLOSING BENDING MOMENT.-----	148
FIGURE 5. 60. END ROTATION VS REACTION MOMENT FOR 12" PIPE WITH 1D BEND RADIUS. -----	149
FIGURE 5. 61. END ROTATION VS REACTION MOMENT FOR 42" PIPE WITH 1D BEND RADIUS. -----	149
FIGURE 5. 62. END ROTATION VS REACTION MOMENT FOR 12" PIPE WITH 5D BEND RADIUS. -----	149
FIGURE 5. 63. END ROTATION VS REACTION MOMENT FOR 42" PIPE WITH 5D BEND RADIUS. -----	149
FIGURE 5. 64. MID-LAYER VON MISES STRESS VS REACTION MOMENT FOR 12" PIPE WITH 1D BEND RADIUS. -----	151
FIGURE 5. 65. MID-LAYER VON MISES STRESS VS REACTION MOMENT FOR 42" PIPE WITH 1D BEND RADIUS. -----	151
FIGURE 5. 66. MID-LAYER VON MISES STRESS VS REACTION MOMENT FOR 12" PIPE WITH 1D BEND RADIUS. -----	152
FIGURE 5. 67. MID-LAYER VON MISES STRESS VS REACTION MOMENT FOR 42" PIPE WITH 1D BEND RADIUS. -----	152
FIGURE 5. 68. VON MISES STRESS VS REACTION MOMENT FOR 12" PIPE WITH 1D BEND RADIUS.-----	153
FIGURE 5. 69. VON MISES STRESS VS REACTION MOMENT FOR 12" PIPE WITH 1D BEND RADIUS.-----	153
FIGURE 5. 70. VON MISES STRESS VS REACTION MOMENT FOR 12" PIPE WITH 1D BEND RADIUS.-----	153
FIGURE 5. 71. VON MISES STRESS VS REACTION MOMENT FOR 12" PIPE WITH 1D BEND RADIUS.-----	153
FIGURE 5. 72. MID-LAYER VON MISES STRESS VS BEND ANGLE (A) FOR PIPES WITH LONG BEND RADIUS ($R = 5D$). -----	154
FIGURE 5. 73. INNER LAYER VON MISES STRESS VS BEND ANGLE (A) FOR PIPES WITH LONG BEND RADIUS ($R = 3D$). -----	154
FIGURE 5. 74. OUTER LAYER VON MISES STRESS VS BEND ANGLE (A) FOR PIPES WITH LONG BEND RADIUS ($R = 5D$). -----	155
FIGURE 5. 75. MID-LAYER VON MISES STRESS VS BEND ANGLE (A) FOR PIPES WITH SHORT BEND RADIUS ($R = 1D$).-----	155
FIGURE 5. 76. INNER LAYER VON MISES STRESS VS BEND ANGLE (A) FOR PIPES WITH SHORT BEND RADIUS ($R = 1D$). -----	155
FIGURE 5. 77. OUTER LAYER VON MISES STRESS VS BEND ANGLE (A) FOR PIPES WITH SHORT BEND RADIUS ($R = 1D$). -----	155
FIGURE 5. 78. MID-LAYER VON MISES STRESSES FROM FEA COMPARED WITH THE CSA RESULTS FOR PIPE BENDS WITH SHORT BEND RADIUS ($R = 1D$) AND BEND ANGLE 20-----	156
FIGURE 5. 79. MID-LAYER VON MISES STRESSES FROM FEA COMPARED WITH THE CSA RESULTS FOR PIPE BENDS WITH LONG BEND RADIUS ($R = 5D$) AND BEND ANGLE 140-----	156
FIGURE 5. 80. INNER LAYER VON MISES STRESSES FROM FEA COMPARED WITH THE CSA RESULTS FOR PIPE BENDS WITH SHORT BEND RADIUS ($R = 1D$) AND BEND ANGLE 40-----	157
FIGURE 5. 81. INNER LAYER VON MISES STRESSES FROM FEA COMPARED WITH THE CSA RESULTS FOR PIPE BENDS WITH LONG BEND RADIUS ($R = 3D$) AND BEND ANGLE 20-----	157
FIGURE 5. 82. OUTER LAYER VON MISES STRESSES FROM FEA COMPARED WITH THE CSA RESULTS FOR PIPE BENDS WITH SHORT BEND RADIUS ($R = 1D$) AND BEND ANGLE 20-----	157
FIGURE 5. 83. OUTER LAYER VON MISES STRESSES FROM FEA COMPARED WITH THE CSA RESULTS FOR PIPE BENDS WITH LONG BEND RADIUS ($R = 5D$) AND BEND ANGLE 20-----	157

FIGURE 5. 84. HOOP STRESS DISTRIBUTION ACROSS THE PIPE CIRCUMFERENCE FOR A 12" PIPE WITH SHORT BEND RADIUS (R=1D) AND 20 BEND ANGLE SUBJECTED TO INTERNAL PRESSURE.-----	159
FIGURE 5. 85. LONGITUDINAL STRESS DISTRIBUTION ACROSS THE PIPE CIRCUMFERENCE FOR A 12" PIPE WITH SHORT BEND RADIUS (R=1D) AND 20 BEND ANGLE SUBJECTED TO INTERNAL PRESSURE.-----	159
FIGURE 5. 86. HOOP STRESS DISTRIBUTION ACROSS THE PIPE CIRCUMFERENCE FOR A 42" PIPE WITH SHORT BEND RADIUS (R=1D) AND 20 BEND ANGLE SUBJECTED TO INTERNAL PRESSURE.-----	160
FIGURE 5. 87. LONGITUDINAL STRESS DISTRIBUTION ACROSS THE PIPE CIRCUMFERENCE FOR A 42" PIPE WITH SHORT BEND RADIUS (R=1D) AND 20 BEND ANGLE SUBJECTED TO INTERNAL PRESSURE.-----	160
FIGURE 5. 88. VON MISES STRESS DISTRIBUTION ACROSS THE PIPE CIRCUMFERENCE FOR A 42" PIPE WITH SHORT BEND RADIUS (R=1D) AND 20 BEND ANGLE SUBJECTED TO INTERNAL PRESSURE.-----	160
FIGURE 5. 89. THE CROSS-SECTIONAL OVALIZATION AT THE MID-LENGTH OF THE PIPE BEND SUBJECTED TO AN OPENING BENDING MOMENT.-----	162
FIGURE 5. 90. THE CROSS-SECTIONAL FLATTENING DEFORMATION AT THE MID-LENGTH OF THE PIPE BEND SUBJECTED TO A CLOSING BENDING MOMENT.-----	162
FIGURE 5. 91. HOOP STRESS DISTRIBUTION ALONG THE CRITICAL SECTION OF A NPS 12 PIPE BEND WITH BEND ANGLE 20o AND SHORT BEND RADIUS (R = 1D) SUBJECTED TO OPENING BENDING.-----	163
FIGURE 5. 92. LONGITUDINAL STRESS DISTRIBUTION ALONG THE CRITICAL SECTION OF A NPS 12 PIPE BEND WITH BEND ANGLE 20o AND SHORT BEND RADIUS (R = 1D) SUBJECTED TO OPENING BENDING.-----	163
FIGURE 5. 93. HOOP STRESS DISTRIBUTION ALONG THE CRITICAL SECTION OF A NPS 12 PIPE BEND WITH BEND ANGLE 20o AND SHORT BEND RADIUS (R = 1D) SUBJECTED TO CLOSING BENDING.-----	163
FIGURE 5. 94. LONGITUDINAL STRESS DISTRIBUTION ALONG THE CRITICAL SECTION OF A NPS 12 PIPE BEND WITH BEND ANGLE 20o AND SHORT BEND RADIUS (R = 1D) SUBJECTED TO CLOSING BENDING.-----	163
FIGURE 5. 95. DEFORMED SECTION FOR A SHORT BEND RADIUS PIPE (R=1D) AT THE END OF STEP 1 (INTERNAL PRESSURE LOADING)---	165
FIGURE 5. 96. DEFORMED SECTION FOR A SHORT BEND RADIUS PIPE (R=1D) AT THE END OF STEP 2 (INTERNAL PRESSURE AND CLOSING BENDING LOADING)-----	165
FIGURE 5. 97. HOOP STRESS DISTRIBUTION ON THE CRITICAL SECTION CIRCUMFERENCE OF A 12" PIPE WITH 20-DEGREE BEND ANGLE AND SHORT BEND RADIUS SUBJECTED TO INTERNAL PRESSURE.-----	166
FIGURE 5. 98. HOOP STRESS DISTRIBUTION ON THE CRITICAL SECTION CIRCUMFERENCE OF A 12" PIPE WITH 20-DEGREE BEND ANGLE AND SHORT BEND RADIUS SUBJECTED TO INTERNAL PRESSURE AND CLOSING BENDING MOMENT.-----	166
FIGURE 5. 99. LONGITUDINAL STRESS DISTRIBUTION ON THE CRITICAL SECTION CIRCUMFERENCE OF A 12" PIPE WITH 20-DEGREE BEND ANGLE AND SHORT BEND RADIUS SUBJECTED TO INTERNAL PRESSURE.-----	166
FIGURE 5. 100. LONGITUDINAL STRESS DISTRIBUTION ON THE CRITICAL SECTION CIRCUMFERENCE OF A 12" PIPE WITH 20-DEGREE BEND ANGLE AND SHORT BEND RADIUS SUBJECTED TO INTERNAL PRESSURE AND CLOSING BENDING MOMENT.-----	166
FIGURE 5. 101 VON MISES STRESS DISTRIBUTION ON THE CRITICAL SECTION CIRCUMFERENCE OF A 12" PIPE WITH 20-DEGREE BEND ANGLE AND SHORT BEND RADIUS FOR STEP 1 (INTERNAL PRESSURE) AND STEP 2 (INTERNAL PRESSURE AND CLOSING BENDING).-----	167
FIGURE 5. 102. DEFORMED SECTION FOR A LONG BEND RADIUS PIPE (R=5D) AT THE END OF STEP 1 (INTERNAL PRESSURE LOADING) --	167
FIGURE 5. 103. DEFORMED SECTION FOR A LONG BEND RADIUS PIPE (R=5D) AT THE END OF STEP 2 (INTERNAL PRESSURE AND CLOSING BENDING MOMENT LOADING)-----	167
FIGURE 5. 104. HOOP STRESS DISTRIBUTION ON THE CRITICAL SECTION CIRCUMFERENCE OF A 12" PIPE WITH 20-DEGREE BEND ANGLE AND LONG BEND RADIUS SUBJECTED TO INTERNAL PRESSURE.-----	168
FIGURE 5. 105. HOOP STRESS DISTRIBUTION ON THE CRITICAL SECTION CIRCUMFERENCE OF A 12" PIPE WITH 20-DEGREE BEND ANGLE AND LONG BEND RADIUS SUBJECTED TO INTERNAL PRESSURE AND CLOSING BENDING MOMENT.-----	168
FIGURE 5. 106. LONGITUDINAL STRESS DISTRIBUTION ON THE CRITICAL SECTION CIRCUMFERENCE OF A 12" PIPE WITH 20-DEGREE BEND ANGLE AND LONG BEND RADIUS SUBJECTED TO INTERNAL PRESSURE.-----	168
FIGURE 5. 107. LONGITUDINAL STRESS DISTRIBUTION ON THE CRITICAL SECTION CIRCUMFERENCE OF A 12" PIPE WITH 20-DEGREE BEND ANGLE AND LONG BEND RADIUS SUBJECTED TO INTERNAL PRESSURE AND CLOSING BENDING MOMENT.-----	168
FIGURE 5. 108 VON MISES STRESS DISTRIBUTION ON THE CRITICAL SECTION CIRCUMFERENCE OF A 12" PIPE WITH 20-DEGREE BEND ANGLE AND SHORT BEND RADIUS FOR STEP 1 (INTERNAL PRESSURE) AND STEP 2 (INTERNAL PRESSURE AND CLOSING BENDING).-----	169
FIGURE 6. 1. STRESS INTENSIFICATION FACTORS FOR SHORT RADIUS PIPE BENDS WITH VARIOUS BEND ANGLES AND PIPE SIZES.-----	173
FIGURE 6. 2. STRESS INTENSIFICATION FACTORS FOR LONG RADIUS PIPE BENDS WITH VARIOUS BEND ANGLES AND PIPE SIZES.-----	173
FIGURE 6. 3. STRESS INTENSIFICATION FACTORS FOR PIPE BENDS SUBJECTED TO OPENING BENDING MOMENT.-----	174
FIGURE 6. 4. STRESS INTENSIFICATION FACTORS FOR PIPE BENDS SUBJECTED TO CLOSING BENDING MOMENT.-----	174
FIGURE 6. 5. PRESSURE EFFECT FACTORS FOR PIPE BENDS WITH 20 DEGREES BEND ANGLES AND VARYING R/R RATIOS.-----	175
FIGURE 6. 6. PRESSURE EFFECT FACTORS FOR PIPE BENDS WITH 40 DEGREES BEND ANGLES AND VARYING R/R RATIOS.-----	175
FIGURE 6. 7. PRESSURE EFFECT FACTORS FOR PIPE BENDS WITH 90 DEGREES BEND ANGLES AND VARYING R/R RATIOS.-----	176
FIGURE 6. 8. PRESSURE EFFECT FACTORS FOR PIPE BENDS WITH 140 DEGREES BEND ANGLES AND VARYING R/R RATIOS.-----	176

FIGURE 6. 9. PRESSURE EFFECT FACTORS FOR PIPE BENDS WITH SHORT BEND RADIUS AND VARIOUS BEND ANGLES. -----	176
FIGURE 6. 10. PRESSURE EFFECT FACTORS FOR PIPE BENDS WITH LONG BEND RADIUS AND VARIOUS BEND ANGLES. -----	176
FIGURE 6. 11. PRESSURE EFFECT FACTORS FOR PIPE BENDS WITH SHORT BEND RADIUS VERSUS THE P/E RATIO. -----	177
FIGURE 6. 12. PRESSURE EFFECT FACTORS FOR PIPE BENDS WITH LONG BEND RADIUS VERSUS THE P/E RATIO. -----	177
FIGURE 6. 15. PRESSURE EFFECT FACTORS FOR SHORT RADIUS PIPE BENDS WITH VARIOUS BEND ANGLES. -----	177
FIGURE 6. 16. PRESSURE EFFECT FACTORS FOR LONG RADIUS PIPE BENDS WITH VARIOUS BEND ANGLES. -----	177
FIGURE 6. 17. THE MID-LAYER FEA SIF (DOTTED) COMPARED TO THE PROPOSED SIF FORMULA (BLUE LINE) FOR BENDS WITH BEND ANGLE = 100 -----	179
FIGURE 6. 18. THE MID-LAYER FEA SIF (DOTTED) COMPARED TO THE PROPOSED SIF FORMULA (BLUE LINE) FOR NPS12 BENDS WITH BEND RADIUS (R=3D) -----	179
FIGURE 6. 19. THE MID-LAYER FEA SIF (DOTTED) COMPARED TO THE PROPOSED SIF FORMULA (BLUE LINE) FOR BENDS WITH BEND ANGLE = 400 -----	180
FIGURE 6. 20. DEVIATION OF THE SIF DEVELOPED FORMULA FROM THE FEA RESULTS FOR THE MID-LAYER OF THE WALL THICKNESS ---	180
FIGURE 6. 21. DEVIATION OF THE SIF DEVELOPED FORMULA FROM THE FEA RESULTS FOR THE INNER LAYER OF THE WALL THICKNESS -	180
FIGURE 6. 22. DEVIATION OF THE SIF DEVELOPED FORMULA FROM THE FEA RESULTS FOR THE OUTER LAYER OF THE WALL THICKNESS	181
FIGURE 6. 23. THE MID-LAYER FEA SIF (DOTTED) COMPARED TO THE PROPOSED SIF FORMULA (BLUE LINE) FOR NPS12 BENDS WITH SHORT BEND RADIUS (R=1D) -----	182
FIGURE 6. 24. THE MID-LAYER FEA SIF (DOTTED) COMPARED TO THE PROPOSED SIF FORMULA (BLUE LINE) FOR BENDS WITH BEND ANGLE = 400 -----	182
FIGURE 6. 25. DEVIATION OF THE SIF DEVELOPED FORMULA FROM THE FEA RESULTS FOR THE MID-LAYER OF THE WALL THICKNESS ---	183
FIGURE 6. 26. DEVIATION OF THE SIF DEVELOPED FORMULA FROM THE FEA RESULTS FOR THE INNER LAYER OF THE WALL THICKNESS -	183
FIGURE 6. 27. DEVIATION OF THE SIF DEVELOPED FORMULA FROM THE FEA RESULTS FOR THE OUTER LAYER OF THE WALL THICKNESS	183
FIGURE 6. 28. DEVIATION OF THE PRESSURE REDUCTION FACTOR DEVELOPED FORMULA FROM THE FEA RESULTS FOR THE MID-LAYER OF THE WALL THICKNESS FOR BENDS UNDER OPENING BENDING MOMENT -----	185
FIGURE 6. 29. DEVIATION OF THE PRESSURE REDUCTION FACTOR DEVELOPED FORMULA FROM THE FEA RESULTS FOR THE MID-LAYER OF THE WALL THICKNESS FOR BENDS UNDER CLOSING BENDING MOMENT -----	185
FIGURE 6. 30. COMPARISON BETWEEN THE STRESS INTENSIFICATION FACTORS FOR BC-1 AND BC-2 FOR SHORT RADIUS BENDS UNDER OPENING BENDING MOMENT. -----	186
FIGURE 6. 31. COMPARISON BETWEEN THE STRESS INTENSIFICATION FACTORS FOR BC-1 AND BC-2 FOR SHORT RADIUS BENDS UNDER CLOSING BENDING MOMENT. -----	186

LIST OF TABLES

TABLE 2. 1. GEOMETRIC PARAMETERS OF PIPE ELBOW. -----	22
TABLE 2. 2. THE PIPE GEOMETRY AND LOADING FOR EACH TEST. -----	26
TABLE 2. 3. REACTION FORCES FROM FEA COMPARED TO THE PROPOSED MATHEMATICAL MODEL.-----	32
TABLE 2. 4. TRESCA STRESS RESULTS FROM SHELL (S4R) ELEMENT VS THE CSA COMBINED STRESS RESULTS FOR PIPE BENDS SUBJECTED TO INTERNAL PRESSURE CAUSING 80 % SMYS HOOP STRESS. -----	35
TABLE 2. 5. THE DATA POINTS USED IN THE REGRESSION ANALYSIS AND THE DEVELOPED PRESSURE FACTOR (Kp) PIPE BENDS SUBJECTED TO INTERNAL PRESSURE CAUSING 80 % SMYS HOOP STRESS. -----	38
TABLE 2. 6. ACCURACY OF THE MODIFIED CSA-Z662 EQUATION COMPARED TO S4R MODEL RESULTS FOR PIPE BENDS SUBJECTED TO INTERNAL PRESSURE RESULTING IN 80% SMYS HOOP STRESS-----	39
TABLE 2. 7. ACCURACY OF THE MODIFIED CSA-Z662 EQUATION COMPARED TO S4R MODEL RESULTS FOR PIPE BENDS SUBJECTED TO INTERNAL PRESSURE RESULTING IN 30% SMYS HOOP STRESS-----	40
TABLE 2. 8. COMPARISON BETWEEN THE PROPOSED MODELLING APPROACH RESULTS AND THE S4R MODEL RESULTS FOR PIPE BENDS SUBJECTED TO INTERNAL PRESSURE RESULTING IN 80% SMYS HOOP STRESS -----	44
TABLE 2. 9. STRESS RESULTS AT SECTION (A-A) : COMPARISON BETWEEN THE PROPOSED MODELLING APPROACH RESULTS USING PIPE AND ELBOW ELEMENTS VERSUS THE S4R MODEL RESULTS AT THE PIPE BEND LOCATION. -----	47
TABLE 2. 10. STRESS RESULTS AT SECTION (B-B): COMPARISON BETWEEN THE PROPOSED MODELLING APPROACH RESULTS AND THE S4R MODEL RESULTS AT STRAIGHT PIPE LOCATION. -----	47
TABLE 2. 11. DISPLACEMENTS (IN MM) EVALUATED AT SECTION (C-C): COMPARISON BETWEEN THE PROPOSED MODELLING APPROACH RESULTS AND THE S4R MODEL RESULTS -----	47
TABLE 2. 12. STRESS RESULTS AT SECTION (A-A) : THE TRESCA STRESS RESULTS USING PIPE AND ELBOW ELEMENTS AT THE PIPE BEND LOCATION WITHOUT MODIFYING THE INTERNAL PRESSURE. -----	48
TABLE 2. 13. STRESS RESULTS AT SECTION (B-B) : THE TRESCA STRESS RESULTS USING PIPE AND ELBOW ELEMENTS AT THE STRAIGHT PIPE LOCATION WITHOUT MODIFYING THE INTERNAL PRESSURE. -----	48
TABLE 2. 14. THE EVALUATED STRESSES FROM DIFFERENT PROPOSED FORMULAS AND THE SHELL ELEMENT MODEL FROM THE CURRENT STUDY. -----	49
TABLE 2. 15. THE ACCURACY OF EACH PROPOSED FORMULA COMPARED TO THE FEA RESULTS -----	50
TABLE 3. 1 GEOMETRIC PARAMETERS OF PIPE ELBOW. -----	64
TABLE 3. 2 DIMENSIONS OF TESTED PIPES (GROSS, 1952) -----	65
TABLE 4. 1. COEFFICIENTS FOR THE OPENING BENDING MOMENT STRESS INTENSIFICATION FACTOR PRESENTED IN EQUATION (4. 1) ----	111
TABLE 4. 2. COEFFICIENTS FOR THE OPENING BENDING MOMENT STRESS INTENSIFICATION FACTOR PRESENTED IN EQUATION (4. 6) ----	114
TABLE 5. 1. EVALUATED BOURDON FORCES USING DEVELOPED EQUATION COMPARED TO THE FEA EXTRACTED FORCES.-----	130
TABLE 6. 1. COEFFICIENTS FOR THE OPENING BENDING MOMENT STRESS INTENSIFICATION FACTOR PRESENTED IN EQUATION (6. 6) ----	178
TABLE 6. 2. THE ACCURACY OF THE PROPOSED EQUATION (6. 6). -----	179
TABLE 6. 3. COEFFICIENTS FOR THE OPENING BENDING MOMENT STRESS INTENSIFICATION FACTOR PRESENTED IN EQUATION (6. 7) ----	181
TABLE 6. 4. THE ACCURACY OF THE PROPOSED EQUATION (6. 7). -----	182
TABLE 6. 3. COEFFICIENTS OF EQUATION (6. 8) FOR THE PROPOSED PRESSURE REDUCTION FACTOR. -----	184
TABLE 6. 6. THE ACCURACY OF THE PROPOSED EQUATION (6. 8). -----	185

NOTATIONS

FEA	Finite Element Analysis
NPS	Nominal Pipe Size
R	Pipe bend radius, mm
r	Radius of the pipe cross-section, mm
D	Outer diameter, mm
t	pipe wall nominal thickness, mm
E	Modulus of elasticity
P	Internal pressure, MPa
I	Second moment of inertia, mm ⁴
λ	Beam parameter or pipe factor ($\lambda = tR/r^2$)
\emptyset	Circumferential angle across the cross-section, degrees
SMYS or "S"	Specified minimum yield strength, MPa
α	Bend angle, degrees
SIF or i	Stress Intensification Factor
ν	Poisson's ratio
Extrados	The point on the pipe cross-section furthest from the torus centre.
Intrados	The point on the pipe cross-section closest to the torus centre.
F	Design factor in CSA-Z662
L	Location factor in CSA-Z662
T	Temperature factor in CSA-Z662
J	Joint factor in CSA-Z662
X proposed	Pressure correction Factor
Kp	Pressure Factor

CHAPTER 1: INTRODUCTION AND LITERATURE REVIEW

1.1. INTRODUCTION

Pipelines are used in several industries nowadays such as oil refineries, power plants, chemical industry, and in the oil and gas industry. In these industrial applications, the product is transported from the producer to the market through pipeline transmission systems that travels for long distances buried under the ground where mainly the pipes run straight. However, sometimes the plant plan or the land topography may lead to a change in the pipeline direction or level. One way to change the directions is to introduce pipe elbows and bends into the pipeline network.

In the past, it was known from experimental and theoretical studies (Bantlin, 1910; Von Kármán, 1911) that curved pipes tend to have higher flexibility than straight pipes. Therefore, elbows and bends were introduced to the pipeline system to absorb any thermal expansions and to provide higher flexibility to the pipeline network (Turner & Ford, 1957). The pipe bend flexibility is gained from its shell-type behaviour. The bend cross-section is able to deform from its initially circular cross-section into an oval shape accompanied by an out-of-plane deformation of the cross-section known as warping. This behaviour adds to the bend flexibility when compared to straight pipes that behave more as beams. Bantlin (1910) was the first to experimentally show that pipe bends respond differently under load than predicted by simple beam theory ($\sigma = Mr/I$). This discrepancy was explained by Von Kármán in (1911) using a theoretical stress analysis method that resulted in a flexibility factor for pipe bends. As a result of the high flexibility, the pipe bend is considered a critical component and a location of high stress levels in any pipeline system. Therefore, the integrity of the pipeline industry is considered crucial and a thorough understanding of the behaviour of piping components is required under different loading conditions.

The simple beam theory has been used to analyse the bending for straight pipes with circular cross-section and it is found to be very satisfactory according to past studies. In addition, the Barlow's equation used to evaluate the stresses on a pressurized straight pipe is very simple and evaluates the stresses accurately. However, when it comes to thin-walled curved pipes as pipe bends and elbows, there is no simple closed-form solution to evaluate the stresses neither from bending nor internal pressure. It is even more complicated when a combined load of internal

pressure and bending is applied at a pipe bend which turns it into a very complex problem that requires finite element methods and non-linear solutions.

The behaviour of a pipe bend depends on the type of load applied. Internal pressure loading tends to expand the cross-section of the bend. Moreover, an outward external force is generated due to the surface geometric characteristics of pipe bends that tends to straighten out the bend. This phenomenon is known as the “Bourdon effect”. There is a lack of understanding of the behaviour of bends under internal pressure since the Bourdon effect was not thoroughly covered in past studies and is not clearly addressed by the design codes. On the other hand, in-plane bending moment generates a different behaviour and it depends on the direction of bending. An in-plane closing bending moment flattens the cross-section in a shape where the major axis is perpendicular to the plane of bending. As the deformed cross-section flattens, the second moment of area decreases leading to a decrease in the pipe bend stiffness. However, an in-plane opening bending moment results in an oval deformed cross-section where the major axis is in the plane of bending. The ovalized shape results in a higher second moment of area consequently generating a stiffer bend. The combined loading of internal pressure and in-plane bending is quite complex since the in-plane opening bending moment tends to increase the deformations resulted from the internal pressure since they both act in the same direction. However, the in-plane closing bending moment acts in an opposite action to the internal pressure. The interaction between the two loads need further study. Even the level of internal pressure to bending moment applied may affect the behaviour of the bend and result in a different stress distribution than expected. Especially, with the in-plane closing bending moment where the internal pressure may overcome the stresses from the bending if the pressure level is high enough. Otherwise, the closing bending overcomes the internal pressure stresses and leads to a totally different distribution with a different behaviour. Several parameters need to be considered in the design of pipe bends to ensure a safe design.

Several past studies (Kármán, 1911; Clark and Reissner, 1951) investigated the behaviour of bends under closing in-plane bending moment and a stress intensification factor was developed based on theoretical or experimental studies. These stress intensification factors are presented in and used by the current design codes (ASME B31.1, ASME B31.3 and CSA Z662-15). Then the effect of adding internal pressure to a closing in-plane bending moment was investigated (Kafka & Dunn, 1956; Rodabaugh & George, 1957) and a pressure reduction factor is developed and is incorporated

in the current design codes (Process piping design code ASME B31.3). In the following section, a background on the Bourdon effect and the Stress Intensification Factors is presented.

There are two philosophies in designing pipelines. The first is based on limiting the stress in the pipe wall due to service and installation loads and maintaining the pipeline in the elastic zone. This is known as the stress based design. On the other hand, another method allows an extension to the stress design to take advantage of the steel plasticity while maintaining stability. This is known as the strain-based design. In this study, the stress-based design is used to limit the stresses on the pipe bends and any plastic deformations are not allowed.

1.2. LITERATURE REVIEW

1.2.1. Pipe Bends Under Internal Pressure Loading

Eugene Bourdon in 1849 developed a pressure gauge that is mainly based on a flattened curved tube that tends to straighten out or regain its circular cross-section when pressurized. The principle of this instrument was discovered by accident (Worthington, 1890). The Bourdon pressure gauge consists of a flattened copper thin-walled pipe with closed-end tube that is connected at the hollow end to a fixed pipe containing the pressurized media to be measured as shown in figure (1. 1). As the pressure increases, the closed end moves in an arc form, and this motion is converted into the rotation of a gear where a pointer is attached. The pointer rotates and gives the pressure reading on a dial. Although the change in the tube cross-section due to the pressure may be small and involves small stress levels, however, the tube is bent into a curved shape to magnify the strain on the tube as it is pressurized since the entire tube tends to straighten out. The tendency of the tube to straighten out when subjected to internal pressure is known as the “Bourdon effect”.

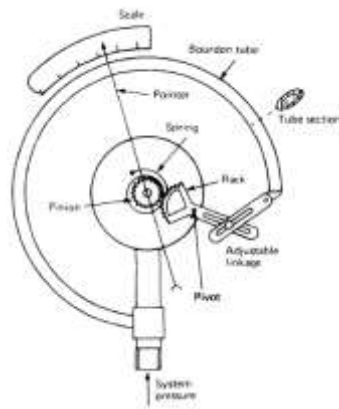


Figure 1. 1. Mechanical interior side of the Bourdon pressure gauge.

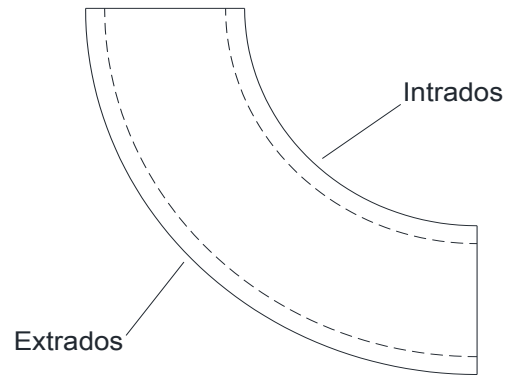


Figure 1. 2. The Intrados and Extradados of Pipe bend.

The Bourdon effect phenomenon with the same concept exists in pipe elbows and bends that are subjected to internal pressure. The pipe bend tends to straighten out causing additional stresses on the pipe walls. Due to the difference of surface area between the extradados and intrados of the pipe bend as shown in figure (1. 2), an outward force exists when pipe bends are subjected to internal pressure. These additional forces will tend to straighten out the pipe bend leading to a higher stress level and higher deformations.

The stresses on a smooth pipe bend with constant wall thickness and initial circular cross-section can be approximately estimated using theoretical methods based on linear shell theory. Flügge (1973) proposed an equation for the longitudinal and hoop stresses for a toroidal shell under internal pressure with an initially circular cross-section. This equation was derived using the equilibrium of shell elements ignoring the bending of the pipe surface. Flügge's proposed formulas show that the toroidal effect influences the hoop stress leaving the longitudinal stress unaltered than that of a straight pipe. His proposed formulas are as follows;

$$\sigma_L = \frac{Pr}{2t} \tag{1. 1}$$

$$\sigma_h = \frac{Pr}{2t} \left[\frac{2\rho + \sin \phi}{\rho + \sin \phi} \right] \tag{1. 2}$$

Where,

ρ : Radius ratio, $\rho = R/r$

ϕ : is the circumferential angle measured from the crown towards the extrados as per figure (1.3).

(Varying from $\phi=0$ at the crown, $\phi=\pi/2$ at the extrados and $\phi=3\pi/2$ at the intrados)

This analytical method considered the effect of toroidal shape on the hoop stresses. However, the cross-sectional deformation was not considered. Moreover, the effect of the additional outward forces on the pipe bend stresses was not considered in this method.

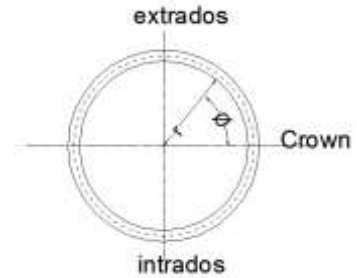


Figure 1. 3. Section of toroidal shell

Goodall (1978) derived an analytical elastic stress solution for thin-walled bends under internal pressure. Only the hoop stresses was affected by the curvature of the pipe. Same as Flügge’s proposed formula, Goodall’s elastic solution is independent of the location along the longitudinal direction of the pipe bend. He proposed the following stress solution for thin-walled bends under internal pressure;

$$\sigma_h = \frac{Pr_i}{t} \left[\frac{2R + r_m \cos \theta}{2R + 2 r_m \cos \theta} \right] \tag{1. 3}$$

θ : is the circumferential angle measured from the intrados towards the extrados. (Varying from $\theta = 0$ at the extrados and $\theta = \pi$ at the intrados).

In recent studies, numerical analysis is used to investigate the behaviour of pipe bends under internal pressure loading. Hong, Seok-Pyo, et al., (2010) extended the work of Flügge (1973) and Goodall (1978) to cover thin-walled and thick-walled pipe bends simulated using FEA. He presented a closed-form approximation to estimate elastic stresses in thick and thin-walled bends under internal pressure based on FEA analysis. He used Goodall’s formula for thin-walled elbows to extend it for thick-walled bends. Goodall’s and Flügge’s formulas are based on a toroidal shape pipe. The existing and extended solutions show that the bend curvature affects the hoop stress only and that the maximum hoop stresses exist in the intrados of the pipe bend and higher than that of a straight pipe, while the minimum is at the extrados and lower than that of a straight pipe. Seok-Pyo Hong compared the proposed

approximation for the hoop stress formula with the FEA results and found that the proposed approximation can be applied on 90 and 45-degree bends and on U-bends as well. Flügge, Goodall and Hong's proposed formulas are developed for pipe bends taking into consideration the surface geometry of a toroid. However, any additional forces resulting from the outward pipe deformation or the cross-sectional deformation was not considered in the hoop stresses. Therefore, the Bourdon and Ovalization effect were ignored from these studies.

Flügge's study was based on an initially circular cross-sectional pipe bend that maintains its cross-sectional shape after deformation. However, initial imperfection was found to have some effects on the pipe bend stress levels. A.R.Veerappan (2006) studied the effect of ovality and thinning introduced during the forming process of pipe bends on the allowable pressure ratio. It was found that the allowable pressure ratio increases, attains a maximum, and then decreases as the values of ovality and thinning are increased. A mathematical model is developed to estimate the allowable pressure in terms of bend ratio (R/D), pipe ratio (D/t), percent of thinning and percent of ovality.

In 2014, K. Muntaseer, et al., constructed a method for the geometric analysis of pipe elbows using 3D scanning to be able to consider the actual pipe elbow geometry in finite element models and investigate the effect of initial imperfections on the pipe behaviour. Two straight pipes were attached to the pipe bend and the system was fixed at both ends. The pipes were subjected to internal pressure that causes 80% SMYS hoop stress. It was found that a translation of the elbows occurred outwards that will affect the support system used to fix this elbow in position by a lateral force (Bourdon effect). The FEA analysis results showed that the von Mises stress distribution was higher at the intrados compared to the extrados. Moreover, the maximum hoop stresses due to the applied internal pressure were found to be greater than that intended to be applied (80% SMYS). It was concluded in this study that using the next higher wall thickness reduced the outward translation of the elbow and the hoop stresses were almost equal to the expected values (80% SMYS).

F.Shemirani, et al. (2014) investigated the influence of the Bourdon effect on the stress and ovalization of the elbows. The study was based on FEA analysis of pipe elbows connected to straight pipes with various lengths. Different pipe sizes and different straight pipe lengths were considered. The actual scanned pipe geometry from the work of K.Muntaseer (2014) was used in this study. The outward displacement of the middle section of the elbow was considered a measurement of the Bourdon effect.

It was found that increasing the elbow thickness with respect to the straight pipe would reduce the outward displacement of the elbow. Increasing the straight pipe length reduces the influence of the end constraints and leads to an increase in the elbow outward displacement. It was suggested in this paper that the displacement due to the Bourdon effect could be restricted by selecting a proper straight pipe length. Moreover, it showed that in case of pipe elbows having same thickness of the straight pipe, the hoop stresses exceeds the 80% SMYS which means a reduction in the safety factor of the elbow section.

1.2.2. Pipe bends under pressure and bending moments

Many studies developed closed-form solutions for pipe bends under bending moments. These studies followed different approaches in defining the mathematical problem and solving the equations. The approaches used in past studies are the “minimum potential energy” approach first used by Von Kármán in 1911, the “mechanics-of-materials” approach used by Turner and Ford in 1957, and the “Thin-shell theory” approach used by Clark and Reissner in 1951. Much of the theoretical work presented after Kármán’s study was an extension of his work, or based on the same assumptions.

Although Kármán proposed a flexibility factor and stress intensification factor to be used as a general approach in the design of piping systems, but other studies aim to extend Kármán’s work and provide more accurate factors and in a form that can be simplified and easily used by the designer.

1.2.2.1. Minimum Potential Energy Approach

Von Kármán (1911) was the first to present a rational explanation of the curved pipe complex behaviour using a theoretical study and that the curve pipe responds differently under bending than predicted by simple beam theory. Most of the following theoretical work was an extension of Kármán’s work and based on the same potential energy minimization using mostly the same assumptions. The general approach followed was to develop a factor that accounts for the increase in flexibility and stresses of pipe bends known as the “flexibility” and “Stress intensification” factors which are simply the ratios of the actual flexibility and stress of a pipe bend to those predicted by simple beam theory. The studies that followed Kármán’s approach were aiming at providing a more accurate factor that could be simplified and usable in the design of pipelines.

Von Kármán (1911) published the first theoretical stress analysis for the curved pipes subjected to in-plane bending. He investigated a long bend radius pipe subjected to in-plane moment increasing the curvature of the pipe. The flattening of the cross-section was the main deformation mode considered in his study. Kármán concluded that the deformation in the cross-section reduced the longitudinal stresses at both the intrados and extrados of the pipe, however, the crown longitudinal stresses increases. He expressed the strain energy for a thin ring cut from the pipe bend as a function of the radial displacement component (ω_r) only, as shown in figures (1. 4) & (1. 5). The pipe bend wall deformation presented in his study as the radial displacement was expressed by a trigonometric series (Eqn. 1.4) and the coefficients were obtained by minimizing the total potential energy.

$$\omega_r = C_1 \cos 2\theta + C_2 \cos 4\theta + \dots + C_n \cos 2n\theta \quad (1.4)$$

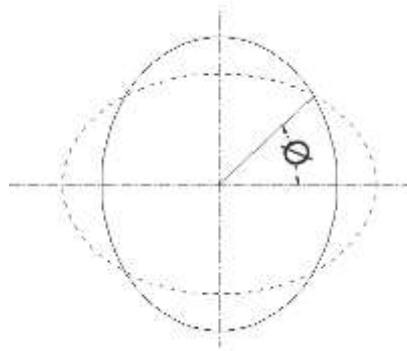


Figure 1. 4. Deformation of the mid-layer of the pipe bend cross-section

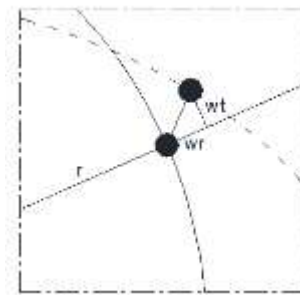


Figure 1. 5. Displacement of a point at the circumference of the mid-layer of the cross-section

In order to simplify the analysis, Von Kármán neglected the small value terms from the displacement trigonometric series presented in equation (1.4) and considered only the first term of the series, this equation was later on known as the First approximation. Some of Kármán's major assumptions are;

- 1- A standalone bend was considered in this investigation ignoring the end effects.
- 2- The circumferential membrane strain was assumed zero. Assuming that the length of any segment of the circumference of the pipe wall remains constant.
- 3- The bend's cross-section remains plane and perpendicular to the pipe's centre-line after deformation ignoring any warping effect on the flexibility of the bend.
- 4- The cross-sectional ovalization is constant along the pipe length.

- 5- The pipe radius (r) is neglected compared to the bend radius (R) for long radius bends. The bore term ($R \pm r$) is approximated to (R).

An expression for the flexibility factor was proposed by Von Kármán and known as the first approximation. The proposed flexibility factor (K) is as follows;

$$K = \frac{12\lambda^2 + 10}{12\lambda^2 + 1} \quad (1.5)$$

Where, λ is a dimensionless pipe bend parameter considering a uniaxial stress-strain relationship and defined as follows;

$$\lambda = \frac{tR}{r^2}$$

t = Pipe wall thickness, mm,

R = Pipe bend radius, mm,

r = pipe cross-section radius, mm.

The drawback in Von Kármán's study is that any deformation occurring to the centre-line of the cross-section leaves the length unchanged according to his assumptions. This means that the hoop stress was assumed to be much smaller than the longitudinal stress and was not significantly affecting the strain energy.

In 1955, Kafka and Dunn suggested that the influence of the internal pressure is rather small for heavy pipes (Thick-walled pipes) used in the industry back then. However, for thin-walled pipes, neglecting the internal pressure leads to an overestimation of the flexibility and stress intensification factors. He presented a method for computing the flexibility and stress intensification factors for plane pipelines with internal pressure and made the same assumptions of Von Kármán. He added to the potential energy expression, a term for the work done by internal pressure. The effect of internal pressure is to reduce the deformation caused by the closing in-plane bending moment. Hence, the internal pressure tends to reduce the flexibility of the pipe bend when added to a closing bending moment and it reduces the bending stresses on the pipe.

Rodabaugh and George in 1957 derived the flexibility and stress intensification factors for pressurized pipe bends under in-plane closing bending moment. In this study, the internal pressure is

added to the potential energy equation as a work done to change the cross-sectional area of the pipe. They followed Von Kármán's assumptions and used an inextensible cross-section to simplify the mathematical procedure and developed the factors for long radius bends. The pipe wall thickness (t) and the cross-sectional radius (r) were ignored compared to the bend radius (R). The effect of the internal pressure was considered by a simple extension of the energy method used by Kármán. A more comprehensive analysis is done by Rodabaugh and George where up to the fourth term of the series equation of the energy were considered to obtain explicit expressions for the flexibility and stress intensification factors. By including the internal pressure, the flexibility and the stress intensification factors depend not only on the beam parameter (λ) but also on a new parameter ($\psi = PR^2/Ert$). The derived third and fourth approximation equations are complicated and time-consuming to apply. Therefore, a simplified approximated formula is derived where these factors are currently used in the nuclear power piping code (B31.1) and presented as follows;

$$K_p = \frac{K}{1 + \frac{S}{E} X_k}, \geq 1 \quad (1.6)$$

$$i_p = \frac{i}{1 + \frac{S}{E} X_i}, \geq 1 \quad (1.7)$$

Where,

$S = Pr/t =$ stress due to internal pressure in a straight pipe, psi,

$P =$ internal pressure, psi

$E =$ modulus of elasticity of pipe material, psi

$$X_k = 6 \left(\frac{r}{t} \right)^{4/3} \left(\frac{R}{r} \right)^{1/3}$$

$$X_i = 3.25 \left(\frac{r}{t} \right)^{3/2} \left(\frac{R}{r} \right)^{2/3}$$

Past studies were concerned with bends with a pipe factor (λ) greater than 0.3. Nicol Gross (1953) studied the flexibility of short radius bends of thin-walled section pipes subjected to internal pressure and in-plane closing bending moments. His main concern was to validate the adequacy of Kármán's factors for short bend radius with small pipe factor ($\lambda < 0.3$). He showed that the theoretical method based on Kármán's assumptions and analysis is inadequate for predicting the stresses and flexibility of bends of this type. In his analysis, Von Kármán assumed that the longitudinal stresses are the main reason behind the cross-sectional deformation and ignored the circumferential membrane strain for the sake of simplicity. This assumption helps in simplifying the mathematical analysis especially

when it deals with the displacements only. Although, when bending is applied to a pipe bend, the longitudinal stresses acting on the extrados and intrados of the pipe walls produce a resultant radial force which has to be balanced out. Since the radial stresses in a thin-walled pipe are negligible, compressive hoop stresses must exist to balance the radial stresses. This hoop stress is known as the hoop direct stress which is neglected by Von Kármán throughout the analysis. He assumed that the hoop direct stress was much smaller than the longitudinal stress thus not significantly affecting the strain energy. Gross determined the circumferential membrane force needed to sustain equilibrium by assuming that Kármán obtained the correct longitudinal membrane force in his analysis. He modified the circumferential stress on pipe bends by adding a corrective term “Transverse compressive stress due to bending”. He compared his theoretical results with experimental work and the modification is shown to be satisfactory down to values of pipe factor equal to 0.09 and R/r of 2.2. The drawback of his analysis is that the moment is only considered to be increasing the pipe bend curvature (Closing bending moment).

1.2.2.2. Mechanics-of-Materials Approach

Other researchers followed a different approach to analyse in-plane bending of pipe bends without internal pressure. Turner and Ford (1957) used a mechanics-of-materials approach to study pipe bends subjected to in-plane closing bending moment. Some of Kármán’s assumptions were considered in this study. However, Turner and Ford avoided two major assumptions in their analysis. The r/R parameter was not neglected relative to 1, nor was the cross-section assumed to be inextensible. These considerations made the derived formula applicable for both short and long radius bends. It may appear that ignoring the bore term ($R \pm r$) is critical for the case of “Short radius” bends. However, since the maximum stresses occur at the crown ($\varnothing=90^\circ$) where the bore term is actually (R), then the maximum stresses are unaffected by this assumption. This assumption may affect the regions closer to the intrados and extrados although the stresses in these areas are low; therefore, they are not critical for the design consideration. The error at the intrados and extrados arose from ignoring the bore term and was found to range between of 10% and 20%. However, ignoring the variation in the longitudinal strain through the wall thickness may result in an error of 40% and it may increase if the bore term is ignored at the same time. In their study, they ignored the effect of end conditions on the pipe bend behaviour and they assumed that plane sections remain plane and thus ignored the warping effect which increases the flexibility as well. However, the neutral axis after deformation needs not to remain at the centre of

the pipe cross-section. The formulas obtained from this approach showed good agreement with Kármán's results, with an error of 5% to 10%. However, due to the complexity of this approach, no further studies were done using this method to improve the results or include the effect of internal pressure.

1.2.2.3. Thin-Shell Theory Approach

In 1951, Clark and Reissner found that the simple formula of von Kármán was not accurate for the case of large diameter and thin-walled pipes (small Rt/r^2 values), and more terms in the radial displacement trigonometric series should be considered to obtain better results which may lead to a more complicated formula. They considered the curved pipe subjected to bending moment from the point of view of the thin elastic shell theory. In order to simplify the solution some approximations were assumed similar to Von Kármán assumptions. Clark and Reissner assumed small deformations for curvature and neglected the small displacement terms. The circumferential strain was assumed zero where the centreline circumferential length will not change after deformation. The plane sections perpendicular to the middle surface of the cross-section was assumed to remain plane after deformation. The developed flexibility (K) and stress-intensification factors (γ) by Clark and Reissner are presented currently in codes in the following simplified formula:

$$K = \frac{1.65}{\lambda} \quad (1.8)$$

$$\gamma = \frac{1.89}{\lambda^{2/3}} \quad (1.9)$$

1.2.2.4. Experimental Work

In 1952, Markl conducted an extensive series of fatigue tests on pipe bends subjected to in-plane and out-of-plane bending. From his fatigue test results, he derived a flexibility factor which exactly coincides with that proposed by Clark and Reissner. However, the stress intensification factor was half the factor from Clark and Reissner. The fatigue tests showed that the stress intensification factor for in-plane bending was slightly higher than the out-of-plane bending. The difference between the two

factors is not practically significant, therefore, for the sake of simplicity; the higher stress intensification factor is used for both in-plane and out-of-plane bending. The derived factors from Markl's fatigue tests are as follows;

$$K = \frac{1.65}{\lambda}$$

$$i = \frac{0.9}{\lambda^3}$$

The developed stress intensification factors are applicable only to the range of pipe sizes considered in the fatigue tests. However, the developed design factors based on these results are currently presented in the codes and applied to a wide size of range of bends. The flexibility factor derived from Clark and Reissner's analysis and from Markl's fatigue tests are currently presented in the codes such as; CSA Z662-15, ASME B31.1 and ASME B31.3. The Stress Intensification Factor from Markl's fatigue test is the one used in the current codes.

Nicol Gross (1953), conducted a series of experiments on short-bend radius pipes with thin-walled sections to investigate the strength and flexibility of seamless and welded bends subjected to in-plane closing bending with and without internal pressure. Since none of the previous studies deals with cases in which the R/r ratio is less than five, Gross found it necessary to establish whether the existing theory for curved tubes could be applied to short-radius bends where the bend radius (R) is only three times the pipe radius (r). The measured strains showed that the maximum strain on the inner surface is significantly larger than the strain on the outer layer of the pipe wall. Moreover, if a linear distribution of hoop strain is assumed, it was found that the hoop strain at the mid-layer is a compressive strain which indicates that Von Kármán's assumption is not justified. In addition, Gross showed that the additional hoop direct stress is more significant for short radius bends than long radius bends. The second assumption made by Kármán was that plane sections remain plane and that the cross-sectional ovalization is assumed equal along the bend length was proven to be invalid by Gross. He showed that the maximum ovalization of the cross-section is at the mid-length of the bend and tends to decrease as it approaches the end of the tangent attached pipes. As for the effect of internal pressure, it only improves the load-carrying capacity of the bend. Even if a lower internal pressure level was applied, the effect in improving the bend strength would be less noticeable but the bend is not weakened by internal pressure in any case.

1.2.2.5. Numerical Analysis Approach

Matzen and Yu (1998) investigated the B2 stress indices for pipe elbows subjected to in-plane opening and closing bending moments and out-of-plane bending. A 90-degree elbow with two attached straight pipes of length 5D are modelled using the Finite Element software ANSYS. They found that the minimum length for the straight pipe required in order to avoid the end boundary conditions effect on the elbow stresses is 5D. The results showed that the case of closing bending moment is governing the design since it has higher stress indices than the opening bending moment.

Joong-Hyok, et al. (2011) quantifies the elastic stresses at the mid-length of 90-degrees pipe elbows under in-plane opening and closing bending using detailed FE analysis. The pipe elbows are attached to two straight pipes with length 16 or 40 times the mean cross-sectional radius. Joong-Hyok extended the elastic stress limit analysis on pipe elbows to include a wider range of pipe diameter to wall thickness ratio from 10 to 25. He showed that for 90° pipe elbows, an in-plane bending moment produce axial and hoop bending stress components that are larger than the axial membrane stress. These components increase with the variation of the radius-to-thickness ratio and are found to be greatest at the crown location of the cross-section.

Shalaby and Younan (1999) investigated the plastic instability of 90-degrees standalone pipe elbows subjected to internal pressure and in-plane bending moment for the purpose of determining the limit loads for pipe elbows. The considered pipe elbows had a short radius bend ($R = 1.5 D$) and a pipe bend factor (λ) ranging from 0.0632 to 0.4417. They found that the direction of bending moment has no effect on the pipe elbows behaviour in the elastic range since they both yielded at the same bending moment value. However, in the plastic regime, the behaviour is affected by the bending moment direction since the cross-sectional ovalization starts to affect the elbow's stiffness. For unpressurized pipe elbows, the opening bending moment case reaches much higher loads and deformations than that of a closing bending moment. For pressurized pipes, the stiffness of elbows in the closing case is lower than the opening case since the deformation was higher. This study was based on short radius bends where the bend radius is three times the cross-sectional radius of the pipe ($R = 1.5 D$). Since the purpose of this study was to investigate the pipe elbow without any attached straight pipes, therefore, the end constraint effect was ignored. The effect of bend angle was not included in the study.

Chattopadhyay (2000) extended the work of Shalaby and Younan by adding two attached straight pipes to a 90-degrees pipe elbow and studied the behaviour under internal pressure and in-

plane bending. Chattopadhyay proposed closed-form collapse moment equations for pressurized pipe elbows subjected to opening or closing bending moments. The studied pipes had a D/t ratio ranging from 10 to 25 with an elbow factor (λ) of 0.24 to 0.6. The FEA results showed that the internal pressure enhances the collapse moment of an elbow up to a certain point beyond which it starts to decrease again. The ovalization of the cross-section plays an important role in determining the collapse moment since the internal pressure opposes the ovalization of the elbow thus delaying the occurrence of collapse. However, if the internal pressure exceeds a certain limit, the hoop stress due to the internal pressure overshadows the moment effect and leads to a reduction in the collapse moment.

1.3. PROBLEM STATEMENT

To date, the research studies on pipe bends and elbows were mostly focusing on studying the effect of bending moment on curved pipes. These studies investigated the ovalization of the pipe bend under in-plane or out-of-plane bending whether closing or opening moments and its influence on the pipe stresses. However, the effect of internal pressure loading on the bend behaviour was not thoroughly investigated and not clearly addressed in past studies. Past theoretical studies that attempted to develop a formula to estimate the hoop and longitudinal stresses on pipe bends considered the toroidal geometry on the stresses without considering the effect of the Bourdon forces on these stresses. Flügge (1973) and Goodall (1978) used the equilibrium of shell elements to propose an elastic stress solution for thin-walled elbows under internal pressure. The membrane bending of the bend cross-section resulting from the cross-sectional deformation was ignored, as well as the effect of the bend angle. A better understanding of the behaviour of pipe bends under internal pressure is investigated in this current study using finite element modelling and a factor is proposed to account for the Bourdon effect.

The main focus of the past research on pipe bends is directed towards the effect of bending moment on the stress solutions. In 1951, Clark and Reissner modified the factors proposed earlier by Von Kármán to cover a wider range of pipe bend geometry and pipe sizes. These flexibility factors (K) proposed by Clark & Reissner (1951) are based on a closing in-plane bending moment only and considered a standalone pipe neglecting any end effects. The obtained expressions were solved only for long radius bends and the final solution is almost similar to Von Kármán's. These factors are used in the current design codes as ASME B31.1, ASME B31.3 and CSA Z662-15 for the design of pipe elbows. These

studies were based on 90-degree pipe bends with long bend radius. The studies that followed Von Kármán used a different approach in solving the problem than what Kármán used but they followed his assumptions. The common drawback in these studies is that the circumferential length of the bend is considered inextensible where the circumferential strain is considered zero. The other common assumption is ignoring the pipe cross-sectional radius (r) with respect to the bend radius (R) which is only applicable for long bend radius pipes. The stress intensification factor currently used by the design codes are based on an extensive experimental study done by Markl (1952) where fatigue tests were carried on curved pipes with a particular range of bend sizes under closing in-plane bending moment. The resulted stress intensification factors are half the factors proposed by Clark and Reissner (1952).

The effect of adding internal pressure to the in-plane bending moment is quite complex since the superposition is not applicable due to the nonlinearity in the behaviour. Rodabaugh and George (1957) investigated the effect of adding an internal pressure to a closing bending moment on the flexibility and stress intensification factors. They found that the internal pressure would resist the ovalization of the pipe bend when subjected to bending moment, which accordingly will reduce the pipe bend flexibility and reduce the stress levels. They proposed a pressure reduction factor to modify the flexibility and SIF factors. Rodabaugh and George explained that the modified factors took into consideration the effect of internal pressure on the ovality and flexibility of the bend. However, it is not clear whether the Bourdon effect was considered or not in these modified factors. Moreover, Rodabaugh and George formulas were based on some approximations such as neglecting the second and higher order terms from the radial displacement trigonometric equation. They stated in their study that this approximation is accepted for pipe bends with beam parameter (λ) greater than or equal 0.5. Recent studies conducted by L. Asnawi & T. Boyle (2004) showed that the Rodabaugh and George proposed formulas are not accurate in case of thin-walled pipes with large diameters. The ASME B31.3 process piping design code adopted the modified formulas from Rodabaugh and George (1957) that considered the internal pressure as a load resisting the ovalization only. However, it is also important to include the "loading effect" due to the unbalance thrust forces occurring at the elbow location. Rodabaugh and George (1957) assumed an inextensible circumferential strain as well and by making this assumption, they neglected the direct circumferential strains and considered the bending circumferential strains only. Considering the circumferential strain of the mid-layer of the wall thickness in the solution may change the hoop stresses by 36% according to Nicol Gross (1952). Moreover, all

studies considered uniform ovalization along the pipe bend length. However, experimental tests showed that the ovalization varies and will affect the flexibility factor value (Findlay & Spence 1966).

The flexibility and SIF factors presented in the current design codes are shown to be used to magnify the bending stresses due to external loading such as dead loads and live loads however the factors are not used to magnify the stresses due to internal pressure. This is an observation that needs to be investigated since it is explained earlier that the internal pressure will cause an increase in the hoop and longitudinal stresses. Moreover, the factors presented in the design codes considered the effect of the bend radius, pipe radius and wall thickness, and the internal pressure was only considered in the ASME B31.3. However, the bend angle and the straight pipe length are not considered in these factors. These factors are important to be investigated as well.

While most of the studies focused on the effect of the internal pressure in reducing the stresses resulting from a closing bending moment on the pipe wall due to resisting the ovalization, they ignored the fact that the internal pressure causes the pipe bend to straighten out. Moreover, the effect of adding internal pressure to an opening bending moment is considered the critical case and was not considered in the proposed factors used by the current codes. The Bourdon effect resulting from the internal pressure was not thoroughly investigated in past studies and is not clearly addressed in any of the current design codes (CSA Z662-15, ASME B31.1 and ASME B31.3). These additional forces resulting from the internal pressure effect will cause unanticipated deformations and high stress levels that are not taken into account using the traditional design methods. Therefore, it is of great importance to study the influence of Bourdon effect as a function of pipe diameter, wall thickness, bend radius, bend angle, unrestrained pipe length and internal pressure.

1.4. AIM OF THE THESIS

The main objective of this study is to investigate the effect of internal pressure and in-plane opening and closing bending moment individually on the bend behaviour. The complex behaviour resulting from the interaction between the internal pressure and bending moment is investigated as well. A reassessment of the stress intensification factors and the pressure reduction factor equation is conducted using finite element analysis. An extensive study on the nonlinear behaviour of pipe bends is presented taking into consideration a wide range of pipe sizes, bend radius and bend angles. Based on

this study, a mathematical model is proposed to estimate the unbalanced outward thrust forces resulting from the internal pressure loading, known as the “Bourdon effect”. A “Pressure factor” is proposed that accounts for the increase in stresses due to the Bourdon effect. In this research study, the behaviour of pipe elbows is analysed numerically using ABAQUS 6.14 software. Based on an extensive parametric study, a new stress intensification factor and pressure reduction factor are proposed to account for the different bending moment directions and cover wide range of bend angles and geometries.

CHAPTER 2: THE BOURDON EFFECT AND BEHAVIOUR OF PRESSURIZED PIPE BENDS

2.1. INTRODUCTION

In the past, expansion bends and curved pipes were used in practice to absorb the expansion of a straight pipeline. Expansion bends were used under the condition that the bend is not overstressed and that the force that will deflect the bend by a required amount is not greater than what the pipeline or its anchorage can safely sustain (Turner & Ford, 1957). Nowadays, Elbows or pipe bends are considered one of the main components in any pipeline system and are frequently used to change directions. The location of pipe elbows in the pipeline system is often the location that shows high-stress levels and this is due to its high flexibility. The increase in flexibility of pipe bends compared to straight pipes is a result of the ability of the pipe bend to straighten out and the cross-section to ovalize. When a smooth pipe bend is subjected to internal pressure, an outward force is generated due to the difference between the intrados and extrados surface area that cause the bend to straighten out. This phenomenon is known as the “Bourdon effect” which results in an increase in the displacement and stress levels in pipe bends. When the pipe bend tends to straighten out, cross-sectional deformation takes place leading to additional bending stresses on the pipe wall and this phenomenon is known as the “Ovalization effect”. Past studies investigated the “Ovalization effect” for pipe bends subjected to bending moment only and developed stress intensification factors “SIF” to account for the increase in pipe stresses (Bantlin, 1910; Von Kármán, 1911; Clark & Reissner, 1951). These SIF factors are representing the increase in stresses due to the ovalization effect resulting from the applied bending moment, although the ovalization of the cross-section could occur due to internal pressure as well depending on the level of internal pressure applied. Past studies investigated the effect of adding internal pressure loading to the bending moment but the Bourdon effect was not clearly mentioned and was not evaluated (Rodabaugh & George. 1957). If these effects due to the internal pressure loading are not taken into consideration during the design of pipe bends and elbows, unanticipated deformations and high-stress levels could occur at the elbow location that may not be accounted for in traditional stress analysis. A better understanding of the influence of the Bourdon effect on the pipe bend behaviour is required.

Numerical and analytical analyses are used in this investigation on a range of pipe sizes (NPS) with different bend angles (α) and bend radii (R). The objective of this study is to get a better understanding of the “Bourdon effect” and its influence on the pipe bend behaviour. The FEA stress results are compared to the predicted stresses using the current design code formulas to investigate the applicability of the Design Code criteria for pipe bends. In the current study, a theoretical method is used to derive a mathematical model that estimates the outward forces resulting from the Bourdon effect. The proposed mathematical model is verified using finite element analysis models. A proposed pressure factor (K_p) is developed to account for the increase in stresses resulting from the Bourdon and Ovalization effects. Based on the understanding of the influence of internal pressure on pipe bends, an approach of modelling pipeline systems using Beam elements is proposed by which the Bourdon and Ovalization effects are incorporated in the FEA analysis. ABAQUS software is used where a study is conducted on the different elements provided by the software. The difference in stress results between modelling pipe bends using Shell elements and Beam elements are investigated and presented as well.

2.2. METHODOLOGY

This section is divided into four parts. The first part presents an analytical method used to estimate the outward forces resulting from the Bourdon effect on pipe bends. The second part aims to evaluate the influence of the Bourdon effect on pipe stresses using the Finite Element Analysis method and proposing a new pressure factor that accounts for the increased stresses. The third part presents a proposed approach of modelling pipe bends in ABAQUS using beam elements taking into consideration the ovalization and Bourdon effect. The applicability of this approach for different piping software programs used by the industry could be studied in the future. The proposed modelling approach aim to provide a design criterion that maintains the pipeline safety and integrity as well as the safety of the environment. The fourth and last part presents some developed formulas from past studies that were proposed to estimate the stresses on pipe bends subjected to internal pressure and a comparison with the current study results is conducted as well.

2.2.1. Developing a mathematical model for the Bourdon effect forces

The outward forces resulting from the Bourdon effect on a pipe elbow is derived from the equilibrium of a shell element. An infinitesimal area of the pipe elbow is studied under the effect of internal pressure loading as shown in figure (2. 1). The internal pressure is assumed to be acting perpendicular to the infinitesimal area. The total force acting on the bend is obtained by integrating the pressure acting on the infinitesimal area assuming a circular cross-sectional pipe bend with a variable bend angle (α).

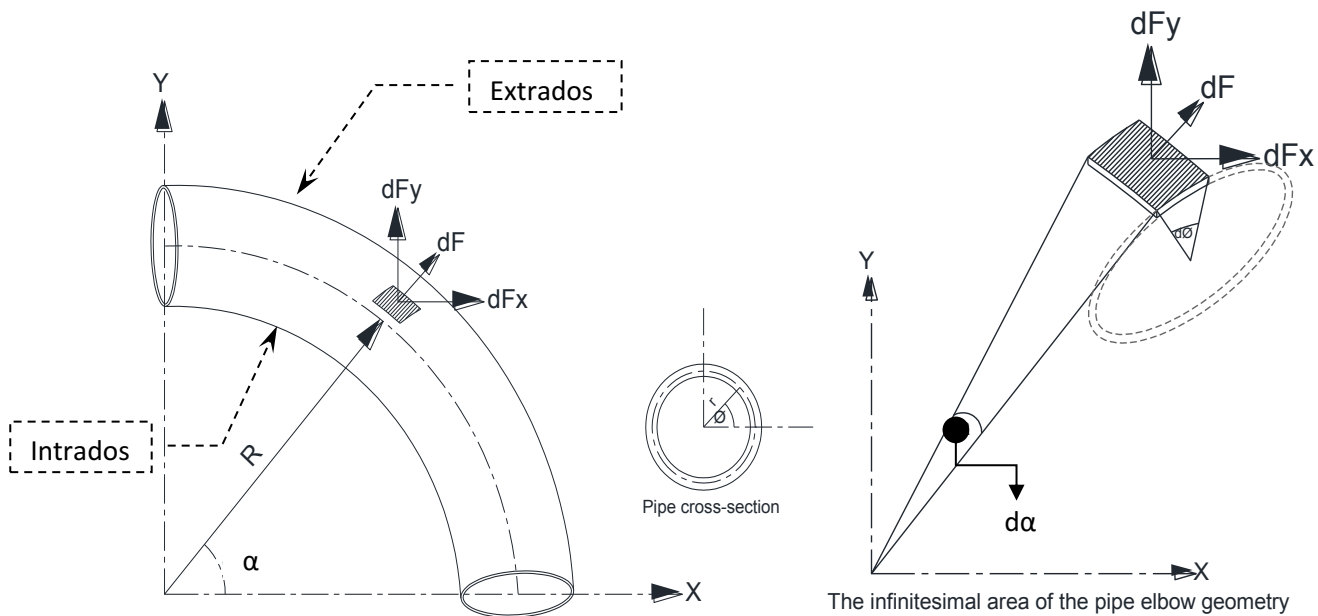


Figure 2. 1. The infinitesimal area on pipe elbow surface.

The infinitesimal area defined by the in-plane angle (α) and circumferential angle (ϕ) is as follows;

$$dA=(R+r \cos\phi)d\alpha.r d\phi$$

The force (dF) acting on the infinitesimal area (dA) resulting from the internal pressure (P) can be computed as;

$$dF=(PRr+Pr^2\cos\phi)d\alpha. d\phi$$

The two components of the in-plane outward total forces are computed as follows;

$$dF_x = dF \cdot \cos\phi \cdot \cos\alpha$$

$$dF_y = dF \cdot \cos\phi \cdot \sin\alpha$$

The components of the total outward force resulting from the Bourdon effect acting on the elbow surface is derived for a circular cross-sectional pipe by integrating the two force components (dF_x & dF_y) over the cross section (ϕ : 0 to 2π) and with respect to the bend angle (α). The total outward force in-plane components will be as follows;

$$F_x = \int_0^{2\pi} (PRr + Pr^2 \cos\phi) \cos\phi \cdot \cos\alpha \, d\phi \cdot d\alpha$$

$$= Pr \cos\alpha \cdot d\alpha \int_0^{2\pi} (R \cos\phi + r \cos^2\phi) \, d\phi = Pr^2 \pi \cos\alpha \cdot d\alpha = \int_0^\alpha Pr^2 \pi \cos\alpha \cdot d\alpha = Pr^2 \pi \sin\alpha \quad (2.1)$$

$$F_y = (PRr + Pr^2 \cos\phi) \cos\phi \cdot \sin\alpha \cdot d\phi = Pr^2 \pi \sin\alpha \cdot d\alpha = \int_0^\alpha Pr^2 \pi \sin\alpha \cdot d\alpha = -Pr^2 \pi \cos\alpha \quad (2.2)$$

The proposed model (equations 2. 1 & 2. 2) agrees with a past study that proposed the same mathematical model (Thiagarajan, 2013). A fixed-free standalone pipe bend is modelled using ABAQUS software in order to validate the proposed mathematical model. In these validation models, symmetry of the pipe bends geometry and loading is considered and half of the bend is modelled. A reference point is assigned at one of the pipe ends and denoted RP-1 as shown in figure (2. 2). This point is fixed while the other end of the pipe is free to rotate and translate. The circumference of the pipe at the fixed end is tied to RP-1 using a kinematic coupling constraint and the radial translation is allowed to enable the pipe to expand under internal pressure. The lines of intersection between the pipe wall and the plane of symmetry are prevented from translation in the direction perpendicular to the plane of symmetry (Y-direction) and rotation about X and Z axes is prevented as well as shown in figure (2. 2). Shell element (S4R) is used to model the pipe bends with an element size of 20x20. The pipe elbows are subjected to internal pressure that results in 80% SMYS hoop stress for steel grade X52. The mathematical model is verified for pipe elbows with bend angle equal to 40, 90 and 140 degrees. The matrix for the pipe sizes and geometry used in the verification are presented in table (2. 1).

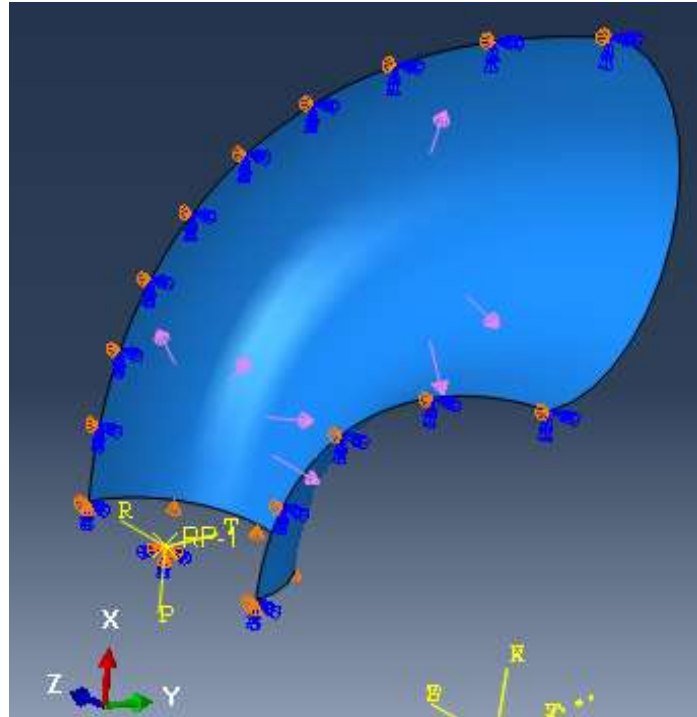


Figure 2. 2 Boundary conditions and loading for a stand-alone pipe elbow.

Table 2. 1. Geometric parameters of pipe elbow.

NPS	Outer Diameter (D, mm)	Bend radius (R, mm)	Elbow thickness (t, mm)	Bend angle (α)	Internal pressure (P, MPa)
12	323.85	323.85	9.525	40	16.94
				90	
				140	
24	609.6	609.6	9.525	40	9
				90	
				140	
42	1066.8	1066.8	9.525	40	5.143
				90	
				140	

2.2.2. Evaluating the Bourdon effect using Shell element models

First, a summary of the CSA-Z662 design methodology is presented in this section to show the equation used in predicting the stresses on pipe bends. Following it with a demonstration of the finite element model used to simulate the actual behaviour of pipe bends under the effect of internal

pressure and to quantify the influence of the Bourdon effect on the pipe bend stresses. Shell elements are used in the modelling to simulate the actual behaviour of bends and to consider the cross-sectional deformations. The FEA stress results are compared to the current CSA stress results to study the applicability of the code design criteria for pipe bends.

2.2.2.1. Current design Methodology by CSA-Z662

The Canadian Standards Association Code of Practice (CSA-Z662) provides a method to design a pipeline system under pressure and other external loadings. The methodology first proposes a pipe wall thickness using equation (2. 3) to sustain a given specific design pressure. After that the combined stresses are checked against the code limitations according to the given loading conditions.

$$P = \frac{2St}{D} F * L * T * J \quad (2. 3)$$

Where;

S: minimum tensile stress,

F: Design factor in CSA-Z662

L: Location factor in CSA-Z662

T: Temperature factor in CSA-Z662

J: Joint factor in CSA-Z662

The estimated combined stresses and the limitations presented in the CSA-Z662 differ according to the loading and the boundary conditions. To ensure the stability of the pipeline, the hoop stress due to the internal pressure combined with the net longitudinal stress due to the internal pressure and the temperature changes should be limited as follows;

$$S_h - S_L \leq 0.9 S X T \quad (2. 4)$$

Where,

S_h =Hoop stress due to design pressure, MPa.

$$S_h = \frac{PD}{2t}$$

S_L = Longitudinal compression stress, MPa.

$$S_L = US_h - E\alpha (T_1 - T_2) \quad (S_L \text{ is only considered if compression})$$

The combined stresses according to the code are shown to be the difference between the hoop stress and the net longitudinal compressive stress which is twice the maximum shear stress. For pipe bends subjected to internal pressure only, the longitudinal stress is ignored since it results in a tensile stress. Therefore, the combined stress is equal to the hoop stresses. Equation (2.4) which is presented in the CSA-Z662 lacks to differentiate between straight pipes and pipe bends, i.e., the Bourdon effect is not included. Therefore, Finite Element Modelling (FEM) is used in the next section to evaluate the increase in stresses on pipe bends subjected to internal pressure compared to straight pipes.

2.2.2.2. Modelling pipe bends using SHELL elements in ABAQUS

A pipeline system consisting of perfectly circular smooth pipes with constant thickness are modelled in ABAQUS using a 4-node reduced integrated Shell element (S4R) to capture the nonlinear complex behaviour of pipe bends. The pipeline system consists of a pipe bend with two attached straight pipes having fixed-fixed end constraints. Half of the pipe system is modelled for simplicity since the pipe system is considered to be symmetric about the X-Z plane as shown in figure (2. 3). The attached straight pipes have a length of 10 times the pipe outer diameter (D). According to a past study conducted by Matzen (1998), the length of the attached straight pipes considered in modelling to avoid the end effects should not be less than 10 D. The size of the attached straight pipes is the same as the pipe bend for each model. At the two ends of the pipe system, a reference point is assigned at the centre of the cross-section where the rotation and translation are fixed in all directions. These two reference points are tied to the circumference of the pipe at these locations using a kinematic coupling constraint where the radial deformation is allowed to enable expansion of the pipe under the effect of internal pressure. Moreover, the lines of intersection between the pipe wall and the plane of symmetry are prevented from translation in the direction perpendicular to the plane of symmetry (X-Z plane) and rotation about the X & Y axis as shown figure (2. 3). The pipe is meshed using a revolved sweep meshing with an element size of 15x15mm. The pipe system is subjected to internal pressure causing 80% SMYS

hoop stress (Steel grade X52). Nonlinear geometry is enabled in the analysis to account for large deformations and any nonlinearity in the behaviour.

In this study, the output from the FEA models is the Tresca stress and the displacement at the end of the pipe bend. The Tresca stresses extracted from ABAQUS is defined as the difference between the principle stresses, known as the hoop and longitudinal stress in this case. Therefore, using the Tresca criterion is found to be suitable since it is compared to the CSA-Z662 estimated combined stress. The combined stress according to CSA-Z662 is double the maximum shear stress which represents the same stress estimated by the Tresca criterion. The Tresca stress measured from the FEA is compared to the combined stress estimated using the CSA-Z662 formulas. The Tresca stress is defined as the maximum difference between the principal stresses which is considered twice the maximum shear stress. The critical section is at the mid-length of the pipe bend at section (A-A) as shown in figure (2. 4). The displacement of the pipe bend is measured at the end of the bend at section (B-B) as shown in figure (2. 4). Table (2. 2) shows the pipe geometry and loading for each model.

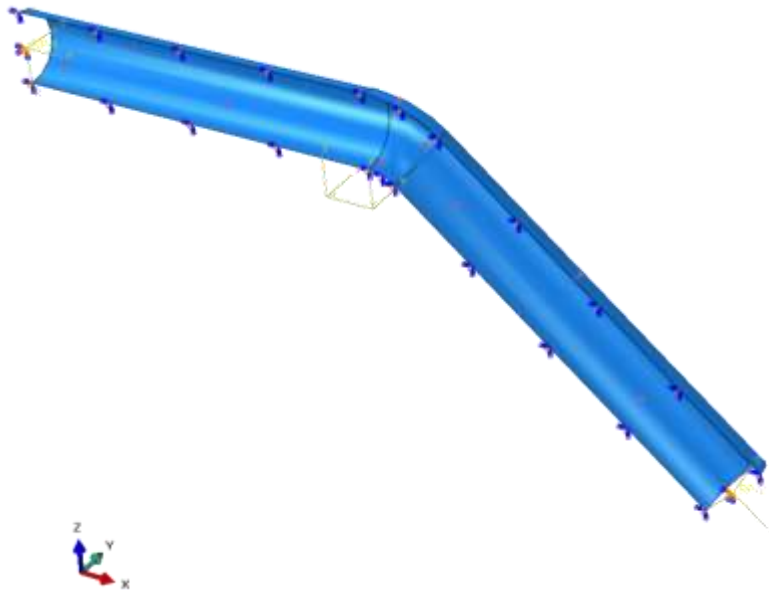


Figure 2. 3. Boundary conditions and geometry of the pipe model.

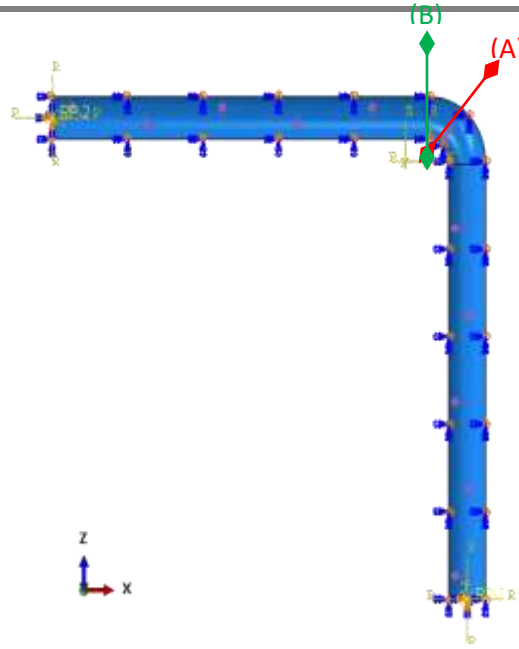


Figure 2. 4. Stress and displacement evaluated at Section (A-A) & (B-B).

Table 2. 2. The pipe geometry and loading for each test.

NPS	Beam parameter (λ)*	Outer diameter (D,mm)	Straight pipe length (L, mm)	Bend radius (R, mm)	Internal Pressure (P, MPa)	Bend angle (α , degrees)
12	0.125	323.85	3238.5	323.85	16.94	40
24	0.064	609.6	6096	609.6	9.00	40
42	0.036	1066.8	10668	1066.8	5.14	40
12	0.624	323.85	3238.5	1619.25	16.94	40
24	0.322	609.6	6096	3048	9.00	40
42	0.182	1066.8	10668	5334	5.14	40
12	0.125	323.85	3238.5	323.85	16.94	90
24	0.064	609.6	6096	609.6	9.00	90
42	0.036	1066.8	10668	1066.8	5.14	90
12	0.624	323.85	3238.5	1619.25	16.94	90
24	0.322	609.6	6096	3048	9.00	90
42	0.182	1066.8	10668	5334	5.14	90
12	0.125	323.85	3238.5	323.85	16.94	140
24	0.064	609.6	6096	609.6	9.00	140
42	0.036	1066.8	10668	1066.8	5.14	140
12	0.624	323.85	3238.5	1619.25	16.94	140
24	0.322	609.6	6096	3048	9.00	140

42	0.182	1066.8	10668	5334	5.14	140
----	-------	--------	-------	------	------	-----

* $\lambda = Rt/r^2$.

2.2.2.3. Developing a pressure factor K_p

A pressure factor (K_p) is developed in this section to account for the increase in the stresses due to the internal pressure acting on the inner surface of the pipe bend. First, a sensitivity analysis is conducted to evaluate the influence of each parameter considered in the new proposed factor. These parameters are the pipe cross-sectional outer radius (r), the bend radius (R) and the bend angle (α). Then a regression analysis is conducted to find an expression that best fits the relation between the increase in stress and the independent parameters. The ratio of the internal pressure causing a difference between the FEA and CSA stress results to the actual applied internal pressure are used as the data points in the regression analysis ($1+ \Delta P/P$). The equation used to evaluate the data points is as follows;

$$K_p = 1 + \frac{\Delta P}{P} = 1 + \left[\frac{(\sigma_s - \sigma_c)}{\sigma_c} \right] \tag{2.5}$$

Where,

$$\Delta P = \frac{\Delta \sigma * 2t}{D}$$

$$\Delta \sigma = \sigma_s - \sigma_c$$

ΔP = the internal pressure resulting in an increase in combined stresses between the Shell element and CSA results

σ_s = Tresca stress from the SHELL element ABAQUS model.

σ_c = $S_h - S_L$ (Combined stress according to CSA code.)

An expression that best fits the data points is developed and used to improve the CSA current design equation. The CSA equation used to evaluate the combined stress is modified by the proposed pressure factor (K_p) as shown in equation (2. 6).

$$K_p * (S_h - S_L) \leq 0.9 S X T \tag{2.6}$$

2.2.3. Propose a modelling approach

The objective of this section is to study the different elements incorporated in ABAQUS (Shell, Pipe and Elbow element). The accuracy of the computed deformations and stresses for a pipeline using different elements are compared and the results are discussed. Based on this investigation, an approach of modelling is proposed considering the Bourdon effect and the ovalization effect on the pipe stresses.

2.2.3.1. Different elements used in modelling

2.2.3.1.1. Beam element (PIPE31)

The beam element in ABAQUS follows the Euler-Bernoulli beam theory where the plane sections remain plane after deformation and perpendicular to the neutral axis. This means that any warping occurs to the cross-section as a result of the overall bend deformation or the cross-sectional deformation is not taken into consideration. ABAQUS ignores warping in the case of closed (thin-walled) sections such as pipes. A beam element is a one-dimensional line element in three-dimensional space. The simplicity in the Beam element's geometry is achieved by assuming that the beam member's deformation depends totally on variables that are function of position along the longitudinal axis of the beam (ABAQUS Users' Manual version 6.13). Another assumption is considered in the beam elements where the beam cross-section cannot deform in its own plane neglecting the ovalization effect. The "PIPE31" element is provided by ABAQUS to model beam with circular cross-sections. Two formulations are available for PIPE31 element in ABAQUS; the thin-walled and thick-walled formulations. The thin-walled pipe formulation is used in this investigation since the pipe wall thickness are small compared to the diameter ($D/t > 20$). The thin-walled pipe formulation assumes constant hoop stress across the cross-section and neglects the radial stress.

2.2.3.1.2. Elbow element (ELBOW31)

The Elbow elements are intended to provide accurate modelling of the nonlinear response of initially circular pipes and pipe bends when distortion of the cross-section by ovalization and warping dominates the behaviour. Element type "ELBOW31" is the most complete elbow element. In this element the ovalization of the pipe wall is made continuous from one element to the next, thus modelling such effects as the interaction between pipe bends (elbows) and adjacent straight segments of the pipeline (ABAQUS Users' Manual version 6.13). The integration points for the elbow section are

chosen to be 6 Fourier modes and 18 integration point around the pipe as recommended by ABAQUS for thin-walled pipes. The stress results are extracted at the Gauss integration points.

2.2.3.2. Finite element modelling

The pipe models are similar to the models presented in section (2.2.2) however beam elements are used instead of shell elements. A pipe bend with two attached straight pipes are modelled using ABAQUS. The lengths of the attached pipes are constant for all models and equal to 10 times the outer diameter of the pipe cross-section. The pipe bend and the straight pipes have consistent pipe size in each model. The pipes are assigned a beam profile section where the inner and outer diameters are defined. The pipes are modelled once using the “PIPE31” element and then using “ELBOW31”. The element size was controlled to be 20x20mm to have a consistent comparison with the Shell element model results. Two fixed constraints are assigned at the ends of the pipe system as shown in figure (2. 5). For pipes modelled using element “ELBOW31”, the nonlinear geometry is enabled in the analysis in order to account for the nonlinear strains in the cross-section such as the ovalization and warping, and the overall deformation of the pipe model. The internal pressure is assigned at the inner diameter of each pipe with a pressure causing 80% SMYS hoop stress. The difference in stress between the PIPE31, ELBOW31 and SHELL (S4R) elements are evaluated to get a better understanding on the limitations of each element. Based on this study a modelling approach is proposed to account for the increase in stresses due to the Bourdon effect. The proposed approach is based on magnifying the value of applied internal pressure at the elbow location by a value of K_p , which is the proposed pressure factor. For validation, the stress and displacement results from the PIPE31 and ELBOW31 element models are compared to the results of the SHELL element models.

In this section, the Tresca stresses at the mid-section of the elbow at section (A-A) are evaluated from ABAQUS for both PIPE31 and ELBOW31 elements. The average Tresca stress of the outer and inner surface of the pipe wall thickness is used in the case of ELBOW element. For the case of PIPE31 element, the hoop stresses are considered constant through the pipe wall thickness and the stress output is for the mean surface. The displacement of the pipe bend is evaluated at the end of the bend at section (B-B) as shown in figure (2. 5).



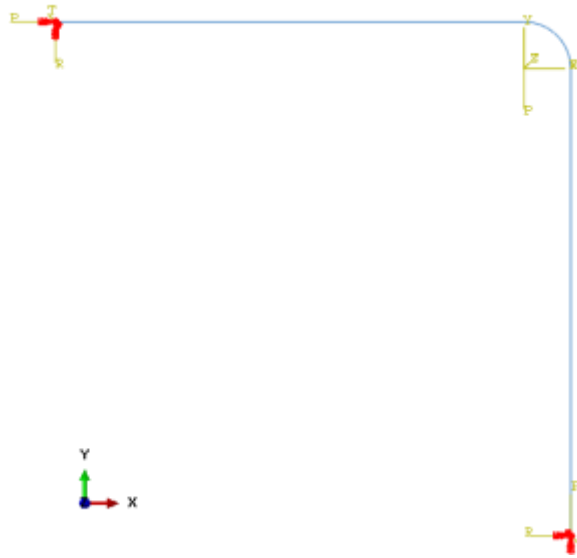


Figure 2. 5. Geometry and boundary conditions for pipe models using Beam element.

2.2.3.3. Check validity of the proposed modelling approach for back-to-back pipe bends

The proposed approach of modelling pipe bends is checked in this section for different pipeline systems. Two 90-degree pipe bends with short bend radius ($R = 1D$) are connected together with a straight pipe of length $5D$. Two straight pipes with length $20D$ are attached to the other end of the pipe bends as shown in figures (2. 6) and (2. 7). All connected pipes have the same pipe size and the average diameter is used in modelling these pipes. The two ends of the S-shape pipe system are fixed using a reference point tied to the circumference of the pipe using a kinematic coupling constraint as explained before in section (2.2.2). Half of the pipeline system is modelled due to the symmetry. Therefore, the lines of intersection between the pipe wall and the plane of symmetry are prevented from translation in the direction perpendicular to the plane of symmetry (X-Z plane) as shown figure (2. 6). The pipe is meshed using a revolved sweep meshing with an element size of $15 \times 15 \text{mm}$. The pipe system is subjected to internal pressure causing 80% SMYS hoop stress. The Tresca stresses at the pipe bend (section A-A) and at the horizontal straight pipe (section B-B) location shown in figure (2. 7) are measured and compared to the stresses from the pipe element model at the same locations.

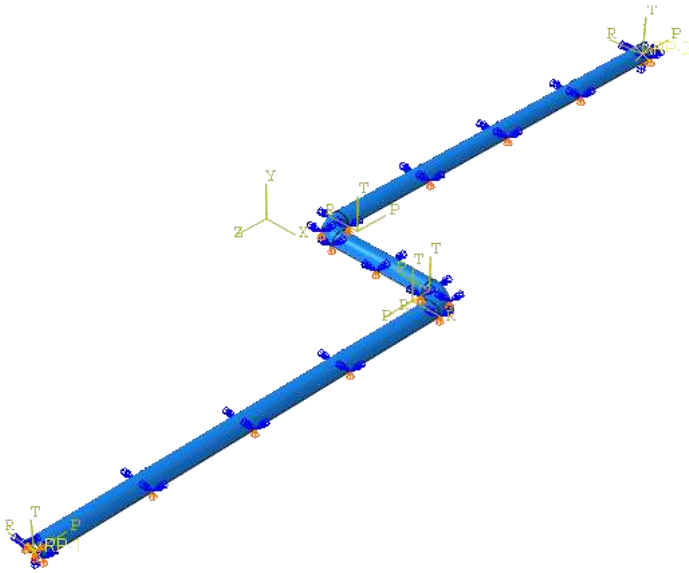


Figure 2. 6. Geometry and boundary condition for a back to back S-shape pipeline system using shell elements (S4R).

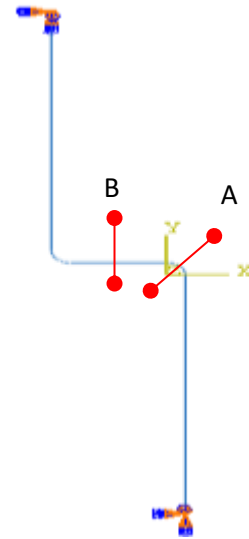


Figure 2. 7. Geometry and boundary condition for a back to back S-shape pipeline system using pipe elements (PIPE31).

The objective of this investigation is to ensure that the proposed modelling approach is valid for different pipeline systems and that the displacement resulted from the additional internal pressure at the pipe elbow is not affecting the whole pipeline system.

2.2.4. Comparison between FEA results and past studies

Several past studies attempted to develop mathematical models to evaluate the stresses on a curved pipe. These studies conducted a theoretical analysis based on the Shell theory to develop formulas for the stresses of a pipe bend. In this section, two past studies are compared to the FEA results of the current study (Goodall, 1978; Seok-Pyo Hong, 2010).

Goodall (1978) derived an analytical elastic stress solution for initially circular thin-walled elbows under internal pressure. This equation was derived using the equilibrium of shell elements ignoring the bending of the pipe wall. Goodall's proposed formulas shows that the toroidal effect

influences only the hoop stress leaving the longitudinal stress unaltered from that of a straight pipe. Goodall's elastic solution ignored the variation of hoop stress along the pipe bend length. However, it evaluates the hoop stresses at the mid-length of the pipe bend which is the critical location and the point of interest for the designer. He proposed the following stress solution for thin-walled elbows under internal pressure;

$$\sigma_h = \frac{Pr_i}{t} \left[\frac{2R + r_m \cos \phi}{2R + 2 r_m \cos \phi} \right] \quad (2.7)$$

$$\sigma_L = \frac{Pr}{2t} \quad (2.8)$$

Where,

r_m : mean radius of the pipe bend cross-section,

ϕ : is the circumferential angle measured from the intrados towards the extrados. (Varying from $\phi=0$ at the extrados and $\phi=\pi$ at the intrados).

Seok-Pyo Hong (2010), extended the work of Goodall (1978) to evaluate hoop stresses for thick-walled elbows. Moreover, he proposed an equation to evaluate the hoop stress at any point along the longitudinal direction of the pipe bend. His formula depends on the mean radius and the circumferential angle as defined by Goodall. This current study is compared to Hong's thin-walled formula for the location of maximum hoop stresses which is the mid-length of the pipe bend. Hong's formula is as follows where " ϕ " is as explained before for Goodall's formula;

$$\sigma_h = \frac{Pr_i}{t} \left[\frac{4R + 3 r_m \cos \phi}{4R + 4 r_m \cos \phi} \right] \quad (2.9)$$

2.3. RESULTS

2.3.1. Validating the proposed mathematical model for the Bourdon effect forces

The outward forces determined from the proposed mathematical models equations (2. 1) and (2. 2) are compared to the fixed end reaction forces obtained from the FEA for the bends with different

bend angles. Comparison between the FEA reactions and the proposed model predictions are shown in Table (2. 3). The proposed mathematical model showed an excellent agreement with the FEA results.

Table 2. 3. Reaction forces from FEA compared to the proposed mathematical model.

NPS	Bend angle (α)	F _x (FEA) (KN)	F _y (FEA) (KN)	F _x (Eqn.) (KN)	F _y (Eqn.) (KN)	F resultant (FEA) (KN)	F resultant (Eqn.) (KN)
12	40	843.67	307.07	845.29	307.66	897.81	899.54
	90	1313.602	1313.602	1315.03	1315.03	1857.71	1859.73
	140	843.67	2317.96	845.29	2322.41	2466.72	2471.46
24	40	1635.43	595.25	1636.76	595.73	1740.39	1741.80
	90	2543.44	2543.44	2544.04	2544.04	3596.97	3597.82
	140	1635.43	4493.3	1636.76	4496.97	4781.67	4785.57
42	40	2901.86	1056.19	2903.41	1056.75	3088.09	3089.74
	90	4595.9	4595.9	4598.83	4598.83	6499.58	6503.73
	140	2901.86	7972.76	2903.41	7977.04	8484.44	8488.99

Equations (2. 1) & (2. 2) show that the Bourdon forces are independent of the bend radius. To verify this conclusion, A pipe bend with pipe size NPS 12 and bend angle 90° is modelled with a bend radius (R) equal to 5D and compared with the result of the second model presented in table (2. 3) which is a similar bend but with short radius bend (R=1D). The Bourdon forces from the long radius bend (R=5D) is 1313.602 KN and 1313.602 KN in X and Y directions, respectively. The results are exactly similar to the short radius bend which shows the accuracy and validity of the developed mathematical model.

2.3.2. Evaluating the Bourdon effect using Shell element models

2.3.2.1. Current Methodology by CSA-Z662

Figures (2. 8) to (2. 11) show the Tresca stress results versus the beam parameter (λ) for pipe bends with different bend angles (α) and variable pipe sizes (NPS 12, 24 & 42). The beam parameter is an indication of the pipe bend flexibility. As the beam parameter decrease, the bend flexibility increase which leads to an increase in the stress levels on the pipe bend. Table (2. 4) shows the value of Tresca stresses from each FEA model and the corresponding estimated CSA combined stress and the difference between these two values defined as $\Delta\sigma$. Table (2. 4) shows a column presenting an additional value of

internal pressure (ΔP). This value of internal pressure (ΔP) is the value resulting in a hoop stress with a value of ($\Delta \sigma$). Figures (2. 8) and (2. 9) show the Tresca stress results for pipe bends subjected to internal pressure resulting in 80% SMYS hoop stresses. While, figures (2. 10) and (2. 11) show the stress results for pipe bends subjected to internal pressure resulting in 30% SMYS hoop stress. For the short bend radius pipes ($R= 1D$) subjected to internal pressure causing 80% SMYS hoops stress, the critical case is the pipe bends with size NPS 42 with bend angle 90 or 140 degrees where the maximum Tresca stress is 424.33 and 423.41 MPa, respectively. For all the studied bends, the combined stress estimated using CSA formula is 288 MPa since the code equation ignores the bend angle and bend radius. In the case of low internal pressure where the pipes are subjected to internal pressure causing 30% SMYS hoop stress, the maximum Tresca stress is 159 MPa while the CSA combined stress is 108 MPa. The results show that the Bourdon effect causes an increase in the combined stress by up to 47.4% for short bend radius pipes whether the pipe is subjected to a high or low internal pressure level.

For the long bend radius pipes ($R= 5D$) subjected to internal pressure causing 80% SMYS hoop stress, the highest Tresca stress was found to be in pipes NPS 42 with bend angle 140 degrees. The maximum stress is 301.4 MPa while the combined stress estimated using CSA is 288 MPa. In the case of low internal pressure where the pipes are subjected to internal pressure causing 30% SMYS hoop stress, the maximum Tresca stress is 113 MPa, while the CSA combined stress is 108 MPa. The results show that the Bourdon effect increases the combined stresses by up to 4.65% for long bend radius pipes. As the bend radius increases, the pipe bend approaches the behaviour of a straight pipe, therefore the influence of the Bourdon effect on the stresses decreases. Since the CSA estimated stresses are based on the straight pipe formulas, therefore as the bend radius increase, the difference between the FEA and the CSA results decreases. It is concluded that the combined stresses evaluated using the CSA equation is un-conservative since the actual stress on the pipe bend reaches up to 1.5 times the estimated stress.

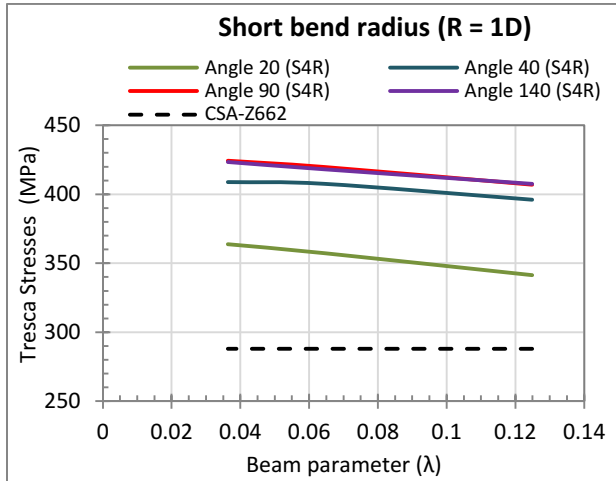


Figure 2. 8. Tresca stress result from the SHELL model vs CSA-Z662 for short radius bends subjected to internal pressure causing 80% SMYS hoop stress.

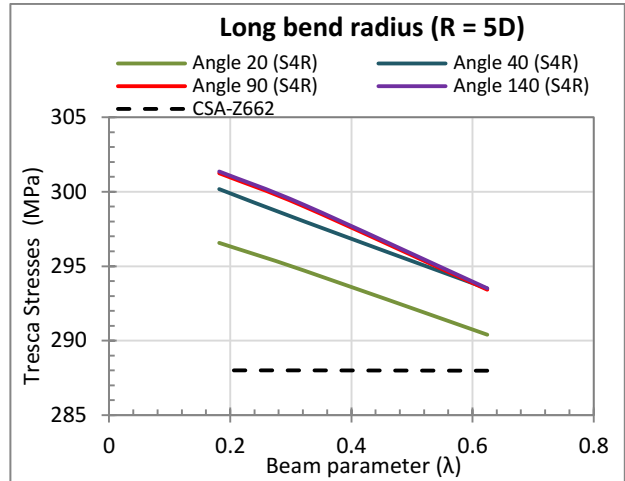


Figure 2. 9. Tresca stress result from the SHELL model vs CSA-Z662 for long radius bends subjected to internal pressure causing 80% SMYS hoop stress.

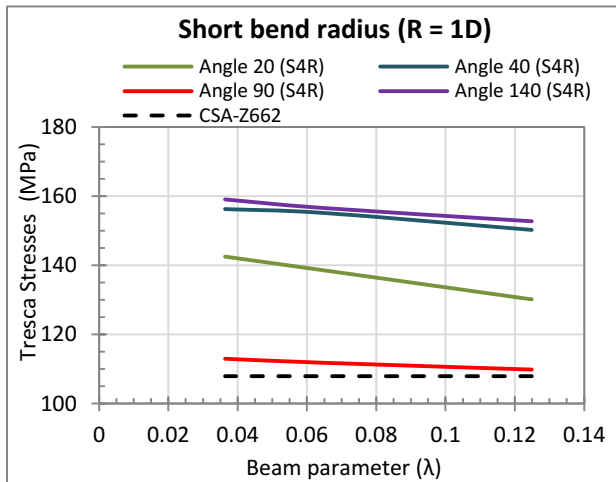


Figure 2. 10. Tresca stress result from the SHELL model vs CSA-Z662 for short radius bends subjected to internal pressure causing 30% SMYS hoop stress.

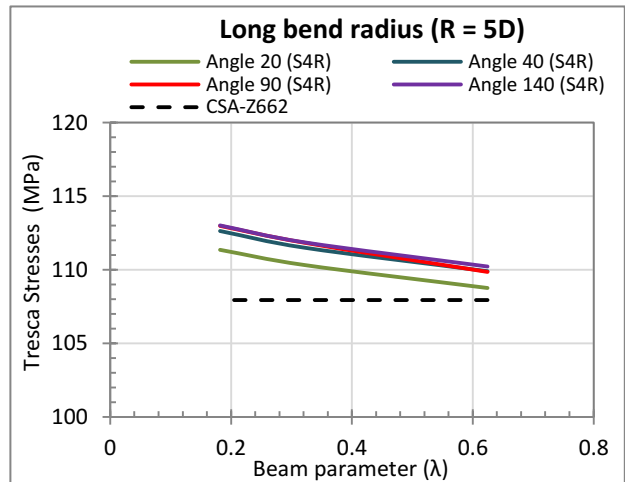


Figure 2. 11. Tresca stress result from the SHELL model vs CSA-Z662 for long radius bends subjected to internal pressure causing 30% SMYS hoop stress.

Table 2. 4. Tresca stress results from SHELL (S4R) element vs the CSA combined stress results for pipe bends subjected to internal pressure causing 80 % SMYS hoop stress.

NPS	Straight pipe length (L, mm)	Bend angle (α , degrees)	Bend radius (R, mm)	Shell Element (S4R) Tresca Stress	CSA-Z662.15 Combined stress (MPa)	Difference between S4R and CSA stress results. $\Delta\sigma$	Difference in internal pressure evaluated from the difference in stresses. ΔP
-----	------------------------------	----------------------------------	---------------------	-----------------------------------	-----------------------------------	---	---

CHAPTER 2

				(MPa)			
12	3238.5	20	323.85	341.373	287.98	53.393	3.14
24	6096	20	609.6	357.282	288	69.282	2.16
42	10668	20	1066.8	363.8035	288	75.8035	1.35
12	3238.5	20	1619.25	290.397	287.98	2.417	0.14
24	6096	20	3048	294.7	288	6.7	0.21
42	10668	20	5334	296.566	288	8.566	0.15
12	3238.5	40	323.85	396.078	287.98	108.078	6.36
24	6096	40	609.6	407.5665	288	119.5665	3.74
42	10668	40	1066.8	408.853	288	120.853	2.16
12	3238.5	40	1619.25	293.497	287.98	5.497	0.32
24	6096	40	3048	298.003	288	10.003	0.31
42	10668	40	5334	300.18	288	12.18	0.22
12	3238.5	90	323.85	406.9445	287.98	118.9445	7.00
24	6096	90	609.6	419.764	288	131.764	4.12
42	10668	90	1066.8	424.3285	288	136.3285	2.43
12	3238.5	90	1619.25	293.422	287.98	5.422	0.32
24	6096	90	3048	299.003	288	11.003	0.34
42	10668	90	5334	301.246	288	13.246	0.24
12	3238.5	140	323.85	407.546	287.98	119.546	7.03
24	6096	140	609.6	418.1155	288	130.1155	4.07
42	10668	140	1066.8	423.4095	288	135.4095	2.42
12	3238.5	140	1619.25	293.5135	287.98	5.5135	0.33
24	6096	140	3048	299.1115	288	11.1115	0.35
42	10668	140	5334	301.362	288	13.362	0.24

Figure (2. 12) shows the results for each pipe bend with different bend angle varying from 20 degrees to 140 degrees. Since the CSA-Z662 does not consider the bend angle in estimating the combined stress, therefore, the combined stress is found to be constant for different bend angles. The FEA results show that the Tresca stresses increase by 16.03 % when the bend angle increase from 20 to 40 degrees. However, the Tresca stress increase by 3.56 % when the bend angle increase from 40 to 140 degrees. Figure (2. 12) shows that as the bend angle increase, the stresses increase by a maximum of 19.4% for short bend radius pipes and by 1.9% for long bend radius pipes. Figure (2. 13) shows the displacement at

the pipe bend end against the bend angle for each pipe size. The results show that the displacement will decrease by 86 % as the bend angle increases from 20 to 140 degrees.

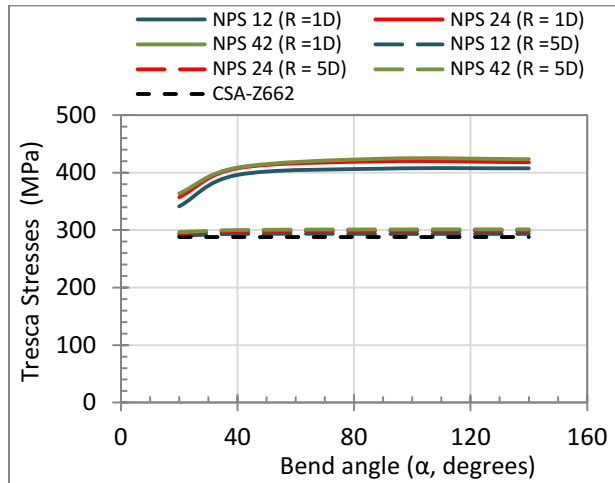


Figure 2. 12. Tresca Stress result vs the bend angle for different pipe bend size subjected to internal pressure causing 80% SMYS hoop stress.

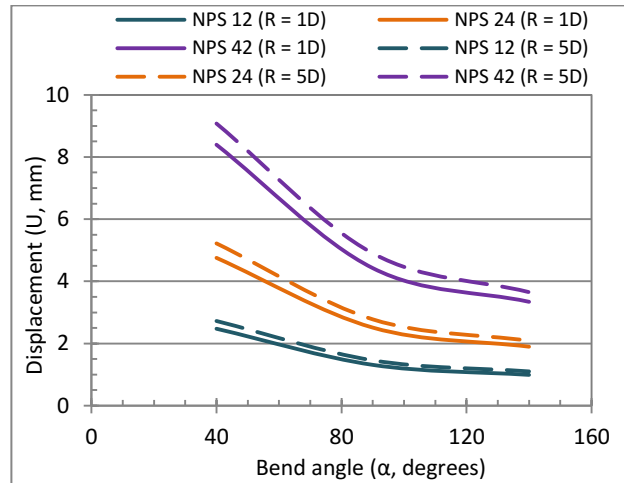


Figure 2. 13. FEA resultant displacement vs the bend angle for different pipe bend size subjected to internal pressure causing 80% SMYS hoop stress.

2.3.2.2. Proposed pressure factor (K_p)

In this section, a new factor is proposed taking into consideration the different effects influencing the pipe stresses where a range of parameters is covered. Figure (2. 14) shows the effect of the radius ratio (R/r) on the Tresca stress results. As the radius ratio increases, the pipe bend tends to approach the behaviour of a straight pipe and the stresses on the pipe decrease by up to 40.86 %. However, when the pipe slenderness (D/t) increases, the pipe gains more flexibility leading to higher stress levels. Figure (2. 15) shows that when the pipe bend slenderness (D/t) increases, the stresses on the pipe bend increase by up to 4.3% for short bend radius pipes and 2.1% for long bend radius pipes. The results show that the slenderness ratio of the pipe has a minor effect on the bend stresses and that the bend angle (α) has an effect when the bend angle is less than 40 degrees. Therefore, the slenderness ratio could be neglected in the proposed pressure factor (K_p) for simplicity.

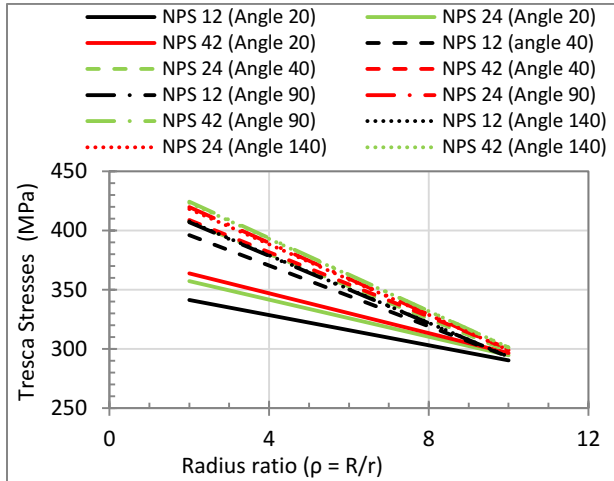


Figure 2. 14. Effect of radius ratio (R/r) on the Tresca stresses for different pipe bend size subjected to internal pressure causing 80% SMYS hoop stress.

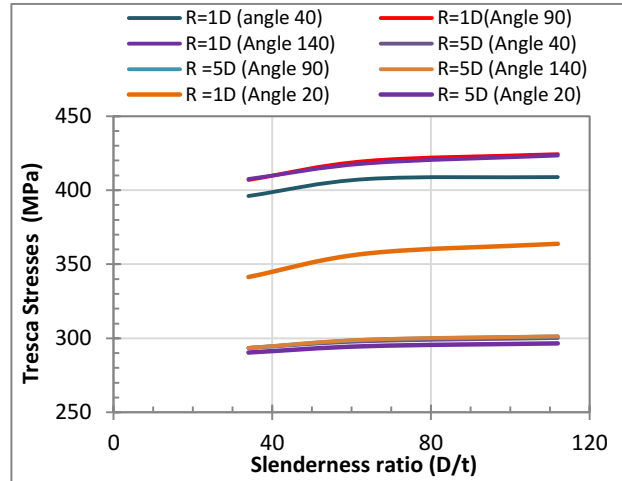


Figure 2. 15. Effect of bend slenderness ratio (D/t) on Tresca stresses for different pipe bend size subjected to internal pressure causing 80% SMYS hoop stress.

Based on the FEA results and the regression analysis, a new factor is proposed that considers the bend angle (α) and the radius ratio (R/r). This formula is developed for pipe bends with D/t ratio ranging from 34 to 112. A relation between the data points (K) shown in table (2. 5) and the considered parameters are expressed in equation (2. 10) as follows;

$$K_p = \left[1 + e^{-0.56\rho} \right] e^{0.031 \alpha} \tag{2. 10}$$

Where,

$$\rho = R/r$$

α : bend angle in radians.

The stress results and data points are presented in Table (2. 5). The pressure factor evaluated from equation (2. 10) is presented as well, along with the accuracy of each proposed factor. The error in this formula is found to lie within 7.9% and 0.63% except for one case where the pipe bend has a small cross-section (NPS 12) and a small bend angle (20 degrees) where the error is 12.43%. The accuracy of the proposed model presented in table (2. 5) is evaluated as follows;

$$\frac{\text{proposed factor} - \text{FEA factor}}{\text{FEA factor}} \%$$

Table 2. 5. The data points used in the regression analysis and the developed pressure factor (K_p) pipe bends subjected to internal pressure causing 80 % SMYS hoop stress.

NPS	α	Δ Hoop	ΔP	$\Delta P/P$	Required factor (Data points) (K) (computed by FEA)	New proposed factor (K_p) Eqn (2.10)	% Accuracy (K_p)
12	20	53.39	3.14	0.19	1.19	1.342	12.43%
24	20	69.28	2.17	0.24	1.24	1.342	7.89%
42	20	75.80	1.35	0.26	1.26	1.342	6.09%
12	20	2.42	0.14	0.01	1.01	1.015	0.63%
24	20	6.70	0.21	0.02	1.02	1.015	0.84%
42	20	8.57	0.15	0.03	1.03	1.015	1.47%
12	40	108.10	6.36	0.38	1.3754	1.357	1.33%
24	40	119.57	3.74	0.42	1.4152	1.357	4.19%
42	40	120.85	2.16	0.42	1.4196	1.357	4.50%
12	40	5.52	0.32	0.02	1.0192	1.026	0.65%
24	40	10.00	0.31	0.03	1.0347	1.026	0.87%
42	40	12.18	0.22	0.04	1.0423	1.026	1.59%
12	90	118.96	7.00	0.41	1.4131	1.394	1.33%
24	90	131.76	4.12	0.46	1.4575	1.394	4.42%
42	90	136.33	2.43	0.47	1.4734	1.394	5.50%
12	90	5.44	0.32	0.02	1.0189	1.054	3.39%
24	90	11.00	0.34	0.04	1.0382	1.054	1.51%
42	90	13.25	0.24	0.05	1.0460	1.054	0.77%
12	140	119.57	7.03	0.42	1.4152	1.433	1.24%
24	140	130.12	4.07	0.45	1.4518	1.433	1.32%
42	140	135.41	2.42	0.47	1.4702	1.433	2.57%
12	140	5.53	0.33	0.02	1.0192	1.083	6.07%
24	140	11.11	0.35	0.04	1.0386	1.083	4.19%
42	140	13.36	0.24	0.05	1.0464	1.083	3.44%

Figures (2. 16) & (2. 17) show the results of the FEA shell models compared to the original CSA estimated stresses and the modified CSA estimated stresses presented in equation (2. 6). Tables (2. 6) and (2. 7) show the accuracy of the proposed pressure factor (K_p) when compared to the S4R shell element model stress results where the error lies between 8% to 0.6% for both high and low internal pressure levels. The comparison shows a good agreement.

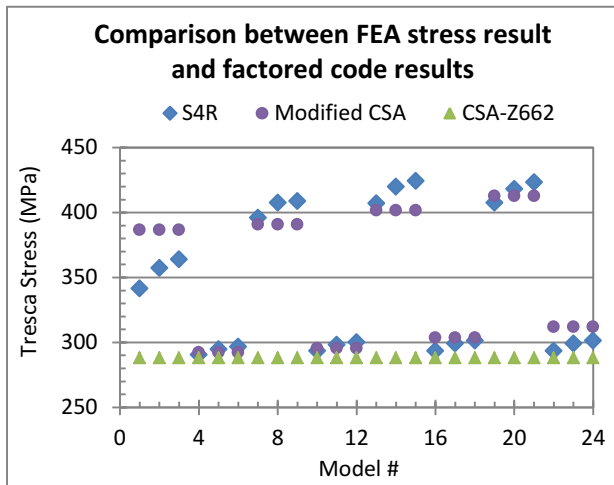


Figure 2. 16. Tresca stress results from the SHELL element model vs the CSA results and the factored CSA results for pipes subjected to internal pressure causing 80% SMYS.

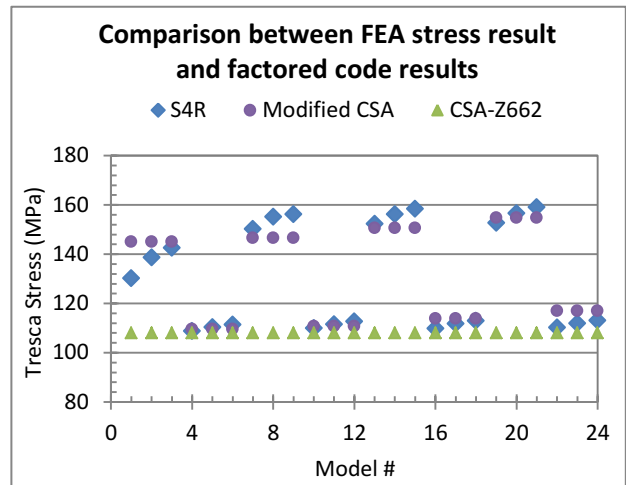


Figure 2. 17. Tresca stress results from the SHELL element model vs the CSA results and the factored CSA results for pipes subjected to internal pressure causing 30% SMYS.

Table 2. 6. Accuracy of the modified CSA-Z662 equation compared to S4R model results for pipe bends subjected to internal pressure resulting in 80% SMYS hoop stress

NPS	Straight pipe length (L, mm)	Bend angle (α , degrees)	Bend radius (R, mm)	Tresca Stress (MPa) Shell Element (S4R)	CSA-Z662 Combined Stress (MPa)	Factored CSA-Z662 Combined Stress (MPa)	% Accuracy
12	3238.5	20	323.85	341.373	288	386.61	12.43%
24	6096	20	609.6	357.282	288	386.64	7.89%
42	10668	20	1066.8	363.8035	288	386.64	6.09%
12	3238.5	20	1619.25	290.397	288	292.23	0.63%
24	6096	20	3048	294.7	288	292.25	0.84%
42	10668	20	5334	296.566	288	292.25	1.47%
12	3238.5	40	323.85	396.078	288	390.83	1.33%
24	6096	40	609.6	407.5665	288	390.86	4.19%
42	10668	40	1066.8	408.853	288	390.86	4.50%
12	3238.5	40	1619.25	293.497	288	295.41	0.65%
24	6096	40	3048	298.003	288	295.44	0.87%
42	10668	40	5334	300.18	288	295.44	1.59%
12	3238.5	90	323.85	406.9445	288	401.58	1.33%
24	6096	90	609.6	419.764	288	401.60	4.42%

CHAPTER 2

42	10668	90	1066.8	424.3285	288	401.60	5.50%
12	3238.5	90	1619.25	293.422	288	303.54	3.39%
24	6096	90	3048	299.003	288	303.56	1.51%
42	10668	90	5334	301.246	288	303.56	0.77%
12	3238.5	140	323.85	407.546	288	412.62	1.24%
24	6096	140	609.6	418.1155	288	412.65	1.32%
42	10668	140	1066.8	423.4095	288	412.65	2.57%
12	3238.5	140	1619.25	293.5135	288	311.88	6.07%
24	6096	140	3048	299.1115	288	311.91	4.19%
42	10668	140	5334	301.362	288	311.91	3.44%

Table 2. 7. Accuracy of the modified CSA-Z662 equation compared to S4R model results for pipe bends subjected to internal pressure resulting in 30% SMYS hoop stress

NPS	Straight pipe length (L, mm)	Bend angle (α , degrees)	Bend radius (R, mm)	Tresca Stress (MPa) Shell Element (S4R)	CSA-Z662 Combined Stress (MPa)	Factored CSA-Z662 Combined Stress (MPa)	% Accuracy
12	3238.5	20	323.85	130.1508	108	144.98	10.78%
24	6096	20	609.6	138.6045	108	144.99	4.50%
42	10668	20	1066.8	142.517	108	144.99	1.72%
12	3238.5	20	1619.25	108.761	108	109.59	0.75%
24	6096	20	3048	110.3153	108	109.59	0.66%
42	10668	20	5334	111.3541	108	109.59	1.59%
12	3238.5	40	323.85	150.2385	108	146.56	2.48%
24	6096	40	609.6	155.167	108	146.57	5.70%
42	10668	40	1066.8	156.257	108	146.57	6.40%
12	3238.5	40	1619.25	109.9007	108	110.78	0.80%
24	6096	40	3048	111.493	108	110.79	0.63%
42	10668	40	5334	112.634	108	110.79	1.65%
12	3238.5	90	323.85	152.337	108	150.59	1.15%
24	6096	90	609.6	156.213	108	150.60	3.66%
42	10668	90	1066.8	158.3845	108	150.60	5.04%
12	3238.5	90	1619.25	109.8545	108	113.83	3.55%
24	6096	90	3048	111.828	108	113.83	1.78%
42	10668	90	5334	112.982	108	113.83	0.75%
12	3238.5	140	323.85	152.733	108	154.73	1.30%
24	6096	140	609.6	156.592	108	154.74	1.19%

42	10668	140	1066.8	159.05	108	154.74	2.75%
12	3238.5	140	1619.25	110.2205	108	116.96	5.93%
24	6096	140	3048	111.856	108	116.96	4.47%
42	10668	140	5334	113.0135	108	116.96	3.44%

2.3.3. Proposed modelling approach:

Figure (2. 18) shows the distribution of Tresca stresses on half of the pipe cross-section starting from the intrados ($\varnothing=0$) going to the extrados ($\varnothing = 180$). The stresses are found to be higher at the outer surface of the pipe at the intrados and extrados location. However, the inner surface of the pipe has higher stresses at the crown location and this depends on the shape of ovalization.

The Tresca stresses are twice the maximum shear stress and since the longitudinal stress is in tension, the maximum shear stress is based on the hoop stresses only. Therefore, in the current chapter, the Tresca stresses are always equal to the hoop stresses. The hoop stress distribution is a result of the bending of the pipe wall. Therefore, the shape of the cross-sectional deformation can be identified from the hoop stress distribution. In this case, it can be concluded from the hoop stress results shown in figure (2. 18) that the intrados and extrados are pulled further away from the pipe centre while the crown is pushed towards the centre of the pipe cross-section resulting in an oval shape with the major axis is in the plane of symmetry. The average of the inner and outer surface stresses is used in the comparison to the PIPE and ELBOW element model.

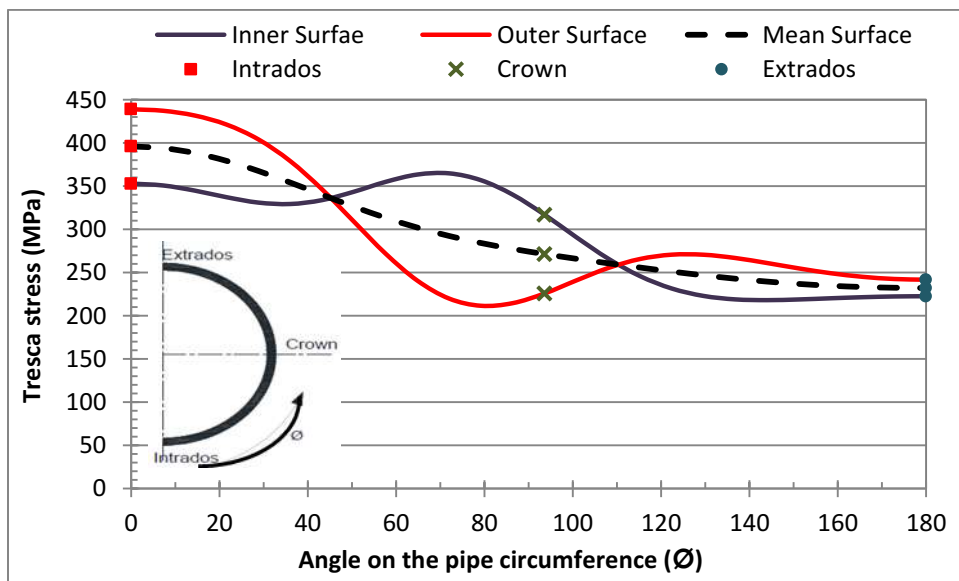


Figure 2. 18 The distribution of Tresca stresses along half the pipe cross-section at the mid-section of pipe bend for Shell element model.

Figure (2. 19) shows the distribution of Tresca stresses along the pipe cross-section in case of using a Pipe element and an Elbow element. These stresses are evaluated at the mid-section of the pipe bend. The Elbow element captures ovalization effect. Therefore, there is an increase in stress considered in the Elbow elements than that from the Pipe elements. In the case of Elbow elements, the stress varies along the pipe cross-section with a maximum value at the intrados which agrees with the Shell element model results. On the other hand, the Pipe element is based on a constant hoop stress along the pipe cross-section. This difference between the two elements will result in Tresca stresses in the Elbow element higher by up to 4% than the Pipe element results. Figure (2. 20) shows the Tresca stresses evaluated from the S4R, PIPE and ELBOW element models plotted for all the studied bends. Figure (2. 21) shows the distribution of stresses from the S4R element model and the ELBOW31 element model where the difference at the intrados is up to 41%. The ELBOW31 element captures the additional stresses generated from the ovalization of the cross-section but ignores the Bourdon effect. Since the cross-sectional deformations (ovalization) due to the internal pressure are not significant, therefore, the major influence on the stresses is the Bourdon effect which is ignored by the ELBOW elements. Therefore, there is a discrepancy in the extracted stresses between the S4R and the ELBOW 31 elements as shown in figure (2. 21).

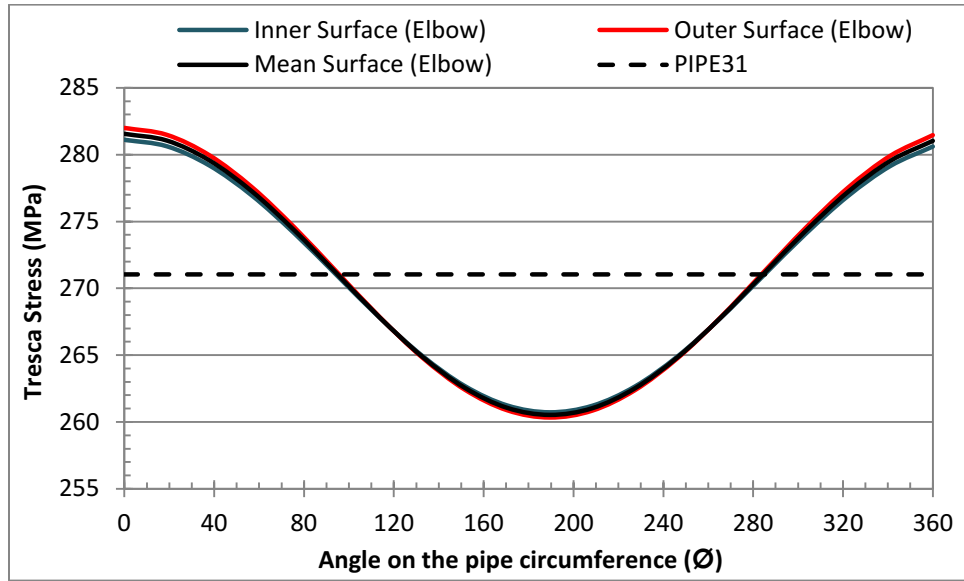


Figure 2. 19. The distribution of hoop stress along the pipe cross-section at mid-section of pipe bend for Pipe and Elbow element model.

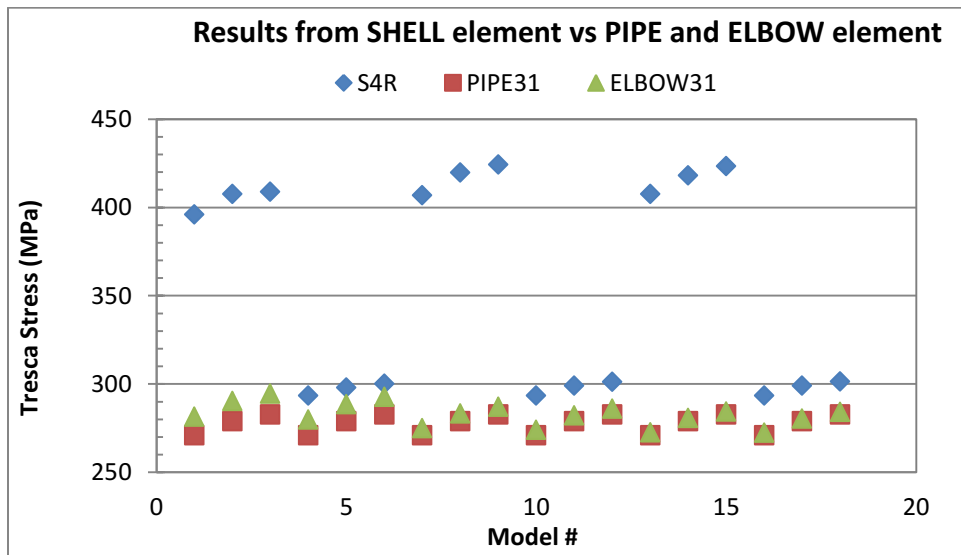


Figure 2. 20. Tresca stress results from pipe model using Shell, PIPE and Elbow element.

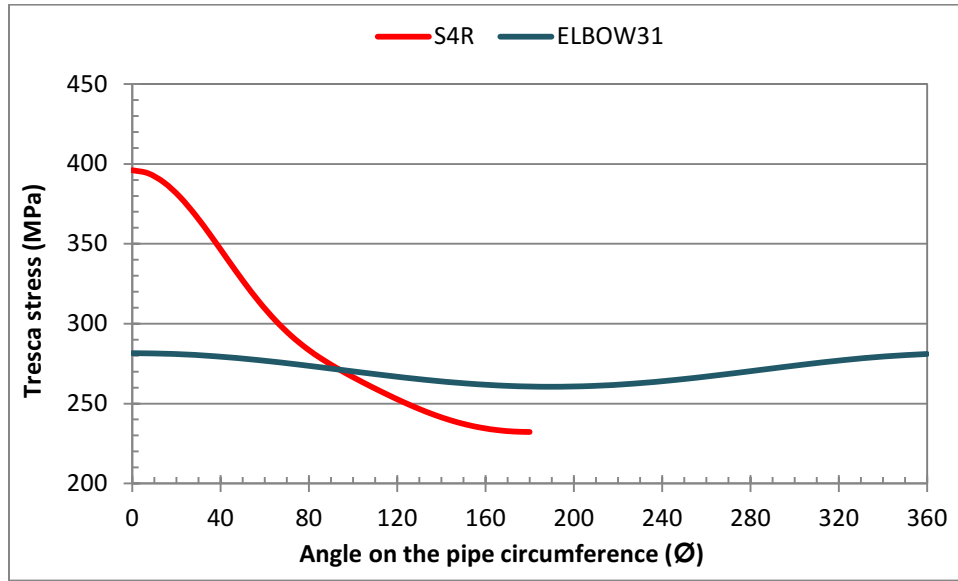


Figure 2. 21. The distribution of Tresca stress along the pipe cross-section at mid-section of pipe bend for Shell element and Elbow element model.

The proposed approach of modelling pipes using beam elements is used and the results from the FEA are compared to the modified CSA code equation results. The FEA results from the SHELL and BEAM elements are presented in figure (2. 22) as well as the modified CSA stress results evaluated using equation (2. 6). The difference in Tresca stress between the Elbow element model and the Shell element model is 6.13%. However, the difference between the Pipe and Shell element model is 6.89% which shows good agreement. Table (2. 8) summarizes the results from the different models and the error found in each model when compared to the Shell element results.

Table 2. 8. Comparison between the proposed modelling approach results and the S4R model results for pipe bends subjected to internal pressure resulting in 80% SMYS hoop stress

NPS	λ	α	R	Tresca stress Shell (S4R)	Magnified Tresca stress PIPE31	% Error	Magnified Tresca stress ELBOW31	% Error
12	0.125	40	323.85	396.078	373.6	5.84%	385.38	2.74%
24	0.064	40	609.6	407.5665	398.04	2.37%	409.67	0.51%
42	0.036	40	1066.8	408.853	421.85	3.13%	433.74	5.91%

12	0.624	40	1619.25	293.497	278.08	5.39%	287.33	2.12%
24	0.322	40	3048	298.003	279	6.59%	288.62	3.20%
42	0.182	40	5334	300.18	295.35	1.62%	305.94	1.90%
12	0.125	90	323.85	406.9445	379.84	6.89%	383.98	5.81%
24	0.064	90	609.6	419.764	404.24	3.77%	408.73	2.66%
42	0.036	90	1066.8	424.3285	428.45	0.97%	433.13	2.05%
12	0.624	90	1619.25	293.422	284.16	3.21%	287.27	2.12%
24	0.322	90	3048	299.003	282.1	5.82%	285.32	4.68%
42	0.182	90	5334	301.246	301.95	0.23%	305.42	1.38%
12	0.125	140	323.85	407.546	381.6	6.58%	383.31	6.13%
24	0.064	140	609.6	418.1155	406.1	2.92%	407.96	2.46%
42	0.036	140	1066.8	423.4095	430.1	1.57%	432.05	2.02%
12	0.624	140	1619.25	293.5135	285.92	2.62%	287.31	2.13%
24	0.322	140	3048	299.1115	283.96	5.20%	285.35	4.71%
42	0.182	140	5334	301.362	304.15	0.92%	305.72	1.44%

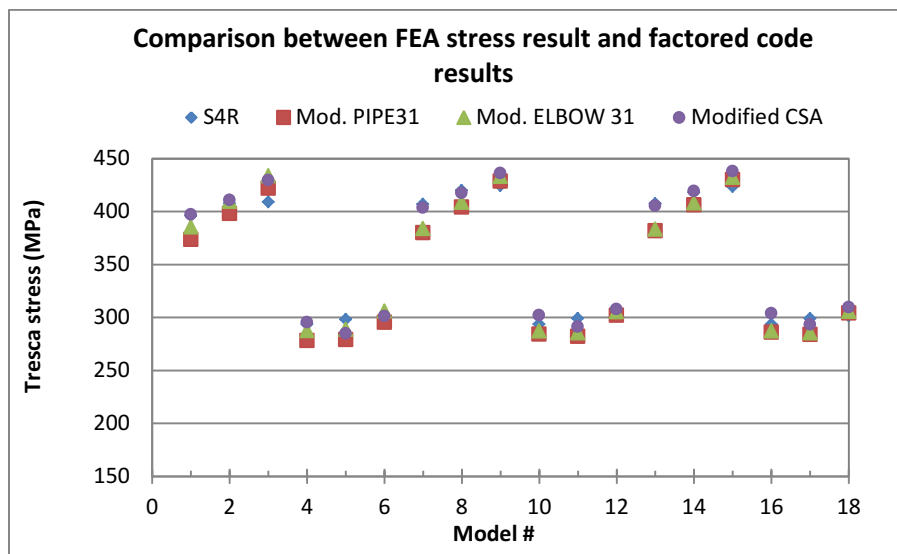


Figure 2. 22. Tresca stress results from the proposed approach of modelling pipe bends using the modified internal pressure load for pipe and elbow elements.

2.3.3.1. Check validity of the proposed modelling approach for back-to-back pipe bends

The results from the Shell element model is compared to the Tresca stresses from the Pipe and Elbow element model in order to validate the proposed approach of modelling pipe bends using beam elements. The magnified internal pressure ($K_p \cdot P$) is applied at the bend location only acting on the inner

surface of the pipe wall for the beam element models. Tables (2. 9) and (2. 10) show the results of the Tresca stresses at section (A-A) and (B-B) as identified in figure (2. 23). The resultant displacement is measured at the end of the pipe bend at section (C-C) from the Shell element model and the beam element model and presented in Table (2. 11). The displacements measured from the proposed modelling approach using PIPE and ELBOW elements show good agreement with the S4R element results. The difference between the S4R element and PIPE element is 12%. However, the difference between the ELBOW and S4R element is 18%. The maximum Tresca stress at the straight pipe (Section (B-B)) is 279.87 MPa for shell element models, however the Tresca stress is 271.04 and 271.26 MPa for the PIPE and ELBOW element model, respectively as shown in table (2. 10). The Tresca stress at the pipe bend (Section (A-A)) from the SHELL element model is 404.47 MPa and from the proposed model using PIPE and ELBOW element model is 379.84 and 387.34 MPa, respectively. The maximum difference in Tresca stresses between the proposed modelling approach and the shell element model is 6.2% at pipe bend and 3.2% at straight pipe, which shows that magnifying the internal pressure at the pipe bend to account for the additional stresses due to the Bourdon effect is not affecting the stresses on the rest of the pipeline system. Using the modified internal pressure at the bend locations will increase the Tresca stress at bend locations by up to 34.4% than the Tresca stress results from the PIPE and ELBOW element models with the actual internal pressure value as presented in table (2. 12). However, using the proposed modified internal pressure at the bend location will cause no change to the Tresca stress at the straight pipes as shown in table (2. 13).

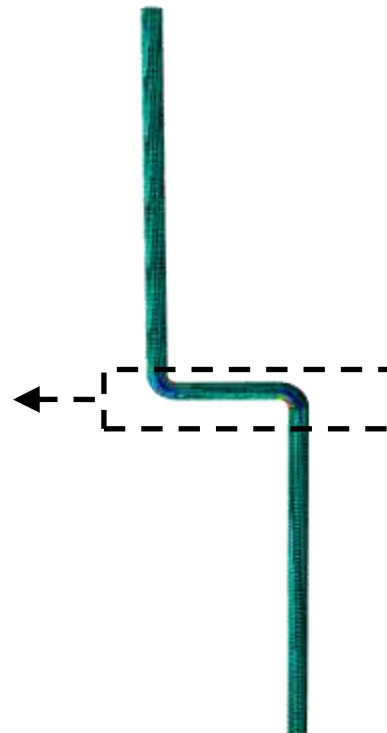
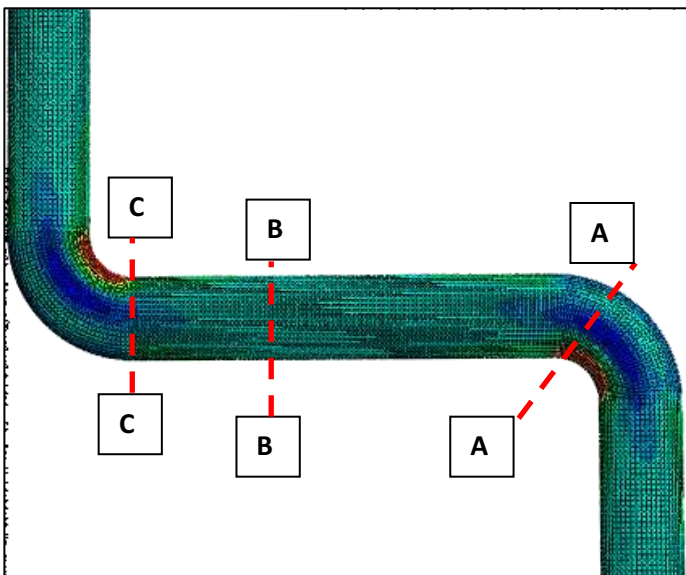


Figure 2. 23. Back to Back 90 degree elow model.

Table 2. 9. Stress results at section (A-A) : Comparison between the proposed modelling approach results using Pipe and Elbow elements versus the S4R model results at the pipe bend location.

NPS	Pressure factor (Kp)	Internal Pressure (Mpa)	Magnified Pressure (Mpa)	Tresca stress (S4R)	Tresca stress (PIPE31) (Kp.p)	Tresca stress (ELBOW31) (Kp.p)	Difference between PIPE31 and S4R	Difference between ELBOW31 and S4R
12	1.38	16.94	23.35	404.47	379.84	387.34	6.28%	4.33%
24	1.43	9.00	12.84	414.22	404.24	412.33	2.44%	0.46%
42	1.49	5.14	7.67	418.90	428.45	436.85	2.25%	4.19%

Table 2. 10. Stress results at section (B-B): Comparison between the proposed modelling approach results and the S4R model results at straight pipe location.

NPS	Pressure factor (Kp)	Internal Pressure (Mpa)	Magnified Pressure (Mpa)	Tresca stress (S4R)	Tresca stress (PIPE31) (Kp.p)	Tresca stress (ELBOW31) (Kp.p)	Difference between PIPE31 and S4R	Difference between ELBOW31 and S4R
12	1.38	16.94	23.35	279.87	271.04	271.26	3.21%	3.12%
24	1.43	9.00	12.84	284.184	279	279.66	1.84%	1.60%
42	1.49	5.14	7.67	286.009	282.7	283.262	1.16%	0.97%

Table 2. 11. Displacements (in mm) evaluated at section (C-C): Comparison between the proposed modelling approach results and the S4R model results

NPS	U- SHELL	U- PIPE	U- ELBOW
-----	----------	---------	----------

12	1.85	1.65	2
24	3.55	3.33	3
42	6.24	6.02	6

Table 2. 12. Stress results at section (A-A) : The Tresca stress results using Pipe and Elbow elements at the pipe bend location without modifying the internal pressure.

NPS	Tresca stress (PIPE31)	Tresca stress (ELBOW31)	Increase in stress between modified and actual internal pressure (PIPE31)	Increase in stress between modified and actual internal pressure (ELBOW31)
12	271.04	278.0463	28.64%	28.22%
24	279	286.5315	30.98%	30.51%
42	282.7	286.53	34.02%	34.41%

Table 2. 13. Stress results at section (B-B) : The Tresca stress results using Pipe and Elbow elements at the straight pipe location without modifying the internal pressure.

NPS	Tresca stress (PIPE31)	Tresca stress (ELBOW31)	Increase in stress between modified and actual internal pressure (PIPE31)	Increase in stress between modified and actual internal pressure (ELBOW31)
12	271.04	271.39	0.00%	-0.05%
24	279	279.1309	0.00%	0.19%
42	282.7	282.83	0.00%	0.15%

2.3.4. Comparison between FEA results and past studies

In this section, two past studies are compared with the FEA results and the modified proposed code equation to verify the accuracy of each mathematical model. For any pipe bend subjected to internal pressure only, the combined stress is equal to the hoop stresses since the longitudinal stress will always be tensile stresses. Therefore, the proposed mathematical model for the hoop stresses from the past studies is used in the comparison with the FEA Tresca stress results.

Table (2. 14) shows the results using Goodall’s and Hong’s proposed formulas. The maximum stresses based on these formulas are found at the intrados, which agrees with the FEA results. All the comparisons are done for the stresses at the intrados. The CSA-Z662 formula shows the highest error when compared to the FEA results by up to 47.3 %. As discussed earlier in this chapter, the high errors in the CSA formula is a result of ignoring the Bourdon effect and the ovalization since it adopts Barlow’s equations for straight pipes without any modifications. Goodall’s and Hong’s formula show better accuracy when compared to the FEA than the CSA results. Goodall’s formula has an error up to 16.8%, however, Hong’s equation has an error of 21.7%. Goodall’s formula is more satisfactory when compared to Hong’s. As presented in table (2. 15), Goodall’s formula has a good accuracy for pipe bends with angles varying from 40 to 140 degrees and for bends with 20-degrees bend angle if it has a long bend radius ($R=5D$). On the other hand, Hong’s formula has a good accuracy for pipes with long bend radius ($R = 5D$), however as the bend radius decreases to $1D$, the percentage of error increases significantly. Figure (2. 24) shows the comparison between Goodall’s, Hong’s and the modified CSA equation. The modified CSA equation proposed in this study shows the best accuracy compared to the FEA results. The accuracy lies within 0.64% and 6%.

Table 2. 14. The evaluated Tresca stresses from different proposed formulas and the SHELL element model from the current study.

NPS	α	R	Tresca stress (FEA)	Goodall (1978) Hoop stress (MPa)			Seok-Pyo Hong (2010) Hoop stress (MPa)			CSA-Z662	Modified CSA
				Intrados	Crown	Extrados	Intrados	Crown	Extrados	Intrados	Intrados
12	20	1D	341.37	398.84	271.06	226.78	334.95	271.06	248.92	288.00	386.64
24	20	1D	357.28	414.21	279.00	232.99	346.60	279.00	255.99	288.00	386.64
42	20	1D	363.80	421.78	282.86	236.00	352.32	282.86	259.43	288.00	386.64
12	20	5D	290.40	285.63	271.06	259.07	278.34	271.06	265.06	288.00	292.25
24	20	5D	294.70	294.23	279.00	266.50	286.62	279.00	272.75	288.00	292.25
42	20	5D	296.57	298.42	282.86	270.10	290.64	282.86	276.48	288.00	292.25
12	40	1D	396.08	398.84	271.06	226.78	334.95	271.06	248.92	288.00	390.85
24	40	1D	407.57	414.21	279.00	232.99	346.60	279.00	255.99	288.00	390.85
42	40	1D	408.85	421.78	282.86	236.00	352.32	282.86	259.43	288.00	390.85
12	40	5D	293.50	285.63	271.06	259.07	278.34	271.06	265.06	288.00	295.43

24	40	5D	298.00	294.23	279.00	266.50	286.62	279.00	272.75	288.00	295.43
42	40	5D	300.18	298.42	282.86	270.10	290.64	282.86	276.48	288.00	295.43
12	90	1D	406.94	398.84	271.06	226.78	334.95	271.06	248.92	288.00	401.60
24	90	1D	419.76	414.21	279.00	232.99	346.60	279.00	255.99	288.00	401.60
42	90	1D	424.33	421.78	282.86	236.00	352.32	282.86	259.43	288.00	401.60
12	90	5D	293.42	285.63	271.06	259.07	278.34	271.06	265.06	288.00	303.55
24	90	5D	299.00	294.23	279.00	266.50	286.62	279.00	272.75	288.00	303.55
42	90	5D	301.25	298.42	282.86	270.10	290.64	282.86	276.48	288.00	303.55
12	140	1D	407.55	398.84	271.06	226.78	334.95	271.06	248.92	288.00	412.63
24	140	1D	418.12	414.21	279.00	232.99	346.60	279.00	255.99	288.00	412.63
42	140	1D	423.41	421.78	282.86	236.00	352.32	282.86	259.43	288.00	412.63
12	140	5D	293.50	285.63	271.06	259.07	278.34	271.06	265.06	288.00	311.90
24	140	5D	299.11	294.23	279.00	266.50	286.62	279.00	272.75	288.00	311.90
42	140	5D	301.36	298.42	282.86	270.10	290.64	282.86	276.48	288.00	311.90

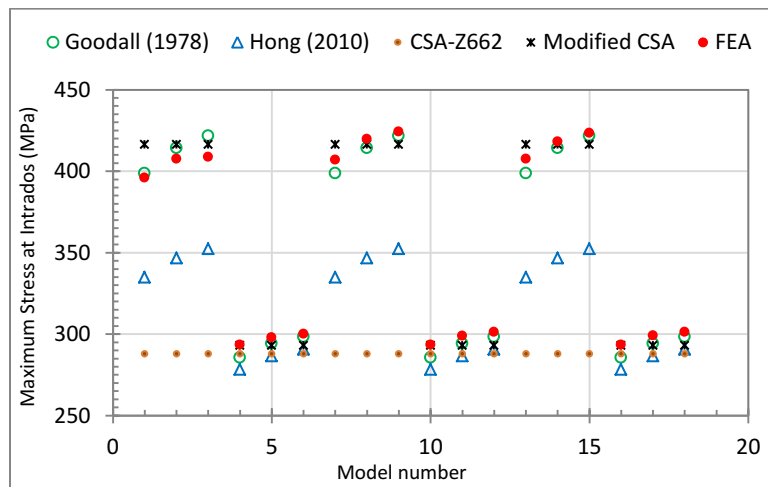


Figure 2. 24. Tresca stress evaluated from past studies compared with the FEA results and the CSA results.

Table 2. 15. The accuracy of each proposed formula compared to the FEA results

Model Number	Goodall Vs FEA	Hong Vs FEA	CSA Vs FEA	Modified CSA Vs FEA
1	16.8%	1.9%	18.5%	13.3%
2	15.9%	3.1%	24.1%	8.2%
3	15.9%	3.3%	26.3%	6.3%
4	1.7%	4.3%	0.8%	0.6%

5	0.2%	2.8%	2.3%	0.8%
6	0.6%	2.0%	3.0%	1.5%
7	0.7%	18.2%	37.5%	1.3%
8	1.6%	17.6%	41.5%	4.3%
9	3.2%	16.0%	42.0%	4.6%
10	2.8%	5.4%	1.9%	0.7%
11	1.3%	4.0%	3.5%	0.9%
12	0.6%	3.3%	4.2%	1.6%
13	2.0%	21.5%	41.3%	1.3%
14	1.3%	21.1%	45.8%	4.5%
15	0.6%	20.4%	47.3%	5.7%
16	2.7%	5.4%	1.9%	3.5%
17	1.6%	4.3%	3.8%	1.5%
18	0.9%	3.7%	4.6%	0.8%
19	2.2%	21.7%	41.5%	1.2%
20	0.9%	20.6%	45.2%	1.3%
21	0.4%	20.2%	47.0%	2.6%
22	2.8%	5.4%	1.9%	6.3%
23	1.7%	4.4%	3.9%	4.3%
24	1.0%	3.7%	4.6%	3.5%

2.4. SIGNIFICANCE OF THE PRESSURE FACTOR (K_p)

2.4.1. Predicting preliminary pipe bend wall thickness:

The FEA results show that the pipe bends have higher stresses than straight pipes subjected to internal pressure. In order to obtain the same hoop stress on a pipe bend compared to a straight pipe, under similar internal pressure levels, the pipe bend should be thicker than that of the straight pipe. Kainat, (2012) showed that the increase in stress for pipe bends could be overcome by using the next higher wall thickness to attain the expected values of hoop stress. In the current study, the proposed pressure factor (K_p) is used to account for the additional stresses resulting from the Bourdon effect. The influence of this effect could be considered from the early first steps in design where the pipe wall thickness is predicted. As presented earlier in this paper, the wall thickness corresponding to a given internal pressure is predicted using the Barlow's formula for hoop stresses according to the CSA-Z662. To account for the Bourdon effect in pipe elbows, the wall thickness could be predicted as follows;

$$K_p P = \frac{2St_e}{D} F * L * T * J \quad (2. 11)$$

By substituting the value of “P” from equation (2. 3) into equation (2. 11), then the relation between the wall thickness for pipe bends (t_e) and wall thickness for straight pipes (t) is as follows;

$$K_p t = t_e$$

This shows that the pipe bend wall thickness could reach up to 1.52 times the straight pipe wall thickness according to the pipe sizes and geometries covered in this study.

Example:

A pipe bend NPS24 has a bend angle 40 degrees and short radius bend ($R=1D$). The wall thickness evaluated using the current CSA code equation results in a thickness of 9.525mm. When the straight pipe wall thickness is used ($t= 9.525$ mm) it results in Tresca stresses from the FEA equals to 407.6 MPa which is 41.5% higher than the expected 80% SMYS hoop stresses. However, by using the proposed modified equation (Eqn. 2. 11), it results in a required wall thickness of 13 mm which results in Tresca stresses equal to 290 MPa which is 0.7% higher than the expected 80% SMYS hoop stresses. Using equation (2. 11) makes it easier for the designer to predict a wall thickness that will sustain the expected stresses. Therefore, it’s a time saving step in the design process.

2.4.2. Design of pipe bends:

Combined stresses on pipe bends could be estimated using the CSA-Z662 equation after introducing the proposed pressure factor into the equation as follows;

$$K_p (S_h - S_L) \leq 0.9 S X T$$

Section (3.4) shows the accuracy of this approach compared to the FEA stress results in table (2. 14). The error found in the pressure factor approach is 8.2% which is satisfactory.

2.4.3. Modelling of pipe bends in ABAQUS:

The proposed pressure factor (K_p) is used in modelling pipelines using beam elements in ABAQUS software. The internal pressure applied at the bend component is magnified by the (K_p) factor where it gives good results for stresses and displacements in the bend component without affecting the straight attached pipes. The accuracy of this approach is 6%.

2.5. DISCUSSION

This chapter investigates the behaviour of pipe bends under internal pressure loading. A proposed mathematical model is presented that estimates the outward forces due to the Bourdon effect. The proposed model is validated against FEA models and the results show a satisfactory agreement. The outward Bourdon forces are found to be dependent on the internal pressure level, pipe cross-section and the bend angle. This means that for two pipe bends with consistent bend angles and pipe size, having different bend radius will not affect the outward force value. The objective behind developing the mathematical models for the outward forces is to get an estimate of these forces that may be affecting the pipeline components surrounding the pipe bend. These mathematical models are not meant to be used in the design of the pipe bends, since most of the pipelines are designed using FEA piping software. However, these estimated outward forces are useful in designing any lateral support located at the pipe bend as shown in figure (2. 25). If these outward forces are not evaluated during the design, then the pipe bend supports will be subjected to lateral forces that are not accounted for in the design that may threaten the pipeline safety.

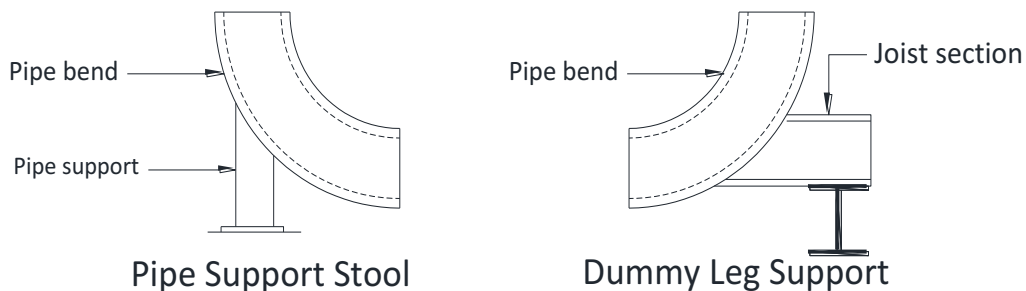


Figure 2. 25. Lateral supports used at pipe bends.

The pipe bend modelled in the FEA is considered a general case where it is not supported laterally. However, if a lateral support is added at the mid-length of the pipe bend, the resulted stress levels will decrease. On the other hand, the outward Bourdon forces are not affected by the lateral

support since the forces are generated from the difference in the surface areas. Therefore, the outward forces are carried by the lateral support and in this case they should be considered in the design of this support.

The design methodology used by the current design codes for pipelines is not differentiating between a straight pipe and a pipe bend when the pipeline is subjected to internal pressure loading. The CSA-Z662 design criteria evaluates the combined stress on a pipe bend based on equation (2. 4), which uses Barlow's formula for straight pipes to evaluate the hoop and longitudinal stresses. Therefore, in the CSA design criteria, the pipe bend is expected to have the same stress levels as a straight pipe when subjected to internal pressure.

In section (2.2), the finite element analysis method is used to evaluate the influence of Bourdon effect on the pipe bend stresses. The FEA results are compared to the CSA estimated stresses to evaluate the difference. Since the CSA combined stress formula ignores the toroidal effect of pipe bends on the stresses, then the evaluated stresses are considered to represent the stresses on a straight pipe. Therefore, the difference between the FEA stresses and the CSA estimated stresses is considered to be the increase in the stress due to the Bourdon effect and the Ovalization effect. This stress difference is used to develop the pressure factor (K_p).

The FEA results show that the Bourdon effect increases the stresses on the pipe bend than that estimated by CSA-Z662 formulas by up to 47.4% and 4.64% for short ($R = 1D$) and long ($R = 5D$) radius bends, respectively which shows that the influence of the Bourdon effect decreases as the bends radius increase. This shows that as the bend radius increases, the pipe bend approaches the behaviour of a straight pipe, which is considered to be a pipe with bend radius equal to infinity ($R = \infty$) and the tendency of the pipe bend to straighten out reduces. This is related to the beam parameter (λ) as well, since the beam parameter increases when the bend radius increases leading to a lower flexibility, the stresses decrease. Moreover, the influence of the Bourdon effect on the pipe bend stresses is found to be significant for low and high pressure levels. Therefore, it should not be ignored when the internal pressure levels are low.

Past studies considered the increase in stresses on a pipe bend due to the surface geometry using the shell theory. Goodall (1978) and Hong (2010) developed mathematical formulas to evaluate the hoop stresses on a pipe bend without considering the ovalization and Bourdon effect. The results

from Goodall's formula are found to be acceptable in the case of bend angles from 40 to 140 degrees where the error is 3.2%. However, for pipe bends with bend angles less than 40 the error reached 16% for short radius bends. Hong's formula had a high percentage of errors for pipe bends with short radius bends that reach up to 21.8%. However, the accuracy for long bend radius is 5.4% which is acceptable.

The FEA results show that the stresses in a pipe bend could reach up to 1.5 times the stresses estimated using the CSA code which could threaten the safety of the pipeline. Therefore, it is of great importance to develop a factor that accounts for the increased stresses due to the Bourdon effect as a function of the radius ratio (R/r), pipe slenderness ratio (D/t), the bend angle (α) and internal pressure (P). The developed pressure factor (K_p) incorporates the influence of ovalization and Bourdon effect in the design. The effect of each parameter on the stress results is investigated. The bend angle has a minor effect on the pipe stresses for the range of bend angles from 40 to 140 degrees. However, when the bend angle is below 40, a significant decrease in stresses is observed. Therefore, a new formula considering the bend angle is proposed. The slenderness ratio (D/t) is found to have a negligible effect on the stress levels on the studied pipe bends, therefore, it was excluded from the analysis for simplicity. The developed pressure factor (K_p) is developed to cover a wide range of bend radius and bend angles. The case of straight pipes are included as well since for a straight pipe, the bend angle is zero and the bend radius is infinity which results in a pressure factor (K_p) equal unity. The accuracy of the proposed factor is investigated by comparing the code stress results modified by the (K_p) factor to the FEA results. The accuracy of the proposed pressure factor is 8.2% with an average of 3.4%. This factor would be beneficial to the industry where it can provide a stress design criteria that maintain the pipeline's integrity.

The most accurate approach in modelling a pipeline system is using Shell elements in any of the finite element software programs. The cross-sectional deformations known as "Ovalization" and the tendency of the pipe to straighten out resulting from the "Bourdon effect" can both be detected using Shell element modelling where the increase in stresses will be considered. Although this method is considered accurate, it is not a practical method to model a whole pipeline system since it is complicated and time-consuming. Therefore, the current piping software used by the industry commonly uses beam elements in modelling and designing pipelines. Beam elements are considered practical and time economic in modelling pipelines but it has many drawbacks. The Beam element ignores the beam cross-sectional deformation, therefore, the ovalization is not considered and the hoop stresses are considered

to be constant along the cross-section of the pipe. Moreover, for closed (Thin-walled) cross-sections, the beam element ignores the warping effect which affects the stress levels on the pipe wall. The ABAQUS software incorporated an Elbow element specifically for modelling pipe bends. The Elbow element considers the ovalization of the pipe bend cross-section but it is not mentioned that it counts for the additional forces resulting from the Bourdon effect. An approach of modelling pipe bends in ABAQUS using beam elements is proposed. This approach is based on the proposed pressure factor (K_p). The pipeline is modelled in ABAQUS using beam elements where the internal pressure is magnified at the bend location by the K_p . Figures (2. 16) & (2. 17) show the results from the modified CSA equation (2. 6) compared with the original CSA equation (2. 4) and the Shell element model results. Figure (2. 16) shows the results for pipe bends subjected to internal pressure resulting in 80% SMYS hoop stress. The difference between the FEA and modified equation is found to be 5% with an average of 1.8%. The modified equation is verified for pipe bends with different internal pressure as well to show its applicability on a wide range of internal pressure levels. Figure (2. 17) show the results for pipe bends subjected to internal pressure resulting in 30% SMYS hoop stress. The maximum difference is 3.87% with an average of 1.45%. The results from the proposed modified CSA equation show excellent agreement with the Shell element model results. The Elbow element accounts for the cross-sectional deformations such as ovalization and warping which cause higher stresses. On the other hand, the Tresca stress results evaluated from the models using PIPE element are equal to the stresses evaluated using the Barlow's formula.

In this study, the effect of residual stresses and initial geometric imperfections are not considered. For pipe bends with initially ovalized cross-section, it is expected to have higher stresses than an initially circular cross-section. Future work may be extended to include the effect of these factors on the pipe bend behaviour and stresses.

2.6. CONCLUSION

This current study concluded the importance of considering the Bourdon effect and its severity on the pipeline integrity. A mathematical model is presented to compute the outward forces resulted from the Bourdon effect on pipe bends. The results from the proposed mathematical model is compared to FEA results for stand-alone pipe bends and showed excellent agreement. It could be concluded that

the outward forces depend mainly on the pipe size and the pipe bend angle. Numerical analysis is used to evaluate the influence of the Bourdon effect on the pipe bend stresses and a proposed pressure factor is developed from this study. The proposed pressure factor depends on the bend angle, bend radius and pipe size. The proposed pressure factor showed to have an important significance in the design of pipe bends since it could be used to estimate a preliminary pipe bend wall thickness. The proposed factor is used as well to magnify the combined stresses evaluated using the CSA-Z662 equation to account for the increase in stress due to the effect of internal pressure on pipe bends.

CHAPTER 3: PIPE BENDS SUBJECTED TO IN-PLANE OPENING AND CLOSING BENDING MOMENTS.

3.1. INTRODUCTION

The stress analysis of pipe bends and elbows has been investigated in the past using theoretical and experimental studies. Bantlin, in 1910, was the first to show experimentally that curved pipes behave differently than predicted by simple beam theory under bending load. Von Kármán, in 1911, was the first to present a theoretical explanation to this phenomenon using the minimum potential energy approach. His study considered a 90 degree pipe bend subjected to an in-plane closing bending moment. Von Kármán's analytical results showed that the angular rotation of plane sections and the maximum stresses were higher for a pipe bend than that for a straight pipe, which agrees with Bantlin's experimental results. The pipe bends were proven to be more flexible in bending than straight pipes of the same configuration. The increased flexibility of pipe bends is due to the tendency of the pipe cross-section to ovalize. The ovalization affected the hoop bending stresses as well and was found to be higher than that of a straight pipe. There was an increase in the longitudinal stresses due to the increase in flexibility. Therefore, Von Kármán developed a factor that accounts for the increase in the pipe bend's flexibility known as the Flexibility factor $\left(K = \frac{10+12\lambda^2}{1+12\lambda^2}\right)$. The flexibility factor is the ratio between the angular rotation for a pipe bend and that of a straight pipe with the same configuration when subjected to bending. The flexibility factors were greater than one and function of a dimensionless beam parameter (λ), $\left(\lambda = \frac{tR}{r^2}\right)$. To simplify the analysis, Von Kármán considered some assumptions in his work. The first assumption was considering the ovalization to be constant over the entire length of the pipe bend. The second assumption is considering the pipe mid-wall radius (r) negligible compared to the bend radius (R), hence the pipe bore term ($R \pm r$) is considered equal to (R), which might be acceptable for long-radius bends. However, recently short-radius bends are being considered by the pipeline industry where this assumption becomes unjustifiable. Third assumption was considering the centre-line of the pipe cross-section to be inextensible where the hoop strains were assumed to be zero. However, past studies showed that the hoop strain at the mid-layer of the pipe cross-section is not equal to zero and has a highly significant compressive value that affects the hoop stresses and consequently affects the equivalent stresses on the pipe bend. In 1951, Clark and Reissner used the thin-shell theory analysis

to investigate the behaviour of curved tubes under bending. Based on the small deformation theory and the pure bending assumption, they obtained two differential equations with variable coefficients. They considered some approximations in their analysis in order to solve these differential equations to obtain the coefficients. The problem is that their assumptions were equivalent to those of Von Kármán's and their final solution is almost identical. The difference is that Clark and Reissner used the approximations to simplify exact mathematical functions, however, Von Kármán used these approximations to obtain simpler mathematical functions throughout his theory. For $\nu = 0.3$, Clark and Reissner developed a flexibility and Stress Intensification Factor (SIF) as follows;

$$K = \frac{1.65}{\lambda}$$

$$i = \frac{1.89}{\lambda^3}$$

In 1952, Markl conducted an extensive series of fatigue tests on pipe bends subjected to in-plane bending. From his fatigue test results, he derived a flexibility factor which is exactly as that proposed by Clark and Reissner. However, the stress intensification factor was half the factor from Clark and Reissner. The derived factors from Markl's fatigue tests are as follows;

$$K = \frac{1.65}{\lambda}$$

$$i = \frac{0.9}{\lambda^3}$$

The flexibility factor derived from Clark and Reissner's analysis and from Markl's fatigue tests are currently presented in the codes such as; CSA Z662-15, ASME B31.1 and ASME B31.3. The Stress Intensification Factor from Markl's fatigue test is the one used in the current codes.

From the past theoretical studies, it is clear that some of the approximations in these theories are questionable especially when applied to short-radius bends or pipe bends with bend angles smaller or larger than 90 degrees. The problem with the currently used stress intensification factors is that they were based on a number of approximations that are either unjustifiable or are not applicable for the range of pipe bend geometry used by the pipeline industry nowadays. These studies were based on in-plane closing bending moment acting on a large-radius bend with 90 degrees bend angle. The effect of changing the direction of applied in-plane bending moment was not covered in these past studies as

well as changing the bend angle. Most of these past studies followed Von Kármán's approximations to obtain a final simplified mathematical function. However, the FE software commonly used nowadays helps to overcome these difficulties and improves the quality of the final derived formulas by reducing the number of approximations considered. For example, the pure bending approximation is ignored in this study since the FEM considers the variation of the deformed cross-section along the pipe bend length. In all studies, the approximations resulted in stress intensification factors that are applicable to a small range of pipelines under particular loading and boundary conditions. In this study, the effect of adding straight pipes attached to the pipe bend is investigated. A more accurate evaluation of the mid-layer stresses is presented in this study without assuming an inextensible pipe cross-section.

The main objective of this study is to investigate the structural behaviour of pipe bends under the effect of the in-plane bending moment and to develop a modified stress intensification factor using finite element analysis. The effect of the direction of applied in-plane bending moment is considered as one of the main parameters in this study. The variation in the pipe bend size and geometry are considered as well such as; the pipe outer diameter (D), pipe bend angle (α) and pipe bend radius (R). In this study, an assessment of the stress intensification factors presented in the current codes is performed to ensure the suitability of using the factors for different pipe bend geometries and different loading directions. The behaviour of pipe bends is analysed numerically and the results are compared with the current design code results. Based on this investigation, a new SIF factor is developed to account for different loading directions and bend angles.

3.2. METHODOLOGY

3.2.1. Finite Element Modelling and Analysis

Finite element modelling and analysis is performed using ABAQUS 6.13. The piping configuration used in this study is a pipe bend connected to two attached straight pipes as shown in figure (3. 1). Since each end of the pipe system is representing a continuously long pipe as the actual situation for any pipeline which usually extends more than 1 Km in most pipelines, therefore, the straight pipe length is considered 10 times the pipe outer diameter to avoid the effect of end conditions ($L = 10 D$). According to a previous study done by Matzen & Yu in 1998, it was shown that the minimum length of the attached straight pipe required to avoid the end condition effect is 5 times the outer diameter of the pipe. If the straight pipe is shorter than $5D$, then the ovalization of the pipe is affected by the end

restraints resulting in higher stress values. The pipe size for the bend and the straight pipe are similar in each model. The wall thickness for all the studied pipes is constant and equal to 0.375" (9.525 mm). The beam parameter of the pipe bend ($\lambda = tR/r^2$) varies by changing the bend radius (R) and pipe outer diameter (D) covering a range from 0.036 up to 0.63. Taking advantage of symmetry about the plane of bending ($X-Z$ plane), half models of the pipe system with symmetric boundaries are built using Shell elements. The pipes are modelled with an initially circular cross-section and a uniform wall thickness without any initial imperfections. Table (3. 1) shows the geometry and dimensions of all the pipe models used in this study. The straight pipes are modelled in a cylindrical coordinate system with an extrusion equal to $10D$. While the bend part is modelled using a spherical coordinate system. The bend is a deformable part with a revolution angle representing the bend angle (α). The pipes are modelled using a four-node quadrilateral shell element with reduced integration (S4R). The size of the mesh in the pipe bend is chosen to be 15×15 mm. While the average mesh size for the attached straight pipes is chosen to be 20×20 mm as shown in figure (3. 2). A linear material is used to define the pipe behaviour where Young's modulus of elasticity is 207000 N/mm^2 and Poisson's ratio is 0.3.

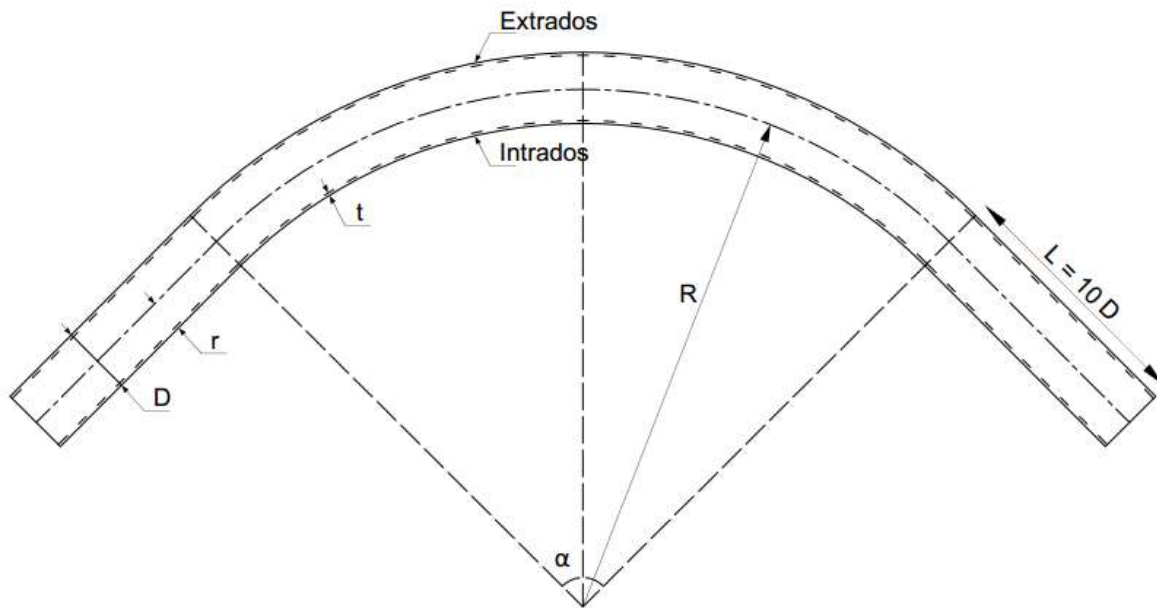


Figure 3. 1. Pipe bend configuration with attached straight pipes.

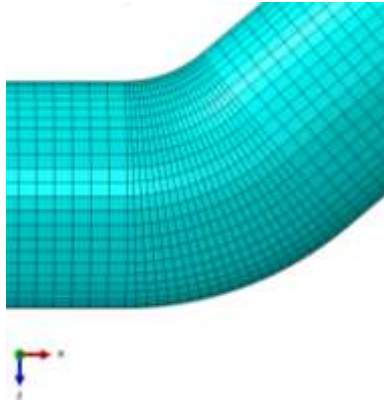


Figure 3. 2. Pipe Meshing

The lines of intersection between the pipe walls and the plane of symmetry (X-Z plane) are restrained from translation in the Y-direction, and the rotation about the X and Z axis are prevented. One end of the pipe is totally fixed from rotation and translation while the other end is free. The end boundary conditions are assigned at reference points RP-1 and RP-2 as shown in figure (3. 3). The reference points are tied to the circumference of the pipe end using a kinematic coupling constraint. In defining the kinematic coupling, the radial movement is permitted to allow for the pipe cross-sectional deformations such as ovalization of the cross-section. The analysis considers the nonlinear geometry to account for the cross-sectional deformations as well as the overall deformation of the pipe.

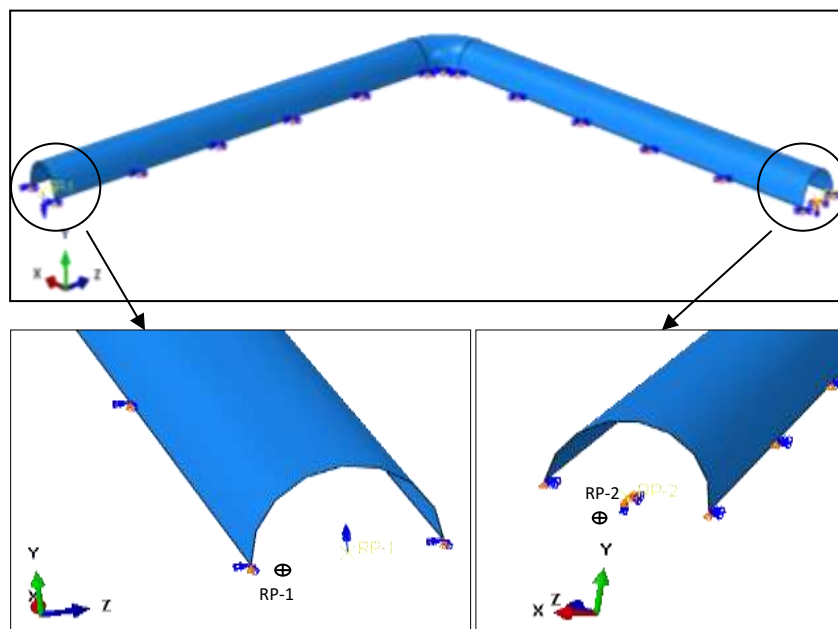


Figure 3. 3. Model boundary conditions.

The displacement control method is used in the finite element analysis to capture the complete behaviour of the pipe including unstable behaviour if present. An end rotational displacement of 0.1 radians is applied at the free end of the pipe as shown in figure (3. 4). The displacement is applied in an increment of 0.025 radians. As will be presented later in this chapter, the applied end rotation (0.1 radians) results in high stresses compared to the pipe capacity and yield stresses of traditional and high strength steels. However, the relationship between the end rotation and the stresses is found to be almost linear as shown in figure (3. 5) and as will be presented later in this chapter. Therefore, by assuming a perfectly linear relationship, the developed stress intensification factors are applicable for the whole range up to 0.1 Radians end rotation.

The Von Mises, hoop and longitudinal stresses are obtained from the FEA numerical models at the location of the critical stresses. These stresses are evaluated at the outer, inner and mid-layer of the pipe wall thickness. The stresses from the FEA models are later compared to the stresses evaluated using the equation presented in the CSA-Z066.

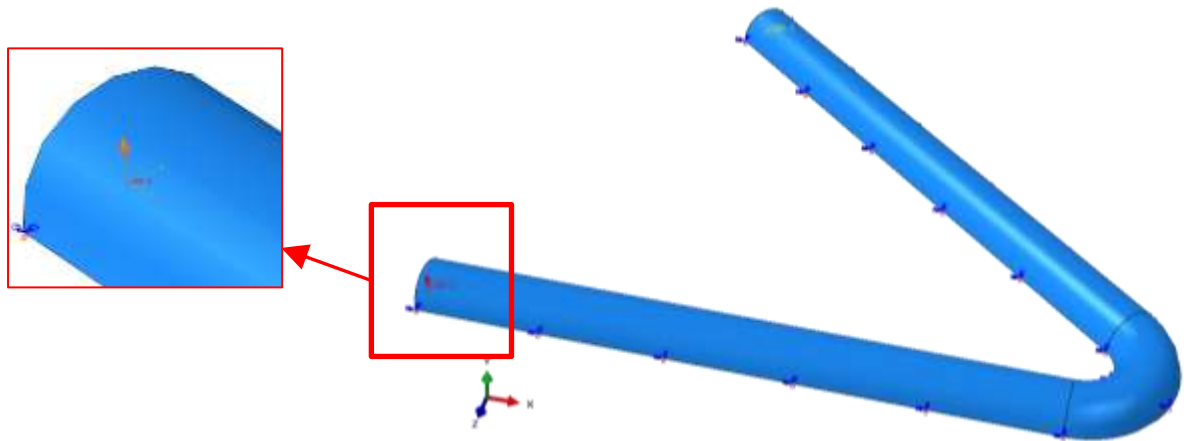


Figure 3. 4. Applied loading and pipe geometry

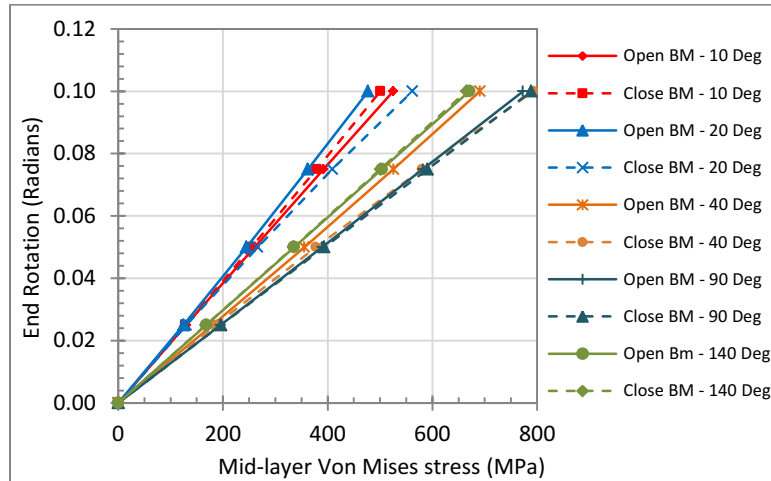


Figure 3. 5. Applied end rotation vs Von Mises stress for NPS 12 pipe bend with short bend radius (R = 1D)

Table 3. 1 Geometric parameters of pipe elbow.

NPS	Outer Diameter (D, mm)	Bend radius (R, mm)			Elbow thickness (t, mm)	Bend angle (α)	Beam Parameter (λ)		
		R = 1D	R = 3D	R = 5D			R= 1D	R= 3D	R= 5D
12	323.85	323.85	971.55	1619.25	9.525	10	0.125	0.353	0.624
						20			
						40			
						90			
						140			
24	609.6	609.6	1828.8	3048	9.525	10	0.065	0.195	0.323
						20			
						40			
						90			
						140			
36	914.4	914.4	2743.2	4572	9.525	10	0.0425	0.127	0.213
						20			
						40			
						90			
						140			
42	1066.8	1066.8	3200.4	5334	9.525	10	0.0364	0.109	0.182
						20			
						40			
						90			
						140			

3.3. RESULTS

3.3.1. Verification of the finite element model

A verification of the finite element model is conducted. The FEA results are compared to the experimental work of Gross (1952). Gross (1952) conducted an experimental study on short bend radius pipes of thin wall thickness subjected to in-plane external moments. The 90-degree bends are attached to two straight pipes with a length considered to eliminate any localized end effects due to the method of loading. The tested pipes are supported vertically and laterally at the bottom end, while the top end is free to rotate and translate vertically. The complete test setup can be found in the original published paper by Nicol Gross, 1953. The displacement results from test “Bend 1” and “Bend 3” are the only available data from this study. Therefore, these two tests are used to verify the FEA model in this current study. The geometry and the pipe size for the tested pipes are presented in table (3. 2). The testing technique applies a load at both ends that exerts a bending moment increasing linearly with distance from the line of loading. The maximum bending moment occurs at the mid-length of the pipe bend being the furthest from the loading line of action. The vertical displacement is measured from these tests and compared to the displacements evaluated from the FEA models for verification.

Table 3. 2 Dimensions of tested pipes (Gross, 1952)

Test	NPS	Outer Diameter (D, mm)	Wall thickness (t, mm)	Bend radius (R, mm)	Straight pipe length (L, mm)
Bend 1	12	314.706	4.7625	457.2	958.85
Bend 3	6	159.7152	3.175	228.6	611.124

A finite element model is built using ABAQUS as presented in section (2.1). Half of the pipes are model due to symmetry using Shell elements. One end of the pipe is free to rotate and translate in the vertical direction while the other end is free to rotate in the plane of symmetry and restricted from translation in the two directions. A vertical load is applied at the free end with a value equal to the failure load from the tested pipes. The vertical displacement at the free end is evaluated during loading and compared with the displacement measured from the tests. The results from the FEA are plotted against the results from the tested pipes in figure (3. 6) and (3. 7). The FEA results show good agreement with the experimental data. Consequently, the FEA model is used in conducting a parametric study on pipe bends considering some minor changes in the verified model such as, adding an end boundary condition or changing the material properties which has no effect on the results.

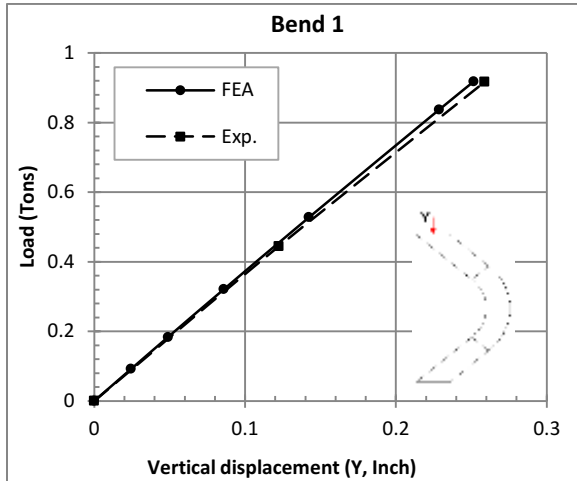


Figure 3. 6. The vertical displacement from the FEA versus the test results for Bend 1.

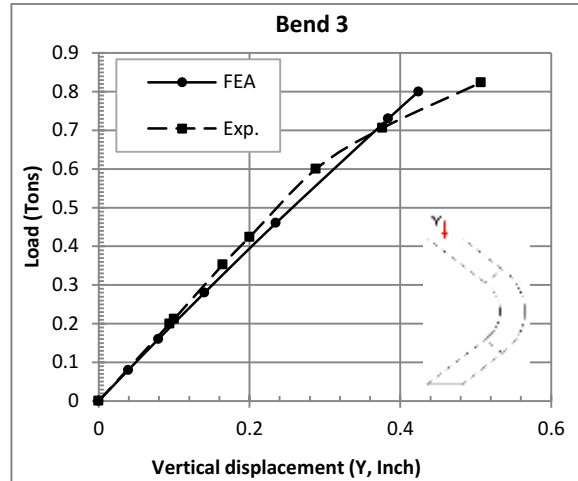


Figure 3. 7. The vertical displacement from the FEA versus the test results for Bend 3.

3.3.2. Shape of Ovalization

A pipe bend subjected to bending moment will undergo deformations in the cross-section in addition to the usual beam deformations. The FEA results show that the shape of ovalization depends on the direction of bending moment, where the cross-section either flattens or ovalizes. The ovalization ratio of the cross-section in this study is measured using equation (3. 1) that captures the location of the major axis with respect to the cross-section deformed shape. The ovalization ratio is measured at the mid-length of the pipe bend (Section A-A), which is found to be the location of maximum stresses as shown in figure (3. 8). For a perfectly circular cross-section, equation (3. 1) results in a zero ovalization ratio. However, if the cross-section flattens or ovalizes, then the ovalization ratio is a negative or positive value, respectively. Figure (3. 8.a) shows a flattened cross-section where the ovalization ratio is negative. While, figure (3. 8.b) shows an ovalised pipe bend where the ovalization ratio is a positive value.

$$\text{Ovalization ratio} = \frac{a-b}{0.5 (a+b)} \tag{3. 1}$$

a: Half the dimension of the axis in the plane of bending.

b: Half the dimension of the axis perpendicular to the plane of bending.

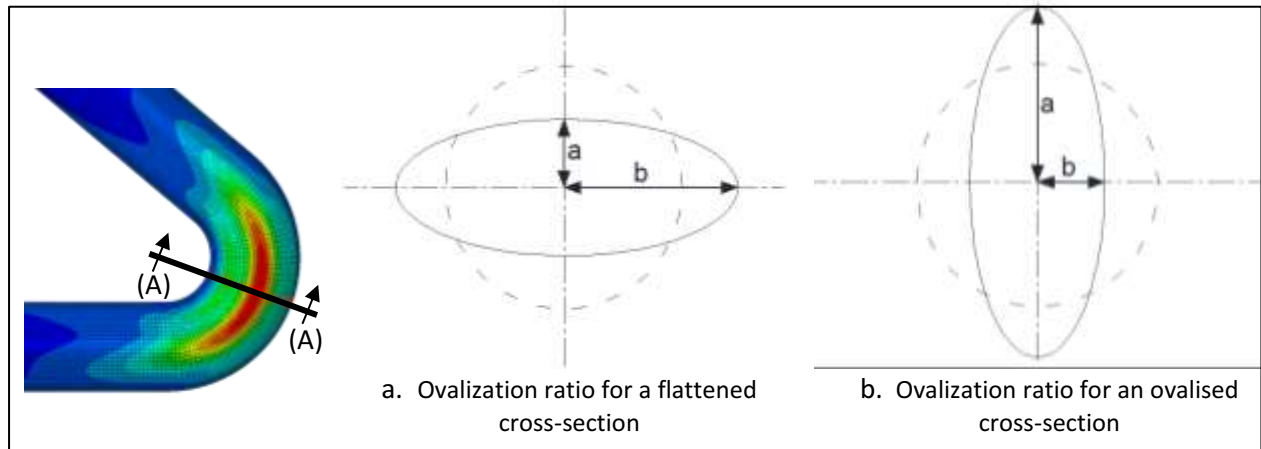


Figure 3. 8. Ovalization equation dimensions

The FEA results show that when a pipe bend is subjected to an opening bending moment, the cross-section at the mid-length of the pipe bend deforms into an oval cross-sectional shape with the major axis lying in the plane of bending. Figure (3. 9.a) shows the un-deformed and deformed cross-section of a pipe bend subjected to an opening bending moment. However, if a closing bending moment is applied to the end of the pipe bend, then the cross-section deforms into a flattened shape where the major axis of the cross-section is perpendicular to the plane of bending as shown in figure (3. 9.b).

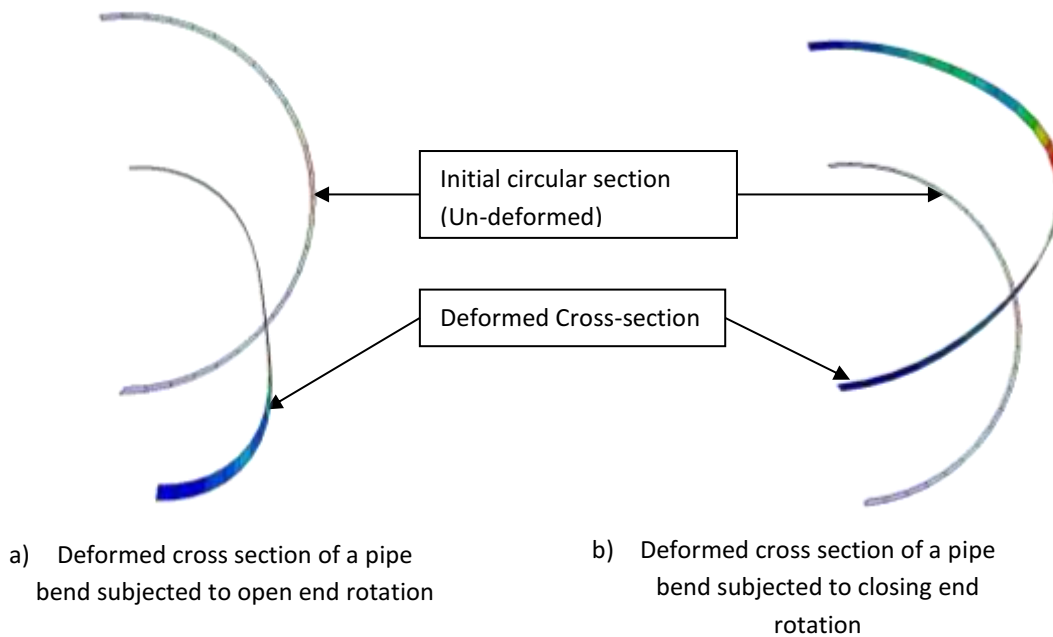


Figure 3. 9. The cross-sectional deformation of half a pipe bend subjected to opening or closing rotations.

Figure (3. 10) shows the FEA results of the ovalization ratio at a particular end rotation (0.1 radians) plotted against the bend angle for pipe bends subjected to opening or closing in-plane bending moment. It is found that as the outer diameter of the pipe bend increases, the ovalization ratio increases as well. By increasing the outer diameter of the pipe bend from 12" to 42", the ovalization ratio increases by up to 15.2% and 27.6% for the opening and closing bending moment, respectively. The results show that the closing bending moment results in higher ovalization ratio than opening bending moment for pipe bends with bend angles 10, 20 and 40 degrees by up to 120%. However, when the bend angle increases to 90 and 140 degrees, the opening bending moment results in higher ovalization ratio than the closing bending moment by up to 58%. In addition, the ovalization ratio is low for pipe bends with 10 degrees bend angle since the pipe bend behaves more as a straight pipe. However, as the bend angle increases to 20 and 40 degrees, the ovalization ratio increases since the toroidal geometry of the pipe affects the deformation of the pipe bend and the cross-section starts to deform. After a certain bend angle, the ovalization ratio starts to decrease again and becomes almost constant. The highest ovalization ratio recorded for pipe bends with bend angles ranging from 10 to 40 degrees is 0.32. For bend angles higher than 40 degrees, the ovalization ratio is up to 0.16. Increasing the bend angle over 90 degrees has a negligible effect on the ovalization ratio. Figures (3. 11) & (3. 12) show the ovalization ratio calculated at a particular applied end rotation (0.1 radians) plotted against the D/t ratio. The results show that as the D/t ratio increases, the ovalization ratio increases. This indicates that the ability of the cross-section to deform increases as the pipe wall thickness gets thinner compared to the outer diameter of the pipe.

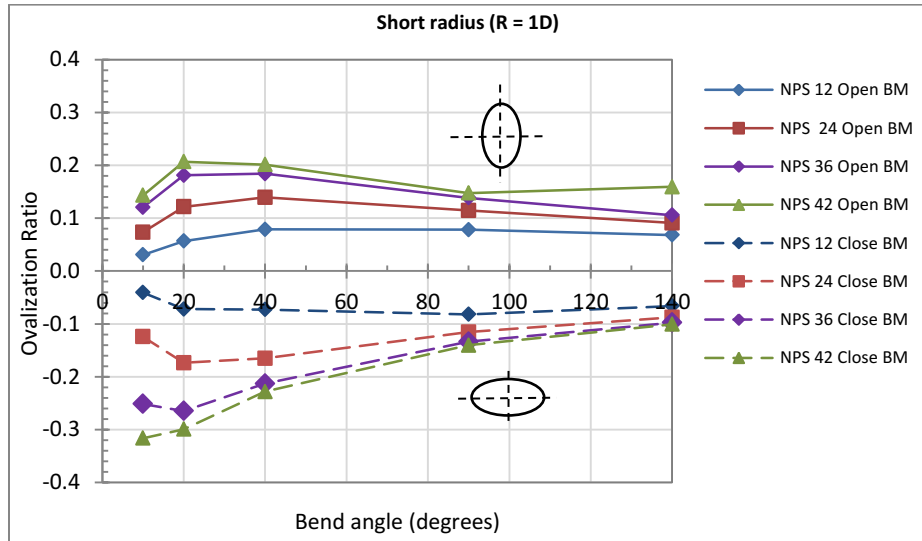


Figure 3. 10. Ovalization ratio vs bend angle for pipe bends with short bend radius (R=1D).

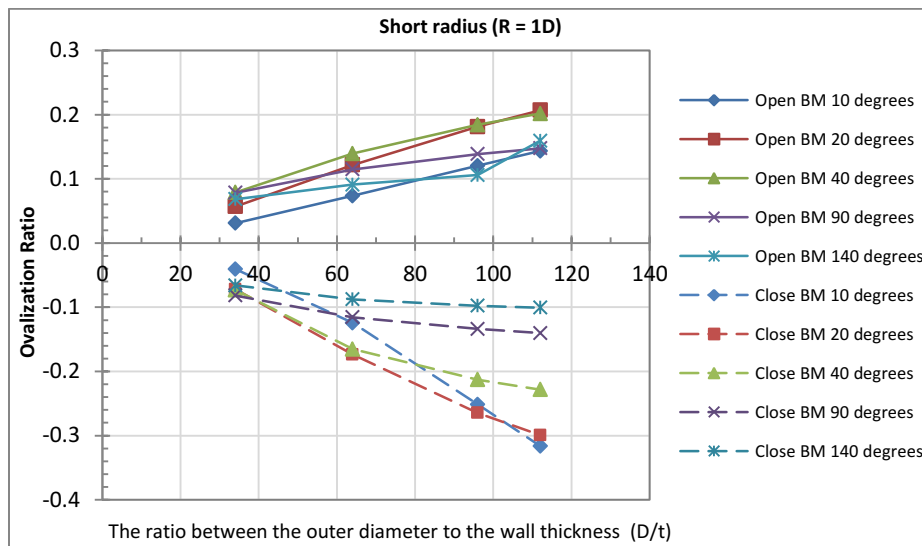


Figure 3. 11. Ovalization ratio vs D/t ratio for pipe bends with short bend radius (R=1D).

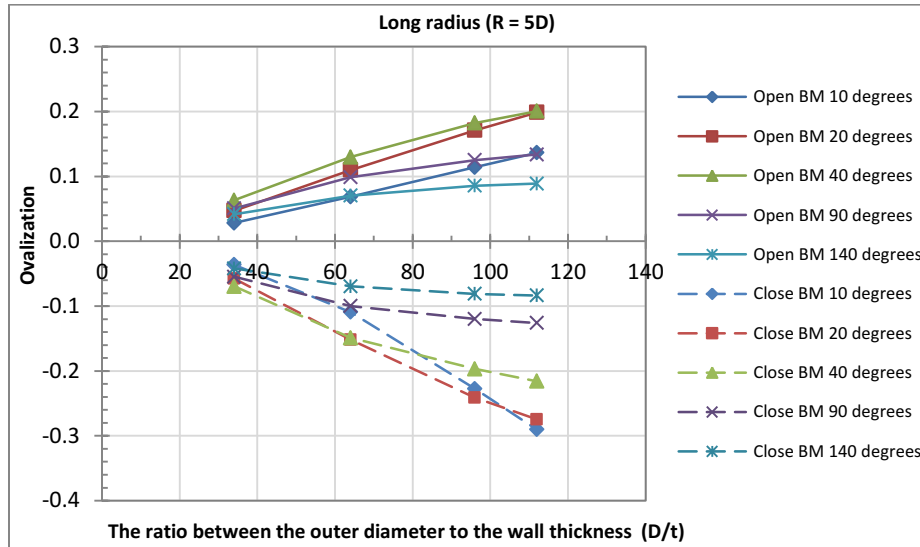


Figure 3. 12. Ovalization ratio vs D/t ratio for pipe bends with long bend radius (R=5D).

3.3.3. Linearity of the response and effect of the bending moment direction

The ovalization phenomenon occurring in pipe bends can affect the linearity of the behaviour. To investigate the behaviour of the pipe bend, the relationship between the applied end rotation and the generated reaction moment is studied. In addition, the relationship between the stresses and the former parameters is investigated as well. Figures (3. 13) and (3. 14) show the results of the generated reaction bending moments versus the applied end rotation at the free end of the straight pipe for short radius pipe bends with 12" and 42" outer diameter, and with a range of bend angles from 10 to 140 degrees. The relation between the end rotation and reaction bending moment is found to be linear for the case of pipe bends with small pipe sizes as NPS 12 (Figure 3. 13). However, as the pipe bend size increases to NPS 42, the relationship tends to be slightly non-linear as shown in figure (3. 14). It is found that by applying an opening end rotation, the results have a concave upward curve where the rate of increase in the reaction moment increases throughout the loading and consequently this means that the pipe bend gains stiffness with loading. However, the case of applying a closing end rotation shows that the results have a concave downward curve, which shows that the rate of increase in reaction moment starts to decrease with time as the pipe bend loses stiffness. For pipe bends with long bend radius (R = 5D), the relationship between the end rotation and reaction moment is linear as shown in figures (3. 15) & (3. 16). The rest of the results showing the linearity of the pipe bend behaviour are presented in Appendix (A).

By looking at figures (3. 13) to (3. 16), the results show that at the same bending moment, the small bend angle pipes have a smaller end rotation than large bend angle pipes. Which means that as the pipe bend angle increases, the pipe bend becomes more flexible therefore tends to have higher deformations under the same applied load. Moreover, at the same bending moment, the end rotation resulting from the opening bending moment is lower than the end rotation resulting from the closing bending moment. In addition to that, the bending moment required to rotate the pipe bend with a particular end rotation (0.1 radians) in the opening direction is up to 2 times higher than that required for the closing direction. Therefore, pipe bends subjected to closing bending moments are more flexible than those subjected to opening bending moments and the flexibility of a pipe bend changes by changing the direction of the applied bending moment. The results show that the bend angle affects the generated reaction moment. For two consistent pipe bends having the same pipe size and bend radius, it is found that pipe bends with bend angle 10 degrees has a reaction moment up to 5.5 times higher than pipe bends with bend angle 140 degrees. Therefore, as the bend angle decreases, the stiffness of the pipe bends increases.

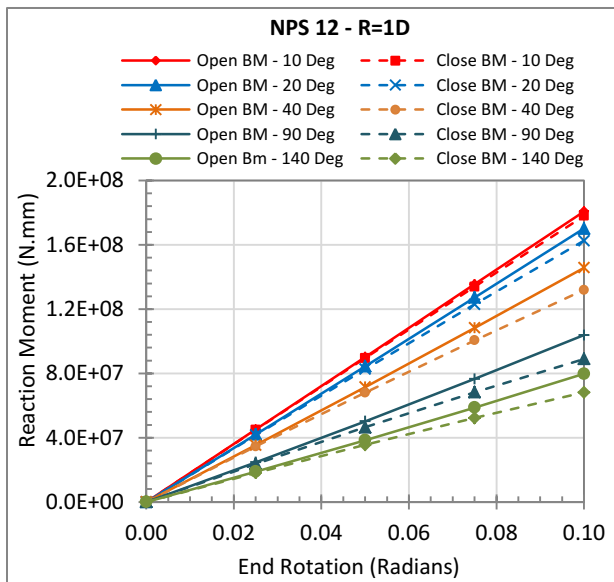


Figure 3. 13. End rotation vs reaction moment for 12” pipe with 1D bend radius.

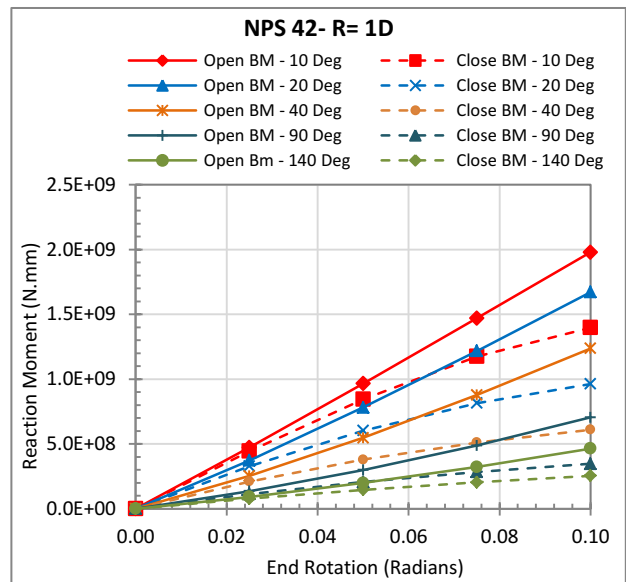


Figure 3. 14. End rotation vs reaction moment for 42” pipe with 1D bend radius.

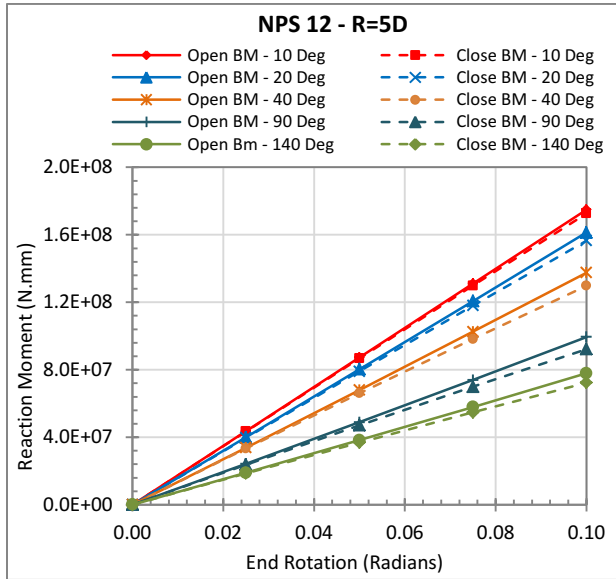


Figure 3. 15. End rotation vs reaction moment for 12” pipe with 5D bend radius.

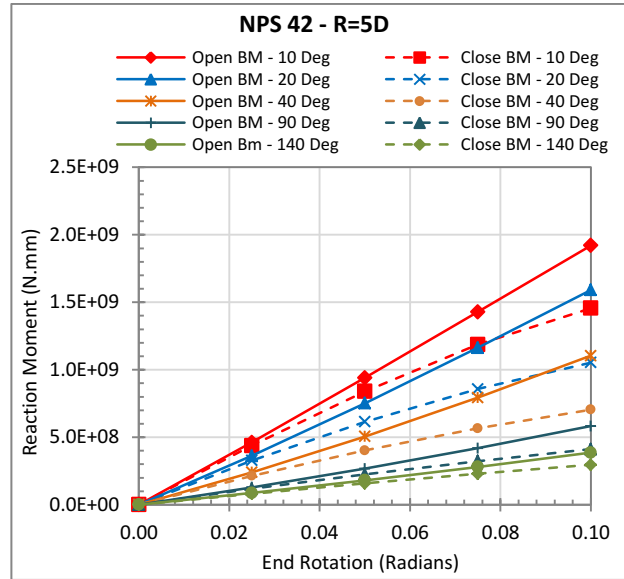


Figure 3. 16. End rotation vs reaction moment for 42” pipe with 5D bend radius.

The linearity in the stress relationships for pipe bends is investigated as well. Figure (3. 17) shows the maximum Von Mises stress results at the mid-layer of a pipe bend with 12” outer diameter and short bend radius ($R = 1D$). Since the code estimates the stresses based on the bending moment, therefore, the comparison is conducted at the same value of the reaction bending moment. The curve shows that at the same bending moment, the Von Mises stress on a pipe bend with a small bend angle is lower than that of a large bend angle pipe. For this pipe configuration, it is noticed that changing the bend angle from 40 to 140 degrees causes an increase in the Von Mises stress by 74%. However, changing the bend angle from 10 to 140 degrees causes an increase of 206% in the Von Mises stress at the mid-layer of the pipe wall. Consequently, this shows that the bend angle has a significant effect on the Von Mises maximum stress measured on the pipe bend. In addition, changing the direction of bending moment affects the Von Mises stress since it affects the pipe flexibility. Figure (3. 17) shows that applying a closing bending moment results in higher stresses than that of an opening bending moment by up to 38% in this studied case. Figure (3. 18) shows the Von Mises stress vs the reaction moment for a pipe bend with 42” outer diameter and short bend radius ($R = 1D$). The stresses resulting from the closing bending moment has a concave downward curve. However, the opening bending moment results in an upward concave stress curve. The nonlinearity can be obviously seen in the larger diameter pipe bends.

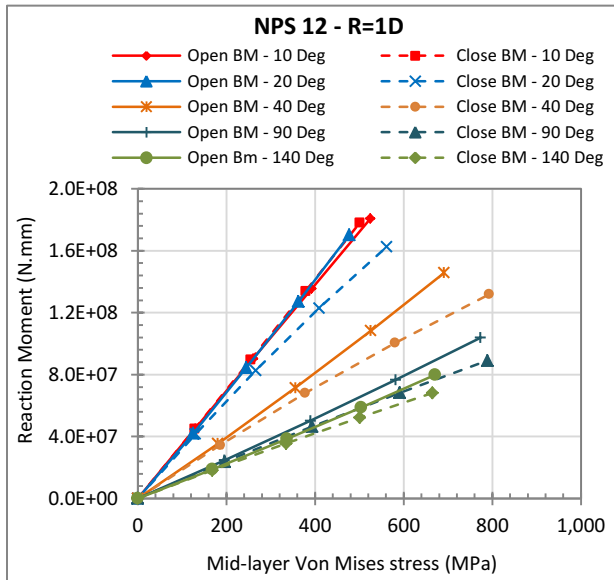


Figure 3. 17. Von Mises stress vs reaction moment for 12” pipe with 1D bend radius.

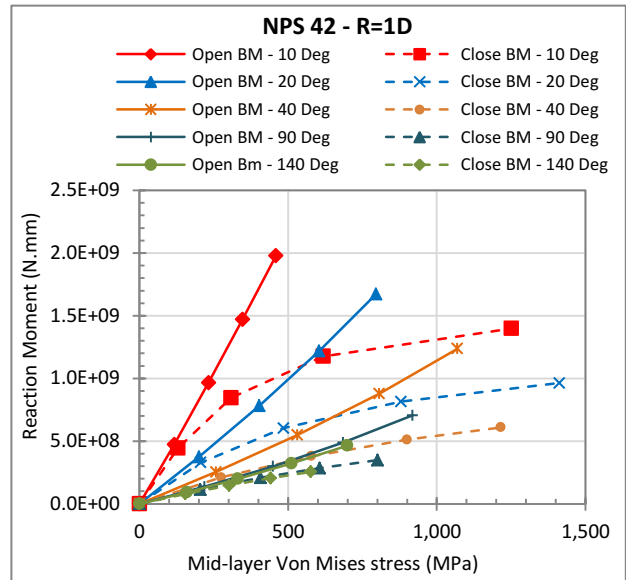


Figure 3. 18. Von Mises stress vs reaction moment for 42” pipe with 1D bend radius.

Figure (3. 19) shows the reaction moment resulting from rotating the pipe bend with a particular end rotation of 0.1 radians versus the bend angle for all studied pipe sizes with short bend radius ($R = 1D$). The pipe size and the bend angle have an effect on the reaction moment required to rotate the pipe. As the pipe size increases, the reaction moment required to rotate the pipe increases as well. While increasing the bend angle results in decreasing the reaction moment. These results show that the flexibility of the pipe is affected by the bend angle which should be one of the parameters in the code factors used in the design.

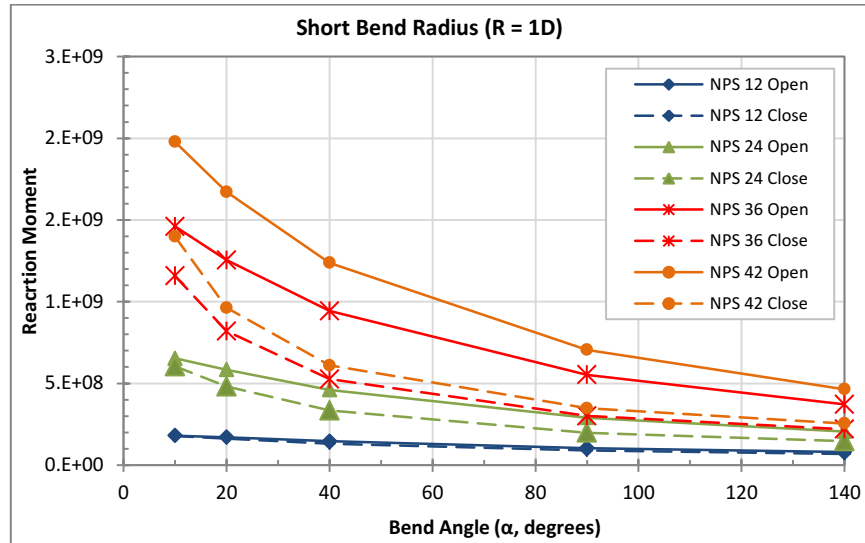


Figure 3. 19. Reaction bending moment vs bend angle for pipe bends with short bend radius (R=1D).

3.3.4. Effect of bending moment direction

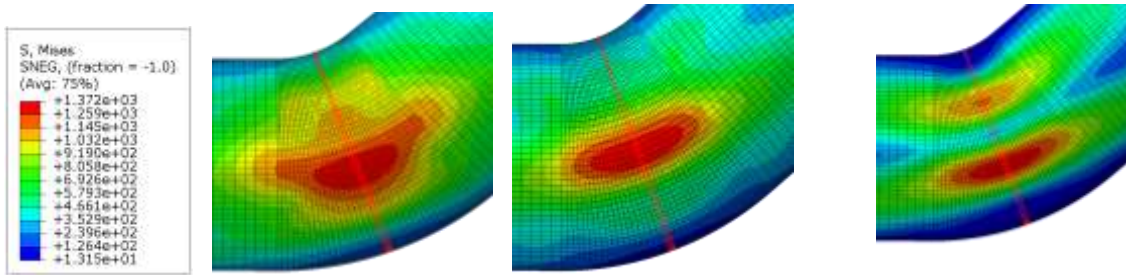
3.3.4.1. Pipe bends with large bend angles (40 to 140 degrees):

The critical section in all the studied pipe bends is at the mid-length of the pipe bend as shown in figure (3. 20) where the maximum stresses are found. The stresses at the critical section are measured at three different layers; inner, outer, and mid-layer of the pipe wall thickness. The FEA results show a typical pattern for the Von Mises stress distribution on most of the pipe bends regardless of the direction of the applied end rotation. The typical stress distribution in the critical cross-section shows a maximum Von Mises stress at the crown location ($\phi = 90^\circ$) for the inner and outer layer. While for the mid-layer, The Von Mises stress distribution has two stress peaks as shown in figure (3. 20). The stress distribution at the critical section is found to be similar for most of the studied pipe bends with bend angle varying from 40 to 140 degrees. However, the stress distribution on some of the pipe bends changes when the bend angle is small as 10 and 20 degrees.

Figures (3. 21) to (3. 26) show the stress distribution on a 90-degree pipe bend with 12” outer diameter (NPS 12 with 0.375” wall thickness) and short bend radius (R =1D) subjected to an opening and closing bending moment. This case is considered one of the typical stress distribution cases for pipe bends. The stress is plotted against the circumferential angle (ϕ) starting from zero at the intrados to

180 degrees at the extrados of the pipe bend. Figure (3. 21) shows that the distribution of the Von Mises stress on the mid-layer of the pipe bend has two maximum points. The two peaks are approximately at a circumferential angle of 60 and 110 degrees. However, for the inner and outer layers, the maximum Von Mises stress is found to be always at the crown location ($\theta = 90$ degrees) regardless the direction of applied end rotation. On the other hand, the hoop and longitudinal stress distributions are affected by the bending moment direction. The ovalization of the cross-section adds bending stresses on the pipe wall that mainly affects the hoop stresses. For the case of an opening bending moment, figure (3. 23) shows the hoop stress distribution on the critical section where the maximum stress is found to be at the crown location for all three layers; inner, outer and mid-layer of the wall thickness. At the outer layer of the pipe wall, the hoop stresses are compression at the crown zone where the circumferential angle is around 55 to 110 degrees, while the rest of the outer layer is in tension. However, the opposite is for the inner layer, where the hoop stresses are tension at the crown zone and compression at the intrados and extrados of the bend. The hoop stresses from the closing bending moment are the opposite of the opening bending moment as shown in figure (3. 24). The hoop stresses at the mid-layer of the pipe wall are considered negligible when compared to the stresses found at the inner and outer layer regardless the direction of the bending moment. The maximum hoop stress is found to be at the inner layer of the pipe wall in all typical models.

The results from all the studied models show that the maximum Von Mises stress through the wall thickness is at the inner layer of the pipe wall. Figures (3. 21) & (3. 22) show that the maximum Von Mises stress is at the inner surface of the pipe bend at the crown location. Therefore, it is expected that for higher stresses, the inner surface of the pipe bend will start yielding. Therefore, the design of pipe bends should not be restricted on the stresses at the mid-layer of the wall thickness only. These results and conclusion agrees with Stromeyer (1907). Stromeyer was the first to draw attention to the fact that unpressurized pipe bends subjected to bending experience cracks at the mid-section of the pipe bend at the crown location where the crack extended from the interior of the tube. The direction of cracks that occurred when the pipeline is in service shows that the circumferential stresses are the reason behind failure. This was mentioned by Gross (1953), but no reference was found.



a. Typical Von Mises stress distribution on the outer (on the left) and inner layer (on the right) of the wall thickness (NPS 42 Open BM, $\alpha=40$)

b. Von Mises stress distribution on the mid-layer of the wall thickness

Figure 3. 20. Typical Von Mises stress distribution for a 40-degree pipe bend with short bend radius ($R = 1D$) subjected to an opening bending moment.

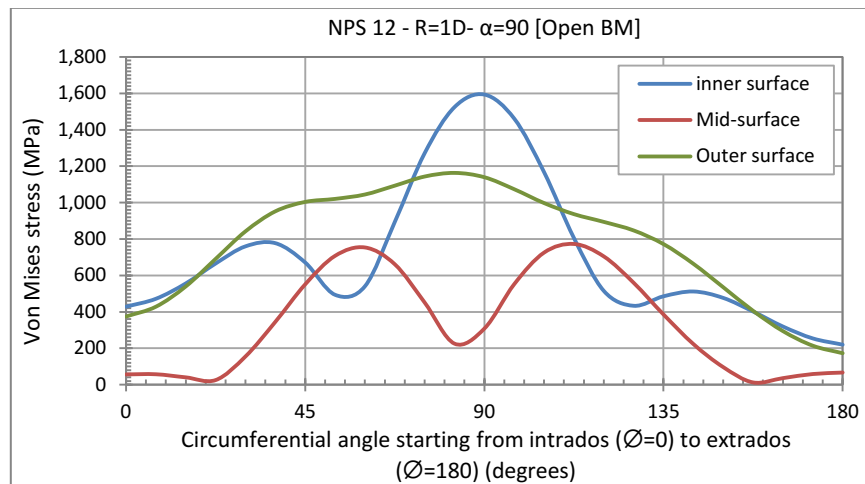


Figure 3. 21. Von Mises stress distribution along the critical section of a pipe bend with bend angle 90° and short bend radius ($R = 1D$) subjected to an open bending moment

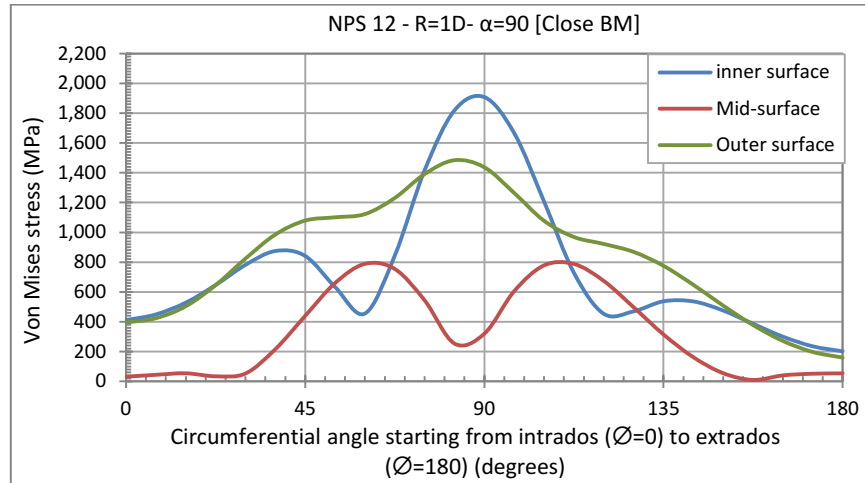


Figure 3. 22. Von Mises stress distribution along the critical section of a pipe bend with bend angle 90° and short bend radius ($R = 1D$) subjected to a closing bending moment

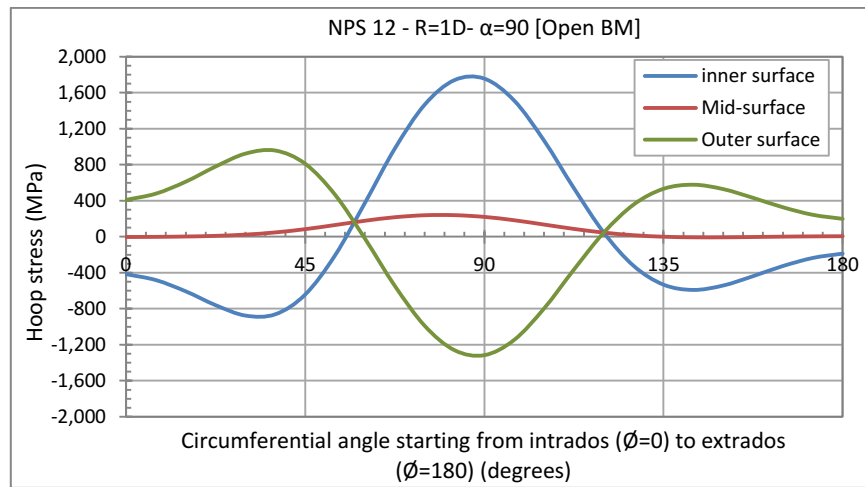


Figure 3. 23. Hoop stress distribution along the critical section of a pipe bend with bend angle 90° and short bend radius ($R = 1D$) subjected to opening bending moment.

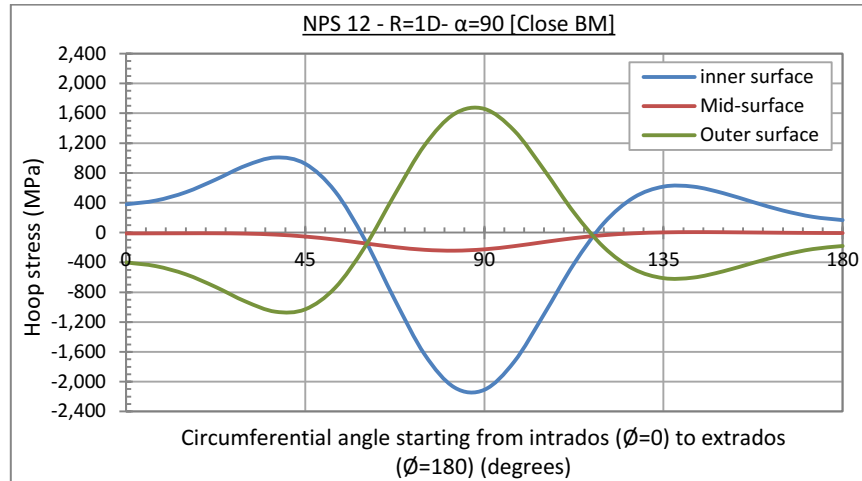


Figure 3. 24. Hoop stress distribution along the critical section of a pipe bend with bend angle 90° and short bend radius ($R = 1D$) subjected to closing bending moment.

According to the beam theory, the maximum longitudinal stresses are expected to be at the intrados and extrados of the pipe bend which are the points furthest to the neutral axis ($\phi = 0^\circ$ & 180°). However, due to the cross-sectional deformations, the longitudinal stress distribution for pipe bends is found to be different. Figure (3. 25) shows the longitudinal stress distribution at the critical section for a pipe bend subjected to an opening bending moment. The maximum longitudinal stresses are found to be in two different regions in the pipe bend. First region is between the intrados and the crown of the pipe bend approximately between a circumferential angle of 50 and 75 degrees, while the second region is between the extrados and the crown between approximately 105 and 130 degrees. The longitudinal stresses across the wall thickness are found to be tension at the intrados area and compression at the extrados area. However, when a closing bending moment is applied, the stresses are mirrored to be tension at the extrados and compression at the intrados as shown in figure (3. 26).

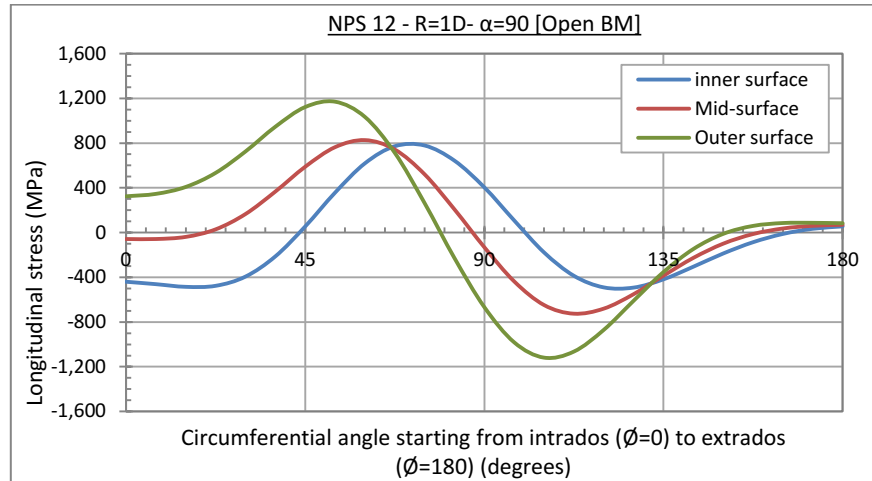


Figure 3. 25. Longitudinal stress distribution along the critical section of a pipe bend with bend angle 90° and short bend radius (R = 1D) subjected to opening bending moment.

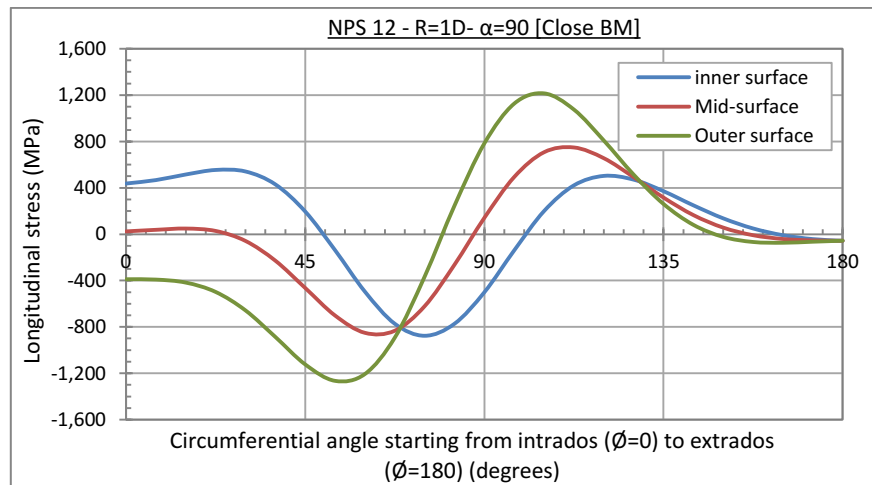


Figure 3. 26. Longitudinal stress distribution along the critical section of a pipe bend with bend angle 90° and short bend radius (R = 1D) subjected to closing bending moment.

3.3.4.2. Pipe bends with small bend angles (10 and 20 degrees):

The behaviour of pipe bends with small bend angles are different than the typical behaviour explained earlier since the small-angled pipe bends start to behave more as a straight pipe. The FEA results started to show a different stress distribution for pipe bends with bend angles 10 and 20

degrees, especially those with small outer diameter bends such as NPS 12 and 24. The FEA results show that as the bend angle decrease, the location of the maximum Von Mises stress along the pipe bend changes from being at the inner layer of the crown to move towards the outer layer of the intrados. This appears in pipe bends of sizes NPS 12, 24, 36 and 42 with bend angle 10 degrees and for pipes NPS 12 with bend angle 20 degrees. Figure (3. 27) shows the Von Mises stress distribution on the three wall thickness layers at the mid-length of a pipe bend with 10 degrees bend angle and pipe size NPS 12 which is considered one of the cases that represents the small bend angle behaviour. The critical section is at the outer layer of the intrados where the maximum Von Mises stress is found. The inner layer of the pipe wall has a Von Mises stress distribution that varies depending on the pipe size and bend angle. For example, small pipe sizes such as NPS 12 and bend angles 10 degrees, the inner layer Von Mises stress will usually have two critical points. One of these critical locations is at the intrados while the other one is at the crown area as shown in figure (3. 28). However, when the bend radius increases and the behaviour approach a straight pipe, the critical point could be seen clearly at the intrados location as shown in figure (3. 29). For pipe bends with larger pipe size as NPS 36, where the outer diameter is relatively large compared to the bend radius, the inner stress distribution changes and the critical Von Mises is at the crown location as shown in figure (3. 30).

On the other hand, the Von Mises stress distribution on the mid-layer changes according to the pipe bend behaviour. For pipe bends behaving as a straight pipe, whether due to long bend radius ($R = 5D$) or the influence of a small bend angle (e.g. 10 degrees) and relatively small pipe outer diameter (e.g. NPS 12), the stresses are found to be negligible at the crown and increases gradually towards the intrados and extrados till it reaches the maximum value at $\theta = 0$ and/or 180 degrees as shown in figures (3. 28) & (3. 29) which looks similar to a straight pipe stress distribution which is mainly affected by the longitudinal stresses. However, when the behaviour is influenced by the toroidal effect of the pipe bend, then the Von Mises stress at the mid-layer has two peaks at a circumferential angle around 60 and 110 degrees as shown in figure (3. 30). This shows that as the bend angle decreases, the behaviour is approaching a straight pipe. For pipe bends with 10 degrees bend angle, the maximum von Mises stresses is at the outer layer of the pipe wall thickness at the intrados. Therefore, it is expected that at higher stresses the outer layer of the pipe bend starts yielding. The FEA results for all the pipe bends with bend angle ranging from 10 to 140 degrees are shown in Appendix (A).

From the FEA results of pipe bends with bend angle 10 degree, it is found that the models that followed this behaviour are those for pipe sizes NPS 12, 24, 36 & 42 when subjected to opening bending moment. However, when a closing bending moment is applied, pipe sizes 12 and 24 only follow this behaviour. When the bend radius increase to 5D, The pipe bend acts more as a straight pipe.

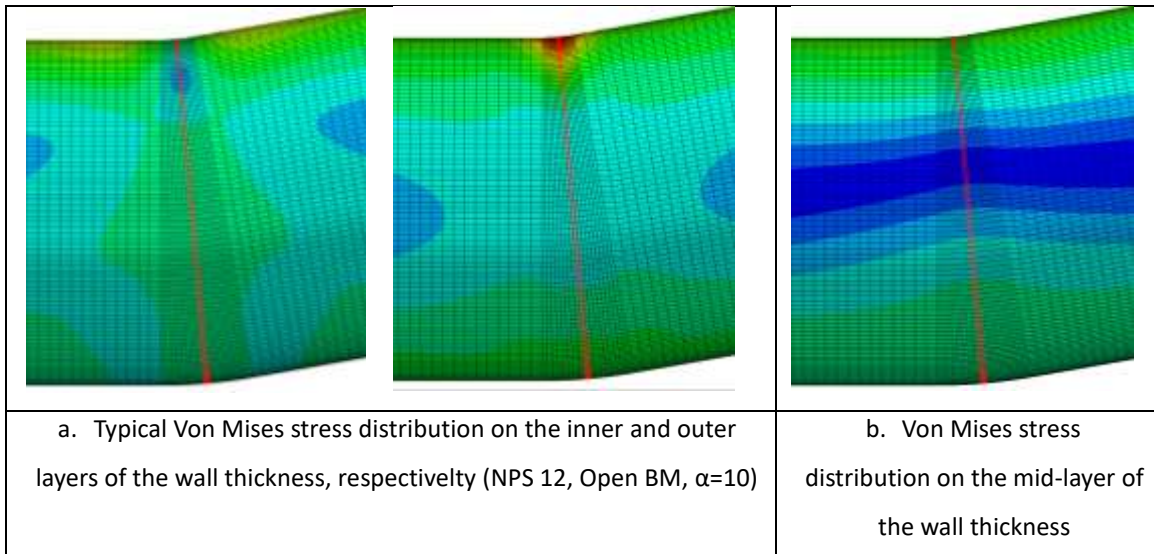


Figure 3. 27. Von Mises stress distribution for 10-degree pipe bends with 12” outer diameter and short bend radius ($R = 1D$) subjected to opening bending moment.

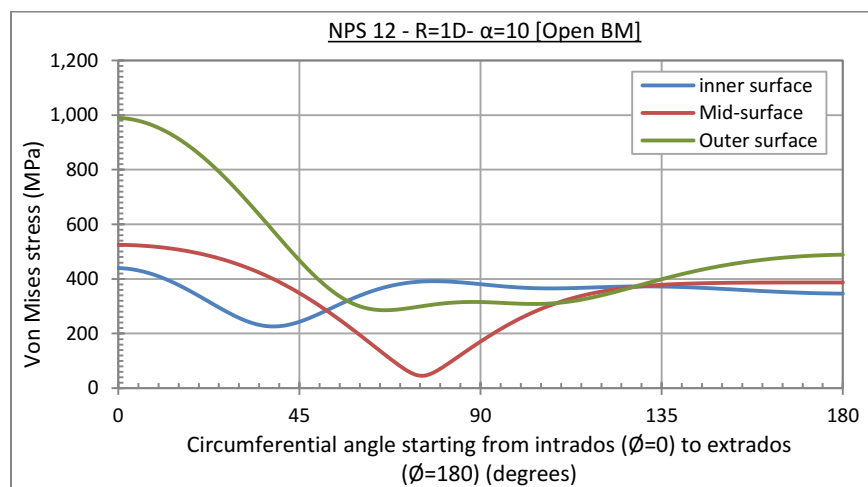


Figure 3. 28. Von Mises stress distribution along the critical section of an NPS 12 pipe bend with bend angle 10° and short bend radius ($R = 1D$)

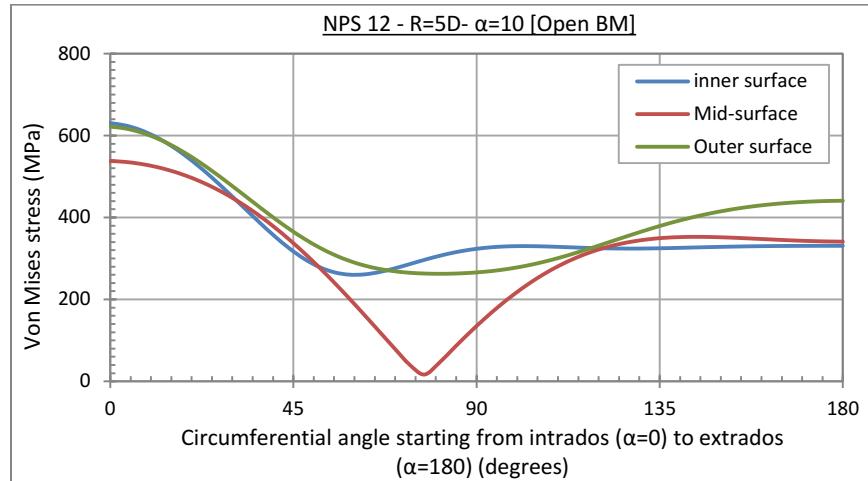


Figure 3. 29. Von Mises stress distribution along the critical section of an NPS 12 pipe bend with bend angle 10° and long bend radius (R = 5D)

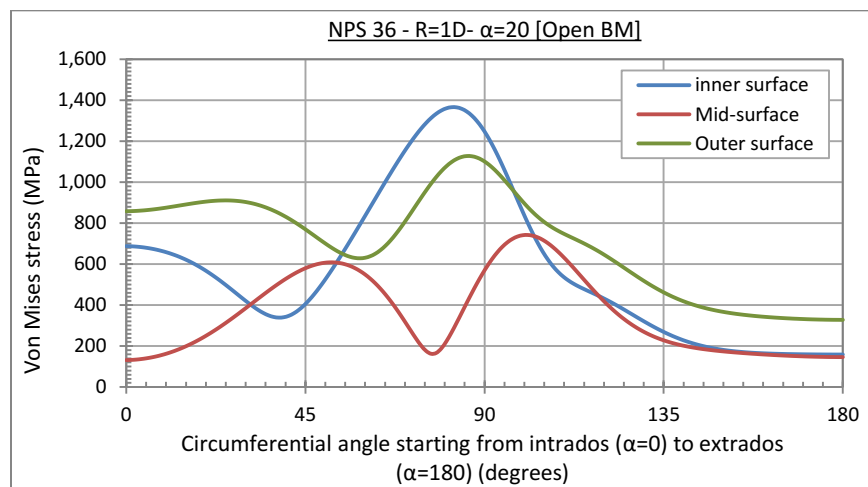


Figure 3. 30. Von Mises stress distribution along the critical section of a NPS 36 pipe bend with bend angle 20° and short bend radius (R = 1D)

The Von Mises stress is an equivalent “distortional” stress that is a function of the differences in the principal stresses, which are considered the longitudinal and hoop stresses in this study. Therefore, the maximum Von Mises stress location depends on the maximum longitudinal and hoop stresses locations. Figures (3. 31) to (3. 36) show the distribution of the longitudinal and hoop stresses across the circumference of the pipe bend from intrados ($\phi = 0$) to extrados ($\phi = 180$) on the inner, outer and mid-

layer. Figures (3. 31) to (3. 34) show that the maximum hoop and longitudinal stress are at the intrados for all three layers for small pipe size (NPS 12) and small bend angle of 10 degrees whether the bend radius is short ($R = 1D$) or long ($R= 5D$). Therefore, the maximum Von Mises stress for this case is at the intrados at the three studied layers. It is noticed that as the bend radius increase, the pipe bend behaves more as a straight pipe. This is concluded from the longitudinal stress distribution shown in figure (3. 34) for long radius pipe bends ($R = 5D$), the behaviour is like a straight pipe since the maximum longitudinal stresses are at the furthest points from the centre of the pipe which is the intrados and extrados, moreover, the maximum stresses are equal in value and opposite in direction. As the pipe size increase to NPS 36, the location of maximum hoop stress for the inner and outer layers are located at the crown as shown in figure (3. 35). While the maximum hoop stress at the mid-layer is around a circumferential angle of 50 degrees and considered negligible compared to the stresses found at the inner and outer layer. The longitudinal stress for the inner layer is around 65 degrees while the outer layer is at the crown. The mid-layer has two maximum longitudinal stress locations around 55 and 100 degrees and is found to be as high as the inner and outer layers as shown in figure (3. 36). The hoop stresses at the inner and outer layers govern the Von Mises stress in the case of large pipe sizes such as NPS 36. The inner and outer layers have maximum Von Mises stress similar to the hoop stress at the crown location while the mid-layer is governed by the longitudinal stress therefore there is two local maximum stress locations. The Von Mises stress depends on the highest of stresses between both, the hoop and longitudinal stress. Therefore, the hoop and longitudinal stresses must be considered in the design of pipelines.

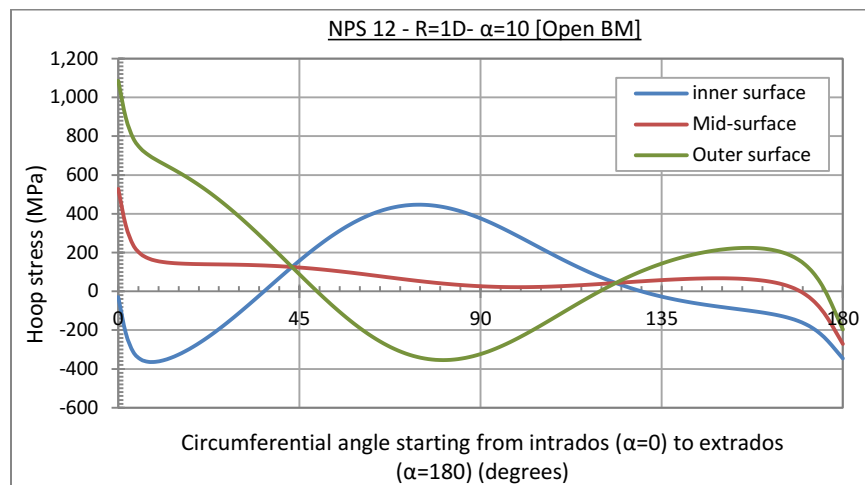


Figure 3. 31. Hoop stress distribution along the critical section of a pipe bend with bend angle 10° and short bend radius ($R = 1D$)

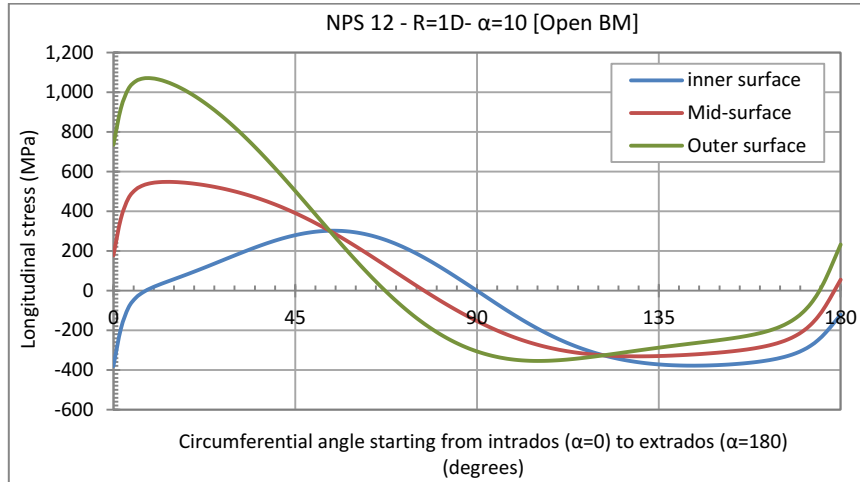


Figure 3. 32. Longitudinal stress distribution along the critical section of a pipe bend with bend angle 10° and short bend radius ($R = 1D$)

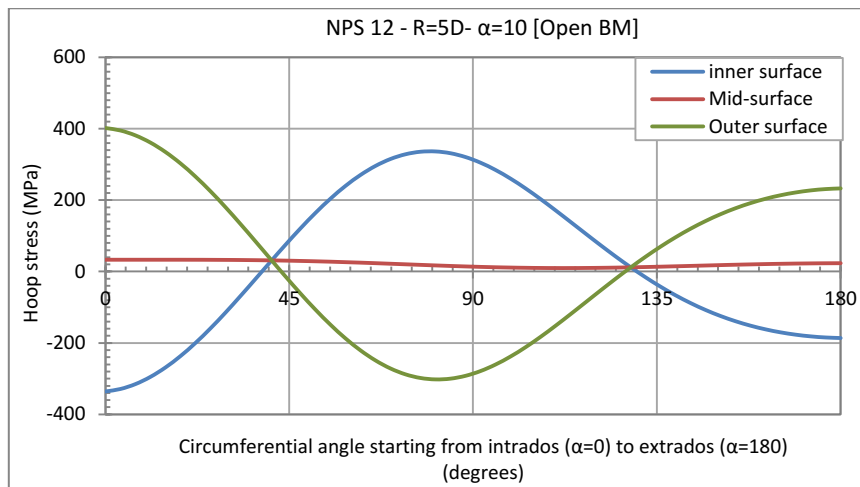


Figure 3. 33. Hoop stress distribution along the critical section of a pipe bend with bend angle 10° and long bend radius ($R = 5D$)

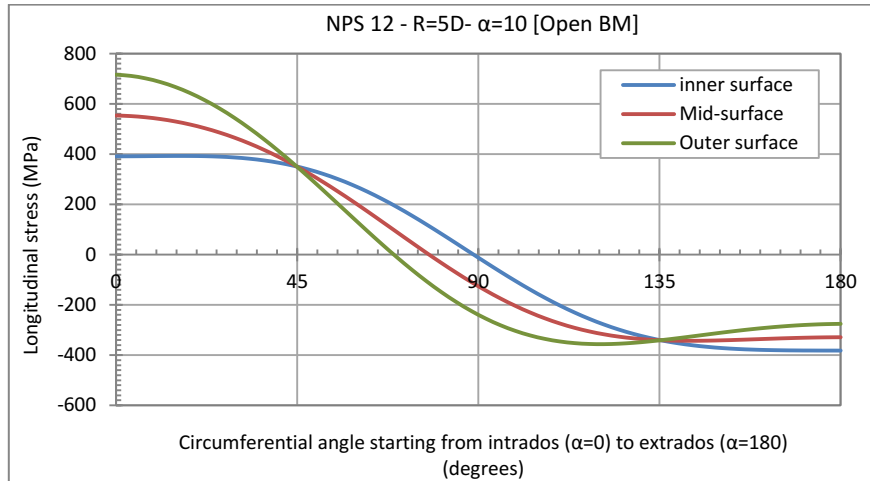


Figure 3. 34. Longitudinal stress distribution along the critical section of a pipe bend with bend angle 10° and long bend radius ($R = 5D$)

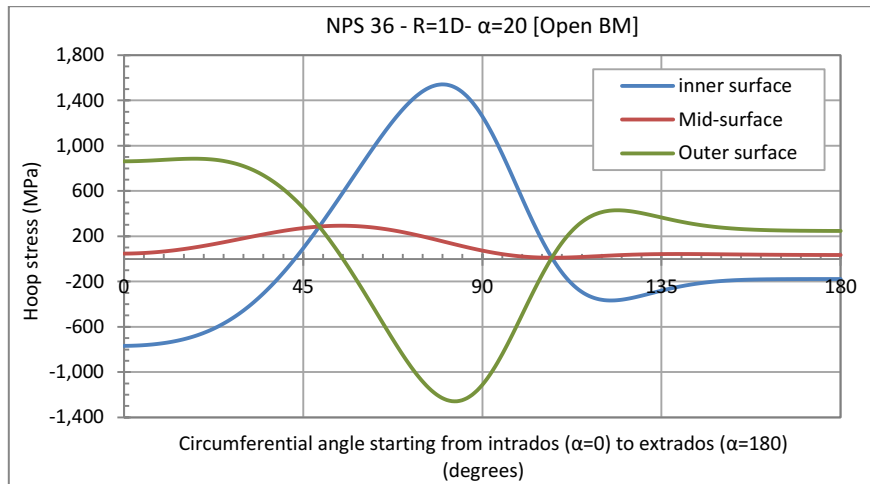


Figure 3. 35. Hoop stress distribution along the critical section of an NPS 36 pipe bend with bend angle 20° and short bend radius ($R = 1D$)

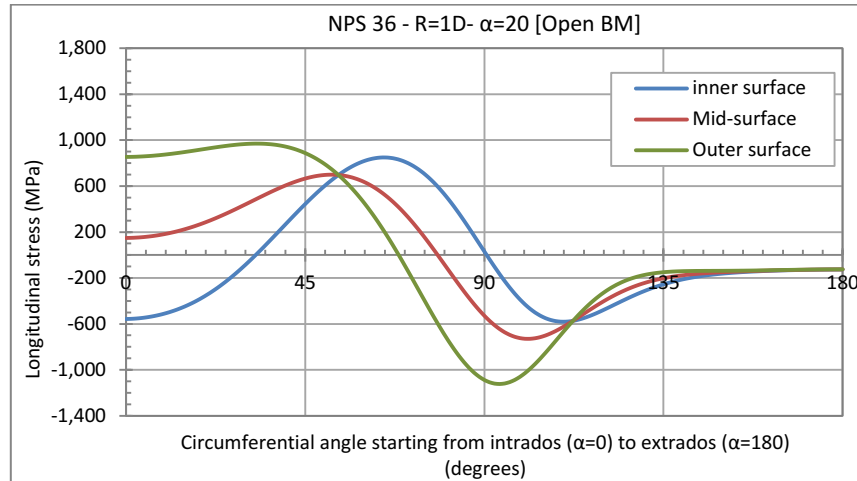


Figure 3. 36. Longitudinal stress distribution along the critical section of an NPS 36 pipe bend with bend angle 20° and short bend radius ($R = 1D$)

3.3.4.3. Stress distribution on the mid-layer of pipe bends

The FEA results show that the Von Mises stress in the mid-layer is affected by the direction of bending moment. For example for small bend angles such as 10, 20 and 40 degrees, the closing bending moment will result in higher Von Mises stress than the opening bending moment. However, when the bend angle increases to 90 and 140 degrees, the opening bending moment results in higher Von Mises stress than the closing bending moment. Figures (3. 37) and (3. 38) show the maximum Von Mises stress in the mid-layer at an end rotation of 0.1 radians plotted against the D/t ratio for pipe bends with short and long bend radius, respectively. The plotted results are for pipe bends with bend angles 10 and 140 degrees subjected to opening bending moment (OBM) and closing bending moment (CBM) which is found to be having the maximum stress difference between the opening and closing bending moment. The curves show that the closing bending moment results in stresses higher than the opening bending moment by up to 172.5% for the 10 degrees bend angle pipes. However, for the 140 degrees bend angle pipes, the opening bending moment results in higher stresses than the closing bending moment by up to 21.35%. The bend radius of the pipe is another parameter that affects the stresses. As the bend radius increase, the difference between the stresses obtained from the opening and closing bending moment decreases as shown in figures (3. 39) and (3. 40). For example, for a pipe bend of size NPS 42 and bend angle 10, the Von Mises stress from the closing bending moment is higher by 172.5% than that from the

opening bending moment for a short radius bend ($R = 1D$). However, as the bend radius increases to $3D$ and $5D$, the difference decreases to 93.99 % and 55.84 %, respectively.

Figures (3. 41) to (3. 43) show the maximum Von Mises stress at a particular end rotation of 0.1 radians due to opening and closing bending moment versus the D/t ratio for pipe bends with different bend radii ($R = 1 D, 3D \& 5D$). The pipe size has an influence on the difference in stresses between the opening and closing bending moment cases. As the bend size increases, the difference in stresses increases as well. For example, pipe bends with short bend radius ($R = 1D$) and bend angle 140 degrees, the difference in stresses is 21.35% for NPS 42 pipes. However, this difference reduces to 0.85% for pipe sizes NPS 12. Therefore, the results show that the difference in stresses is more significant in the case of large pipe sizes than small pipe sizes. The maximum difference in stresses for small pipe sizes such as NPS 12 is found to be 17.7%. While for large pipe sizes as NPS 42, the maximum difference in stresses is 172.5%. Therefore, the direction of bending moment acting on the pipe bend is an important parameter that needs to be included in the flexibility and stress intensification factors.

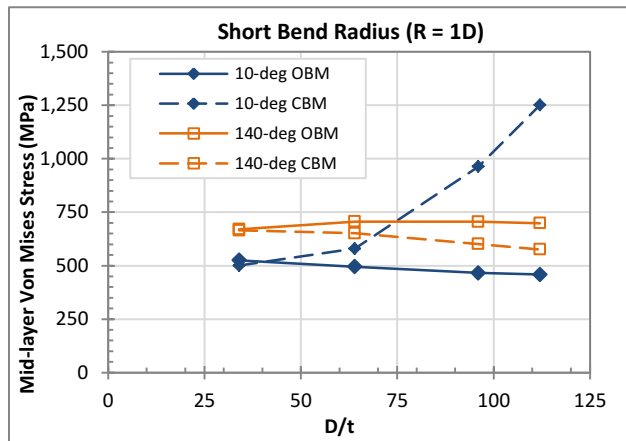


Figure 3. 37. Von Mises stress distribution at mid-layer of pipe wall at an applied end rotation 0.1 radians for different D/t ratios for pipe bends with bend angle 10 and 140 degrees having short bend radius ($R = 1D$).

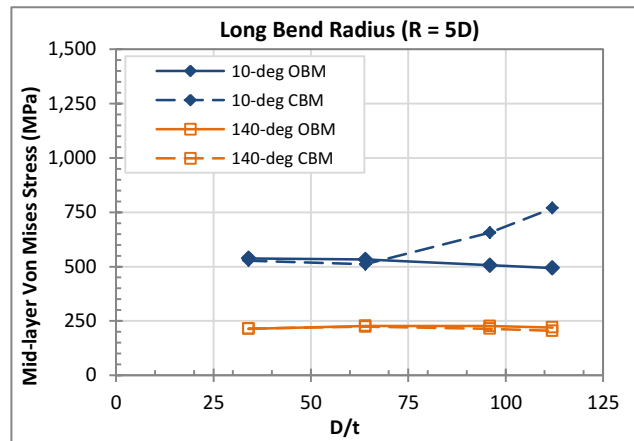


Figure 3. 38. Von Mises stress distribution at mid-layer of pipe wall at an applied end rotation 0.1 radians for different D/t ratios for pipe bends with bend angle 10 and 140 degrees having long bend radius ($R = 5D$).

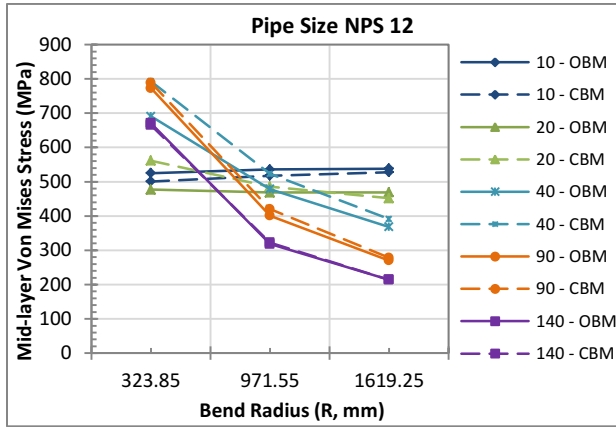


Figure 3. 39. The maximum Von Mises stress vs the bend radius for pipe size NPS 12 with different bend angles.

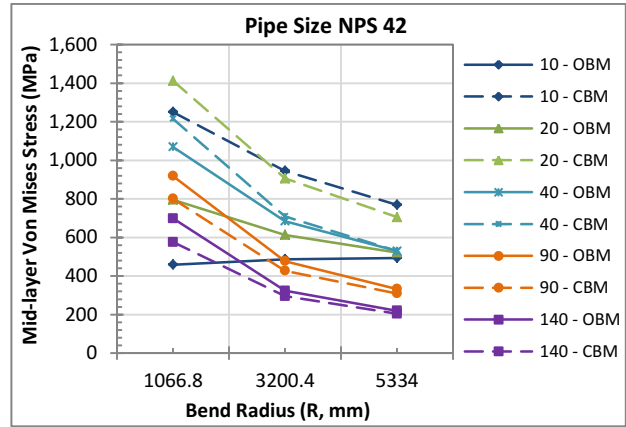


Figure 3. 40. The maximum Von Mises stress vs the bend radius for pipe size NPS 42 with different bend angles.

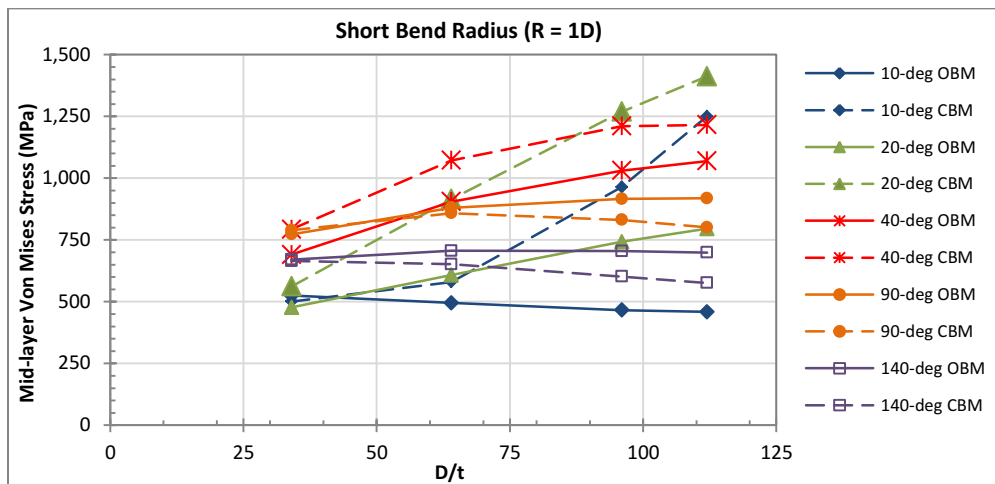


Figure 3. 41. Von Mises stress distribution at mid-layer of pipe wall at an applied end rotation 0.1 radians for different D/t ratios for pipe bends with short bend radius (R = 1D) and varying bend angles.

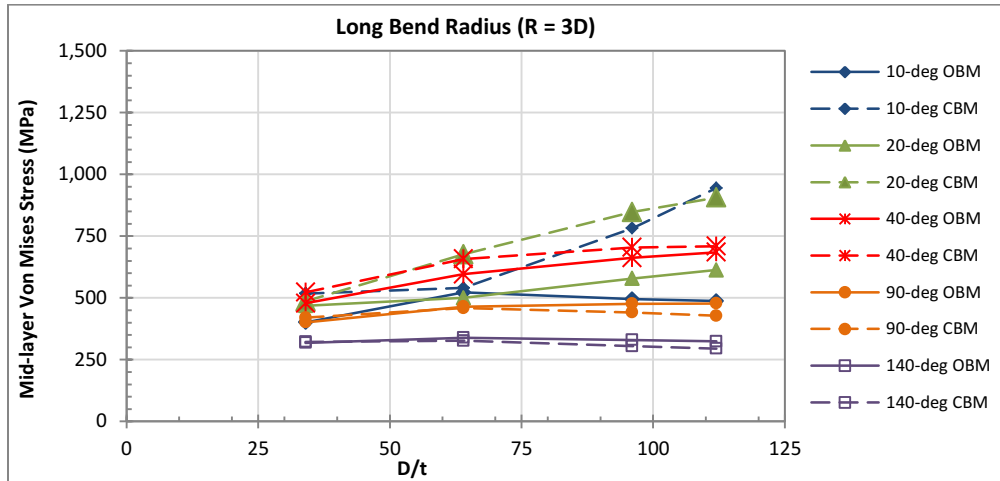


Figure 3. 42. Von Mises stress distribution at mid-layer of pipe wall at an applied end rotation 0.1 radians for different D/t ratios for pipe bends with short bend radius (R = 1D) and varying bend angles.

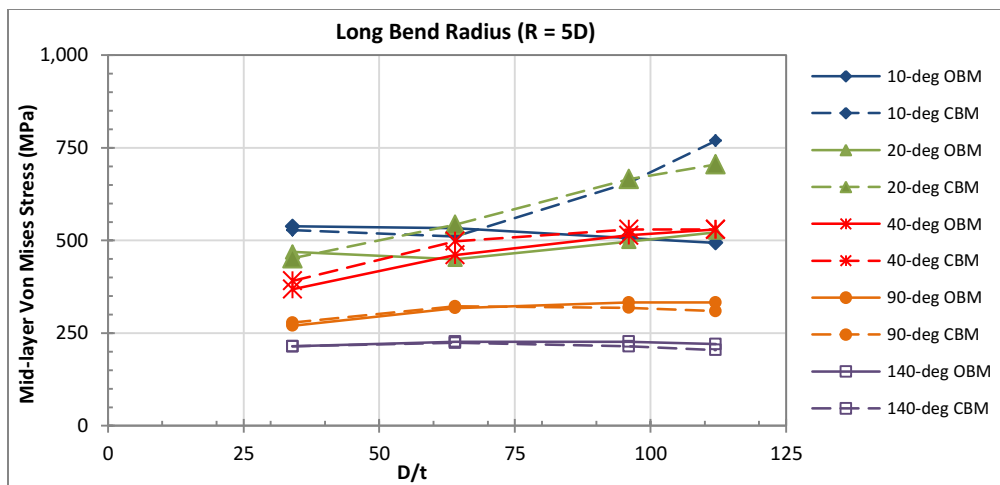


Figure 3. 43. Von Mises stress distribution at mid-layer of pipe wall at an applied end rotation 0.1 radians for different D/t ratios for pipe bends with long bend radius (R = 5D) and varying bend angles.

3.3.5. Comparison between the FEA and the CSA-Z662 Stresses

A comparison between the FEA and the predictive stress according to the CSA-Z662 is conducted in this section to get a better understanding on the methodology used by the current codes to account for the ovalization shape in the design. The results from the FEA models of pipe systems

subjected to opening and closing bending moments are compared to the stress results evaluated using the CSA-Z662 code. The CSA-Z662 evaluates the stresses on a pipe bend under internal pressure and bending moment using equation (3.2). The stresses due to internal pressure (S_h & S_L) are ignored from equation (3.2) since this study is based on pipe bends subjected to bending moments only. The stresses at the mid-layer of the pipe bend are evaluated according to CSA-Z662 as follows;

$$S_h - S_L + S_B \leq S * T \tag{3.2}$$

Where,

S = specified minimum yield strength,

T= temperature factor,

$$S_B = i.M/Z$$

$$i = \frac{0.9}{h^{2/3}}$$

$$h = \frac{tR}{r^2}$$

3.3.5.1. Stresses at mid-layer of the pipe wall thickness

The FEA Von Mises stress results measured at the mid-layer of the pipe bend is compared to the predictive stresses using the CSA-Z662 equation (Eqn. (3.2)) and plotted in figures (3. 44) to (3. 51) versus the D/t ratios. The results show that the CSA estimated stresses is conservative in some cases and un-conservative in others depending on the bend angle, pipe size and the bend radius of the pipe.

Pipe bends with small bend angles tend to behave more as a straight pipe. Therefore, the increase in stresses due to ovalization might not be as high as that for pipe bends with large bend angles. It is expected that the stress intensification factors required for bends with small bend angles to be lower than that of the larger bend angle pipes. Therefore, the CSA estimated stresses are found to be highly conservative for pipes with bend angles 10 and 20 degrees since the CSA

code ignores the bend angle as a parameter in the stress intensification factor. Figures (3. 44) and (3. 45) show the stresses for pipe bends with bend angles 10 and 20 degrees. As predicted, the CSA estimated stresses are highly conservative compared to the stresses evaluated by the FEA by up to 745 % and 333 % for the opening and closing bending moment, respectively. However, as the bend angle increases to 90 degrees, the CSA estimated stress is found to be un-conservative by up to 17.5% in the closing bending moment case as shown in figure (3. 46). As the bend radius increase to 5D, the difference between the CSA estimated stresses and the FEA stresses decreases as well as shown in Figures (3. 48) to (3. 51). The results presented in figures (3. 48) and (3. 49) show that the code estimated results are conservative in the case of long radius pipe bends with bend angle 10 degrees by up to 160% and 65% for the opening and closing bending moment cases, respectively. However, as the bend angle increase to 90 and 140 degrees as shown in figures (3. 50) and (3. 51), the code is un-conservative by up to 12.2%.

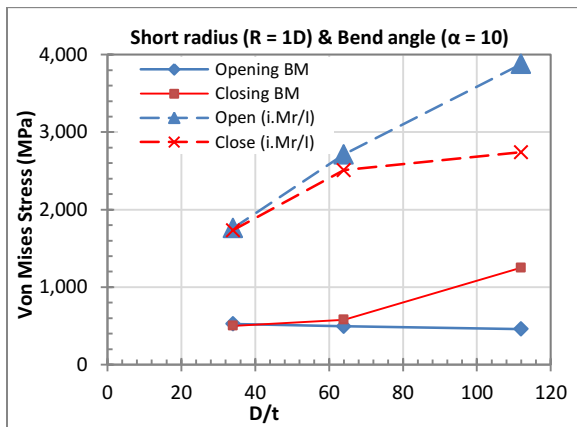


Figure 3. 44. Stress distribution at applied end rotation 0.1 radians for short radius pipe bends with bend angle 10 degrees.

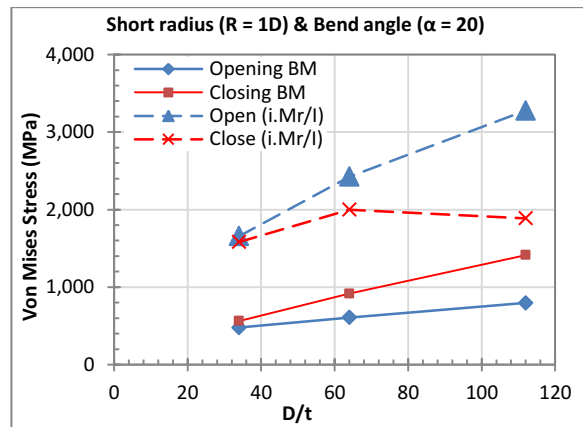


Figure 3. 45. Stress distribution at applied end rotation 0.1 radians for short radius pipe bends with bend angle 20 degrees.

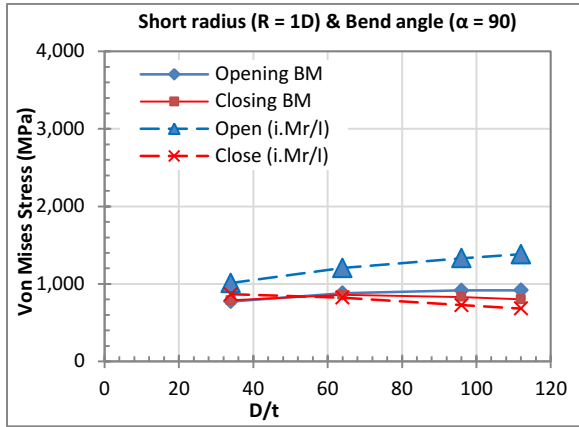


Figure 3. 46. Stress distribution at applied end rotation 0.1 radians for short radius pipe bends with bend angle 90 degrees.

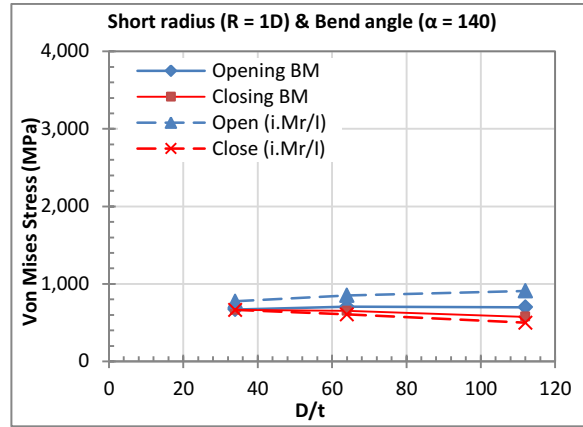


Figure 3. 47. Stress distribution at applied end rotation 0.1 radians for short radius pipe bends with bend angle 140 degrees.

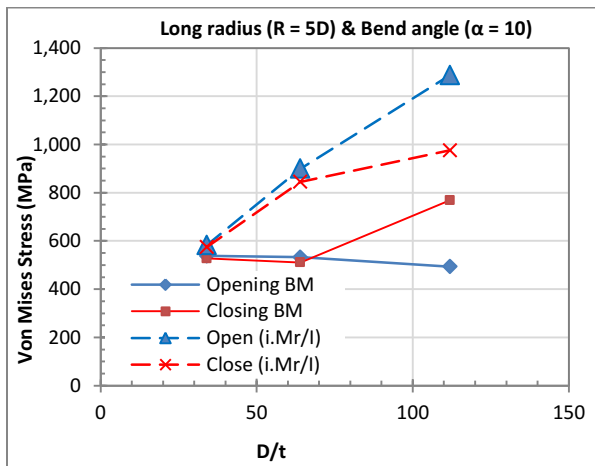


Figure 3. 48. Stress distribution at applied end rotation 0.1 radians for long radius pipe bends with bend angle 10 degrees.

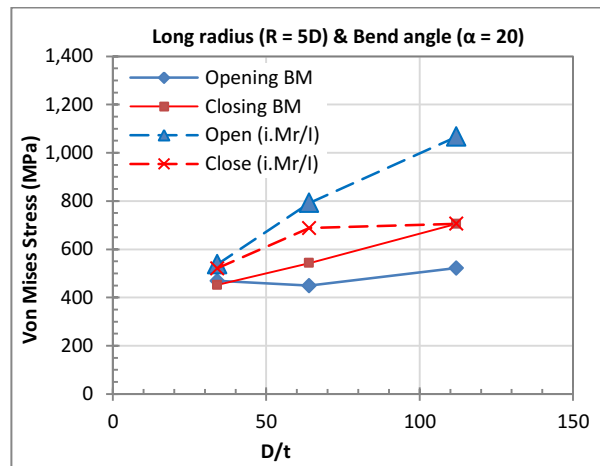


Figure 3. 49. Stress distribution at applied end rotation 0.1 radians for long radius pipe bends with bend angle 20 degrees.

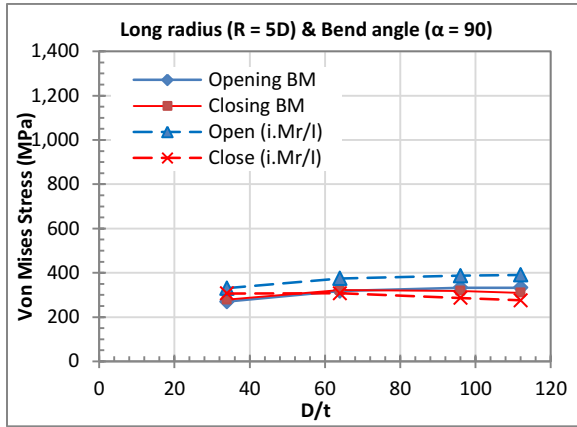


Figure 3. 50. Stress distribution at applied end rotation 0.1 radians for long radius pipe bends with bend angle 90 degrees.

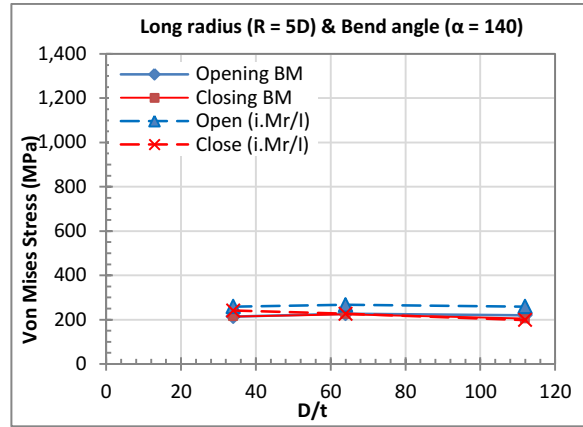


Figure 3. 51. Stress distribution at applied end rotation 0.1 radians for long radius pipe bends with bend angle 140 degrees.

3.3.5.2. Stresses at the inner and outer layer of the pipe wall thickness

The Von Mises stresses presented earlier in this chapter shows that the maximum stresses are not found at the mid-layer of the wall thickness of the pipe bend. However, the critical stresses are at the inner and outer layer where the yielding of the section starts. Therefore, in this section a comparison between the FEA stress results and the estimated stresses by the code at the inner and outer layers is conducted to investigate the conservativeness of the design methodology adopted by the CSA code. The results show that the CSA is un-conservative for most of the studied pipes when the inner and outer layers are investigated.

Figures (3. 52) to (3. 55) show the stresses on the inner layer of pipe bends with short and long bend radii and with bend angles 10, 90 and 140 degrees. The results show that the CSA estimated stresses are highly conservative for pipe bends with short bend radius ($R = 1D$) and small bend angles ($\alpha = 10^\circ$ & 20°) especially when the pipe size is equal to or smaller than NPS 24. However as the bend angle increases, the CSA stresses are un-conservative. Figure (3. 52) shows the FEA stress results at the inner layer of the pipe wall compared to the CSA estimated stresses for short radius pipe bends with bend angle 10 degrees. The code stresses are highly conservative especially in the opening bending moment case where the stresses are higher by up to 421.4% than the FEA stress results. However, the code stresses are conservative by up to 191.7 % in the closing

bending moment cases. As the bend angle increase, the ovalization effect starts to increase and it has higher influence on the stresses. For an opening bending moment, the CSA stresses are found to be un-conservative by up to 83.8 % when compared to the FEA results of pipe bends with 140 degrees bend angles as shown in Figure (3. 53). However, for a closing bending moment, the CSA stresses are un-conservative by up to 219.4 % for pipes with 90 degree bend angle.

Figures (3. 54) and (3. 55) show the stress results on pipe bends with long bend radius ($R = 5D$). The difference in stresses between the estimated CSA and the FEA results decreases as the bend radius increases. However, the un-conservativeness of the CSA code is more noticeable for long bend radius pipes. For small bend angles ($\alpha = 10^\circ$ & 20°), the code is slightly conservative by up to 72.9% for pipes subjected to an opening bending moment. When the bend angle increases, the code is un-conservative by up to 68.9 %. For pipe bends subjected to closing bending moment, the code estimated stresses are un-conservative when compared to the FEA results for the whole range of bend angles by up to 167.6 %.

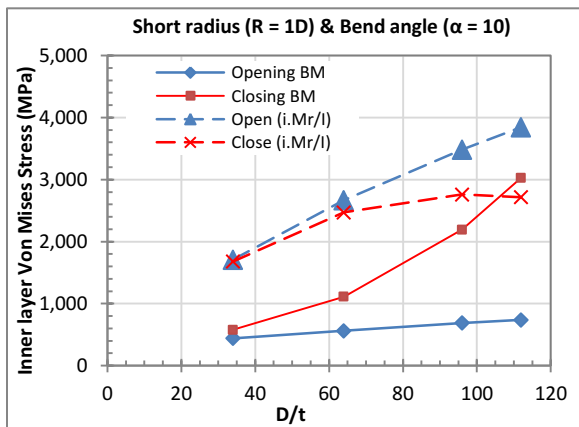


Figure 3. 52. Inner layer stress distribution at applied end rotation 0.1 radians for short radius pipe bends with bend angle 10 degrees.

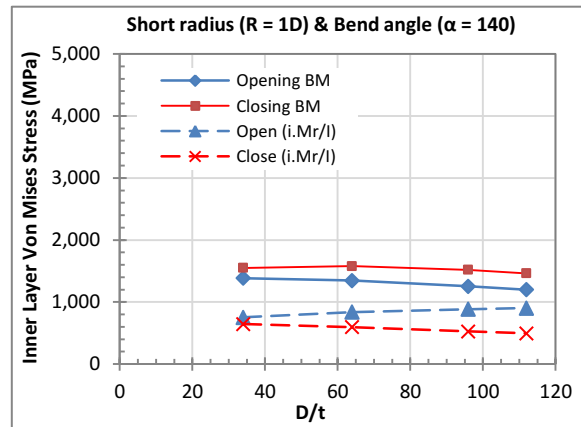


Figure 3. 53. Inner layer stress distribution at applied end rotation 0.1 radians for short radius pipe bends with bend angle 140 degrees.

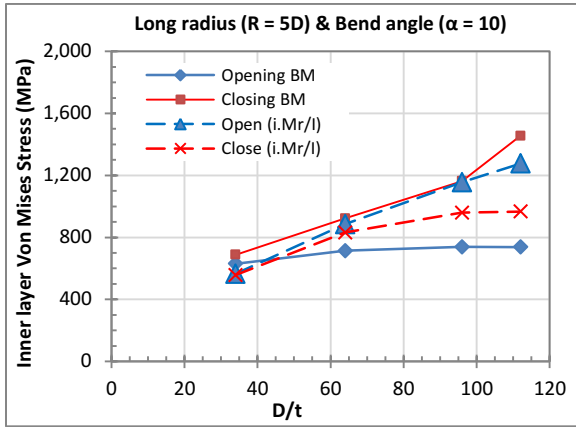


Figure 3. 54. Inner layer stress distribution at applied end rotation 0.1 radians for long radius pipe bends with bend angle 10 degrees.

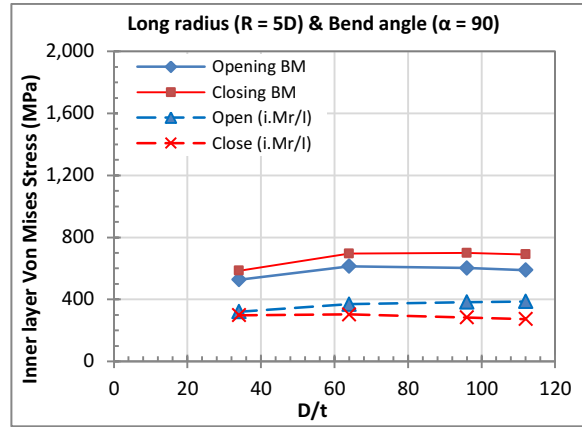


Figure 3. 55. Inner layer stress distribution at applied end rotation 0.1 radians for short radius pipe bends with bend angle 90 degrees.

The investigation of the outer layer of the pipe wall shows the same conclusion as for the inner layer. The maximum Von Mises stress on the outer layer is higher than that of the inner layer for pipe bends with small bend angles as 10 and 20 degrees. Therefore, the code estimated stresses in these cases show less conservativeness than that of the inner layer as shown in figure (3. 56). The code is conservative by up to 268.8% and 64.8 % in the case of opening and closing bending moment, respectively. However, for large bend angles the inner layer has higher maximum Von Mises stress than that of the outer layer. Therefore, the difference between the stresses estimated from the code and evaluated from the FEA are smaller and the un-conservativeness of the code is lower. The highest percentage of code un-conservative results are found in pipe bends with short bend radius and bend angles 90 degrees subjected to closing bending moment as shown in figure (3. 57). For long bend radius pipes with small bend angles ($\alpha = 10^\circ$ & 20°), the closing bending moment results in higher stresses than the opening bending moment leading to an un-conservative code results as shown in figure (3. 57) by up to 177%. However, the code shows conservative results when pipe bends are subjected to opening bending moments by up to 94%. As the bend angle increase, the code results are found to be un-conservative in both the opening and closing bending moments by up to 52% and 107%, respectively as shown in figure (3. 58).

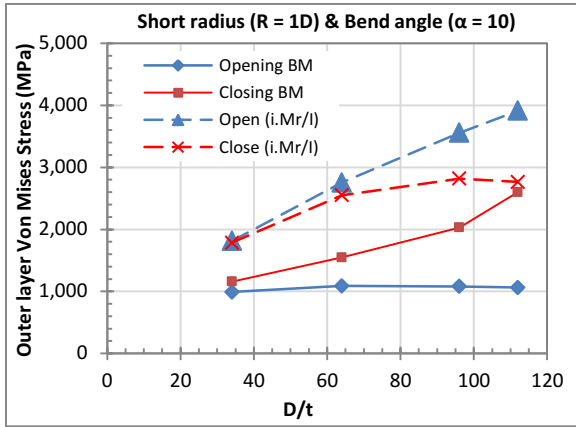


Figure 3. 56. Outer layer stress distribution at applied end rotation 0.1 radians for short radius pipe bends with bend angle 10 degrees.

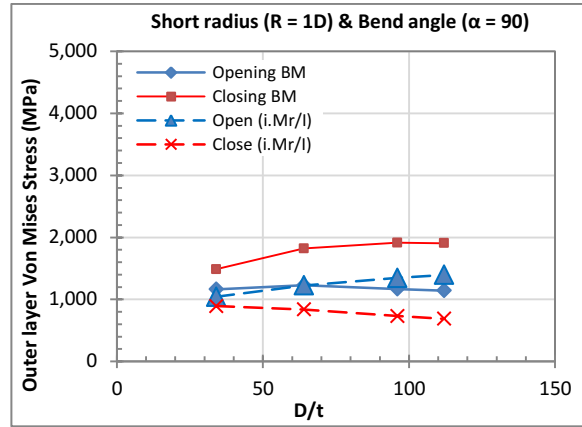


Figure 3. 57. Outer layer stress distribution at applied end rotation 0.1 radians for short radius pipe bends with bend angle 90 degrees.

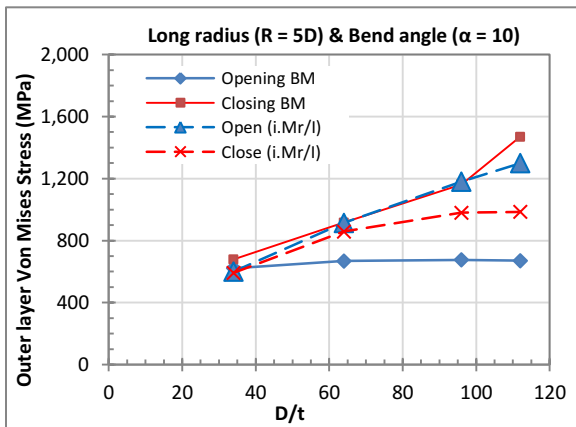


Figure 3. 57. Outer layer stress distribution at applied end rotation 0.1 radians for long radius pipe bends with bend angle 10 degrees.

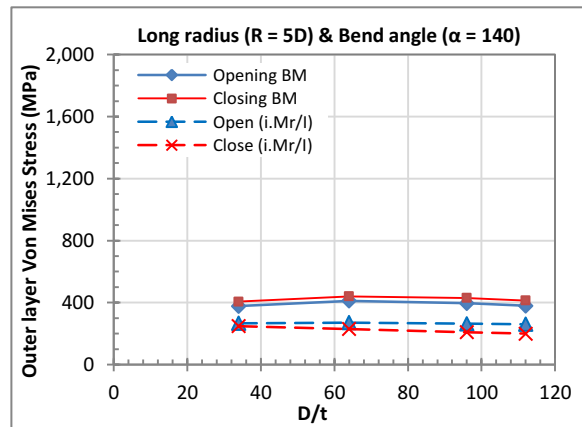


Figure 3. 58. Outer layer stress distribution at applied end rotation 0.1 radians for long radius pipe bends with bend angle 140 degrees.

3.4. DISCUSSION AND CONCLUSION

The FEA results show that the cross-sectional deformed shape depends on the direction of bending moment. The deformed cross-section is shaped according to the longitudinal axial forces resulting from the bending moment. If the pipe bend is subjected to a closing bending moment, then the resulting axial forces are distributed as tension above the neutral axis and compression below the neutral axis as shown in figure (3. 60.a). This leads to a resultant force, at both extrados and intrados of

the bend, pushing the pipe walls towards the neutral axis deforming the cross-section into a flattened shape. However, if an opening bending moment is acting on a pipe bend, then the generated axial forces are distributed as tension below the neutral axis and compression above the neutral axis. A resultant force is generated at the extrados and intrados of the pipe bend pulling the pipe walls away from the neutral axis resulting in an oval shape as shown in figure (3. 60.b).

The cross-sectional deformation occurring at the mid-length of a pipe bend subjected to bending moment is found to be function of many parameters. The main parameters are the direction of bending moment, the bend angle and the size of the pipe bend. For pipe bends subjected to closing bending moments, the cross-section starts to flatten and the diameter in the plane of bending deforms (D') into a smaller dimension than the initial pipe diameter (D). Therefore, during loading, as the bending moment increases and the D' decreases, the longitudinal forces generated at the extrados and intrados of the pipe bend increases as well leading to a higher resultant force pushing the extrados and intrados towards the neutral axis. On the other hand, when opening bending moments are acting on pipe bends, the cross-section ovalizes and the diameter in the plane of bending deforms (D') and increases than the initial pipe diameter (D). Therefore, during loading, as the bending moment increases and the D' increases, the increase in longitudinal forces is not significant leading to a small value of increase in the resultant force pulling the extrados and intrados away from the neutral axis. Therefore, the ovalization ratio could be found higher in the cases of pipe bends subjected to closing bending moments than those subjected to opening bending moment.

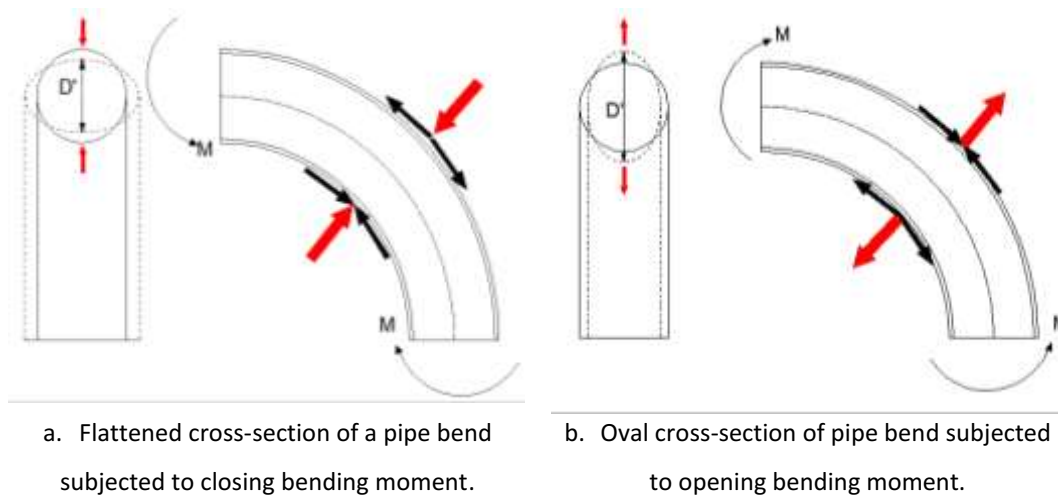


Figure 3. 60. The shape of deformation of a pipe bend subjected to in-plane opening or closing bending moment.

In this study, the wall thickness for all studied pipes are constant and equal to 9.525 mm as mentioned earlier. Therefore, when the pipe outer diameter increases, the slenderness of the pipe ratio (D/t) increases as well which makes it more susceptible to any cross-sectional deformations. In addition, the percent of increase in the bending moment generated to rotate the pipe bend by a particular end rotation is much higher than the percent of increase in the pipe's outer diameter which leads to an increase in the longitudinal forces generated at the extrados and intrados of the pipe. Consequently, the resultant forces increase leading to a higher ovalization ratio. The results show that as the bend radius increases the ovalization ratio tends to increase as well.

The cross-sectional deformation is found to have a notable impact on the pipe bend's stiffness. For the case of an opening bending moment, the second moment of area of the bend starts to increase as the pipe walls at the extrados and intrados are pulled away from the neutral axis leading to an increase in the stiffness of the pipe. Therefore, during the loading process, the bend starts to gain more stiffness and a higher bending moment is required to reach a particular end rotation for this pipe bend, which shows the reason behind the concave upward curve between the reaction moment and end rotation (Figure 3. 14). On the other hand, if a pipe bend is subjected to closing bending moment then the pipe walls at the extrados and intrados will be pushed towards the neutral axis leading to a decrease in the second moment of area. Therefore, during the loading process, the pipe bend's stiffness starts to decrease and a lower bending moment is needed to rotate this pipe bend with a particular end rotation. Therefore, the end rotation vs the reaction bending moment relation is a concave downward curve (Figure 3. 14). The ovalization is the reason behind the nonlinearity of the pipe response and this nonlinearity is obvious in the case of larger pipe sizes. As the pipe size increase the ovalization ratio of the cross-section increases and therefore the nonlinearity is more prominent as shown in figure (3. 61). However, for pipe bends with small outer diameters, the behaviour is linear due to the small ovalization ratios.

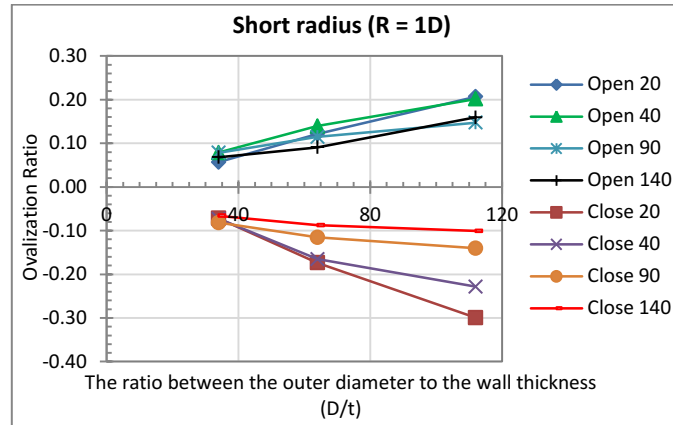


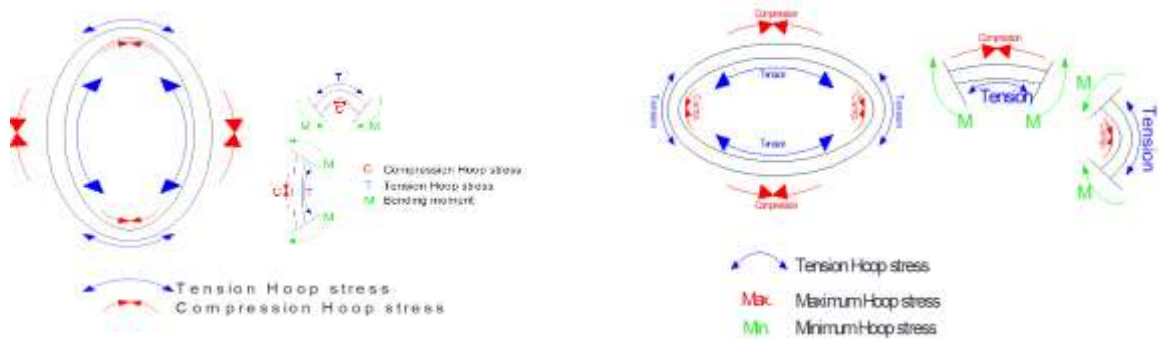
Figure 3. 61. The ratio of the major and minor axis of the oval shape cross-section versus the D/t ratio for different bend angles.

As the ovalization of the cross-section affects the stiffness and linearity of the pipe bend behaviour, it influences the stresses as well. The opening or closing of the pipe bend due to the applied bending generates longitudinal stresses on the pipe wall at the extrados and intrados. However, it generates a direct hoop stress that balances the radial stresses generated as a resultant of these longitudinal forces. This hoop stress is known as the direct hoop stress. In addition, the cross-sectional deformations generate bending stresses on the pipe walls with a distribution that depends on the deformed shape of the cross-section. Consequently the total hoop stresses increase due to the additional bending stresses acting on the pipe wall from the ovalization of the cross-section leading to higher Von Mises stress. Moreover, as the pipe diameter increases, the second moment of inertia of the pipe increases leading to a higher reaction moment required to rotate the pipe end with a specific angle (0.1 radians) resulting in higher stresses. The bend angle is another factor that affects the ovalization ratio and consequently the maximum stresses on the pipe bend. Since the bend angle and the direction of bending moment are two interdependent parameters where changing one will affect the other; therefore, they could not be discussed separately and the relationship between them needs to be investigated. The FEA results showed that by increasing the bend angle (α), the reaction moment required to rotate the pipe bend with a particular end rotation decreases. This means that as the bend angle increases, the pipe starts to be more flexible. The behaviour of a pipe bend is analogous to a corrugated sheet compared to a straight sheet. The corrugated sheet has more flexibility due to the bends existing in it however the corrugation gives it higher strength. Similarly, the pipe bend has higher

flexibility than a straight pipe although it can attain higher stresses. This can be shown in the result section in figure (3. 17), where it shows that the Von Mises stresses on a pipe bend with bend angle 140 degrees is higher than that from a 10 degree bend angle pipe bend at a particular reaction moment. Therefore, due to the higher flexibility, the pipe bend requires lower bending moment to rotate the pipe end with a particular rotation. The ovalization ratio on the other hand changes by changing these two parameters. For small bend angles, the pipe bends behave similar to a straight pipe where the cross-sectional deformations do not exist or is considerably low. Then as the bend angle increases to 20 and 40 degrees, the cross-sectional ovalization occurs and the ovalization effect starts to be significant, which leads to an increase in the ovalization ratio. However, when the bend angle is higher than 40 degrees, the pipe bend starts to gain more flexibility and the reaction moment generated from rotating the pipe bend with a particular end rotation (0.1 radians) decreases leading to a decrease in the longitudinal forces generated on the extrados and intrados of the pipe bend and therefore a decrease in the ovalization ratio occurs. The ovalization ratio shows to be almost constant for bend angles higher than 40 degrees. The flexibility of the pipe bend is affected by the direction of the bending moment as well. The ovalization ratio resulting from the closing bending moment is higher than the opening bending moment for pipe bends with small bend angles such as 10, 20 and 40 degrees. This means that higher bending moment is needed to close the bend compared to opening it with the same angle. The stresses are affected by the flexibility of the pipe bend and by the bend angle as well. Therefore, the Von Mises stresses are higher in the closing bending moment case than that of an opening bending moment case for small bend angle pipe bends. On the other hand, the opening bending moment results in higher ovalization ratio than closing bending moment for large bend angles as 90 and 140 degrees. This shows that the flexibility of the pipe is higher when it is subjected to closing bending moment and that more moment is needed to open the pipe bend. As the pipe gains more flexibility and more deformations takes place, then the stresses increase. In this case, the Von Mises stresses from the opening bending moment are higher than that of the closing bending moment.

The Von Mises stress distribution and the location of the maximum stress is affected by the hoop and longitudinal stress distributions. The hoop stresses are generated mainly from the bending stresses on the pipe wall due to the ovalization of the cross-section. The hoop stress distribution is affected by the cross-sectional deformation. When pipe bends are subjected to opening bending moment, the cross-sectional deformation is an oval shape. In this case, the bending stresses developed on the pipe bend walls push the crown inside and pull the intrados and extrados outside as shown in

figure (3. 62.a). These bending stresses result in a compression stress at the crown location and tension stresses at the intrados and extrados of the pipe bend for the outer layer of the wall thickness, and the opposite is for the inner layer while the mid-layer has almost zero hoop stresses. On the other hand, when a pipe bend is subjected to a closing bending moment, the cross-section flattens resulting in bending stresses acting on the pipe wall trying to pull the pipe walls at the crown location outside and push the extrados and intrados zones inside towards the centre of the pipe as shown in figure (3. 62.b). Consequently, the crown location is under tension at the outer layer while the extrados and intrados are under tension. However, the opposite is for the inner layer. The mid-layer has almost zero stresses in both cases of cross-sectional deformations which are incompatible with the concept of direct hoop stress explained by Gross (1953). On the other hand, the longitudinal stresses are affected by the cross-sectional deformations. From simple beam theory, it is expected to find the maximum longitudinal stresses at the furthest points from the neutral axis. However, the FEA results show that the maximum longitudinal stress is at a point located around 15 degrees away from the intrados and extrados of the pipe bend.



a. Cross-section deformation due to an opening bending moment

b. Cross-section deformation due to a closing bending moment.

Figure 3. 62. Bending stresses resulted from the cross-sectional deformations of the pipe bend subjected to opening and closing bending moment.

For pipe bends with bend angles ranging from 40 to 140 degrees, the maximum Von Mises stress at the inner and outer layers is at the crown location. However, there is two stress peaks for the mid-layer. For the inner and outer layers, the hoop stresses are found to be higher than the longitudinal stresses

and therefore, the hoop stress governs the Von Mises stress. For the inner and outer layer, the maximum hoop stresses are at the crown location, however, the rest of the cross-section has a low hoop stress value. While the longitudinal stress has a relatively low value all over the cross-section compared to the hoop stresses. Therefore, the maximum Von Mises stress is found to be at the crown of the pipe bend and governed by the hoop stress. However, at the mid-layer, the hoop stress has a negligible value which is almost zero while the longitudinal stress has two peaks at circumferential angles approximately equals to (\emptyset) 60 and 110 degrees. In these cases, the Von Mises stress is governed by the longitudinal stress at the mid-layer and shows maximum stresses at around the same circumferential angles as the maximum longitudinal stress. The hoop stress at the mid-layer is found to be almost negligible; indicating that the hoop stresses is generated mostly due to bending of the cross section where the maximum hoop is at the two extreme fibres of the section while the centreline has almost zero stresses. Therefore, the longitudinal stress is the component governing the maximum Von Mises stress location at the mid-layer of the pipe bends.

The behaviour of small bend angle pipes is found to be different than that of large bend angle. The Von Mises, hoop and longitudinal stress distributions are different for pipe bends with small bend angles. The FEA results show that for bend angles 10 and 20 degrees, the maximum Von Mises stresses are located at the intrados for all three layers. This can be explained by looking at the ovalization of the cross-section. The FEM show that the cross-sectional deformation is higher at the intrados than the extrados. The intrados is pushed closer to the neutral axis or pulled away from the neutral axis more than the extrados. Therefore the longitudinal forces are higher at the intrados and the bending stresses acting on the pipe wall generated from the cross-sectional deformation increase as the ovalization increase consequently the hoop stresses are higher at the intrados as well when compared to the extrados. For all the studied pipes, either small or large bend angle, the FEA results show that the Von Mises stresses at the inner layer of the pipe bend is higher than the outer-layer. Consequently, it is expected that for higher stresses, the inner surface of the pipe bend will start yielding before the mid-layer of the pipe wall. Therefore, the design codes should base the stress design on the outer and inner layer as well as the mid-layer of the pipe to ensure a safe design of the pipeline.

In this study a comparison between the FEA stress results and the CSA Z662-15 code estimated stresses is conducted. This comparison showed that the code estimated stresses are highly conservative in pipes with small bend angles and highly un-conservative for pipes with large bend angles. When pipe

bends have small bend angles, they behave more as a straight pipe. Therefore, the stresses on a small bend angle pipe are not much higher than that of a straight pipe (M_r/l) with the same configuration. Consequently, the stress intensification factors are not expected to be high in this case (not much higher than 1.0). On the other hand, as the bend angle increases, the cross-section deforms and the ovalization effect takes place. Therefore, the Stress Intensification Factors for these pipes are expected to be high. This comparison is conducted on all three studied layers of the pipe wall thickness. For the outer and inner layer of the pipe wall, the stress intensification factors evaluated using the code formulas are extremely un-conservative when compared with the FEA developed factors. This is due to the large difference in stresses between the inner and outer layer, even for thin-walled pipes, which was not considered by the past studies while developing the current SIF factors. Therefore, new stress intensification factors are developed in this study for the inner, outer and mid-layer of the pipe wall thickness for pipe bends with varying bend angles and different in-plane bending moment directions.

In the previous studies, the effect of attaching a straight pipe to the pipe bends was not investigated and the effect of the bend angle was considered negligible since it was excluded from the derived factors. Our study conducts an analytical investigation on pipe bends with two attached straight pipes under in-plane opening and closing moment loading using ABAQUS software. A wide range of pipe bend geometry is considered. Bend angles from 10 to 140 degrees and bend radii from 1 up to 5 times the pipe outer diameter is considered. The FEA results show that the direction of applied bending moment with the bend angle have an influence on the flexibility of the pipe bend. On the other hand, the critical section of the pipe bend varied according to the bend angle but in most of the studied pipes it was found that the yielding is initiated at the crown location at the inner layer of the pipe wall. Therefore, it is recommended that the current design procedure adopted by the codes consider evaluating the stresses at the inner and outer layer of the pipe wall as well as the centre-line of the pipe cross-section.

CHAPTER 4: Developed Stress Intensification Factors

4.1. INTRODUCTION & BACKGROUND

Stress intensification factors have been developed in the past to account for the increase in stresses due to the toroidal shape of a pipe bend. The effect of the pipe geometry on the stress distribution has long been investigated and shown to be significantly different than the estimated stresses evaluated from simple beam theory ($\sigma = Mr/I$). Theoretical and experimental work has been conducted in the past and there were many attempts to develop stress intensification factors based on different theories. Following Von Karman's (1911) theoretical study, many studies have been conducted on pipe bends using different approaches to develop a stress intensification factor. Clark and Reissner (1952) developed flexibility and stress intensification factors for pipe bends subjected to in-plane closing bending moment based on Thin-Shell theory approach. In 1952, Markl conducted extensive fatigue tests on pipe bends subjected to in-plane bending to derive these factors. The flexibility factor was similar to Reissner's developed factor, however, the stress intensification from the fatigue tests were half that of the Reissner's theoretical approach. The stress intensification factor developed from Markl's work is presented in the current design codes (CSA Z662, B31.1 & B31.3) and used for pipe sizes and geometries out of the range considered in the tests. These developed factors are function of a beam parameter (λ) that considers the effect of bend radius (R), pipe radius (r) and pipe wall thickness (t) on the stress levels. The stress intensification factor presented in the current codes is as follow;

$$i = \frac{0.9}{\lambda^3}$$

Where; $\lambda = \frac{tR}{r^2}$

In the past theoretical and experimental studies, from which the current code SIF factors are developed, many assumptions were considered and some parameters were ignored in order to simplify the mathematical procedure. However, the common drawback in these studies is that the bend angle and the direction of bending moment were ignored from the SIF factors. Therefore, the effect of these parameters on the stress distribution and stress levels were not considered. In addition to the effect of end boundary conditions since the past studies were conducted on standalone pipe bends.

Based on the results presented in chapter (3), it is found that the CSA stress intensification factors (SIF) are either conservative or un-conservative based on the direction of bending moment, bend angle, pipe bend geometry and the layer of interest within the wall thickness. It is shown that the critical section is located at the mid-length of the pipe bend and specifically found at the inner layer of the crown. In this chapter, new stress intensification factors will be developed to evaluate the stresses at the inner, outer and mid-layer of the pipe bend wall thickness under in-plane opening and closing bending moments.

4.2. METHODOLOGY

A new stress intensification factor (SIF) is developed in this section to account for the increase in the stresses due to the ovalization effect resulted from the opening or closing in-plane bending moment applied at the ends of a pipe bend with two attached straight pipes. First a sensitivity analysis is conducted to evaluate the impact of each parameter on the stress intensification factor. These parameters are the pipe cross-sectional outer radius (r), the bend radius (R) and the bend angle (α). Then a regression analysis is conducted to find an expression that best fits the relation between the increase in stress and the dependant parameters. Based on the relationship between the SIF data points and the considered parameters, a form is chosen as an expression for these factors.

4.2.1. Sensitivity Analysis and Model Formulation

To decide the considered parameters in the developed form for the stress intensification factors, a sensitivity analysis is performed to determine the impact of each parameter on the FEA SIF results. The parameters considered in this analysis are the beam parameter (λ), the bend angle (α) and direction of bending moment. Figures (4. 1) to (4. 4) show the SIF factors as predicted by the numerical models described previously plotted against the bend angle (α) and the beam parameter (λ) for pipe bends under opening and closing bending moments.

The results show that the SIF factor increases in an exponential growth rate as the bend angle increases as shown in figures (4. 1) and (4. 2). As the bend angle increases, the SIF factor value increase

as well till it reaches a certain point where the curve has a plateau and the SIF factor is almost constant even with the increase in the bend angle. The plateau starts earlier in large pipe sizes rather than small pipe sizes. Pipes with bend angles 140 degrees have SIF factor up to 7.6 times higher than 10-degrees bends for short bend radius. However, when the bend radius increases to 5D, the increase in the SIF factor due to increasing the bend angle from 10 to 140 degrees is up to 2.7 times as shown in figure (4. 2). Figure (4. 1) shows that for pipe sizes NPS 42, the plateau in the curve starts at 90 degrees. However for pipes NPS 12, the plateau did not occur. Moreover, the results show that the plateau in the growth rate of SIF factor occurs earlier for long radius bends than short radius bends and occurs earlier for the closing bending moment rather than the opening bending moment. It is observed that the bend angle and the bend radius are interdependently affecting the SIF factors. Based on that, an exponential growth form should express the relation between the SIF factors and bend angle (e^α).

As for the beam parameter (λ), the impact is highly significant at the mid-layer stresses for short radius bends where increasing the beam parameter by 3.5 times results in an increase in the SIF factor by up to 4.8 times. This ratio may go up to 7.5 times if the layer under study is the inner and outer layers of the wall thickness. For long bend radius such as 5D, increasing the beam parameter by 3.5 times results in an increase in the SIF factor by up to 4.2 times. Moreover, the inner and outer layers of the pipe wall thickness are greatly affected by the change in the bend angle and beam parameter more than the mid-layer of the pipe wall. Figures (4. 3) and (4. 4) show the SIF factor plotted against the beam parameter (λ). The SIF factors decrease in an exponential decay form with respect to the beam parameter. The decay rate decreases as the bend radius increases, where a plateau occurs in the curve at which the SIF factor is almost constant. In addition, the plotted results show that as the bend angle decreases the decay occurs earlier than that of a large bend angle. Therefore, an exponential form with a decay rate is chosen for the beam parameter. A term of the equation relates the growth in the bend angle with the decay in the beam parameter which is the ($e^{(m+n\lambda)\alpha}$). While, the other term is related only to the decay rate in the beam parameter ($1/\lambda^d$).

The proposed factor is in the following form:

$$SIF = \frac{(c - e^{(n+m\lambda)\alpha})(f + \lambda j)}{\lambda^d} \quad (4. 1)$$

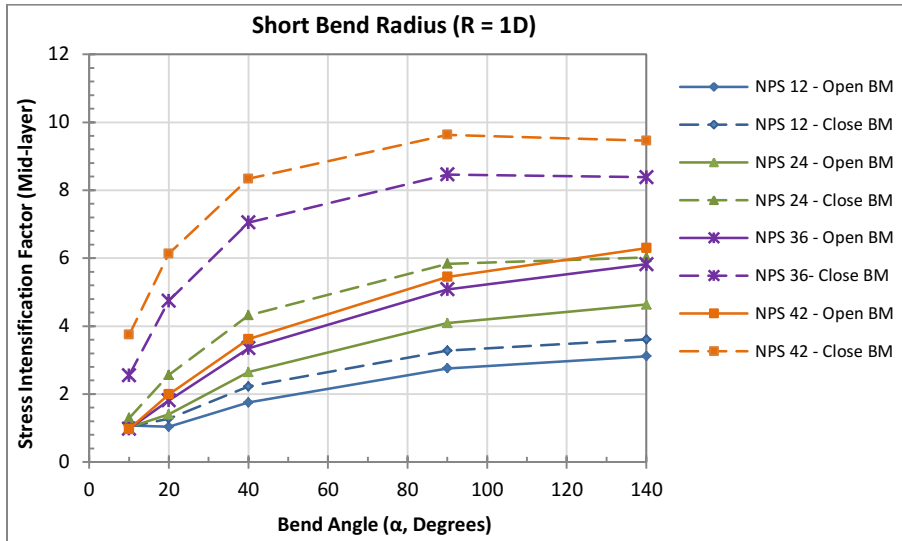


Figure 4. 1. Stress intensification factors for short radius pipe bends with various bend angles.

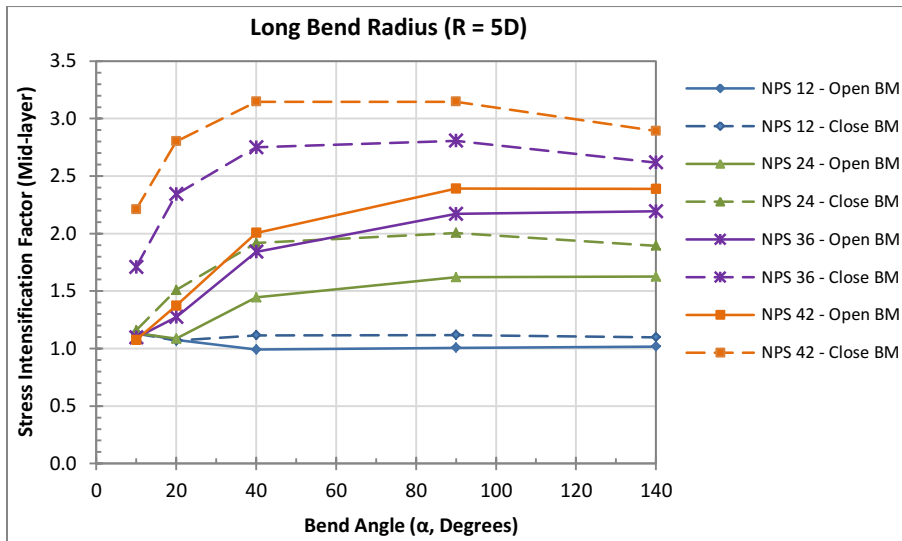


Figure 4. 2. Stress intensification factors for long radius pipe bends with various bend angles.

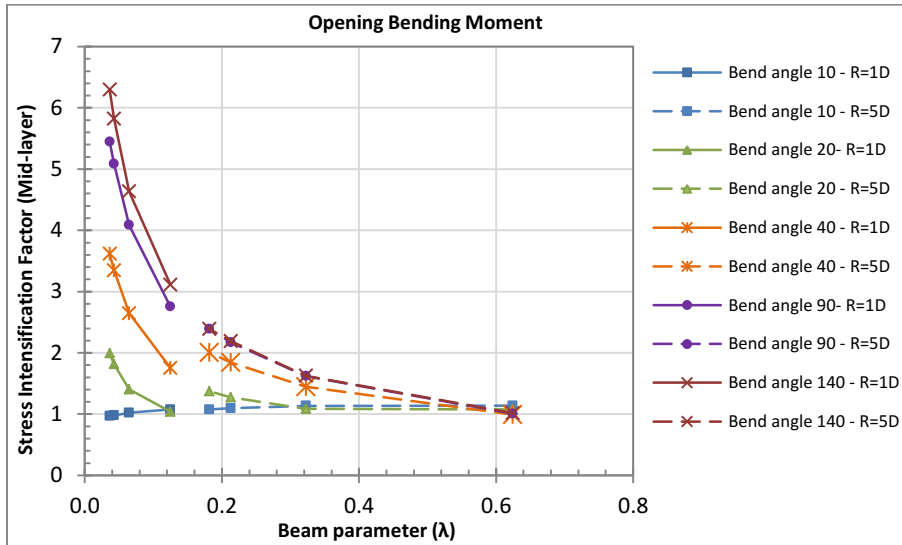


Figure 4. 3. Stress intensification factors pipe bends subjected to opening bending moment.

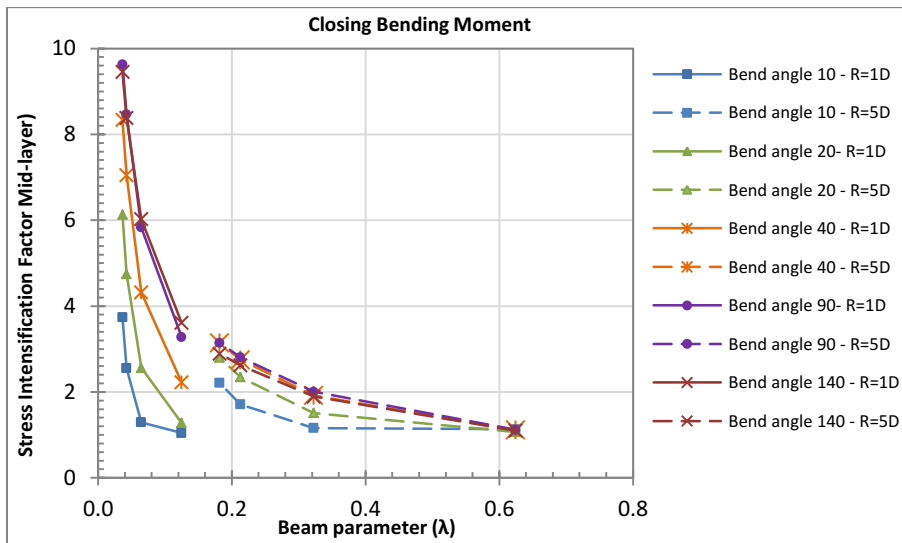


Figure 4. 4. Stress intensification factors pipe bends subjected to closing bending moment.

4.2.2. Regression Analysis

The ratio between the Von Mises stress evaluated from the FEA models presented in Chapter (3) and the stress estimated using the simple beam theory ($\sigma = Mr/I$) is used as the data points in the regression analysis [$\sigma_{VM\ FEA} / (Mr/I)$] and these data points represent the SIF evaluated from the FEA models. The equation used to evaluate the data points is as follows;

$$SIF_{FEA} = \frac{\sigma_{VM}}{Mr/I} \tag{4.2}$$

In nonlinear regression, the model function “SIF” is a nonlinear function of “ λ ” and “ α ” as shown in the proposed form (4. 1), and of the parameters a_1, a_2, \dots, a_m . Given a set of n data points ($SIF_i, \lambda_i, \alpha_i$) with $1 \leq i \leq n$, curve fitting starts by using the assumed model SIF (λ, α) with m parameters. The parameters can be obtained by finding the least squares:

$$S = \sum_{i=1}^n (SIF(\lambda_i, \alpha_i) - SIF_i)^2 \tag{4.3}$$

In order to find the parameters of the model that would minimize S, m equations of the following form are solved:

$$\frac{\partial S}{\partial a_m} = \sum_{i=1}^n \left(2 (SIF(\lambda_i, \alpha_i) - SIF_i) \frac{\partial SIF}{\partial a_m} \Big|_{\lambda=\lambda_i, \alpha=\alpha_i} \right) = 0 \tag{4.4}$$

Since SIF(λ, α) is nonlinear in the coefficients, the m equations formed are also nonlinear and can only be solved using a nonlinear equation solver method such as Newton Raphson method.

Based on the sensitivity analysis, a formula is chosen to express the SIF factors as a function of the considered parameters and a set of unknown constants. Mathematica software is used to solve the nonlinear formula and find the constants that best fit the data points. The Mathematica Wolfram language uses the Newton Raphson as a method to solve the nonlinear system of equations. The derivation of the method for nonlinear system is as follows;

For a nonlinear system of equation of the form:

$$f_1(x_1, x_2, \dots, x_n) = 0$$

$$f_2(x_1, x_2, \dots, x_n) = 0$$

⋮
⋮

$$f_n(x_1, x_2, \dots, x_n) = 0$$

For one iteration (x^i), the components of parameters are defined as; $x_1^i, x_2^i, \dots, x_n^i$, then the Taylor expansion of the first equation around these components is given by:

$$f_1(x_1^{i+1}, x_2^{i+1}, \dots, x_n^{i+1}) \approx f_1(x_1^i, x_2^i, \dots, x_n^i) + \frac{\partial f_1}{\partial x_1} (x_1^{i+1} - x_1^i) + \frac{\partial f_1}{\partial x_2} (x_2^{i+1} - x_2^i) + \dots + \frac{\partial f_1}{\partial x_n} (x_n^{i+1} - x_n^i)$$

Applying the same Taylor expansion for f_1, f_2, \dots, f_n , we obtain a system of linear equations with the unknown (variables) being the vector $x^{(i+1)}$:

$$\begin{pmatrix} f_1(x^{i+1}) \\ f_2(x^{i+1}) \\ \vdots \\ f_n(x^{i+1}) \end{pmatrix} = \begin{pmatrix} f_1(x^i) \\ f_2(x^i) \\ \vdots \\ f_n(x^i) \end{pmatrix} + \begin{pmatrix} \frac{\partial f_1}{\partial x_1} & \frac{\partial f_1}{\partial x_2} & \dots & \frac{\partial f_1}{\partial x_n} \\ \frac{\partial f_2}{\partial x_1} & \frac{\partial f_2}{\partial x_2} & \dots & \frac{\partial f_2}{\partial x_n} \\ \vdots & \vdots & \ddots & \vdots \\ \frac{\partial f_n}{\partial x_1} & \frac{\partial f_n}{\partial x_2} & \dots & \frac{\partial f_n}{\partial x_n} \end{pmatrix} \begin{pmatrix} (x_1^{i+1} - x_1^i) \\ (x_2^{i+1} - x_2^i) \\ \vdots \\ (x_n^{i+1} - x_n^i) \end{pmatrix}$$

The final desired value to be achieved for f_1, f_2, \dots, f_n is zero, therefore, the left hand side of the equation is set equal to zero and the set of equations is written as follows;

$$-\begin{pmatrix} f_1(x^i) \\ f_2(x^i) \\ \vdots \\ f_n(x^i) \end{pmatrix} = \begin{pmatrix} \frac{\partial f_1}{\partial x_1} & \frac{\partial f_1}{\partial x_2} & \dots & \frac{\partial f_1}{\partial x_n} \\ \frac{\partial f_2}{\partial x_1} & \frac{\partial f_2}{\partial x_2} & \dots & \frac{\partial f_2}{\partial x_n} \\ \vdots & \vdots & \ddots & \vdots \\ \frac{\partial f_n}{\partial x_1} & \frac{\partial f_n}{\partial x_2} & \dots & \frac{\partial f_n}{\partial x_n} \end{pmatrix} \begin{pmatrix} (x_1^{i+1} - x_1^i) \\ (x_2^{i+1} - x_2^i) \\ \vdots \\ (x_n^{i+1} - x_n^i) \end{pmatrix}$$

$$-f = K \Delta x$$

This equation can be rewritten as;

$$\Delta x = -K^{-1} f \Rightarrow x^{i+1} = x^i + \Delta x$$

Using the Newton Raphson method, Mathematica software solves the system of equation to get the coefficients that gives the best fit to the proposed formula.

4.3. THE DEVELOPED STRESS INTENSIFICATION FACTORS

Based on the regression analysis, the set of equations are solved to find the coefficients that best fit the proposed form to the data points. Two sets of factors are derived. One equation is for the opening bending moment and another one for the closing bending moment case where three set of coefficients are used for each case to represent the SIF factor at the three considered wall thickness layers.

4.3.1. Opening bending moment:

The developed stress intensification factor is presented in equation (4. 5) and the coefficients are as shown in table (4. 1) based on the pipe wall layer under study.

$$SIF = \frac{(c - e^{b \cdot \lambda})^a}{\lambda^d} \tag{4. 5}$$

Where;

$$a = (f + \lambda j)$$

$$b = (n + m \lambda)$$

$$\lambda = \frac{R t}{r^2}$$

Table 4. 1. Coefficients for the opening bending moment stress intensification factor presented in equation (4. 1)

Wall thickness layer	f	c	m	d	j	n	Standard deviation
Inner layer	1.89	1	-6.93	0.579	-0.59	-0.6	0.3
Mid-layer	0.68	1.015	-10.98	0.71	0.15	-0.48	0.2
Outer layer	1.29	1.158	-6.82	0.63	-0.24	-0.2	0.2

The standard deviation for each proposed factor is provided in table (4. 1) which could be used to shift the curve and ensure conservative predictions. To evaluate the accuracy of the proposed SIF factors, the evaluated factors from the proposed model are compared with the FEA factors. Figures (4. 5) to (4. 7) show the plot of the SIF evaluated from the FEA models against the proposed SIF factors compared to a line that represents an equation where the FEA results equals the evaluated model

results. The proposed SIF factors are scattered in a smooth pattern almost linear with a 45 degree regression line. The stress intensification factor of the mid-layer of the pipe bend wall has one reading with an error of 44.9% which is for NPS 12 with small bend angle and short radius bend ($\alpha = 10^\circ$ & $R = 1D$) as shown in figure (4. 8). However, the rest of the models show a good accuracy with an average percentage of error equal to 7.2%. The inner and outer layers show the same high error of 47.9% and 29.6%, respectively, in the evaluated SIF factor for pipe bend NPS12 with small bend angle and short bend radius ($\alpha = 10^\circ$ & $R = 1D$). The average error for the rest of the models is 5.4% which is acceptable in this study. The developed SIF formulas show better results compared to the FEA for pipe bends with large bend angles such as; 40 to 140 degrees as shown in figure (4. 9). The accuracy of the SIF factors evaluated for pipe bends with bend angle 10-degrees has the highest error as shown in figure (4. 10). The comparison between the proposed model and the FEA SIF factors for all the studied pipe bends are presented in Appendix (B).

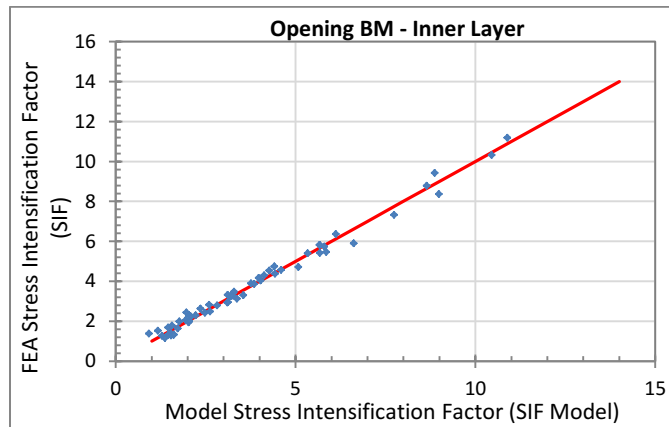


Figure 4. 5. Deviation of the SIF developed formula from the FEA results for the Mid-layer of the wall thickness

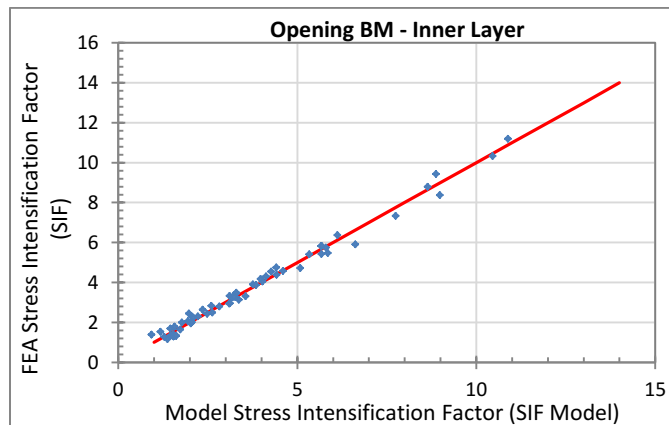


Figure 4. 6. Deviation of the SIF developed formula from the FEA results for the inner layer of the wall thickness

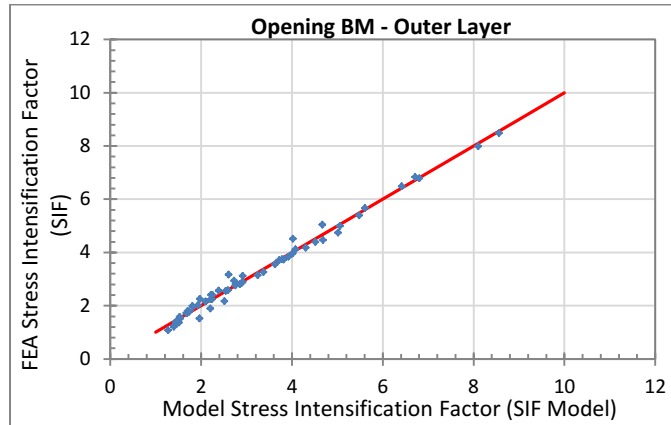


Figure 4. 7. Deviation of the SIF developed formula from the FEA results for the outer layer of the wall thickness

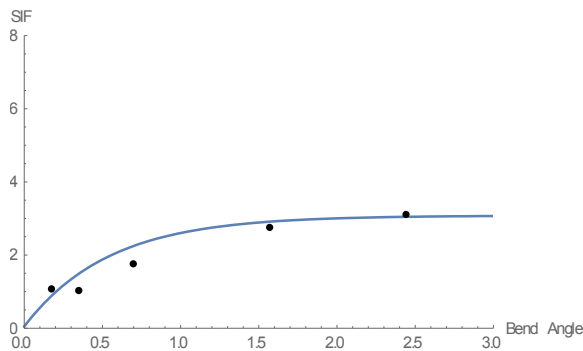


Figure 4. 8. The mid-layer FEA SIF (dotted) compared to the proposed SIF formula (blue line) for NPS12 bends with short bend radius ($R=1D$)

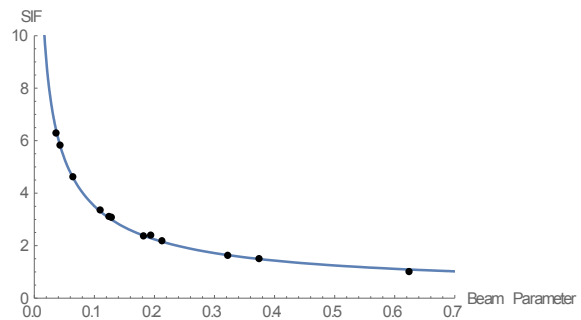


Figure 4. 9. The FEA SIF (dotted) compared to the proposed SIF formula (blue line) for bends with bend angle = 140°

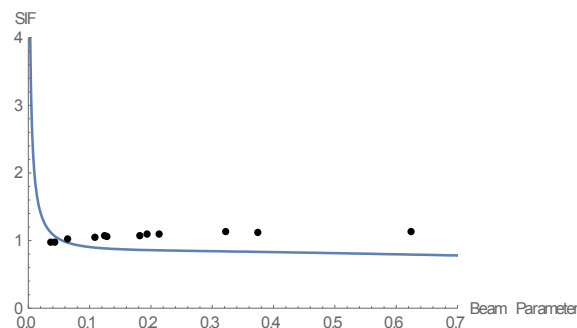


Figure 4. 10. The FEA SIF (dotted) compared to the

proposed SIF formula (blue line) for bends with bend
angle = 10°

4.3.2. Closing bending moment:

The developed stress intensification factor is presented in equation (4. 6). The coefficients are as shown in table (4. 2) based on the pipe wall layer under study.

For the inner and outer layers:

$$SIF = \frac{a * (b - e^{c \alpha})}{\lambda^d} \tag{4. 6}$$

$$SIF = \frac{(c - e^{b \cdot \alpha})(a)}{\lambda^d}$$

Where;

$$a = (f + \lambda j)$$

$$b = (n + m \lambda)$$

$$\lambda = \frac{R t}{r^2}$$

Table 4. 2. Coefficients for the opening bending moment stress intensification factor presented in equation (4. 6)

Wall thickness layer	f	c	m	d	j	n	Standard deviation
Inner layer	2.143	0.815	0	0.8	0	-3.35	1.3
Mid-layer	0.73	0.98	-10.76	0.77	0.278	-2.06	0.5
Outer layer	1.91	0.839	0	0.77	0	-3.55	1.3

The percentage of error in the proposed SIF factors for bends under closing bending moment is found to be higher than that for the opening bending moment. Figures (4. 11) to (4. 13) show the plot of the SIF evaluated from the FEA models against the proposed SIF factors compared to a line that represents an equation where the FEA results equal the evaluated model results. The data points are found to be scattered in a wider range about the 45 degree regression line showing that neither of the

regression lines fits the data well. The highest error is found for pipe bends with small bend angles ($\alpha = 10^\circ$) and bend radius ranging from 1D to 5D and this error is up to 137% as shown in figure (4. 14). However, by neglecting the proposed SIF factor for bends with 10 bend angles, the average error is 15% for all three studied layers of the wall thickness which is a satisfactory accuracy in this study.

The developed SIF formulas show better results compared to the FEA for pipe bends with large bend angles such as; 40 to 140 degrees as shown in figure (4. 15). The comparison between the proposed model and the FEA SIF factors for all the studied pipe bends are presented in Appendix (B).

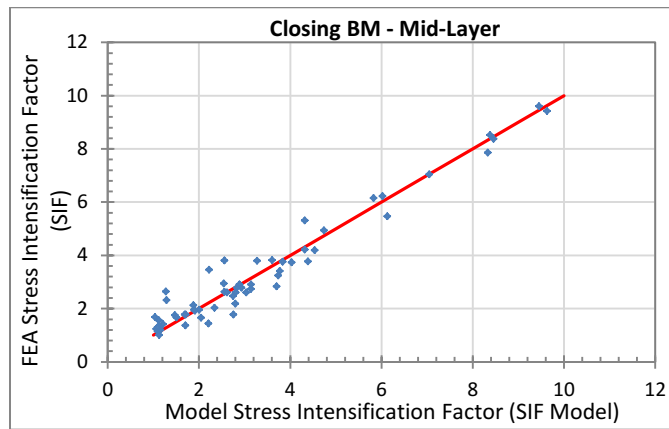


Figure 4. 11. Deviation of the SIF developed formula from the FEA results for the mid-layer of the wall thickness

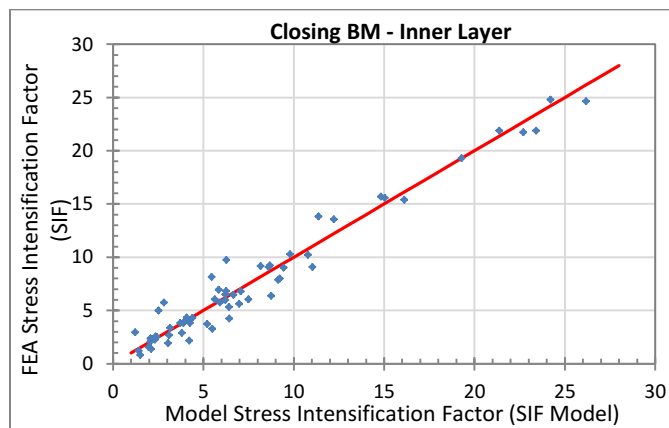


Figure 4. 12. Deviation of the SIF developed formula from the FEA results for the inner layer of the wall thickness

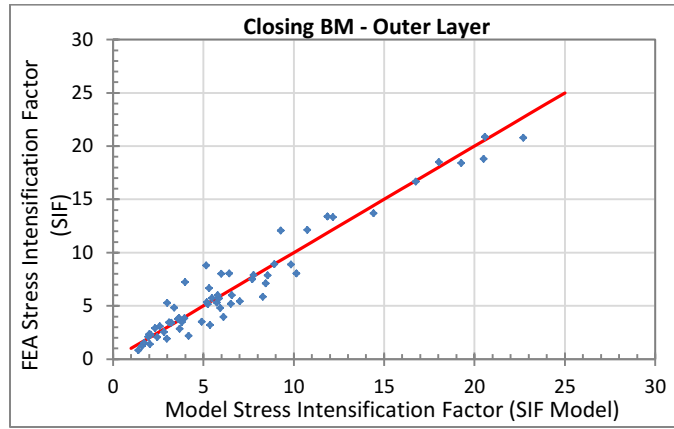


Figure 4. 13. Deviation of the SIF developed formula from the FEA results for the outer layer of the wall thickness

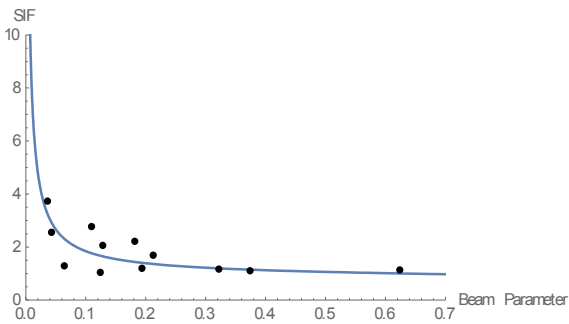


Figure 4. 14. The FEA SIF (dotted) compared to the proposed SIF formula (blue line) for bends with bend angle = 10°

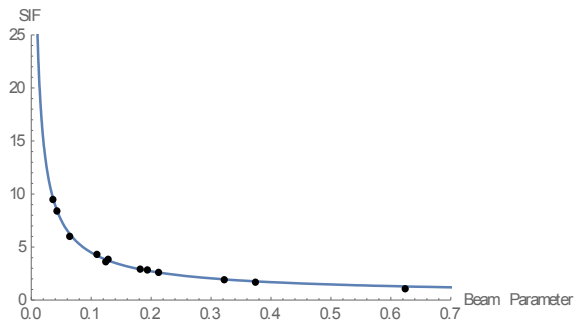


Figure 4. 15. The FEA SIF (dotted) compared to the proposed SIF formula (blue line) for bends with bend angle = 140°

CHAPTER 5: THE INTERACTION BETWEEN THE INTERNAL PRESSURE AND BENDING MOMENT FOR PIPE BENDS

5.1. INTRODUCTION

In previous chapters, the behaviour of pipe bends subjected to bending moment was investigated and shown that based on the direction of bending moment, the initially circular cross-section either flattens or ovalizes. The flexibility of the bend was found to change with the change of bending moment value applied due to the change in the cross-sectional second moment of area. Therefore, bends under in-plane opening bending moment are found to gain stiffness by loading, while bends under closing in-plane bending moment gain flexibility by loading. When an internal pressure loading is added to the in-plane bending, the behaviour becomes quite complex and a closed-form analytical solution is difficult to be obtained. The internal pressure tends to open the bend due to the “Bourdon effect” phenomenon explained in chapter (2) of this study. Therefore, it is expected that when internal pressure is added to an opening in-plane bending moment, the ovalization increases leading to higher stiffness. On the other hand, adding internal pressure to a closing in-plane bending moment increases the stiffness than in the absence of internal pressure and somehow reduces the stress levels. However, the problem is not that simple and the expected behaviour may change based on the ratio of the internal pressure to the bending moment applied to the pipe bend especially in the case of internal pressure and closing bending moment. Moreover, the behaviour and response of the bend to such a combined loading differs based on the pipe geometry and configuration.

The flexibility and stress intensification factors currently used in the design codes in piping analysis are to account for the behaviour of pipe bends under external bending moment. The effect of adding internal pressure loading to the bending moment was first investigated by Kafka and Dunn (1956) where a flexibility factor is derived for the case of internal pressure and closing in-plane bending using the Thin-shell theory approach. In 1957, Rodabaugh and George investigated the effect of adding internal pressure loading to in-plane closing bending moment. They used a simple potential energy approach by extending the work of Von Karman (1911) and Vigness (1943) starting from the energy equations developed by these authors. In this study the internal pressure was added to the potential energy equation as a “second-order” effect where the work presented by the pressure acts against the change in volume leading to an increase in the pipe bends stiffness. Assuming long bend radius,

Rodabaugh and George developed a pressure reduction factor as a modification to the flexibility and stress intensification factors proposed from earlier studies and presented in the current design codes. The pressure reduction factor is currently used by the power piping ASME B31.1 as follows:

$$k_p = \frac{k}{1 + 6 \left(\frac{p}{E}\right) \left(\frac{t}{r}\right)^{7/3} \left(\frac{R}{r}\right)^{5/2}} \quad (5.1)$$

$$i_p = \frac{i}{1 + 3.25 \left(\frac{p}{E}\right) \left(\frac{t}{r}\right)^{5/2} \left(\frac{R}{r}\right)^{2/3}} \quad (5.2)$$

Where p is the internal pressure and E is the Young's modulus of elasticity. In equation (5.1) & (5.2), "k" and "i" are the flexibility and stress intensification factors adopted from the Clark and Reissner (1952) study and modified according to the fatigue tests of Markl (1952) in the absence of internal pressure. Rodabaugh and George pressure reduction factor shows that as the internal pressure level increases, the flexibility of the pipe bend decreases since the internal pressure resists the change in the cross-sectional deformation generated from the bending moment. At the same time, the internal pressure reduces the high stress levels generated from the bending moment loading especially associated with flexible pipe bends. The same behaviour could be found in straight or curved pipes with non-circular cross-section (initial imperfection exists) subjected to internal pressure known as the "Haigh effect", where the flexibility increases and the membrane stresses can be magnified by a factor of six (Asnawi, 2004).

The flexibility and stress intensification factors derived from the past studies are based on a particular loading of internal pressure and in-plane closing bending moment, however, it is continued to be used till now in the piping analysis usually without modifications for the in-plane opening and out-of-plane bending moments. Moreover, the effect of the bend angle and the end effects were not included as well. In this chapter, the commercial finite element package ABAQUS is used to conduct a non-linear analysis of pressurized pipe bends subjected to in-plane opening and closing bending moments with different bend angles and varying pipe geometry. The interaction between the internal pressure and bending moment is investigated. However, the ratio of the internal pressure to the bending moment is constant.

This chapter studies the behaviour of pipe bends under internal pressure and bending moment, and the combined action of both loading on the bend's behaviour. The difference between the models in this chapter and the previous ones is the boundary conditions used. In this chapter, the end boundary

conditions are rollers at the end of the straight attached pipe. The translation in a direction perpendicular to the straight pipe is allowed. However, in the previous chapter, the pipe assembly had a fixed end and another free end where the end rotation is applied. This chapter is divided into three parts. The first part is for bends subjected to internal pressure. The Bourdon forces are evaluated and compared to the proposed mathematical model derived in chapter (2). The second part is for pipe bends subjected to in-plane opening or closing bending moments. The FEA models are compared to Chapter (3) and the effect of changing the boundary conditions on the stresses is presented as well. The third and last part is for bends subjected to both internal pressure and bending moments. In this section, the FEA results are compared to bends under internal pressure loading only to study the effect of adding bending to the internal pressure and to investigate the effect of the bending moment direction.

5.2. METHODOLOGY

5.2.1. Finite Element Modelling and Analysis

The finite element modelling and analysis is performed using ABAQUS 6.13. The piping configuration used in this study is a pipe bend connected to two attached straight pipes with consistent pipe size in each model as shown in figure (5. 1). Similar to the modelling concept used in chapter (3), half models of the pipe system with symmetric boundaries are built using Shell elements. The pipes are modelled with an initially circular cross-section and a uniform wall thickness without any initial imperfections. The straight pipes are modelled in a cylindrical coordinate system with an extrusion equal to 1D. While the bend part is modelled using a spherical coordinate system. The bend is a deformable part with a revolution angle representing the bend angle (α). The length of the attached straight pipe is chosen as 1D to minimize the bending moment at the elbow generated from the straight pipe end reaction. The pipes are modelled using a four-node quadrilateral shell element with reduced integration (S4R). The size of the mesh is chosen to be 15x15 mm as shown in figure (5. 2). A linear material is used to define the pipe behaviour where Young's modulus of elasticity is 207000 N/mm² and Poisson's ratio is 0.3.

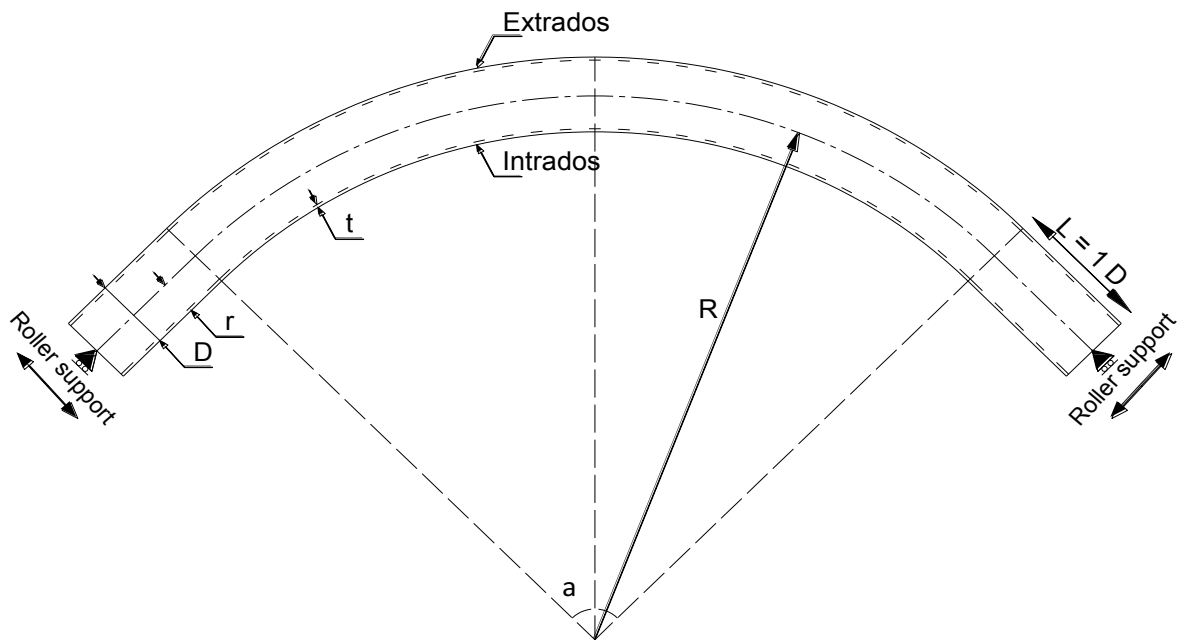


Figure 5. 1. Pipe bend configuration with attached straight pipes.

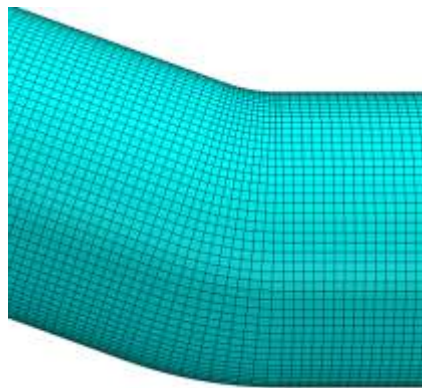


Figure 5. 2. Pipe Meshing

5.2.2. Loading and Boundary Conditions

Considering the symmetry in geometry and loading about the XZ plane, only half of the pipes are modelled. The lines of intersection between the pipe walls and the plane of symmetry (X-Z plane) are restrained from translation in the Y-direction, and the rotation about the X and Z axis are prevented. To apply the end boundary conditions, all the nodes at the circumference of the pipe end are tied to a reference point located at the centre of the cross-section using a kinematic coupling restraint where the

radial movement is permitted to allow for the pipe cross-sectional deformations such as the ovalization of the cross-section. The reference points RP-1 and RP-2 are free to translate in the direction perpendicular to the straight pipes as shown in figure (5. 3). The analysis considers the large displacement theory by activating the nonlinear geometry feature in the software. The large displacement theory is considered when deformations affect the stiffness of the geometry and this is one of the objectives of this study.

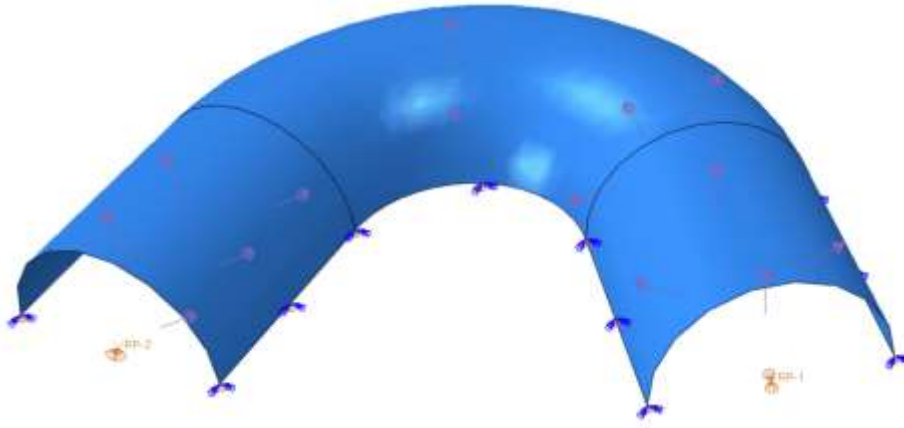


Figure 5. 3. Model boundary conditions.

The load is applied in two steps. The first step is considered the internal pressure acting on the inner surface of the pipe. The second step is the in-plane opening or closing bending moments and applied as a rotational displacement. The rotational displacement loading is applied to the reference points (RF-1 & RF-2) located at the ends of the attached straight pipes. The displacement control method is used in the finite element analysis to capture the complete behaviour of the pipe including unstable behaviour if present. The internal pressure is considered constant in the second step since the pressure generally does not increase during service, whereas the bending moment is applied in an incremental step since it may increase due to any accidental conditions. The applied internal pressure and bending moment are chosen to result in a ratio of 0.24 for the hoop stress due to internal pressure ($PD/2t$) to the longitudinal stresses due to bending (Mr/I). The applied internal pressure is chosen to result in 80% SMYS hoop stress on the pipe. The study is based on pipes of steel grade X100 to ensure that the developed factors would be applicable for a wide range of material properties. The value of the applied end rotation is evaluated such that the Von Mises stress due to bending and internal pressure is

72% SMYS at the pipe bend where the steel grade is considered X100. This ratio results in a stress from bending moment (M_r/l) equal to 19.6% SMYS.

The Von Mises stresses are obtained from the FEA numerical models at the location of the critical stresses. These stresses are measured at the outer, inner and mid-layer of the pipe wall thickness. The stresses from the FEA models are later compared to the stresses evaluated using the equation presented in the CSA-Z662 code.

In this chapter, the objective is to investigate the behaviour of pipe bends under the effect of adding bending moment to the internal pressure loading. The Von Mises stresses due to internal pressure only, bending only and, internal pressure with bending are evaluated from the FEA models and compared to each other and to the code estimated stresses. The end supports are modelled as rollers to allow studying each loading condition individually without being affected by one another, especially in the case of internal pressure with bending. The pipe bend is allowed to straighten out under internal pressure then when the bending is applied, the pipe bend can open out or close without any influence from the previous internal pressure load.

This chapter is divided into three parts. The first part is the results of the FEA models for pipe bends subjected to internal pressure loading only. The second part is the results of pipe bends subjected to bending moment only. These results are compared with the FEA results of Chapter (3) to investigate the effect of different boundary conditions on the behaviour of pipe bends. The third and last part is for pipe bends subjected to internal pressure and bending moment successively. These results are used to get a better understanding of the pipe bend behaviour as a result of adding bending moment to the internal pressure. In addition, new stress intensification factors are proposed based on this study.

5.2.3. Predicted stresses according to the current Design Codes

In this section, the equations used by the CSA and ASME codes to predict the stresses on a pipe bend are presented. The predictive stresses are compared to the FEA stress in the result section of this chapter to investigate the code design limitations and conservativeness.

The CSA-Z662 evaluates the combined stresses on a pipe bend under internal pressure and bending moment using a general equation that evaluates basically the maximum shear stresses on a

pipe using equation (5. 3), which is the difference between the hoop stresses generated from the internal pressure (S_h) and the longitudinal stress generated from both internal pressure (S_L) and bending moment (S_B). For pipes subjected to bending moment only, the internal pressure terms (S_h & S_L) are ignored from the general equation and equation (5. 4) is used instead. However, when the bend is subjected to internal pressure only then equation (5. 5) is used.

$$S_h - S_L + S_B = S \times T \quad (5. 3)$$

$$S_B = S \times T \quad (5. 4)$$

$$S_h - S_L = 0.9 S \times T \quad (5. 5)$$

Where,

S = specified minimum yield strength,

T = temperature factor,

$$S_h = \frac{PD}{2t}$$

$S_L = \nu S_h - E_c \alpha (T_2 - T_1)$; S_L is considered only when in compression (negative stress)

$$S_B = i.M/Z$$

$$i = \frac{0.9}{h^{2/3}}$$

$$h = \frac{tR}{r^2}$$

The ASME B31.1 predicts the stresses on the pipe bend under pure in-plane bending same as CSA-Z662 using equation (5. 4). However, for the case of internal pressure and pure bending, the ASME B31.1 predicts the stresses using Rodabaugh and George (1957) pressure reduction factor. The modified flexibility and stress intensification factors are estimated using equations (5. 6) and (5. 7). Then the stress on a pipe bend subjected to internal pressure and bending moment is evaluated using equation (5. 8) which represents mainly the longitudinal stresses on a pipe bend.

$$k_p = \frac{k}{1 + 6 \left(\frac{P}{E} \right) \left(\frac{t}{r} \right)^{7/3} \left(\frac{R}{r} \right)^{5/2}} \quad (5. 6)$$

$$i_p = \frac{i}{1 + 3.25 \left(\frac{P}{E} \right) \left(\frac{t}{r} \right)^{5/2} \left(\frac{R}{r} \right)^{2/3}} \quad (5. 7)$$

$$\frac{PD}{2t} + i_p \frac{Mr}{I} < \text{allowable stresses} \quad (5.8)$$

5.3. RESULTS

5.3.1. Pipe Bends Under Internal Pressure Loading

The FEA results of the pipe bends subjected to internal pressure only are presented in this section and compared to the code estimated stresses. Figures (5. 4) to (5. 12) show the Von Mises stress results at the inner, outer and mid-layer of the pipe wall thickness versus the outer diameter to wall thickness ratio (D/t). The relationship between the Von Mises stresses and the outer diameter-to- wall thickness ratio (D/t) seems to change based on the layer under study. The Von Mises stresses at the mid-layer show a slight increase in the slope as the D/t ratio increases. Increasing the pipe outer diameter from 12" to 42" leads to an increase in the mid-layer stresses by up to 12% for short radius bends as shown in figure (5. 4). And as the bend radius increase to 3D and 5D, the increase in stresses due to the increase in the D/t ratio is considered negligible. The maximum difference in stresses between the NPS 42 and NPS 12 is found in pipes with small bend angles and short bend radius (e.g. 20° bend angle and bend radius equal to 1D). On the other hand, the inner and outer layers show a different function with the D/t ratio. When the D/t ratio increases, the Von Mises stresses at the inner and outer layers tend to decrease as shown in figures (5. 7) to (5. 12). Increasing the pipe outer diameter from 12" to 42" results in a decrease in the stresses by up to 23.7%. For the inner and outer layers, the percentage of decrease in stresses range from 11% to 23.16% when the pipe size increase from 12" to 42" for long bend radius pipes.

By comparing the FEA stress results to the estimated stresses using the code, it is found that the code is un-conservative in most of the studied pipes, especially for pipe bends with short bend radius (R =1D). And as the bend radius increases, the code estimated stresses approach the conservative side. From the FEA results, it is found that the stresses at the mid-layer have the lowest values compared to the evaluated stresses at the inner and outer layers. The predicted code stresses are un-conservative by up to 30.4 % when compared to the evaluated FEA stresses at the mid-layer. Pipes with short bend radius (e.g. R=1D) and large pipe outer diameter (e.g. NPS 42) show the highest un-conservativeness as shown in figure (5. 4). However, when the bend radius increase to R=3D & 5D, the Code is conservative by up to 7.3 % and shows a negligible 1.4% un-conservative part as shown in figures (5. 5) and (5. 6). On

the other hand, the FEA Von Mises stress evaluated on the inner and outer layers of the pipe bend are un-conservative for short and long bend radius pipes as shown in figures (5. 7) to (5. 12). The estimated code stresses are un-conservative in pipes with short bend radius by up to 93.9% and 110.22% at the inner and outer layer, respectively. However, for long bend radius pipes such as $R= 3D$ and $5D$, the inner and outer layer are un-conservative by up to 38.3% and 21.11%, respectively. The FEA results show that for higher internal pressure levels, the yielding is initiated at the inner or outer layer of the pipe bend where the maximum Von Mises stress is recorded. Therefore, the design criteria need to consider the variation of hoop and longitudinal stresses through the wall thickness of the pipe.

Increasing the bend radius from $1D$ to $5D$ results in a decrease in the Von Mises stresses by up to 73.6% at the outer layer of the pipe bend. However, for the inner layer and mid-layer of the bend, the decrease in stresses reduces to 57.5 % and 36.45 %, respectively. Therefore, the bend radius has a significant influence on the Von Mises stresses of pipe bends.

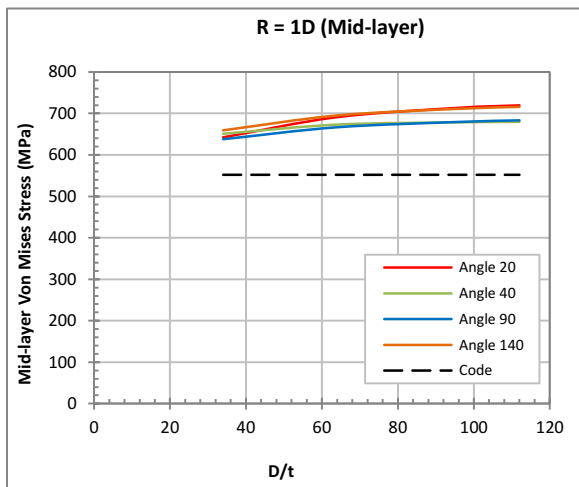


Figure 5. 4. Von Mises stress at mid-layer for pipe bends with short bend radius ($R = 1D$)

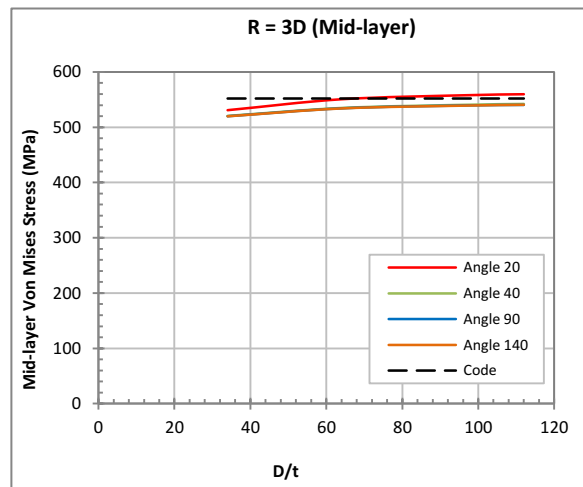


Figure 5. 5. Von Mises stress at mid-layer for pipe bends with long bend radius ($R = 3D$)

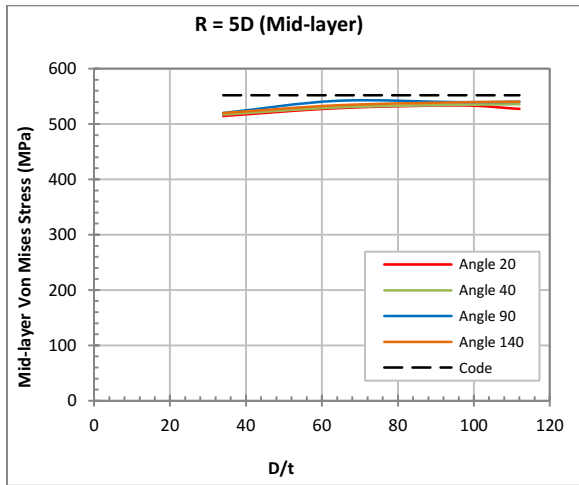


Figure 5. 6. Von Mises stress at mid-layer for pipe bends with long bend radius ($R = 5D$)

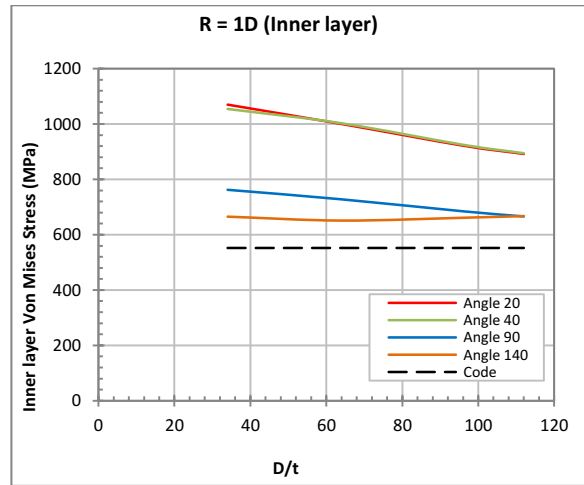


Figure 5. 7. Von Mises stress at inner layer for pipe bends with short bend radius ($R = 1D$)

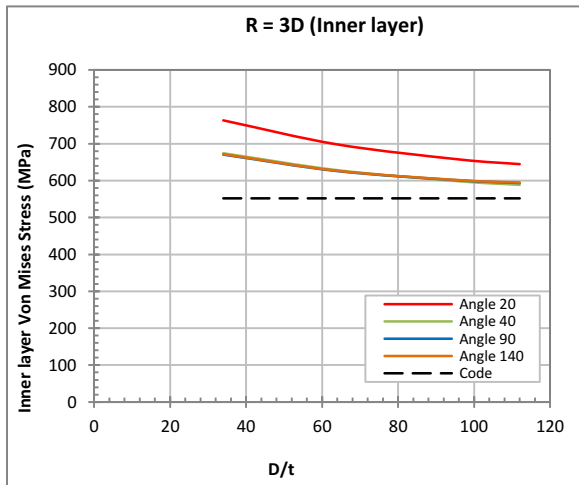


Figure 5. 8. Von Mises stress at inner layer for pipe bends with long bend radius ($R = 3D$)

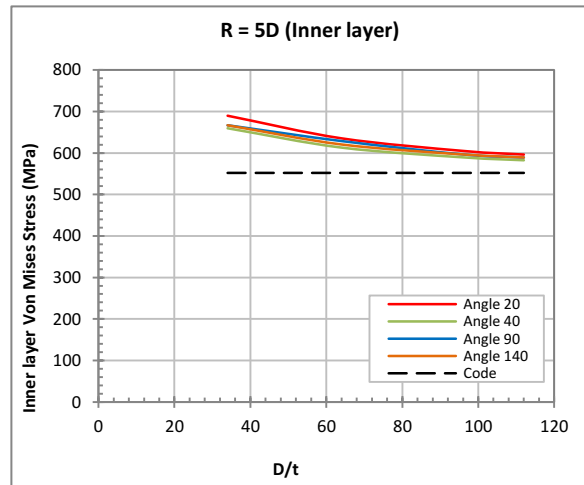


Figure 5. 9. Von Mises stress at inner layer for pipe bends with long bend radius ($R = 5D$)

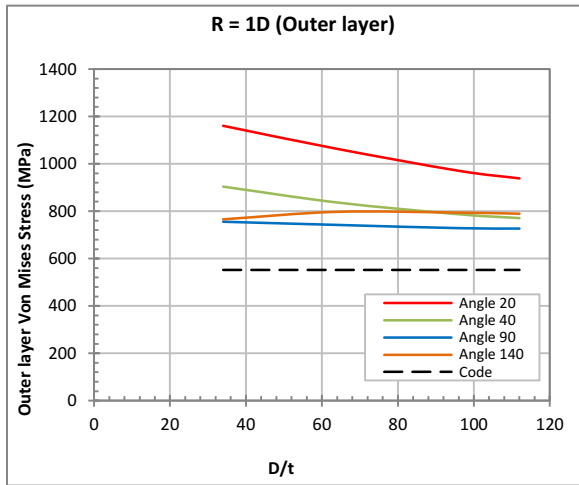


Figure 5. 10. Von Mises stress at outer layer for pipe bends with short bend radius ($R = 1D$)

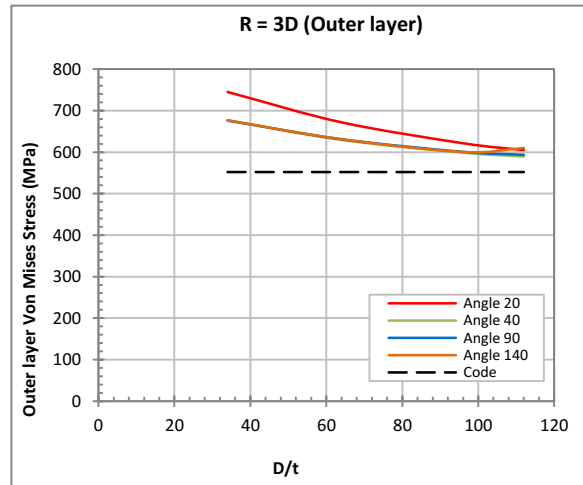


Figure 5. 11. Von Mises stress at outer layer for pipe bends with long bend radius ($R = 3D$)

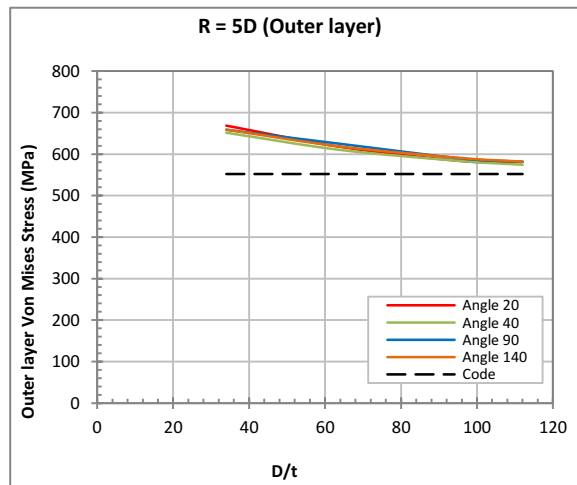


Figure 5. 12. Von Mises stress at outer layer for pipe bends with long bend radius ($R = 5D$)

The Von Mises stress distribution depends on the hoop and longitudinal stress distributions across the pipe bend circumference. Therefore, a typical pipe bend is chosen to present the effect of the outer diameter-to-wall thickness ratio (D/t) on the stress distribution. Figures (5. 13) to (5. 18) show the distribution of stresses across the circumference of the critical section of a 12" and 42" pipe bend with short radius bend ($R = 1D$) and 40-degrees bend angle. The FEA results show that the hoop stresses are

greater than the longitudinal stresses; therefore, the Von Mises stress distribution along the pipe bend circumference is governed by the Hoop stress distribution. Any change occurs in the hoop stress whether a drop or a jump in the maximum value is reflected directly in the same pattern in the Von Mises stress. As shown in figures (5. 13) to (5. 18), the Von Mises stress at the three layers have the same pattern of the hoop stresses. Therefore, when the maximum hoop stress on the critical section circumference of the mid-layer increases due to the increase of the pipe size (D), the Von Mises stress increases as well which explains the upward slope shown in figures (5. 4) to (5. 6). However, from figure (5. 16) it is observed that the maximum hoop stress at the inner and outer layer decreases as the pipe size increases which leads to a decrease in the maximum Von Mises stress. This explains the downward slope shown in figures (5. 7) to (5. 12).

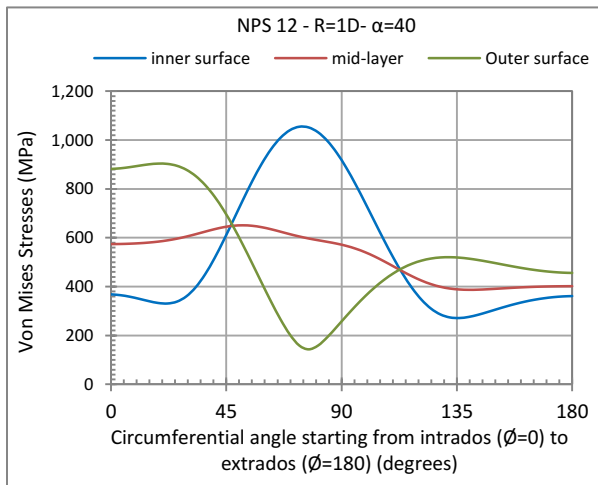


Figure 5. 13. Von Mises stress distribution along the circumference of the critical section of a 12" pipe bend with short bend radius and bend angle 40 degrees.

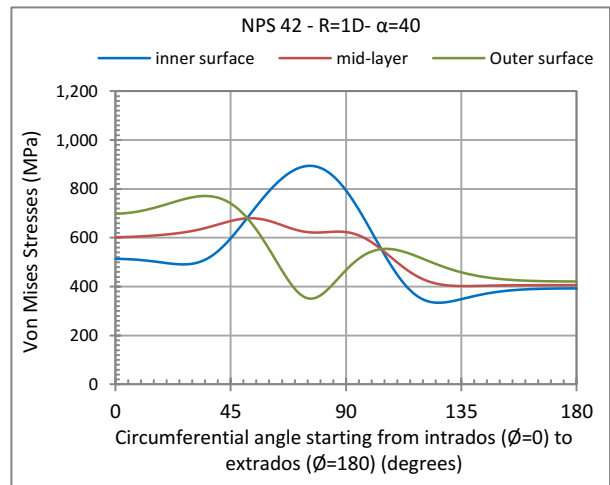


Figure 5. 14. Von Mises stress distribution along the circumference of the critical section of a 42" pipe bend with short bend radius and bend angle 40 degrees.

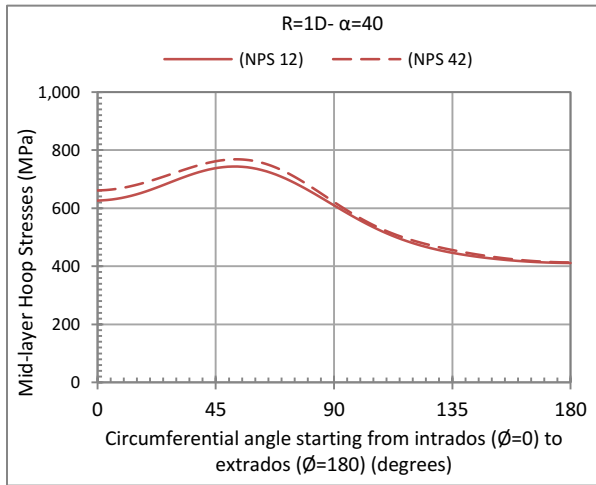


Figure 5.15. Comparison between the mid-layer hoop stresses of the 12" and 42" pipe size.

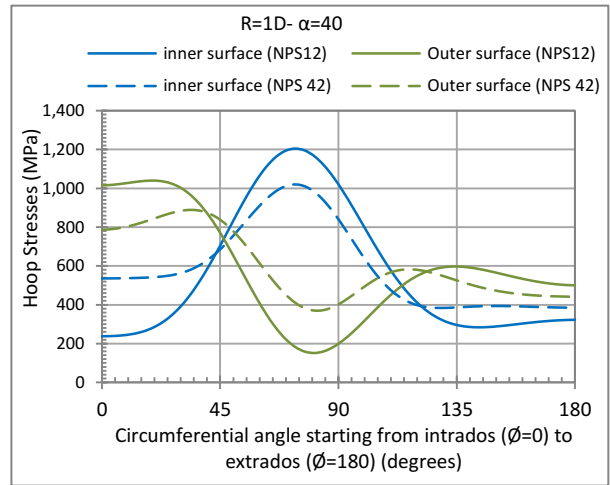


Figure 5.16. Comparison between inner and outer layer hoop stresses of the 12" and 42" pipe size.

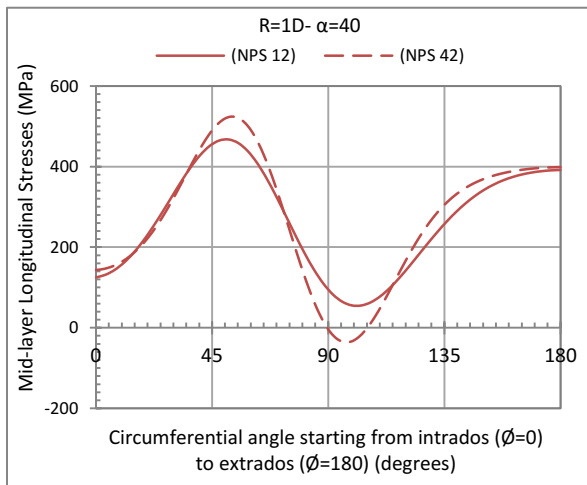


Figure 5.17. Comparison between the mid-layer longitudinal stresses of the 12" and 42" pipe size.

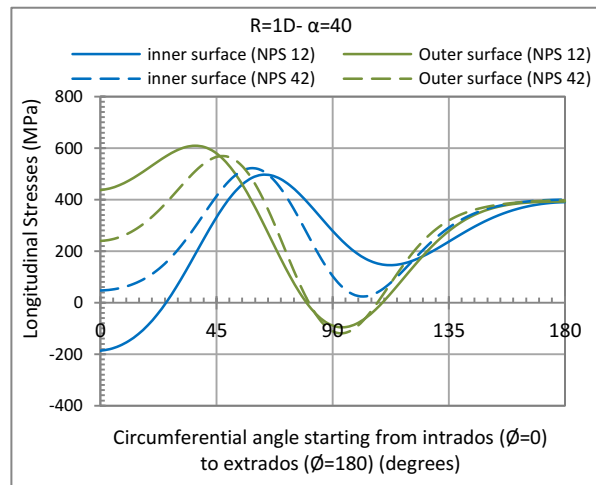


Figure 5.18. Comparison between the mid-layer longitudinal stresses of the 12" and 42" pipe size.

The Bourdon forces acting on a pipe bend as a result of the internal pressure are evaluated for the studied bends and compared to the estimated forces using the developed mathematical model from Chapter (2) and presented in this chapter as equations (5.9) & (5.10). From the body equilibrium of the pipe bend, the Bourdon forces are balanced out with the sum of end reaction at both supports of the bend as shown in figure (5.19). Therefore, the evaluated Bourdon forces from equations (5.9) & (5.10)

are compared to the sum of reactions and presented in table (5. 1) where the positive percentage means that the proposed model is conservative, however, a negative percentage represents an un-conservative case for the proposed model. The maximum error in the developed mathematical model is found to be 7% which is an acceptable percentage.

$$F_x = \int_0^\alpha Pr^2\pi \cos\alpha.d\alpha = Pr^2\pi \sin \alpha \tag{5. 9}$$

$$F_y = \int_0^\alpha Pr^2\pi \sin\alpha.d\alpha = -Pr^2\pi \cos \alpha \tag{5. 10}$$

$$F_x = R_{x1} + R_{x2} \quad \& \quad F_y = R_{y1} + R_{y2}$$

Table 5. 1. Evaluated Bourdon forces using developed equation compared to the FEA extracted forces.

α	NPS	Proposed Model		FEA reactions		Accuracy of the proposed equation	
		Fx	Fz	Fx	Fz	Fx	Fz
20	12	915154.2	161366	855364	150820	7.0%	7.0%
20	24	1722643	303748	1652520	291380	4.2%	4.2%
20	36	2583965	455623	2503140	441380	3.2%	3.2%
20	42	3014626	531560	2927980	516280	3.0%	3.0%
40	12	1719927	626002	1609416	585774	6.9%	6.9%
40	24	3237510	1178357	3108980	1131580	4.1%	4.1%
40	36	4856265	1767536	4708940	1713920	3.1%	3.1%
40	42	5665643	2062125	5508020	2004740	2.9%	2.9%
90	12	2675732	2675732	2518340	2518340	6.2%	6.2%
90	24	5036672	5036672	4871680	4871680	3.4%	3.4%
90	36	7555008	7555008	7382020	7382020	2.3%	2.3%
90	42	8814176	8814176	8635620	8635620	2.1%	2.1%
140	12	1719927	4725462	1624388	4462970	5.9%	5.9%
140	24	3237510	8894987	3145040	8640940	2.9%	2.9%
140	36	4856265	1.3E+07	4766620	13096180	1.9%	-0.7%
140	42	5665643	1.6E+07	5577140	15323080	1.6%	4.4%

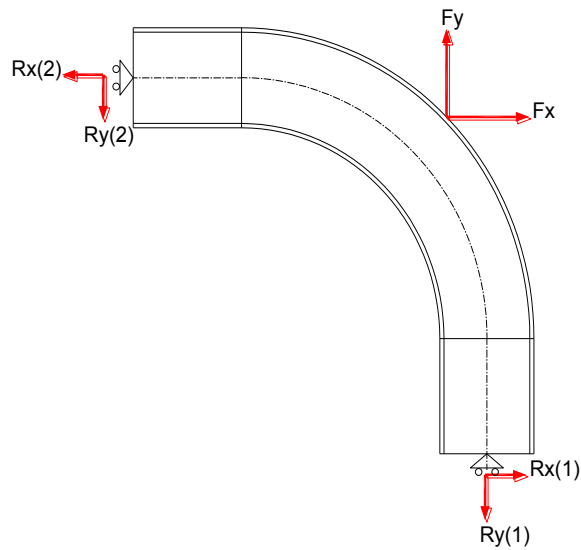


Figure 5. 19. Bourdon forces and end reaction moments on pipe bends.

5.3.2. Bending Moment Loading

5.3.2.1. Linearity of the response

The effect of ovalization on the pipe bend flexibility is investigated by studying the linearity of the behaviour. The relationship between the applied end rotation and the generated reaction moment is investigated. In addition, the relationship between the Mid-layer Von Mises stresses and the reaction moment is studied as well. Figures (5. 20) to (5. 23) show the results of the generated reaction bending moments versus the applied end rotation for short and long bend radius pipes with 12" and 42" outer diameter, and with a range of bend angles from 20 to 140 degrees. For the same pipe bends, figures (5. 24) to (5. 27) show the mid-layer Von Mises stress versus the reaction moment. The relationship is linear for all the studied pipe bends except for the short bend radius 42" diameter pipe with bend angles 90 and 140 degrees as shown in figure (5. 22). These are the only two cases out of 96 studied bends which are found to be nonlinear, therefore, they are considered linear in this study and the nonlinearity in the behaviour is ignored. The results are curve-fitted to a linear relationship leading to some un-conservative points on the curve.

Figures (5. 20) & (5. 21) show the end rotation-reaction moment relationship for 12" diameter pipe bends with short and long bend radius, respectively. The curves show that the cross-sectional

ovalization has an insignificant effect on the behaviour of the pipe bends since the relationship is perfectly linear. The end rotation resulting from a closing bending moment is found to be higher than that from an opening bending moment at the same bending moment values. This means that a pipe bend is more flexible when it is under a closing bending moment than that of an opening bending moment regardless the value of bend angle (α) or the bend radius (R). However, by comparing figures (5. 20) & (5. 21) together, it can be found that having a larger bend radius results in higher flexibility since the generated end rotation is higher when the same bending moment is applied. In addition, the curves indicate that at the same bending moment, the resulted end rotation of a 20° bend is lower than that of a 140° bend for two bends having a consistent size and bend radius. This indicates that increasing the bend angle results in higher flexibility. All these observations are in agreement with the conclusions of Chapter (3). Which means that even by using a different boundary condition, the flexibility of the pipe bend is affected by the bending moment direction and the bend geometry in the same way.

As the pipe size increases, the nonlinearity in the behaviour starts to be significant. Figures (5. 22) & (5. 23) show the end rotation - reaction moment relationship to be nonlinear. The opening bending moment shows almost a linear relationship however it has a slight concave downward curve. This means that by applying a large increment of change in the bending moment results in an insignificant increase in the end rotation. Consequently, meaning that the pipe bends gain more stiffness with loading. However, the closing bending moment shows a concave upward curve where the rate of increase in the end rotation increases throughout the loading and consequently this means that the pipe bend gains flexibility with loading. This shows that applying a closing bending moment leads to increasing the bend's flexibility than that applying an opening bending moment. Consequently, this affects the Stress Intensification Factors (SIF) and clearly these two cases need to be dealt with separately.

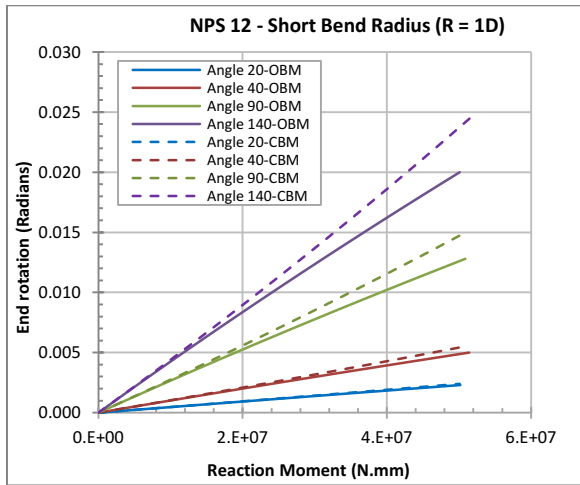


Figure 5. 20. End rotation vs reaction moment for 12” pipe with 1D bend radius.

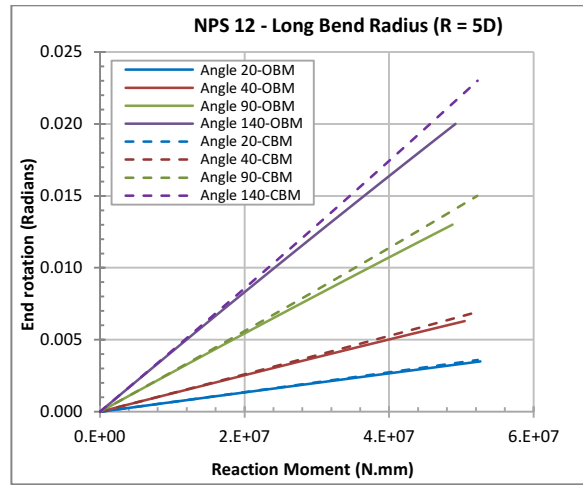


Figure 5. 21. End rotation vs reaction moment for 12” pipe with 5D bend radius.

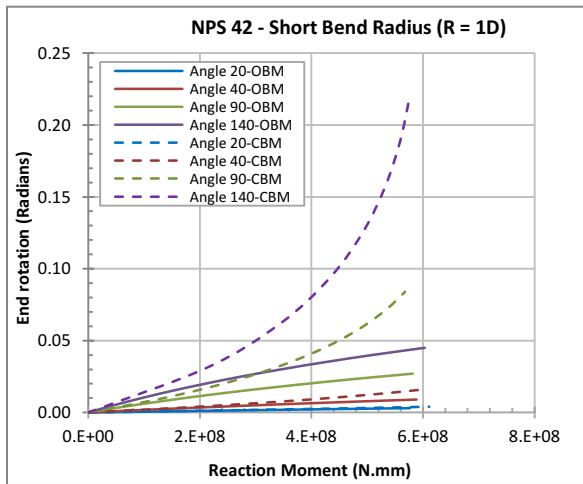


Figure 5. 22. End rotation vs reaction moment for 42” pipe with 1D bend radius.

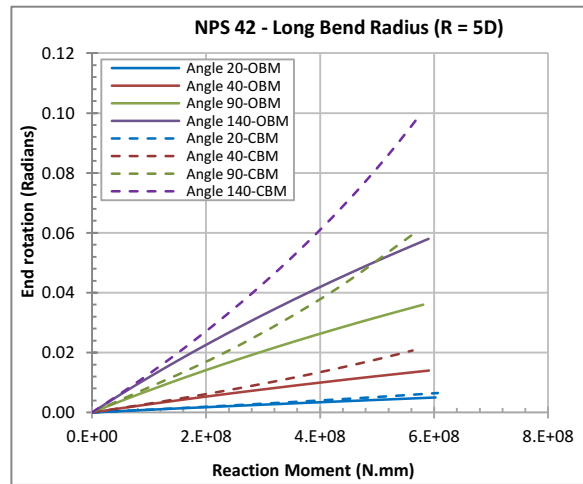


Figure 5. 23. End rotation vs reaction moment for 42” pipe with 5D bend radius.

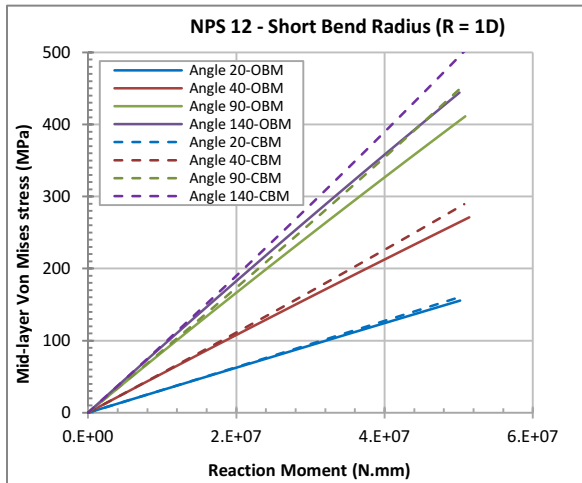


Figure 5. 24. Mid-layer Von Mises stress vs reaction moment for 12” pipe with 1D bend radius.

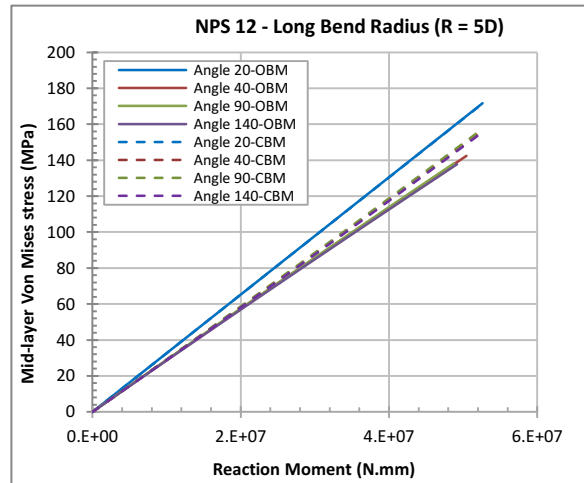


Figure 5. 25. Mid-layer Von Mises stress vs reaction moment for 12” pipe with 5D bend radius.

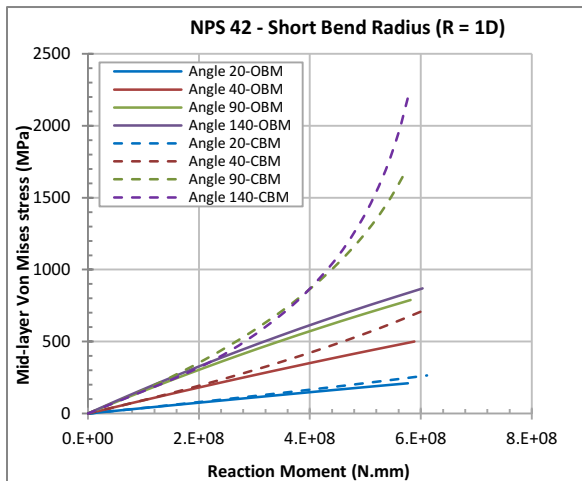


Figure 5. 26. Mid-layer Von Mises stress vs reaction moment for 42” pipe with 1D bend radius.

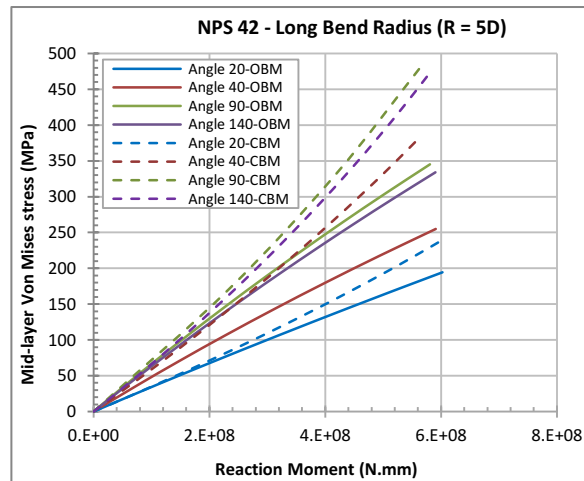
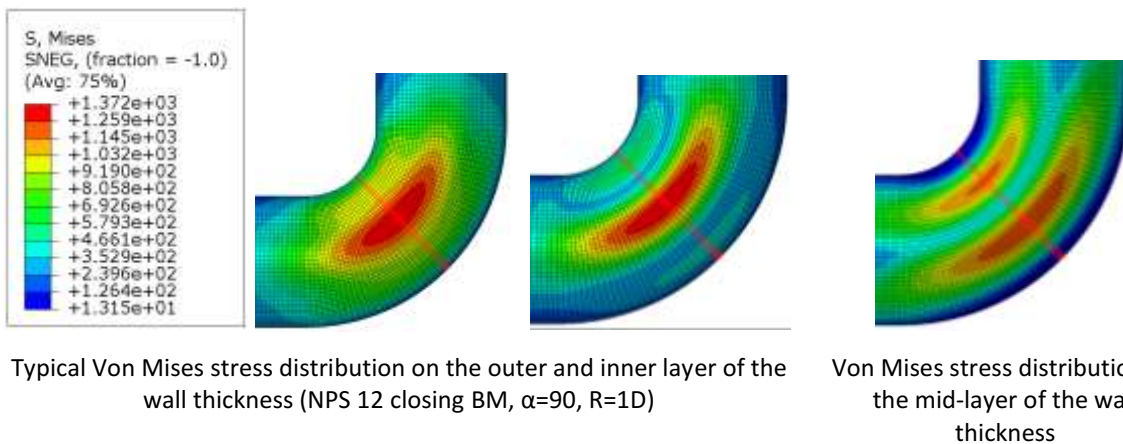


Figure 5. 27. Mid-layer Von Mises stress vs reaction moment for 42” pipe with 5D bend radius.

5.3.2.2. Effect of bending moment direction

As presented from the previous section, the direction of bending moment affects the pipe flexibility. Consequently, the bending direction affects the Von Mises stress distribution across the bend circumference at the critical section. The critical section is defined as the location along the bend length where the maximum Von Mises stresses are recorded at the mid-layer of the pipe wall as shown in figure (5. 28). The stresses at the identified critical section are measured at inner, outer, and mid-layer

of the pipe wall thickness. The Von Mises stress distribution at these three layers is found to be similar for most of the studied pipe bends regardless of the direction of the applied bending. The location of the maximum stress along the critical section may differ from one pipe bend to another based on the geometry where it is found at the crown for large bend angles and changes to be at the intrados of the bend for small bend angles. The stress distribution at the critical section is found to be similar for most of the studied pipe bends with bend angle varying from 40 to 140 degrees. However, the stress distribution on some of the pipe bends changes when the bend angle is as small as 20 degrees. Figure (5. 28) is the Von Mises stress distribution for a 12” diameter pipe with short bend radius ($R = 1D$) and bend angle 90 degrees subjected to a closing bending moment which is considered a typical bend.



Typical Von Mises stress distribution on the outer and inner layer of the wall thickness (NPS 12 closing BM, $\alpha=90$, $R=1D$)

Von Mises stress distribution on the mid-layer of the wall thickness

Figure 5. 28. Typical Von Mises stress distribution for pipe bends with bend angles ranging from 40 to 140 degrees and bend radius from 1D to 5D.

5.3.2.2.1. Pipe bends with large bend angles (40 to 140 degrees):

The Von Mises stress distribution along the critical section is plotted in figures (5. 29) and (5. 30) as a typical distribution for pipe bends with bend angles varying from 40 to 140 degrees. Although, the closing bending moment shows higher stresses than the opening bending moment case, but the curves show the same Von Mises stress pattern along the pipe circumference. Figures (5. 29) and (5. 30) show the stress distribution on a 90-degree pipe bend with 36” outer diameter and bend radius equal to 3D subjected to an opening and closing bending moment, respectively. The Von Mises stress is plotted against the circumferential angle (θ) starting from zero at the intrados to 180 degrees at the extrados of the pipe bend. As shown previously in Chapter (3), the distribution of the Von Mises stress on the mid-layer of the pipe bend has two stress peaks. The two peaks are approximately at a circumferential angle

of 60 and 110 degrees. However, for the inner and outer layers, the maximum Von Mises stress is found to be always at the crown location ($\varnothing = 90$ degrees) regardless the direction of applied bending moment. Figures (5. 31) and (5. 32) show the deformed cross-section of the mid-length section of the pipe bend. The deformed cross-section is ovalized in the opening bending moment case and flattened in the closing bending moment case as explained before in chapter (3). The deformed cross-section is found to be symmetric about the neutral axis which results in a symmetric hoop and longitudinal stress distribution about the crown ($\varnothing = 90$) as shown in figures (5. 33) to (5. 36). Consequently, resulting in a symmetric Von Mises stress whether the bend is subjected to opening or closing bending moment.

The FEA results show that the maximum Von Mises stress is at the inner layer of the wall thickness at the crown location ($\varnothing = 90$ degrees). The Von Mises stresses at the inner layer are 36% higher than that found at the outer layer for both opening and closing bending moment. Moreover, the Von Mises stresses at the inner layer is 115% and 220.3% higher than that found at the mid-layer of the pipe wall thickness for opening and closing bending moments, respectively. Therefore, it is expected that for higher stresses, the inner surface of the pipe bend will start yielding. The same observation is mentioned for pipe bends with fixed-free ends presented in Chapter (3). Therefore, the design of pipe bends should not be restricted to the stresses at the mid-layer of the wall thickness only.

Figures (5. 37) to (5. 39) show the difference in stresses generated from the closing and opening bending moments for all the studied pipe bends at three different layers. As the bend angle increases, the difference in stresses increase as well where the maximum difference is found in pipe bends with 140-degrees bend angle. The closing bending moment results in higher stresses than the opening bending moment in all the studied pipe bends at the three different wall thickness layers. The highest difference in stresses is recorded in pipe bends with short bend radius. For short bend radius ($R=1D$) pipes, the closing bending moment results in up to 5.5 times the Von Mises stress of the opening bending moment at the outer layer. However, for long bend radius ($R=5D$), the closing bending moment results in up to 1.9 times the stresses of the opening bending moment. As the bend radius increases, the difference between the stresses from closing and opening bending decrease but yet considered significant and should be reflected in the SIF factors of the code.

By comparing the Von Mises stresses from Chapter (3) with the stresses presented in this chapter, It shows that the effect of bending moment direction is more significant in this case where both

pipe ends are rollers which is considered to be reflecting the actual end conditions of a pipe bend located in a pipeline. A comparison between the two different cases of end conditions is conducted in the next section since the boundary conditions of a pipe bend affect the stress levels.

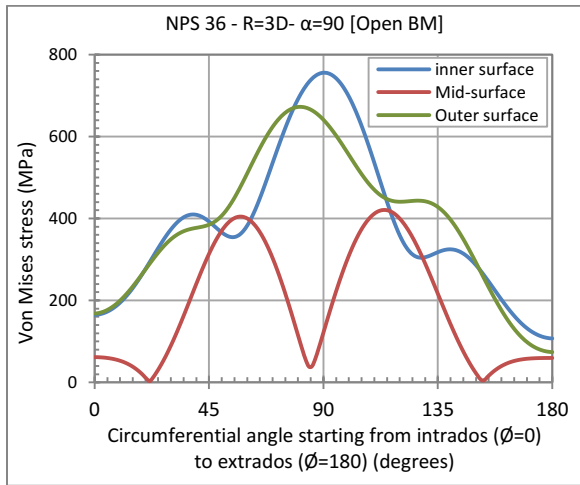


Figure 5. 29. Von Mises stress distribution along the critical section of a pipe bend with bend angle 90o and bend radius (R = 3D) subjected to an opening bending moment.

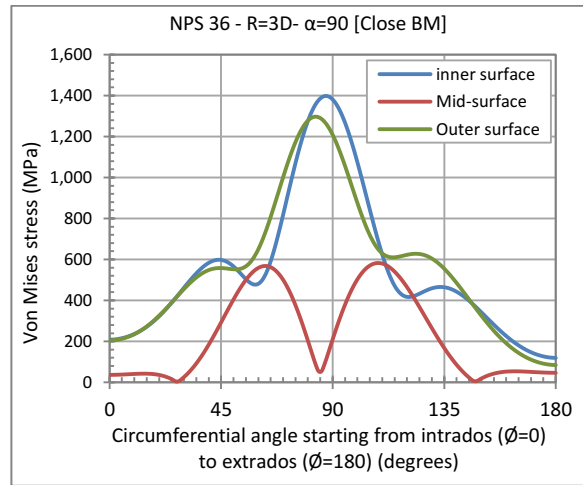


Figure 5. 30. Von Mises stress distribution along the critical section of a pipe bend with bend angle 90o and bend radius (R = 3D) subjected to a closing bending moment.

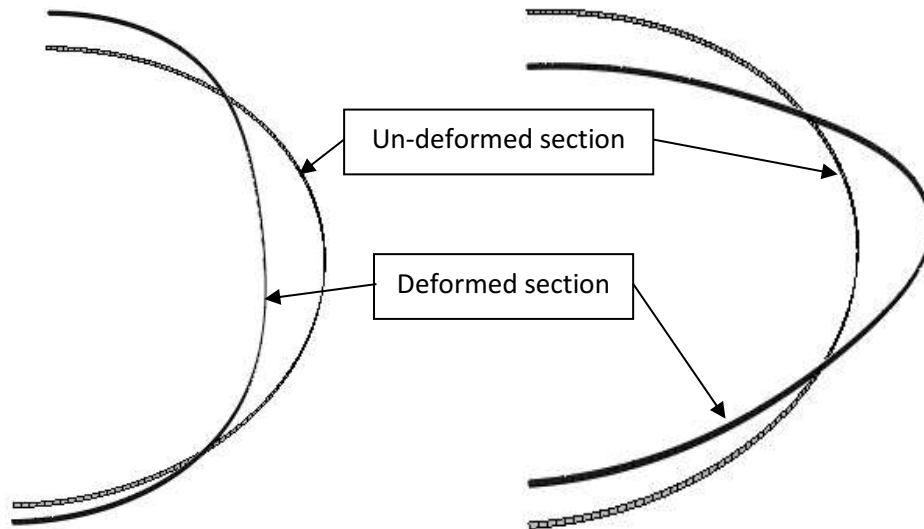


Figure 5. 31. The cross-sectional ovalization at the mid-length of the pipe bend subjected to an opening bending moment.

Figure 5. 32. The cross-sectional flattening deformation at the mid-length of the pipe bend subjected to a closing bending moment.

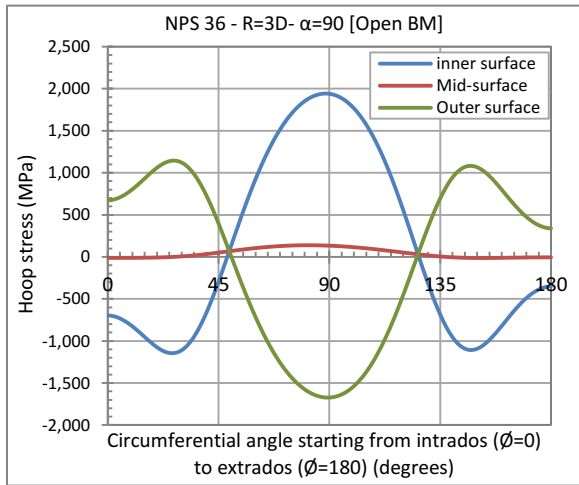


Figure 5. 33. Von Mises stress distribution along the critical section of a pipe bend with bend angle 90o and bend radius (R = 3D) subjected to an opening bending moment.

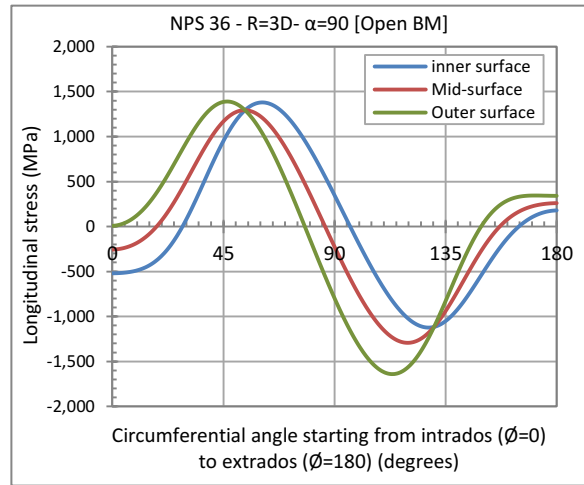


Figure 5. 34. Von Mises stress distribution along the critical section of a pipe bend with bend angle 90o and bend radius (R = 3D) subjected to a closing bending moment.

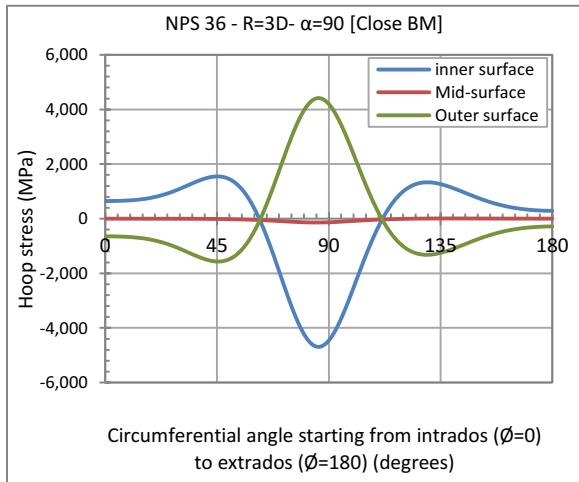


Figure 5. 35. Von Mises stress distribution along the critical section of a pipe bend with bend angle 90o and bend radius (R = 3D) subjected to an opening bending moment.

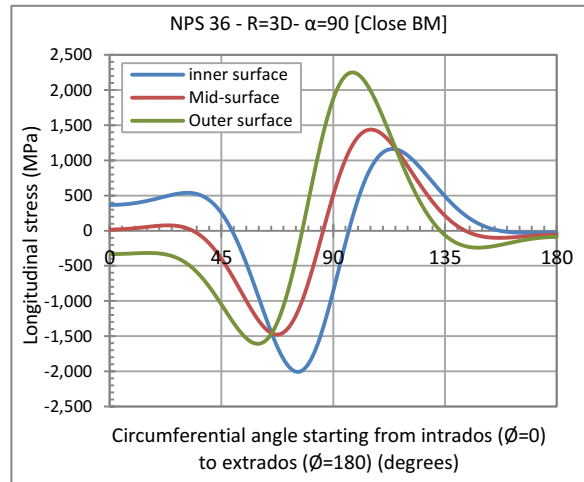


Figure 5. 36. Von Mises stress distribution along the critical section of a pipe bend with bend angle 90o and bend radius (R = 3D) subjected to a closing bending moment.

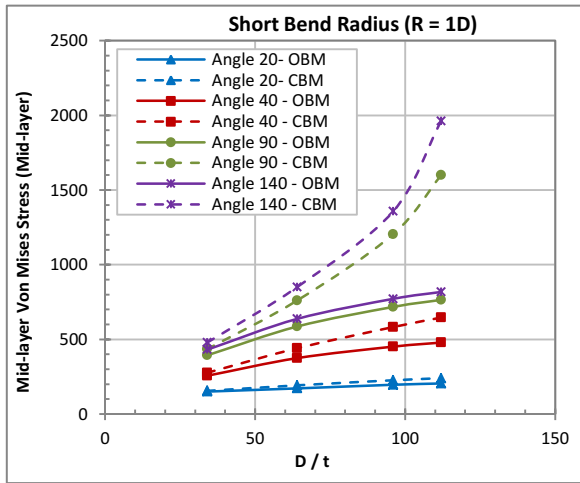


Figure 5.37. Mid-layer Von Mises stress vs the D/t ratio for pipe bends with short bend radius (R=1D).

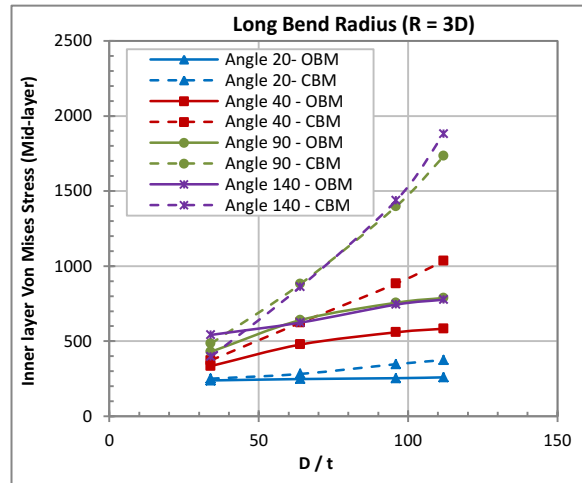


Figure 5.38. Inner-layer Von Mises stress vs the D/t ratio for pipe bends with long bend radius (R=3D).

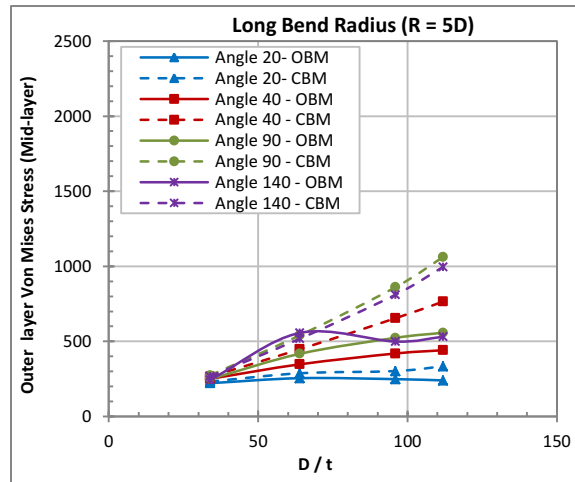
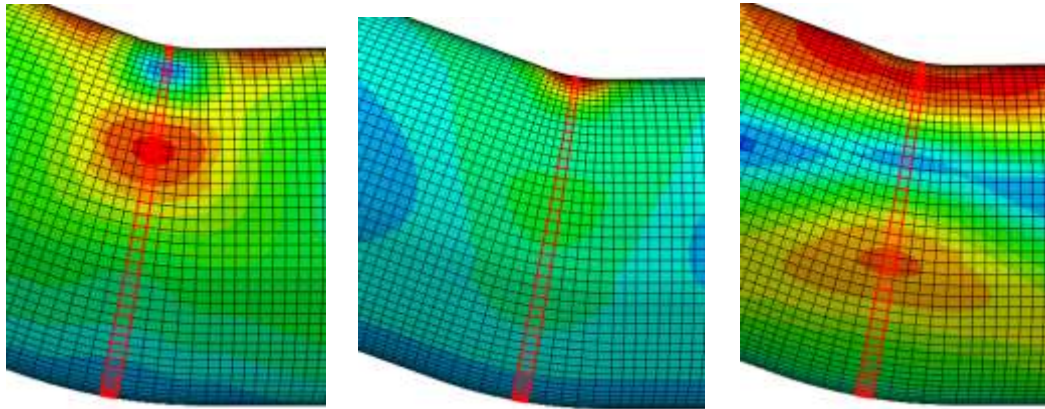


Figure 5.39. Outer-layer Von Mises stress vs the D/t ratio for pipe bends with long bend radius (R=5D).

5.3.2.2.2. Pipe bends with small bend angles (20 degrees):

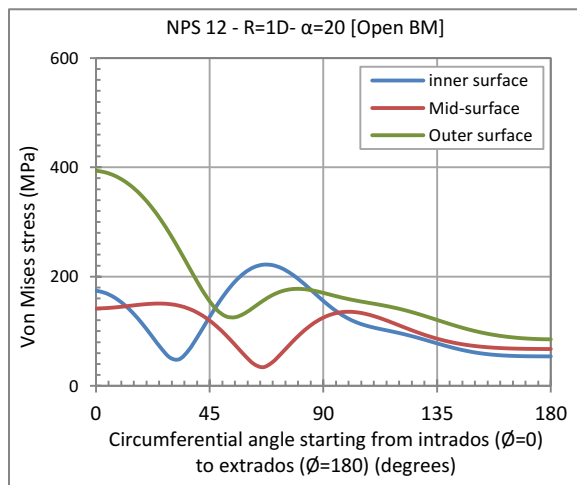
As for pipe bends with small bend angles ($\alpha = 20^\circ$) and small outer diameter (NPS 12 & 24) that are considered to be stiffer, the behaviour tends to be different than the large bend angles presented earlier as shown in figure (5. 40). Figure (5. 41.a) shows the Von Mises stress distribution on a NPS 12 pipe bend subjected to opening bending moment with bend angle equal 20 degrees. The maximum Von Mises stress is at the intrados of the pipe bend and the yielding is initiated from the outer layer of the

pipe wall. However, even if the bend angle is small as 20 degrees but the bend outer diameter and the bend radius increase, the stiffness of the pipe starts to decrease and the Von Mises distribution approaches more the symmetric distribution explained earlier in section (3.2.2.1). Figure (5. 41.b) shows the Von Mises stress on a 42” pipe bend with long bend radius ($R = 5D$) where the maximum stresses are at the crown for the inner and outer layers whereas there are two stress peaks at the mid-layer which resembles the stresses on a large bend angle pipe.

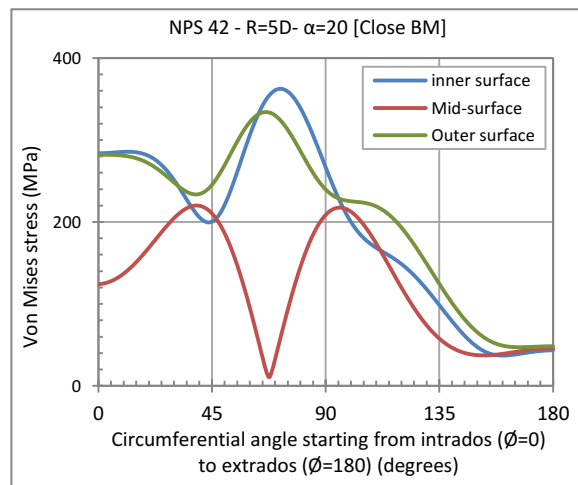


Typical Von Mises stress distribution on the inner and outer layers of the wall thickness, respectively (NPS 12, Open BM, $\alpha=20$) Von Mises stress distribution on the mid-layer of the wall thickness

Figure 5. 40. Von Mises stress distribution for 20-degree pipe bends with 12” outer diameter and short bend radius ($R = 1D$) subjected to opening bending moment.



a. Pipe bend NPS 12 with bend angle 20° and short bend radius ($R = 1D$) under opening bending moment



b. Pipe bend NPS 12 with bend angle 20° and short bend radius ($R = 1D$) under opening bending moment

Figure 5. 41. Von Mises stress distribution for pipe bends with small bend angles.

5.3.2.3. Comparison between the FEA and the CSA-Z662 Code results

The CSA-Z662 code predicts the combined stresses on a pipe bend ignoring the bend angle and the bending moment direction effect on the behaviour of pipe bends. In this section, a comparison between the Von Mises stress results evaluated from the FEA models for pipe bends subjected to opening and closing bending moments and the predictive stress according to the CSA-Z662 is conducted to have a better understanding on the methodology used by the current codes and its limitations. In this section, the internal pressure term is ignored since the bends are subjected to bending moment only. The combined stresses at the pipe bend are evaluated according to CSA-Z662 using equation (5. 2).

Figures (5. 42) to (5. 48) show the FEA maximum Von Mises stresses evaluated at a particular opening and closing bending moments plotted against the D/t ratio of the pipe bends at the three studied wall layers. The code estimated stresses are found to be conservative in some cases and un-conservative in other cases based on the pipe size, bend angle, bend radius and bending moment direction. The layer at which the stresses are evaluated is an important factor as well in the accuracy and integrity of the design. The mid-layer stress results show that for small bend angles (20 and 40 degrees), the CSA estimated stresses are highly conservative especially for short radius bends by up to 436 % as shown in figure (5. 42). However, for large bend angles (90 and 140 degrees) the CSA estimated stresses are found conservative for opening bending moment cases but un-conservative for closing bending moment cases by up to 78.5 % especially for large pipe sizes as shown in figure (5. 43). For long bend radius, the mid-layer stresses are higher than the estimated code stress by up to 67% for both opening and closing bending moments.

On the other hand, the Von Mises stresses at the inner and outer layers are higher than the mid-layer stresses and show higher un-conservative code stresses. For the inner and outer layers, pipe bends with bend angles 40, 90 and 140 degrees with bend radius ranging from 1D to 5D are un-conservative by up to 145.8% and 477% for opening and closing bending moment, respectively as shown in figures (5. 44) and (5. 48).

It is observed that the un-conservativeness of the code estimated stresses is more prominent in the closing bending moment than the opening bending moment case for all studied bends. As the pipe size increases, the un-conservativeness of the code combined stress increases as well. However,

the code estimated stresses are relatively close to the FEA results for small pipe sizes especially in the opening bending moment case. This means that the code's formula for predictive stress might be more accurate for small D/t ratios rather than the large pipes.

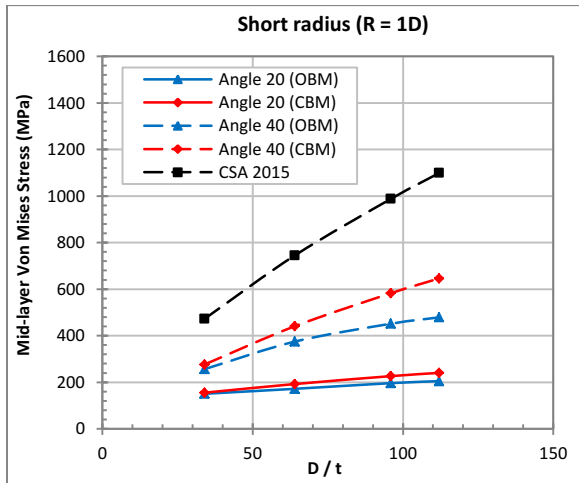


Figure 5. 42. Mid-layer Von Mises stress vs D/t ratio for short radius pipe bends (R =1D) with bend angles 20 & 40 degrees.

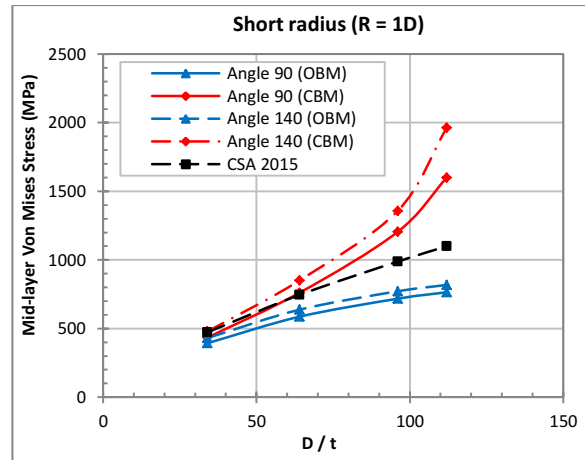


Figure 5. 43. Mid-layer Von Mises stress vs D/t ratio for short radius pipe bends (R =1D) with bend angles 90 & 140 degrees.

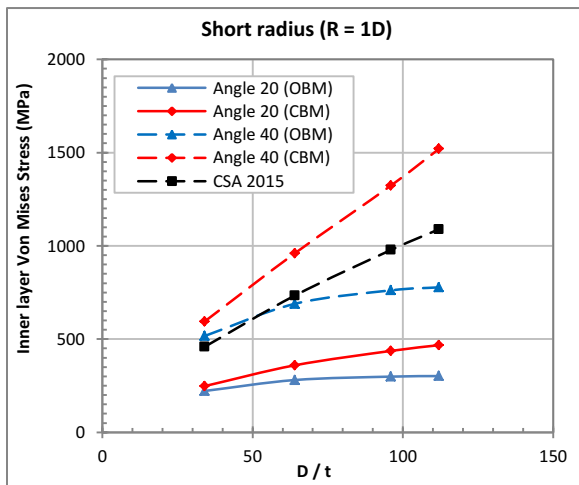


Figure 5. 44. Inner layer Von Mises stress vs D/t ratio for short radius pipe bends (R= 1D) with bend angle 20 & 40 degrees.

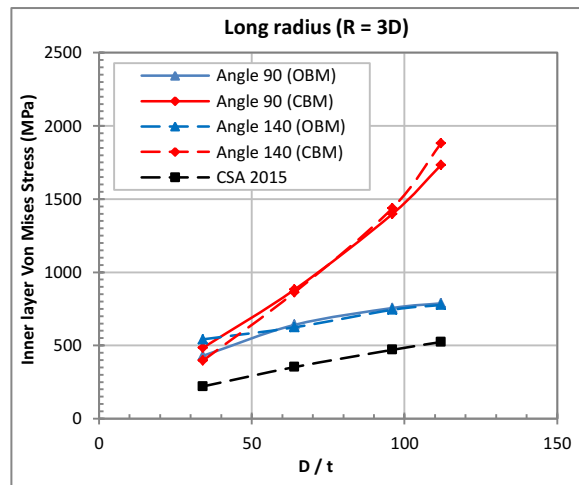


Figure 5. 45. Inner layer Von Mises stress vs D/t ratio for long radius pipe bends (R= 3D) with bend angle 90 & 140 degrees.

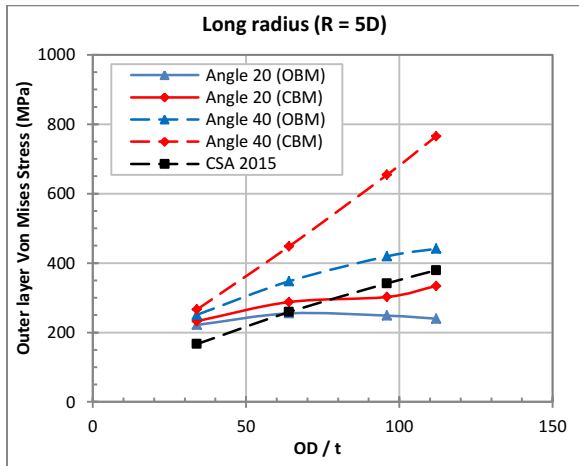


Figure 5. 46. Inner layer Von Mises stress vs D/t ratio for short radius pipe bends (R= 1D) with bend angle 20 & 40 degrees.

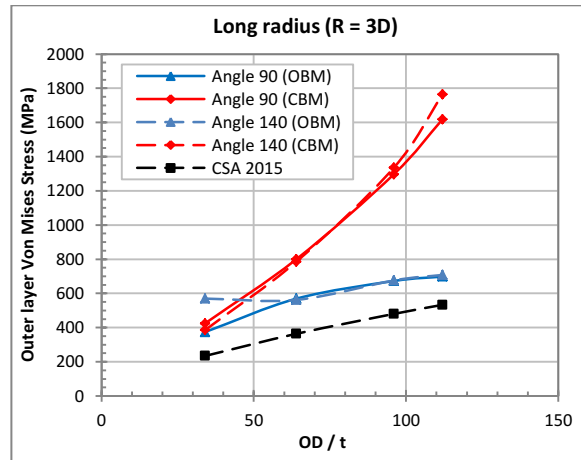


Figure 5. 47. Inner layer Von Mises stress vs D/t ratio for long radius pipe bends (R= 3D) with bend angle 90 & 140 degrees.

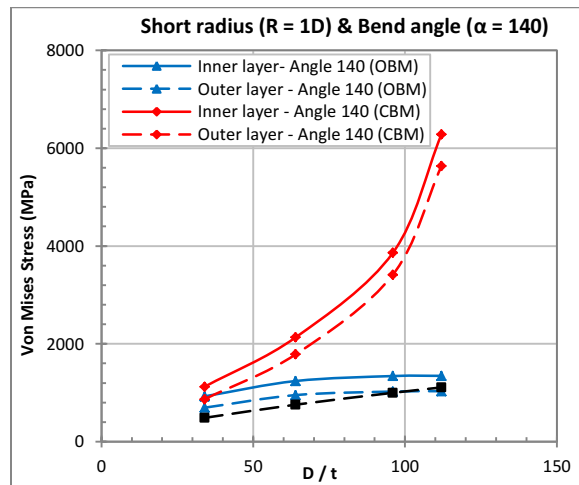


Figure 5. 48. Inner and outer layer Von Mises stress vs D/t ratio for short radius pipe bends (R= 1D) with bend angle 140 degrees.

5.3.2.4. Effect of changing the End Boundary Conditions on the Bend Behaviour

The end boundary conditions of a pipe bend are believed to have an effect on the behaviour and stress distribution along the pipe bend surface. According to a previous study done by Matzen & Yu in 1998, it was shown that the minimum length of the attached straight pipe required to avoid the end

condition effect is 5 times the outer diameter of the pipe. If the straight pipe is shorter than $5D$, then the ovalization of the pipe is affected by the end restraints resulting in higher stress values at the bend mid-length section.

To have a better understanding on the effect of end boundary conditions on the bend behaviour, a comparison between the FEA stress results from the pipe bends modelled in Chapter (3) and the stresses from the current chapter are conducted in this section. In Chapter (3), the pipe bend is modelled with two attached straight pipes of length $10 D$. One of the pipe ends is free to rotate and translate while the other end is fixed. This pipe configuration and boundary condition is referred to as “BC-1” in this section. The pipe bends in this current chapter are modelled as explained earlier, with two roller support ends where the pipe is free to translate in a direction perpendicular to the attached straight pipe and are free to rotate in the plane of symmetry. In addition, the attached straight pipes are of length $1D$ and this pipe configuration is referred to as “BC-2”.

Figures (5. 49) to (5. 51) show the Von Mises stress plotted against the D/t ratio. The results show that the boundary conditions affect the Von Mises maximum stresses on the bend and it varies based on the bend angle (α) and the bend radius (R). For small bend angles as 20 and 40 degrees, the fixed-free pipe bends (BC-1) result in higher stresses than the roller support end bends (BC-2) as shown in figure (5. 49). However, as the bend angle increases to 90 and 140 degrees, the roller support bends (BC-2) show higher stresses than the fixed-free bends (BC-1) regardless the direction of applied bending as shown in figures (5. 50) & (5. 51). And this is observed in the three different layers of the wall thickness and for all the studied bend radii ($R = 1D, 3D \& 5D$).

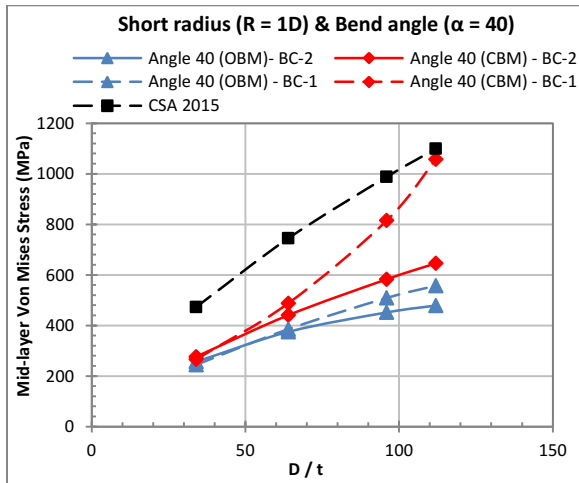


Figure 5. 49. Mid-layer Von Mises stress vs D/t ratio for pipes with 1D bend radius and 40 degrees bend angle.

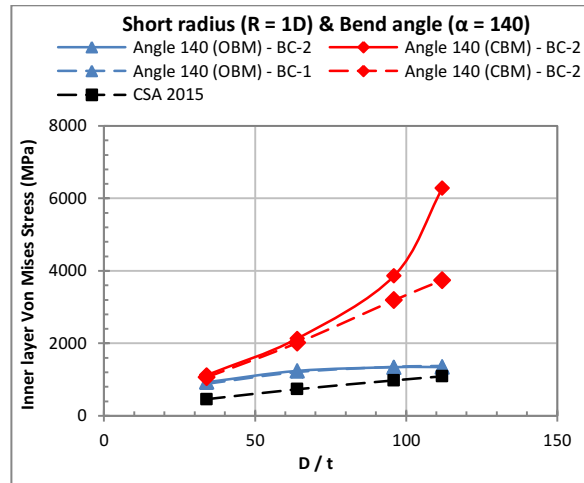


Figure 5. 50. Inner layer Von Mises stress vs D/t ratio for pipes with 1D bend radius and 140 degrees bend angle.

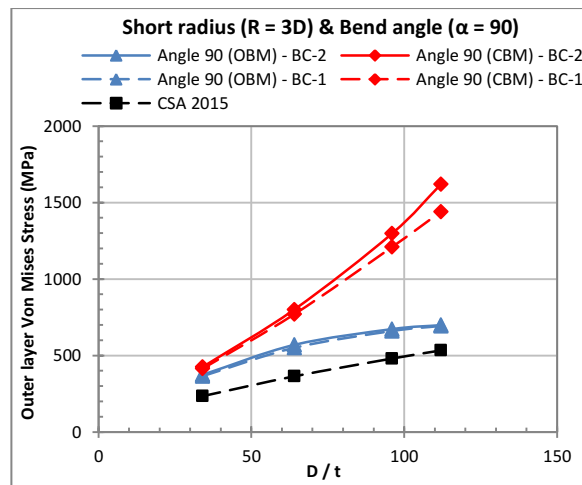


Figure 5. 51. Outer layer Von Mises stress vs D/t ratio for pipes with 3D bend radius and 90 degrees bend angle.

The highest difference in stresses between BC-1 and BC-2 is found in bends with short bend radius ($R=1D$) and large bend outer diameter as 42". For pipe bends with small bend angles as 20 and 40 degrees, the fixed-free boundary condition (BC-1) results in higher stresses than the roller supported end bends (BC-2) at the mid-layer of the wall thickness by up to 48.7% and 109.7% for opening and closing bending moments, respectively, as shown in figures (5. 52) and (5. 53). As shown in figures (5.

54) & (5. 55), as the bend radius increases to 5D, this difference drops to 19.5% and 30.3% for opening and closing bending, respectively.

This difference in stresses is higher and more significant when the comparison is at the inner and outer layer of the wall thickness as shown in figures (5. 56) to (5. 59). For the inner and outer layer of short bend radius pipes ($R=1D$), The stresses from the BC-1 is higher than that of the BC-2 for bends with bend angles 20 and 40 degrees by up to 108.8% and 169.9% for opening and closing bending moments, respectively. As the bend radius increases to 5D, the difference in stresses drops to 43% and 72% for opening and closing bending moments, respectively.

On the other hand, when the bend angle increases to 90 and 140 degrees, the maximum stresses from pipe bends with BC-1 are lower than that of bends with BC-2. At the mid-layer of the wall thickness for pipes with short bend radius ($R = 1D$), the stresses from BC-2 is higher than BC-1 by up to 5.1% and 40.4% for opening and closing bending moments, respectively as shown in figures (5. 52) & (5. 53). This percentage increases at the inner and outer layer of the wall thickness to 4.9% and 71.8% for opening and closing bending moments, respectively as shown in figures (5. 56) & (5. 57). As the bend radius increases, there are some spikes recorded in the stress results that may be due to any FEA accuracy as shown in figures (5. 54), (5. 55) & (5. 58). These models are 3 out of 48 models considered a small percentage of error and ignored in this comparison. For long bend radius ($R=3D$ & $5D$) the ignored models in this comparison are the 24" pipes with bend angle 140 degrees in the opening bending moment loading and the 36" pipe diameter with bend angle 90 degrees in both opening and closing bending moments. For long bend radius pipes, the mid-layer stresses from BC-2 are higher than BC-1 by up to 15.6% and 20.7% for opening and closing bending moment, respectively. However, the differences at the inner and outer layers are 8.9% and 33% for opening and closing bending, respectively.

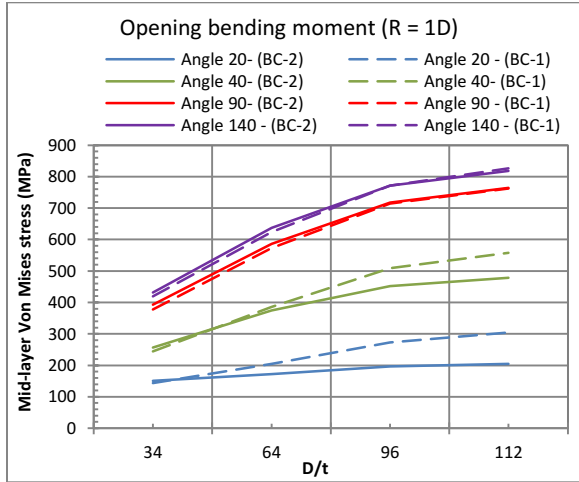


Figure 5. 52. Mid-layer Von Mises stress vs D/t ratio for pipes with 1D bend radius subjected to an opening bending moment.

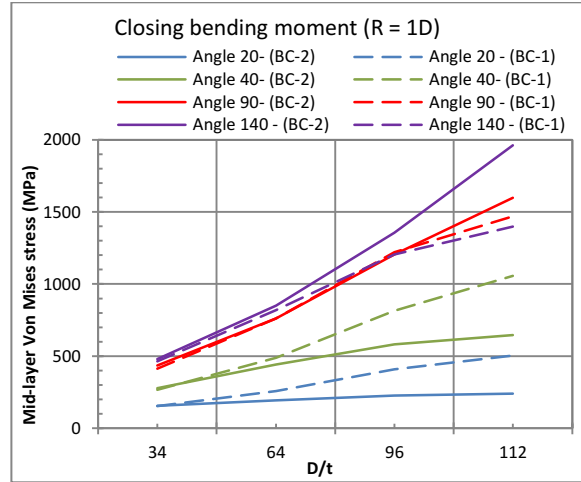


Figure 5. 53. Mid-layer Von Mises stress vs D/t ratio for pipes with 1D bend radius subjected to a closing bending moment.

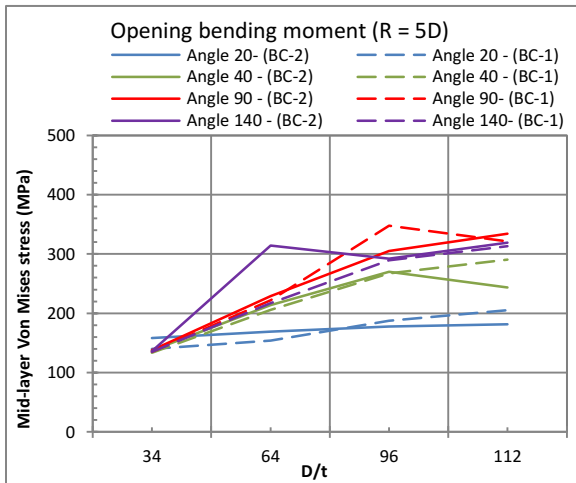


Figure 5. 54. Mid-layer Von Mises stress vs D/t ratio for pipes with 5D bend radius subjected to an opening bending moment.

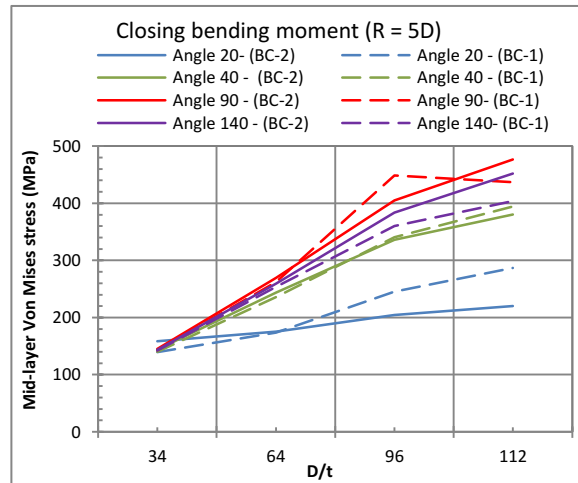


Figure 5. 55. Mid-layer Von Mises stress vs D/t ratio for pipes with 5D bend radius subjected to a closing bending moment.

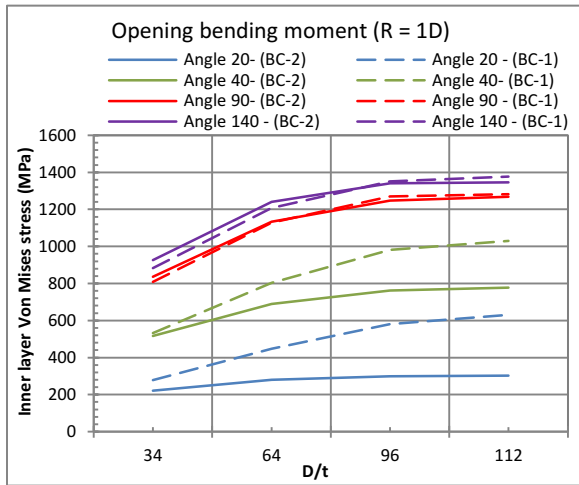


Figure 5. 56. Inner layer Von Mises stress vs D/t ratio for pipes with 1D bend radius subjected to an opening bending moment.

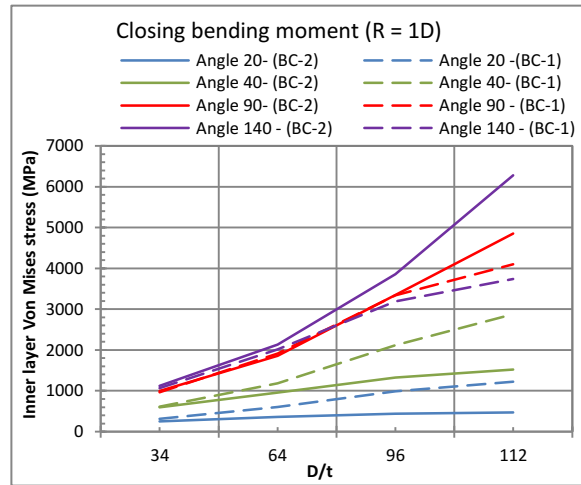


Figure 5. 57. Inner layer Von Mises stress vs D/t ratio for pipes with 1D bend radius subjected to closing bending moment.

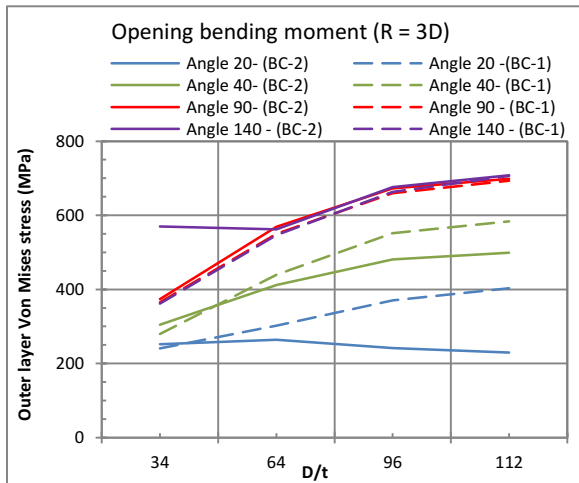


Figure 5. 58. Outer layer Von Mises stress vs D/t ratio for pipes with 3D bend radius subjected to an opening bending moment.

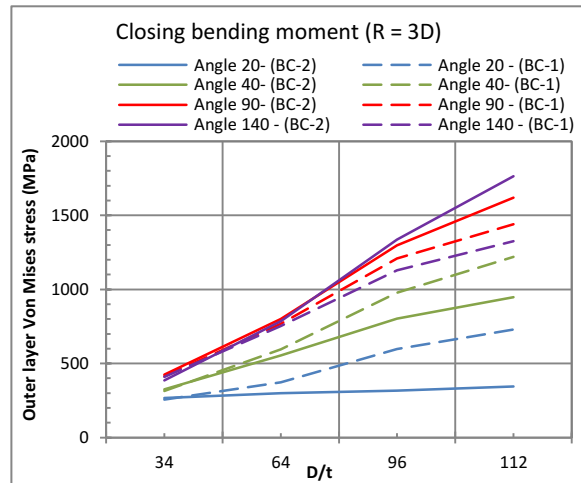


Figure 5. 59. Outer layer Von Mises stress vs D/t ratio for pipes with 3D bend radius subjected to closing bending moment.

5.3.3. Internal Pressure and Bending Moment Loading

5.3.3.1. Linearity of the response and the effect of bending moment direction

The relationship between the bending moment and the end rotation gives an indication of the flexibility of the pipe bends and its behaviour. The relationship is linear for all studied pipes and a sample of these curves is shown in figures (5. 60) to (5. 63). The relationship shows that at the same reaction moment, as the bend angle increases, the end rotation increases. In addition, adding an opening bending moment to the internal pressure results in higher end rotations than that of adding a closing bending moment. Therefore, we can say that the flexibility of the pipe bend increases by increasing the bend angle (α) and increases by applying an opening bending moment rather than a closing bending moment. This finding agrees with a past study by Yu and Matzen (1999) that showed that the internal pressure tends to make the elbow stiffer, with the stiffening changes under closing moment greater than those under opening moment.

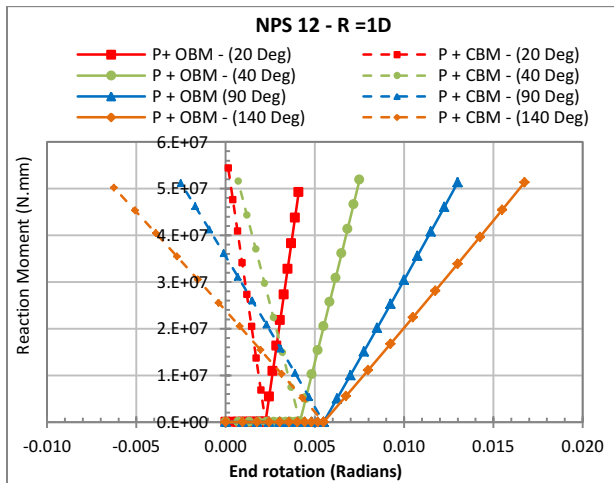


Figure 5. 60. End rotation vs reaction moment for 12” pipe with 1D bend radius.

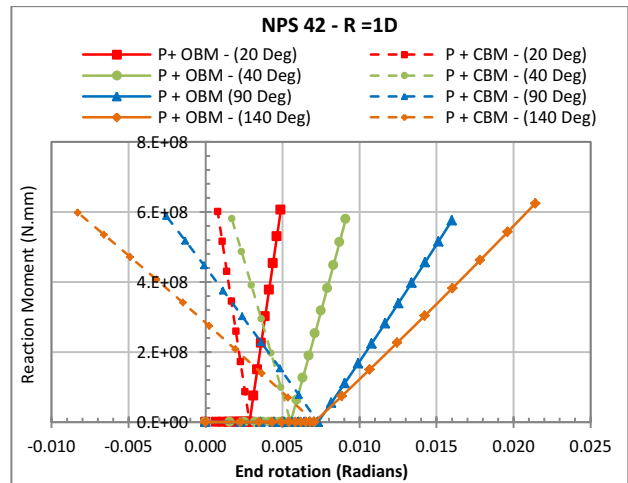


Figure 5. 61. End rotation vs reaction moment for 42” pipe with 1D bend radius.

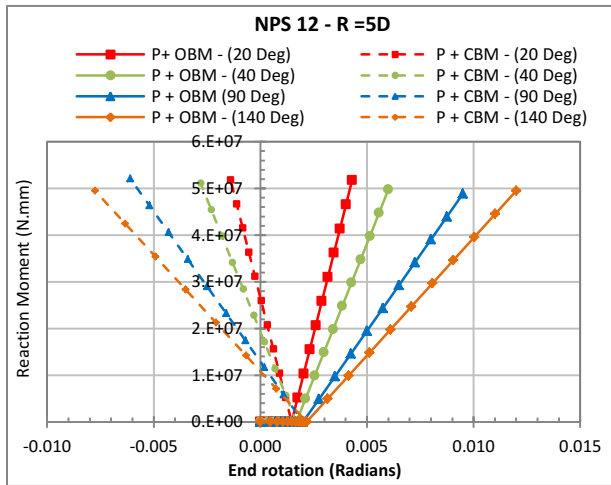


Figure 5. 62. End rotation vs reaction moment for 12" pipe with 5D bend radius.

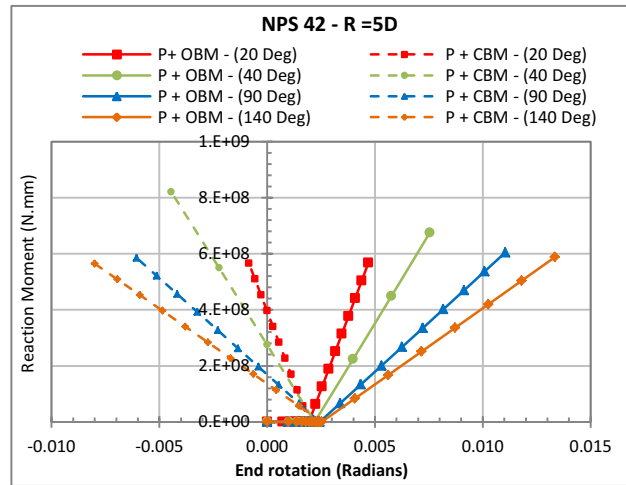


Figure 5. 63. End rotation vs reaction moment for 42" pipe with 5D bend radius.

The linearity in the stress relationships for pipe bends is investigated as well. The Mid-layer Von Mises stress is plotted against the reaction bending moment as shown in figures (5. 64) to (5. 67). Since the two loads are applied at two successive steps, the curves are broken into two parts. The first step where the internal pressure is applied results in some stresses on the pipe wall. However, no reaction bending moment is generated at the end supports due to the internal pressure loading. The second step is the bending moment loading which either increases or decreases the Von Mises stresses from the first step based on the direction of bending moment. Although, the Von Mises stresses from the internal pressure loading is independent of the direction of applied bending moment. However, the curves show that the Von Mises stress from the first step might not be equal in some cases. This occurs when the maximum Von Mises stress location changes in the opening bending than the closing bending case and the stresses are measured at a different location along the critical section circumference of the pipe. In this case, the Von Mises stresses from the internal pressure are different as shown in figure (5. 64) for the 90-degree bend and figures (5. 65) to (5. 67) for all bend angles since they are measured at different locations along the critical section circumference.

The Von Mises stress relationship with the reaction moment is considered almost linear. However, some pipe bends show slight nonlinearity in the relationship. The behaviour of pipe bends with small bend radius is somehow different than those of long bend radius. Figures (5. 64) & (5. 65) show that the internal pressure and opening bending moment case have a concave downward curve

which means that adding an increment of change in the bending moment results in a relatively significant increase in the Von Mises stress. This confirms that adding an opening bending moment to the internal pressure increases the bend's flexibility. However, the internal pressure and closing bending loading case have a concave upward curve where adding a bending moment increment of change leads to a small decrease in the stress. This shows that adding a closing bending moment to the internal pressure leads to lower flexibility than the opening bending case. The behaviour is a bit different for long bend radius pipes ($R=5D$), where adding an opening or closing bending moment to the internal pressure results in a concave downward curve. However, the slope of the closing bending moment curve is steeper than the opening moment curve as shown in figures (5. 66) & (5. 67). Therefore, the rate of increase in the flexibility of the bend is higher in the closing bending moment case than that of the opening bending moment. However, at the same reaction moment, the resulting Von Mises stress is higher in the opening bending than the closing bending. Which is an expected result since the closing bending moment is acting in an opposite direction to the internal pressure loading. Therefore, it decreases the stress until the bending load overcomes the internal pressure and results in a stress that is opposite in direction but higher in value than the internal pressure.

For short radius bends ($R = 1D$), the difference between the opening and closing bending moment case increases by increasing the applied bending load. However, for long radius bends, the difference between the stresses from the opening and closing bending decreases as the applied bending value increases. The comparison between the stresses is conducted at the end of the applied load when the longitudinal stresses due to bending are 0.24 of the stresses due to internal pressure. However, if the difference in stresses between the opening and closing bending is evaluated at a lower bending moment, the recorded difference in stresses will be lower in short radius bends ($R=1D$) and higher for long radius bends ($R= 5D$). Figures (5. 64) & (5. 65) show the Von Mises stress at the mid-layer for pipe bends with 12" and 42" outer diameter and short bend radius ($R=1D$). For short bend radius, the maximum difference in stresses between the opening and closing bending moment for pressurized bends is 29.3 %. This difference increases up to 72.4% when the comparison is conducted for the inner and outer layers of the wall thickness. As the bend radius increases to 5D, the difference between the Von Mises stress at the mid-layer measured from the opening and closing bending moments drops to 2.4% at the end of the loading step as shown in figures (5. 66) & (5. 67). For the inner and outer layer, the difference is found to be up to 28.4% for long radius bends ($R = 3D$ & $5D$).

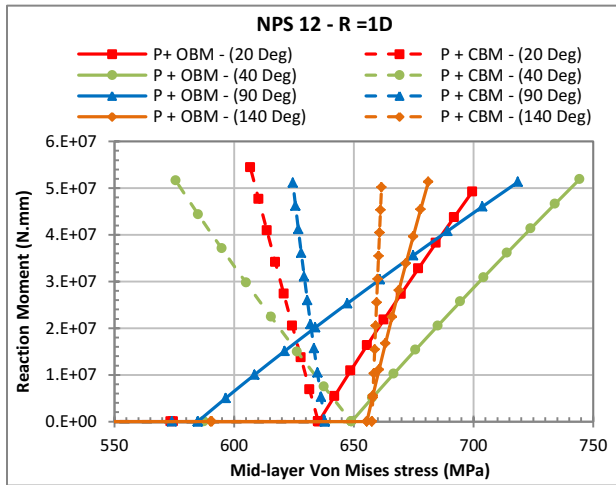


Figure 5. 64. Mid-layer Von Mises stress vs reaction moment for 12” pipe with 1D bend radius.

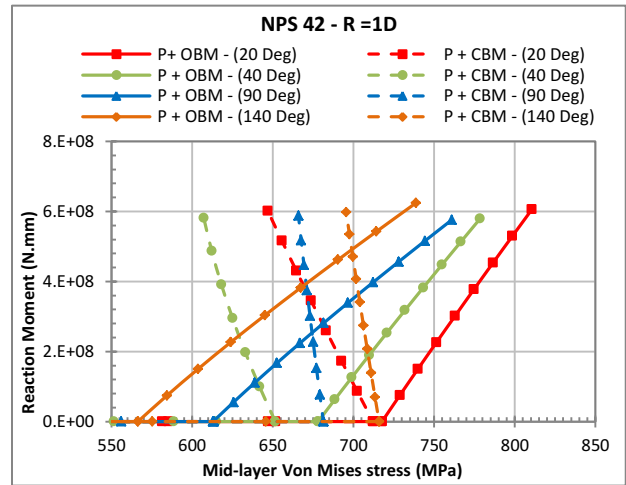


Figure 5. 65. Mid-layer Von Mises stress vs reaction moment for 42” pipe with 1D bend radius.

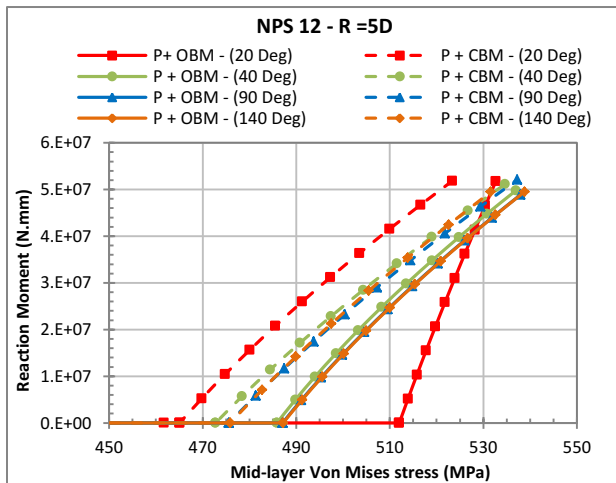


Figure 5. 66. Mid-layer Von Mises stress vs reaction moment for 12” pipe with 5D bend radius.

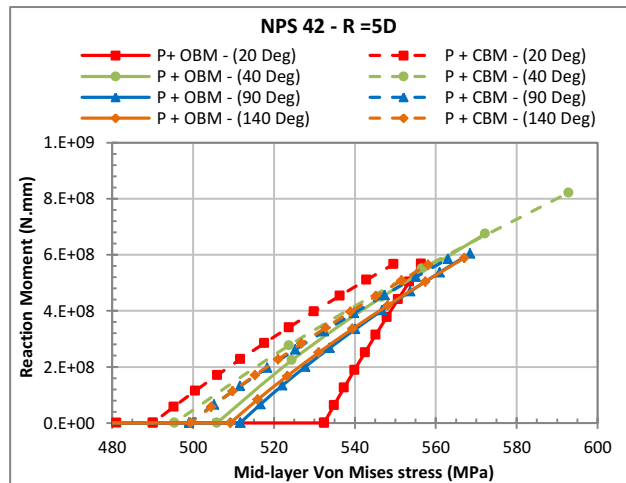


Figure 5. 67. Mid-layer Von Mises stress vs reaction moment for 42” pipe with 5D bend radius.

By investigating the linearity of the stresses at the inner and outer layer, it is found to be different than the mid-layer stresses. Although the stresses on the mid-layer increase by adding opening bending to internal pressure and decrease by adding closing bending, but the inner and outer layer are not following the same pattern. For short bend radius, increasing the bend angle to 90 and 140 degrees changes the behaviour of bends hence the stresses increase by adding closing bending to internal pressure as shown in figures (5. 68) and (5. 69). As the bend radius increase to 5D, the inner layer Von Mises stress decreases by adding closing bending moment to the internal pressure as shown in figure (5.

70). However, the outer layer stresses decreases for pipes with 40, 90 & 140 degrees bend angle when subjected to closing bending moment as shown in figure (5. 71).

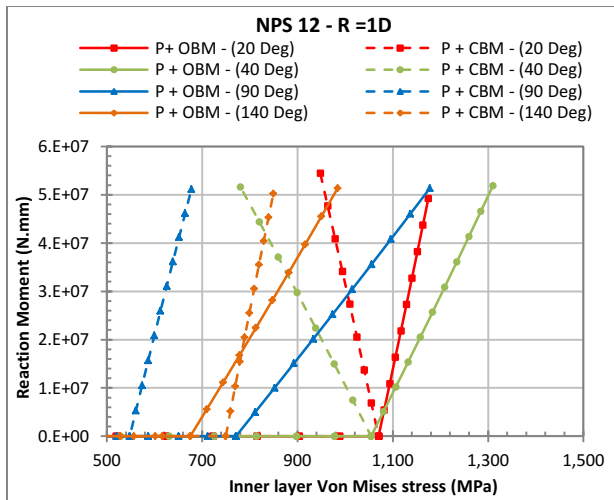


Figure 5. 68. Von Mises stress vs reaction moment for 12” pipe with 1D bend radius.

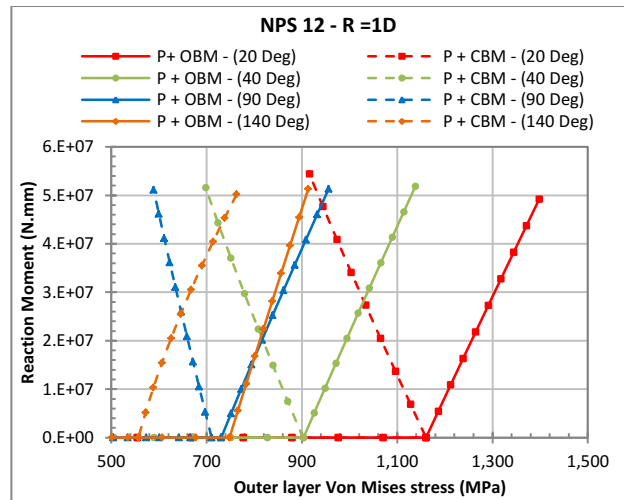


Figure 5. 69. Von Mises stress vs reaction moment for 12” pipe with 1D bend radius.

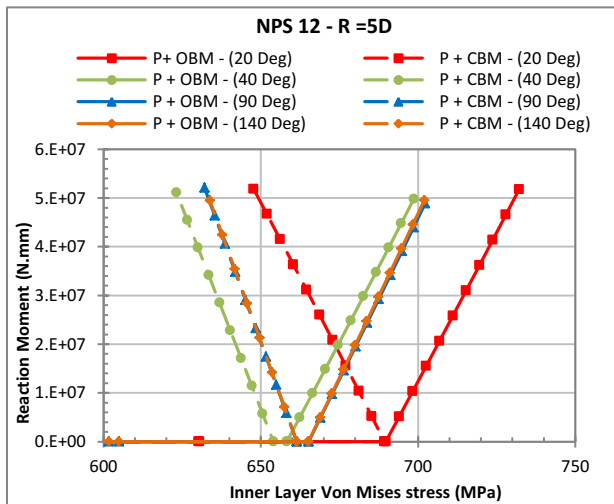


Figure 5. 70. Von Mises stress vs reaction moment for 12” pipe with 5D bend radius.

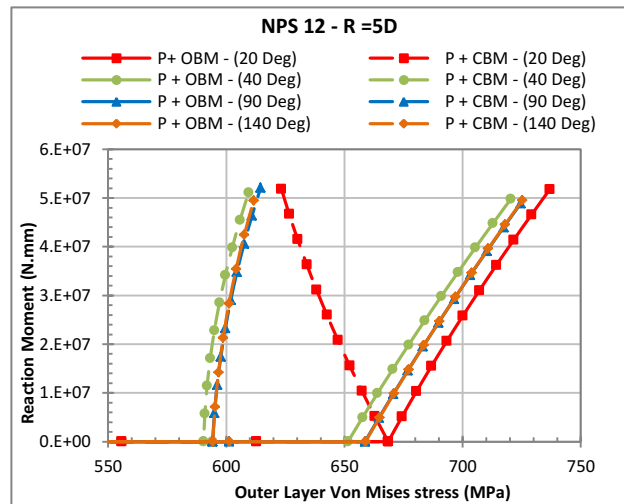


Figure 5. 71. Von Mises stress vs reaction moment for 12” pipe with 5D bend radius.

5.3.3.2. Effect of Bend Angle (α) on the stress distribution

The effect of bend angle is negligible for long bend radius pipes ($R=3D$ & $5D$) whether on the inner, outer or mid-layer of the wall thickness as shown in figures (5. 72) to (5. 74). However, for the short bend radius, it is noticed that as the bend angle increases the mid-layer Von Mises stress

decreases by up to 11.7% for bends subjected to internal pressure and opening bending moment. However, bends subjected to internal pressure and closing bending moment show a 7% decrease in the mid-layer Von Mises stresses when the bend angle decreases from 20 to 40 degrees. Then the stresses increases again when the bend angle increases from 40 to 140 degrees by up to 15.3% as shown in figure (5. 75). For the inner layer Von Mises stresses, adding an opening bending moment to the internal pressure shows a decrease in stresses as the bend angle increases as shown in figure (5. 76). An increase in the bend angle from 20 to 40 degrees leads to an increase in the stresses by up to 11%. Whereas increasing the bend angle beyond 40 degrees results in a decrease in stresses by up to 36.8%. Pipe bends subjected to closing bending moment and internal pressure show a decrease in stress by up to 20.6% when bend angles increases from 20 to 40 degrees followed by an increase in stress which is negligible beyond the 40 degrees as shown in figure (5. 76). The outer layer stresses show almost the same behaviour as the inner layer for the closing bending moment. Pipe bends subjected to opening or closing bending moment and internal pressure show a decrease in the stresses by up to 32% when the bend angle increases from 20 to 40 degrees However, the reduction in stresses beyond the 40 degree bend angle is up to 24% for opening bending and negligible in the case of closing bending as shown in figure (5. 77).

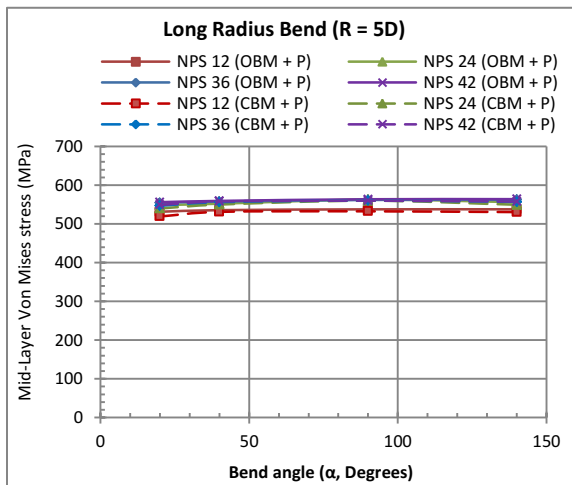


Figure 5. 72. Mid-layer Von Mises stress vs bend angle (α) for pipes with long bend radius (R = 5D).

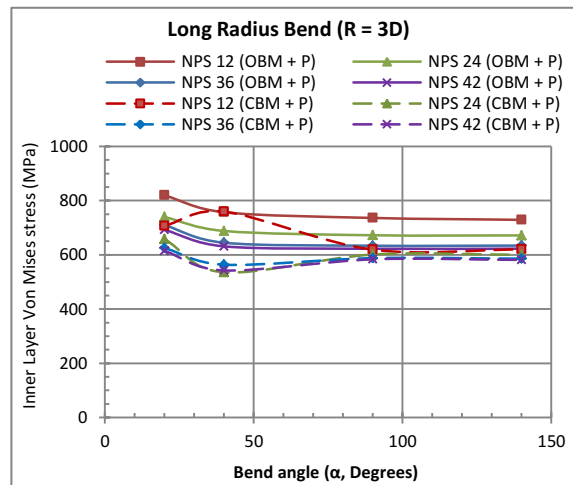


Figure 5. 73. Inner layer Von Mises stress vs bend angle (α) for pipes with long bend radius (R = 3D).

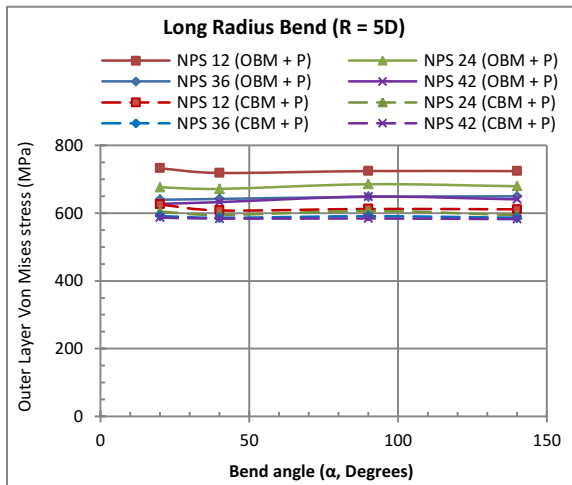


Figure 5. 74. Outer layer Von Mises stress vs bend angle (α) for pipes with long bend radius ($R = 5D$).

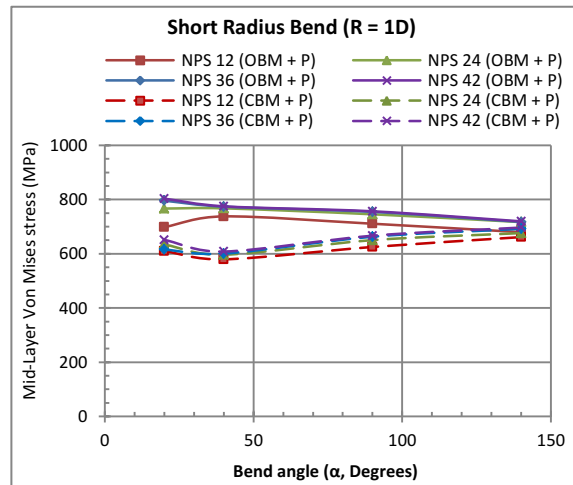


Figure 5. 75. Mid-layer Von Mises stress vs bend angle (α) for pipes with short bend radius ($R = 1D$).

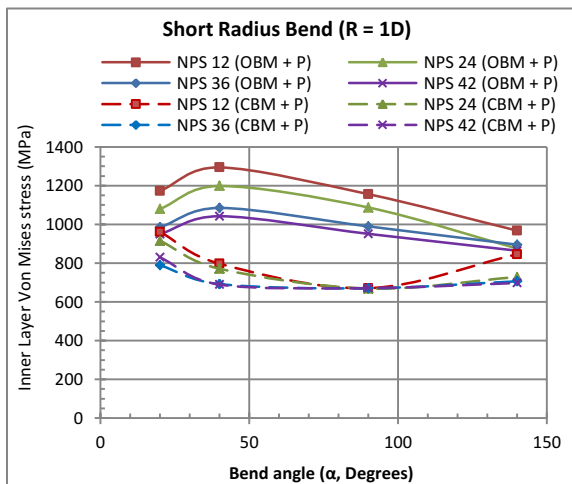


Figure 5. 76. Inner layer Von Mises stress vs bend angle (α) for pipes with short bend radius ($R = 1D$).

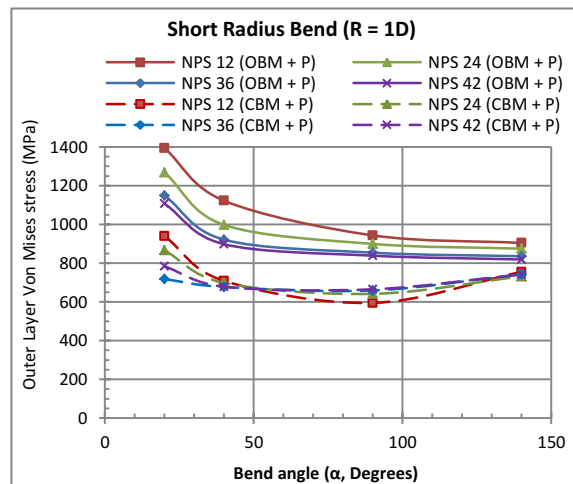


Figure 5. 77. Outer layer Von Mises stress vs bend angle (α) for pipes with short bend radius ($R = 1D$).

5.3.3.3. Comparison between the FEA with CSA-Z662 and ASME B31.1

The FEA Von Mises stress results measured at the inner, outer and mid-layer of the pipe bend are compared to the predictive stresses using the CSA-Z662 Equation (Eqn. 5. 1) and ASME B31.1 equation (5. 7). Samples of the stresses from random models are plotted in figures (5. 78) to (5. 83) against the D/t ratios. The FEA results show that the CSA predictive stresses are highly conservative when compared to the FEA Von Mises stress on the mid-layer of the pipe wall thickness as shown in figures (5. 78) and (5. 79). The CSA is conservative by up to 171.4% for short radius bends and 97.3% for

long radius bends. However, for the inner and outer layers, the CSA is found to be un-conservative only in the case of internal pressure loading succeeded with opening bending moment and for bends with small pipe size as shown in figures (5. 80) to (5. 83). The CSA predictive stress is un-conservative by up to 34.2% for the inner and outer layer.

The ASME B31.1 predictive stress equation is found to be un-conservative for some pipe bends, especially those with short bend radius ($R = 1D$). The un-conservativeness of the B31.1 predictive stress is more pronounced in the opening bending moment case following the internal pressure. For the inner layer stresses, the FEA Von Mises stresses are higher than the ASME B31.1 predictive stress by up to 65% and 22% for the opening and closing bending moment cases, respectively, as shown in figures (5. 80) & (5. 81). However, for the outer layer stress the FEA is higher than the code by up to 74% for the opening bending moment and 18% for the closing bending moment as in figures (5. 82) & (5. 83). Figures (5. 78) & (5. 79) shows the mid-layer stresses to be the less un-conservative percentage for the ASME predictive stresses when compared to the FEA results. The ASME B31.1 results are unconservative by up to 12% for the opening bending moment and found to be conservative in the closing bending moment by up to 27%. The un-conservative results in the ASME B31.1 are found to be in the models with short radius bends ($R = 1D$) and small bend angles as 20 and 40 degrees.

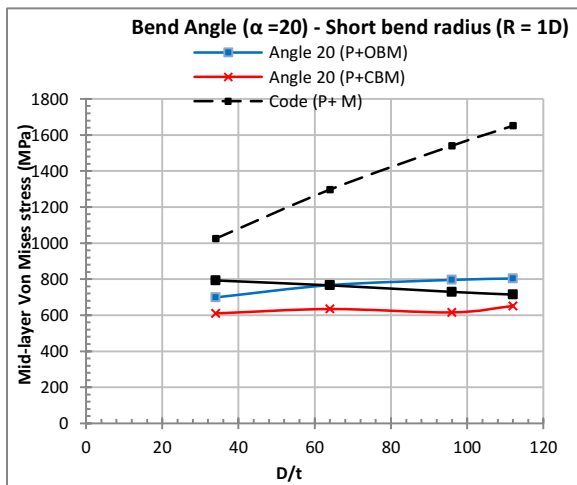


Figure 5. 78. Mid-layer Von Mises stresses from FEA compared with the CSA results for pipe bends with short bend radius ($R = 1D$) and bend angle 20

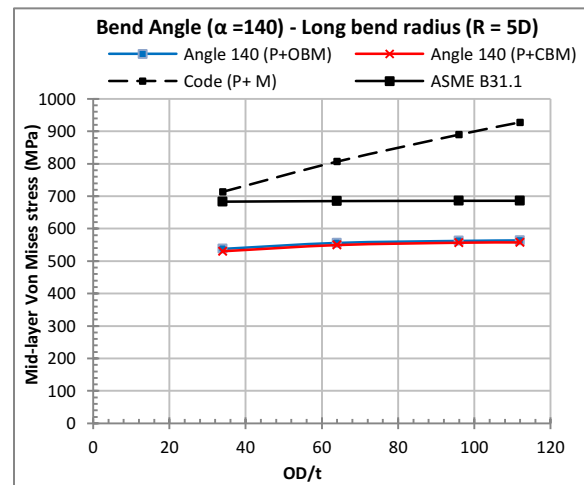


Figure 5. 79. Mid-layer Von Mises stresses from FEA compared with the CSA results for pipe bends with long bend radius ($R = 5D$) and bend angle 140

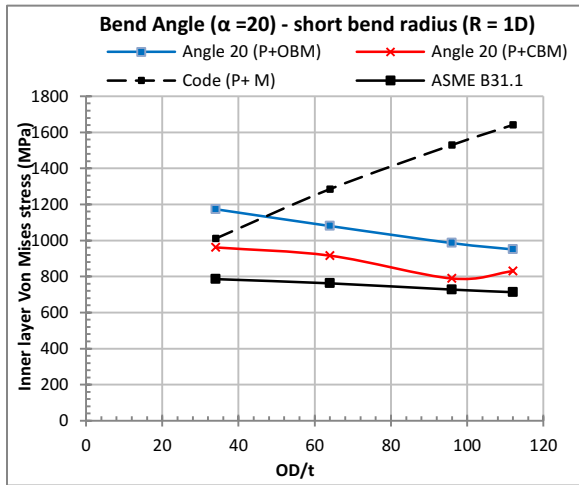


Figure 5. 80. Inner layer Von Mises stresses from FEA compared with the CSA results for pipe bends with short bend radius ($R = 1D$) and bend angle 20

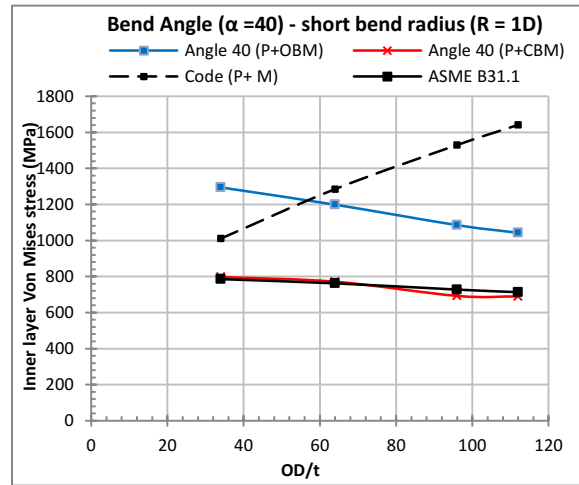


Figure 5. 81. Inner layer Von Mises stresses from FEA compared with the CSA results for pipe bends with long bend radius ($R = 3D$) and bend angle 40

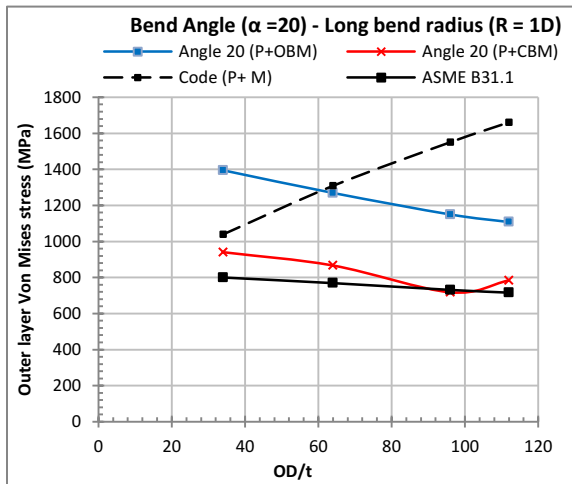


Figure 5. 82. Outer layer Von Mises stresses from FEA compared with the CSA results for pipe bends with short bend radius ($R = 1D$) and bend angle 20

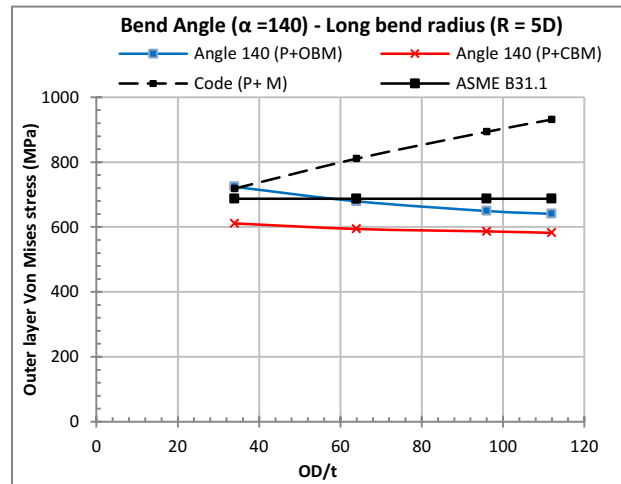


Figure 5. 83. Outer layer Von Mises stresses from FEA compared with the CSA results for pipe bends with long bend radius ($R = 5D$) and bend angle 140

5.4. DISCUSSION

Pipe bends subjected to internal pressure undergo some deformations due to the Bourdon effect and some ovalization from the overall deformation of the pipe generated from the straightening-out action. The proposed mathematical models developed in Chapter (2) (Equations 2.1 & 2.2) to evaluate the outward Bourdon forces are validated with the FEA results in this chapter and it shows a

satisfactory accuracy within a range of 1.6% to 7% showing that the developed models are suitable for different boundary conditions.

Since all the pipe models are subjected to an internal pressure that causes 80% SMYS hoop stresses, then the evaluated stress from the FEA is expected to be close to the 80% SMYS. However, it is observed that the evaluated FEA stresses are much higher than the predicted stress due to the Bourdon effect and the cross-sectional deformations.

Based on the developed Bourdon force formulas, the Bourdon forces increase by the increase of the pipe bend's outer diameter leading to higher deformations and higher stress levels on the pipe. As the D/t ratio increases and the pipe bend starts to gain more flexibility, this leads to higher average stresses on the pipe bend which represents the mid-layer Von Mises stress in this study as shown in figure (5. 15) in the results section. To understand the change in the Von Mises stresses, the hoop and longitudinal stresses are investigated as well. The increase in the mid-layer hoop and longitudinal stresses is shown by comparing figures (5. 84) & (5. 85) to figures (5. 86) & (5. 87). The mid-layer hoop stress is significantly affected by the increase of the D/t ratio as presented in figure (5. 84) & (5. 86). In contrast, the longitudinal stresses show a minor increase at the mid-layer as in figures (5. 85) & (5. 87). Since the hoop stress is higher than the longitudinal stress, it governs the Von Mises stress level. However, since the bend tends to approach more the thin-walled pipe behaviour as the D/t ratio increases, then the variation in stresses between the inner and outer layers decrease leading to a lower stress at the intrados outer surface and higher stress at the intrados inner surface as shown in figures (5. 86) & (5. 87). This explains figures (5. 4) to (5. 12) presented in the results section where the mid-layer stress increase, and the inner and outer layers stresses decrease with the increase in D/t ratio.

If the level of stress is maintained equal in the design, then changing the pipe diameter results in increasing the mid-layer stress and decreasing the variation between the inner and outer layers. However, if the same internal pressure value is applied at two similar bends but with different pipe outer diameter (12" and 42"), the NPS 42 show higher stresses than the NPS 12 at all three layers as shown in figure (5. 88). This shows that as the pipe diameter increases, the flexibility increases as well leading to a higher stress on the pipe bend.

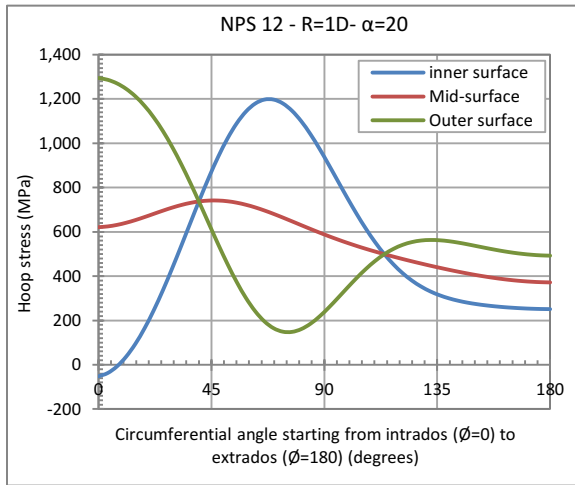


Figure 5.84. Hoop stress distribution across the pipe circumference for a 12" pipe with short bend radius ($R=1D$) and 20 bend angle subjected to internal pressure.

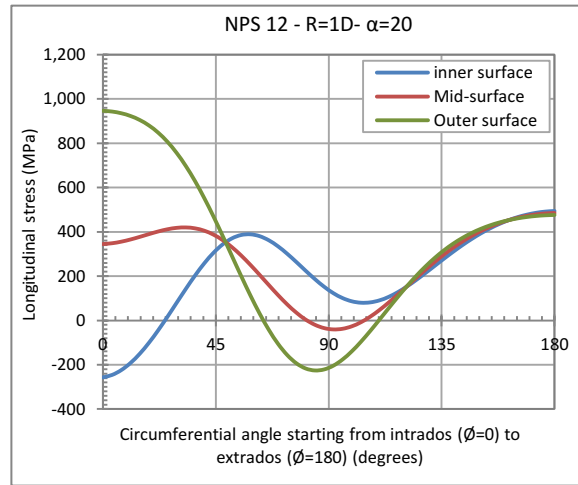


Figure 5.85. Longitudinal stress distribution across the pipe circumference for a 12" pipe with short bend radius ($R=1D$) and 20 bend angle subjected to internal pressure.

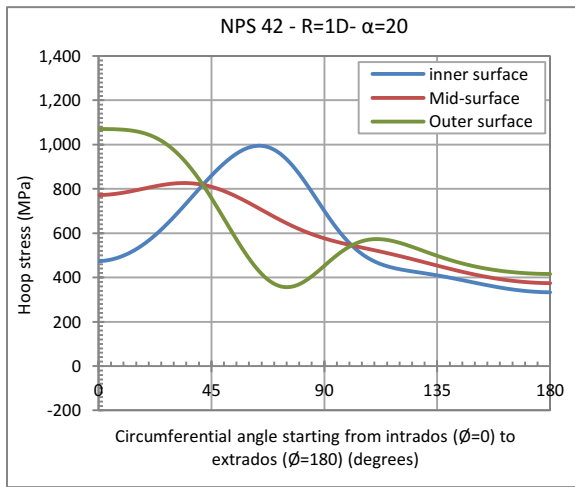


Figure 5.86. Hoop stress distribution across the pipe circumference for a 42" pipe with short bend radius ($R=1D$) and 20 bend angle subjected to internal pressure.

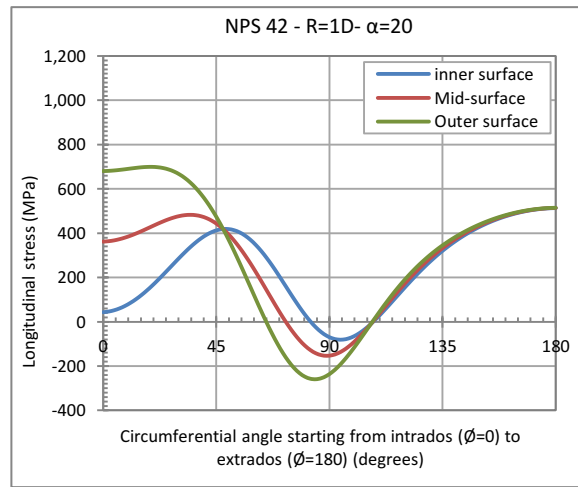


Figure 5.87. Longitudinal stress distribution across the pipe circumference for a 42" pipe with short bend radius ($R=1D$) and 20 bend angle subjected to internal pressure.

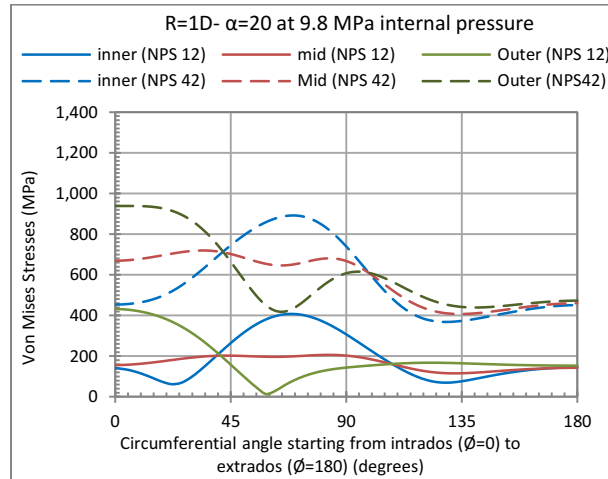


Figure 5. 88. Von Mises stress distribution across the pipe circumference for a 42" pipe with short bend radius ($R=1D$) and 20 bend angle subjected to internal pressure.

For pipe bends subjected to bending moment only, the flexibility of the bend depends on the bend geometry as in the case of internal pressure loading and on the direction of bending moment as well. The FEA results show that as the bend radius and bend angle increase, the flexibility of the bend increases as well. This was concluded and explained in chapter (3) where the pipe bend is compared to the behaviour of a corrugated sheet. As the corrugation increases, it gives it more flexibility but increases its strength as well. In addition, the bending moment direction affects the flexibility where the closing bending moment results in higher flexibility than opening bending moments.

The results show that as the bend angle increase, the flexibility of the bend increases as well leading to higher stresses on the pipe bend. For relatively flexible pipe bends, the deformation in the cross-section as a result of the bending moment is symmetric about a horizontal axis passing through the centre of the cross-section and the crown. The stress distribution along the bend cross-section is decided mainly by the shape of the deformed cross-section. As explained in the results section, pipe bends are considered flexible when the bend angles vary from 40 to 140 degrees and especially when the outer diameter is large. Consequently, the cross-sectional deformation is symmetric leading to a symmetric stress-distribution along the cross-section with a maximum stress at the inner layer of the crown location. On the other hand, a stiffer bend is studied where the bend angle and the pipe outer diameter are relatively small. Due to the stiff behaviour of the bend, the cross-sectional deformation is un-symmetric as shown in figures (5. 89) and (5. 90) leading to an un-symmetrical Von Mises stress distribution along the circumference of the critical section of the bend with a maximum stress at the

outer layer of the intrados location. For the opening and closing bending moment cases, the highest cross-sectional deformation is at the intrados part of the bend leading to a lot of generated bending stresses.

For a bend subjected to opening bending moment, the intrados side has the highest cross-sectional deformation as shown in figure (5. 89), therefore, the hoop stresses are maximum at the intrados due to the membrane bending stresses generated from the cross-sectional ovalization as shown in figure (5. 91). The cross-sectional deformations lead to a downward shift in the neutral axis towards the extrados where the intrados and part of the crown zone are in tension whereas the extrados part is in compression. This is clearly shown in the longitudinal stress distribution on the pipe section at the three wall layers as shown in figure (5. 92). On the other hand, if a pipe bend is subjected to a closing bending moment, then the cross-section flattens as shown in figure (5. 90) and the intrados side shows a lot of deformations leading to high membrane bending stresses at this side of the cross-section. The un-symmetric deformed shape has a new shifted neutral axis where the intrados part is in compression and the extrados is in tension. This can be concluded from the longitudinal stress distribution in figure (5. 94) where high compressive longitudinal stresses are at the intrados and start to diminish as it approaches the extrados. Therefore, from the hoop and longitudinal stresses it can be concluded that the Von Mises stress distribution is different and un-symmetrical for small bend angle pipes. In addition, the high cross-sectional deformations at the intrados results in a large variation in stresses between the inner and outer layers. However, at the extrados side, the cross-section almost translated with negligible wall bending deformations resulting in a minor variation in stresses between the inner and outer layers as shown in figures (5. 91) to (5. 94).

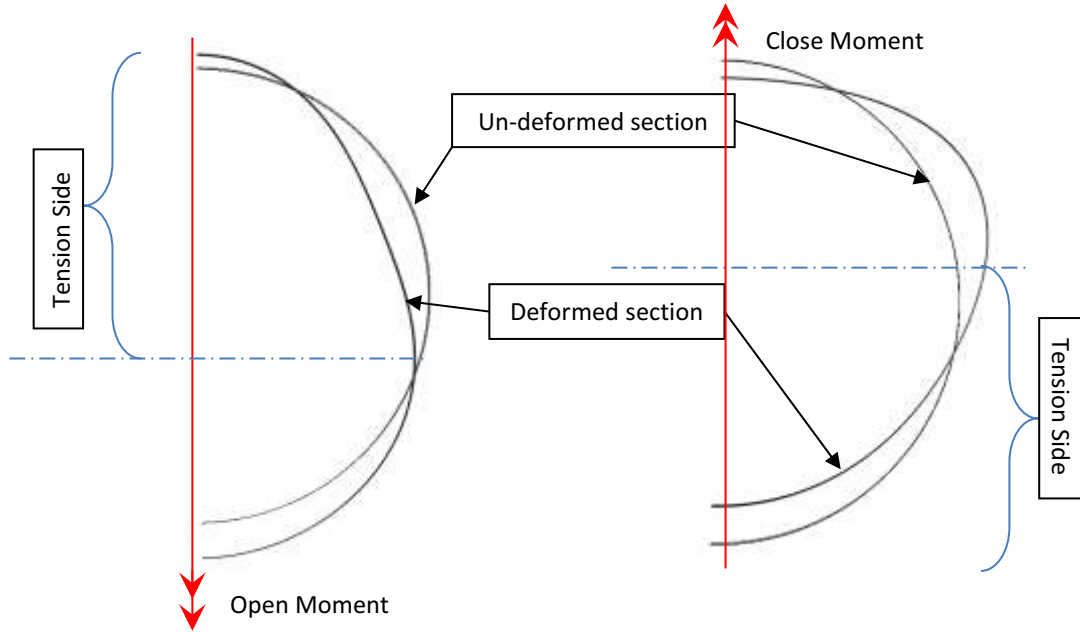


Figure 5.89. The cross-sectional ovalization at the mid-length of the pipe bend subjected to an opening bending moment.

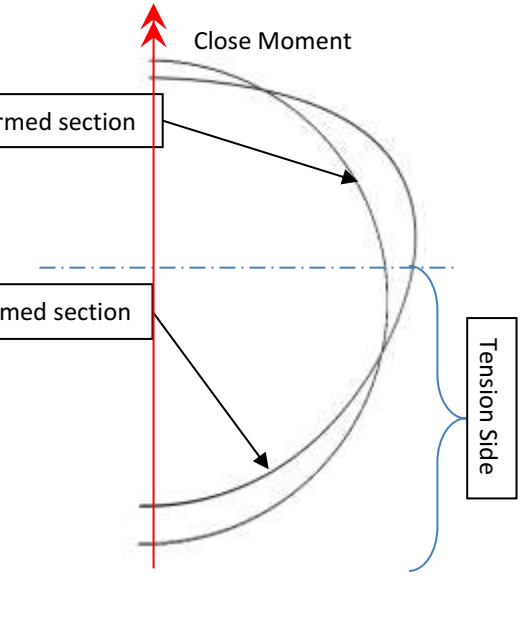


Figure 5.90. The cross-sectional flattening deformation at the mid-length of the pipe bend subjected to a closing bending moment.

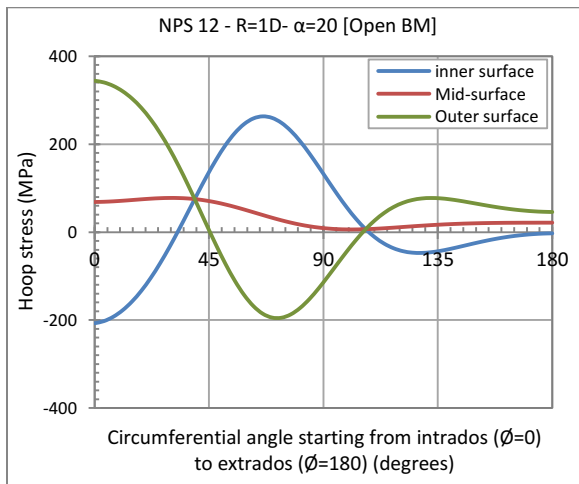


Figure 5.91. Hoop stress distribution along the critical section of a NPS 12 pipe bend with bend angle 20° and short bend radius ($R = 1D$) subjected to opening bending.

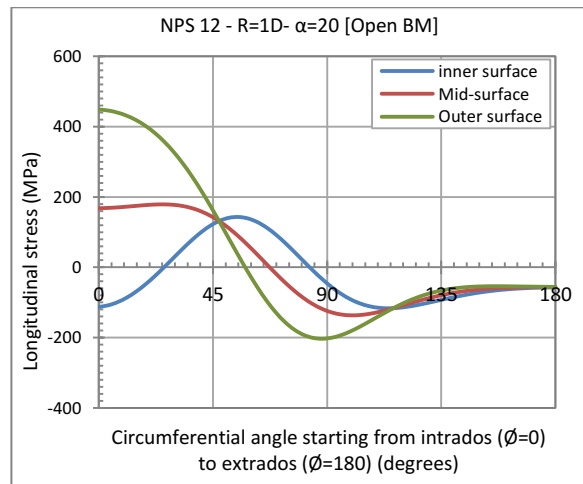


Figure 5.92. Longitudinal stress distribution along the critical section of a NPS 12 pipe bend with bend angle 20° and short bend radius ($R = 1D$) subjected to opening bending.

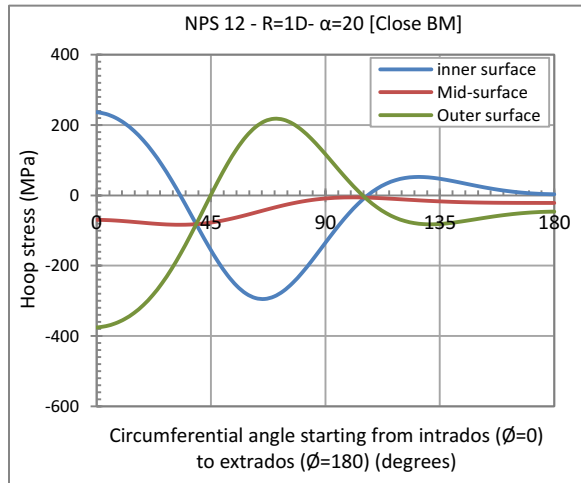


Figure 5.93. Hoop stress distribution along the critical section of a NPS 12 pipe bend with bend angle 20° and short bend radius ($R = 1D$) subjected to closing bending.

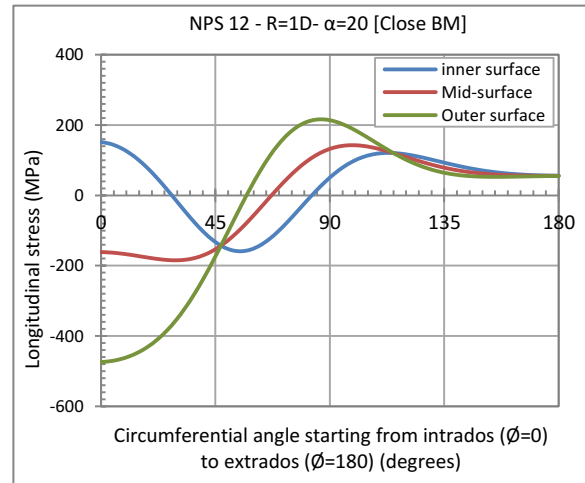


Figure 5.94. Longitudinal stress distribution along the critical section of a NPS 12 pipe bend with bend angle 20° and short bend radius ($R = 1D$) subjected to closing bending.

Following the internal pressure with a bending moment load changes the flexibility and behaviour of pipe bends. The FEA results show that adding opening bending moment to the internal pressure results in increasing the Von Mises stress since both loads are opening the pipe bend, therefore, they both exert stresses in the same direction. However, following the internal pressure with a closing bending moment results in decreasing the Von Mises stress since the closing bending moment has an opposite action on the bend than the internal pressure load which is opening the bend. Therefore, adding an opening bending moment to the internal pressure results in higher stresses than that of adding a closing bending. A different behaviour is observed for pipe bends with long bend radius ($R = 5D$). When the internal pressure is followed by a closing bending moment, the Von Mises stress increases as shown in figures (5.66) & (5.67).

When a bend is subjected to internal pressure loading, the bend straightens-out and the cross-section deforms into an oval shape as shown in figures (5.95) & (5.102). The studied bends are thin-walled pipes. Therefore, the tensile radial stresses generated from the internal pressure as a result of the cross-sectional expansion is transferred into tensile hoop stresses which increase through the wall thickness from the inner to the outer surface of the wall. Therefore, applying an internal pressure to the bend (whether it is of a short or long radius) results mainly in tensile hoop stresses at all three layers as

shown in figures (5. 97) & (5. 104). Since the internal pressure loading causes the cross-section to deform into an oval shape with the major axis in the plane of bending, therefore, it is noticed that the hoop stresses are in tension at the outer surface of the intrados and extrados while its compression at the crown outer surface and vice versa. As for the longitudinal stress, it is found to have the highest variation through the thickness at the intrados of the bend and this variation starts to decrease until it almost vanishes at the extrados as shown in figures (5. 99) and (5. 106).

Following the internal pressure with a closing bending moment tends to restore the bend initial shape. Short radius bends are found to be stiff as shown in the results, therefore, when a closing bending moment is applied and tends to deform the bend in an opposite direction of the internal pressure action, the bend starts to resist and the resulting deformation tends to restore the bend's circular cross-section as shown in figure (5. 96). Since the closing bending moment restores the cross-sectional shape, as a result the pipe wall deformation decreases (after step 2 loading), the hoop stresses generated from the membrane bending decreases as well as shown in figure (5. 98). However, the longitudinal stresses decrease at the intrados and increase at the extrados as shown in figure (5. 100). By superposition, the equivalent stress of the hoop and longitudinal stresses is decreased in the second step as shown in figure (5. 101). In this case, the bending moment is not high enough to overcome the deformations and stresses generated from the internal pressure. Therefore, the stresses at the end of the second loading step is lower than the stresses from the first loading step.

On the other hand, the large radius bends are very flexible compared to the short radius bends. Therefore, the applied bending moment generates a large deformation compared to that generated from the internal pressure and are opposite in direction as shown in figures (5. 102) & (5. 103). Therefore, the bending moment deformation overcomes the internal pressure deformation and results in an overall high stress after succeeding the internal pressure by a closing bending moment load. The longitudinal stresses are significantly affected by the closing bending moment where the location of maximum stresses shift from the intrados to the extrados of the bend as shown in figure (5. 107). However, the hoop stress is slightly affected since the overall bend deformation is higher compared to the cross-sectional ovalization. Consequently, there are two scenarios that could take place in the Von Mises stress distribution. The first scenario is that the increase in longitudinal stresses is significantly high, even though the location shifted where the hoop stress is low but it results in an equivalent high stress which means that the Von Mises stress might slightly increase by adding the closing bending

moment as shown in figure (5. 108). The second scenario is that the increase in longitudinal stress is negligible and shifts to a location of low hoop stresses which consequently results in a decrease in the Von Mises stress. Both scenarios exist in this study and it depends on the pipe size and geometry which may affect the bend flexibility. However, changing the level of applied internal pressure to a lower value may change this pattern. Therefore, it is difficult to identify the point at which the closing bending moment increases or decreases the stresses and it needs further study.

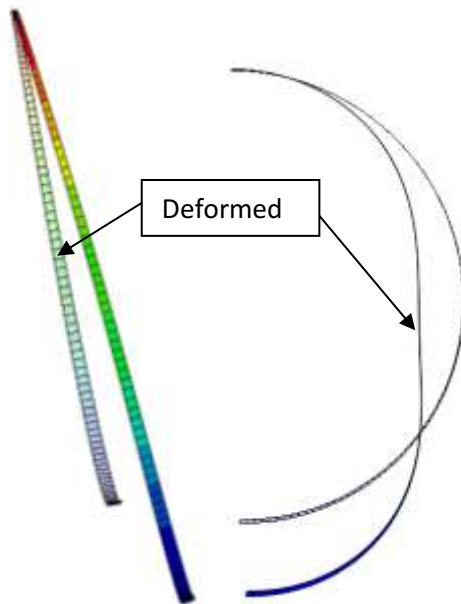


Figure 5. 95. Deformed section for a short bend radius pipe ($R=1D$) at the end of step 1 (internal pressure loading)

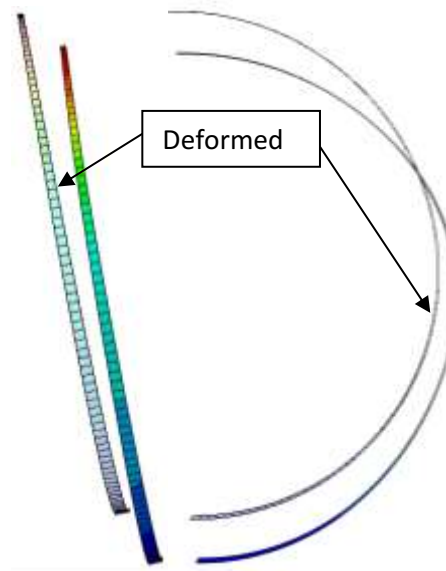


Figure 5. 96. Deformed section for a short bend radius pipe ($R=1D$) at the end of step 2 (internal pressure and closing bending loading)

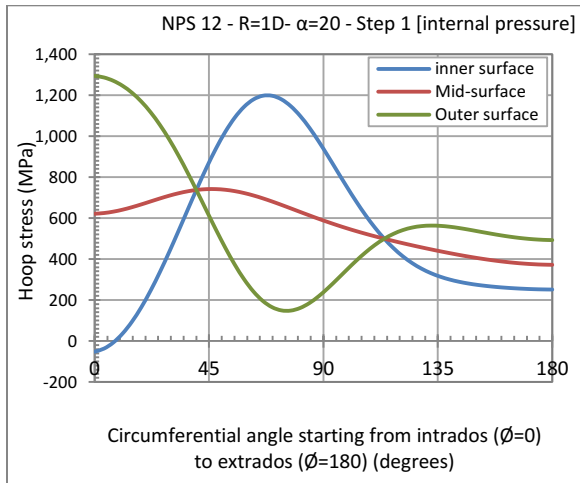


Figure 5.97. Hoop stress distribution on the critical section circumference of a 12" pipe with 20-degree bend angle and short bend radius subjected to internal pressure.

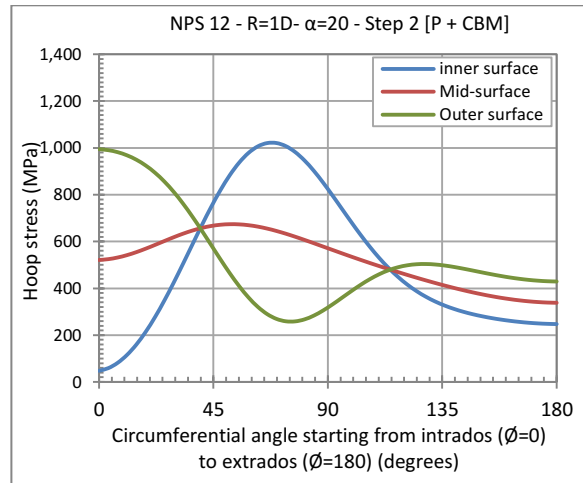


Figure 5.98. Hoop stress distribution on the critical section circumference of a 12" pipe with 20-degree bend angle and short bend radius subjected to internal pressure and closing bending moment.

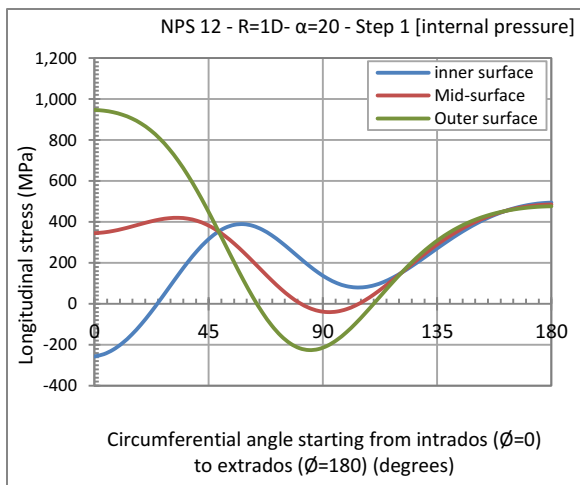


Figure 5.99. Longitudinal stress distribution on the critical section circumference of a 12" pipe with 20-degree bend angle and short bend radius subjected to internal pressure.

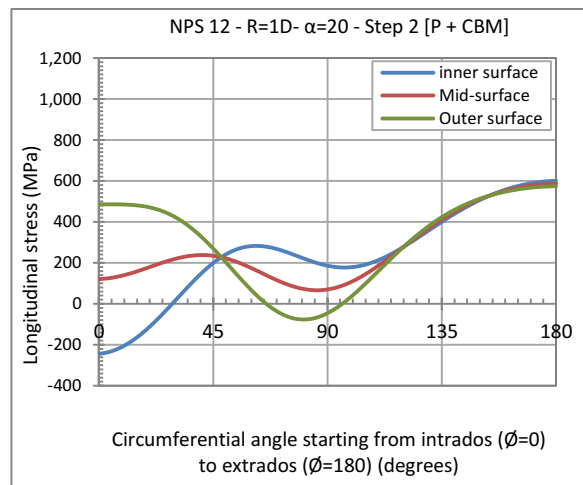


Figure 5.100. Longitudinal stress distribution on the critical section circumference of a 12" pipe with 20-degree bend angle and short bend radius subjected to internal pressure and closing bending moment.

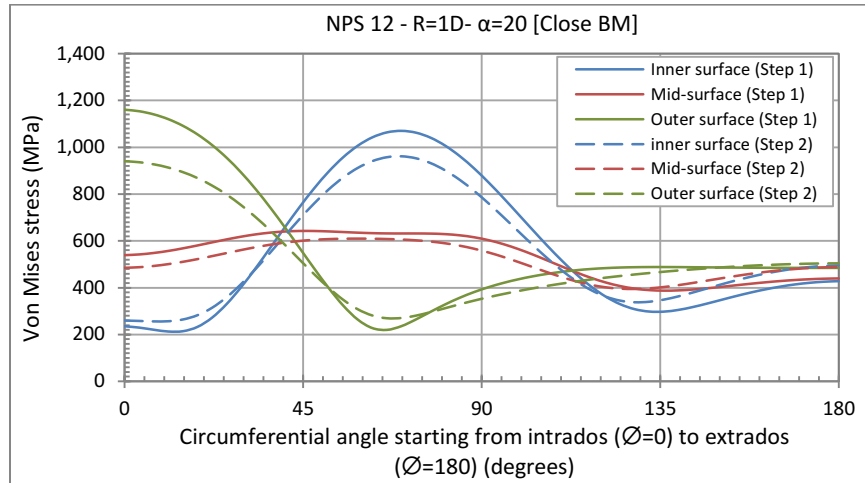


Figure 5. 101 Von Mises stress distribution on the critical section circumference of a 12" pipe with 20-degree bend angle and short bend radius for step 1 (internal pressure) and step 2 (internal pressure and closing bending).

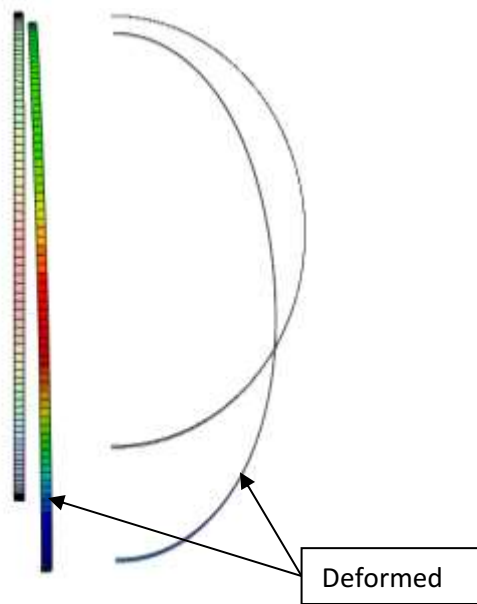


Figure 5. 102. Deformed section for a long bend radius pipe (R=5D) at the end of step 1 (internal pressure loading)

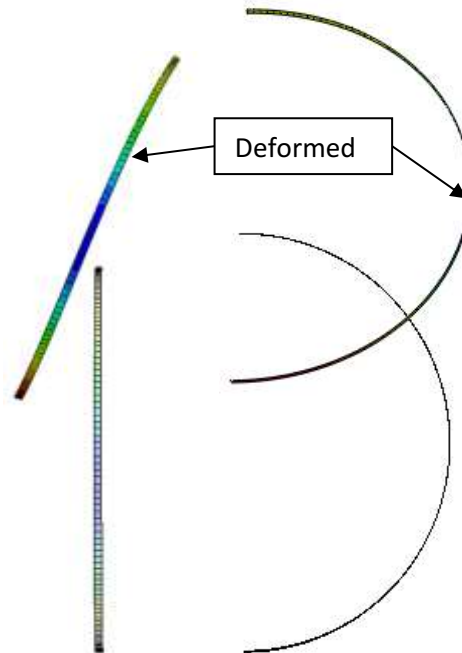


Figure 5. 103. Deformed section for a long bend radius pipe (R=5D) at the end of step 2 (internal pressure and closing bending moment loading)

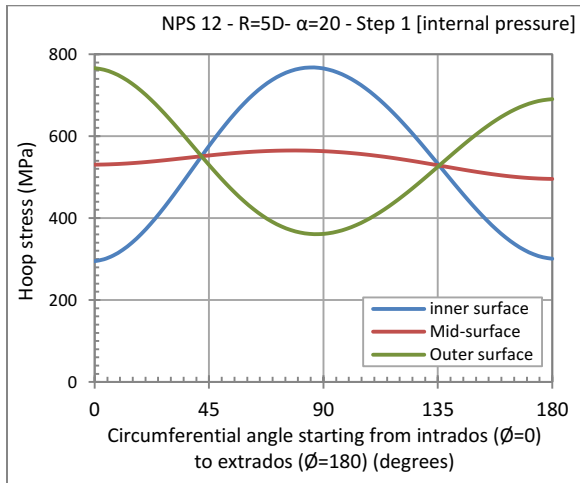


Figure 5. 104. Hoop stress distribution on the critical section circumference of a 12" pipe with 20-degree bend angle and long bend radius subjected to internal pressure.

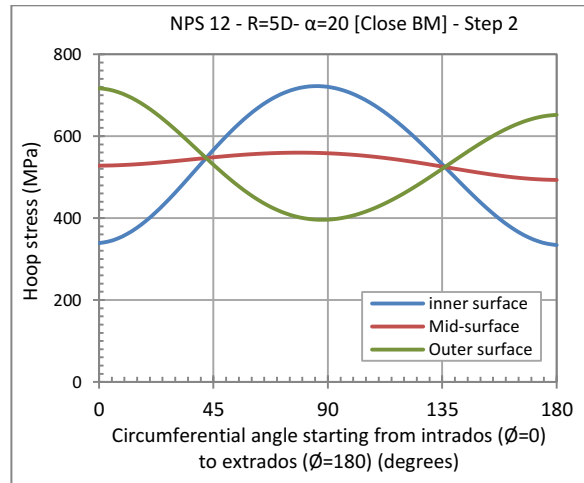


Figure 5. 105. Hoop stress distribution on the critical section circumference of a 12" pipe with 20-degree bend angle and long bend radius subjected to internal pressure and closing bending moment.

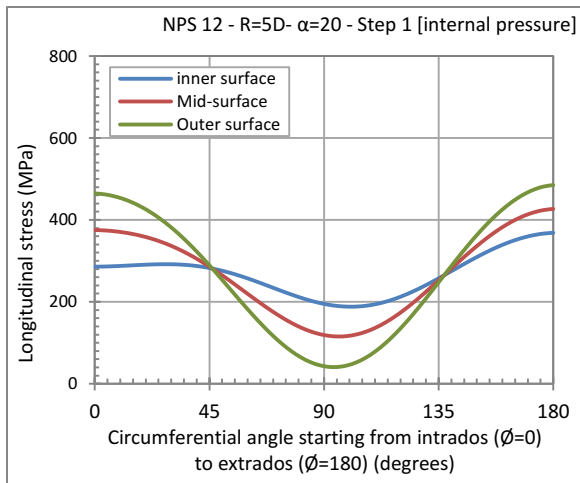


Figure 5. 106. Longitudinal stress distribution on the critical section circumference of a 12" pipe with 20-degree bend angle and long bend radius subjected to internal pressure.

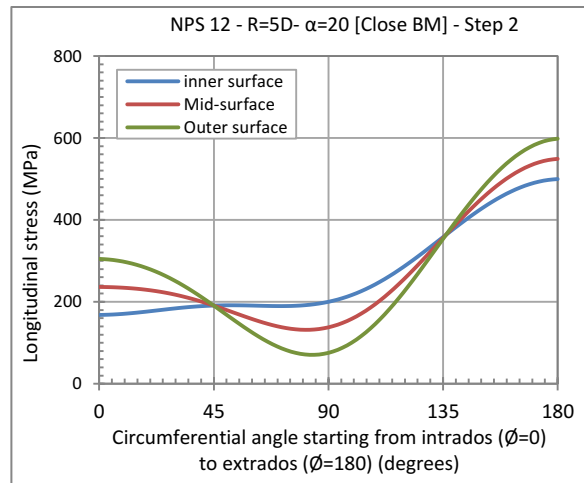


Figure 5. 107. Longitudinal stress distribution on the critical section circumference of a 12" pipe with 20-degree bend angle and long bend radius subjected to internal pressure and closing bending moment.

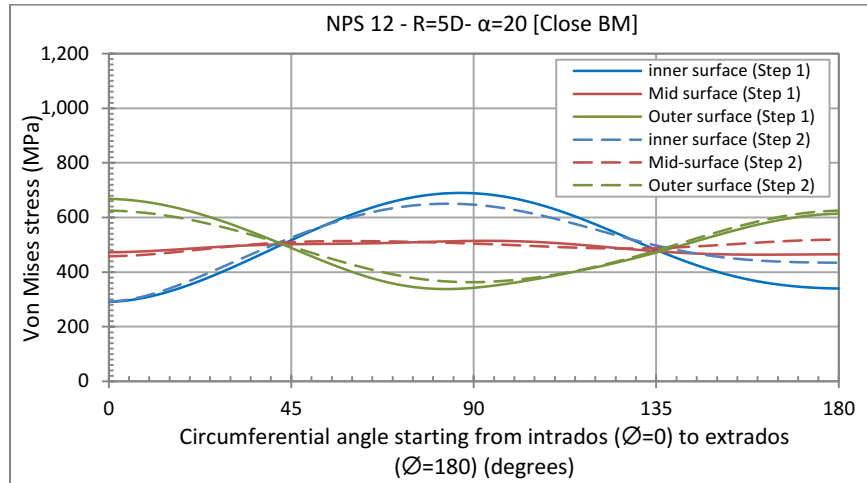


Figure 5. 108 Von Mises stress distribution on the critical section circumference of a 12" pipe with 20-degree bend angle and short bend radius for step 1 (internal pressure) and step 2 (internal pressure and closing bending).

CHAPTER 6: DEVELOPED STRESS INTENSIFICATION FACTORS FOR BENDS UNDER INTERNAL PRESSURE AND BENDING MOMENT

6.1. INTRODUCTION & BACKGROUND

A theoretical study was conducted by Rodabaugh and George in 1957 to derive a pressure reduction factor that accounts for the increase in pipe bend stiffness due to the internal pressure loading. In their study, the work of Von Karman was extended from the pure in-plane closing bending moment to include the work done by internal pressure in reducing the cross-sectional deformation volume. The work done by the internal pressure was added as a “Secondary effect” to the potential energy equation from which the flexibility and stress intensification modification factors were derived. They followed Von Karman’s assumption in their study which may need justification in the case of short radius bends. The pressure reduction factor was derived for a particular case of loading which is pure in-plane closing bending and internal pressure, however, it is used without modification for in-plane opening bending and out-of-plane bending moments till this day. The nonlinear interaction between bending and pressure is quite complex and not simple to be detected by theoretical methods. Therefore, in this study the finite element analysis is used to simulate the pipe bend behaviour under internal pressure and bending, and derive a new pressure reduction factor.

Based on the results presented in chapter (5), it is found that the CSA stress intensification factors (SIF) are either conservative or un-conservative based on the direction of bending moment, bend angle, pipe bend geometry and the layer of interest within the wall thickness. However, the pressure reduction factor presented in the ASME B31.1 used to modify the stress intensification factors results in highly un-conservative predicted stresses as presented earlier in chapter (5).

In this chapter, a stress intensification factor and a pressure effect factor is derived for the case of pure in-plane bending and the case of combined internal pressure and bending moment loading, respectively, for a pipe bend with two straight attached pipes having end roller supports. The derived factors are based on the FEA results presented in chapter (5). The difference between the stress intensification factor in this current chapter and those derived in chapter (4) is the end boundary conditions of the pipe bend with attached straight pipes under in-plane bending. The study aims to

reflect the importance and the influence of the end boundary condition on these factors and consequently on the stress levels on pipe bends.

6.2. METHODOLOGY

A sensitivity analysis is conducted for the case of in-plane bending only, then for bends subjected to a combined loading of internal pressure and in-plane bending moment to study the impact of each parameter on the proposed factors. Then, based on the sensitivity analysis, a form to express these factors is proposed.

6.2.1. Evaluating the data points required for the regression analysis

In this section, the extraction of the data points from the FEA results is presented. The data points are used later in the regression analysis to find the best fit for the proposed factors formulation.

6.2.1.1. In-plane bending moment (Stress Intensification Factor)

The ratio between the Von Mises stress evaluated from the FEA models for pipe bends under in-plane bending moment only presented in Chapter (5) and the stress estimated using the simple beam theory ($\sigma = Mr/I$) is used as the data points in the regression analysis [SIF_{FEA}] and these data points represent the SIF evaluated from the FEA models. The equation used to evaluate the data points is as follows;

$$SIF_{FEA} = \frac{\sigma_{VM}}{Mr/I}$$

6.2.1.2. Internal pressure and in-plane bending moment (Pressure Effect Factor)

From the FEA results in chapter (5) for the bends under internal pressure and in-plane bending, the pressure effect factors ($X_{proposed}$) are evaluated using the Von Mises stress from the FEA and comparing it with the Von Mises stress formula but introducing a stress intensification factor ($i_{proposed}$)

with the bending moment load to account for the increased stress due to the ovalization effect as follows:

$$\sigma_{VM} = \sqrt{\frac{(\sigma_h^2 + \sigma_l^2 + (\sigma_h^2 - \sigma_l^2))}{2}} \quad (6.1)$$

$$\sigma_{VM} = \sqrt{\frac{\left(\left(\frac{PD}{2t}\right)^2 + \left(\frac{PD}{4t} + \frac{Mr_i}{I_{proposed}}\right)^2 + \left(\frac{PD}{2t} - \left(\frac{PD}{4t} + \frac{Mr_i}{I_{proposed}}\right)\right)^2\right)}{2}} \quad (6.2)$$

$$i_{proposed} = \frac{1}{Mr} \sqrt{\frac{\left(2\sigma_{VM}^2 - \left(\frac{PD}{2t}\right)^2 - 2\left(\frac{PD}{4t}\right)^2\right)}{2}} \quad (6.3)$$

Based on the values of the evaluated stress intensification factors ($i_{proposed}$), the pressure effect factor ($X_{proposed}$) is derived based on the following equation:

$$X_{proposed} = \frac{K}{i_{proposed}} = \frac{0.9/\lambda^{2/3}}{i_{proposed}} \quad (6.4)$$

Where, “K” is the stress intensification factor presented in the current codes (CSA Z-662, B31.1 & B31.3) for the case of pure in-plane bending moment. The proposed pressure effect factor ($X_{proposed}$) is derived as a modification and an improvement to the current factors used by the ASME B31.1 code which is based on the Rodabaugh and George (1957) study. The improvement done by the new proposed factor is to account for the direction of bending moment and differentiates between the effect of internal pressure on a closing and opening bending moment. Moreover, it includes the bend angle parameter therefore it is applicable on a wider range of pipe bend geometries. The bend radius considered in this study is short and long bend radii ranging from 1D to 5D. The pipe sizes range from a D/t ratio as low as 34 up to 112. Therefore, this study covers thin-walled pipes only since the D/t ratio is greater than 20.

6.2.2. Sensitivity Analysis and Model Formulation

6.2.2.1. In-plane bending moment

The stress intensification factors (SIF) evaluated from the FEA results are plotted against the bend angle (α) and the beam parameter (λ) in figures (6. 1) to (6. 4). The results show the same

conclusion observed in chapter (4), the SIF factors increase by the increase of the bend angle in an exponential growth form as shown in figures (6. 1) and (6. 2). The effect of the bend angle is more pronounced in short radius bends rather than long radius bends. Moreover, the change in bend angles affects the SIF factors for large pipe sizes more than small pipes. Based on that, an exponential growth form should express the relation between the SIF factors and bend angle (e^α).

As for the beam parameter (λ), The SIF factors decrease in an exponential decay form with respect to the beam parameter. The decay rate decreases as the bend radius increases, where a plateau occurs in the curve at which the SIF factor is almost constant. In addition, the plotted results show that as the bend angle decreases the decay occurs earlier than that of a large bend angle. Therefore, an exponential form with a decay rate is chosen for the beam parameter. A term of the equation relates the growth in the bend angle with the decay in the beam parameter which is the ($e^{(m+n\lambda)\alpha}$), while, the other term is related only to the decay rate in the beam parameter ($1/\lambda^d$).

Therefore, the proposed factor is in the following form:

$$SIF = \frac{(c - e^{(n+m\lambda)\alpha})(f + \lambda j)}{\lambda^d} \tag{6.5}$$

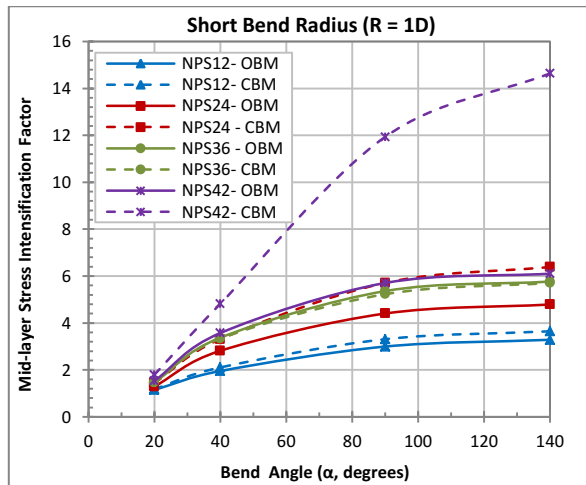


Figure 6. 1. Stress intensification factors for short radius pipe bends with various bend angles and pipe sizes.

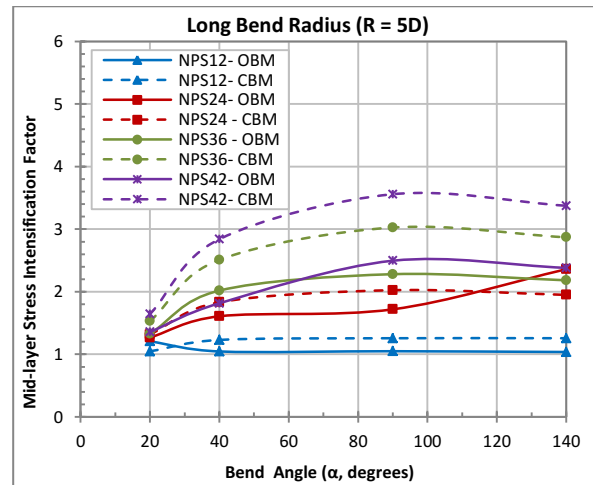


Figure 6. 2. Stress intensification factors for long radius pipe bends with various bend angles and pipe sizes.

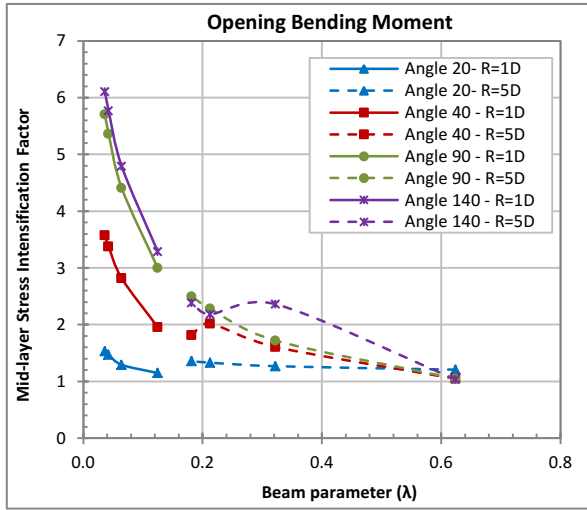


Figure 6. 3. Stress intensification factors for pipe bends subjected to opening bending moment.

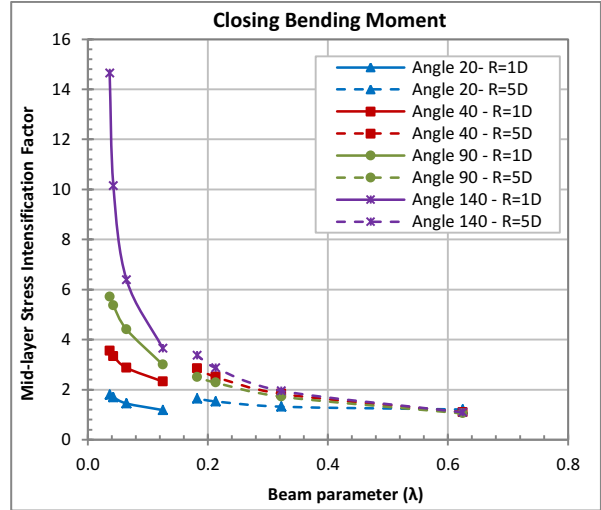


Figure 6. 4. Stress intensification factors for pipe bends subjected to closing bending moment.

6.2.2.2. Internal pressure and In-plane bending moment

First a sensitivity analysis is conducted to evaluate the influence of each parameter considered in the new proposed factor. These parameters are the bend radius to pipe radius ratio (R/r), the bend angle (α), the internal pressure to the Young’s elastic modulus (P/E) and the pipe outer diameter to wall thickness ratio (D/t). To identify the parameters to be considered in the developed form for the pressure effect factor ($X_{proposed}$), a sensitivity analysis is performed to determine the impact of each parameter on the FEA $X_{proposed}$ results. Figures (6. 5) to (6. 8) show the $X_{proposed}$ factors as predicted by the numerical models described previously plotted against the (R/r) ratio for different bend angles (α). It can be seen that the $X_{proposed}$ has a linear relationship with the (R/r) ratio for bend angles 20 and 40 degrees. However, as the bend angle increases to 90 and 140 degrees, the relationship is slightly nonlinear with a downward concave curve showing a decay in the $X_{proposed}$ factor as the R/r ratio increase. In general, the R/r ratio is inversely proportional to the $X_{proposed}$ factor in a slightly nonlinear form, therefore, $X_{proposed} = f\{(R/r)^{-d}\}$. Moreover, the effect factor for the closing bending moment case is found to be higher than the opening bending moment case by up to 72%. Therefore, two different pressure effect factors need to be derived to distinguish between the different bending moments directions.

Figures (6. 9) and (6. 10) show the relationship between the D/t ratio with the $X_{proposed}$ factor for short and long radius bends. As the D/t ratio increase the $X_{proposed}$ increases as well in a proportional linear form. The impact of the D/t ratio is high since it can be seen from the results that changing the D/t ratio may result in an increase up to 105% in the $X_{proposed}$ factor.

The P/E ratio plotted against the $X_{proposed}$ factor is presented in figures (6. 11) and (6. 12) and found to have a nonlinear inversely proportional relationship with the $X_{proposed}$ factor. As the P/E ratio decrease the $X_{proposed}$ factor increases.

The bend angle has an altering effect on the $X_{proposed}$ factor. It is observed that the bend angle has an exponential growth rate in the opening bending moment case. However, it changes to an exponential decay rate for closing bending moment. Therefore, a proper expression for the bend angle term is (α^c) , where the coefficient “C” controls the rate based on its value (decay rate for $c < 0$, growth rate for $c > 0$).

Based on the relation between the $X_{proposed}$ factor and the considered parameters, a form to express the pressure effect factor is proposed where a nonlinear regression analysis is used to obtain the unknown coefficients;

$$X_{proposed} = \frac{a \left(\frac{D}{t}\right)^b (\alpha)^c}{\left(\frac{R}{r}\right)^d \left(\frac{P}{E}\right)^f}$$

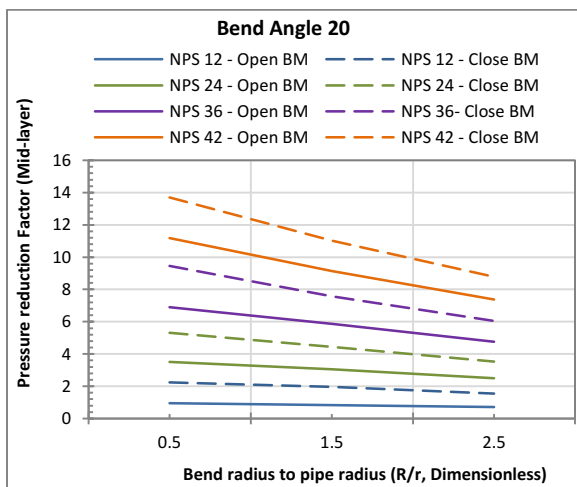


Figure 6. 5. Pressure Effect factors for pipe bends with 20 degrees bend angles and varying R/r ratios.

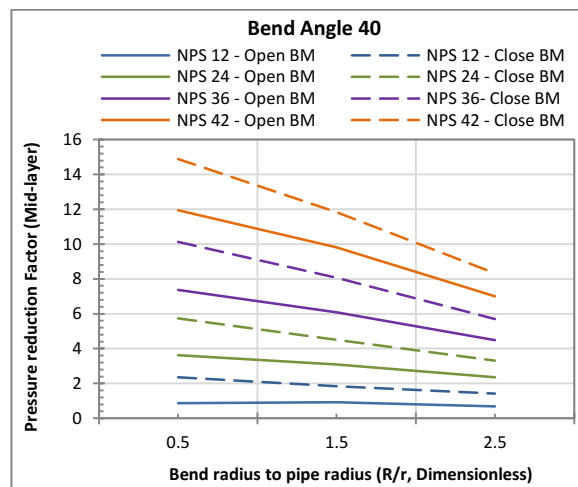


Figure 6. 6. Pressure Effect factors for pipe bends with 40 degrees bend angles and varying R/r ratios.

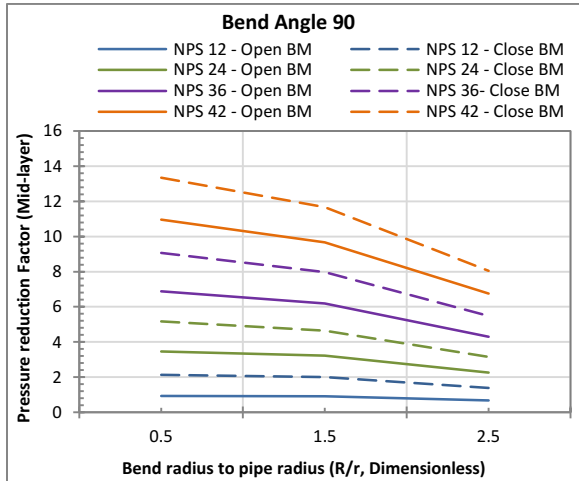


Figure 6. 7. Pressure Effect factors for pipe bends with 90 degrees bend angles and varying R/r ratios.

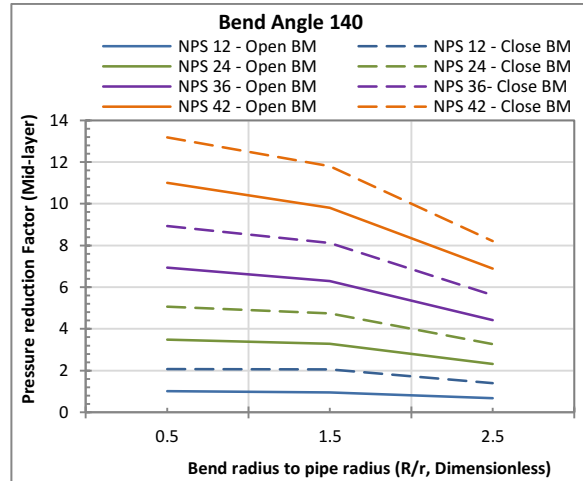


Figure 6. 8. Pressure Effect factors for pipe bends with 140 degrees bend angles and varying R/r ratios.

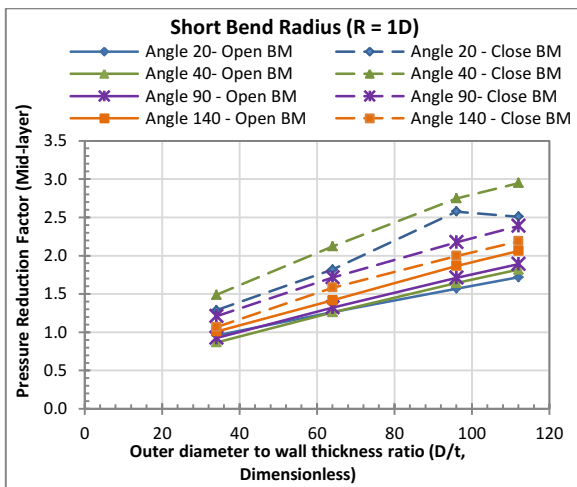


Figure 6. 9. Pressure Effect factors for pipe bends with short bend radius and various bend angles.

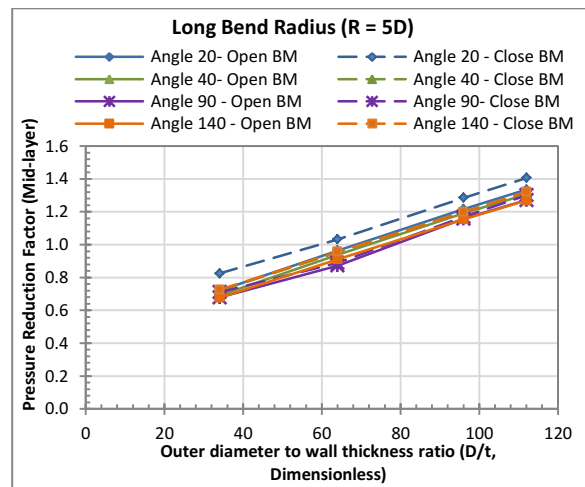


Figure 6. 10. Pressure Effect factors for pipe bends with long bend radius and various bend angles.

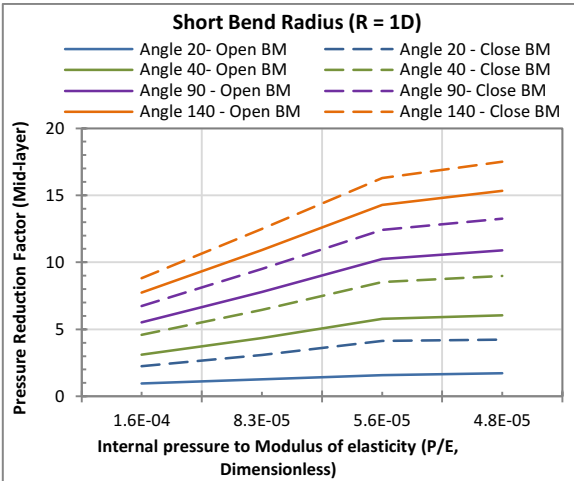


Figure 6. 11. Pressure Effect factors for pipe bends with short bend radius versus the P/E ratio.

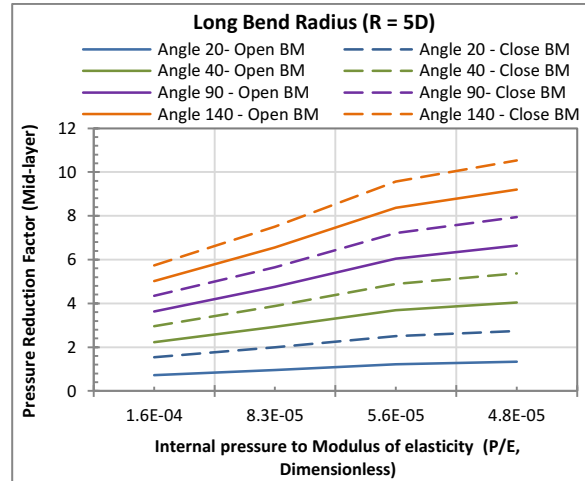


Figure 6. 12. Pressure Effect factors for pipe bends with long bend radius versus the P/E ratio.

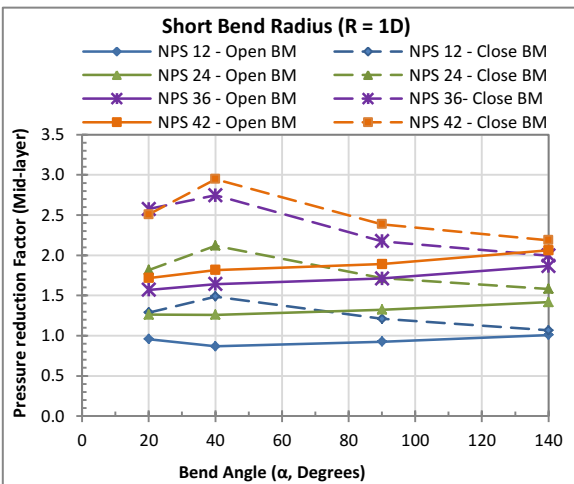


Figure 6. 15. Pressure Effect factors for short radius pipe bends with various bend angles.

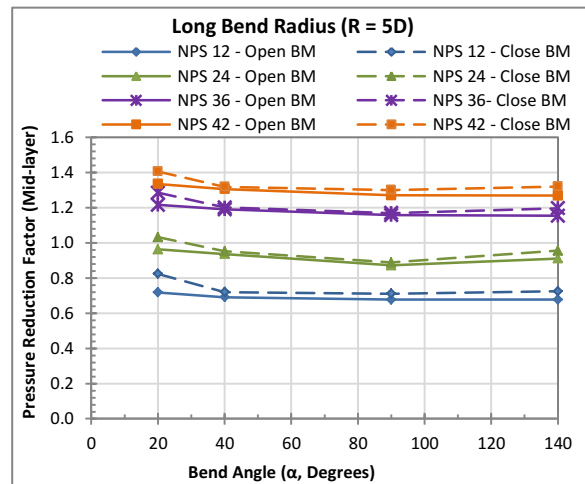


Figure 6. 16. Pressure Effect factors for long radius pipe bends with various bend angles.

6.3. Equations Development:

The regression analysis is conducted as explained in chapter (4) section (2.2). After proposing a form for the factor as a function of the parameters and the unknown coefficients, the parameters are obtained by finding the least squares. Consequently, a set of nonlinear equations is obtained and solved using a nonlinear equation solver method such as the Newton Raphson method.

6.3.1. The developed Stress Intensification Factor

Based on the regression analysis, the set of equations are solved to find the coefficients that best fit the proposed form to the data points. Two sets of factors are derived. One equation is for the opening bending moment and another one for the closing bending moment case where three set of coefficients are used for each case to represent the SIF factor at the three considered wall thickness layers.

a. For the opening bending moment Mid-layer stress:

The developed stress intensification factor is presented in equation (6. 6) and the coefficients are as presented in table (6. 1) based on the pipe wall layer under study.

$$SIF = \frac{(c - e^{b \cdot \alpha}) \cdot a}{\lambda^d} \tag{6. 6}$$

Where;

$$a = (f + \lambda j)$$

$$b = (n + m \lambda)$$

$$\lambda = \frac{R t}{r^2}$$

Table 6. 1. Coefficients for the opening bending moment stress intensification factor presented in equation (6. 6)

Wall thickness layer	f	c	m	d	j	n	Standard deviation
Inner layer	3.8	0.77	-4.95	0.42	-1.92	-1.48	0.61
Mid-layer	1.39	0.77	-7.4	0.541	-0.2	-1.26	0.226
Outer layer	3.14	0.95	-3.27	0.316	-1.93	-1.24	0.33

The accuracy of the proposed SIF factors is presented in table (6. 2). The maximum errors are usually found for the small D/t ratios and it is usually 2 out of 48 models for each layer which could be discarded. The average error is below 15% which is considered satisfactory in this study. The highest errors are found for pipe bends with small bend angles as figure (6. 17) and for NPS 12 pipe bends as shown in figure (6. 18). However, as the pipe size and bend angle increase, the accuracy of the proposed

model is better. Figure (6. 19) shows the results from the proposed model plotted against the FEA results for pipe bends with 40-degrees bend angles and shows a good accuracy. The linear regression of the proposed model results with the data points are presented in figures (6. 20) to (6. 22) and shows a good agreement. The comparison between the proposed model and FEA results are all presented in Appendix (C).

Table 6. 2. The accuracy of the proposed equation (6. 6).

Wall thickness layer	Maximum error%	Average error%
Inner layer	41%	14%
Mid-layer	67%	7.9%
Outer layer	34%	8.6%

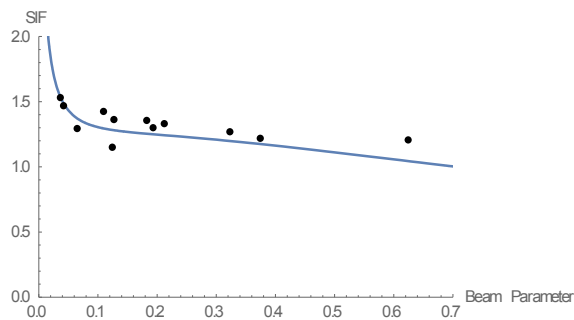


Figure 6. 17. The mid-layer FEA SIF (dotted) compared to the proposed SIF formula (blue line) for bends with bend angle = 10°

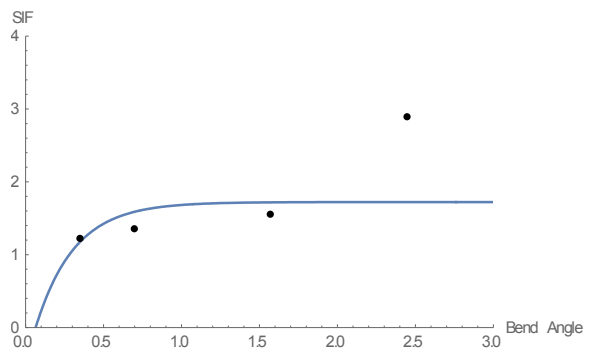


Figure 6. 18. The mid-layer FEA SIF (dotted) compared to the proposed SIF formula (blue line) for NPS12 bends with bend radius (R=3D)

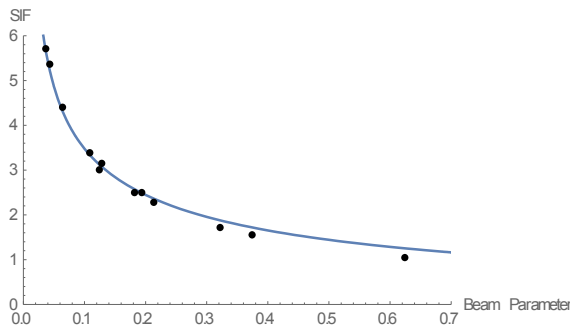


Figure 6. 19. The mid-layer FEA SIF (dotted) compared to the proposed SIF formula (blue line) for bends with bend angle = 40°

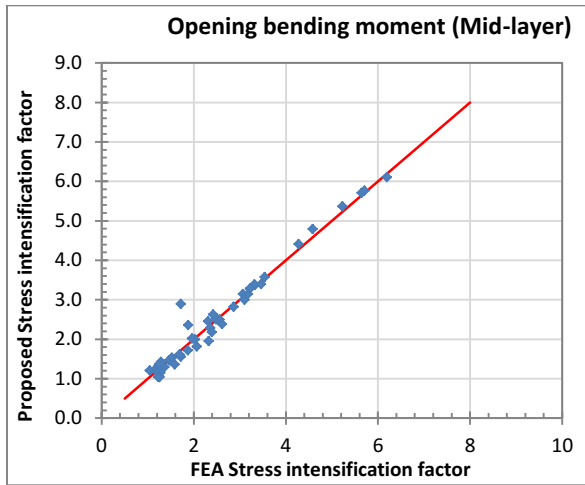


Figure 6. 20. Deviation of the SIF developed formula from the FEA results for the Mid-layer of the wall thickness

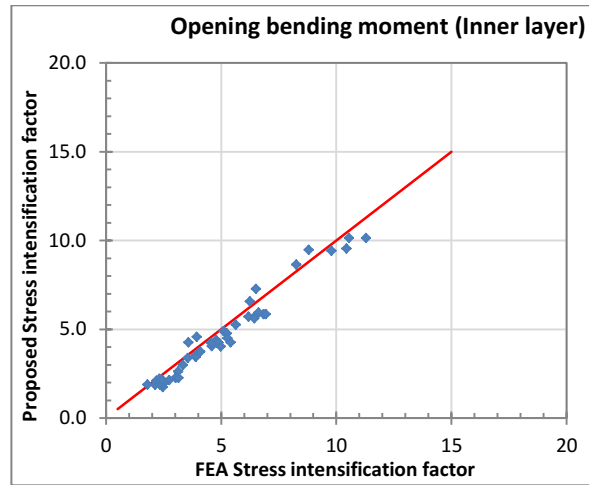


Figure 6. 21. Deviation of the SIF developed formula from the FEA results for the Inner layer of the wall thickness

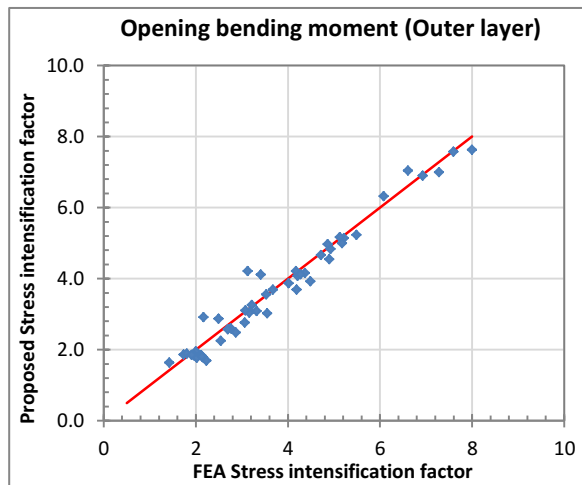


Figure 6. 22. Deviation of the SIF developed formula from the FEA results for the Outer layer of the wall thickness

- a. For the closing bending moment Mid-layer stress:

The developed stress intensification factor is presented in equation (6. 7) and the coefficients are as presented in table (6. 3) based on the pipe wall layer under study.

$$SIF = \frac{(c - e^{b \cdot \alpha})^a}{\lambda^d} \tag{6.7}$$

Where;

$$a = (f + \lambda j)$$

$$b = (n + m \lambda)$$

$$\lambda = \frac{R t}{r^2}$$

Table 6. 3. Coefficients for the opening bending moment stress intensification factor presented in equation (6. 7)

Wall thickness layer	f	c	m	d	j	n	Standard deviation
Inner layer	0.124	0.813	-6.04	1.78	1.76	-0.51	1.88
Mid-layer	0.07	0.81	-9.2	1.55	1.161	-0.577	0.512
Outer layer	0.11	0.83	-6.23	1.77	1.53	-0.46	1.9

The accuracy of the proposed SIF factors is presented in table (6. 4). The average error is below 17% which is considered satisfactory in this study. The highest errors are found for pipe bends with small sizes as NPS 12 pipe bends presented in figure (6. 23). However, as the pipe size and bend angle increase, the accuracy of the proposed model is better. Figure (6. 24) shows the results from the proposed model plotted against the FEA results for pipe bends with 40-degrees bend angles and shows a good accuracy. The linear regression of the proposed model results with the data points are presented in figures (6. 25) to (6. 27) and shows a good agreement. The comparison between the proposed model and FEA results for all studied beds are presented in Appendix (C).

Table 6. 4. The accuracy of the proposed equation (6. 7).

Wall thickness layer	Maximum error%	Average error%
Inner layer	35%	14%
Mid-layer	47%	9%
Outer layer	46%	17%

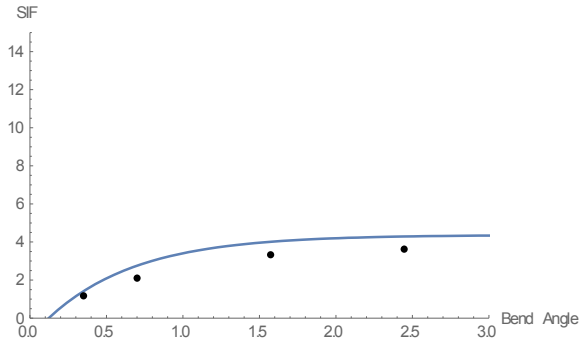


Figure 6. 23. The mid-layer FEA SIF (dotted) compared to the proposed SIF formula (blue line) for NPS12 bends with short bend radius (R=1D)

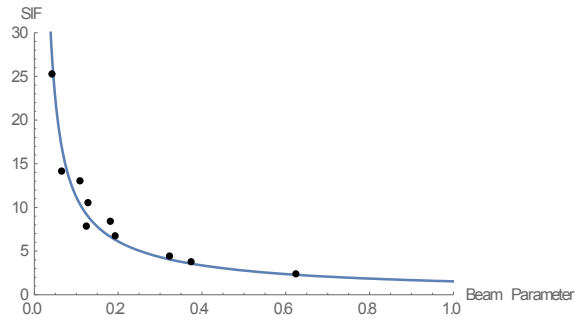


Figure 6. 24. The mid-layer FEA SIF (dotted) compared to the proposed SIF formula (blue line) for bends with bend angle = 40°

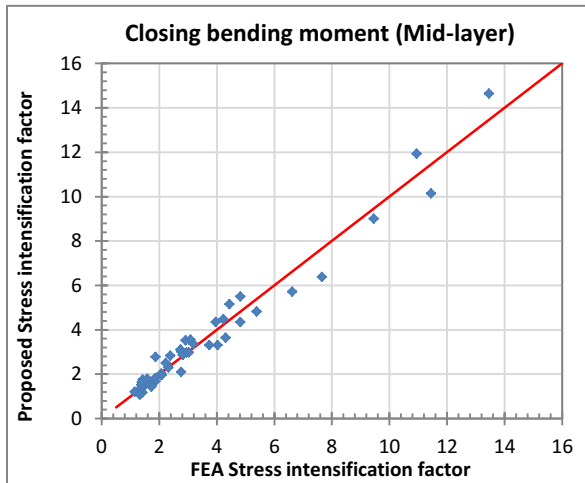


Figure 6. 25. Deviation of the SIF developed formula from the FEA results for the Mid-layer of the wall thickness

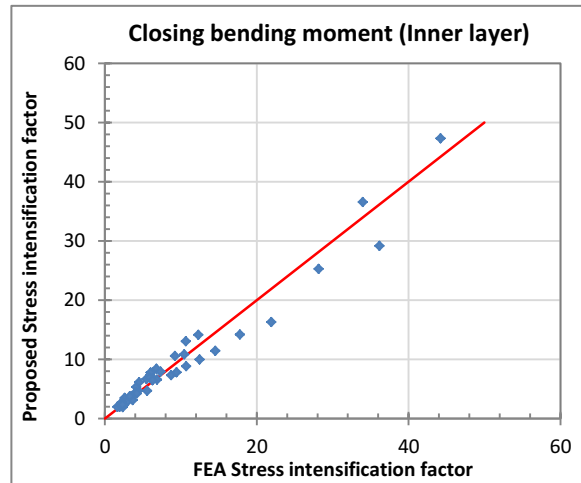


Figure 6. 26. Deviation of the SIF developed formula from the FEA results for the Inner layer of the wall thickness

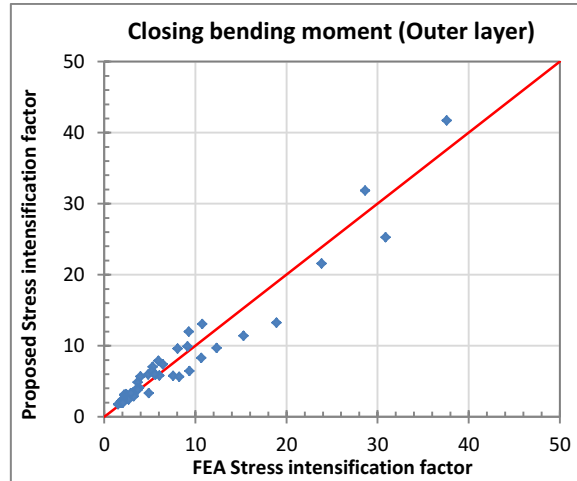


Figure 6. 27. Deviation of the SIF developed formula from the FEA results for the Outer layer of the wall thickness

6.3.2. The developed Pressure Reduction Factor ($X_{proposed}$)

A regression analysis is conducted to find the coefficients of equation (6. 8) that best fits the relation between the pressure reduction factor and the dependant parameters. Based on the relationship between the data points and the considered parameters, a form is chosen as an expression for these factors and the coefficients for each case are presented in table (6. 3).

$$X_{proposed} = \frac{a \left(\frac{D}{t}\right)^b (\alpha)^c}{\left(\frac{R}{r}\right)^d \left(\frac{P}{E}\right)^f} \tag{6. 8}$$

Table 6. 3. Coefficients of equation (6. 8) for the proposed pressure reduction factor.

Wall thickness layer	Bending moment	a	b	c	d	f	Standard deviation
Inner layer	Open	0.0148	0.942	0.0377	0.0015	0.16	0.09
	Close	0.0317	0.843	0.078	0.005	0.3	0.2
Mid-layer	Open	0.0973	0.605	0.038	0.007	0.188	0.15
	Close	0.129	0.58	-0.06	0.0039	0.34	0.18
Outer layer	Open	0.0166	0.91	0.1063	0.0027	0.29	0.08
	Close	0.046	0.77	0.052	0.003	0.34	0.21

The pressure reduction factor is derived using the Von Mises stresses from the FEA analysis. Therefore, the application of these developed factors are not anymore used with the Tresca stresses as per the codes, however, it is used as a modification factor to the Von Mises stresses. To evaluate the stresses on any pipe bend under internal pressure and in-plane bending moment, the design procedure is as follows;

- i. The proposed stress intensification factor is evaluated based on the direction of bending moment and the layer of wall thickness under study.

$$i_{\text{proposed}} = \frac{0.9/\lambda^{2/3}}{X_{\text{proposed}}} = \frac{0.9/\lambda^{2/3} \left(\frac{R}{r}\right)^d \left(\frac{P}{E}\right)^f}{a \left(\frac{D}{t}\right)^b (\alpha)^c}$$

- ii. The Von Mises stresses are evaluated by magnifying the bending moment term using the proposed stress intensification factor and compared with the allowable stresses presented in the code based on the pipe steel grade.

$$\sigma_{\text{VM}} = \sqrt{\frac{\left(\left(\frac{PD}{2t}\right)^2 + \left(\frac{PD}{4t} + \frac{Mr}{I} i_{\text{proposed}}\right)^2 + \left(\frac{PD}{2t} - \left(\frac{PD}{4t} + \frac{Mr}{I} i_{\text{proposed}}\right)\right)^2\right)}{2}}$$

To evaluate the accuracy of the proposed pressure reduction factors, the evaluated factors are compared with the FEA factors. Figures (6. 28) and (6. 29) show the plot of the proposed pressure reduction factor from the proposed model versus the pressure reduction factor evaluated from the FEA using equation (6. 4). The maximum error for both the opening and closing bending moment proposed factors are 26% and found in the case of a pipe bend with large bend angles (140 degrees). However, the average error is found to be up to 6.2% which is a satisfactory percentage considering that this proposed factor accounts for the change in bend angle and bending moment direction. The maximum and average error for the proposed model of each case is presented in table (6. 6).

Table 6. 6. The accuracy of the proposed equation (6. 8).

Wall thickness layer	Bending moment	Maximum error %	Average error %
Inner layer	Open	16.6 %	5.1 %
	Close	19.6 %	5.3 %
Mid-layer	Open	9.2 %	3.4 %
	Close	6.8 %	3.1 %
Outer layer	Open	22 %	4.8 %
	Close	23.4 %	6.2 %

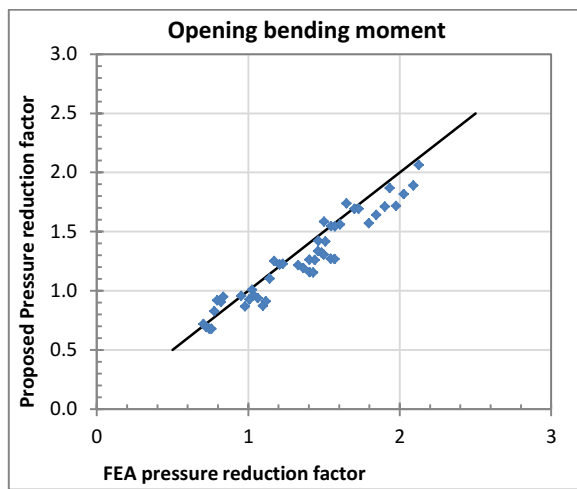


Figure 6. 28. Deviation of the pressure reduction factor developed formula from the FEA results for the Mid-layer of the wall thickness for bends under opening bending moment

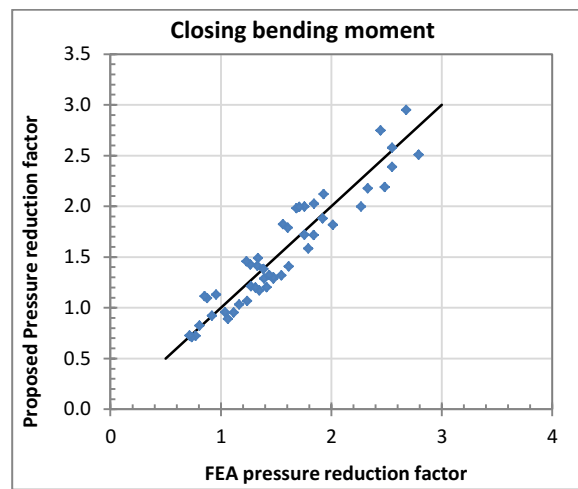


Figure 6. 29. Deviation of the pressure reduction factor developed formula from the FEA results for the Mid-layer of the wall thickness for bends under closing bending moment

6.4. Influence of the End Effects

The proposed stress intensification factor from this chapter is compared to the factors derived in chapter (4). The difference between the factors is the end boundary condition of the attached straight pipes. In chapter (4) the pipe has a fixed-free end and denoted BC-1 in this comparison. While in this chapter, the pipe both ends has a roller support and denoted BC-2. The results show that the SIF factors from the roller end bends (BC-2) is higher than the fixed-free bends (BC-1). The difference between the two boundary conditions in the opening bending moment case is

up to 32% which is found in the case of short radius bends ($R=1D$) with bend angle 10-degrees. However, the maximum difference found in the rest of the models is 19.4% which is the bends with bend radius 3D and bend angle 10 degrees. The results of the stress intensification factors for both boundary conditions are presented in figure (6. 30) for the opening bending moment case. The difference between the stress intensification factors is found to be higher in the closing bending moment case where it reaches up to 97.4% for short bend radius and small bend angles ($R=1D$, $\alpha =10^\circ$) as shown in figure (6. 31).

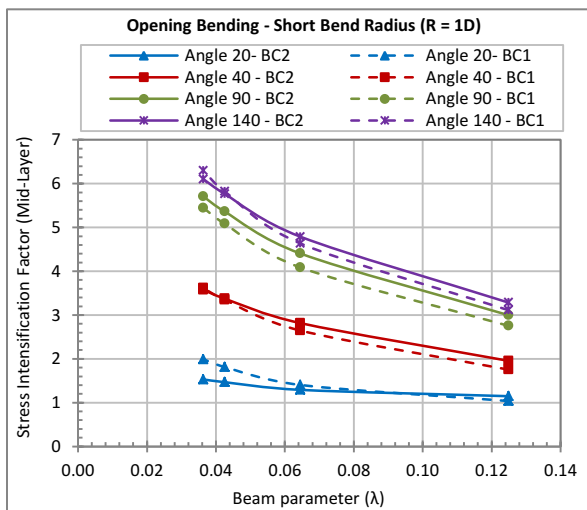


Figure 6. 30. Comparison between the stress intensification factors for BC-1 and BC-2 for short radius bends under opening bending moment.

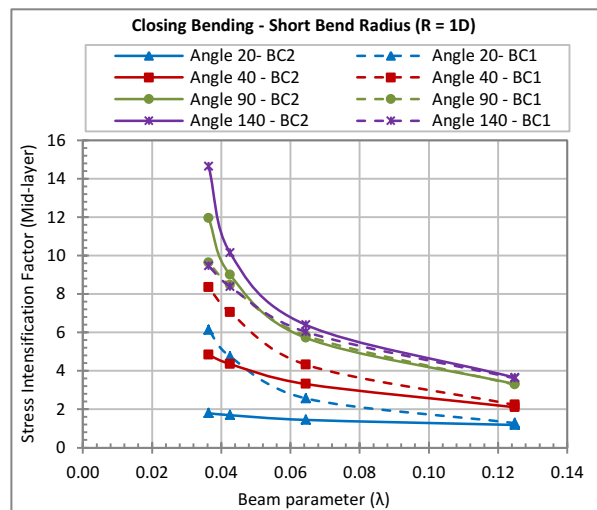


Figure 6. 31. Comparison between the stress intensification factors for BC-1 and BC-2 for short radius bends under closing bending moment.

CHAPTER 7: CONCLUSIONS AND RECOMMENDATIONS

An analytical study is conducted on pipe bends with a wide range of bend angles and pipe geometry subjected to internal pressure and in-plane bending moment loadings. The commercial finite element package ABAQUS 6.14 was used throughout this study where pipe bends were represented in a SHELL element form with a linear elastic material, and large deformation analysis. The main aim of this study was to study the Bourdon effect due to internal pressure and to reassess the stress intensification factors used currently by the design codes and define its limitations.

7.1. CONCLUSIONS

Pipe bends and elbows under internal pressure undergo a cross-sectional and global deformation where the pipe bend tends to straighten out generating higher stress levels than estimated using simple beam theory. This phenomenon is known as the “Bourdon effect”. The outward forces generated from the Bourdon effect are found to be dependent on the internal pressure level applied, pipe radius (r) and the bend angle (α). Therefore, changing the bend radius will not help in reducing the outward deformation or the high stress levels.

A proposed model to evaluate the Bourdon outward forces is derived from this study for a standalone pipe bend with a fixed-free end conditions. These proposed models are of high significance for the design of any lateral support located at the pipe bend or any other component connecting the bend with the rest of the pipeline system. If these forces are not estimated during the design procedure, the lateral supports may be subjected to loads that are not accounted for in the design.

The current design codes are dealing with pipe bends under internal pressure in a similar way as a straight pipe. The predictive code stresses are based on Barlow’s formulas without any modification to account for the increase in stresses. However, the analytical study conducted in this research using the commercial finite element package “ABAQUS” shows that the Bourdon effect results in an increase in stresses of pipe bends by up to 47% than that predicted by the current codes (CSA-Z662) which could threaten the safety of the pipeline and the surrounding environment. Therefore, there is an urge to develop a factor that accounts for the Bourdon effect in pipe bends as a function of the radius ratio (R/r), pipe slenderness ratio (D/t), the bend angle (α) and internal pressure (P). Based on an extensive analytical study, a pressure factor (K_p) is derived to account for the increase in stresses. The pipe bends

covered in this study have a range of D/t ratios from 34 to 112 with bend angles from 40 to 140 degrees and bend radius from $1D$ to $5D$. The accuracy of the proposed factor is investigated by comparing the code stress results modified by the (K_p) factor to the FEA results. The accuracy of the proposed pressure factor is 8.2% with an average of 3.4%. This factor would be beneficial to the industry where it can provide a stress design criterion that maintains the pipeline's integrity. An approach of modelling pipe bends using "Beam" elements is proposed in this study by incorporating the proposed (K_p) factor to account for the Bourdon effect in the FEA modelling.

Behaviour of pipe bends under in-plane bending moment has a different phenomenon affecting the stress distribution. This phenomenon is known as the "ovalization effect" which arises from the resultant forces acting on the pipe wall. The ovalization or deformation of the cross-section depends on the direction of bending moment based on the analytical study presented in chapter (3). It was shown from the FEA results that for a bend under in-plane opening bending moment, the pipe gains stiffness with loading as a result of the oval deformed cross-section. However, the bend gains flexibility in the case of an in-plane closing bending moment since the cross-section flattens more with loading resulting in a reduction of the second moment of area. Therefore, for two identical bends, the ovalization ratio could be found higher in the cases of pipe bends subjected to closing bending moments than those subjected to opening bending moment. Moreover, the FEA results show that the Von Mises stress from the closing bending moment is higher than the opening bending moment by up to 173%.

For pipe bends subjected to in-plane opening or closing bending moment, the critical section is found at the mid-length of the pipe bend where the stresses are maximum at the inner layer of the wall thickness at the crown location ($\theta = 90$). Based on the FEA results in this study, the stresses at the inner and outer layers are found to be higher than the mid-layer stress by up to 200% which, if ignored, may result in the failure of the pipe bend. Therefore, the stresses need to be checked at the critical layer of the pipe wall thickness not just the mid-layer of the pipe.

The CSA-Z662 design methodology was revisited in this study and compared to the FEA results to reassess the stress intensification factors. The study shows that the CSA-Z662 design criteria is highly conservative for small bend angle pipes (Such as; 10 and 20 degrees). However, as the bend angles increase the CSA-Z662 is un-conservative by up to 18% for mid-layer and may go up to 219% for inner and outer layers.

Based on the FEA results of chapter (3) a stress intensification factor is developed for in-plane opening and closing bending moment to evaluate the stress on the three different layers of wall thickness considered in this study. These SIF factors are based on a pipe bend with attached straight pipes having fixed-free end conditions. The factors show good accuracy when compared to the FEA results with an average error of 15%. These factors included the effect of bend angle and the direction of bending moment on the stresses to the formula, which was ignored from the factors proposed in the past studies.

A different end boundary condition is considered in this study and presented in chapter (5) where the bend attached to a straight pipe has two roller ends. The results were compared to the fixed-free models and a difference was noticed. Despite the large length of the straight pipe considered, which is more than 10D, as recommended by Matzen and Yu (1998), the end boundary condition affected the results especially for pipe bends with large D/t ratios.

The flexibility of the pipe bend is highly affected when the internal pressure load is followed with an in-plane bending moment. The opening bending moment tends to increase the stresses on the bend. However, the closing bending moment has an opposite effect on the bend than the internal pressure resulting in lower stresses if the pressure level is high. In the case of low pressure levels, the closing in-plane bending moment may overcome the deformation and stresses resulted from the internal pressure leading to an increase in the stresses rather than a decrease.

The combination of internal pressure and in-plane bending moment is a complex problem that requires further study since changing any of both loading values alters the behaviour of the bend totally. The effect of the ratio between the internal pressure and the bending moment on the stress levels remains vague and needs further investigation.

The CSA-Z662 is found to be highly conservative for bends subjected to internal pressure and in-plane bending moment since the reduction factor due to the presence of internal pressure is not included. On the other hand, the pressure reduction factor developed by Rodabaugh and George and adopted by the ASME B31.1 code is highly un-conservative when compared to the FEA results especially for the case of opening in-plane bending moment.

A new pressure reduction factor is proposed in this study that takes into consideration the difference between the effect of adding in-plane opening or closing bending moment to the internal

pressure. Moreover, another parameter was considered in the proposed factor which is the bend angle. Therefore, this factor is applicable for a wider range of pipe geometries and different loading conditions. The accuracy of the proposed pressure reduction factor shows a good agreement with the FEA results and has an average error of 12%.

The proposed Stress Intensification Factor and Pressure Correction Factors are found to be un-conservative for some of the modelled pipes since it was based on a best fit for the data points. Therefore, the standard deviation for all the proposed factors is provided to enable shifting the curve ensuring conservative predictions. Another method is to conduct rigorous reliability analysis to identify the needed factor to ensure the reliability of the predictions.

7.2. RECOMMENDATIONS AND FUTURE WORK

1. The effect of residual stresses and initial geometric imperfections may affect the stresses on pipe bends. Therefore, future study is recommended to include these parameters into the investigation and evaluate the increase in stresses generated from them.
2. The effect of the end boundary conditions could be investigated since it was concluded from this current study that even by considering long attached straight pipes, the flexibility of the bend's mid-length section was affected by the end effect.
3. In this study the stress intensification factor and the pressure reduction factors were revisited. Another study could investigate the same change in parameters on the flexibility factors and propose a modification to consider the bend angles and the bending moment direction.
4. Based on this study, it was concluded that following the internal pressure with a closing bending moment may increase or decrease the stresses based on the pipe bend flexibility. However, the level of bending moment applied with respect to the applied internal pressure will affect these results as well. Therefore, it is recommended to consider different ratios of internal pressure to bending moment loading in future studies and this ratio could be considered as one of the variables affecting the Pressure Correction Factors.

REFERENCES

- [1] Bourdon, Eugene. "Notes on Bourdon Pressure Gauges", 1849.
- [2] Worthington, A. M. "Bourdon's pressure gauge." *Nature* 41 (1890): 296.
- [3] Flügge, Wilhelm. "Stress in shells." Berlin and New York: Springer-Verlag (1973).
- [4] Goodall, I. W. "Lower bound limit analysis of curved tubes loaded by combined internal pressure and in-plane bending moment." *Research Division Report RD/B N 4360* (1978): 14.
- [5] Hong, Seok-Pyo, et al. "Approximate elastic stress estimates for elbows under internal pressure." *International Journal of Mechanical Sciences* 53.7 (2011): 526-535.
- [6] Veerappan, A. R., and S. Shanmugam. "Stress analysis of pipe bends subjected to internal fluid pressure using the finite element technique." *The Journal of Strain Analysis for Engineering Design* 41.8 (2006): 561-573.
- [7] Kainat, Muntaseer, et al. "Identifying Initial Imperfection Patterns of Energy Pipes Using a 3D Laser Scanner." 2012 9th International Pipeline Conference. American Society of Mechanical Engineers, 2012.
- [8] Shemirani, Farzad M., et al. "Investigation of the Influence of the Bourdon Effect on the Stress and Ovalization in Elbows." 2014 10th International Pipeline Conference. American Society of Mechanical Engineers, 2014.
- [9] KÁRMÁN, Th. "v.(1912): Festigkeitsversuche unter allseitigem Druck." German.) *Mitt. Forsch. Ingwes.* ed. VDI 118 (1911): 37-68.
- [10] Kafka, P. G., and M. B. Dunn. *Stiffness of curved circular tubes with internal pressure.* No. D-14025. Boeing Airplane Co., 1953.
- [11] Rodabaugh, ECf, and H. H. George. "Effect of internal pressure on flexibility and stress-intensification factors of curved pipe or welding elbows." *Trans. ASMe* 79.4 (1957): 939-948.
- [12] Gross, Nicol. "Experiments on short-radius pipe-bends." *Proceedings of the Institution of Mechanical Engineers, Part B: Management and engineering manufacture* 1.1-12 (1953): 465-479.

-
- [13] Gross, Nicol, and Hugh Ford. "The flexibility of short-radius pipe-bends." Proceedings of the Institution of Mechanical Engineers, Part B: Management and engineering manufacture 1.1-12 (1953): 480-509
- [14] Turner, C. E., and Hugh Ford. "Examination of the theories for calculating the stresses in pipe bends subjected to in-plane bending." Proceedings of the Institution of Mechanical Engineers 171.1 (1957): 513-525.
- [15] Clark, R. A., and Reissner, E. - 1951: Bending of Curved Tubes. In Advances in Applied Mechanics, Vol. II, pp. 93 - 122, edited by Richard von Mises and Theodore von Karman, Academic Press Inc.
- [16] Markl, A. R. C., and K. Y. Louisville. "Fatigue tests of piping components." Trans. ASME 74.3 (1952): 287-303.
- [17] Matzen, Vernon C., and Lixin Yu. "Elbow stress indices using finite element analysis." Nuclear engineering and design 181.1 (1998): 257-265.
- [18] Yu, L., and Matzen, V. C. - 1999: B2 Stress Index for Elbow Analysis. Nuclear Engineering and Design, Vol. 192, pp. 261- 70, Elsevier.
- [19] An, Joong-Hyok, et al. "Elastic stresses for 90° elbows under in-plane bending." International Journal of Mechanical Sciences 53.9 (2011): 762-776.
- [20] Shalaby MA, Younan MA. Limit Loads for Pipe Elbows Subjected to In-Plane Opening Moments and Internal Pressure. ASME. J. Pressure Vessel Technol. 1999;121(1):17-23. doi:10.1115/1.2883661.
- [21] Chattopadhyay JJ, Nathani DK, Dutta BK, Kushwaha HS. Closed-Form Collapse Moment Equations of Elbows Under Combined Internal Pressure and In-Plane Bending Moment. ASME. J. Pressure Vessel Technol. 2000;122(4):431-436. doi:10.1115/1.1285988.
- [22] Findlay, G. E., and J. Spence. "In-plane bending of a large 90° smooth bend." Journal of Strain Analysis 1.4 (1966): 290-300.
- [23] CSA Standard Z662-15, Canadian Code for Oil and Gas Pipeline Systems, Canadian Standards Association, 2015.
- [24] ASME B31.1: Power piping. ASME Code for pressure piping.
- [25] ASME B31.3: Process piping code. ASME Code for pressure piping.

[26] Bantlin, Albert. Formänderung und Beanspruchung federnder Ausgleichsrohre. Springer, 1910.

[27] Thiagarajan, N. "Estimation of Pipe Elbow Anchor Loads Due to Internal Pressure." International Journal of Engineering and Innovative Technology 2.7 (2013).

[28] Simulia ABAQUS. 2013. Users' Manual version 6.13 documentation.

[29] Lubis, Asnawi, and James T. Boyle. "The pressure reduction effect in smooth piping elbows—revisited." International journal of pressure vessels and piping 81.2 (2004): 119-125.

[30] Vigness, Irwin. "Elastic properties of curved tubes." Trans. ASME 65.2 (1943): 105-120.

APPENDIX (A): PIPE BENDS UNDER IN-PLANE BENDING MOMENT

1. Linearity of the response

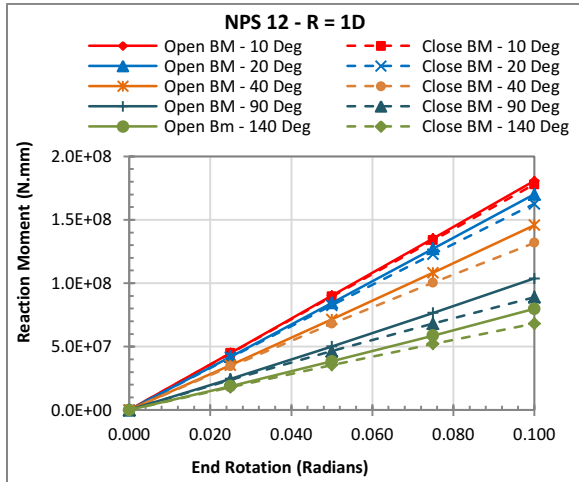


Figure 1. End rotation – reaction moment relationship for 12” pipe with 1D bend radius.

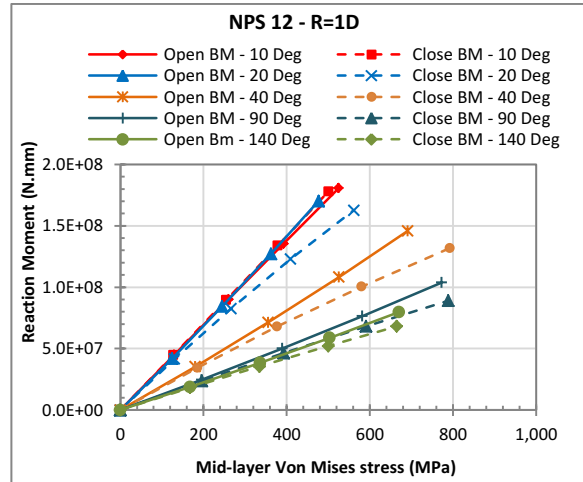


Figure 2. Von Mises stress – reaction moment relationship at midlayer wall thickness for 12” pipe with 1D bend radius.

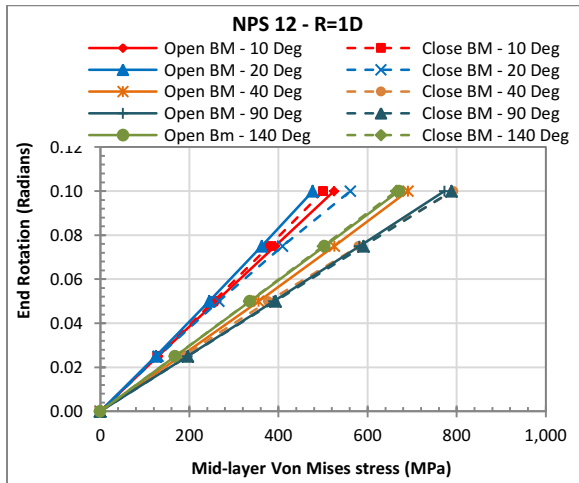


Figure 3. Von Mises stress – End rotation relationship at midlayer wall thickness for 12” pipe with 1D bend radius.

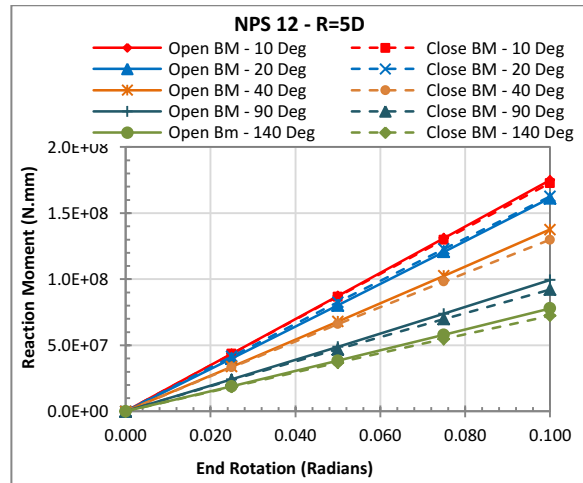


Figure 4. End rotation – reaction moment relationship for 12” pipe with 5D bend radius.

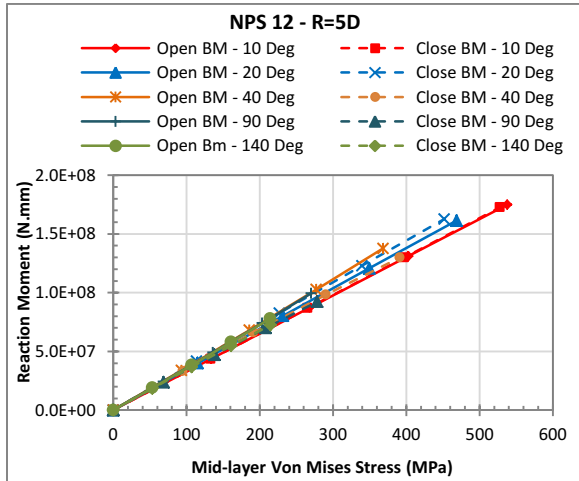


Figure 5. Von Mises stress – reaction moment relationship at midlayer wall thickness for 12" pipe with 5D bend radius.

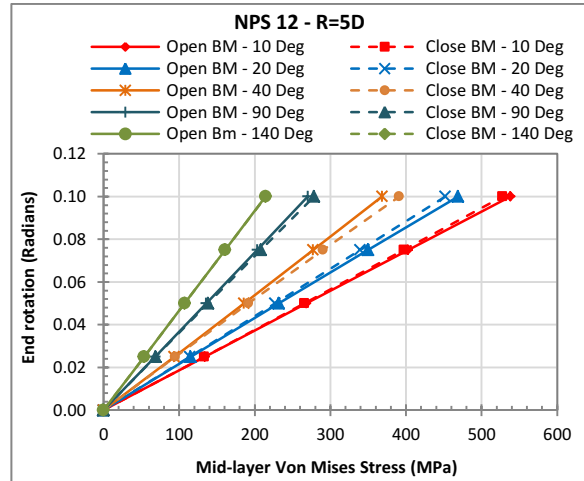


Figure 6. Von Mises stress – End rotation relationship at midlayer wall thickness for 12" pipe with 5D bend radius.

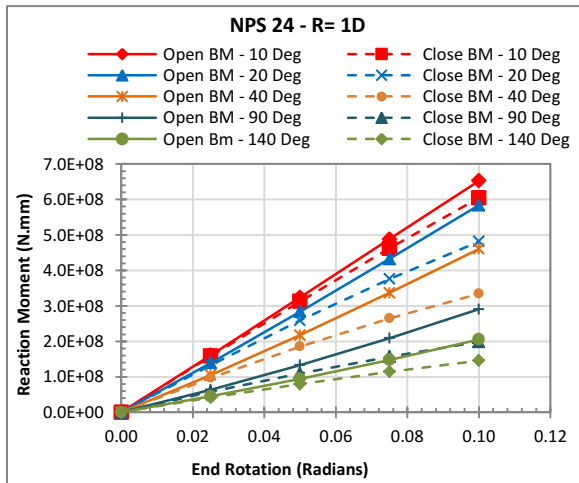


Figure 7. End rotation – reaction moment relationship for 24" pipe with 1D bend radius.

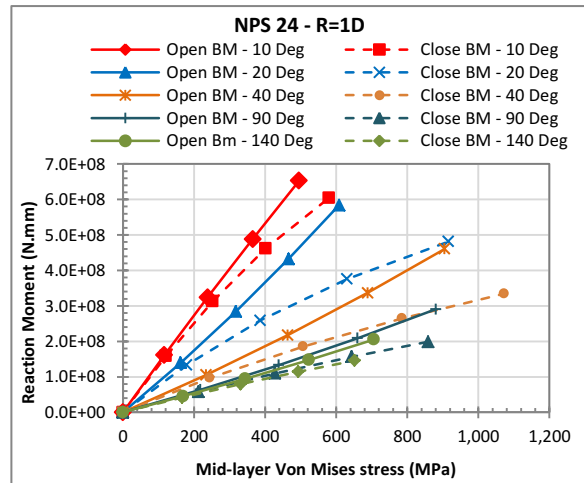


Figure 8. Von Mises stress – reaction moment relationship at midlayer wall thickness for 24" pipe with 1D bend radius.

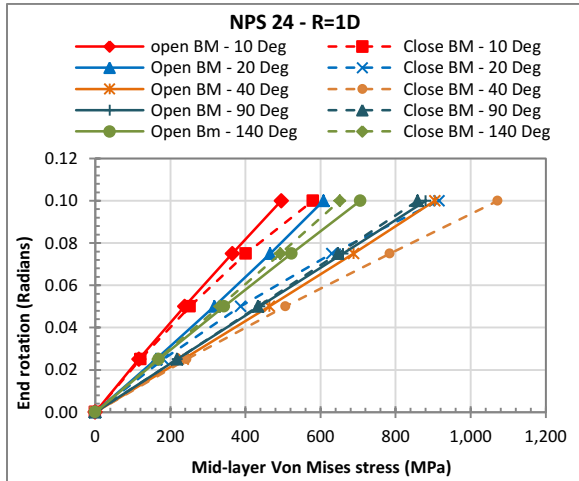


Figure 9. Von Mises stress – End rotation relationship at mid-layer wall thickness for 24” pipe with 1D bend radius.

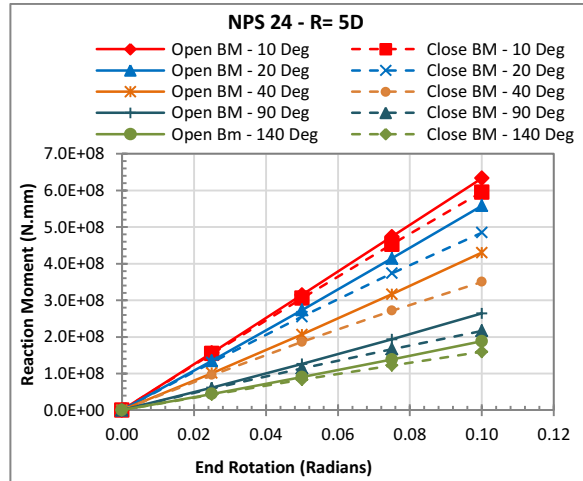


Figure 10. End rotation – reaction moment relationship for 24” pipe with 5D bend radius.

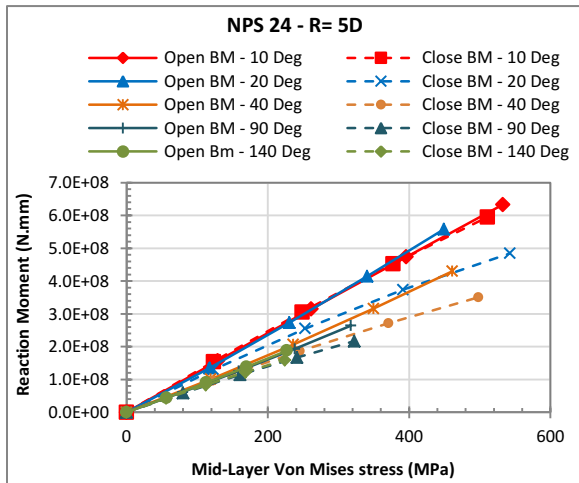


Figure 11. Von Mises stress – reaction moment relationship at mid-layer wall thickness for 24” pipe with 5D bend radius.

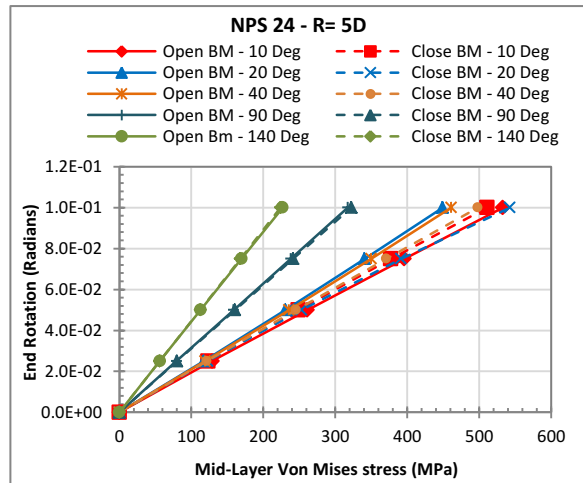


Figure 12. Von Mises stress – End rotation relationship at mid-layer wall thickness for 24” pipe with 5D bend radius.

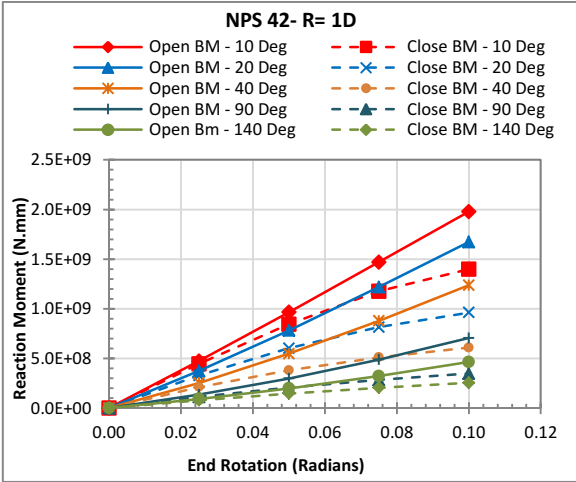


Figure 13. End rotation – reaction moment relationship for 42” pipe with 1D bend radius.

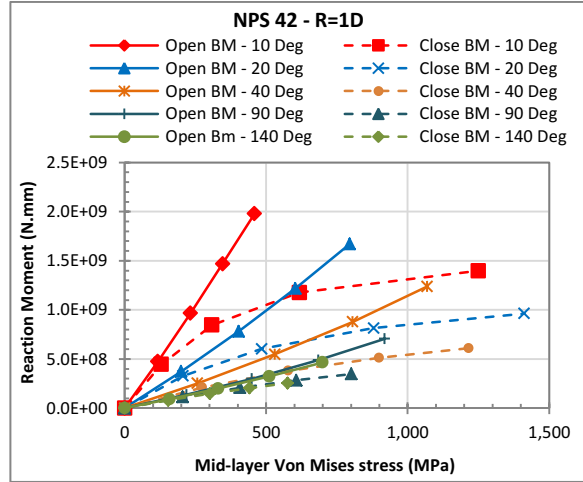


Figure 14. Von Mises stress – reaction moment relationship at mid-layer wall thickness for 42” pipe with 1D bend radius.

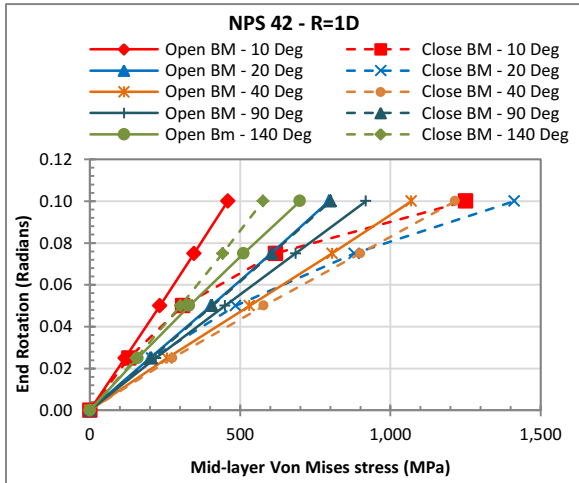


Figure 15. Von Mises stress – End rotation relationship at mid-layer wall thickness for 42” pipe with 1D bend radius.

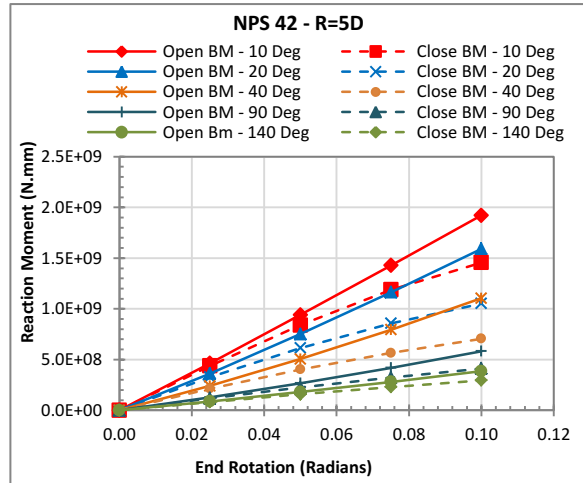


Figure 16. End rotation – reaction moment relationship for 42” pipe with 5D bend radius.

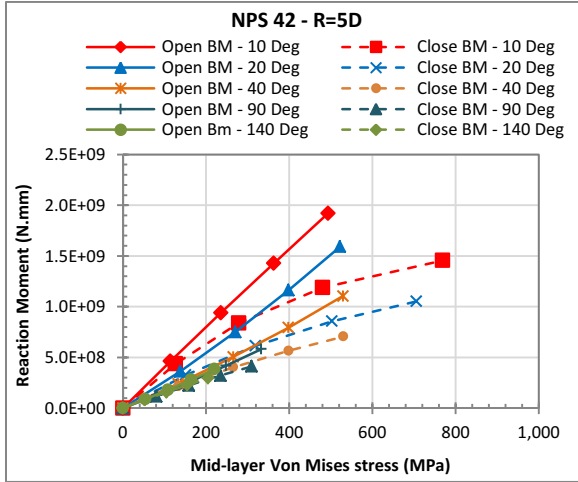


Figure 17. Von Mises stress – reaction moment relationship at mid-layer wall thickness for 42” pipe with 5D bend radius.

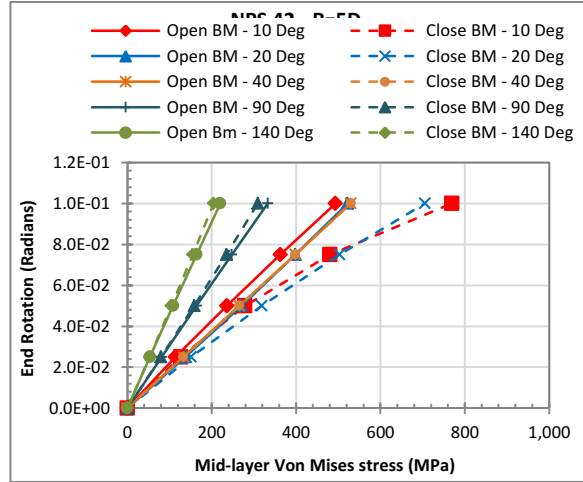


Figure 18. Von Mises stress – End rotation relationship at mid-layer wall thickness for 42” pipe with 5D bend radius.

2. Effect of bending moment direction
a. Opening Bending Moment

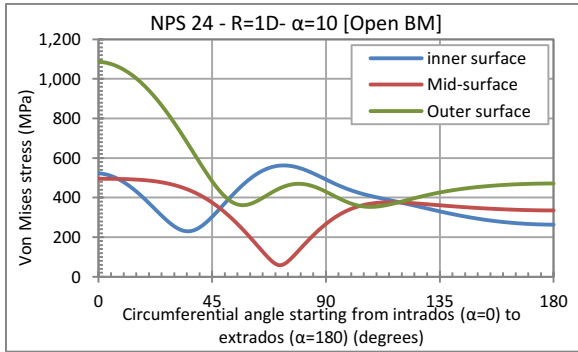


Figure 19. Von Mises stress distribution on NPS 24 bend with short radius and bend angle 10-degrees under opening bending moment

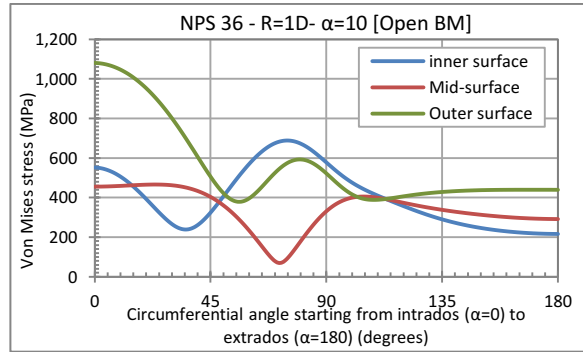


Figure 20. Von Mises stress distribution on NPS 36 bend with short radius and bend angle 10-degrees under opening bending moment

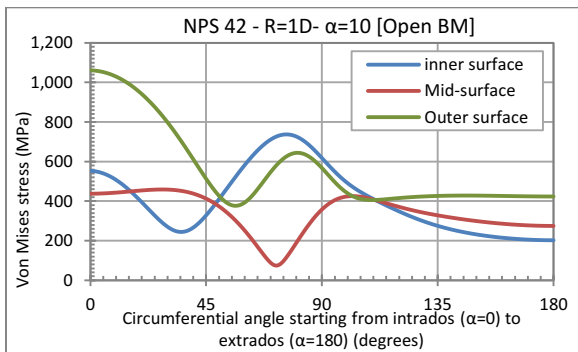


Figure 21. Von Mises stress distribution on NPS 42 bend with short radius and bend angle 10-degrees under opening bending moment

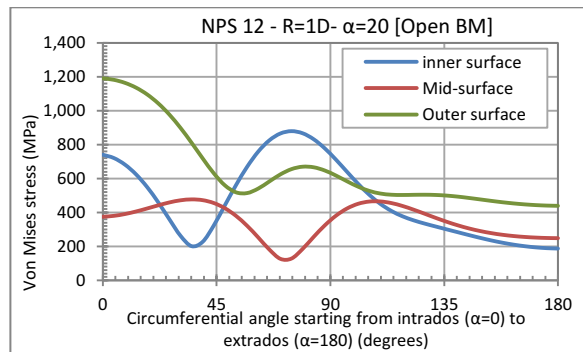


Figure 22. Von Mises stress distribution on NPS 12 bend with short radius and bend angle 20-degrees under opening bending moment

opening bending moment

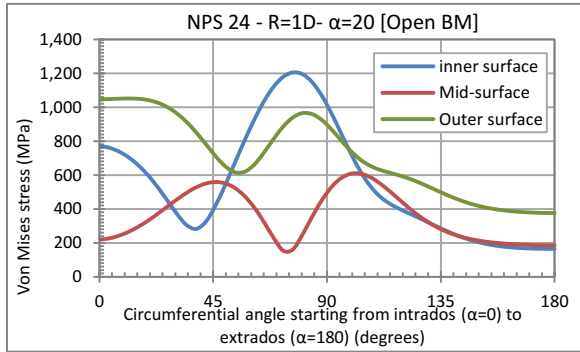


Figure 23. Von Mises stress distribution on NPS 24 bend with short radius and bend angle 20-degrees under opening bending moment

opening bending moment

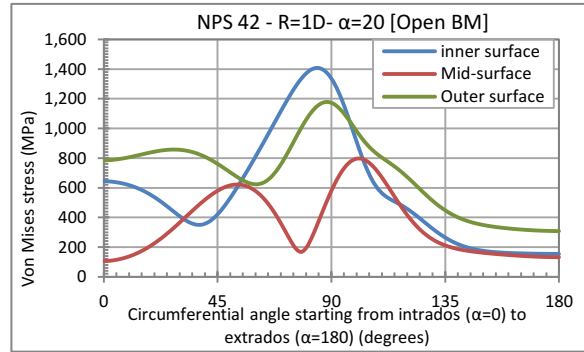


Figure 24. Von Mises stress distribution on NPS 42 bend with short radius and bend angle 20-degrees under opening bending moment

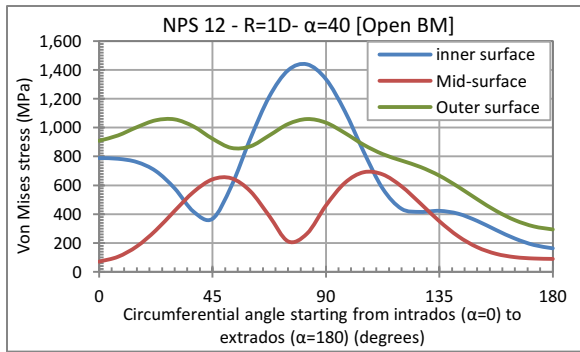


Figure 25. Von Mises stress distribution on NPS 12 bend with short radius and bend angle 40-degrees under opening bending moment

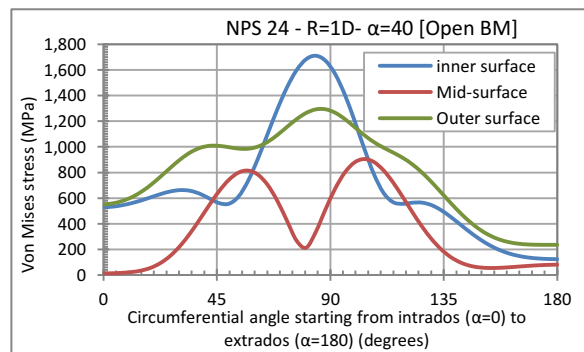


Figure 26. Von Mises stress distribution on NPS 24 bend with short radius and bend angle 40-degrees under opening bending moment

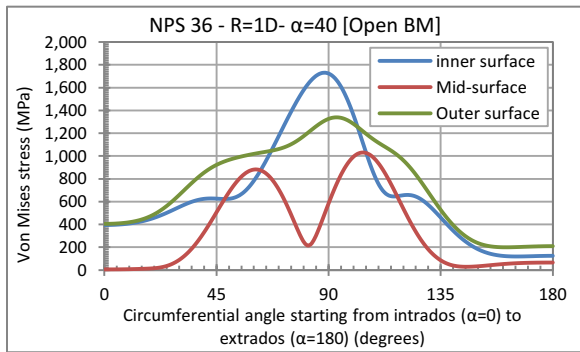


Figure 27. Von Mises stress distribution on NPS 36 bend with short radius and bend angle 40-degrees under opening bending moment

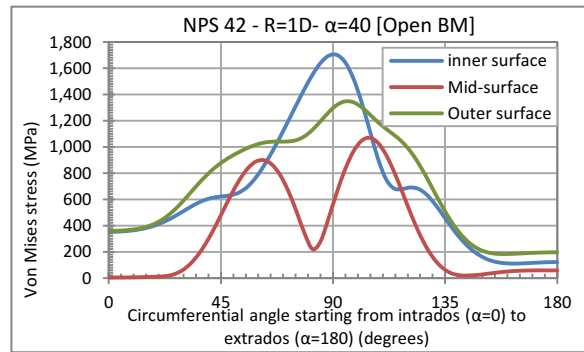


Figure 28. Von Mises stress distribution on NPS 42 bend with short radius and bend angle 40-degrees under opening bending moment

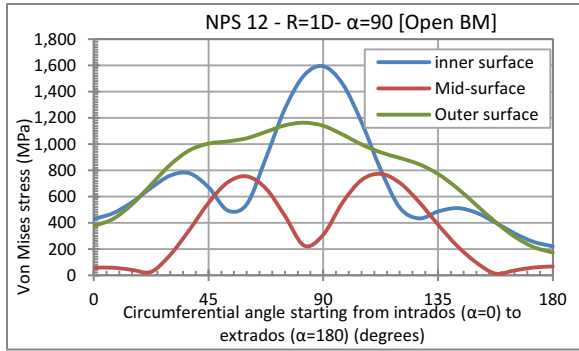


Figure 29. Von Mises stress distribution on NPS 12 bend with short radius and bend angle 90-degrees under opening bending moment

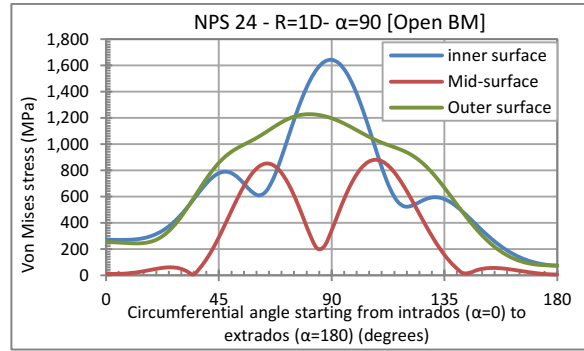


Figure 30. Von Mises stress distribution on NPS 24 bend with short radius and bend angle 90-degrees under opening bending moment

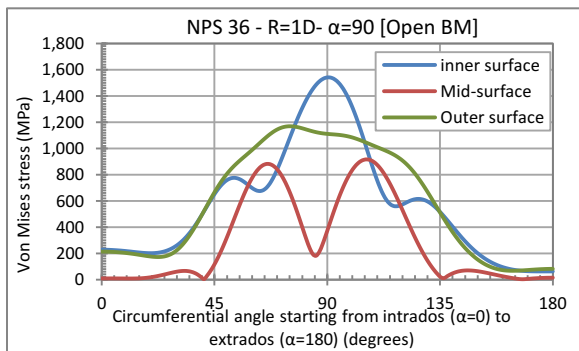


Figure 31. Von Mises stress distribution on NPS 36 bend with short radius and bend angle 90-degrees under opening bending moment

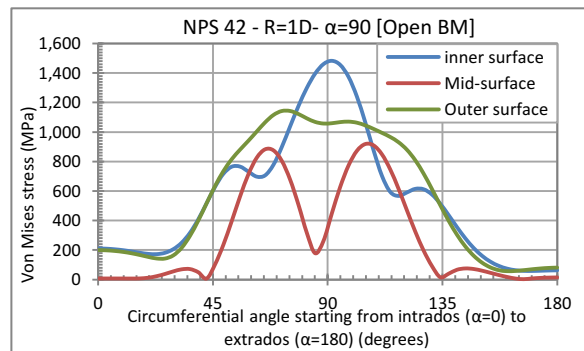


Figure 32. Von Mises stress distribution on NPS 42 bend with short radius and bend angle 90-degrees under opening bending moment

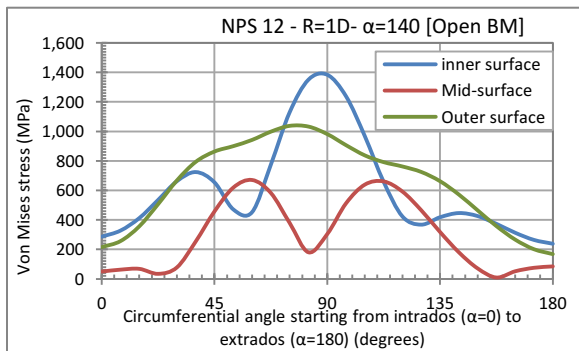


Figure 33. Von Mises stress distribution on NPS 12 bend with short radius and bend angle 140-degrees under opening bending moment

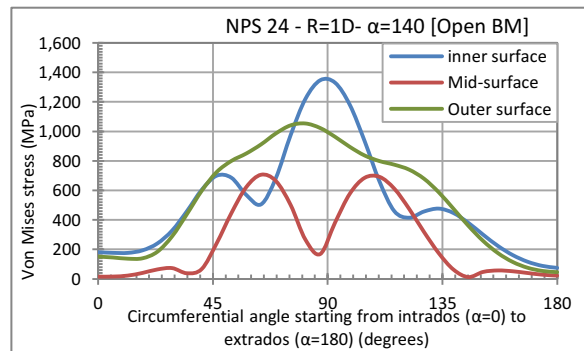


Figure 34. Von Mises stress distribution on NPS 24 bend with short radius and bend angle 140-degrees under opening bending moment

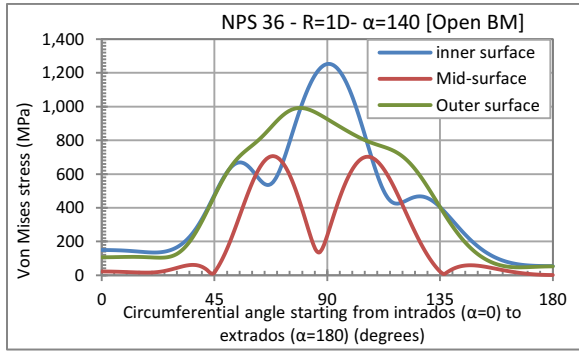


Figure 35. Von Mises stress distribution on NPS 36 bend with short radius and bend angle 140-degrees under opening bending moment

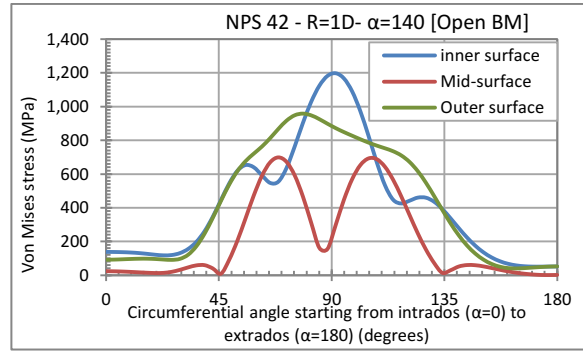


Figure 36. Von Mises stress distribution on NPS 42 bend with short radius and bend angle 140-degrees under opening bending moment

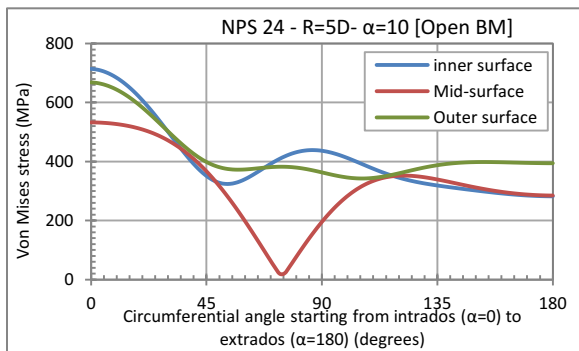


Figure 37. Von Mises stress distribution on NPS 24 bend with long radius and bend angle 10-degrees under opening bending moment

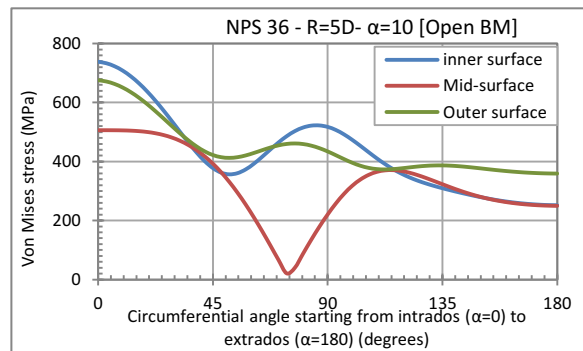


Figure 38. Von Mises stress distribution on NPS 36 bend with long radius and bend angle 10-degrees under opening bending moment

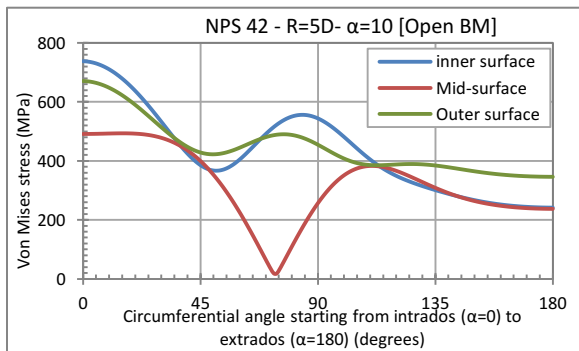


Figure 39. Von Mises stress distribution on NPS 42 bend with long radius and bend angle 10-degrees under opening bending moment

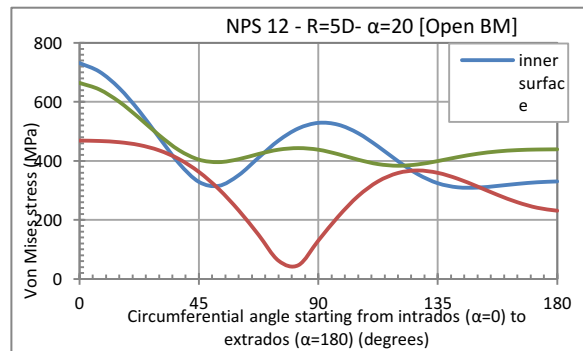


Figure 40. Von Mises stress distribution on NPS 12 bend with long radius and bend angle 20-degrees under opening bending moment

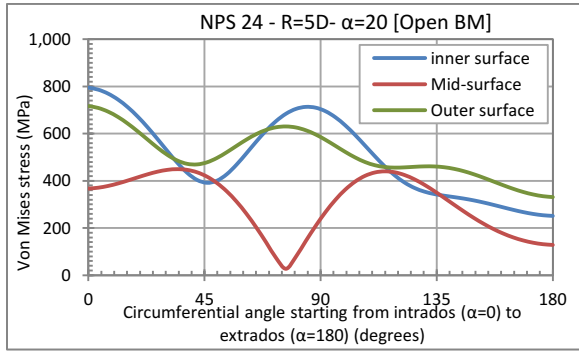


Figure 41. Von Mises stress distribution on NPS 24 bend with long radius and bend angle 20-degrees under opening bending moment

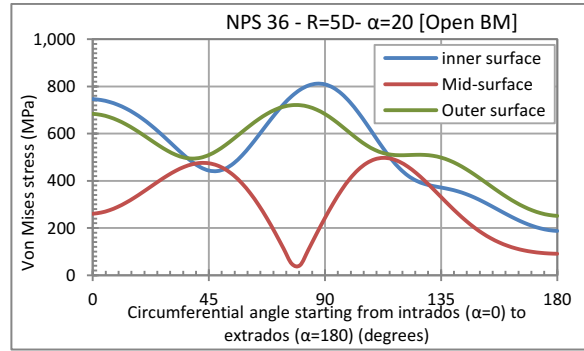


Figure 42. Von Mises stress distribution on NPS 36 bend with long radius and bend angle 20-degrees under opening bending moment

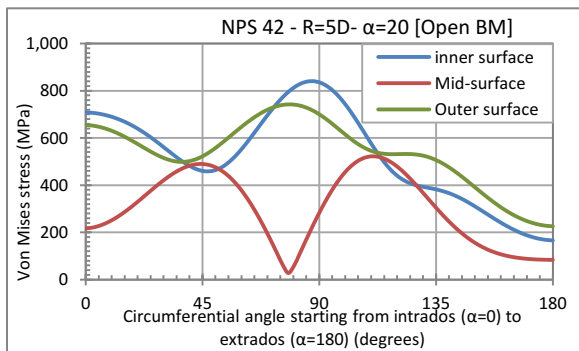


Figure 43. Von Mises stress distribution on NPS 42 bend with long radius and bend angle 20-degrees under opening bending moment

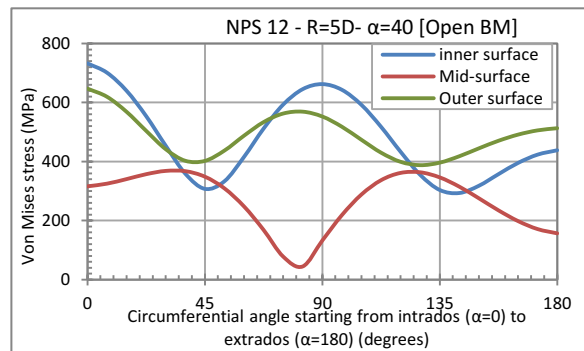


Figure 44. Von Mises stress distribution on NPS 12 bend with long radius and bend angle 40-degrees under opening bending moment

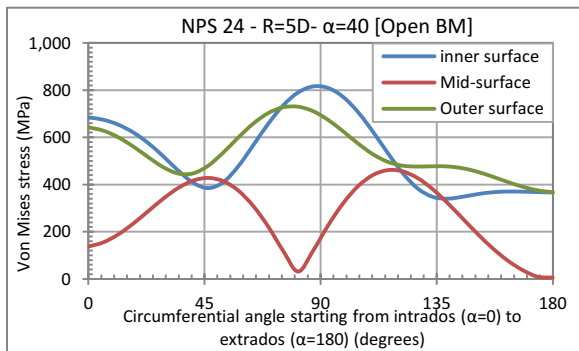


Figure 45. Von Mises stress distribution on NPS 24 bend with long radius and bend angle 40-degrees under opening bending moment

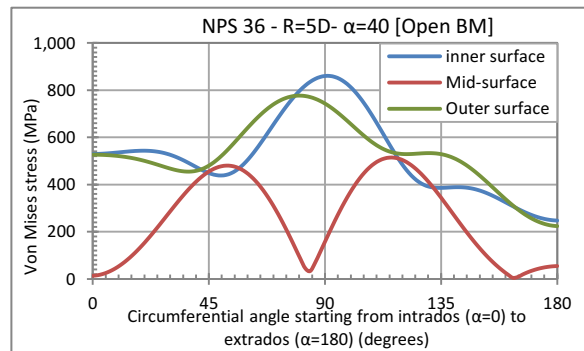


Figure 46. Von Mises stress distribution on NPS 36 bend with long radius and bend angle 40-degrees under opening bending moment

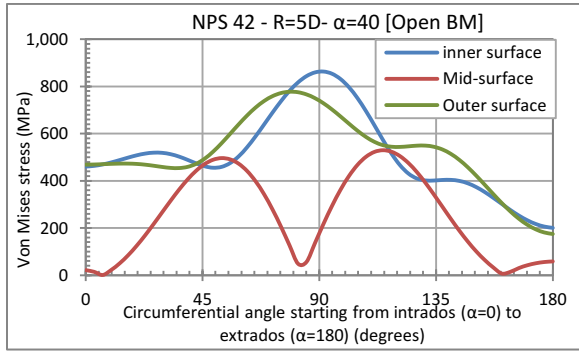


Figure 47. Von Mises stress distribution on NPS 42 bend with long radius and bend angle 40-degrees under opening bending moment

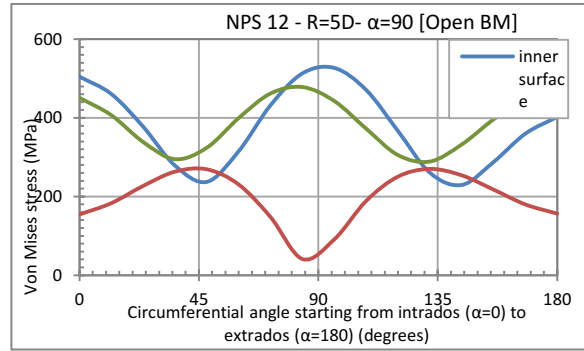


Figure 48. Von Mises stress distribution on NPS 12 bend with long radius and bend angle 90-degrees under opening bending moment

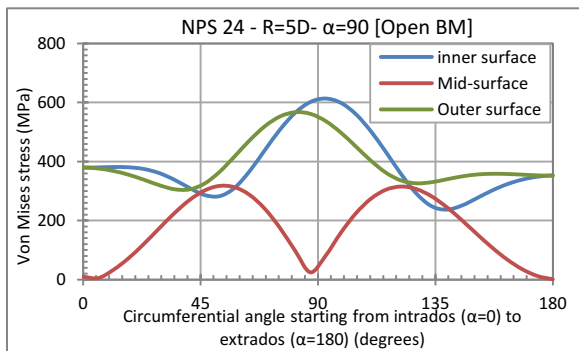


Figure 49. Von Mises stress distribution on NPS 24 bend with long radius and bend angle 90-degrees under opening bending moment

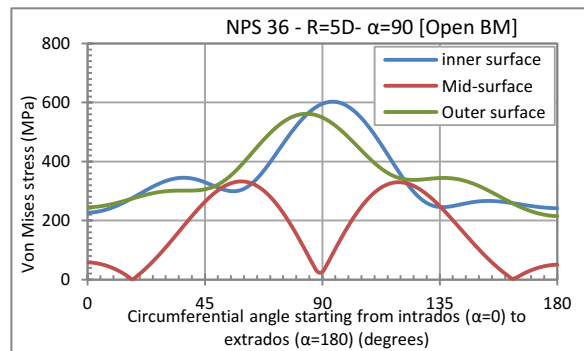


Figure 50. Von Mises stress distribution on NPS 36 bend with long radius and bend angle 90-degrees under opening bending moment

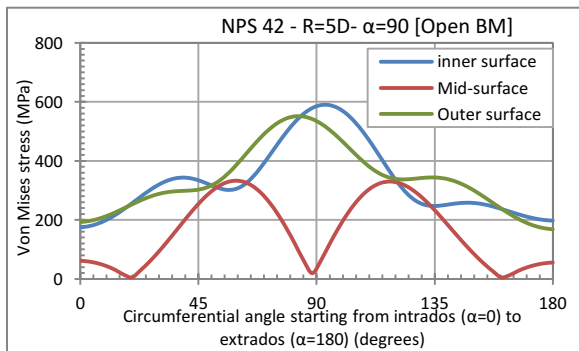


Figure 51. Von Mises stress distribution on NPS 42 bend with long radius and bend angle 90-degrees under opening bending moment

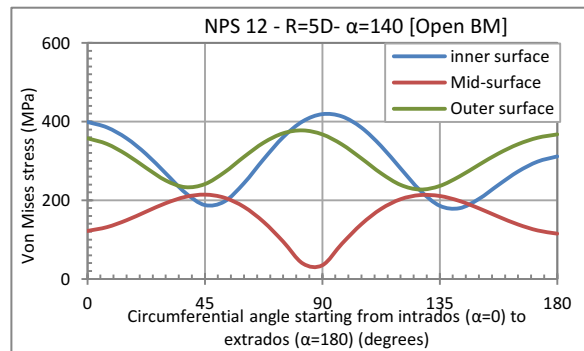


Figure 52. Von Mises stress distribution on NPS 12 bend with long radius and bend angle 140-degrees under opening bending moment

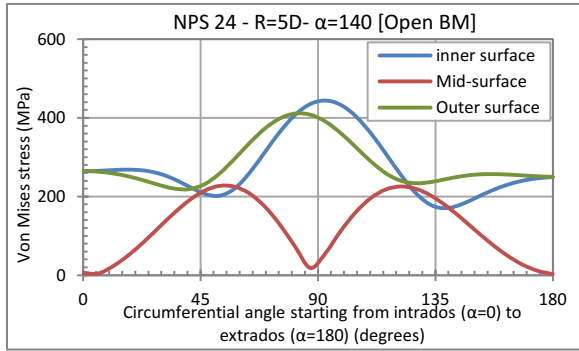


Figure 53. Von Mises stress distribution on NPS 24 bend with long radius and bend angle 140-degrees under opening bending moment

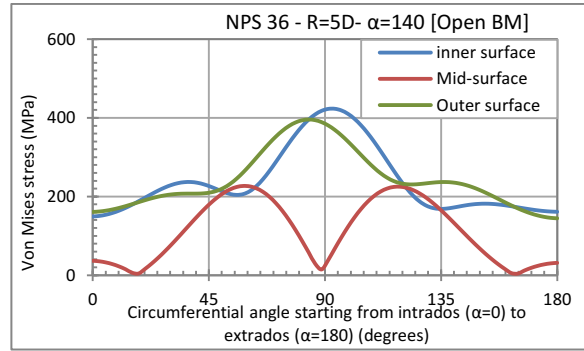


Figure 54. Von Mises stress distribution on NPS 36 bend with long radius and bend angle 140-degrees under opening bending moment

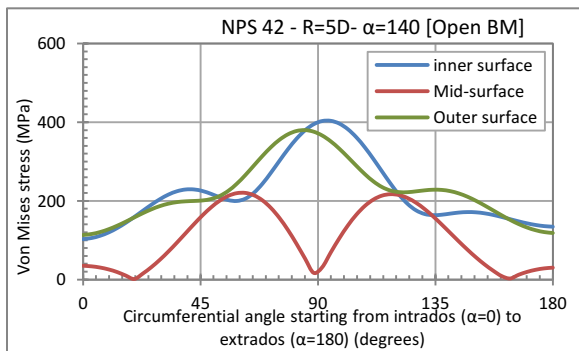


Figure 55. Von Mises stress distribution on NPS 42 bend with long radius and bend angle 140-degrees under opening bending moment

b. Closing Bending Moment

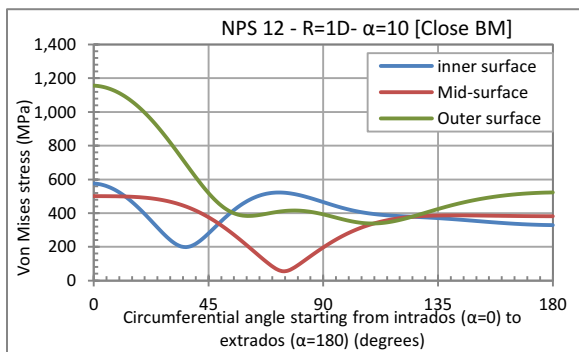


Figure 56. Von Mises stress distribution on NPS 12 bend with short radius and bend angle 10-degrees under closing bending moment

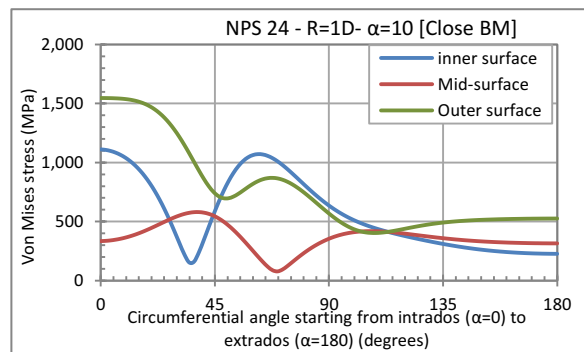


Figure 57. Von Mises stress distribution on NPS 24 bend with short radius and bend angle 10-degrees under closing bending moment

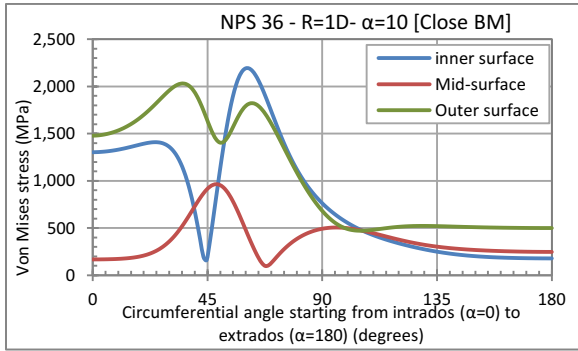


Figure 58. Von Mises stress distribution on NPS 36 bend with short radius and bend angle 10-degrees under closing bending moment

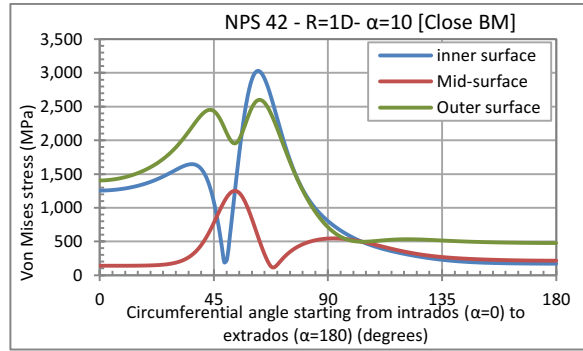


Figure 59. Von Mises stress distribution on NPS 42 bend with short radius and bend angle 20-degrees under closing bending moment

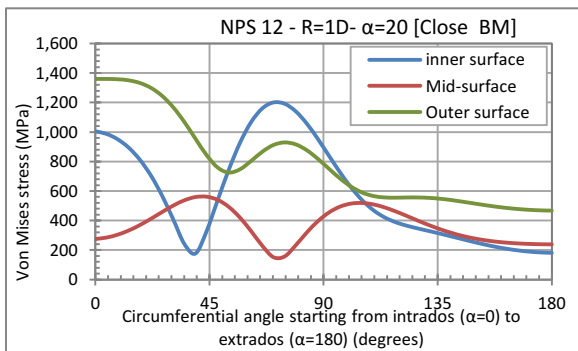


Figure 60. Von Mises stress distribution on NPS 12 bend with short radius and bend angle 20-degrees under closing bending moment

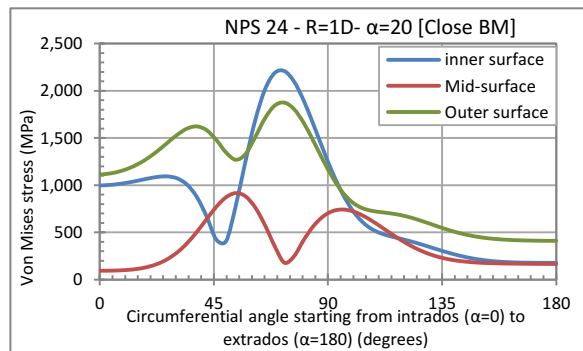


Figure 61. Von Mises stress distribution on NPS 24 bend with short radius and bend angle 20-degrees under closing bending moment

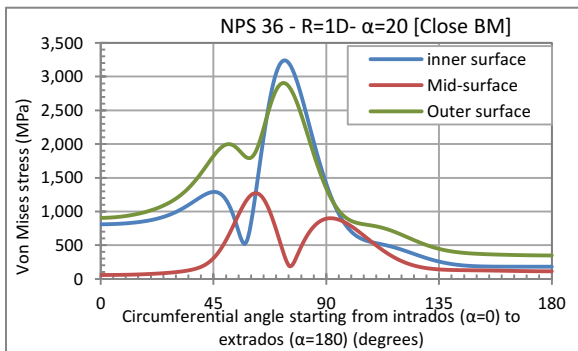


Figure 62. Von Mises stress distribution on NPS 36 bend with short radius and bend angle 20-degrees under closing bending moment

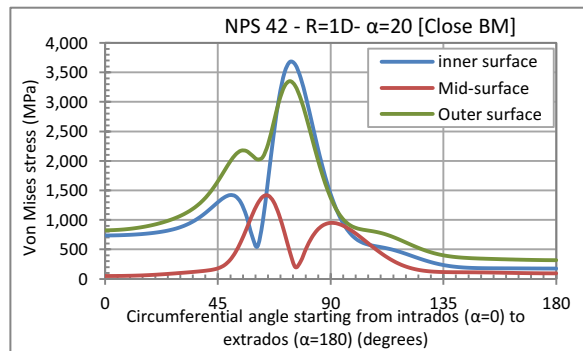


Figure 63. Von Mises stress distribution on NPS 42 bend with short radius and bend angle 20-degrees under closing bending moment

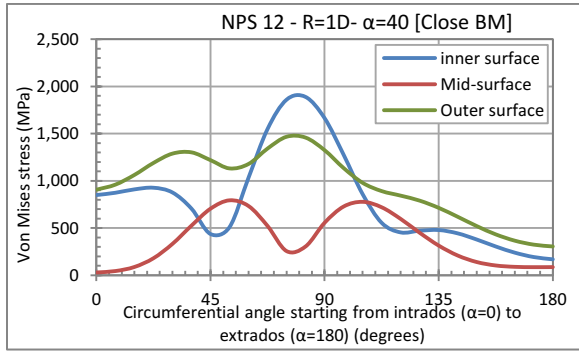


Figure 64. Von Mises stress distribution on NPS 12 bend with short radius and bend angle 40-degrees under closing bending moment

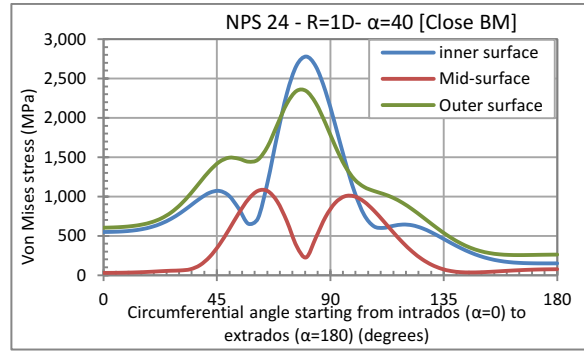


Figure 65. Von Mises stress distribution on NPS 24 bend with short radius and bend angle 40-degrees under closing bending moment

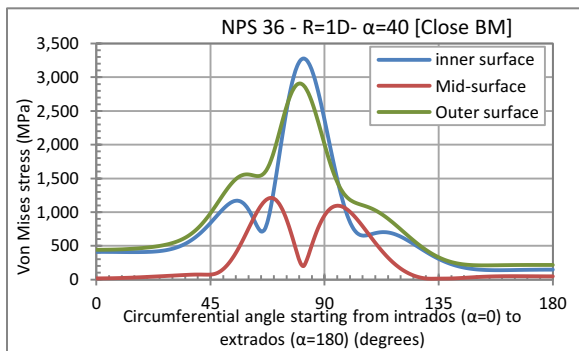


Figure 66. Von Mises stress distribution on NPS 36 bend with short radius and bend angle 40-degrees under closing bending moment

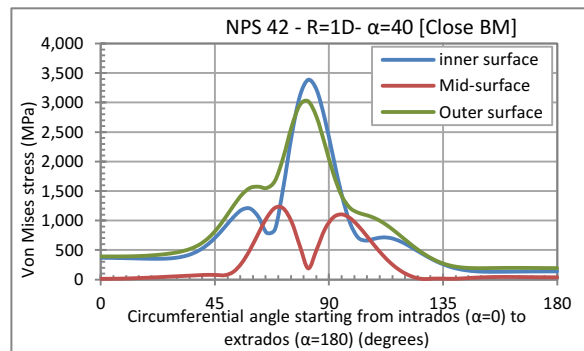


Figure 67. Von Mises stress distribution on NPS 42 bend with short radius and bend angle 40-degrees under closing bending moment

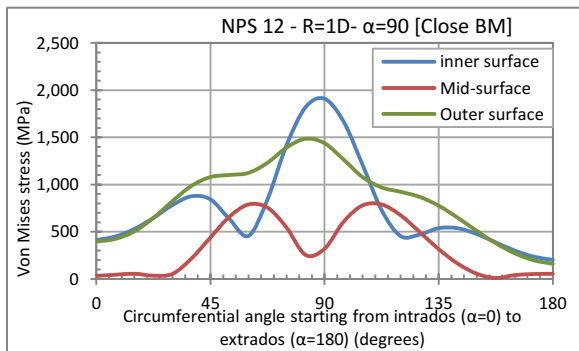


Figure 68. Von Mises stress distribution on NPS 12 bend with short radius and bend angle 90-degrees under closing bending moment

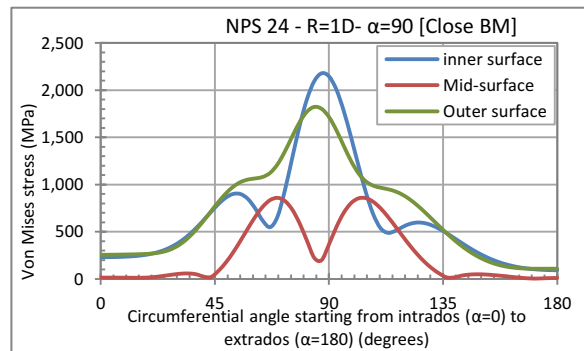


Figure 69. Von Mises stress distribution on NPS 24 bend with short radius and bend angle 90-degrees under closing bending moment

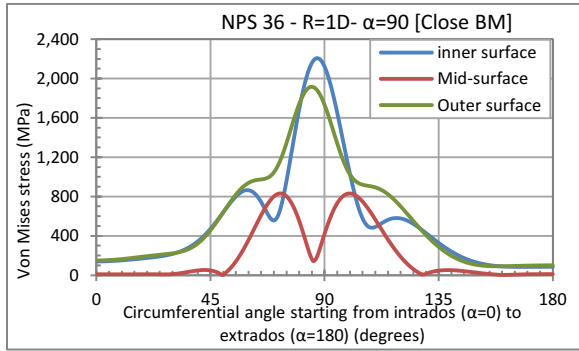


Figure 70. Von Mises stress distribution on NPS 36 bend with short radius and bend angle 90-degrees under closing bending moment

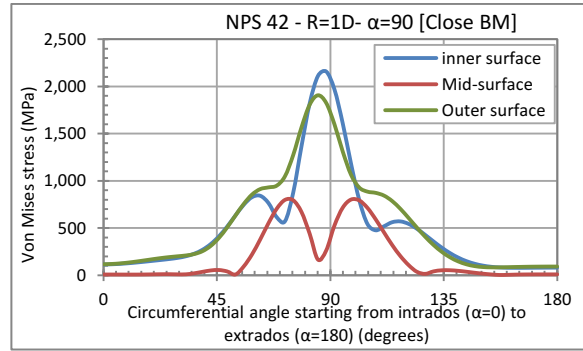


Figure 71. Von Mises stress distribution on NPS 42 bend with short radius and bend angle 90-degrees under closing bending moment

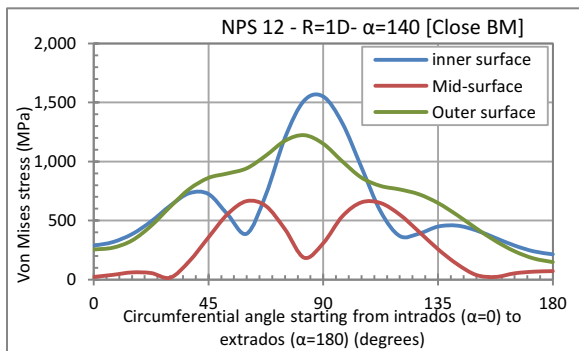


Figure 72. Von Mises stress distribution on NPS 12 bend with short radius and bend angle 140-degrees under closing bending moment

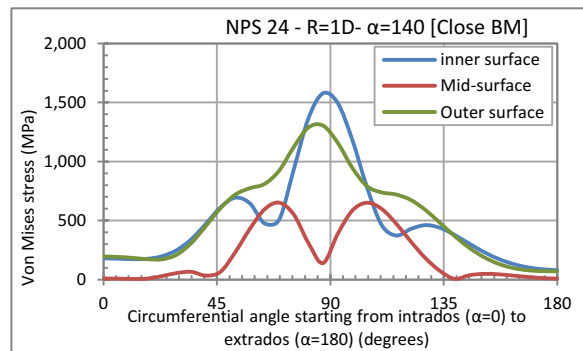


Figure 73. Von Mises stress distribution on NPS 24 bend with short radius and bend angle 140-degrees under closing bending moment

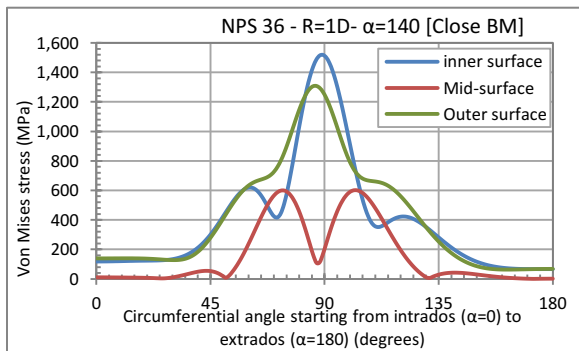


Figure 74. Von Mises stress distribution on NPS 36 bend with short radius and bend angle 140-degrees under closing bending moment

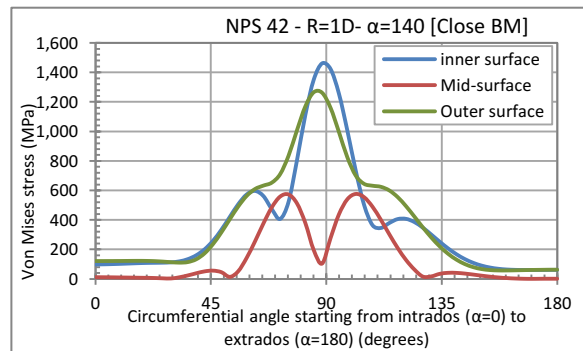


Figure 75. Von Mises stress distribution on NPS 42 bend with short radius and bend angle 140-degrees under closing bending moment

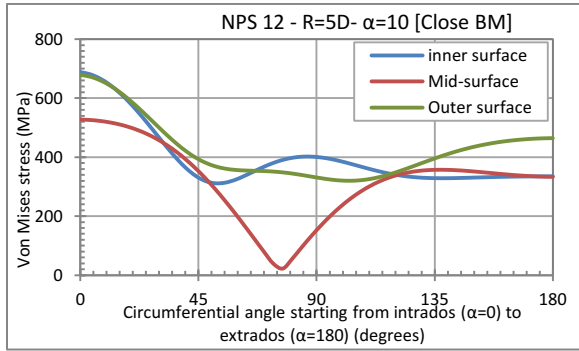


Figure 76. Von Mises stress distribution on NPS 12 bend with long radius and bend angle 10-degrees under closing bending moment

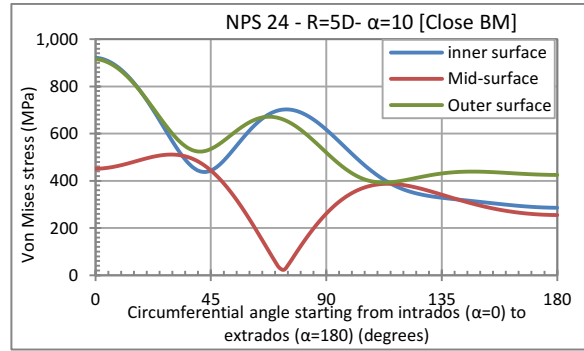


Figure 77. Von Mises stress distribution on NPS 24 bend with long radius and bend angle 10-degrees under closing bending moment

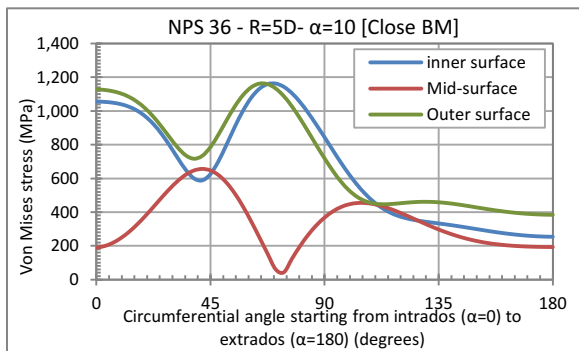


Figure 78. Von Mises stress distribution on NPS 36 bend with long radius and bend angle 10-degrees under closing bending moment

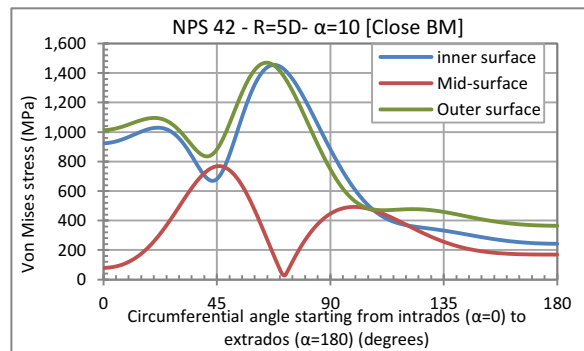


Figure 79. Von Mises stress distribution on NPS 42 bend with long radius and bend angle 10-degrees under closing bending moment

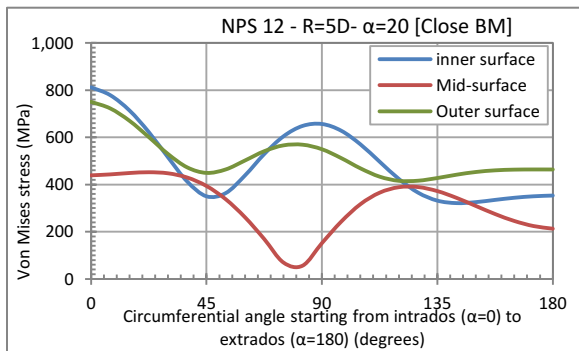


Figure 80. Von Mises stress distribution on NPS 12 bend with long radius and bend angle 20-degrees under closing bending moment

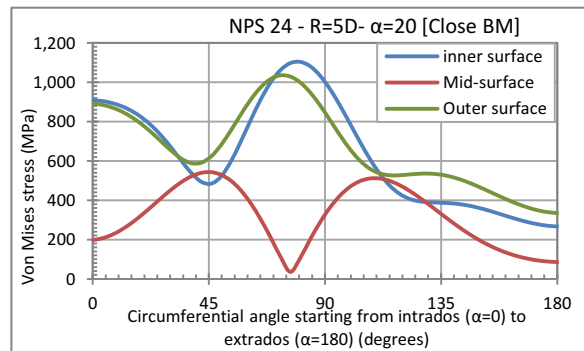


Figure 81. Von Mises stress distribution on NPS 24 bend with long radius and bend angle 20-degrees under closing bending moment

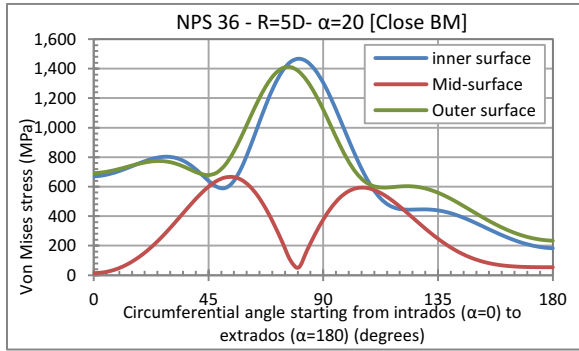


Figure 82. Von Mises stress distribution on NPS 36 bend with long radius and bend angle 20-degrees under closing bending moment

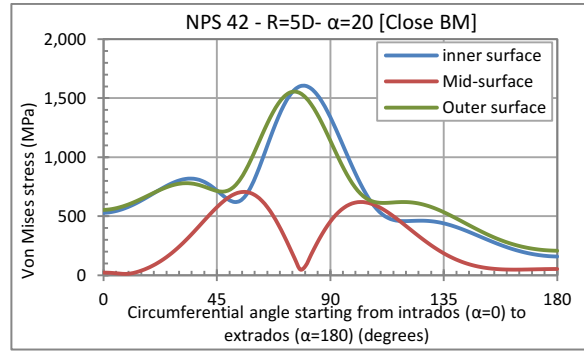


Figure 83. Von Mises stress distribution on NPS 42 bend with long radius and bend angle 20-degrees under closing bending moment

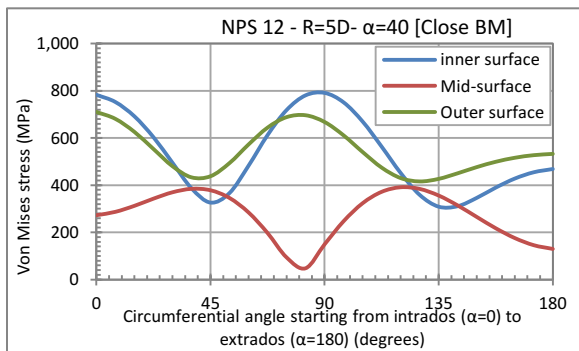


Figure 84. Von Mises stress distribution on NPS 12 bend with long radius and bend angle 40-degrees under closing bending moment

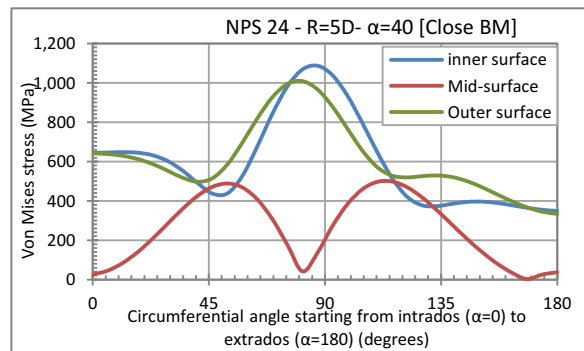


Figure 85. Von Mises stress distribution on NPS 24 bend with long radius and bend angle 40-degrees under closing bending moment

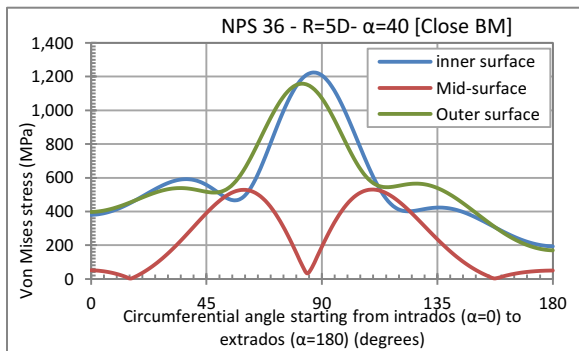


Figure 86. Von Mises stress distribution on NPS 36 bend with long radius and bend angle 40-degrees under closing bending moment

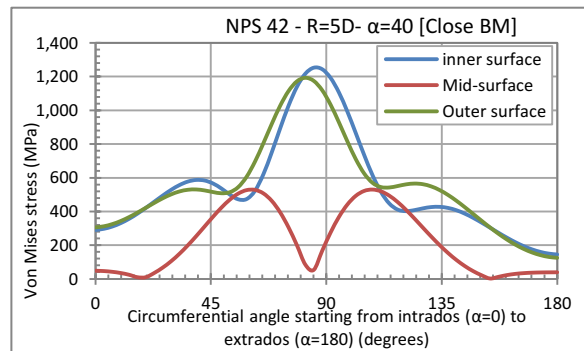


Figure 87. Von Mises stress distribution on NPS 42 bend with long radius and bend angle 40-degrees under closing bending moment

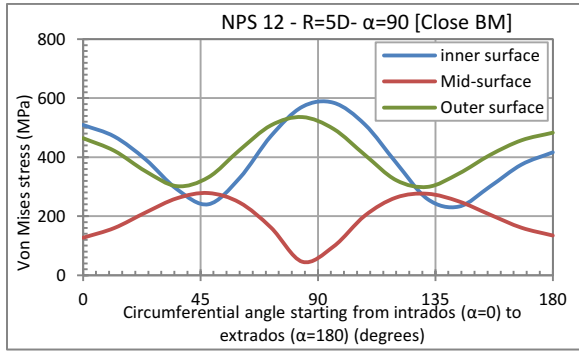


Figure 88. Von Mises stress distribution on NPS 12 bend with long radius and bend angle 90-degrees under closing bending moment

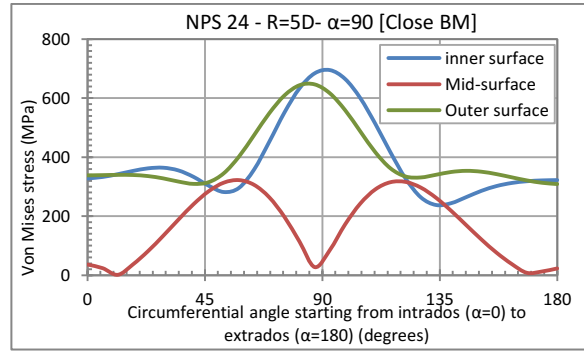


Figure 89. Von Mises stress distribution on NPS 24 bend with long radius and bend angle 90-degrees under closing bending moment

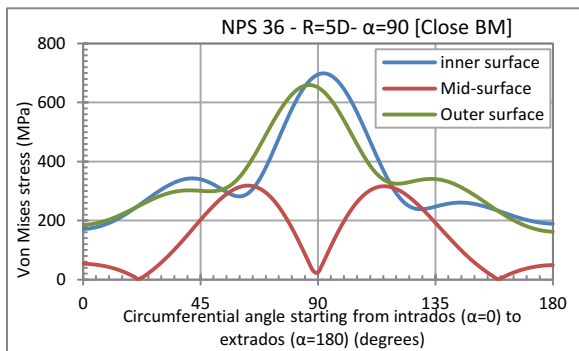


Figure 90. Von Mises stress distribution on NPS 36 bend with long radius and bend angle 90-degrees under closing bending moment

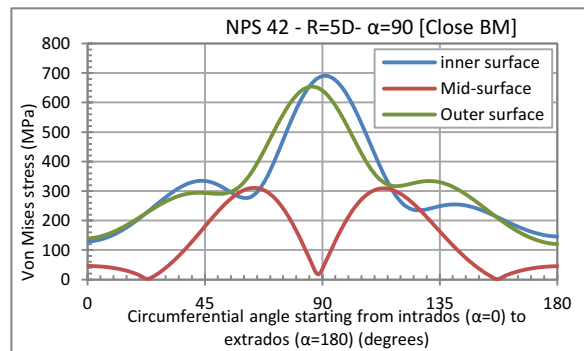


Figure 91. Von Mises stress distribution on NPS 42 bend with long radius and bend angle 90-degrees under closing bending moment

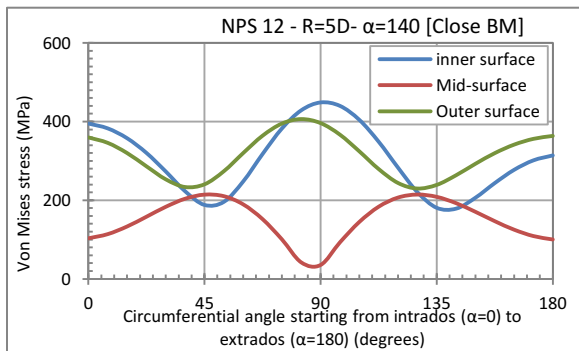


Figure 92. Von Mises stress distribution on NPS 12 bend with long radius and bend angle 140-degrees under closing bending moment

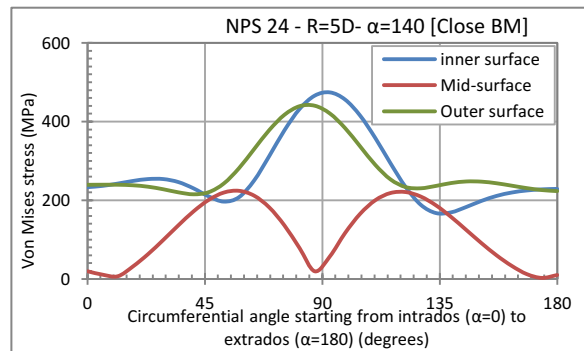


Figure 93. Von Mises stress distribution on NPS 24 bend with long radius and bend angle 140-degrees under closing bending moment

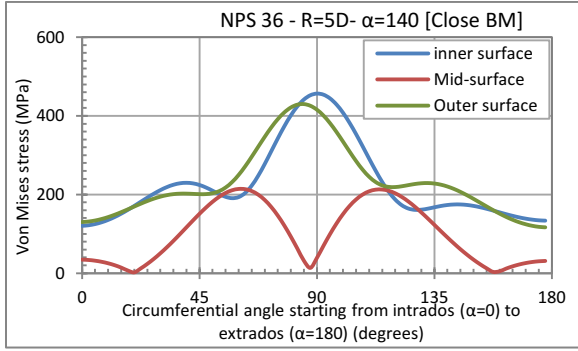


Figure 94. Von Mises stress distribution on NPS 36 bend with long radius and bend angle 140-degrees under closing bending moment

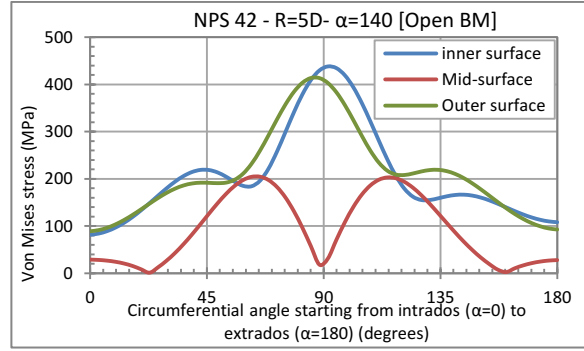


Figure 95. Von Mises stress distribution on NPS 42 bend with long radius and bend angle 140-degrees under closing bending moment

1. Comparison between FEA and CSA-Z662 stresses

a. Mid-layer stresses

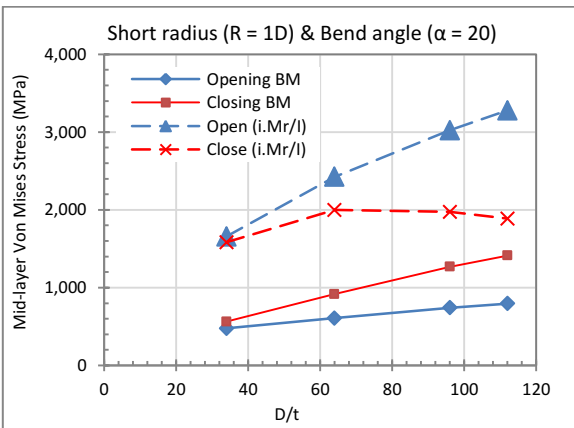


Figure 96. Maximum Von Mises stress for short radius bends with bend angle 20-degrees.

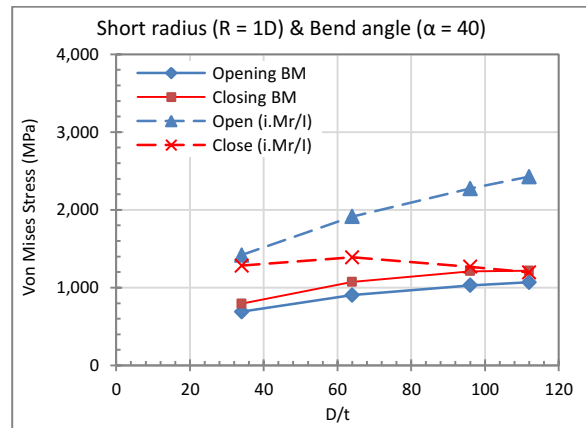


Figure 97. Maximum Von Mises stress for short radius bends with bend angle 40-degrees.

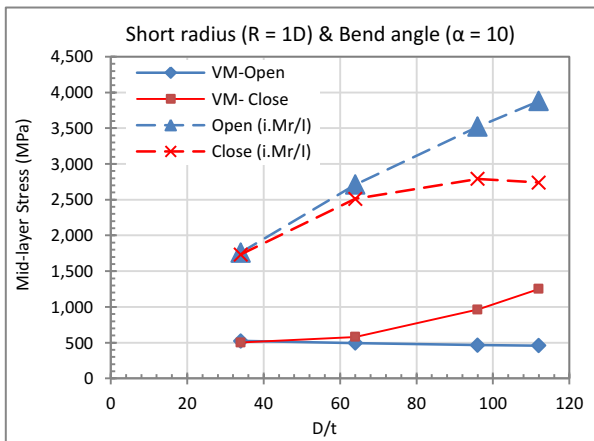


Figure 98. Maximum Von Mises stress for short radius bends with bend angle 10-degrees.

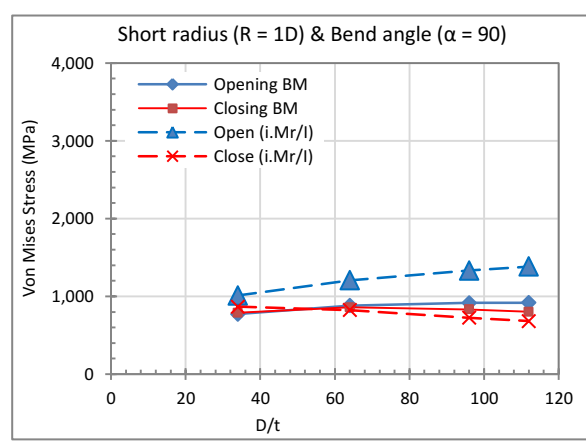


Figure 99. Maximum Von Mises stress for short radius bends with bend angle 90-degrees.

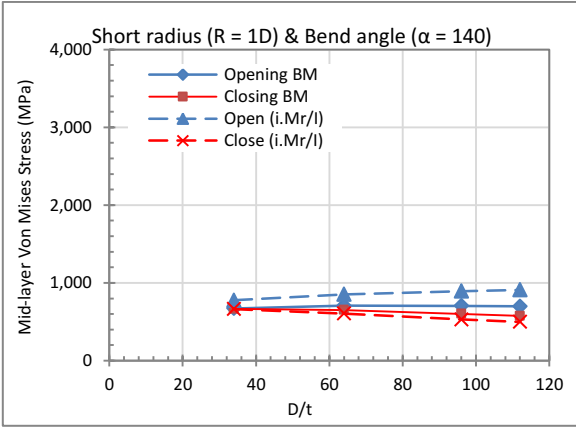


Figure 100. Maximum Von Mises stress for short radius bends with bend angle 140-degrees.

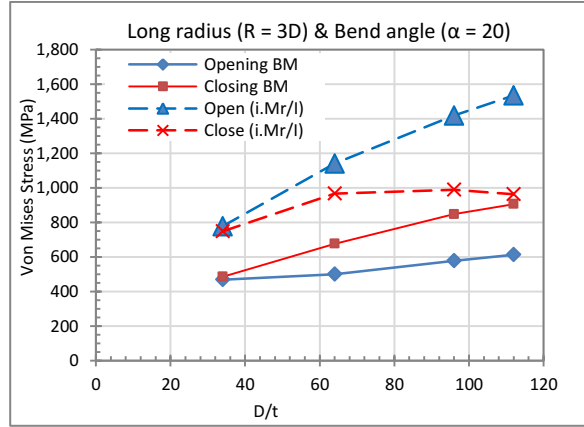


Figure 101. Maximum Von Mises stress for long radius bends with bend angle 20-degrees.

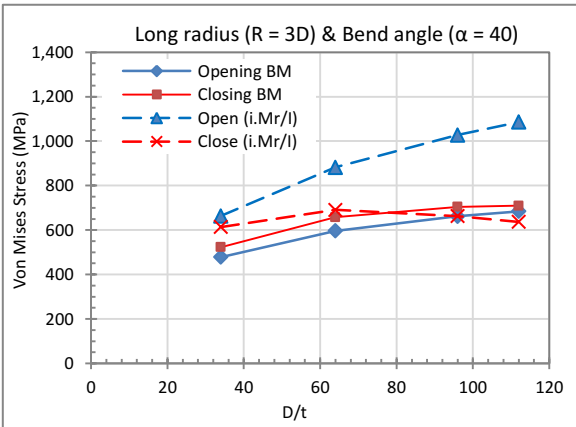


Figure 102. Maximum Von Mises stress for long radius bends with bend angle 40-degrees.

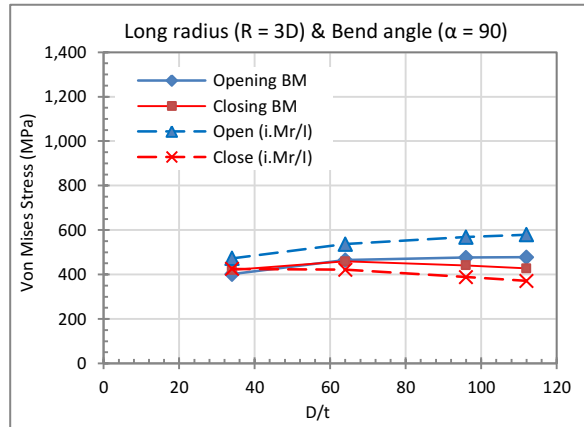


Figure 103. Maximum Von Mises stress for long radius bends with bend angle 90-degrees.

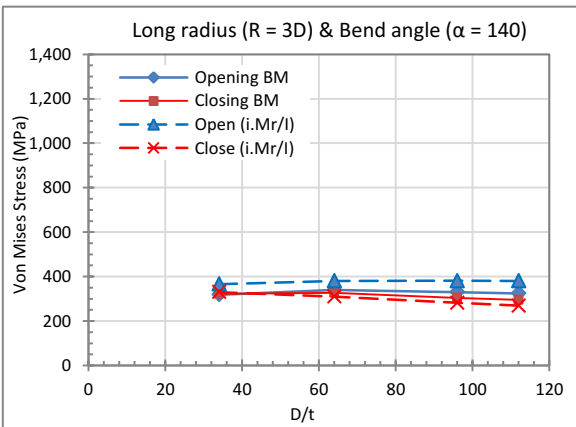


Figure 104. Maximum Von Mises stress for long radius bends with bend angle 140-degrees.

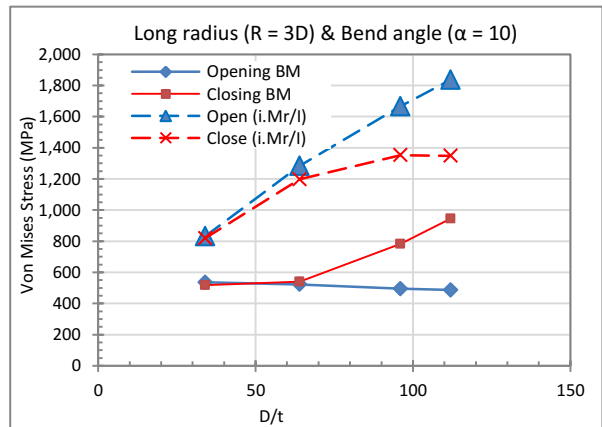


Figure 105. Maximum Von Mises stress for long radius bends with bend angle 10-degrees.

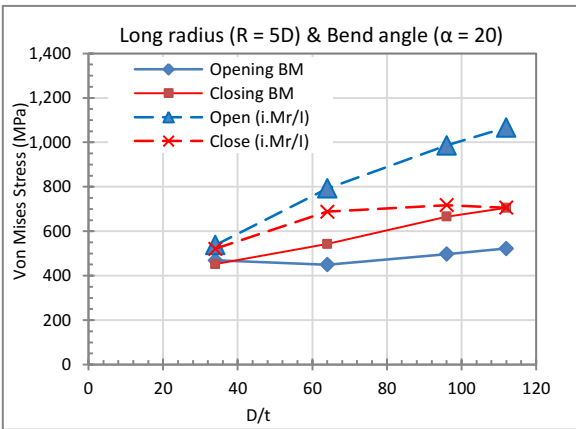


Figure 106. Maximum Von Mises stress for long radius bends with bend angle 20-degrees.

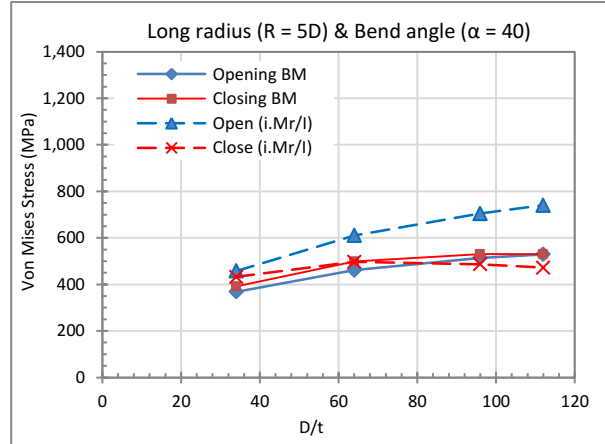


Figure 107. Maximum Von Mises stress for long radius bends with bend angle 40-degrees.

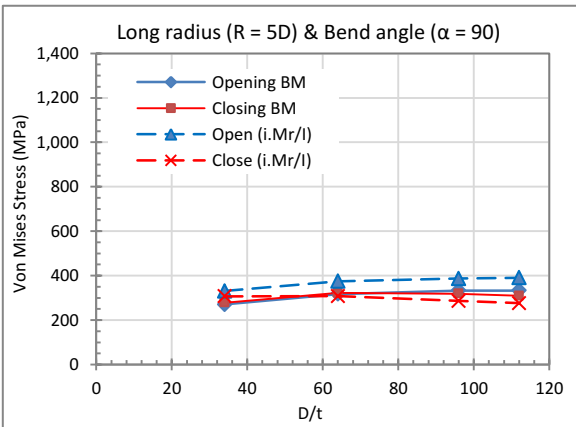


Figure 108. Maximum Von Mises stress for long radius bends with bend angle 90-degrees.

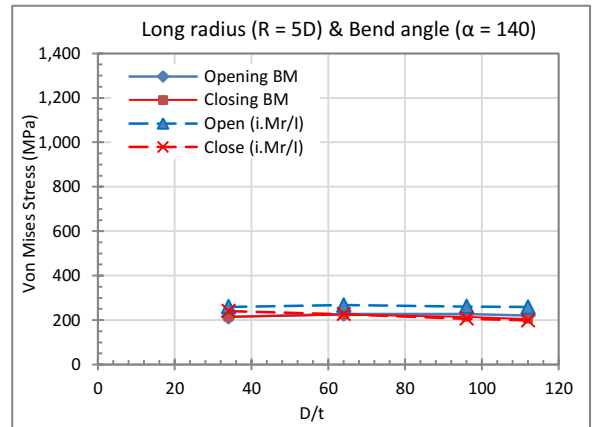


Figure 109. Maximum Von Mises stress for long radius bends with bend angle 140-degrees.

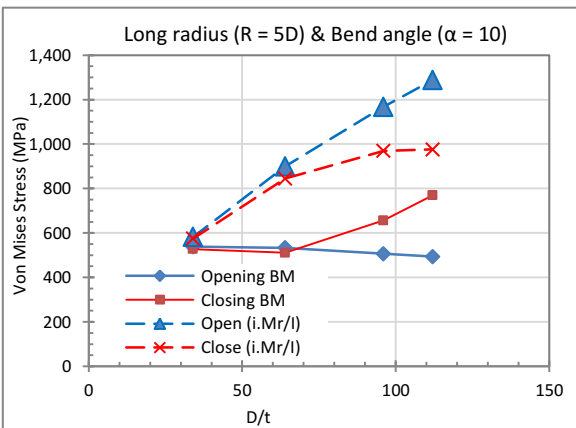


Figure 110. Maximum Von Mises stress for long radius bends with bend angle 140-degrees.

b. Inner layer stresses

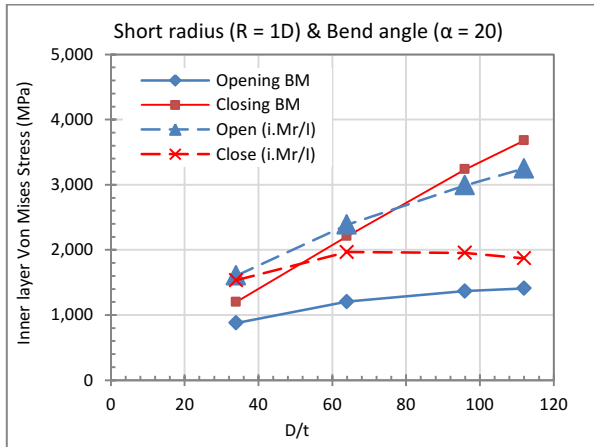


Figure 111. Maximum Von Mises stress for short radius bends with bend angle 20-degrees.

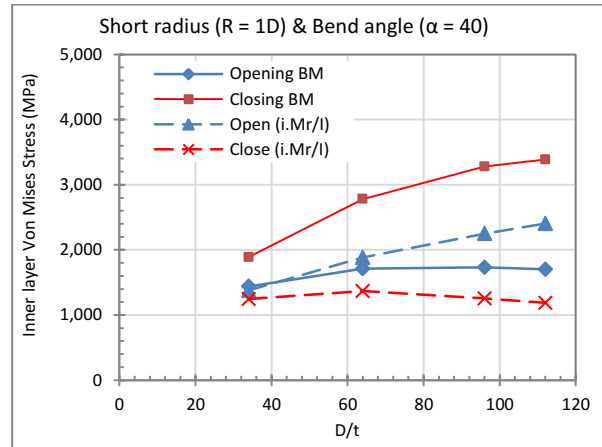


Figure 112. Maximum Von Mises stress for short radius bends with bend angle 40-degrees.

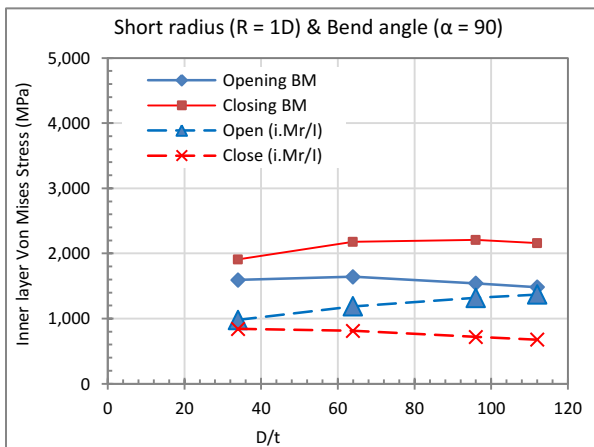


Figure 113. Maximum Von Mises stress for short radius bends with bend angle 90-degrees.

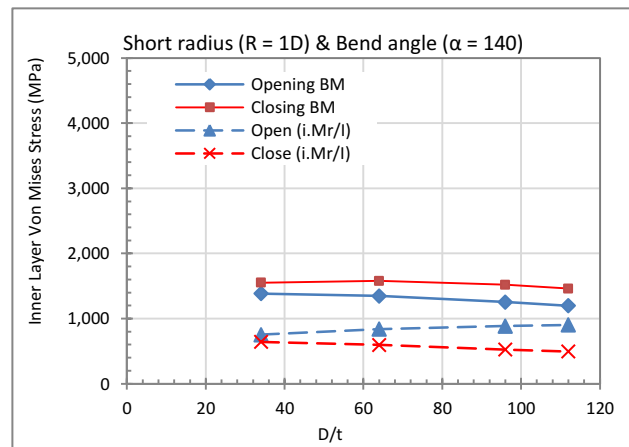


Figure 114. Maximum Von Mises stress for short radius bends with bend angle 140-degrees.

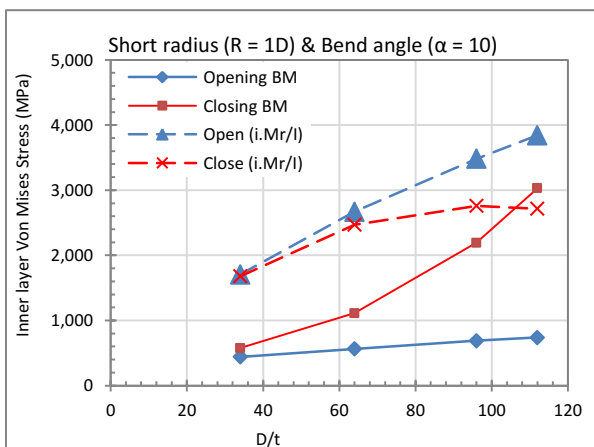


Figure 115. Maximum Von Mises stress for short radius bends with bend angle 10-degrees.

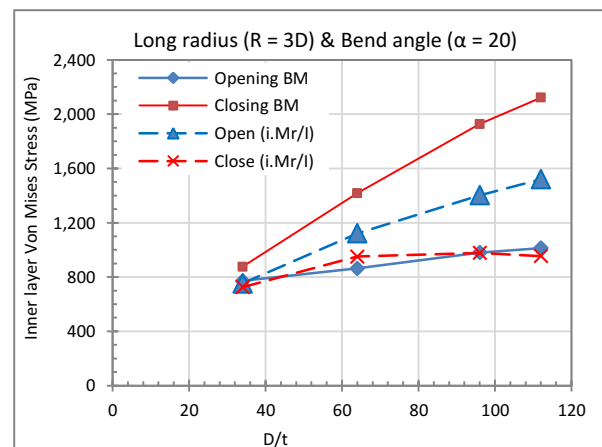


Figure 116. Maximum Von Mises stress for long radius bends with bend angle 20-degrees.

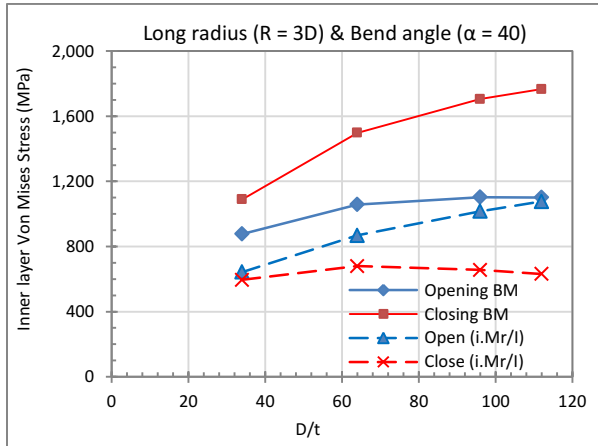


Figure 117. Maximum Von Mises stress for long radius bends with bend angle 40-degrees.

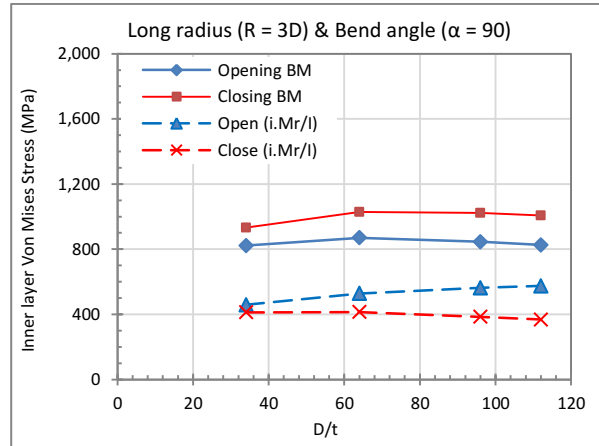


Figure 118. Maximum Von Mises stress for long radius bends with bend angle 90-degrees.

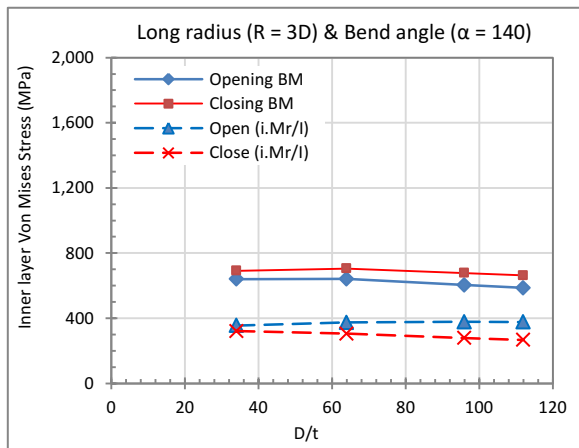


Figure 119. Maximum Von Mises stress for long radius bends with bend angle 140-degrees.

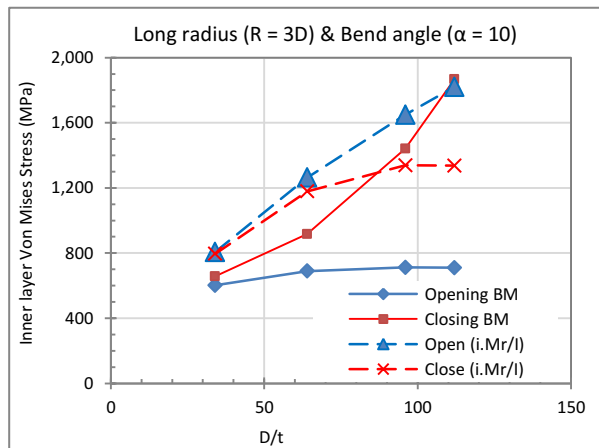


Figure 120. Maximum Von Mises stress for long radius bends with bend angle 10-degrees.

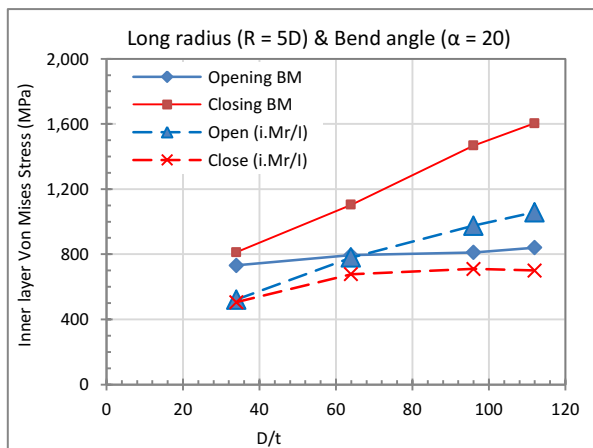


Figure 121. Maximum Von Mises stress for long radius bends with bend angle 20-degrees.

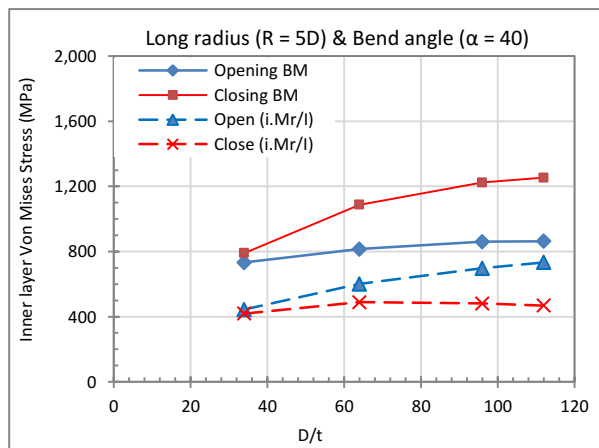


Figure 122. Maximum Von Mises stress for long radius bends with bend angle 40-degrees.

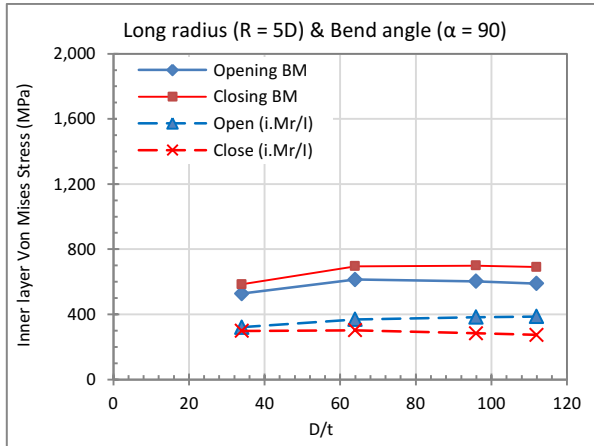


Figure 123. Maximum Von Mises stress for long radius bends with bend angle 90-degrees.

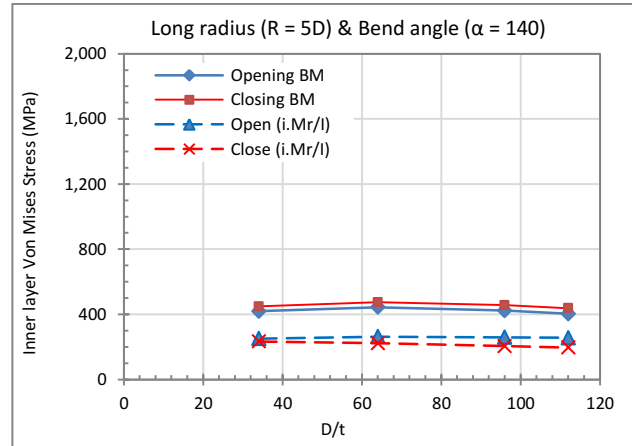


Figure 124. Maximum Von Mises stress for long radius bends with bend angle 140-degrees.

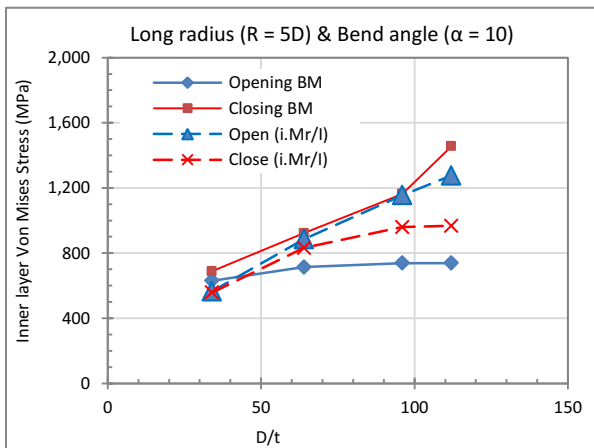


Figure 125. Maximum Von Mises stress for long radius bends with bend angle 140-degrees.

c. Outer layer stresses

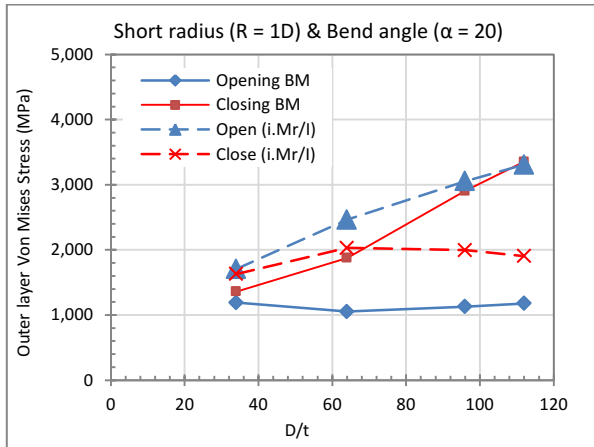


Figure 126. Maximum Von Mises stress for short radius bends with bend angle 20-degrees.

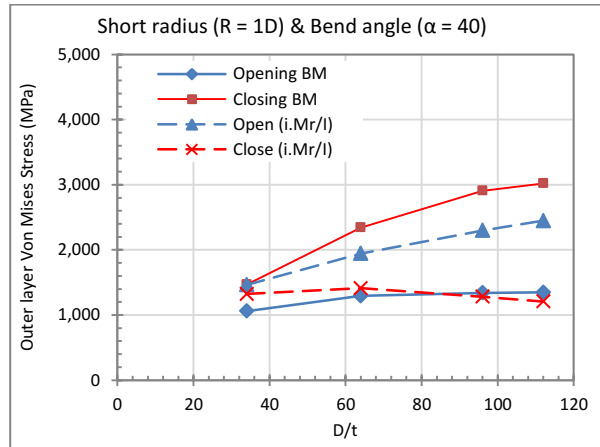


Figure 127. Maximum Von Mises stress for short radius bends with bend angle 40-degrees.

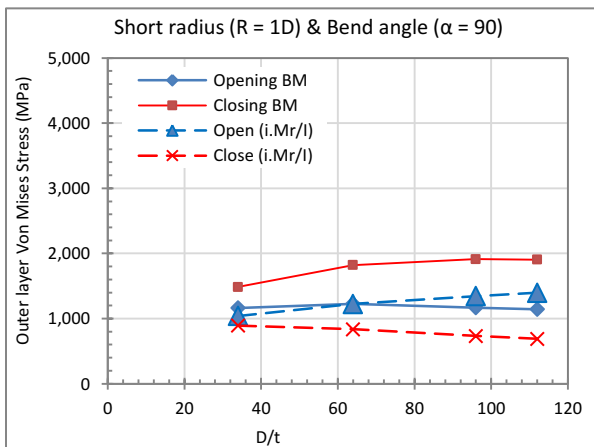


Figure 128. Maximum Von Mises stress for short radius bends with bend angle 90-degrees.

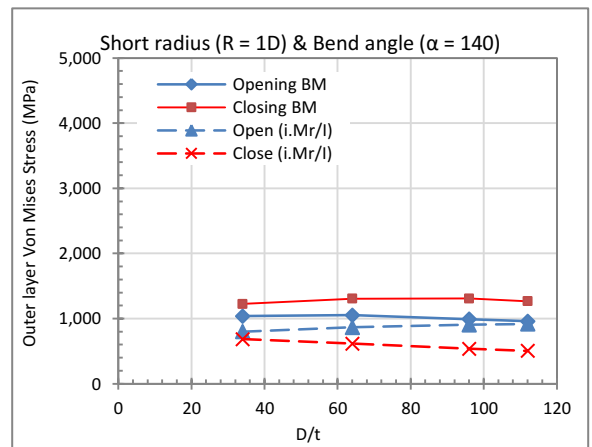


Figure 129. Maximum Von Mises stress for short radius bends with bend angle 140-degrees.

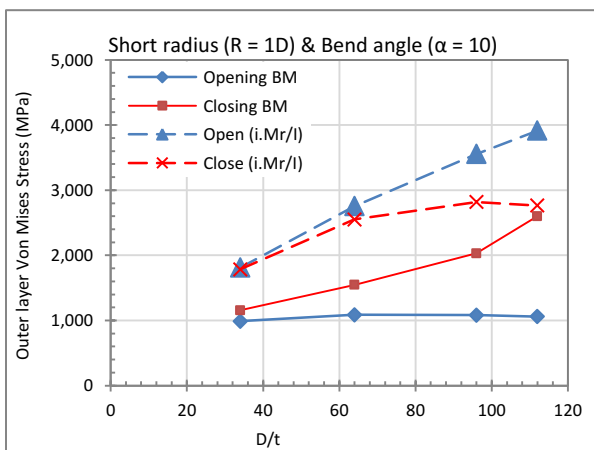


Figure 130. Maximum Von Mises stress for short radius bends with bend angle 10-degrees.

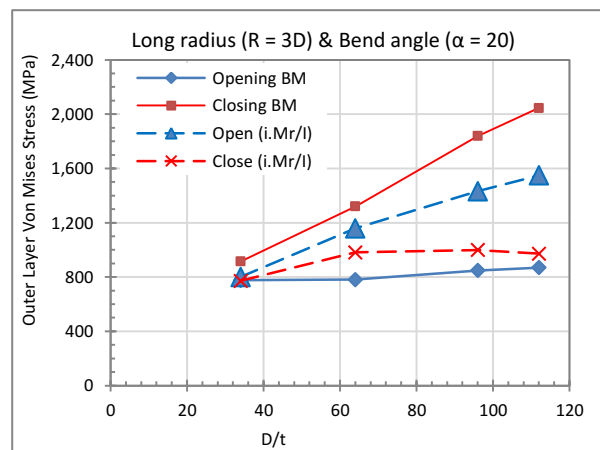


Figure 131. Maximum Von Mises stress for long radius bends with bend angle 20-degrees.

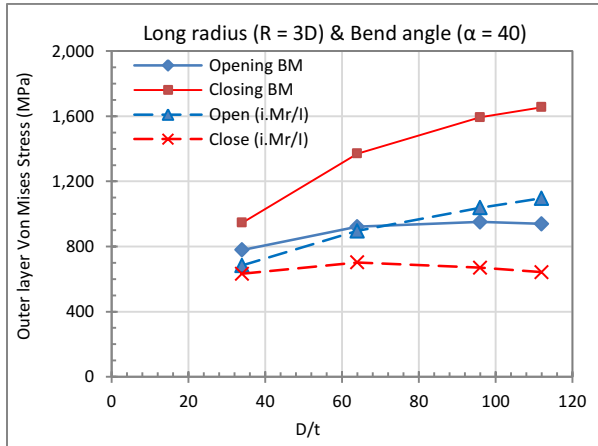


Figure 132. Maximum Von Mises stress for long radius bends with bend angle 40-degrees.

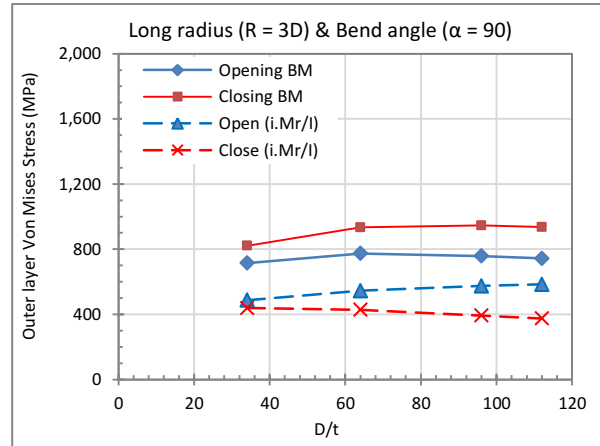


Figure 133. Maximum Von Mises stress for long radius bends with bend angle 90-degrees.

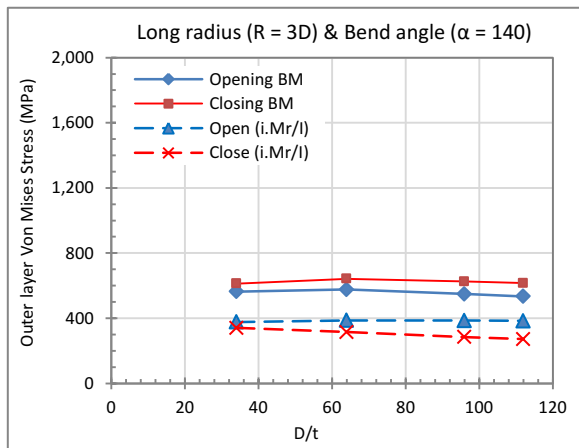


Figure 134. Maximum Von Mises stress for long radius bends with bend angle 140-degrees.

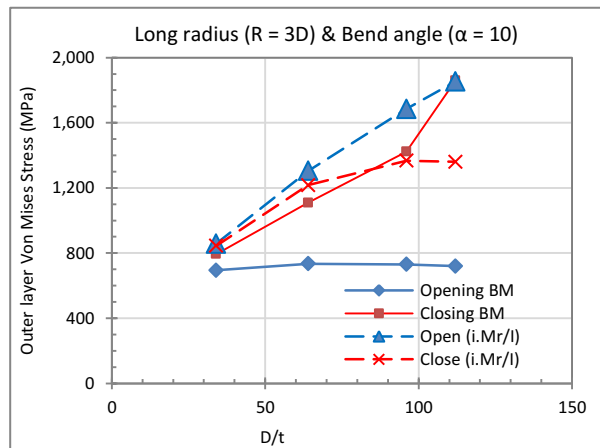


Figure 135. Maximum Von Mises stress for long radius bends with bend angle 10-degrees.

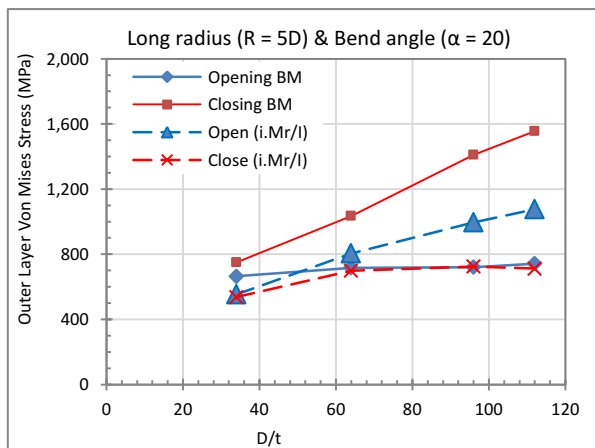


Figure 136. Maximum Von Mises stress for long radius bends with bend angle 20-degrees.

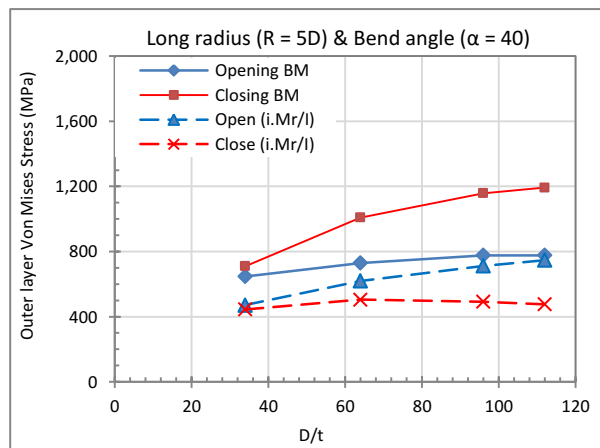


Figure 137. Maximum Von Mises stress for long radius bends with bend angle 40-degrees.

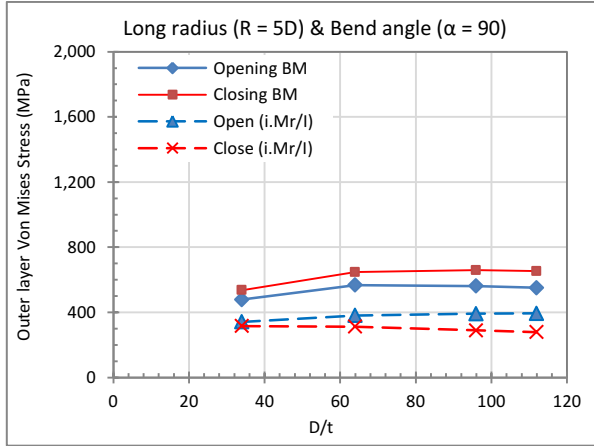


Figure 138. Maximum Von Mises stress for long radius bends with bend angle 90-degrees.

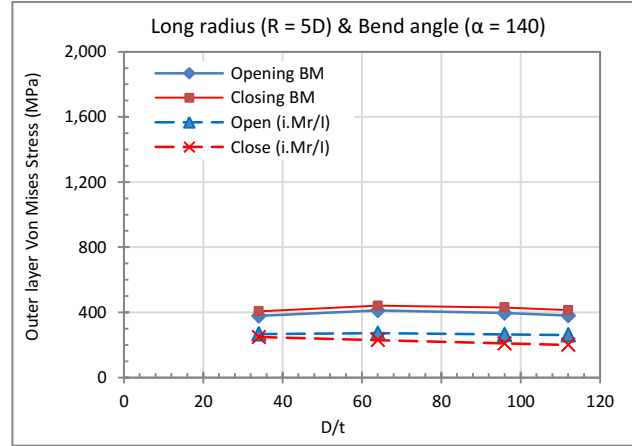


Figure 139. Maximum Von Mises stress for long radius bends with bend angle 140-degrees.

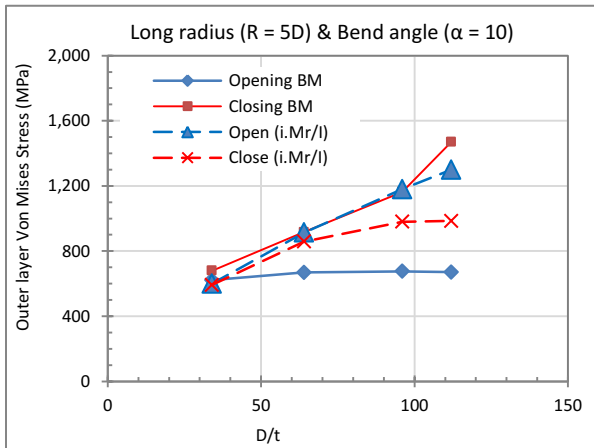


Figure 140. Maximum Von Mises stress for long radius bends with bend angle 140-degrees.

Table A.1. Ovalization ratio for pipe bends under opening and closing in-plane bending moment.

α	NPS	R	Ovalization Ratio %	
			Oval open	Oval close
10	12	323.85	3.1%	-4.1%
10	24	609.6	7.4%	-12.4%
10	36	914.4	12.1%	-25.1%
10	42	1066.8	14.3%	-31.6%
20	12	323.85	5.7%	-7.2%
20	24	609.6	12.2%	-17.4%
20	36	914.4	18.1%	-26.5%
20	42	1066.8	20.7%	-29.9%

40	12	323.85	7.9%	-7.3%
40	24	609.6	13.9%	-16.5%
40	36	914.4	18.4%	-21.3%
40	42	1066.8	20.2%	-22.8%
90	12	323.85	7.8%	-8.2%
90	24	609.6	11.5%	-11.6%
90	36	914.4	13.9%	-13.4%
90	42	1066.8	14.7%	-14.0%
140	12	323.85	6.8%	-6.6%
140	24	609.6	9.1%	-8.8%
140	36	914.4	10.6%	-9.8%
140	42	1066.8	15.9%	-10.1%
10	12	1619.25	2.8%	-3.6%
10	24	3048	6.9%	-10.9%
10	36	4572	11.4%	-22.8%
10	42	5334	13.7%	-29.0%
20	12	1619.25	4.7%	-5.8%
20	24	3048	11.0%	-15.2%
20	36	4572	17.1%	-24.1%
20	42	5334	19.9%	-27.5%
40	12	1619.25	6.3%	-6.9%
40	24	3048	13.0%	-14.9%
40	36	4572	18.2%	-19.7%
40	42	5334	20.1%	-21.6%
90	12	1619.25	5.1%	-5.5%
90	24	3048	9.9%	-10.0%
90	36	4572	12.5%	-12.0%
90	42	5334	13.4%	-12.6%
140	12	1619.25	4.2%	-4.2%
140	24	3048	7.0%	-6.9%
140	36	4572	8.6%	-8.1%
140	42	5334	8.9%	-8.3%

APPENDIX (B): DEVELOPED STRESS INTENSIFICATION FACTORS

1.1. Opening Bending Moment

1.1.1. Comparison between the FEA and SIF proposed models

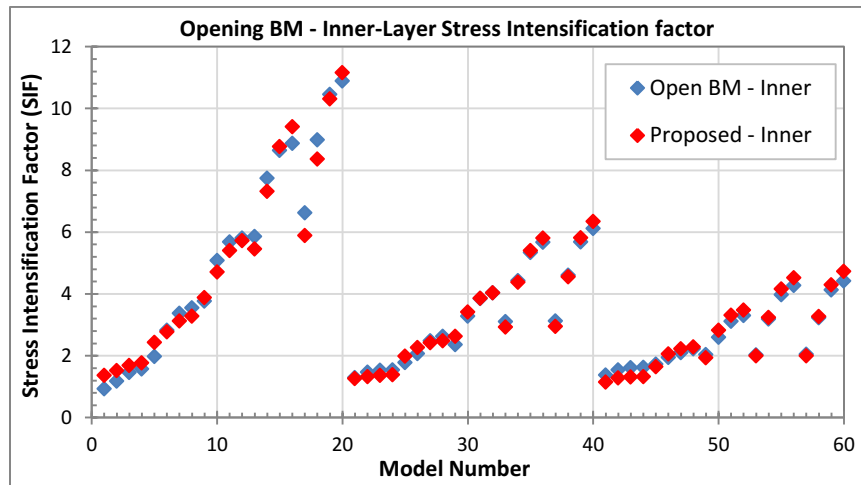


Figure 141. Proposed factor compared to FEA results for the inner layer of pipe bends

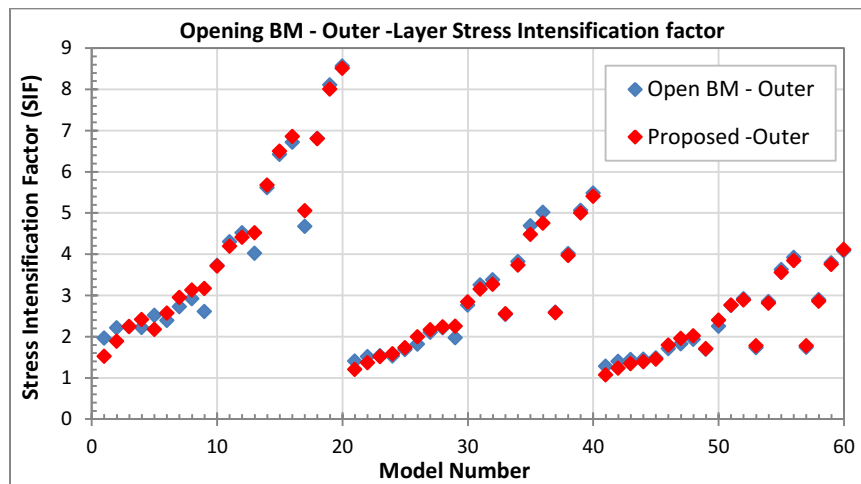


Figure 142. Proposed factor compared to FEA results for the Mid-layer of pipe bends

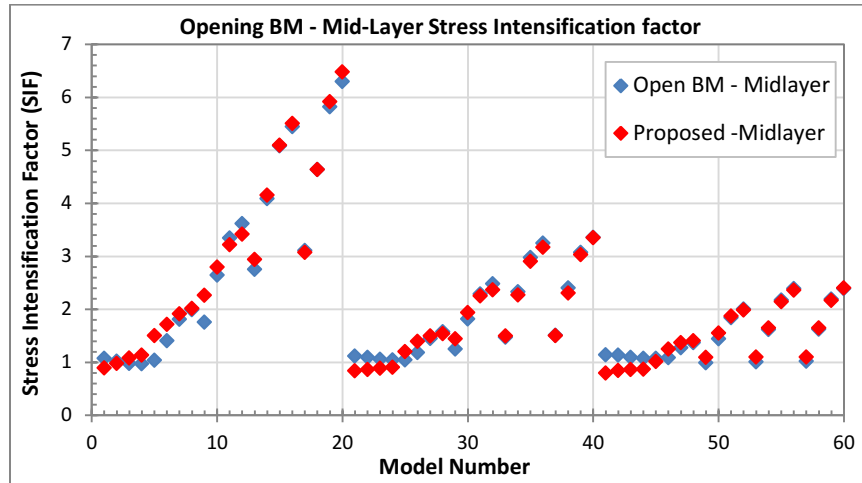


Figure 143. Proposed factor compared to FEA results for the outer layer of pipe bends

1.1.2. The FEA plotted against the proposed SIF formula for each set of models

1.1.2.1. Mid-layer results

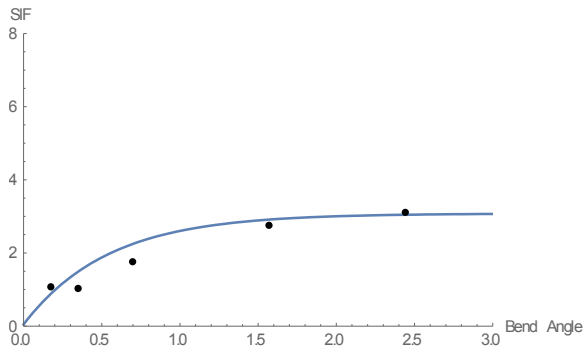


Figure 144. NPS 12 and R=1D

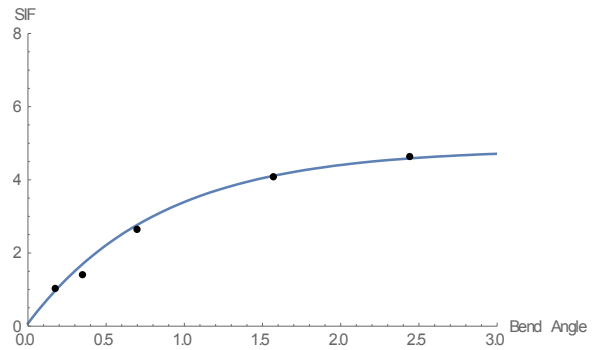


Figure 145. NPS 24 and R=1D

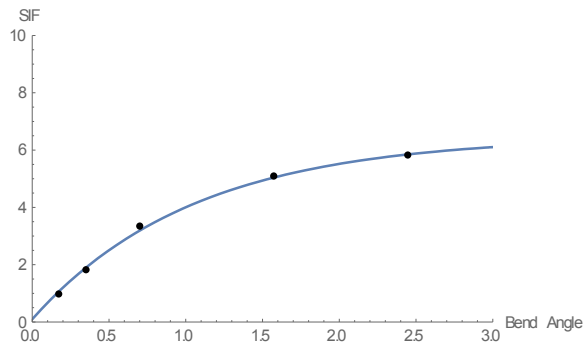


Figure 146. NPS 36 and R=1D

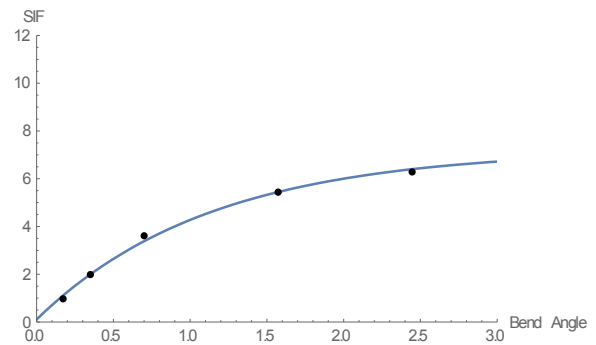


Figure 147. NPS 42 and R=1D

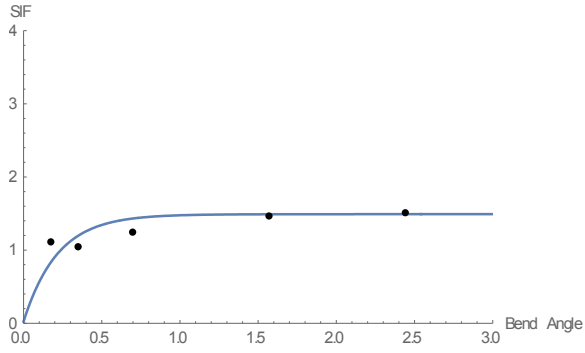


Figure 148. NPS 12 and R=3D

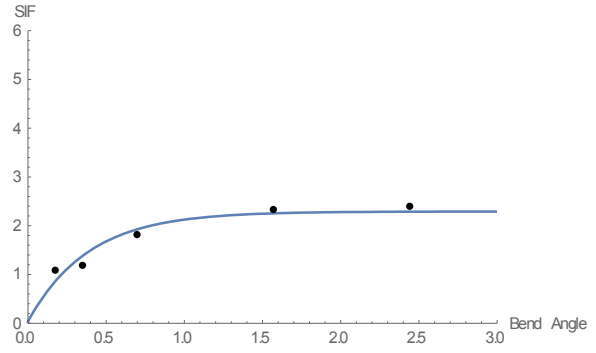


Figure 149. NPS 24 and R=3D

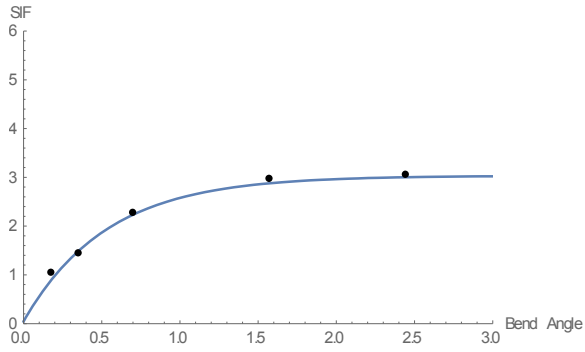


Figure 150. NPS 36 and R=3D

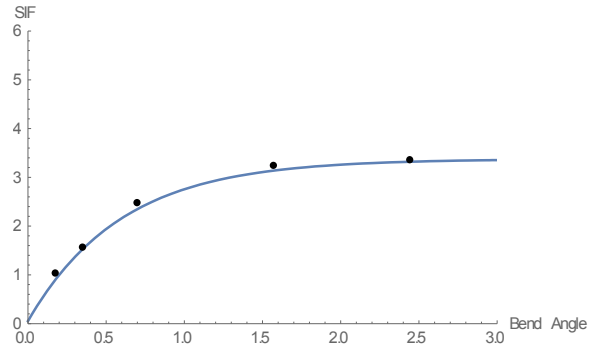


Figure 151. NPS 42 and R=3D

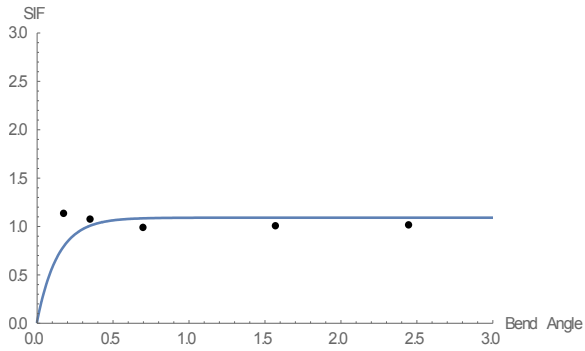


Figure 152. NPS 12 and R=5D

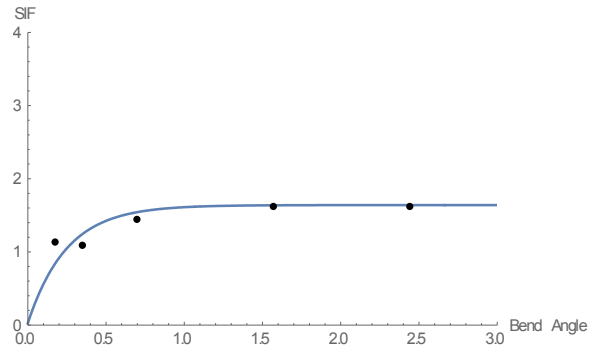


Figure 153. NPS 24 and R=5D

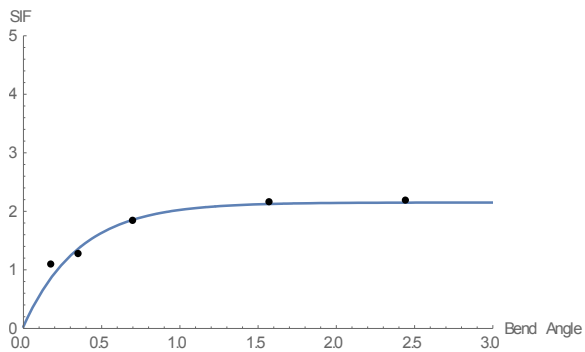


Figure 154. NPS 36 and R=5D

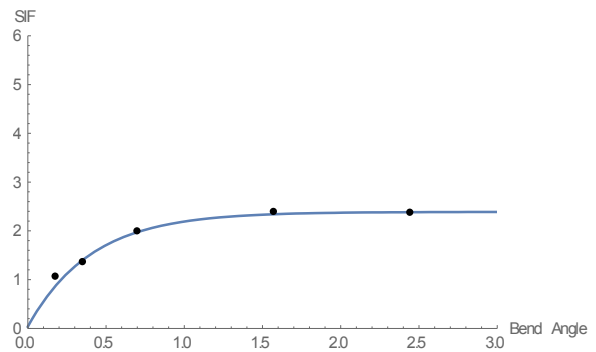


Figure 155. NPS 42 and R=5D

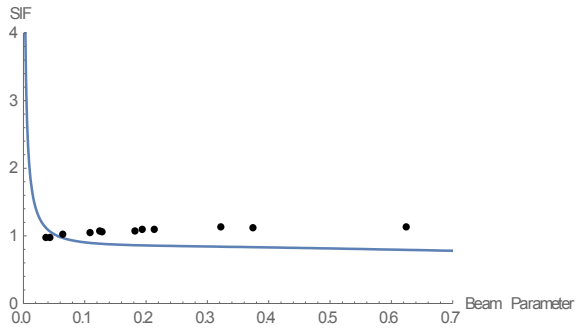


Figure 156. Bend angle 10°

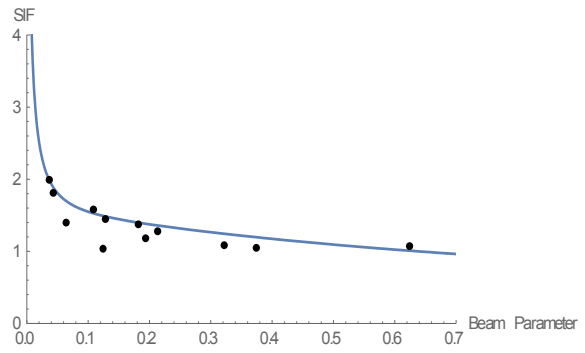


Figure 157. Bend angle 20°

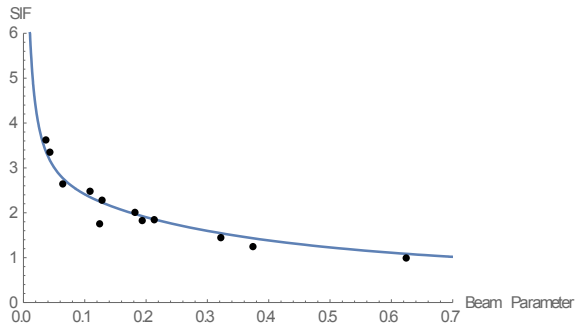


Figure 158. Bend angle 40°

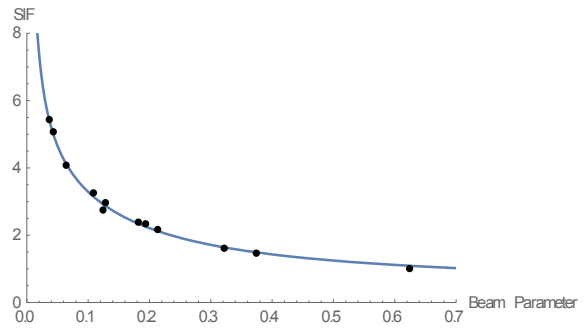


Figure 159. Bend angle 90°

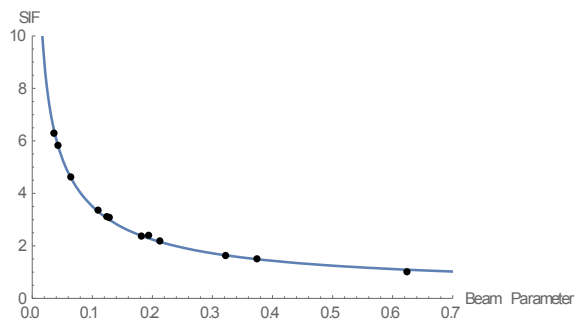


Figure 160. Bend angle 140°

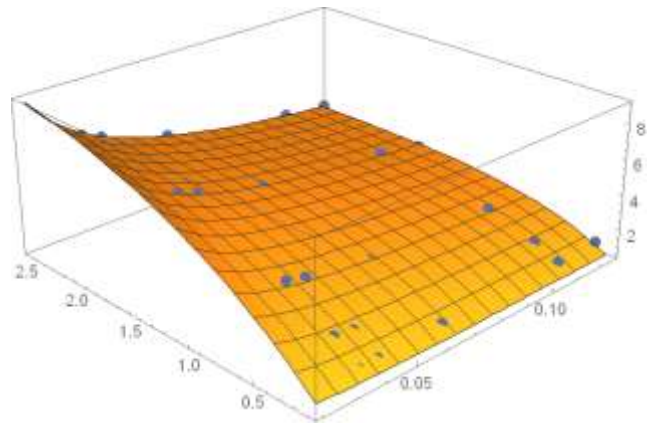


Figure 161. The proposed SIF formula surface

1.1.2.2. Inner layer results

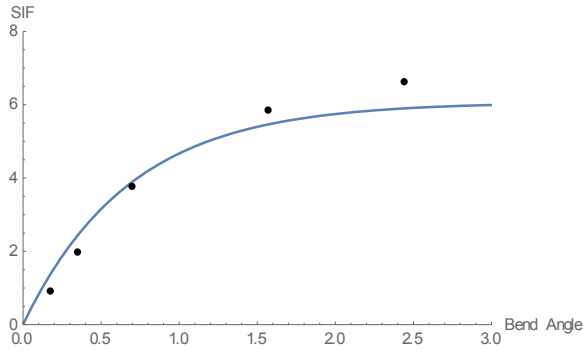


Figure 162. NPS 12 and R=1D

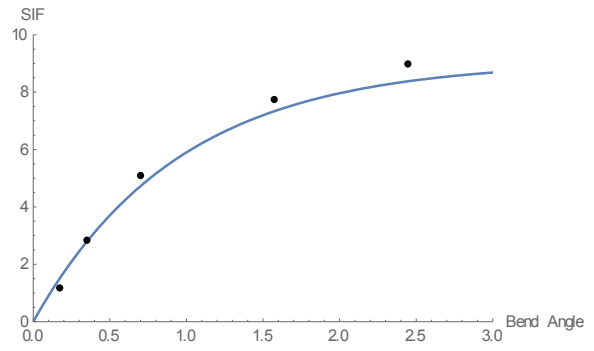


Figure 163. NPS 24 and R=1D

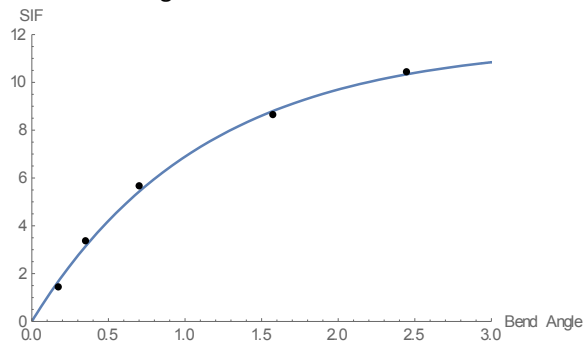


Figure 164. NPS 36 and R=1D

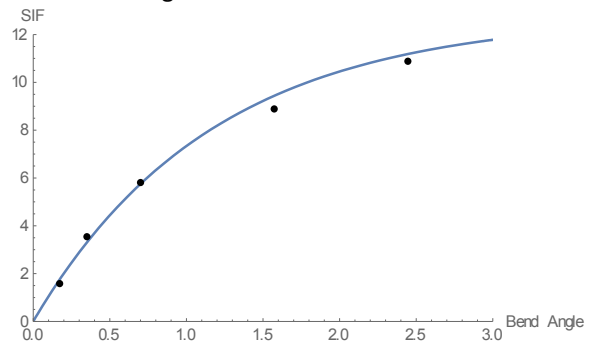


Figure 165. NPS 42 and R=1D

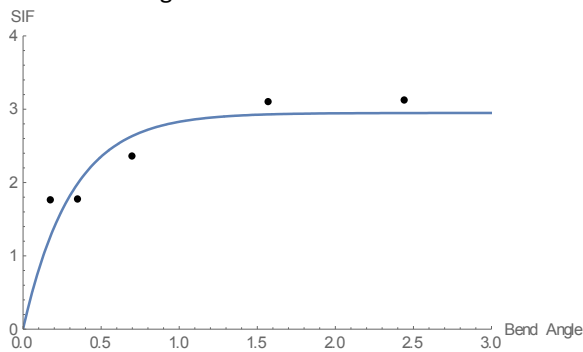


Figure 166. NPS 12 and R=3D

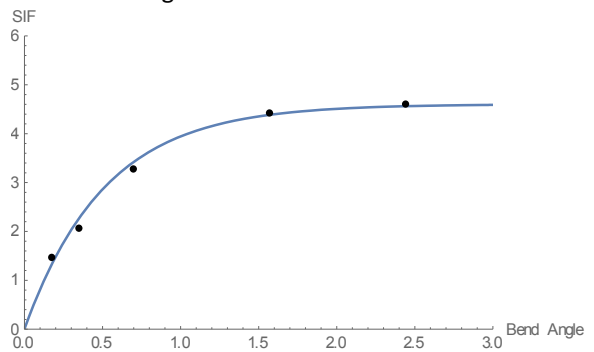


Figure 167. NPS 24 and R=3D

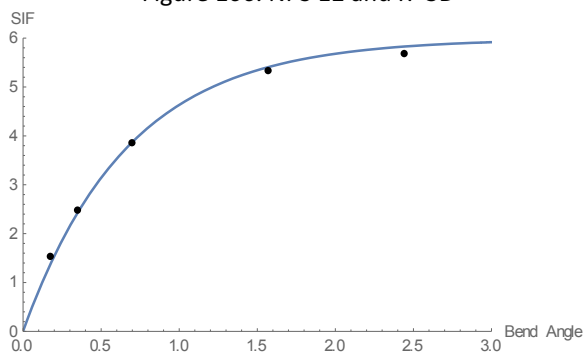


Figure 168. NPS 36 and R=3D

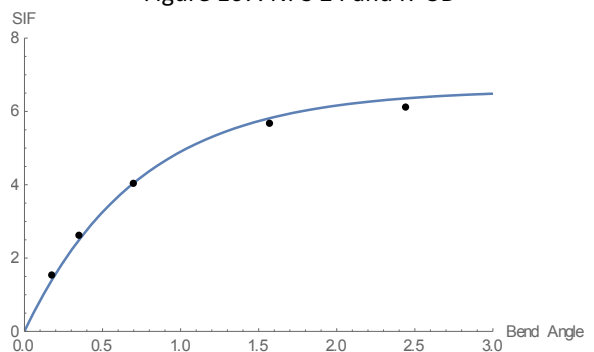


Figure 169. NPS 42 and R=3D

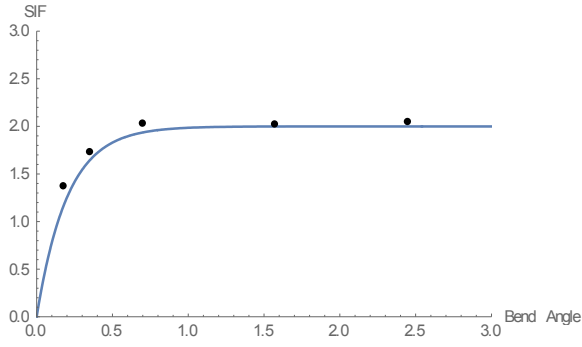


Figure 170. NPS 12 and R=5D

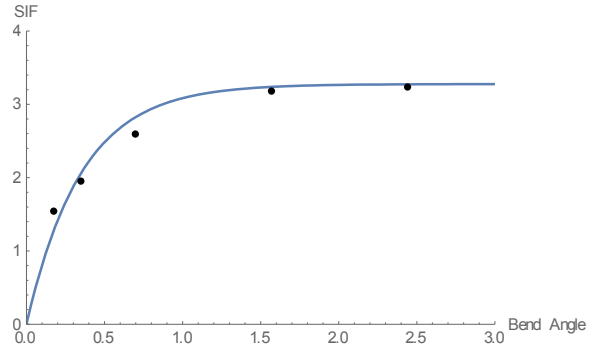


Figure 171. NPS 24 and R=5D

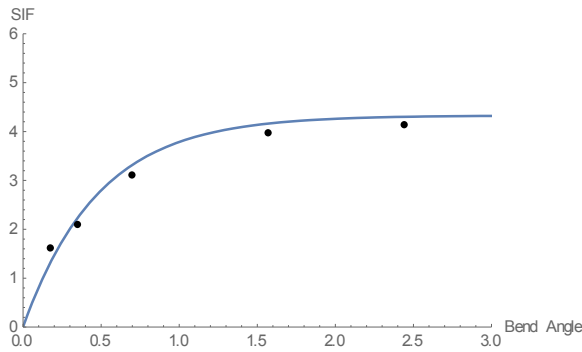


Figure 172. NPS 36 and R=5D

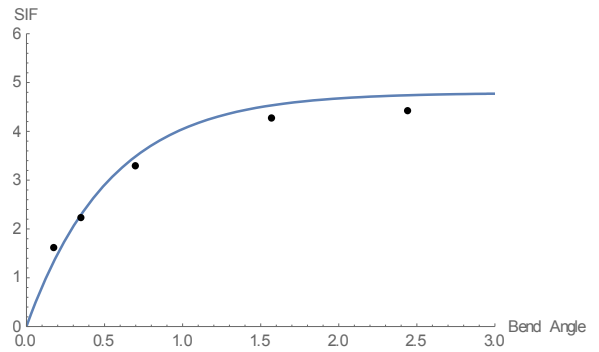


Figure 173. NPS 42 and R=5D

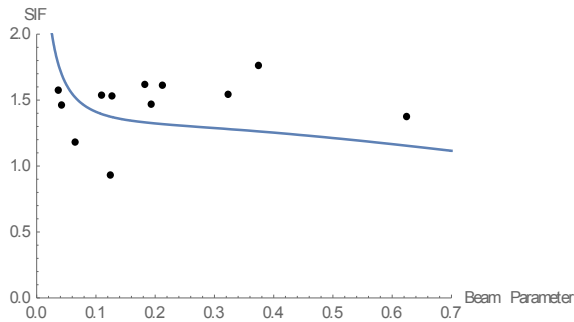


Figure 174. Bend angle 10°

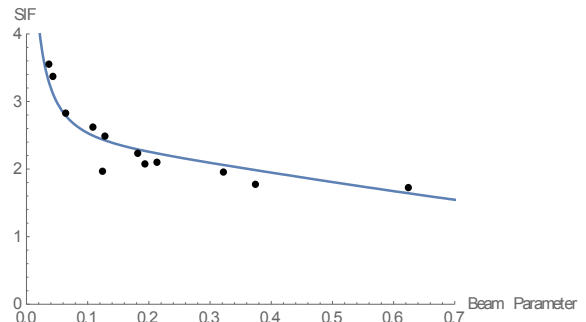


Figure 175. Bend angle 20°

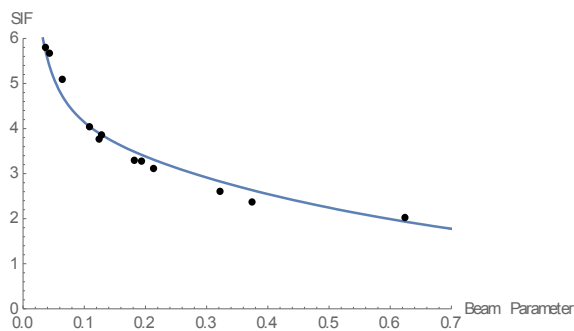


Figure 176. Bend angle 40°

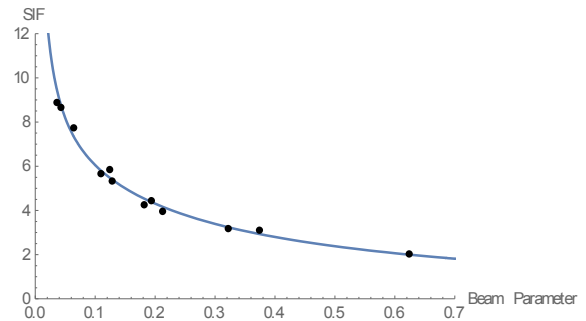


Figure 177. Bend angle 90°

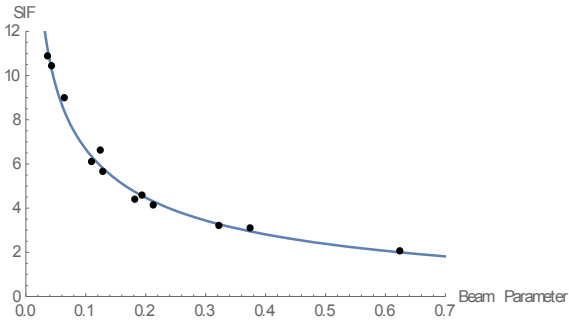


Figure 178. Bend angle 140°

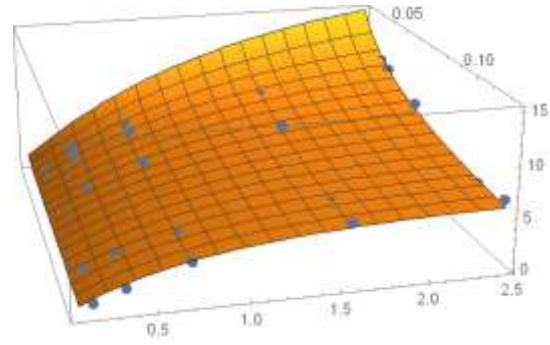


Figure 179. The proposed SIF formula surface

1.1.2.3. Outer layer results

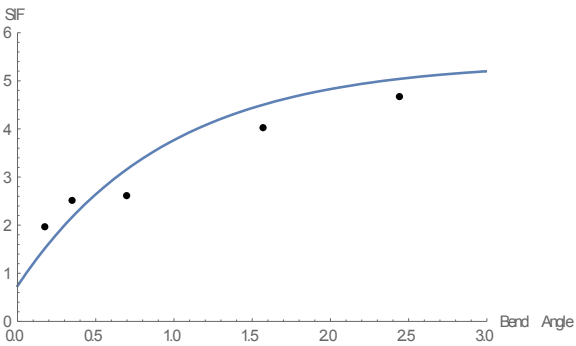


Figure 180. NPS 12 and R=1D

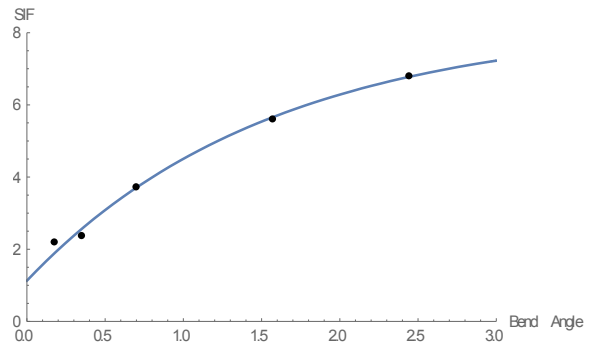


Figure 181. NPS 24 and R=1D

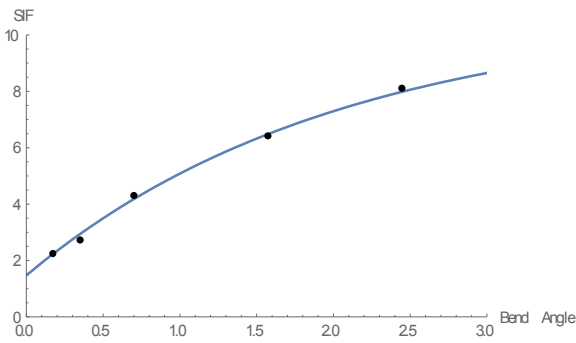


Figure 182. NPS 36 and R=1D

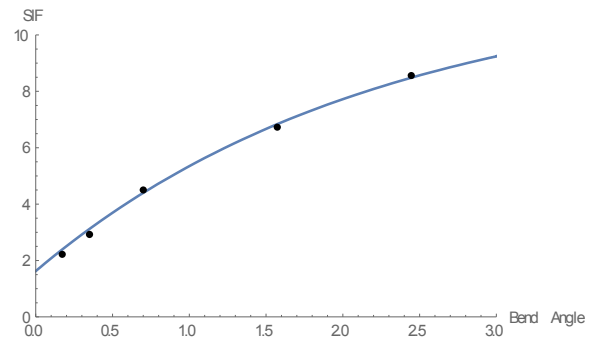


Figure 183. NPS 42 and R=1D

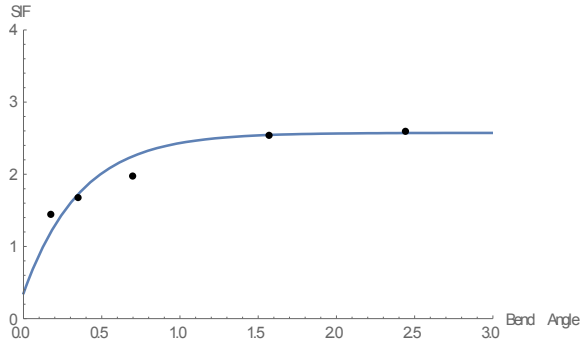


Figure 184. NPS 12 and R=3D

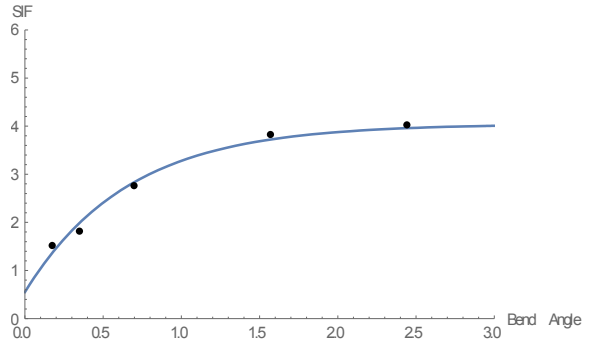


Figure 185. NPS 24 and R=3D

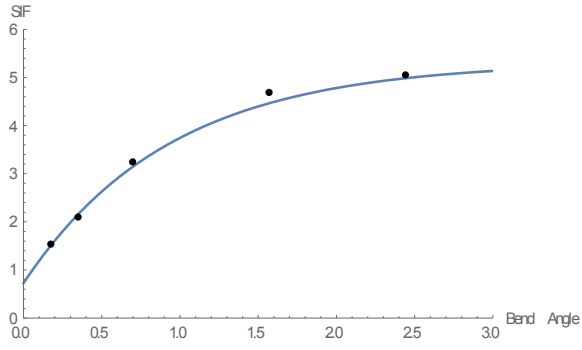


Figure 186. NPS 36 and R=3D

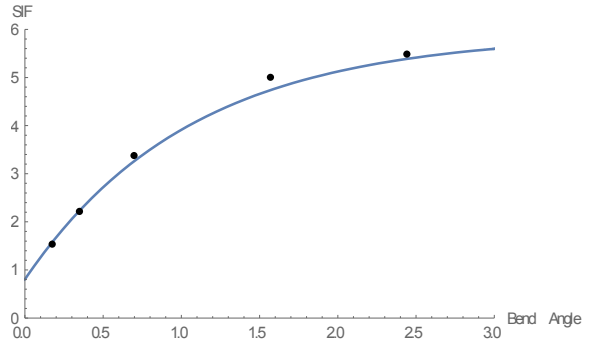


Figure 187. NPS 42 and R=3D

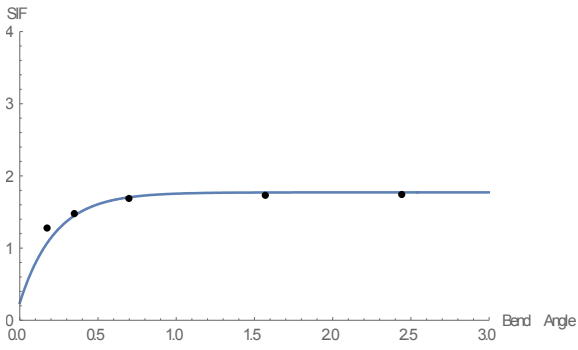


Figure 188. NPS 12 and R=5D

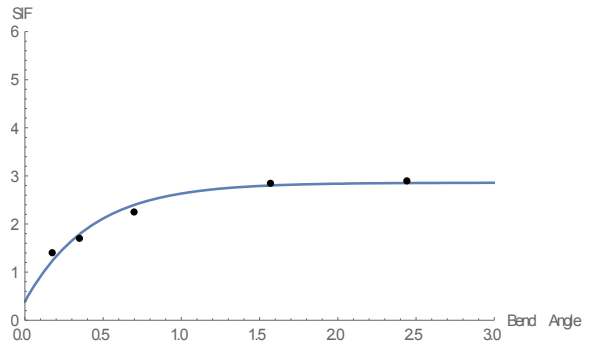


Figure 189. NPS 24 and R=5D

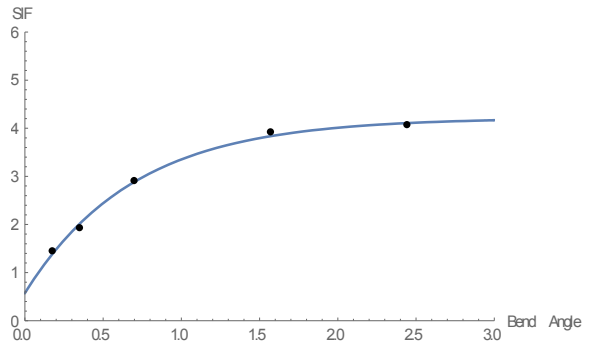
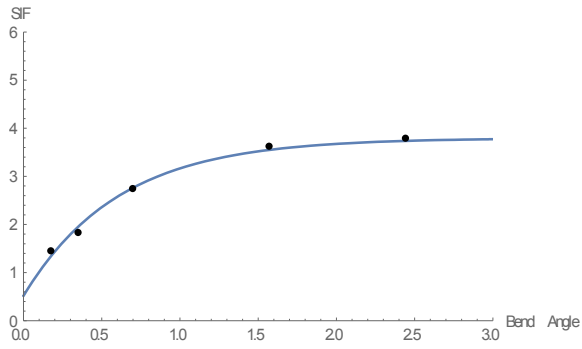


Figure 190. NPS 36 and R=5D

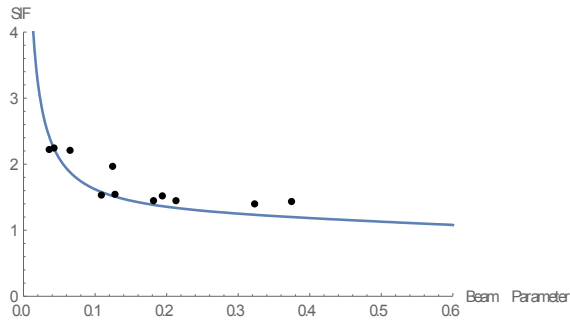


Figure 191. NPS 42 and R=5D

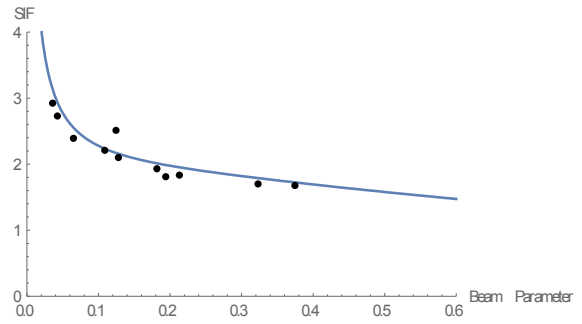


Figure 192. Bend angle 10°

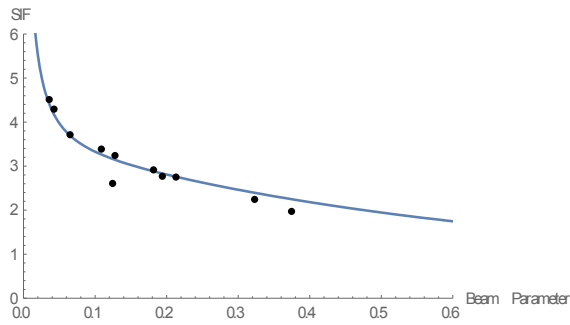


Figure 193. Bend angle 20°

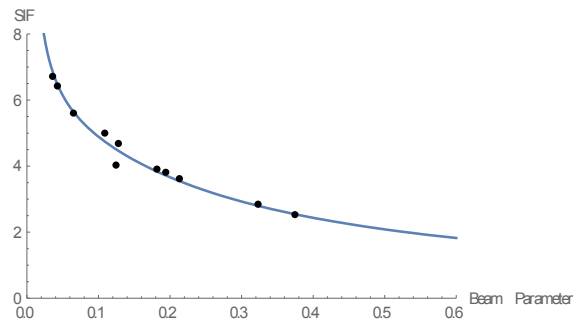


Figure 194. Bend angle 40°

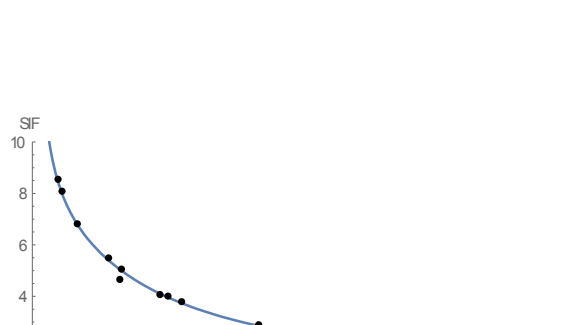


Figure 195. Bend angle 90°

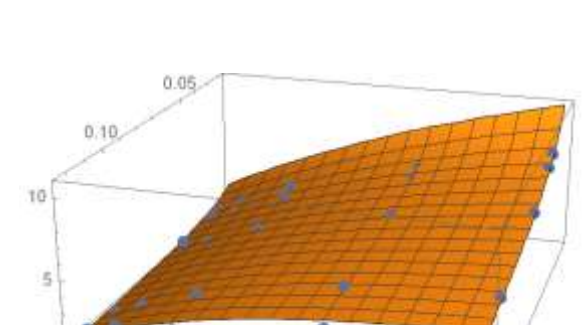


Figure 196. Bend angle 140°

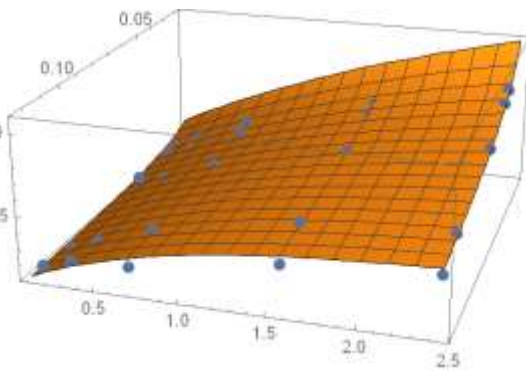
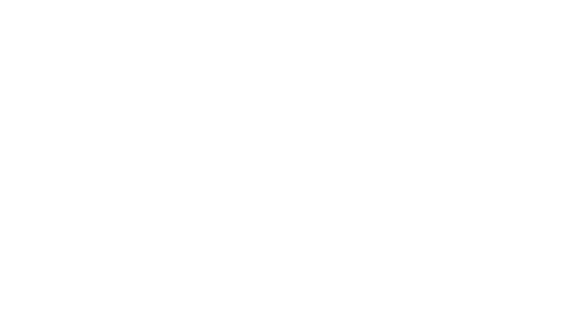


Figure 197. The proposed SIF formula surface

1.2. Closing Bending Moment

1.2.1. Comparison between the FEA and SIF proposed models

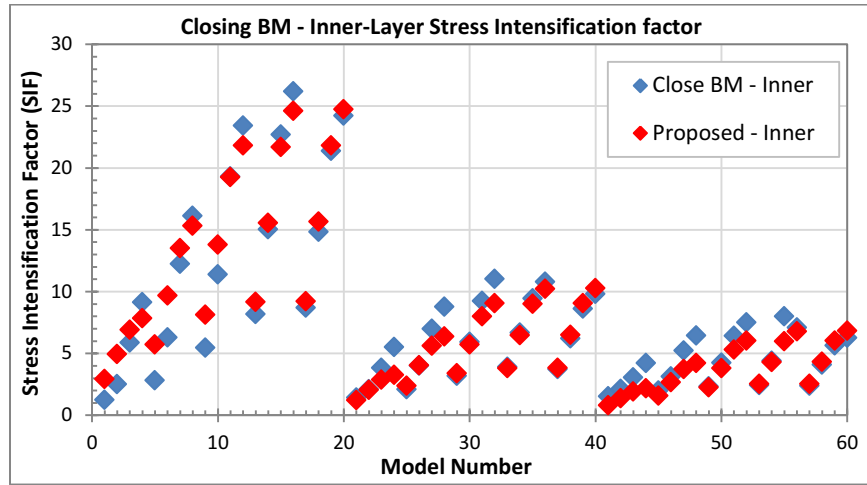


Figure 198. Proposed factor compared to FEA results for the inner layer of pipe bends

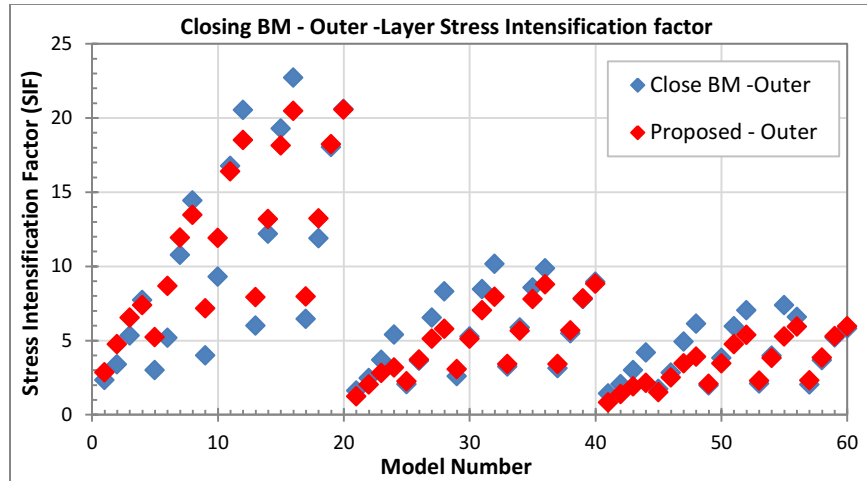


Figure 199. Proposed factor compared to FEA results for the outer layer of pipe bends

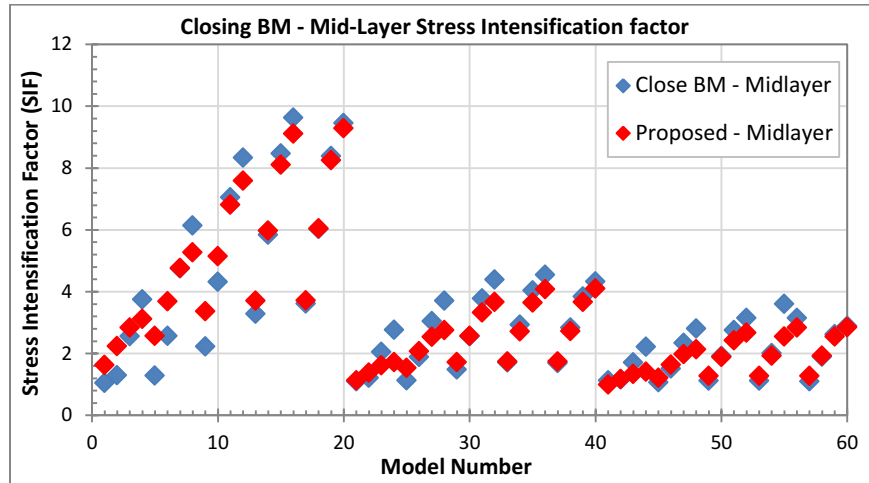


Figure 200. Proposed factor compared to FEA results for the Mid- layer of pipe bends

1.2.2. The FEA plotted against the proposed SIF formula for each set of models

1.2.2.1. Mid-layer results

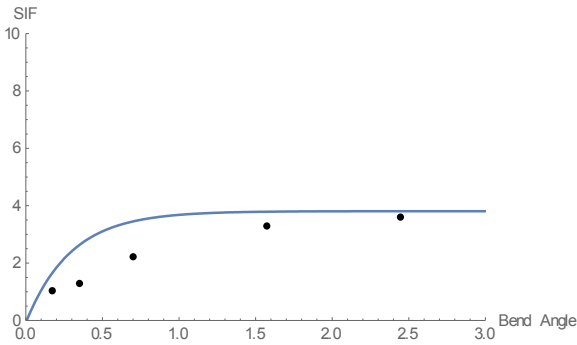


Figure 201. NPS 12 and R=1D

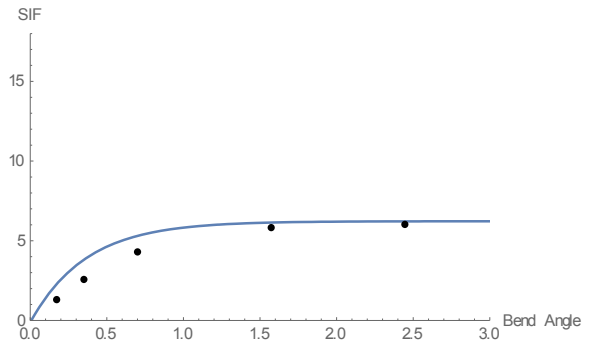


Figure 202. NPS 24 and R=1D

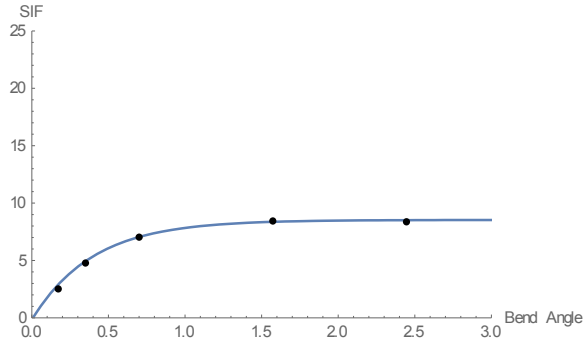


Figure 203. NPS 36 and R=1D

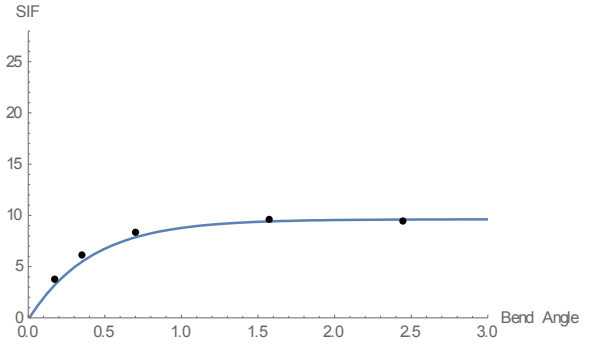


Figure 204. NPS 42 and R=1D

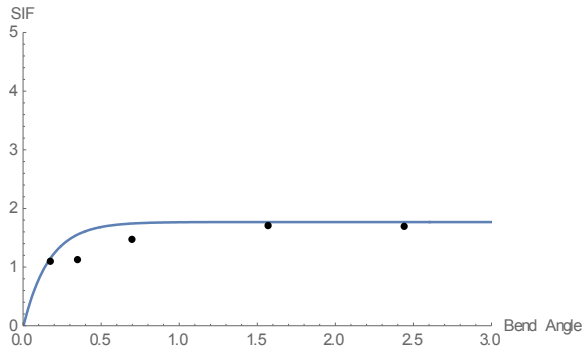


Figure 205. NPS 12 and R=3D

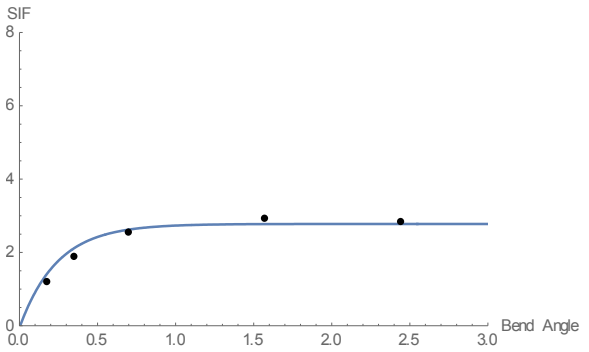


Figure 206. NPS 24 and R=3D

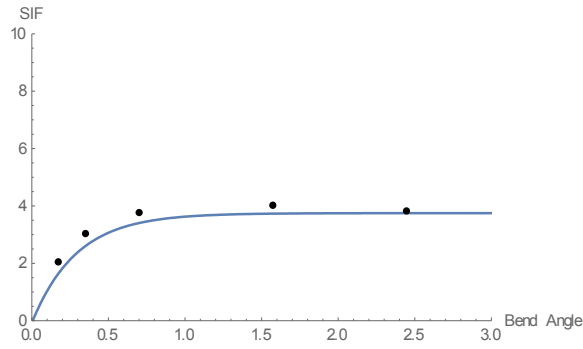


Figure 207. NPS 36 and R=3D

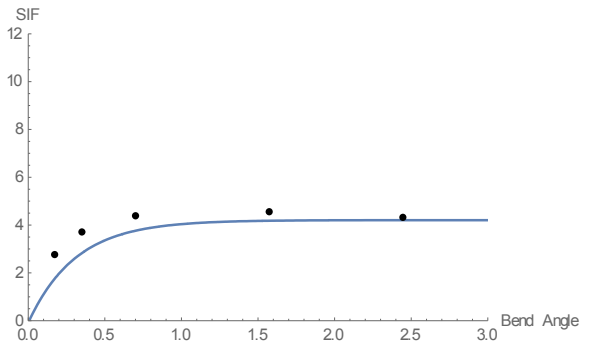


Figure 208. NPS 42 and R=3D

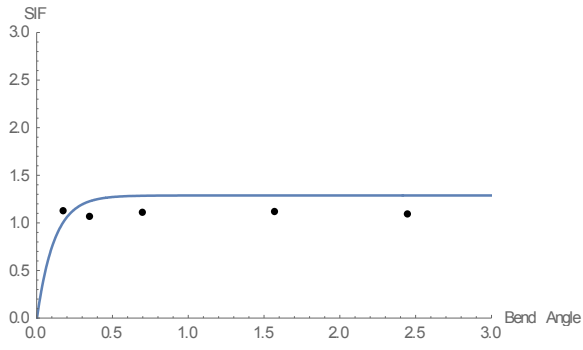


Figure 209. NPS 12 and R=5D

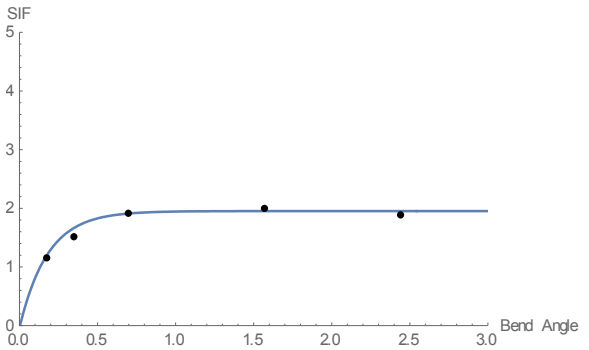


Figure 210. NPS 24 and R=5D

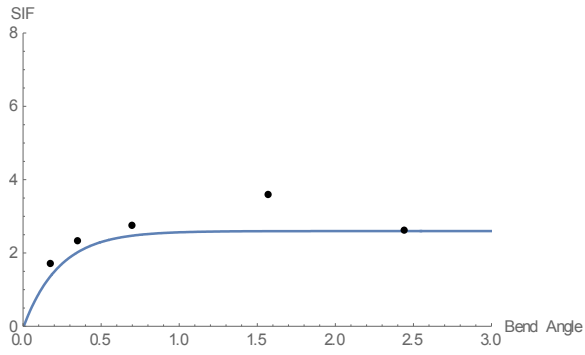


Figure 211. NPS 36 and R=5D

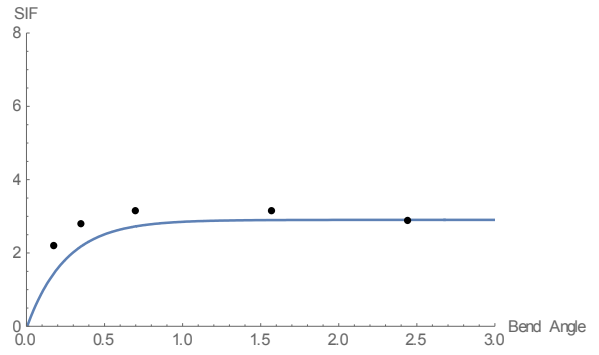


Figure 212. NPS 42 and R=5D

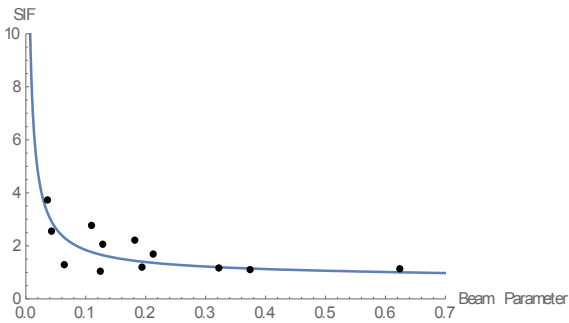


Figure 213. Bend angle 10°

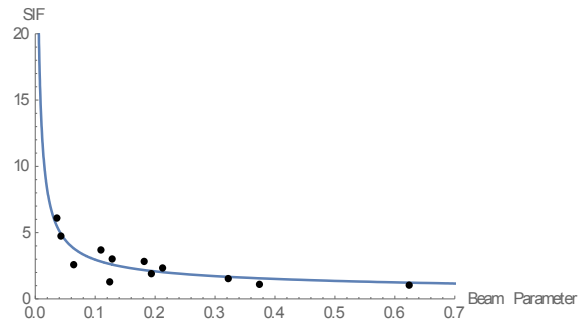


Figure 214. Bend angle 20°

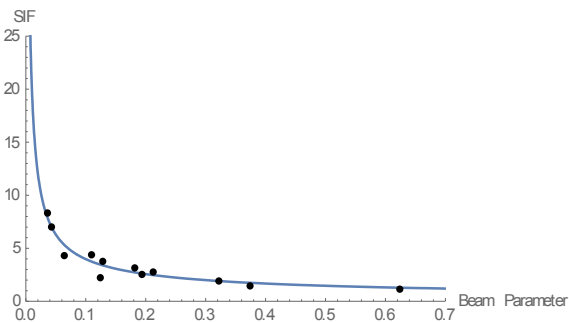


Figure 215. Bend angle 40°

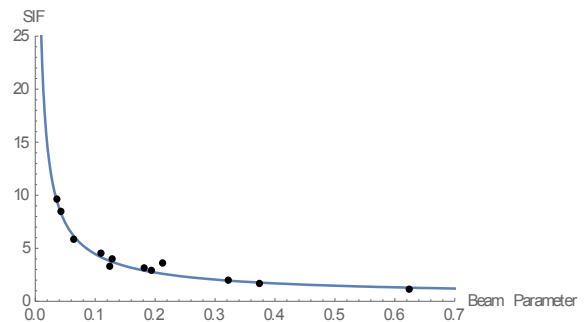


Figure 216. Bend angle 90°

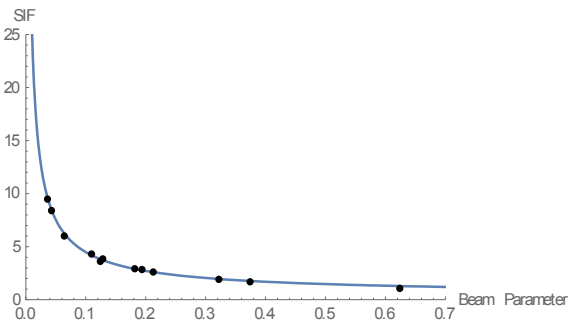


Figure 217. Bend angle 140°

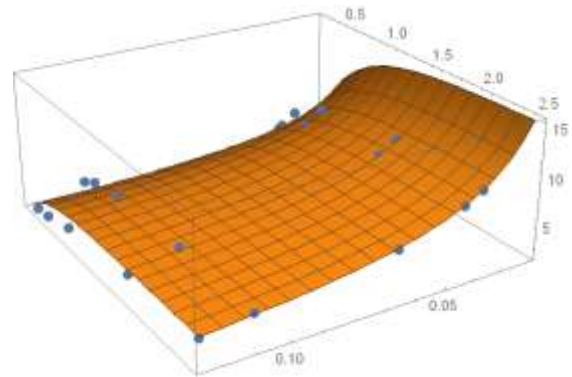


Figure 218. The proposed SIF formula surface

1.2.2.2. Inner layer results

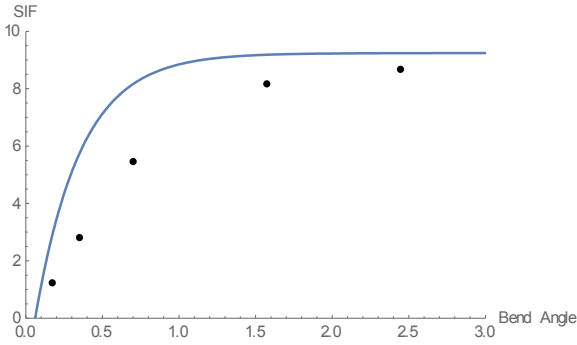


Figure 219. NPS 12 and R=1D

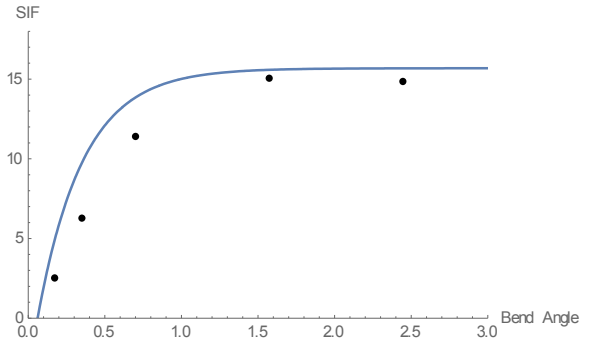


Figure 220. NPS 24 and R=1D

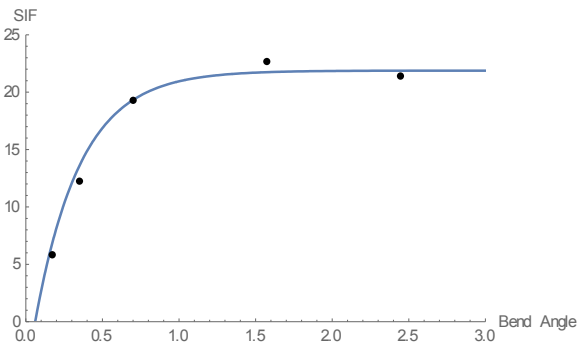


Figure 221. NPS 36 and R=1D

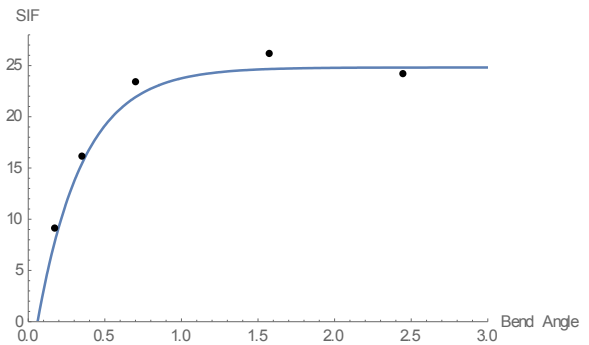


Figure 222. NPS 42 and R=1D

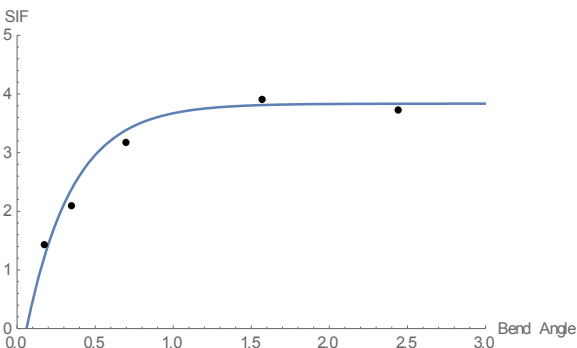


Figure 223. NPS 12 and R=3D

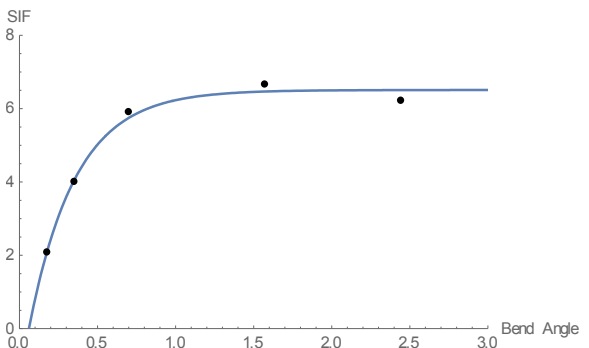


Figure 224. NPS 24 and R=3D

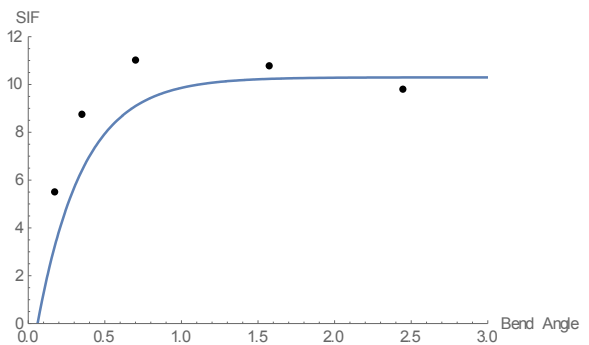
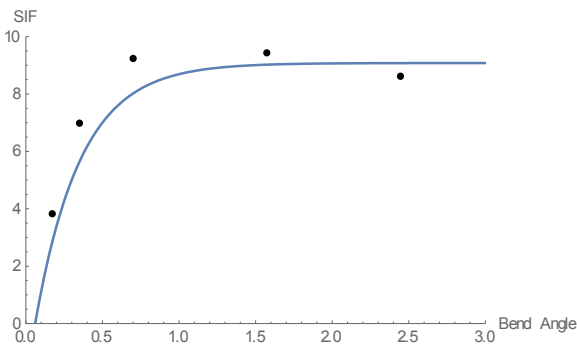


Figure 225. NPS 36 and R=3D

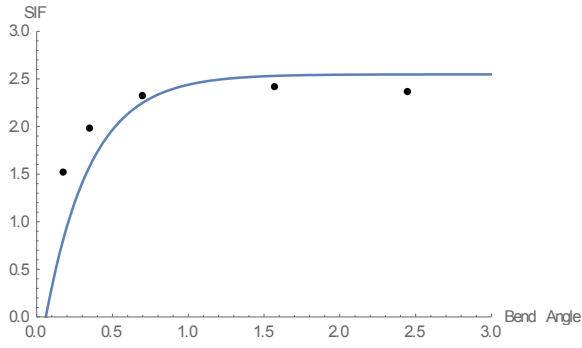


Figure 226. NPS 42 and R=3D

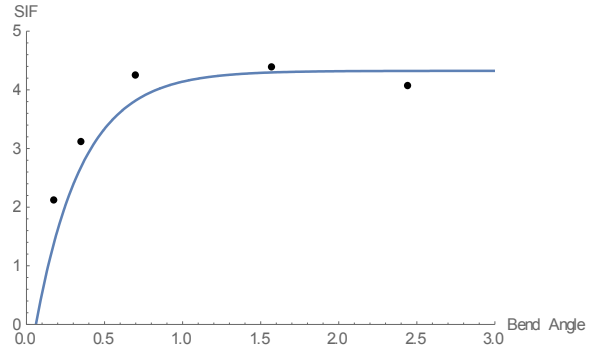


Figure 227. NPS 12 and R=5D

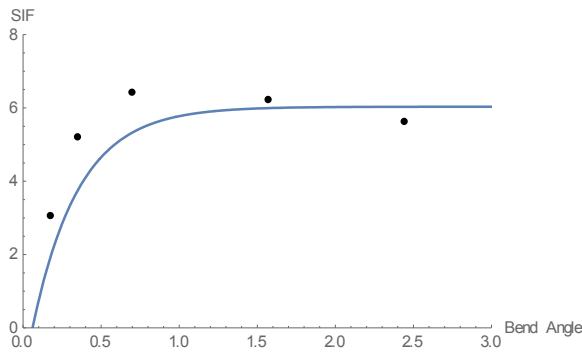


Figure 228. NPS 24 and R=5D

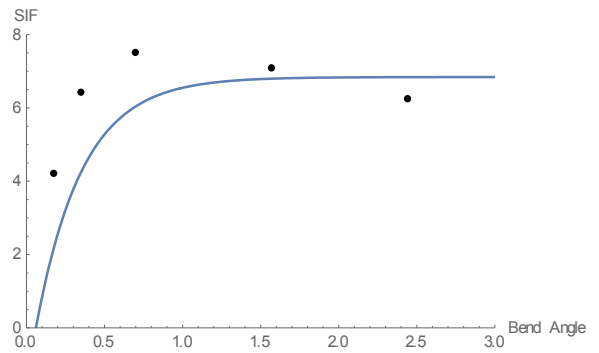


Figure 229. NPS 36 and R=5D

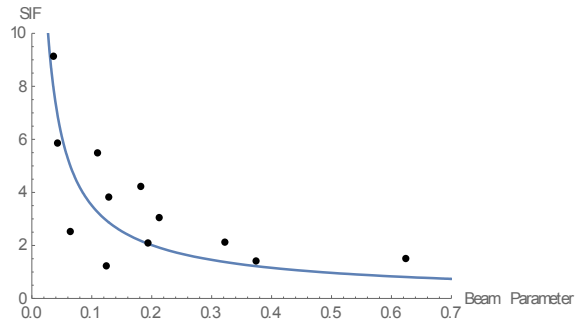


Figure 230. NPS 42 and R=5D

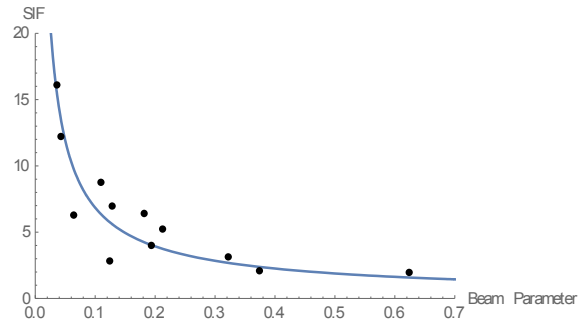


Figure 231. Bend angle 10°

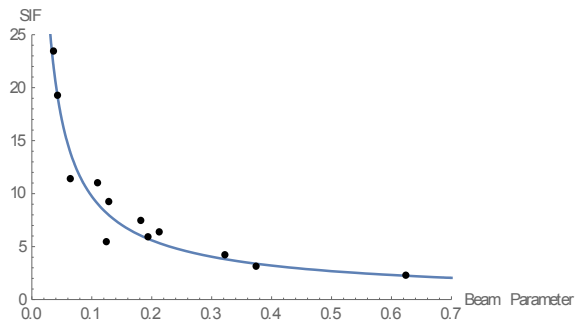


Figure 232. Bend angle 20°

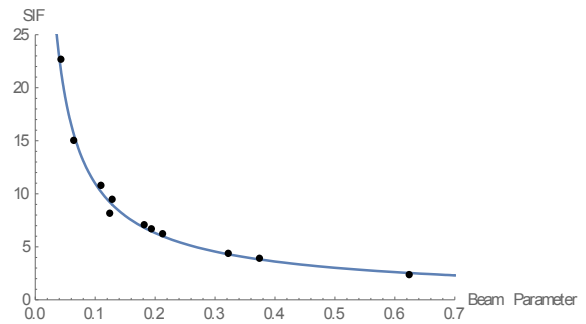


Figure 233. Bend angle 40°

Figure 234. Bend angle 90°

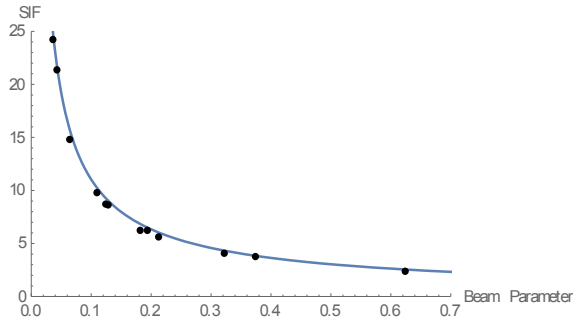


Figure 235. Bend angle 140°

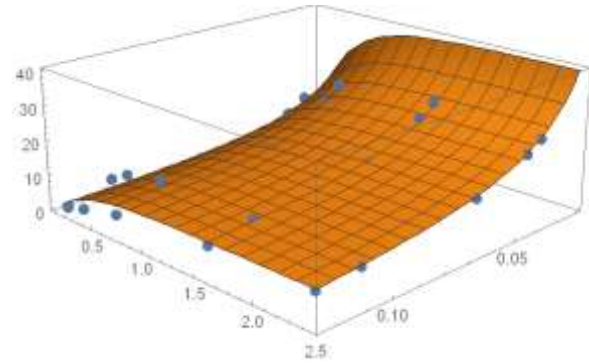


Figure 236. The proposed SIF formula surface

1.2.2.3. Outer layer results

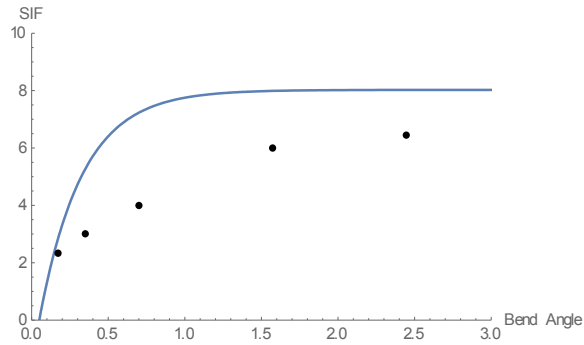


Figure 237. NPS 12 and R=1D

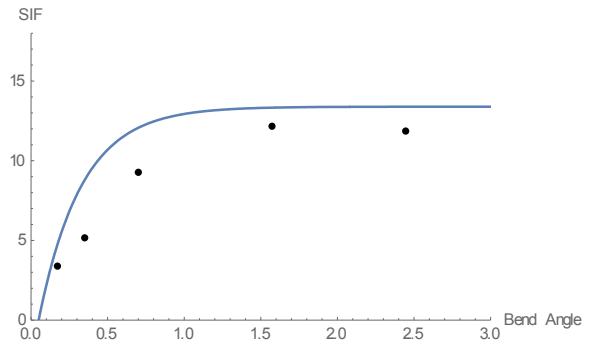


Figure 238. NPS 24 and R=1D

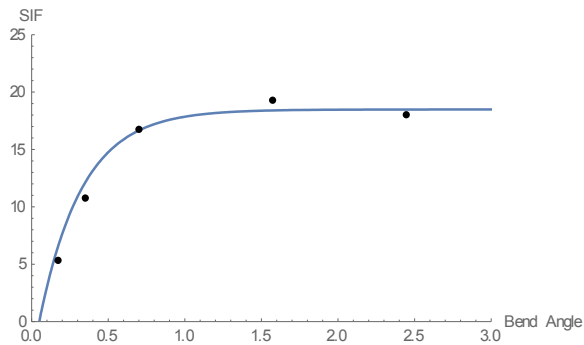


Figure 239. NPS 36 and R=1D

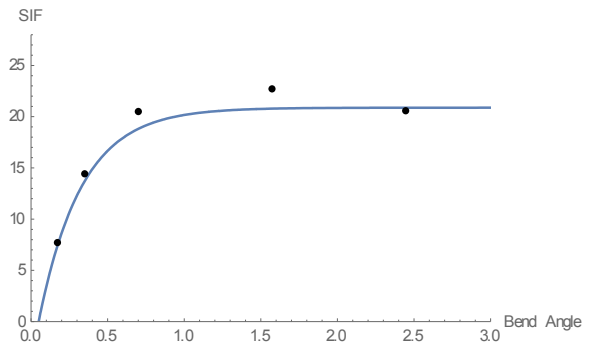


Figure 240. NPS 42 and R=1D

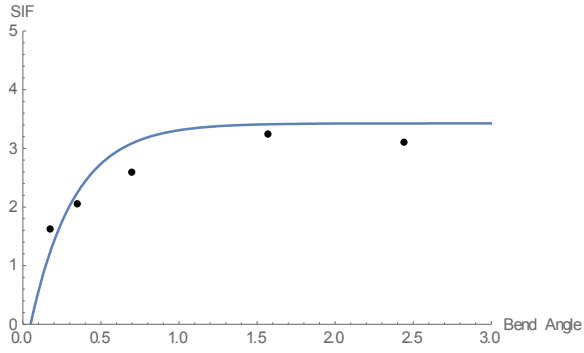


Figure 241. NPS 12 and R=3D

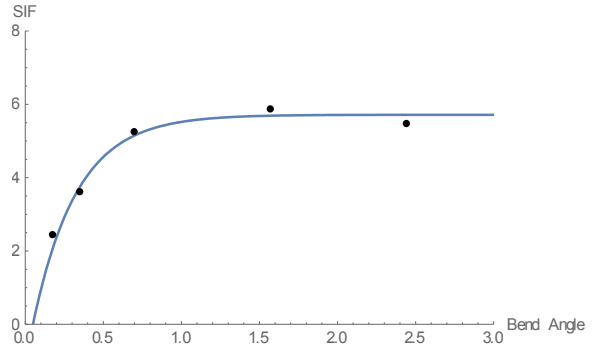


Figure 242. NPS 24 and R=3D

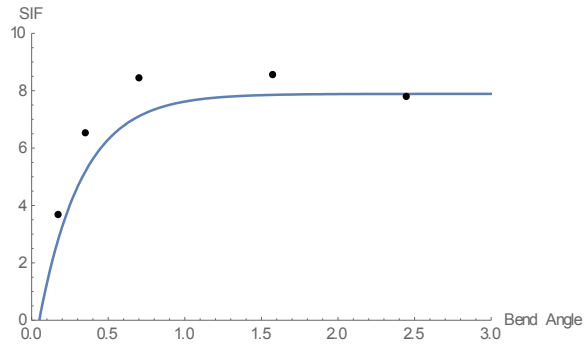


Figure 243. NPS 36 and R=3D

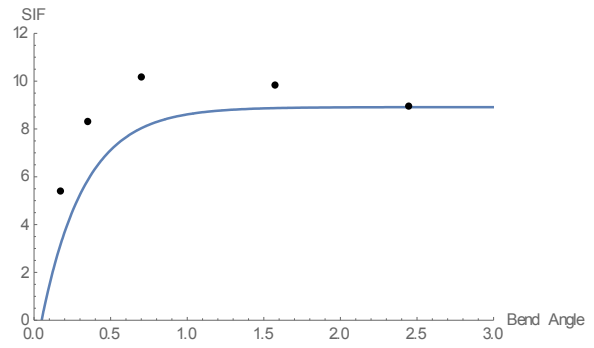


Figure 244. NPS 42 and R=3D

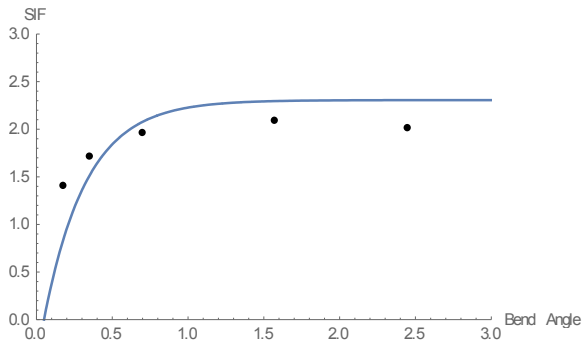


Figure 245. NPS 12 and R=5D

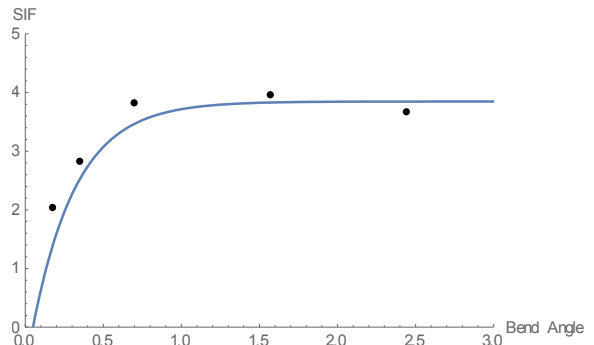


Figure 246. NPS 24 and R=5D

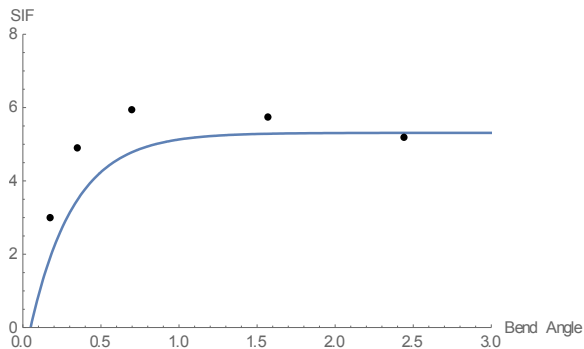


Figure 247. NPS 36 and R=5D

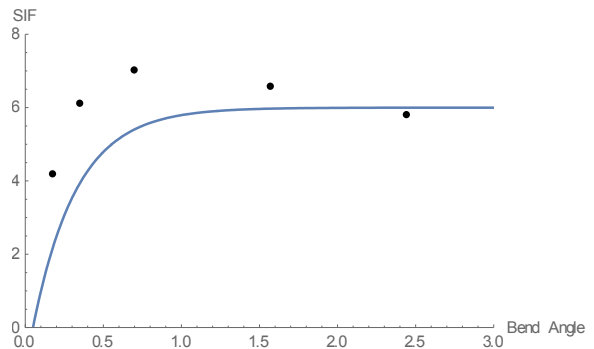


Figure 248. NPS 42 and R=5D

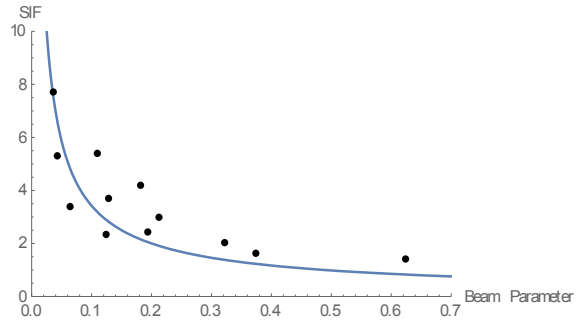


Figure 249. Bend angle 10°

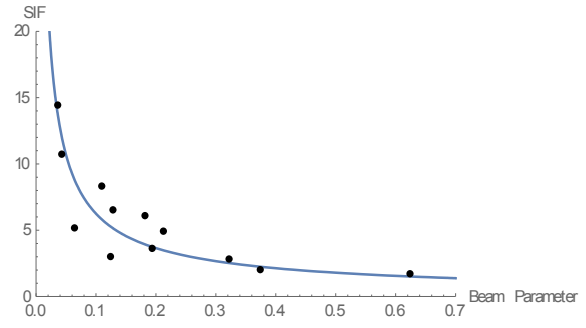


Figure 250. Bend angle 20°

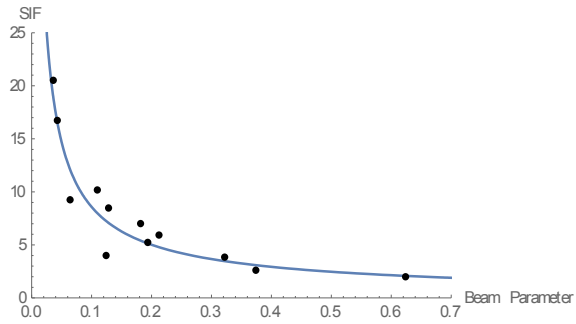


Figure 251. Bend angle 40°

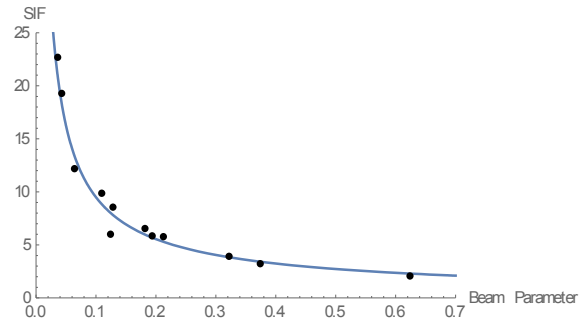


Figure 252. Bend angle 90°

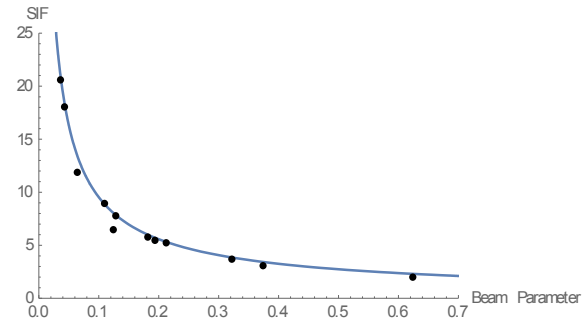


Figure 253. Bend angle 140°

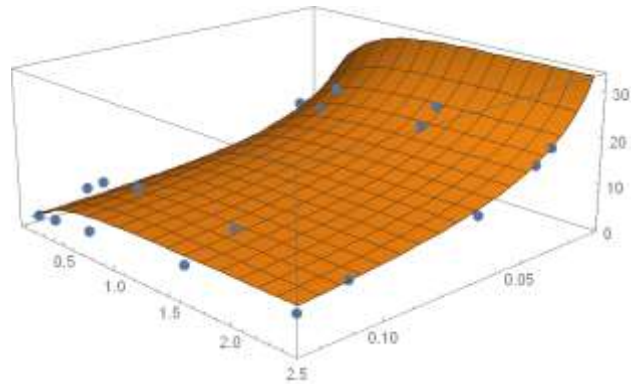


Figure 254. The proposed SIF formula surface

APPENDIX (C): DEVELOPED STRESS INTENSIFICATION FACTORS FOR BENDS UNDER INTERNAL PRESSURE AND BENDING MOMENT

1.3. Opening Bending Moment

1.3.1. Comparison between the FEA and SIF proposed models

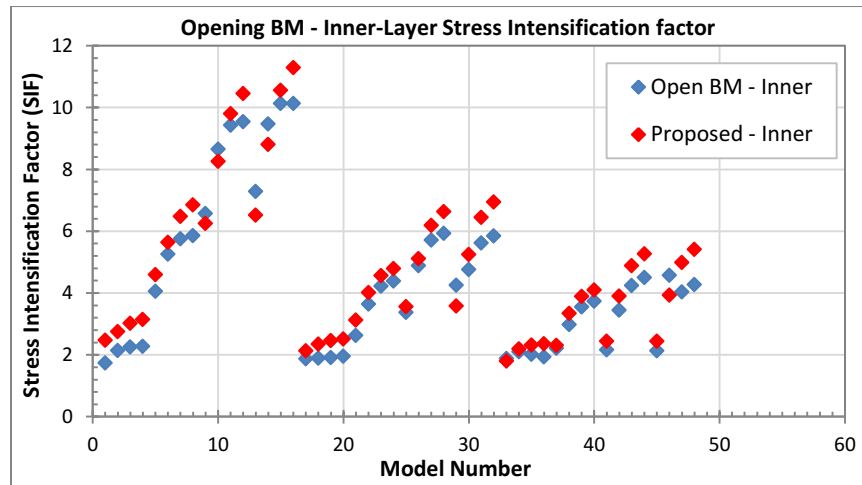


Figure 255. Proposed factor compared to FEA results for the inner layer of pipe bends

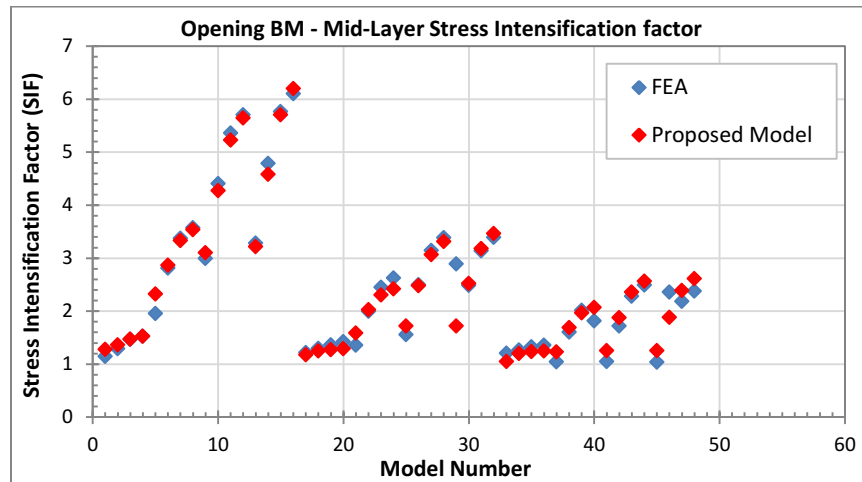


Figure 256. Proposed factor compared to FEA results for the Mid-layer of pipe bends

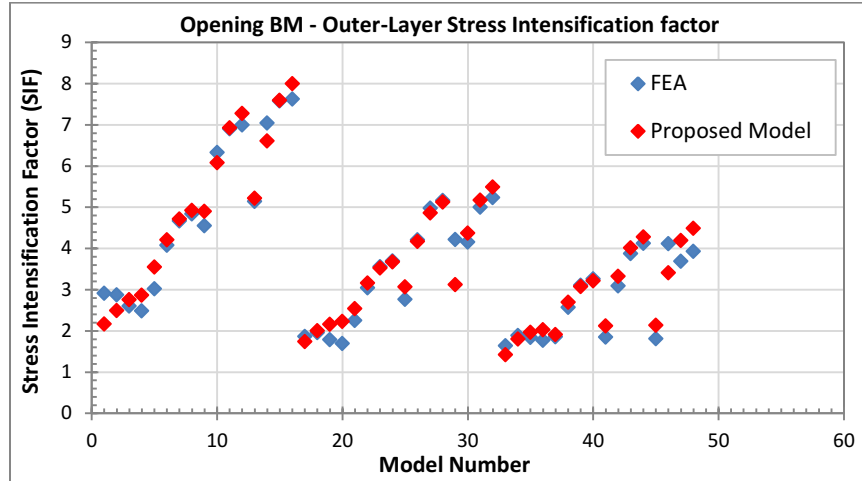


Figure 257. Proposed factor compared to FEA results for the outer layer of pipe bends

1.3.2. The FEA plotted against the proposed SIF formula for each set of models

1.3.2.1. Mid-layer results

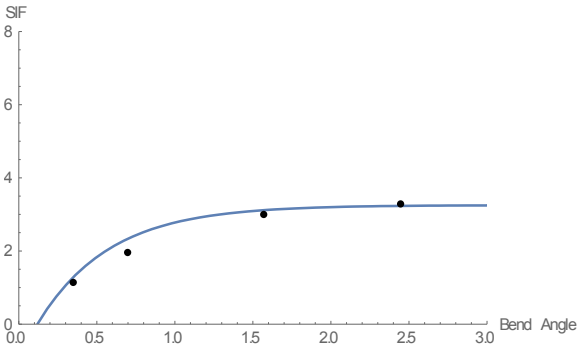


Figure 258. NPS 12 and R=1D

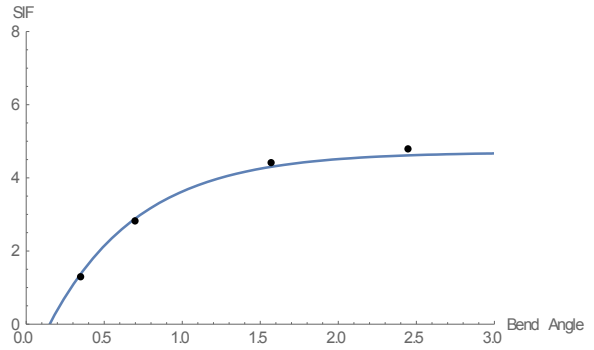


Figure 259. NPS 24 and R=1D

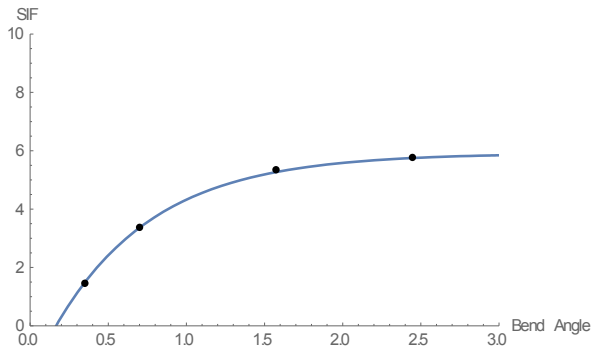


Figure 260. NPS 36 and R=1D

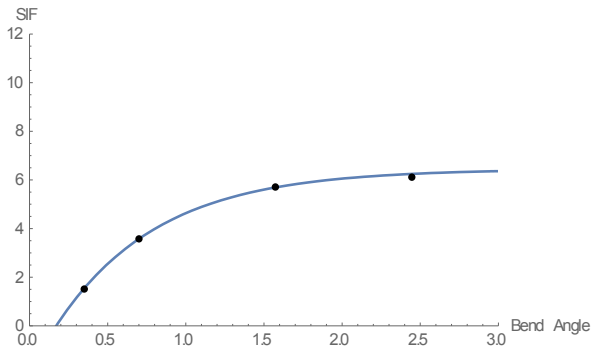


Figure 261. NPS 42 and R=1D

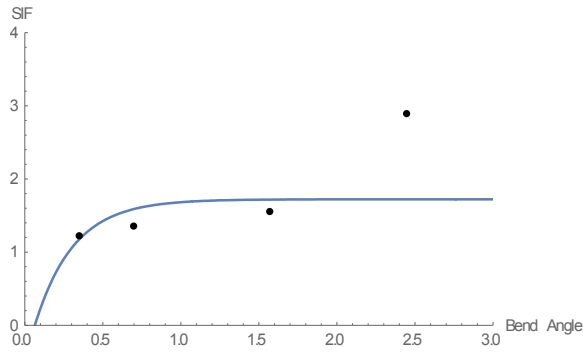


Figure 262. NPS 12 and R=3D

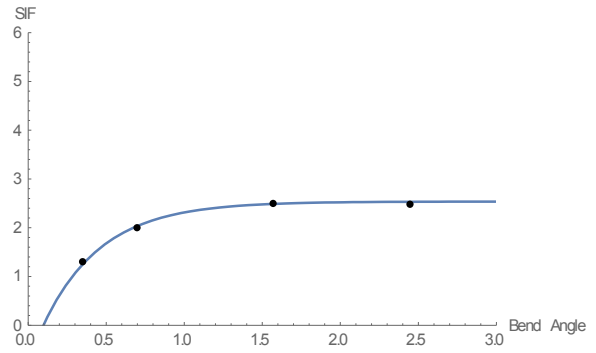


Figure 263. NPS 24 and R=3D

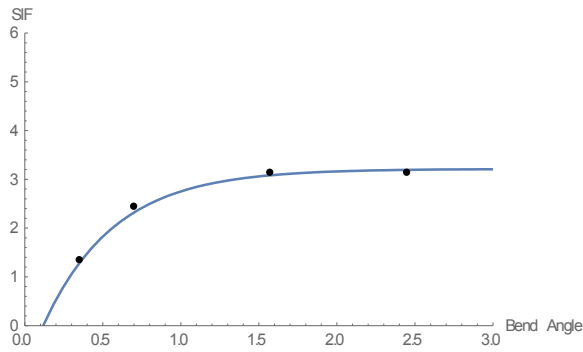


Figure 264. NPS 36 and R=3D

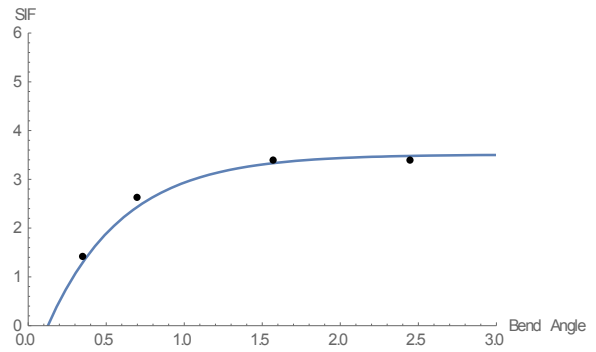


Figure 265. NPS 42 and R=3D

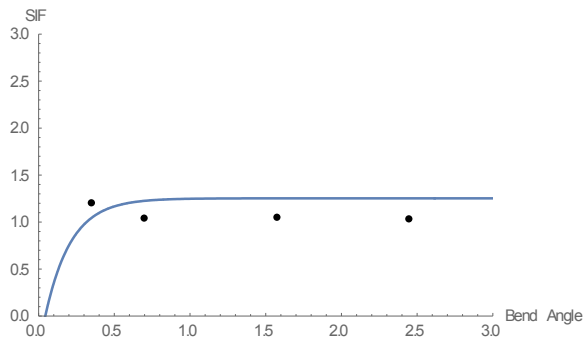


Figure 266. NPS 12 and R=5D

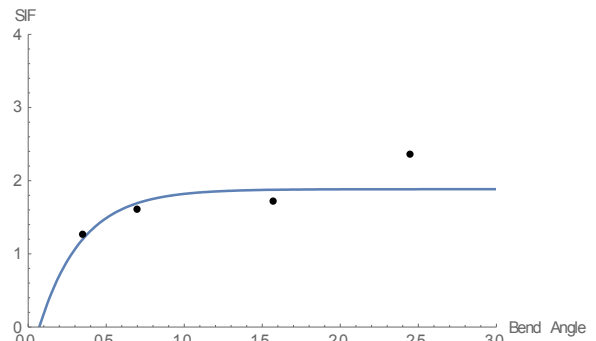


Figure 267. NPS 24 and R=5D

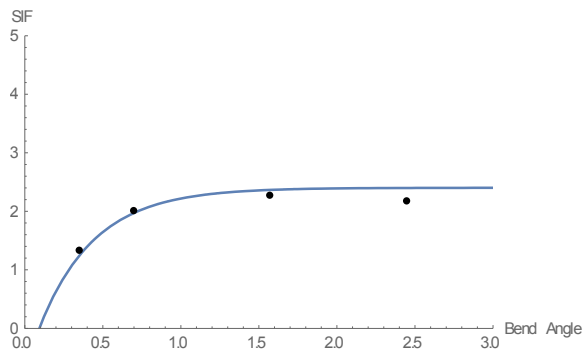


Figure 268. NPS 36 and R=5D

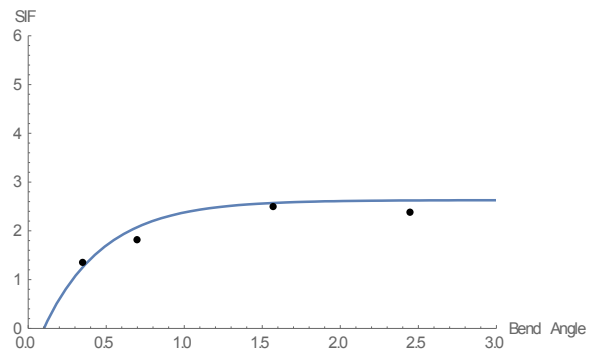


Figure 269. NPS 42 and R=5D

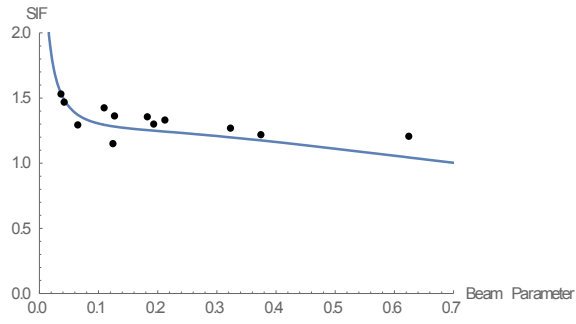


Figure 270. Bend angle 10°

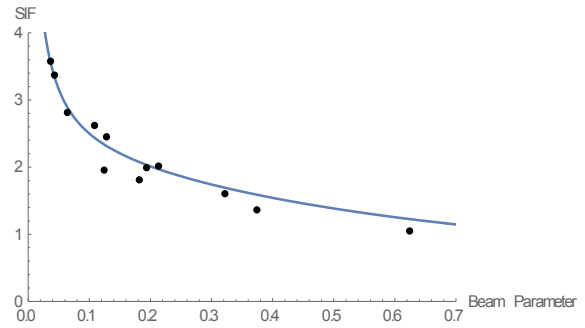


Figure 271. Bend angle 20°

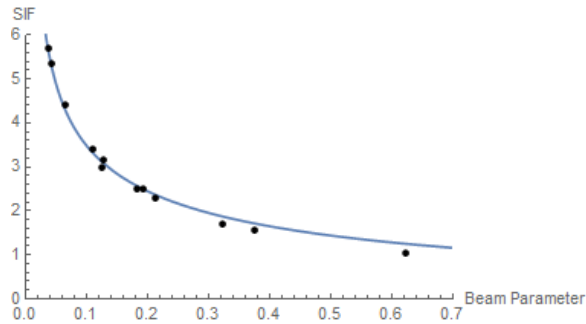


Figure 272. Bend angle 40°

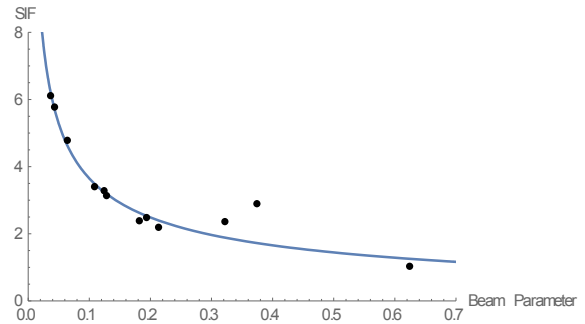


Figure 273. Bend angle 90°

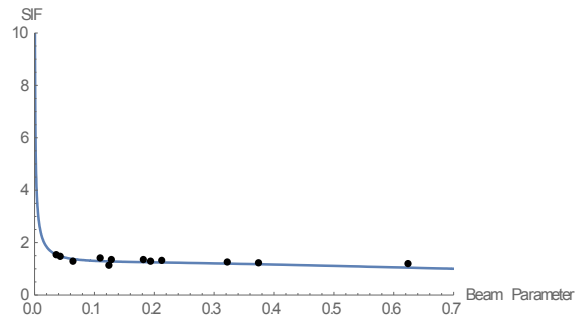


Figure 274. Bend angle 140°

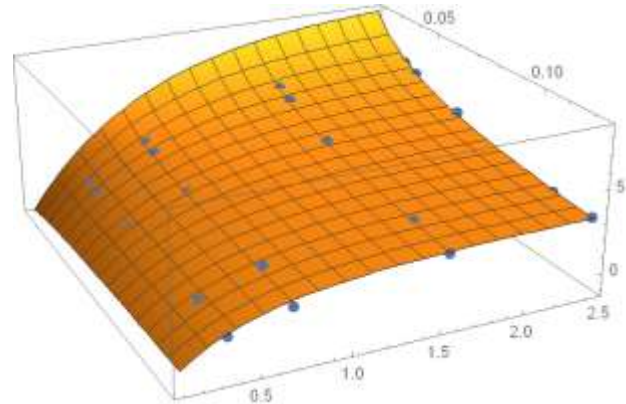


Figure 275. The proposed SIF formula surface

1.3.2.2. Inner layer results

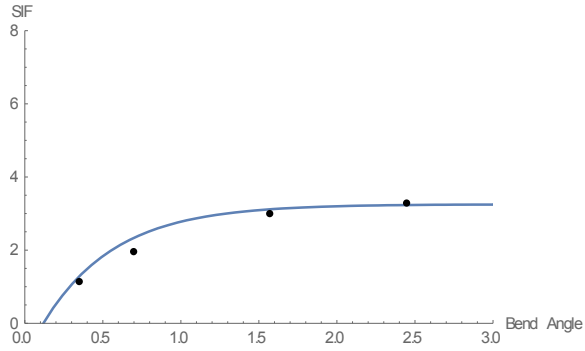


Figure 276. NPS 12 and R=1D

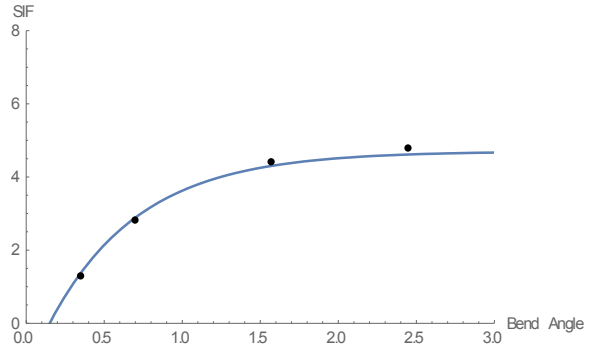


Figure 277. NPS 24 and R=1D

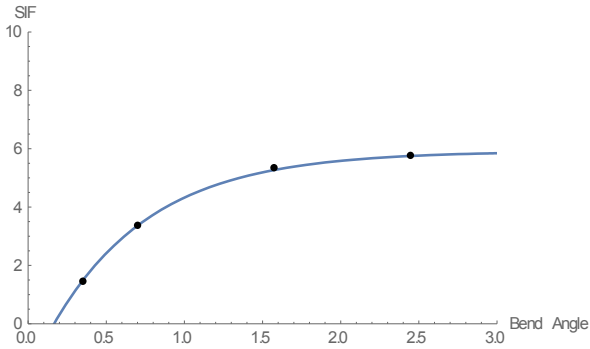


Figure 278. NPS 36 and R=1D

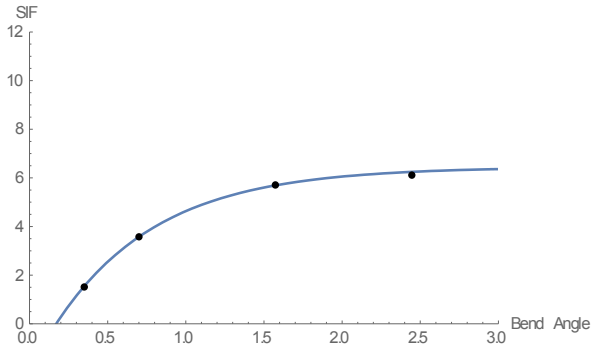


Figure 279. NPS 42 and R=1D

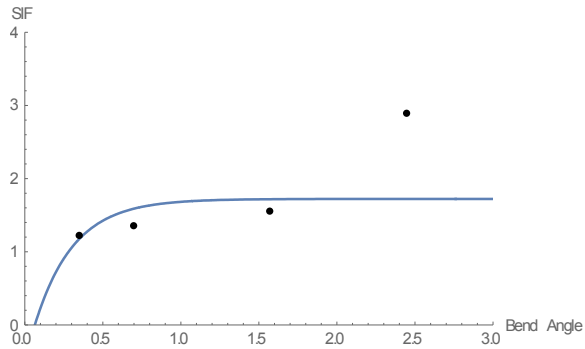


Figure 280. NPS 12 and R=3D

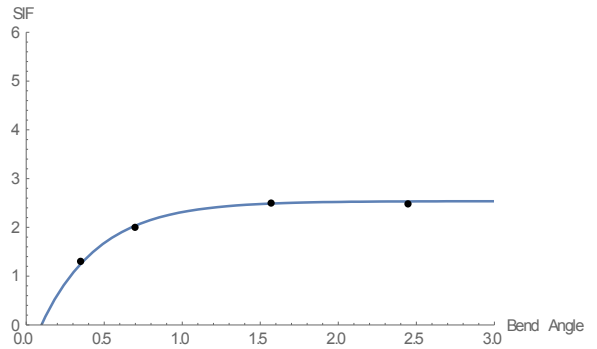


Figure 281. NPS 24 and R=3D

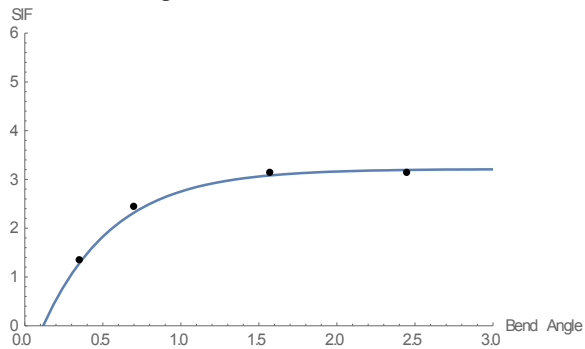


Figure 282. NPS 36 and R=3D

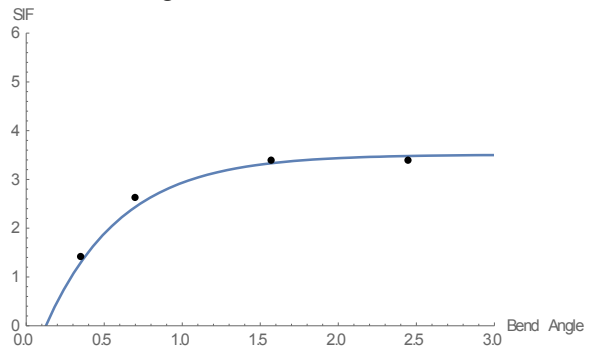


Figure 283. NPS 42 and R=3D

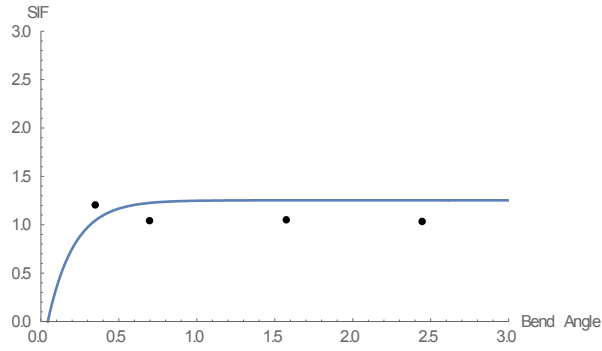


Figure 284. NPS 12 and R=5D

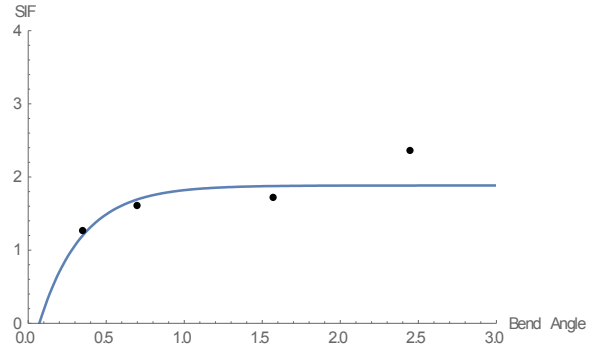


Figure 285. NPS 24 and R=5D

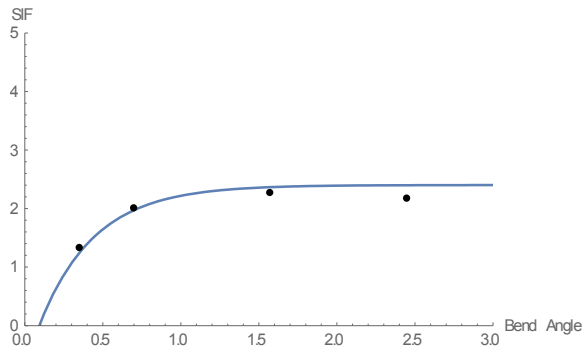


Figure 286. NPS 36 and R=5D

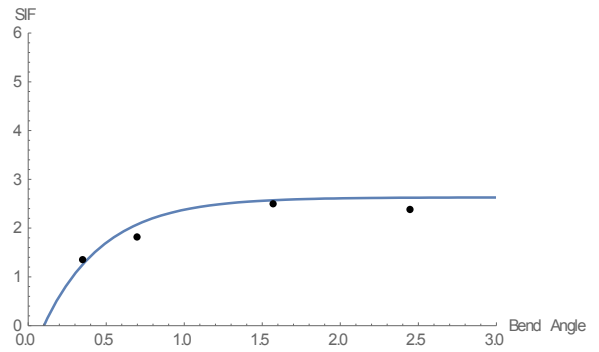


Figure 287. NPS 42 and R=5D

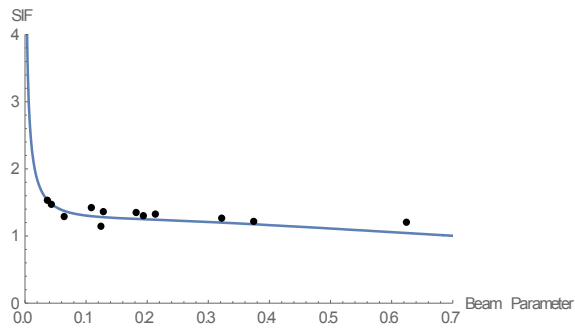


Figure 288. Bend angle 10°

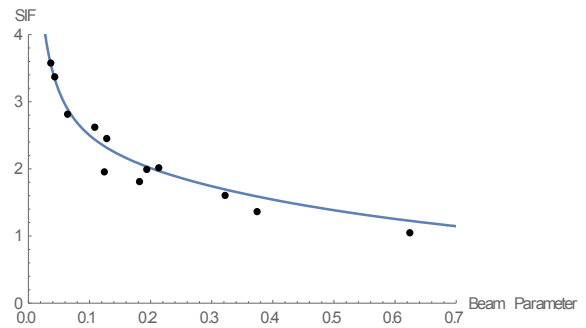


Figure 289. Bend angle 20°

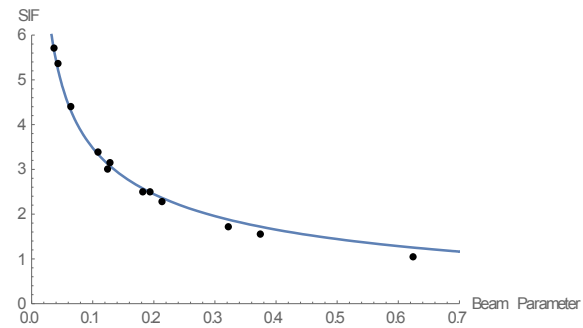


Figure 290. Bend angle 40°

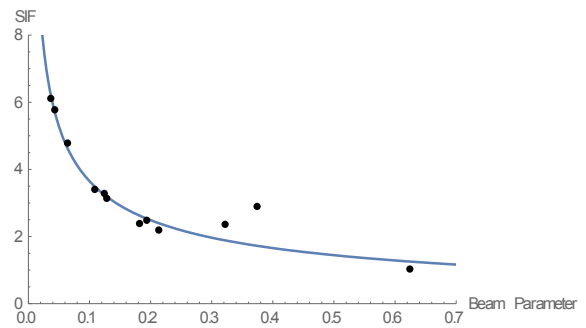


Figure 291. Bend angle 90°

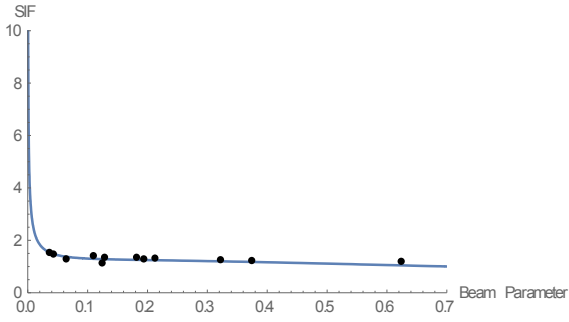


Figure 292. Bend angle 140°

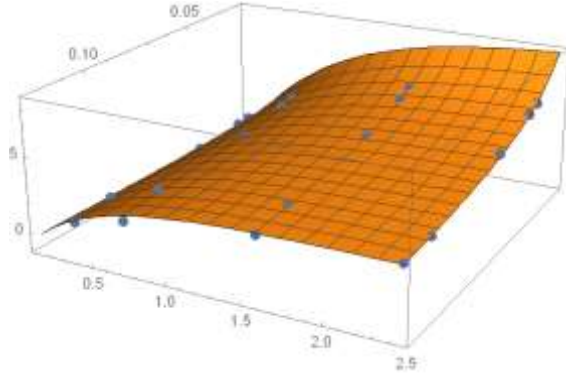


Figure 293. The proposed SIF formula surface

1.3.2.3. Outer layer results

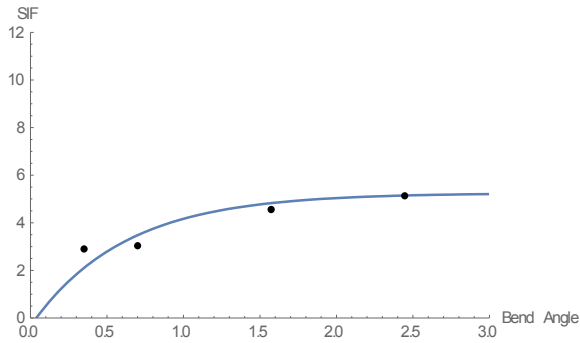


Figure 294. NPS 12 and R=1D

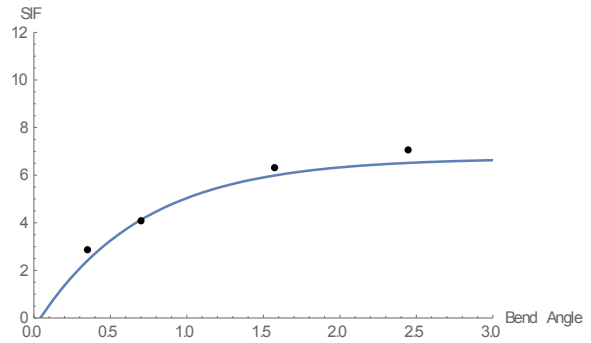


Figure 295. NPS 24 and R=1D

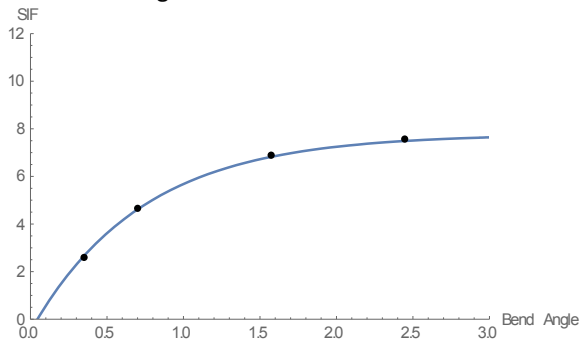


Figure 296. NPS 36 and R=1D

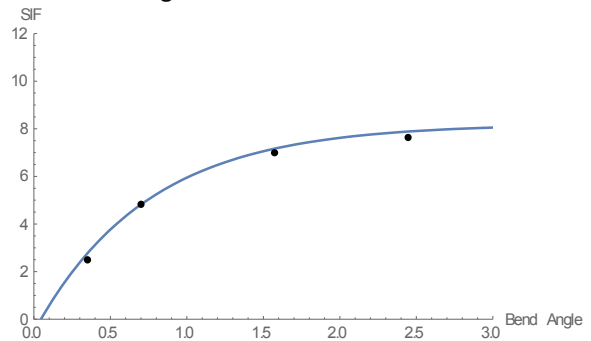


Figure 297. NPS 42 and R=1D

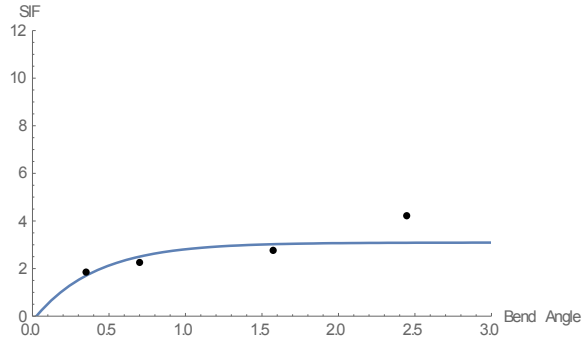


Figure 298. NPS 12 and R=3D

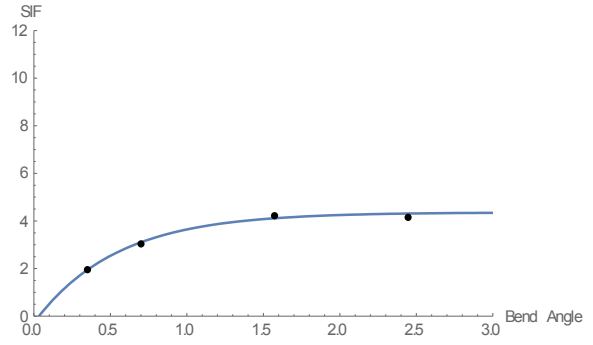


Figure 299. NPS 24 and R=3D

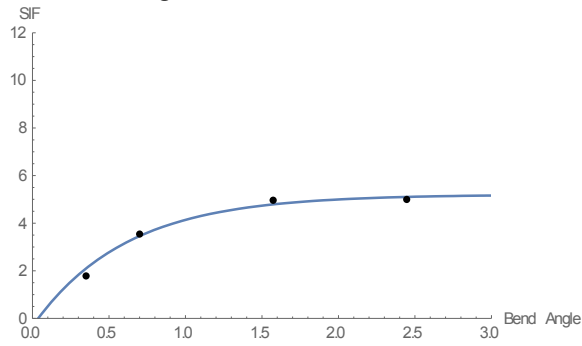


Figure 300. NPS 36 and R=3D

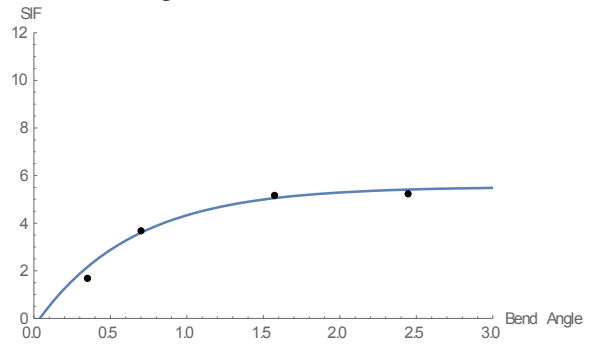


Figure 301. NPS 42 and R=3D

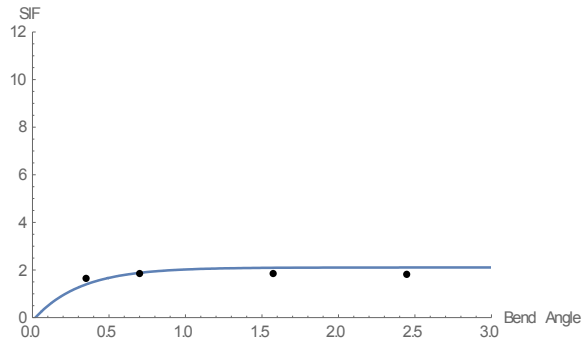


Figure 302. NPS 12 and R=5D

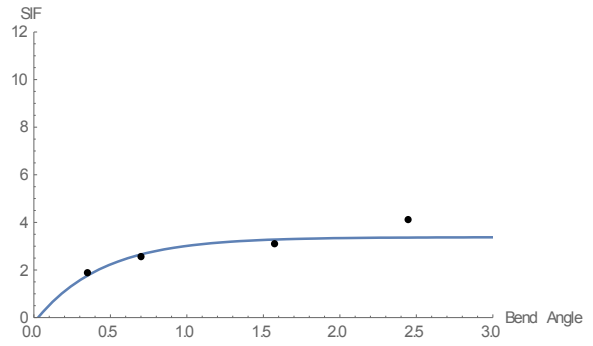


Figure 303. NPS 24 and R=5D

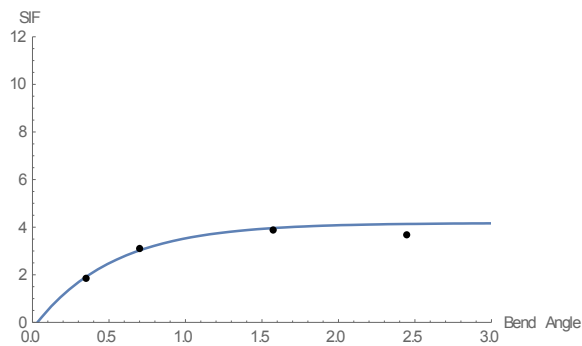


Figure 304. NPS 36 and R=5D

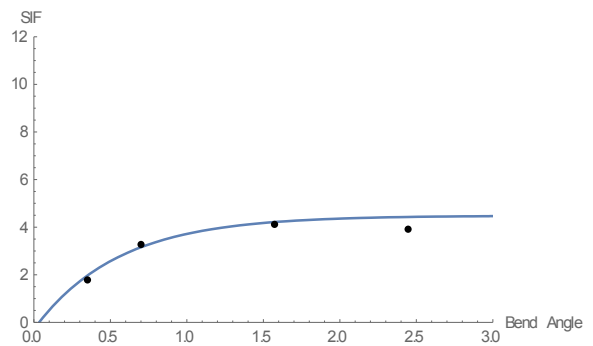


Figure 305. NPS 42 and R=5D

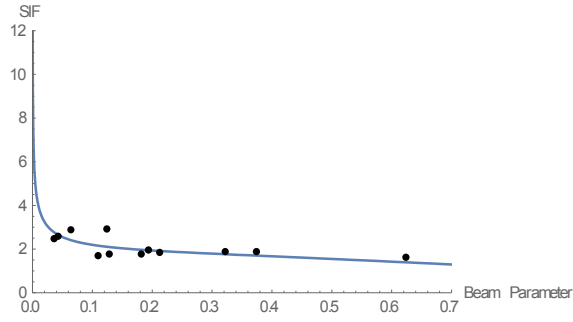


Figure 306. Bend angle 10°

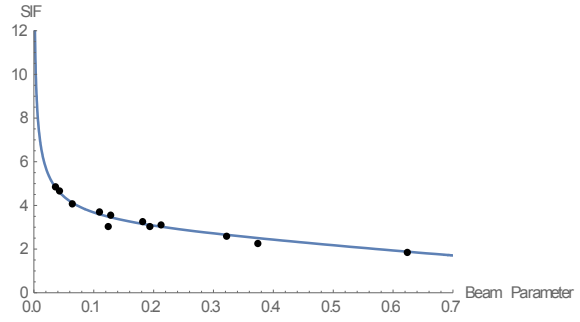


Figure 307. Bend angle 20°

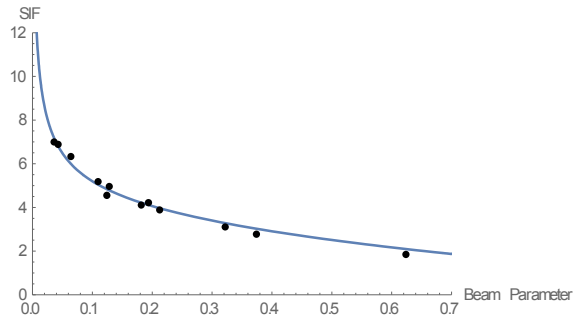


Figure 308. Bend angle 40°

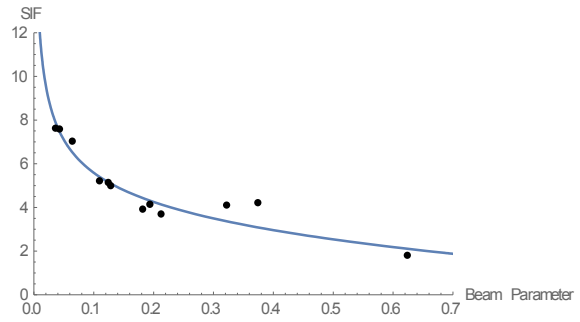


Figure 309. Bend angle 90°

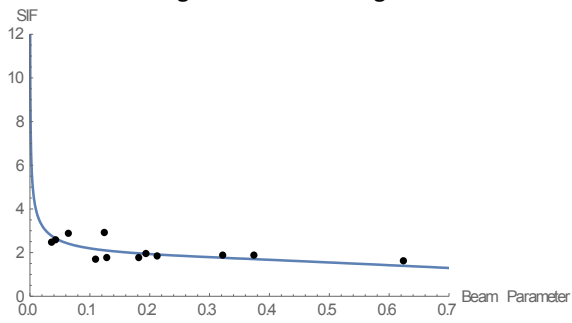


Figure 310. Bend angle 140°

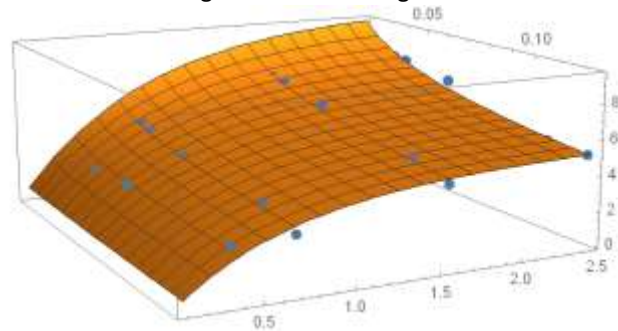


Figure 311. The proposed SIF formula surface

1.4. Closing Bending Moment

1.4.1. Comparison between the FEA and SIF proposed models

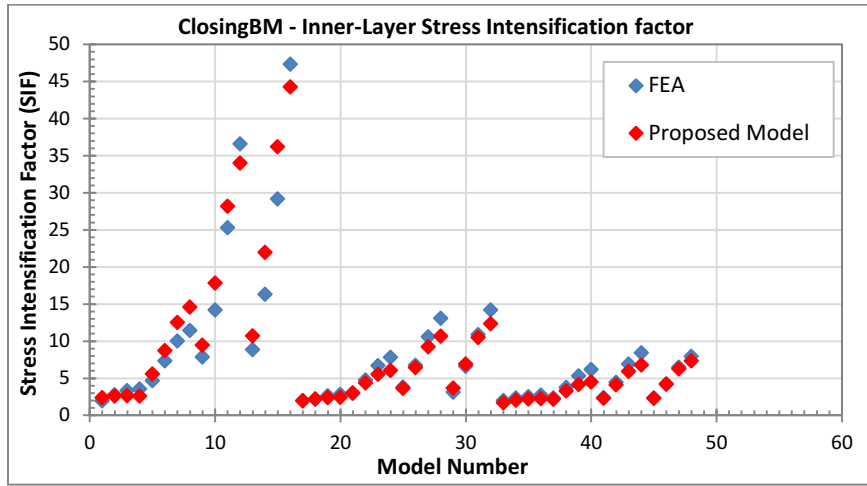


Figure 312. Proposed factor compared to FEA results for the inner layer of pipe bends

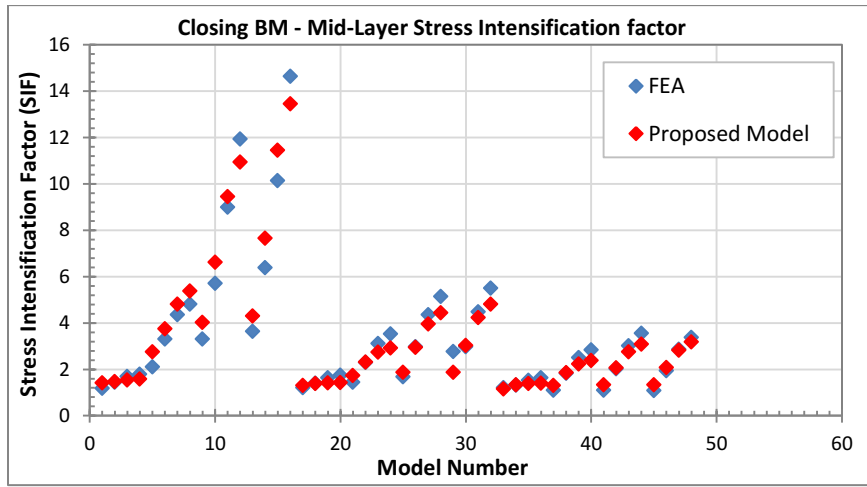


Figure 313. Proposed factor compared to FEA results for the inner layer of pipe bends

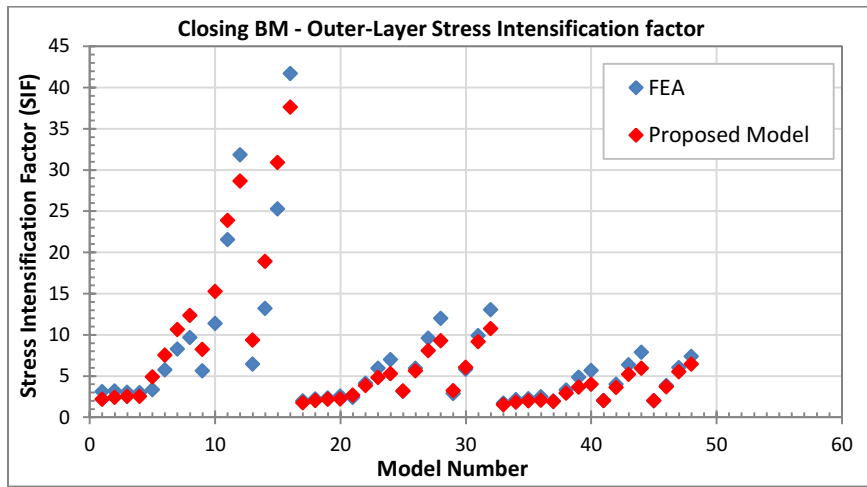


Figure 314. Proposed factor compared to FEA results for the inner layer of pipe bends

1.4.2. The FEA plotted against the proposed SIF formula for each set of models

1.4.2.1. Mid-layer results

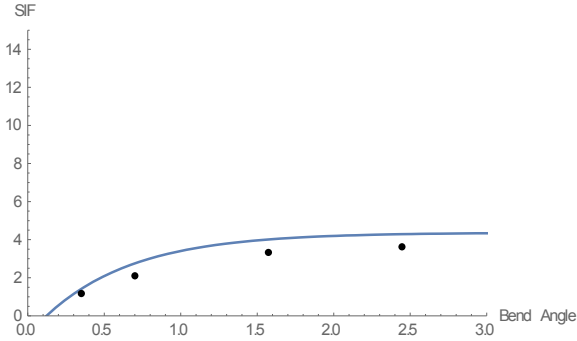


Figure 315. NPS 12 and R=1D

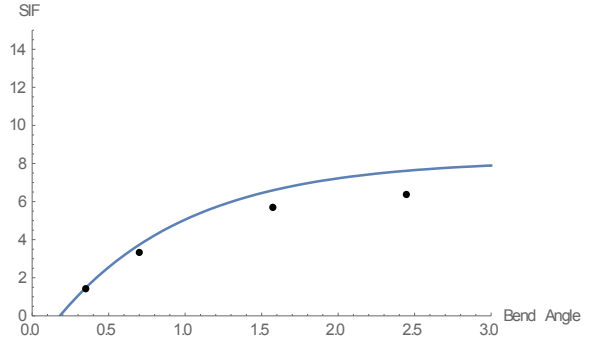


Figure 316. NPS 24 and R=1D

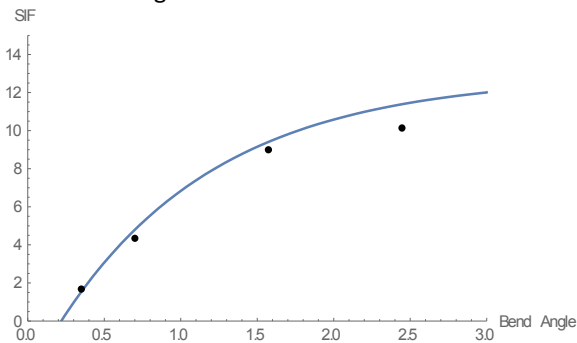


Figure 317. NPS 36 and R=1D

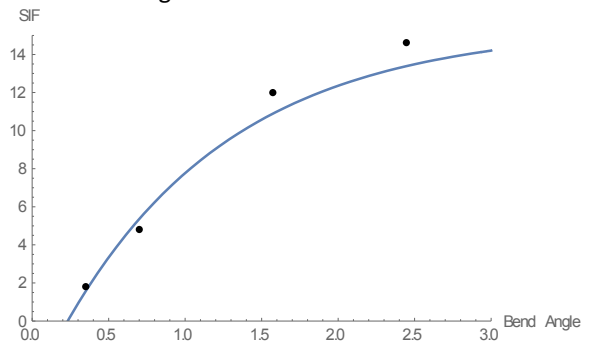


Figure 318. NPS 42 and R=1D

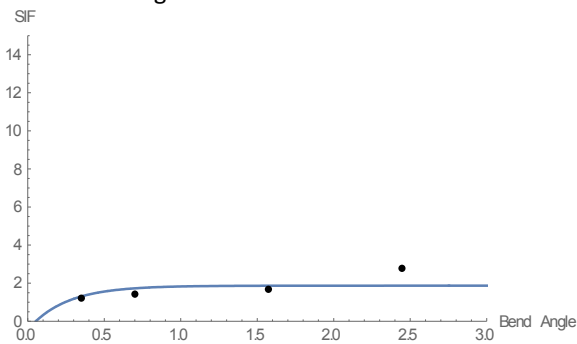


Figure 319. NPS 12 and R=3D

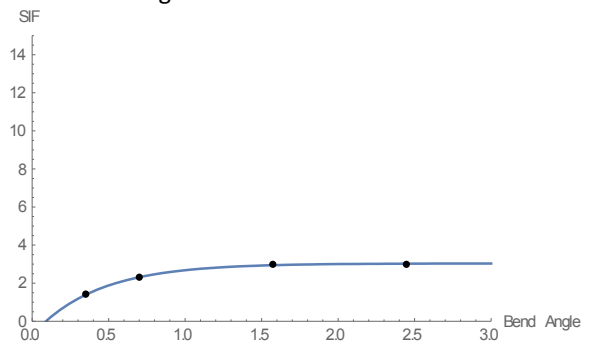


Figure 320. NPS 24 and R=3D

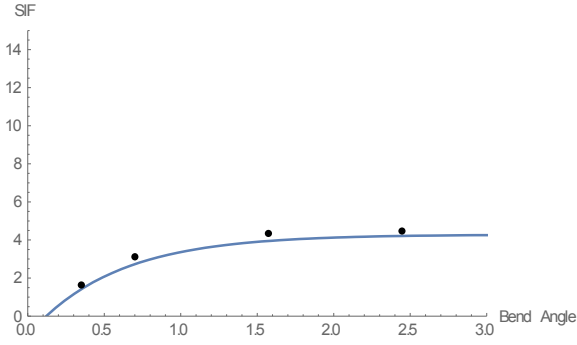


Figure 321. NPS 36 and R=3D

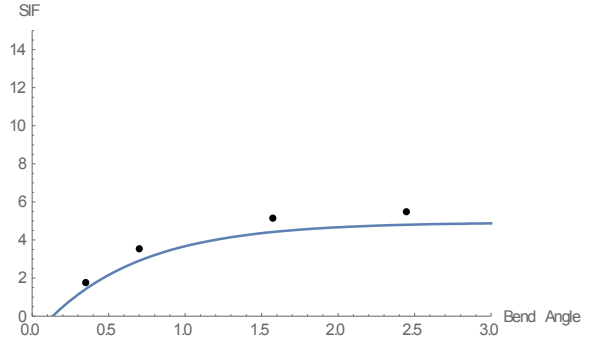


Figure 322. NPS 42 and R=3D

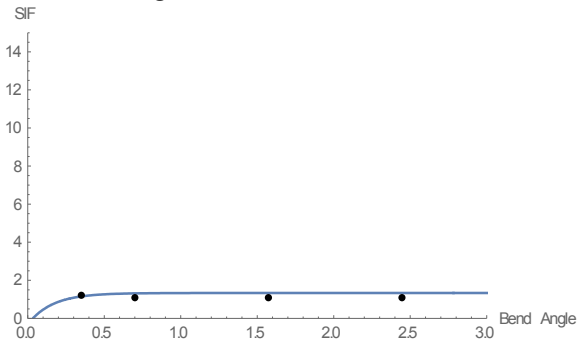


Figure 323. NPS 12 and R=5D

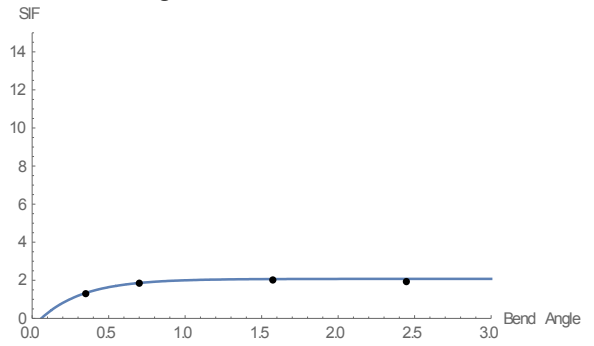


Figure 324. NPS 24 and R=5D

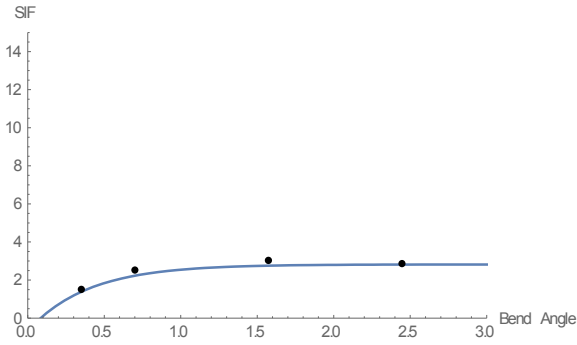


Figure 325. NPS 36 and R=5D

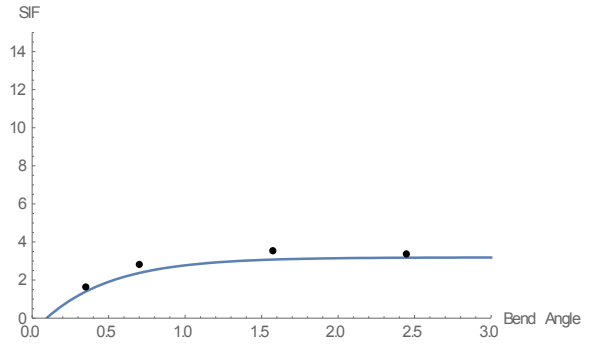


Figure 326. NPS 42 and R=5D

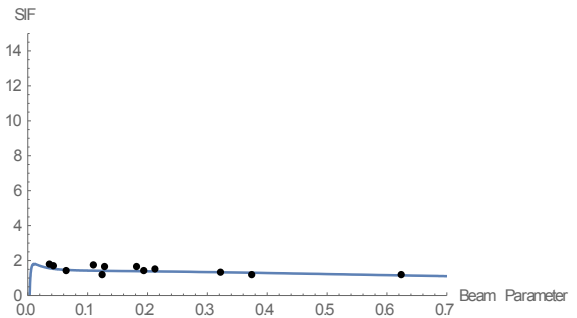


Figure 327. Bend angle 10°

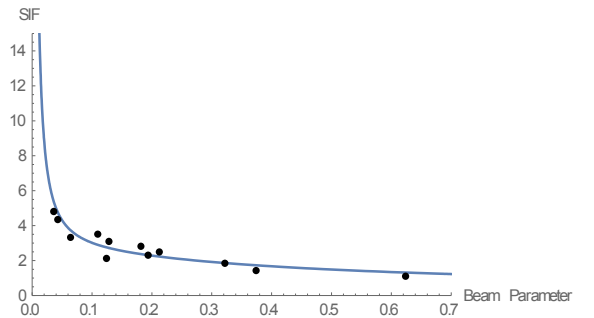


Figure 328. Bend angle 20°

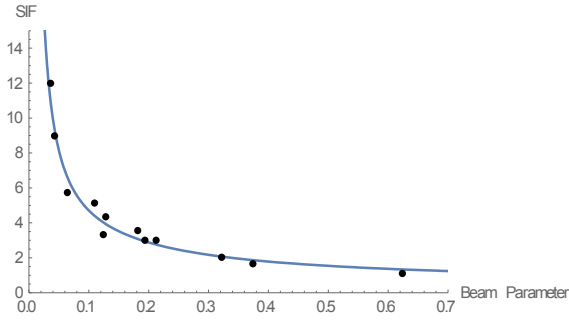


Figure 329. Bend angle 40°

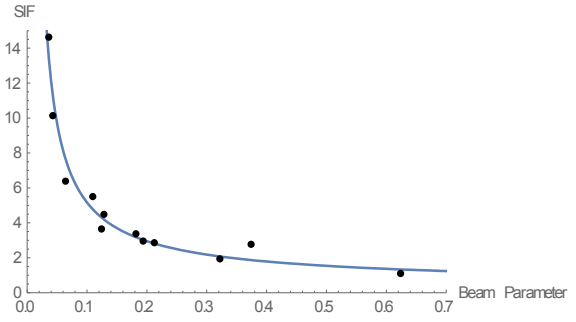


Figure 330. Bend angle 90°

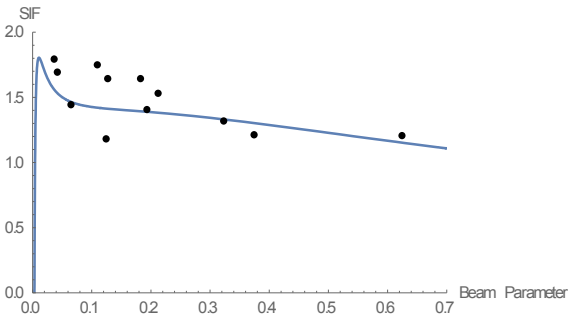


Figure 331. Bend angle 140°

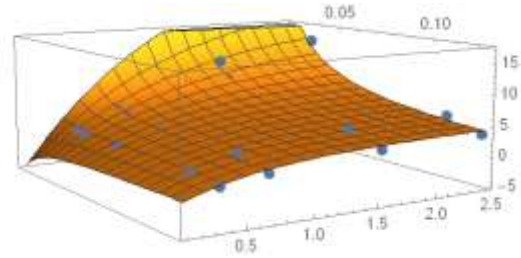


Figure 332. The proposed SIF formula surface

1.4.2.2. Inner layer results

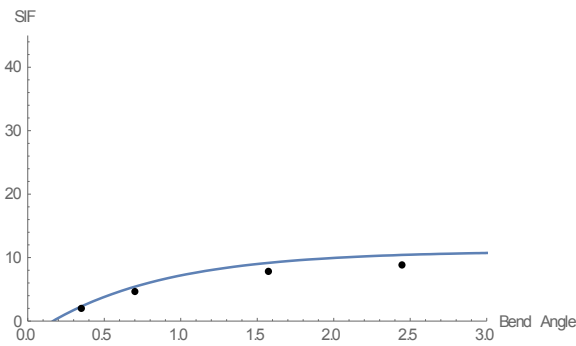


Figure 333. NPS 12 and R=1D

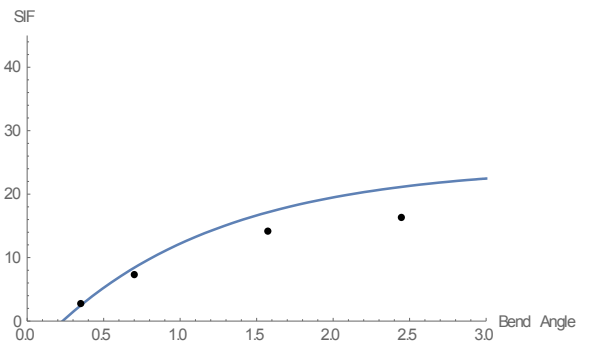


Figure 334. NPS 24 and R=1D

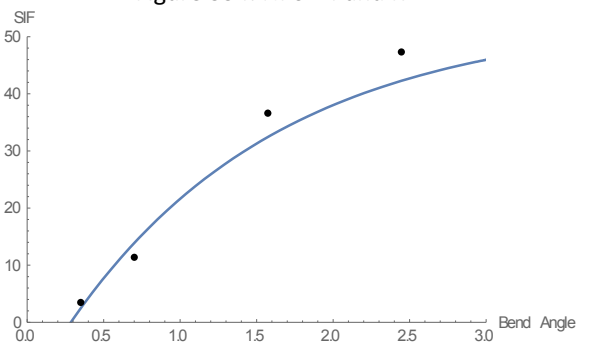
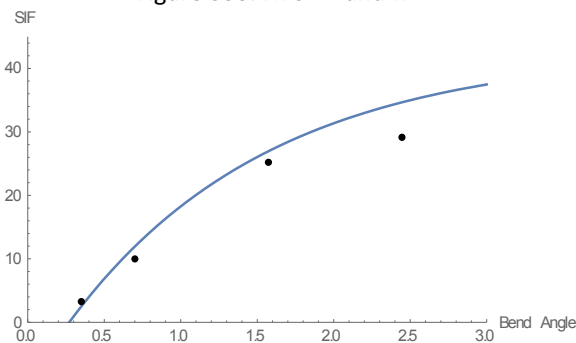


Figure 335. NPS 36 and R=1D

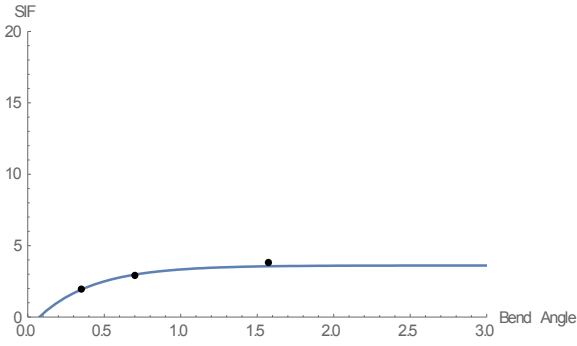


Figure 336. NPS 42 and R=1D

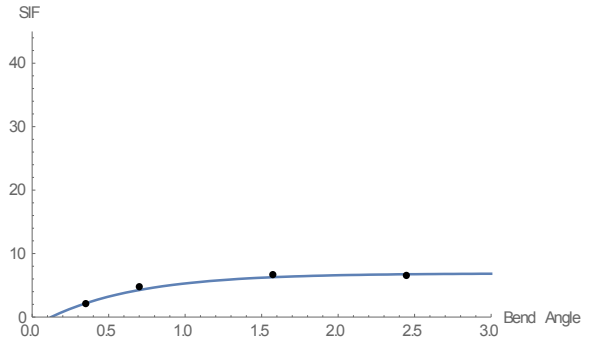


Figure 337. NPS 12 and R=3D

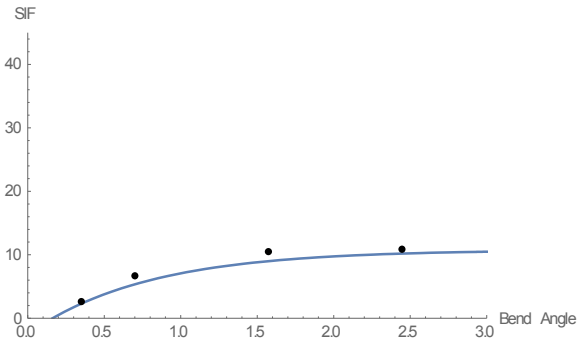


Figure 338. NPS 24 and R=3D

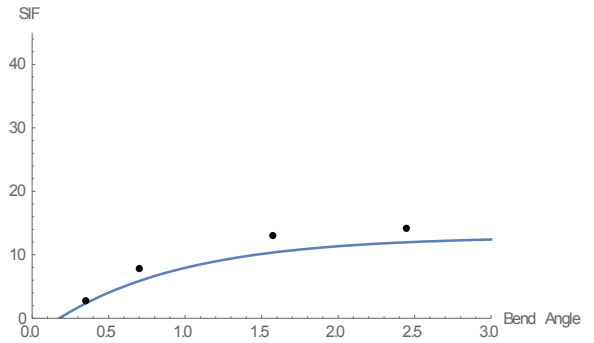


Figure 339. NPS 36 and R=3D

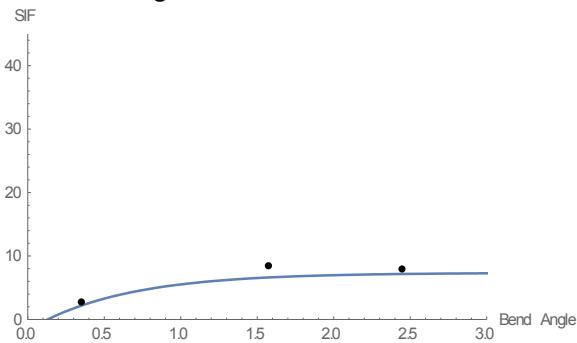


Figure 340. NPS 42 and R=3D

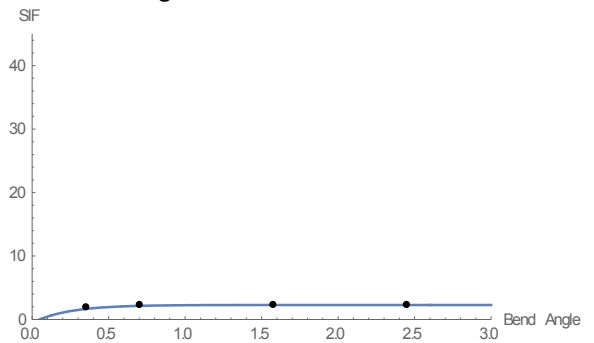


Figure 341. NPS 12 and R=5D

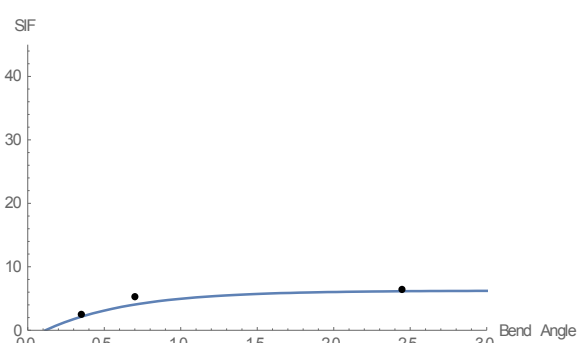


Figure 342. NPS 24 and R=5D

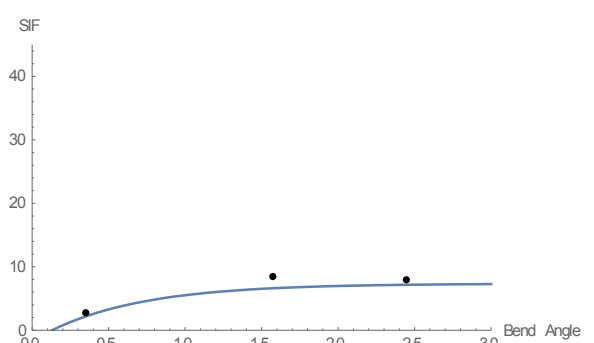


Figure 343. NPS 36 and R=5D



Figure 344. NPS 42 and R=5D



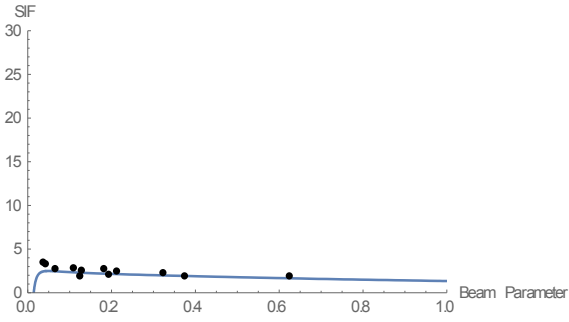


Figure 345. Bend angle 10°

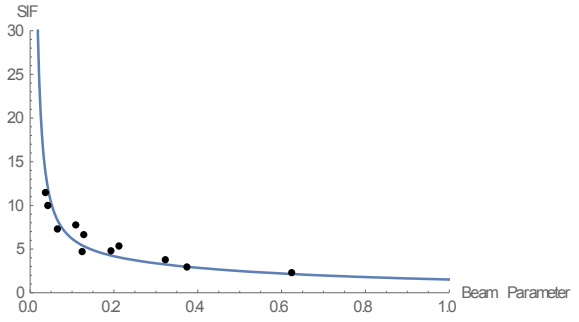


Figure 346. Bend angle 20°

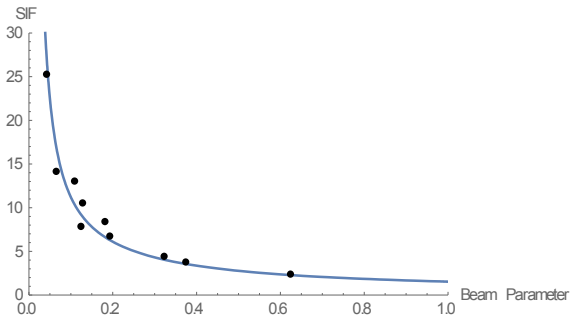


Figure 347. Bend angle 40°

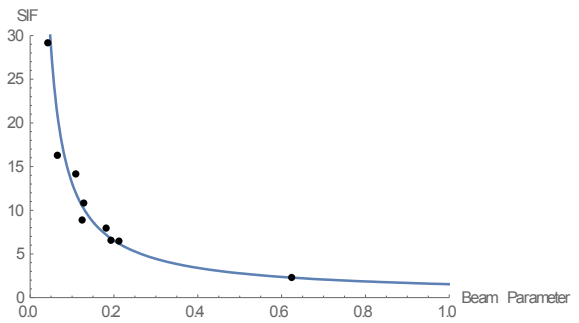


Figure 348. Bend angle 90°

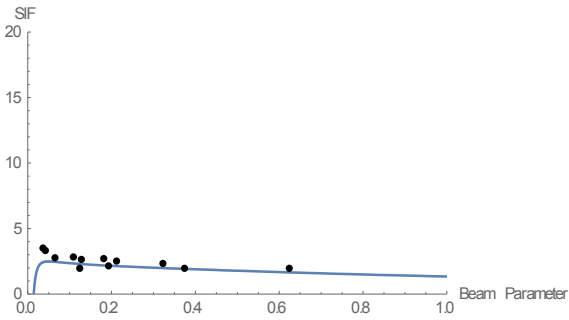


Figure 349. Bend angle 140°

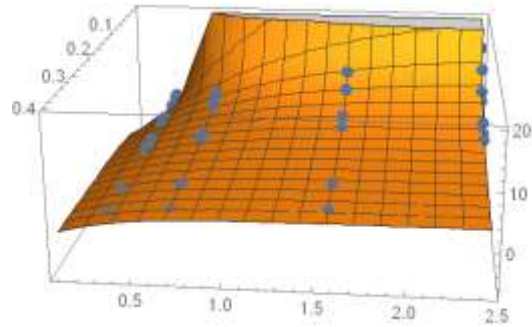


Figure 350. The proposed SIF formula surface

1.4.2.3. Outer layer results

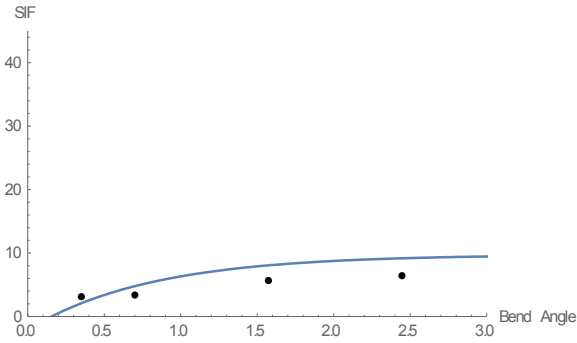


Figure 351. NPS 12 and R=1D

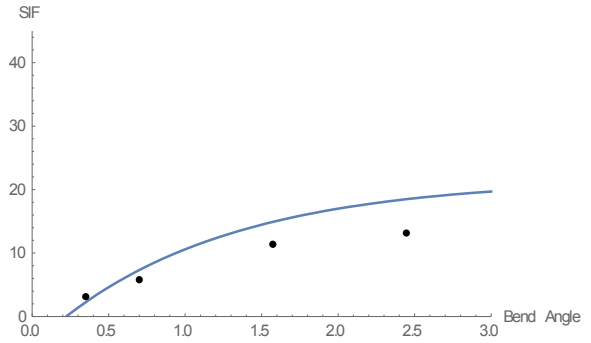


Figure 352. NPS 24 and R=1D

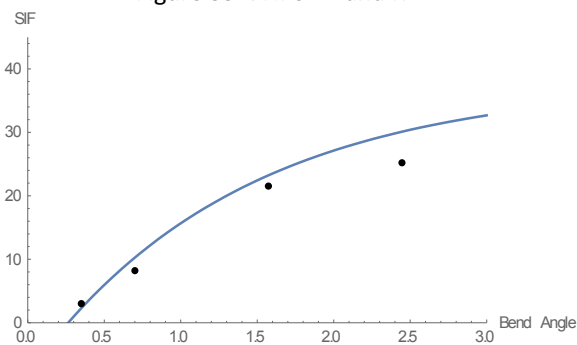


Figure 353. NPS 36 and R=1D

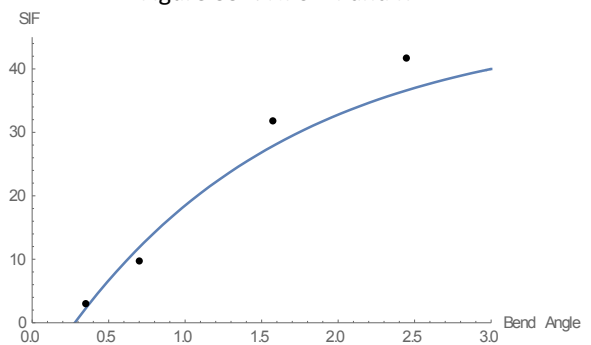


Figure 354. NPS 42 and R=1D

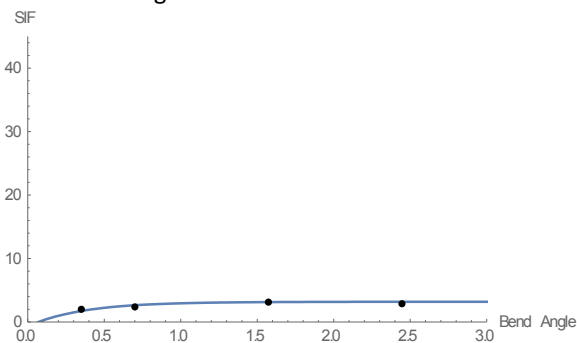


Figure 355. NPS 12 and R=3D

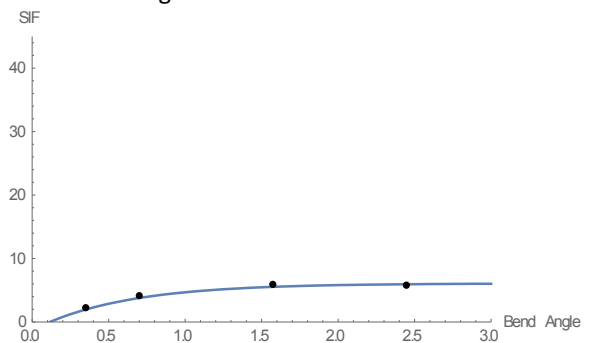


Figure 356. NPS 24 and R=3D

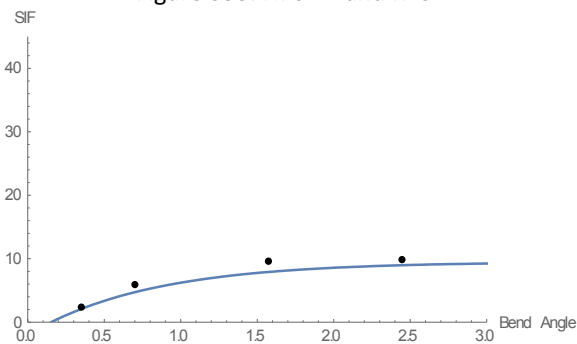


Figure 357. NPS 36 and R=3D

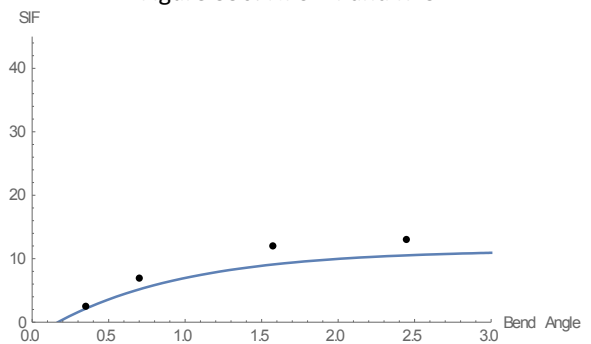


Figure 358. NPS 42 and R=3D

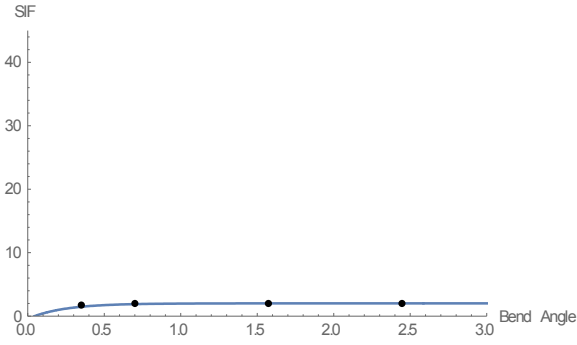


Figure 359. NPS 12 and R=5D

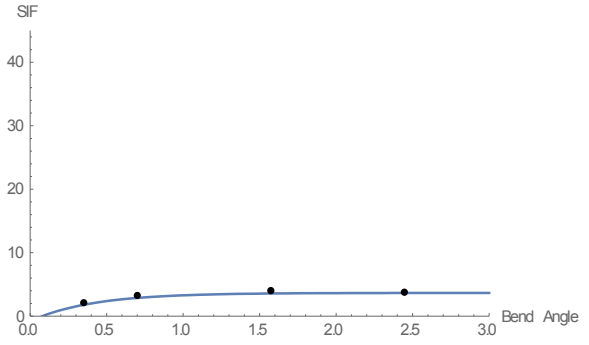


Figure 360. NPS 24 and R=5D

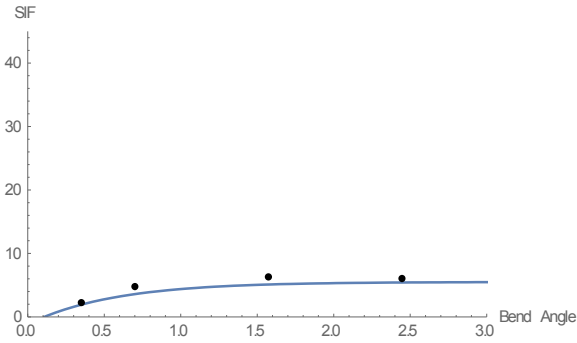


Figure 361. NPS 36 and R=5D

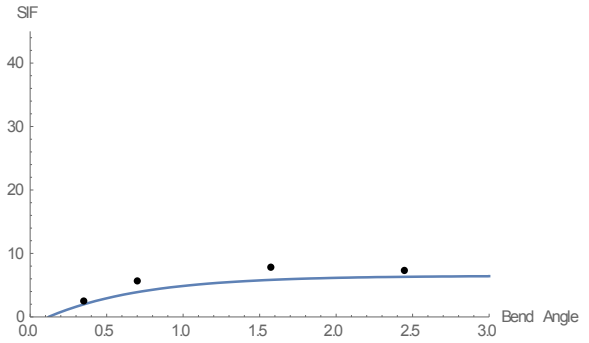


Figure 362. NPS 42 and R=5D

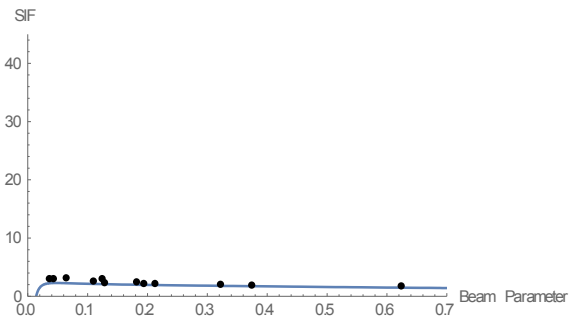


Figure 363. Bend angle 10°

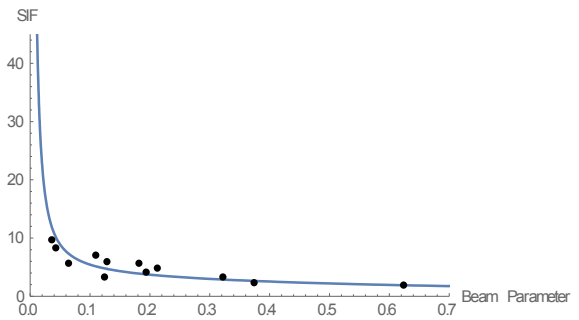


Figure 364. Bend angle 20°

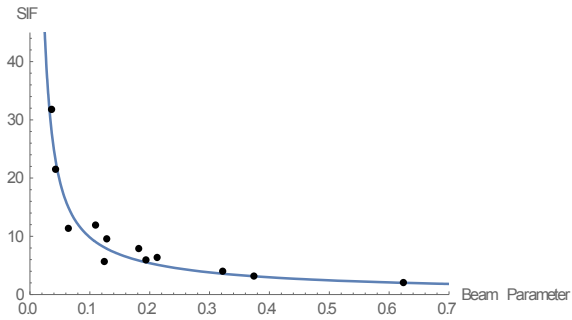


Figure 365. Bend angle 40°

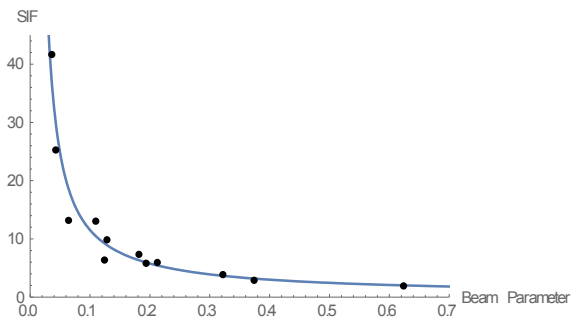


Figure 366. Bend angle 90°

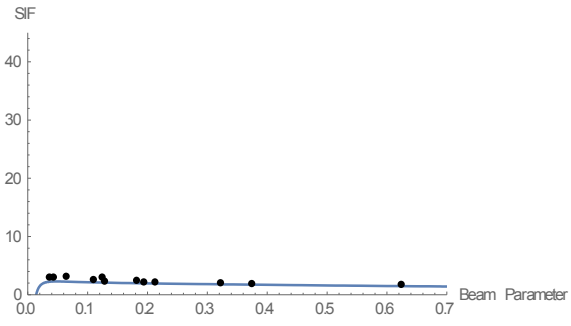


Figure 367. Bend angle 140°

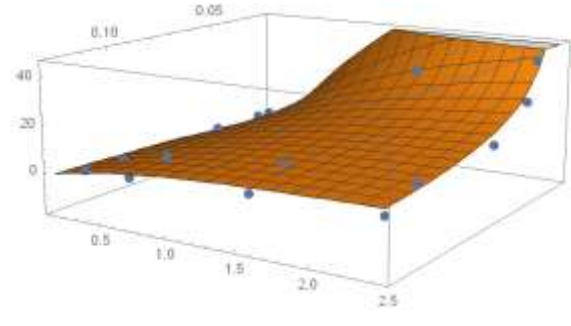


Figure 368. The proposed SIF formula surface